Physics of the Solid State, Vol. 47, No. 3, 2005, pp. 397–404. Translated from Fizika Tverdogo Tela, Vol. 47, No. 3, 2005, pp. 387–394.

METALS AND SUPERCONDUCTORS

Specific Features of the Hydrogen-Induced Discrete (Jumplike) Structural Evolution in Pd–Ta–H and Pd–Mo–H Alloys

V. M. Avdyukhina, A. A. Anishchenko, A. A. Katsnel'son, and G. P. Revkevich

Moscow State University, Leninskie gory, Moscow, 119992 Russia

e-mail: albert@solst.phys.msu.ru

Received May 11, 2004

Abstract—The nonmonotonic structural evolution observed in Pd–Ta–H and Pd–Mo–H hydrogenated alloys is shown to be discrete (jumplike) in character, which is due to the thermodynamic potential having a multivalley fractal structure in reciprocal space. This structure arises in the initial state and is fairly stable. Transformations occur as a result of hopping of the system between the long-lived states corresponding to local minima of the thermodynamic potential at both stages of rapid degassing and of stochastic oscillations of the centroids of diffraction maxima. The jumps are associated with the migration of hydrogen atoms and vacancies between the matrix and defect complexes and are accompanied by an increase or a decrease in the diffraction angles. © *2005 Pleiades Publishing, Inc.*

1. INTRODUCTION

As shown in [1–4] and earlier studies, the kinetics of structural transformations in palladium alloys after hydrogenation is nonmonotonic. Long-term oscillatory variations in the diffraction characteristics of a defect structure have been found to occur in Pd–W–H alloys, and the multiphase decomposition and stochastic changes in the number and volume fractions of coexisting phases have been observed in Pd–Ta and Mo–Pd alloys during long-term relaxation after hydrogenation of deformed surface layers [2, 4]. These phenomena are associated with the nonequilibrium state produced by hydrogenation; therefore, the appearance of complicated structures that change irregularly in time correlates well with the well-known principle that, in systems far from equilibrium, there appear various structures, which Prigogine [5] named dissipative. In [6–8], synergetic models were proposed for some of the phenomena reported in [1–4]. These models assume that the transition from the initial to the final structure generally occurs via intermediate structures; the most typical case is the appearance of one-dimensional long-period structures, which has been observed to occur during diffusionless transformations and the formation of certain superstructures, Laves phases, etc. [9–13]. The thermodynamic conditions for such structures to appear are the occurrence of volume and thermal effects, the smallness of the energy of formation of inhomogeneities [9], the significant effect of long-range fields [10, 14], and a high degree of saturation with dopant elements in the single-phase region [9].

It is significant that one-dimensional long-period structures correspond to a nonequilibrium state; therefore, standard thermodynamic methods are inapplicable to them. It is also important that the thermodynamic potential $\Phi(k)$ in the cases under study possesses a multivalley structure in reciprocal space and, hence, has a variety of local minima k_a (a = 1, 2, …), as shown in Fig. 1 [12]. The deepest minima correspond to rational numbers m/n with small m and n. Obviously, there are many minima with higher values of m and n between the deepest minima; the structure of the thermodynamic potential is fractal in character. For example, in the case where a sudden transformation from a closely packed hexagonal structure to a face-centered cubic structure takes place, correlated shifts of individual closely packed layers in minimal clusters occur first, which corresponds to filling of the shallowest minima in the $\Phi(k)$ dependence. Then, due to correlation, the minimal clusters coalesce, which corresponds to filling of deeper minima, and so on. Thus, in the course of a sequence of structural transformations associated with the formation of one-dimensional long-period structures, step-by-step coalescence of clusters occurs. Since the energy of formation of a one-dimensional long-period structure is small, it is energetically favorable for clusters with this structure to grow step by step

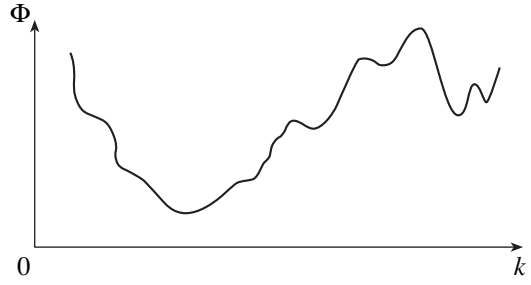

Fig. 1. Thermodynamic potential as a function of k for a multivalley system (schematic).

1063-7834/05/4703-0397$26.00 © 2005 Pleiades Publishing, Inc.

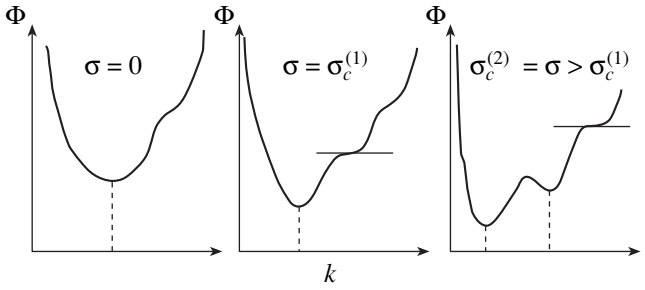

Fig. 2. Formation of a multivalley structure under an increasing load above a critical level (schematic).

through their correlation rather than through the motion of their boundaries, as in first-order phase transformations. The thermodynamic-potential multivalley structure can also arise as a result of the application of a load to a system [12], at least if a load causes the formation of defects in the system, as shown in Fig. 2 [12].

The synergetic models proposed in [6–8] assume that the multiphase decomposition of Pd–Ta and Pd–Mo alloys observed in [2–4] is essentially associated with the multivalley fractal structure of the thermodynamic potential in reciprocal space. The existence of a multivalley structure also explains the new phenomenon reported in [4, 15–17], namely, the observation of a discrete distribution of the positions of the diffraction peak components in 2θ space (which indicate the formation of a multiphase system and its transformation) after hydrogenation of an alloy and in the course of subsequent relaxation. The point is that the probability of a metastable state forming at a local energy minimum is significantly higher than that at a local barrier; therefore, the components of a diffraction peak correspond to local minima of a multivalley structure. As a result, the observed diffraction peaks consist of several components and their structure changes jumpwise. In [4, 15–17], it was not elucidated whether the multivalley structure appears in the initial state or after hydrogenation and some issues also remained unresolved, such as the effect of cyclic treatment on this structure and the fractal nature of the structure. These issues are dealt with in this paper. The specific features of the discrete structural evolution in Pd-based alloys are investigated immediately after hydrogenation of deformed samples and also after several cycles of saturation with hydrogen. The factors determining these features are established, and the model of this phenomenon is developed further with allowance for new experimental data.

2. SAMPLES AND EXPERIMENTAL TECHNIQUE

Pd–Mo and Pd–Ta alloys [1, 4] were studied using x-ray diffraction (monochromatized Cu–$K_{\alpha 1}$ radiation). The alloys were melted from high-purity metals in an electric-arc furnace and then homogenized at 900°C over 24 h. After cutting, the samples were ground and polished; the thickness of the deformed surface layer was greater than the x-ray penetration depth. The alloys were saturated with hydrogen electrolytically. The shape of the diffraction peaks was analyzed with the Origin program package.

The angular positions of the diffraction peaks for the initial state corresponded to the Reuss formula for deformed materials [18], according to which the dependence of a_{hkl} on the Miller indices has the form

$$a_{hkl} = a_0 + a_0 \sigma K_{hkl}. \quad (1)$$

Here, a_0 is the lattice parameter of a cubic alloy, σ is the elastic strain in the surface plane, and K_{hkl} depends on the Miller indices and the elastic compliances.

The compressive elastic stresses along the surface caused by the mechanical treatment produce tensile strains along the normal to the surface due to interstitial defect complexes (*D–M* complexes), which are generated in the course of the mechanical treatment [1–3]. The saturation of Pd-based alloys with hydrogen was observed in [1–3] to cause a change in the sign of the elastic stresses (thereby producing compressive strains along the normal to the surface).

The values of a_0 and σ were determined with an accuracy of 0.0004 Å and 3 kg/mm^2, respectively, by using the technique of least squares.

3. EXPERIMENTAL RESULTS

3.1. Multiphase States and the Hydrogen-Induced Discrete Evolution of the Structure in Pd–Mo–H Alloys

Experimental diffraction peaks measured immediately after hydrogenation and in the course of subsequent relaxation have a complex structure, which indicates the existence of multiphase states in the alloys [4]. For example, after hydrogenation, the single (200) diffraction peak of a Pd–Mo alloy transforms into several peaks differing in height and shifts to a higher value of a_{200} (Fig. 3). Then, all components of the peak shift to a lower value of a_{200}, and after 22 h this quantity becomes smaller than its initial value.

The following fact is of special interest [4]: over certain time periods, it was clearly seen that the peak components appeared and disappeared or transformed one into another. This phenomenon was detected in [4] for the (200) diffraction peak during the evolution of a Pd–Mo–H alloy over the period from 23.6 to 121 h after saturating the alloy with hydrogen. In [15–17], an analogous phenomenon was observed in a Pd–Ta–H alloy and was referred to as discrete (jumplike) evolution. It can be seen from Fig. 3 that, after 23.6 h of relaxation in the Pd–Mo–H alloy, there appear indications of the presence of diffraction lines of two phases that noticeably differ in intensity. After the next 3.5 h, their intensities become similar, although their positions remain almost unchanged. Then, after 3.5 h, a clearly visible

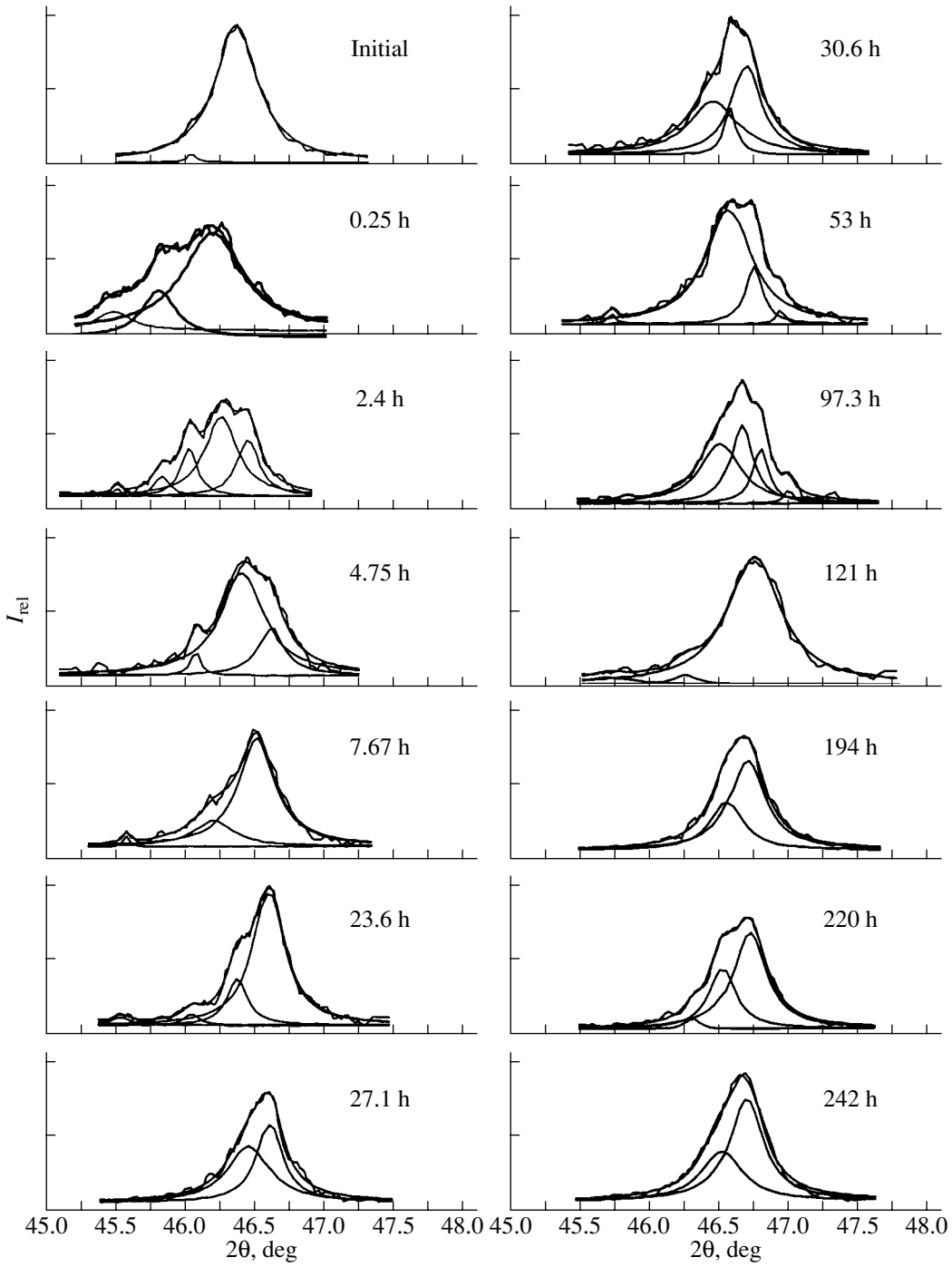

Fig. 3. Evolution of the (200) diffraction peak from a Pd–Mo–H alloy with relaxation time.

weak peak of another phase arises between the peaks of the two phases, and this peak becomes dominant after the next day. One of the former two peaks (at a larger value of 2θ) remains almost unchanged, while the other peak (at a smaller value of 2θ) almost vanishes. Next, after approximately two days, the three peaks that appeared in one form or another for the preceding three days become clearly visible. After the next day, these three peaks coalesce into a single broad peak, which then again becomes a double peak and assumes a complex shape. These changes suggest that the observed structural transformations involve only a few (3–5) phases of a certain composition. Within the first several hours after hydrogenation, the Pd–Mo–H system becomes multiphase, and the structure of this multiphase state varies with time. After the next several

hours, the system again becomes nearly single phase but then once more decomposes into a few phases. The transformation from a single-phase into a multiphase state and vice versa is repeated many times. Similar transformations also occur a long time, $(16–22) \times 10^3$ h, after hydrogenation [19].

3.2. Jumplike Structural Transformations in Pd–Ta–H Alloys

In order to reinforce the statement that the experimental data reported in [4] indicate a new phenomenon, special studies were also performed on Pd–Ta–H alloys and the results were published in [15–17], which described the evolution of the (311) diffraction peak after the sixth saturation with hydrogen and of the (220) peak after the fifth saturation of a Pd–Ta–H alloy. The results showed that the structural evolution in this alloy is also discrete (jumplike) in character. In this subsection, we discuss the structural evolution of the Pd–Ta–H alloy using the example of the evolution of the (220) diffraction peak after the first and sixth saturations with hydrogen. The study of the evolution after the first saturation is of importance because it may reveal whether or not the multivalley structure arises even in the initial state.

Tables 1–3 list the experimental positions (the values of the angle 2θ in degrees) of the maxima of the peak components. The subscripts indicate the relative intensity (in percentage) of the corresponding components. We note that the data obtained after other saturations and for other diffraction peaks are basically the same as those given in this paper.

Based on more extensive data, these tables provide support for the earlier conclusion that the positions of the diffraction peak components are divided into groups (columns). Therefore, the data published in [4, 15–17] do indeed reveal a new phenomenon, namely, discrete (jumplike) structural evolution. Furthermore, new features of this evolution are uncovered in this work. First, let us discuss the specific features of the data given in these tables. Note that, based on the data obtained for all saturations, a new numbering of the groups of peak components is used in this paper. Unfortunately, this numbering is arbitrary as yet.

The first feature to note is that the peak components for the initial state fall within two groups (8, 9) constructed on the basis of the data for hydrogenated alloys. This result indicates that the thermodynamic potential has a multivalley structure even in the initial state. It is important that the same results were obtained for the (311) diffraction peak. (Since the data on this peak are not given in the tables, we point out that the peak components for the initial state in this case correspond to values of the diffraction angle (2θ) of 81.35° and 81.75°; the diffraction-angle ranges for the respective groups are 81.32°–81.37° and 81.69°–81.76°, respectively.) The doublet is transformed into a triplet 1.2 h after the first saturation with hydrogen; its components fall within groups 8, 10, and 16, with the first and last components being the strongest. The analysis performed in [2] shows that, 1.2 h after saturation, the increase in the lattice parameter due to the hydrogen dissolving in the system is replaced by a decrease in the interplanar spacing due to elastic stresses. Therefore, even after 1.2 h, a strong peak component appears that is associated with the elastic stresses produced in a large portion of the system. This fact, in turn, indicates the appearance of significant inhomogeneities in this system. After the next 2.8 h, a quintuplet arises. However, its two extreme components are faint. The other components correspond to groups 9, 11, and 14, with the last two being the strongest. By 51.5 h after hydrogenation, there appears a quasi-single state correspond-

Table 1. Structural evolution of the (220) diffraction peak after the first saturation

Relaxation time, h	Group no.											⟨2θ⟩, deg
	5	8	9	10	11	12	13	14	15	16	17	
Initial state		67.67_{20}	67.88_{80}									67.85
1.2		67.74_{40}		67.94_{17}						68.40_{43}		68.06
4	67.40_{02}		67.80_{09}		68.05_{43}			68.23_{44}		68.40_{02}		68.11
6.8				67.94_{56}			68.19_{44}					68.05
9.7			67.83_{24}		68.04_{24}			68.22_{49}			68.49_{03}	68.09
24.5		67.69_{03}		67.95_{29}		68.14_{41}			68.31_{27}			68.12
31				68.01_{33}			68.17_{67}					68.12
51.5				67.94_{04}		68.12_{93}			68.36_{03}			68.12
59				67.95_{40}		68.14_{17}			68.30_{43}			68.13
73			67.86_{18}				68.18_{82}					68.12
103			67.84_{20}				68.18_{80}					68.11
173				67.95_{27}			68.20_{73}					68.13

Table 2. Structural evolution of the (220) diffraction peak after the sixth saturation (stage of rapid degassing)

Relaxation time	Group no.											⟨2θ⟩, deg
	1	3	4	5	7	8	9	10	11	14	16	
3500 h after the fifth saturation										68.25_{80}	68.41_{20}	68.29
0.8	68.88_{07}	67.20_{79}		67.47_{14}								67.22
3.2		67.24_{42}		67.47_{42}		67.73_{16}						67.42
5.7				67.45_{94}			67.78_{06}					67.50
7.7				67.41_{60}	67.62_{33}				68.04_{07}			67.52
10.3		67.19_{07}			67.57_{60}		67.80_{33}					67.62
24.1			67.36_{05}				67.85_{95}					67.83
26.8					67.63_{27}		67.81_{06}	67.96_{67}				67.86

Table 3. Structural evolution of the (220) diffraction peak after the sixth saturation (stage of stochastic oscillations of the peak position)

Relaxation time	Group no.									⟨2θ⟩, deg
	8	9	10	11	12	13	14	15	16	
33		67.84_{62}	67.99_{21}			68.17_{17}				67.93
49		67.85_{38}			68.10_{62}					68.01
53		67.77_{34}		68.06_{41}			68.22_{06}		68.35_{19}	68.02
57			67.96_{30}			68.17_{70}				68.11
73			67.97_{08}	68.03_{76}	68.11_{08}		68.24_{08}			68.05
76	67.74_{13}		67.97_{23}		68.13_{37}			68.31_{27}		68.09
80			67.95_{42}			68.17_{58}				68.08
97		67.77_{06}	68.00_{11}			68.18_{83}				68.14
101			67.93_{27}			68.17_{73}				68.11
127			67.98_{26}		68.15_{74}					69.11
167				68.03_{55}		68.20_{45}				68.10
174					68.12_{94}			68.30_{06}		68.13
195		67.81_{05}			68.13_{95}					68.11
218				68.07_{81}	68.14_{11}			68.30_{08}		68.10
243	67.74_{06}		67.96_{20}			68.19_{74}				68.12
266					68.11_{100}					68.11
293					68.09_{79}		68.26_{21}			68.12
339			67.96_{34}			68.19_{66}				68.11

ing to group 12, which is then transformed into a three-phase state with components corresponding to groups 10, 12, and 15. By 73 h, this state becomes two-phase; it remains unchanged over 30 h and changes only weakly over the next 70 h.

The initial state for the sixth saturation was the state reached 3.5×10^3 h after the fifth saturation. In this state, two peak components belonging to groups 14 and 16 are seen. After 0.8 h, the diffraction peak components transfer to groups 3 and 5 (one of the weak components at the periphery of the diffraction peak has an intensity of as low as 7% and is not covered by the numbered groups, which indicates once more that our classification of the groups is arbitrary); this transfer is associated with the hydrogen dissolving in the system. Then, hydrogen begins to emerge from the system, which causes the peak and its components to shift toward larger diffraction angles. Simultaneously, the transformation into a state with a greater number of phases occurs, and these phases sometimes coalesce into one phase. For example, after 3.2 h, the diffraction peak has three components; after 5.7 h, there is virtually

only one component; after 7.7 h, the peak again has three components; after 24.1 h, there is again virtually only one component; and after 26.8 h, the number of components again begins to increase. Here, it is of interest that one of the components appears at a noticeably smaller angle, even though the peak has not ceased to shift toward larger angles. The increase and decrease in the number of peak components continue to alternate even after the centroid of the peak ceases to shift toward larger angles and begins to oscillate stochastically.

Now, we will discuss specific features that have not been mentioned earlier. First, the number of components in a group depends nonmonotonically on the number of the group. Second, the character of this nonmonotonic dependence varies irregularly from one saturation with hydrogen to another. For example, the number of components is maximum in groups 10 and 13 after the first saturation, in groups 9–12 and 14 after the second saturation, in groups 9 and 10 after the fifth saturation (we do not give detailed data on the second and fifth saturations in this paper), and again in groups 9, 10, 12, and 13 after the sixth saturation. These distinctions may be due to the various defect structures produced by different saturations with hydrogen.

A comparison of the data on diffraction peaks (311) (from [15–17]) and (220) (given in this paper) shows that the occurrence of nonmonotonic structural evolution is beyond question in both cases, although the specific features and details of this evolution are different. The differences can be explained in terms of the model in which the structure of an alloy is assumed to pass through a series of intermediate metastable states rather than to pass immediately to the final state. For the alloys in question, the intermediate states are one-dimensional long-period structures [9, 10]. In certain cases, these structures are associated with specific features of the electronic spectrum [11] that occur as the nonspherical Fermi surface approaches the Brillouin zone boundary. An important feature of the diffraction patterns from these long-period structures is their significantly different behavior depending on the reciprocal-lattice site and, hence, on the diffraction peak. This feature was observed in the studies mentioned above.

Let us sum up the results obtained.

First, it has been found that the positions of the components of the (220) diffraction peak (as well as of other peaks not presented in this paper) for the initial state of alloys belong to the same groups as those for the states after hydrogenation. This finding indicates that the thermodynamic potential has a multivalley structure in reciprocal space even in the initial state. The fact that the structural transformations occur differently for different diffraction peaks suggests that the multivalley structure in the alloys at hand is associated with the specific features of the electronic structure, the long-range (elastic and electrostatic) interactions [9–14], etc.

Second, the interval boundaries within which the peak components lie vary only weakly in going from the first to the sixth saturation. Therefore, the structure of groups (columns) is very stable and depends only weakly on the amount of absorbed hydrogen and vacancies, as well as on the defect structure resulting from hydrogenation. This feature lends support to the above conclusion that the multivalley structure is mainly determined by the basic properties of the Pd-based alloys in question and, therefore, is highly stable.

Third, the number of peak components in a group (column) has been found to depend nonmonotonically on the number of the group. Since the probability that the peak component corresponding to a given local minimum will be observed depends on the depth of the minimum, a larger number of observed peak components must correspond to a higher probability of these components, i.e., to a larger depth or width of the corresponding local minima. Therefore, the depth and width of local minima are random functions of the reciprocal-space vector, which can be due to the thermodynamic-potential distribution in reciprocal space being fractal in nature. In our opinion, this remarkable property is associated with the fact that the amount of absorbed hydrogen and the defect structure of the system depend on the number of saturations with hydrogen performed. Apparently, the positions of groups of peak components are determined by the type of reciprocal-space vector, whereas the depth of local minima also depends on the defect structure, the amount of dissolved hydrogen, etc. Note that the possible influence of the defect structure on the thermodynamic-potential distribution in reciprocal space was pointed out in [12, Fig. 2].

Fourth, the jumplike structural changes have been observed to be irregular; therefore, the nonmonotonic structural evolution is associated with stochastic structural transformations.

Fifth, the structural evolution is accompanied by both an increase and a decrease in the diffraction angles. Therefore, the structural transformations in a system saturated with hydrogen are caused by the migration of both hydrogen atoms and vacancies.

4. DISCUSSION OF THE RESULTS

The decomposition observed in the system in question after saturating the system with hydrogen and thereby producing vacancies and various complexes (containing hydrogen atoms and vacancies) may be due to the system becoming unstable. The situation in this case is similar to that in a highly dislocated crystal system [12, 20]. The theory of multiphase decomposition was developed in [7] on the basis of the Edwards thermodynamic representation under the assumption that the internal energy (thermodynamic potential) of a system saturated with hydrogen has a complicated relief in the space of states with a great number of local minima separated by barriers (multivalley structure; see Fig. 1). Obviously, a structure corresponding to minima of this

relief arises with significantly higher probability than does a structure corresponding to maxima (i.e., the former structure is a long-lived one). This fact is likely the reason for the discrete values of the angle 2θ at which diffraction peak components were observed in [4, 15–17].

As indicated above, the difference in structure between the diffraction peaks may be due to the initial crystal structure passing into the final structure by going through a series of intermediate metastable states. Furthermore, the k dependence of the potential energy of the systems in question can be fractal in nature [21].

The behavior of a hydrogenated system can be complicated by various types of complexes (clusters), which can appear in the system, transform into a hierarchical defect structure, and, in addition, can cause various elastic stresses to arise. The evolution of the system is generally associated with its redistribution between minima that are relatively close together, which was also observed in this study.

Further evolution of the system is associated with the redistribution of hydrogen atoms and vacancies between the matrix (crystallites) and defect complexes (traps). The traps form at the initial stage of evolution of the system and remain enriched in hydrogen and especially vacancies over the entire period of observation. In the course of this evolution, the system undergoes various fluctuations; therefore, it is not improbable that noise-induced transitions take place in the system in question [22]. Since the evolution of the system is associated with transitions between phases that differ significantly in structure, these transitions must occur in a jumplike manner.

As already pointed out in [17], it is important that the diffraction peaks (or their components), as a rule, remain fairly narrow at all stages of the studies reported in [1–3] and this paper. This finding can be explained by the fact that the multilevel system under study is separated into intermediate-sized regions, a peculiar sort of quasi-cells analogous to Benard cells [5, 23], each of which corresponds to a long-lived thermodynamic state. These thermodynamic states are comparatively few in number. In the course of its evolution, the system relaxes due to migration of hydrogen atoms and vacancies and passes in a jumplike manner ("falls down") from one thermodynamic state (local minimum) to another; each time, only a few of these states coexist in the system. For this reason, the diffraction peaks consist of several components rather than being simply broadened. The width of each component is determined by the size of the coherent-scattering domains (CSDs) of the corresponding phases and by the state of the defect structure in these domains. Therefore, the width of the peak components varies only slightly with time. Due to the migration of hydrogen atoms and vacancies between the matrix and defect regions, the coexisting phases are replaced over the course of time (in a jumplike manner, as shown above).

In the course of the subsequent relaxation, hydrogen atoms and then defects can escape from the system. Clearly, the escape rates for different peak components are different. Therefore, the thermodynamic stability of the imperfect system can vary with time in a very complicated manner. For example, in the case where hydrogen atoms escape from the matrix (palladium-rich CSDs) but the amount of vacancies (V) remains unchanged, the thermodynamic stability of the system becomes lower rather than higher. In addition to the escape of hydrogen atoms into the surface (or grain boundaries), various hydrogen–defect complexes can form. For example, the transformation of interstitial defect complexes (*D–M* complexes; see Section 2) into hydrogen–defect–metal–vacancy (H–*D–M–V*) complexes causes anisotropic compression (increase in σ), which also renders the matrix less stable and causes opposing processes to occur. Thus, the transformations of the system containing hydrogen and vacancies are the result of the formation of an unstable complicated defect structure, which causes cooperative transfer of hydrogen and vacancies. The transfer of vacancies between the matrix (presumably H–*V* complexes) and H–*D–M–V* defect regions is likely of primary importance, as already indicated in [19, 24].

5. CONCLUSIONS

Thus, new experimental data have been obtained. The data indicating that the multivalley structure of the thermodynamic-potential distribution arises even in the initial state are of particular interest. This structure is highly stable and has a fractal character, which is influenced by saturation with hydrogen and by the defect structure transforming during hydrogenation and subsequent relaxation.

During relaxation, hydrogen atoms and vacancies can escape from the matrix (at different escape rates). They can escape both into the surface and H–*D–M–V* defect complexes. For this reason, the thermodynamic stability of the system varies in a complicated manner. The transfer of hydrogen and vacancies causes transformations to occur when the system undergoes a transition to a lower local minimum. As a result, nonmonotonic jumplike structural evolutionary changes will occur in the system. In the case where only hydrogen atoms (or, alternatively, vacancies) transfer from the matrix to defect complexes, the lattice parameter decreases (increases). These two processes cause jumps (that are opposite in sign) and, on the whole, lead to complicated nonmonotonic stochastic evolution.

ACKNOWLEDGMENTS

This study was supported by the Russian Foundation for Basic Research, project no. 02-02-16537.

REFERENCES

1. V. M. Avdyukhina, A. A. Katsnel'son, and G. P. Revkevich, Kristallografiya **44** (1), 49 (1999) [Crystallogr. Rep. **44**, 44 (1999)].
2. V. M. Avdyukhina, A. A. Katsnel'son, G. P. Revkevich, Han Ha Sok, A. V. Sedletskiĭ, A. A. Anishchenko, and A. A. Sidorchuk, Al'tern. Énerg. Ékol. **1** (1), 11 (2000).
3. V. M. Avdyukhina, A. A. Katsnelson, and G. P. Revkevich, Platinum Met. Rev. **46** (4), 169 (2002).
4. V. M. Avdyukhina, A. A. Anishchenko, A. A. Katsnel'son, and G. P. Revkevich, Perspekt. Mater., No. 6, 12 (2001).
5. I. Prigogine, *The End of Certainty: Time, Chaos, and the New Laws of Nature* (Free Press, New York, 1997; Regul. Khaot. Din., Izhevsk, 1999).
6. A. A. Katsnel'son, V. M. Avdyukhina, A. I. Olemskoĭ, D. A. Olemskoĭ, and G. P. Revkevich, Fiz. Met. Metalloved. **88** (6), 63 (1999) [Phys. Met. Metallogr. **88**, 576 (1999)].
7. V. M. Avdyukhina, A. A. Katsnel'son, A. I. Olemskoĭ, D. A. Olemskoĭ, and G. P. Revkevich, Fiz. Tverd. Tela (St. Petersburg) **44** (6), 979 (2002) [Phys. Solid State **44**, 1022 (2002)].
8. V. M. Avdyukhina, A. A. Katsnel'son, A. I. Olemskoĭ, and G. P. Revkevich, Perspekt. Mater., No. 3, 5 (2001).
9. V. I. Nikolin, *Multilayered Structures and Polytypism in Metal Alloys* (Naukova Dumka, Kiev, 1984) [in Russian].
10. D. A. Vul' and M. A. Krivoglaz, Fiz. Met. Metalloved. **51**, 231 (1981).
11. S. C. Moss, Phys. Rev. Lett. **22** (21), 1108 (1969).
12. A. I. Olemskoĭ and A. A. Katsnel'son, *Synergetics of Condensed Media* (URSS, Moscow, 2003) [in Russian].
13. A. I. Ustinov, A. Yu. Gaevskiĭ, A. D. Rud', V. S. Skorodzievskiĭ, and K. V. Chuistov, Fiz. Met. Metalloved. **62**, 519 (1986).
14. V. V. Kondrat'ev, Metallofizika (Kiev), No. 6, 13 (1981).
15. A. A. Katsnel'son, V. M. Avdyukhina, A. A. Anishchenko, and G. P. Revkevich, in *Abstracts of II International Symposium on Safety and Economics of Hydrogen Transport, IFSSEHT-2003* (Sarov, 2003), p. 74.
16. V. M. Avdyukhina, A. A. Anishchenko, A. A. Katsnel'son, and G. P. Revkevich, Vestn. Mosk. Univ., Ser. 3: Fiz., Astron. **44** (6), 62 (2003).
17. V. M. Avdyukhina, A. A. Anishchenko, A. A. Katsnel'son, A. I. Olemskoĭ, and G. P. Revkevich, Fiz. Tverd. Tela (St. Petersburg) **46** (3), 401 (2004) [Phys. Solid State **46**, 411 (2004)].
18. Ya. S. Umanskiĭ, *X-ray Diffractometry of Metals and Semiconductors* (Metallurgiya, Moscow, 1969) [in Russian].
19. V. M. Avdyukhina, A. A. Anishchenko, A. A. Katsnel'son, and G. P. Revkevich, Perspekt. Mater., No. 4, 5 (2002).
20. G. A. Malygin, Usp. Fiz. Nauk **169** (6), 979 (1999) [Phys. Usp. **42**, 887 (1999)].
21. A. I. Olemskoĭ and A. Ya. Flat, Usp. Fiz. Nauk **163** (12), 1 (1993) [Phys. Usp. **36**, 1087 (1993)].
22. W. Horsthemke and R. Lefever, *Noise-Induced Transitions: Theory and Applications in Physics, Chemistry, and Biology* (Springer, Heidelberg, 1984; Mir, Moscow, 1987).
23. H. Haken, *Synergetics: An Introduction* (Springer, Berlin, 1977; Mir, Moscow, 1980).
24. V. M. Avdyukhina, A. A. Anishchenko, A. A. Katsnel'son, and G. P. Revkevich, Zavod. Lab.: Diagn. Mater. **69** (9), 25 (2003).

Translated by Yu. Epifanov

Physics of the Solid State, Vol. 47, No. 3, 2005, pp. 405–410. Translated from Fizika Tverdogo Tela, Vol. 47, No. 3, 2005, pp. 395–399.

METALS AND SUPERCONDUCTORS

Nonlinear Elastic Characteristics of $Zr_{52.5}Ti_5Cu_{17.9}Ni_{14.6}Al_{10}$ and $Pd_{40}Cu_{30}Ni_{10}P_{20}$ Bulk Metallic Glasses

N. P. Kobelev*, E. L. Kolyvanov*, and V. A. Khonik**

** Institute of Solid-State Physics, Russian Academy of Sciences, Chernogolovka, Moscow oblast, 142432 Russia*
e-mail: kobelev@issp.ac.ru
*** Voronezh State Pedagogical University, ul. Lenina 86, Voronezh, 394043 Russia*

Received May 11, 2004; in final form, July 7, 2004

Abstract—The influence of uniaxial compression on the propagation of sound in $Zr_{52.5}Ti_5Cu_{17.9}Ni_{14.6}Al_{10}$ and $Pd_{40}Cu_{30}Ni_{10}P_{20}$ bulk metallic glasses is investigated, and the third-order elastic moduli of these glasses are determined. © *2005 Pleiades Publishing, Inc.*

1. INTRODUCTION

Owing to the unique combination of their physical properties, metallic glasses have been a subject of intensive experimental investigations for a long time. These investigations have been aimed at solving both applied and fundamental problems, especially those regarding the nature of the amorphous state. However, until very recently, conventional metallic glasses could be produced only in the form of thin ribbons or wires and, hence, a number of experimental techniques could not be used as efficient tools for studying these materials. The discovery of so-called bulk metallic glasses (alloys with a very low critical rate of cooling occurring without crystallization that make it possible to prepare large-sized metallic glass samples for use in various measurements) [1] and considerable recent progress achieved in the technology for producing these materials have opened up strong possibilities for their study using different modern techniques. In particular, since bulk metallic glasses possess good strength characteristics, it has become possible to investigate the influence of elastic deformation on the parameters of propagation of acoustic waves in these glasses and to obtain reliable data on their nonlinear elastic properties over a wide range of applied loads. Similar measurements can provide complementary important information on the force parameters of interatomic interactions occurring in a metallic glass and, consequently, on the specific features of its atomic configuration. To the best of our knowledge, such comprehensive research in bulk metallic glasses has never been performed in full measure. In [2–5], the influence of hydrostatic pressure on ultrasonic velocity was experimentally investigated for a large number of bulk amorphous alloys of different compositions. However, those experimental studies have permitted one to derive information only on specific linear combinations of third-order elastic moduli rather than on all these characteristics. In this respect, the purpose of the present work was to investigate the influence of uniaxial compression on the velocity of propagation of ultrasonic waves in $Zr_{52.5}Ti_5Cu_{17.9}Ni_{14.6}Al_{10}$ and $Pd_{40}Cu_{30}Ni_{10}P_{20}$ bulk amorphous alloys and to determine the complete set of their third-order elastic moduli from the results obtained.

2. SAMPLE PREPARATION AND EXPERIMENTAL TECHNIQUE

A master alloy of the composition $Pd_{40}Cu_{30}Ni_{10}P_{20}$ was prepared by two-zone direct melting of components in a silica tube at a controlled phosphorus partial pressure. Another master alloy of the composition $Zr_{52.5}Ti_5Cu_{17.9}Ni_{14.6}Al_{10}$ was produced by induction levitation melting under vacuum. Samples of both alloys in the amorphous state were prepared by quenching the melt into a copper mold. The quenching rate in the vicinity of the glass transition temperature was approximately equal to 100 K/s. The procedure for quenching melts was described in detail in [6]. The ingots thus prepared were $3 \times 6 \times 60$ mm in size. For measurements, samples (cross section, ~3×6 mm; length, 12–16 mm) were produced by electric-arc cutting from the ingots with subsequent mechanical grinding and polishing. The structural state (amorphicity) of the samples was checked using x-ray diffraction analysis on a SIEMENS D-500 diffractometer (CuK_α radiation). The densities of the $Zr_{52.5}Ti_5Cu_{17.9}Ni_{14.6}Al_{10}$ and $Pd_{40}Cu_{30}Ni_{10}P_{20}$ glasses were estimated at ~6.68 and ~9.27 g/cm^3, respectively.

Elastic deformation was accomplished by compressing the samples along their long axes on an Instron testing machine up to applied stresses of approximately 1 GPa. These stresses were considerably less than the ultimate compressive stress of the glasses under investigation. The ultimate compressive stress was approximately equal to 1.4–1.5 GPa for the $Pd_{40}Cu_{30}Ni_{10}P_{20}$

1063-7834/05/4703-0405$26.00 © 2005 Pleiades Publishing, Inc.

glass and 1.5–1.7 GPa for the $Zr_{52.5}Ti_5Cu_{17.9}Ni_{14.6}Al_{10}$ glass. For the samples used in the experiments, the onset of plastic flow was observed at stresses amounting to approximately 0.9 of the ultimate compressive stress, whereas the plastic strain to failure did not exceed 0.3%. The applied load was changed at testing machine speeds ranging from 0.02 to 0.10 mm/min. The acoustical measurements were carried out at a constant stress.

In testing of the bulk metallic glasses, the velocity of sound was measured by the high-frequency resonance method [7] with the use of longitudinal and transverse ultrasonic vibrations at frequencies ranging from 4 to 10 MHz along the short axis (perpendicular to the loading axis) of the sample. The measurements were carried out using lithium niobate or ceramic piezoelectric transducers. The piezoelectric transducers were cemented to the samples with a liquid epoxy resin for measuring longitudinal ultrasonic vibrations and with wax for transverse vibrations. In the case of transverse ultrasonic waves, the polarization vector was directed either parallel or perpendicular to the loading axis of the sample. The relative accuracies in measuring the resonant frequency $\Delta f/f$ ($f \sim V/L$, where V is the velocity of sound and L is the sample size in the direction of propagation of ultrasonic waves) with a change in the applied load were equal to 1×10^{-4} and 2×10^{-4} for transverse waves and 2×10^{-4} and 4×10^{-4} for longitudinal waves in the $Zr_{52.5}Ti_5Cu_{17.9}Ni_{14.6}Al_{10}$ and $Pd_{40}Cu_{30}Ni_{10}P_{20}$ bulk metallic glasses, respectively. All the measurements were performed at room temperature.

3. BASIC RELATIONSHIPS USED IN MEASUREMENTS OF THIRD-ORDER ELASTIC MODULI

The third-order elastic moduli are defined as the third derivatives of the internal energy U (adiabatic derivatives) or the free energy (isothermal derivatives) with respect to the strain of the material in a natural state. (For an isotropic solid, the number of third-order independent elastic moduli is equal to 3.) These elastic moduli can be interpreted as additions (linear in the strain) to the second-order elastic moduli. According to this interpretation, the third-order elastic moduli can be determined from the dependences of the second-order elastic moduli (or the velocities of sound) on the applied stress. The dependences of the velocities of acoustic waves in a solid on the applied static load were first calculated by Hughes and Kelly [8]. For anisotropic materials, these dependences were thoroughly examined by Thurston [9]. A brief derivation of the basic relationships used for calculating the third-order elastic moduli is given below.

Let us assume that s_i and u_i are the displacements caused by an acoustic wave and an applied load, respectively. In this case, the total displacements can be written in the form $v_i = s_i + u_i = (x_i - X_i) + (X_i - a_i)$, where x_i are the current coordinates, X_i are the initial coordinates in a strained state, and a_i are the natural (reference) coordinates of a material point. It is also assumed that the strains induced by the applied load are constant in time, uniform over the sample, and small (but finite) in magnitude and that the strain amplitude in the acoustic wave is infinitesimal. Therefore, the derivative with respect to x_i can be replaced by the derivative with respect to X_i [9] and only the terms of the first order in s_i can be retained in the equation of motion:

$$\rho\frac{\partial^2 v_i}{\partial t^2} = \rho\frac{\partial^2 s_i}{\partial t^2} = \frac{\partial \sigma_{ji}}{\partial x_j} = \frac{\partial \sigma_{ji}}{\partial X_j}, \tag{1}$$

where ρ is the density. By changing over from the elastic stresses σ_{ji} to the thermodynamic stresses t_{ji} [9], we obtain (to the first order in $\partial u_i/\partial a_j$)

$$\begin{aligned}\rho\frac{\partial^2 s_i}{\partial t^2} &= \frac{\partial}{\partial X_j}\left(\frac{1}{J}\frac{\partial x_j}{\partial a_k}\frac{\partial x_i}{\partial a_m}t_{km}\right)\\ &= \frac{1}{J}\left(\delta_{jk}\delta_{lm}t_{km}\frac{\partial^2 s_i}{\partial X_j \partial X_l} + \frac{\partial X_j}{\partial a_k}\frac{\partial X_i}{\partial a_m}\frac{\partial t_{km}}{\partial X_j}\right),\end{aligned} \tag{2}$$

where $J = \rho_0/\rho = \det\|\partial x_i/\partial a_j\|$ and ρ_0 is the density of the material in the initial state. Within the approximation used, in expression (2), we have

$$\begin{aligned}\frac{\partial t_{km}}{\partial X_j} &= \left(\frac{\partial t_{km}}{\partial \varepsilon_{rt}}\right)_S\left(\frac{\partial \varepsilon_{rt}}{\partial X_j}\right)\\ &= (c^S_{kmrt} + c^{ST}_{kmrtpq}\varepsilon_{pq})\left(\frac{\partial X_s}{\partial a_r}\frac{\partial X_e}{\partial a_t}\right)\frac{\partial^2 s_e}{\partial X_s \partial X_j}\end{aligned}$$

and $t_{km} = c^T_{kmls}\varepsilon_{ls}$, where c_{ijkl} are the isothermal or adiabatic elastic moduli of the second order,

$$c^{ST}_{ijklmn} = \left(\frac{\partial c^S_{ijkl}}{\partial \varepsilon_{mn}}\right)_T = \rho_0\left(\frac{\partial}{\partial \varepsilon_{mn}}\left(\frac{\partial^2 U}{\partial \varepsilon_{kl}\varepsilon_{ij}}\right)_S\right)_T$$

are the third-order mixed elastic moduli, and ε_{ij} is the Green's strain tensor. As a result, we obtain

$$\begin{aligned}\rho_0 V^2 s_i = c^S_{kmrt}\Bigg(&\delta_{jk}\delta_{im}\delta_{sr}\delta_{et} + \delta_{im}\delta_{sr}\delta_{et}\frac{\partial u_j}{\partial a_k}\\ &+ \delta_{jk}\delta_{sr}\delta_{et}\frac{\partial u_i}{\partial a_m} + \delta_{jk}\delta_{im}\delta_{et}\frac{\partial u_s}{\partial a_r}\\ &+ \delta_{jk}\delta_{im}\delta_{sr}\frac{\partial u_e}{\partial a_t}\Bigg)s_e n_s n_j\\ &+ c^T_{jmpq}\left(\frac{\partial u_p}{\partial a_q} + \frac{\partial u_q}{\partial a_p}\right)s_i n_j n_m/2\\ &+ c^{ST}_{jirtpq}\left(\frac{\partial u_p}{\partial a_q} + \frac{\partial u_q}{\partial a_p}\right)s_t n_j n_r/2.\end{aligned} \tag{3}$$

Here, n_i are the direction cosines of the wave vector and the relationship between the applied load and the strain components can be obtained in a linear approximation.

In the case under consideration (which is characterized by an isotropic medium, a uniaxial stress, a wave vector perpendicular to the loading axis of the sample, and a polarization vector parallel or perpendicular to the loading axis), relationship (3) can be significantly simplified. In particular, for a longitudinal acoustic wave, we have

$$\rho_0 V_l^2 = (K_S + 4/3\mu)(1 + 4\alpha) + 2A^{ST}\alpha + 2B^{ST}(4\alpha + \gamma) + 2C^{ST}(2\alpha + \gamma), \quad (4)$$

where K_S is the adiabatic bulk modulus; μ is the shear modulus; A, B, and C are the third-order elastic moduli in the Landau notation (hereafter, the indices on these moduli will be omitted); and α and γ are the strains of the sample in the transverse and longitudinal directions about the loading axis, respectively. Similar relationships can be written for transverse acoustic waves. By expressing the strains α and γ through the external compressive stress P, we obtain the following formulas relating the change in the velocities of sound to the external compressive stress P:

$$\left(\frac{\Delta V}{V}\right)_l = \left(\frac{K_T - 2/3\mu}{\mu} + \frac{K_T - 2/3\mu}{2C_l}\frac{A}{\mu} + \frac{K_T - 5/3\mu}{C_l}\frac{B}{\mu} - \frac{C}{C_l}\right)\frac{P}{3K_T}, \quad (5)$$

$$\left(\frac{\Delta V}{V}\right)_{t1} = \left(-\frac{K_T + 4/3\mu}{2\mu} - \frac{K_T + 4/3\mu}{8\mu}\frac{A}{\mu} - \frac{B}{2\mu}\right)\frac{P}{3K_T}, \quad (6)$$

$$\left(\frac{\Delta V}{V}\right)_{t2} = \left(\frac{K_T - 2/3\mu}{\mu} + \frac{K_T - 2/3\mu}{4\mu}\frac{A}{\mu} - \frac{B}{2\mu}\right)\frac{P}{3K_T}, \quad (7)$$

where K_T is the isothermal bulk modulus; $C_l = K_S + 4/3\mu$ is the adiabatic longitudinal elastic modulus; and V_{t1} and V_{t2} are the velocities of the transverse acoustic waves with polarization vectors parallel and perpendicular to the loading axis of the sample, respectively. Since the propagation time of an acoustic wave or, as in our case, the resonant frequency is directly measured in real experiments rather than the velocity of sound, it is expedient to write the expression relating the relative change in the velocity of sound to the relative change in the resonant frequency:

$$\frac{\Delta f}{f} = \frac{\Delta V}{V} - \frac{K_T - 2/3\mu}{2\mu}\frac{P}{3K_T}. \quad (8)$$

It can be seen from relationships (5)–(8) that, knowing the dependences of the velocities of sound on the external stress, we can calculate all the three third-order elastic moduli under consideration.

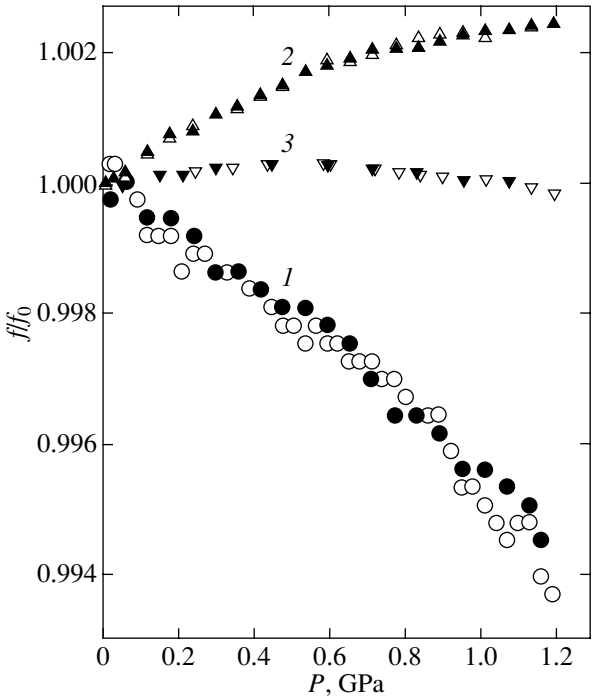

Fig. 1. Dependences of the relative change in the resonant frequency of (*1*) longitudinal vibrations and (*2*, *3*) transverse vibrations with a polarization vector directed (*2*) parallel and (*3*) perpendicular to the loading axis on the uniaxial compressive stress in the $Zr_{52.5}Ti_5Cu_{17.9}Ni_{14.6}Al_{10}$ bulk amorphous alloy. Open and closed symbols represent the results obtained in the loading and unloading cycles, respectively.

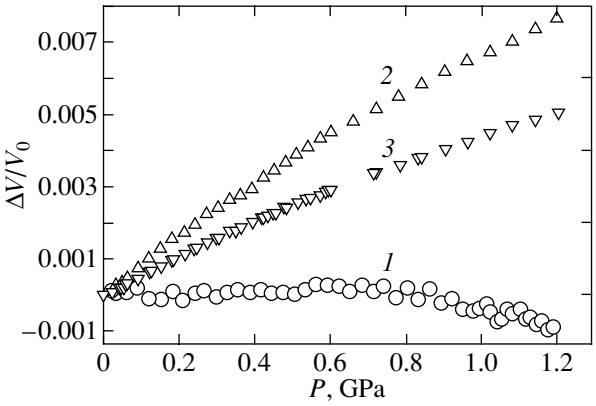

Fig. 2. Dependences of the relative change in the velocity of (*1*) longitudinal ultrasonic waves and (*2*, *3*) transverse ultrasonic waves with a polarization vector directed (*2*) parallel and (*3*) perpendicular to the loading axis on the compressive stress in the $Zr_{52.5}Ti_5Cu_{17.9}Ni_{14.6}Al_{10}$ bulk amorphous alloy.

4. RESULTS AND DISCUSSION

The magnitudes of the velocities of sound in the initial samples of both alloys were measured using the pulse echo technique and high-frequency resonance.

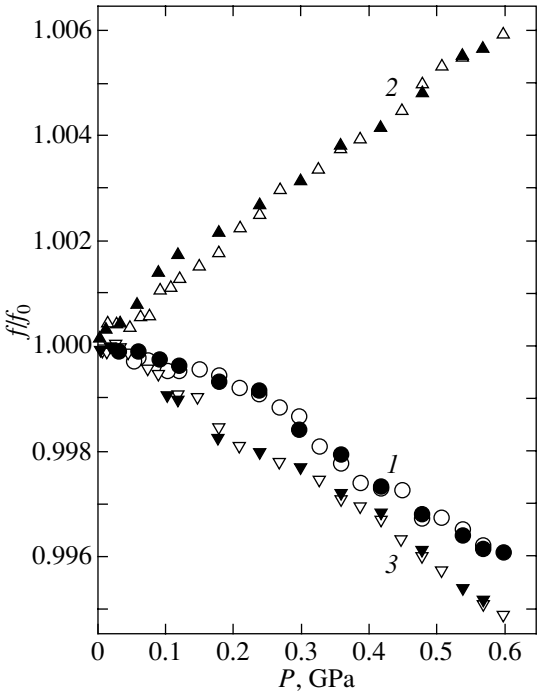

Fig. 3. Dependences of the relative change in the resonant frequency of (*1*) longitudinal vibrations and (*2*, *3*) transverse vibrations with a polarization vector directed (*2*) parallel and (*3*) perpendicular to the loading axis on the compressive stress in the $Pd_{40}Cu_{30}Ni_{10}P_{20}$ bulk amorphous alloy. Open and closed symbols represent the results obtained in the loading and unloading cycles, respectively.

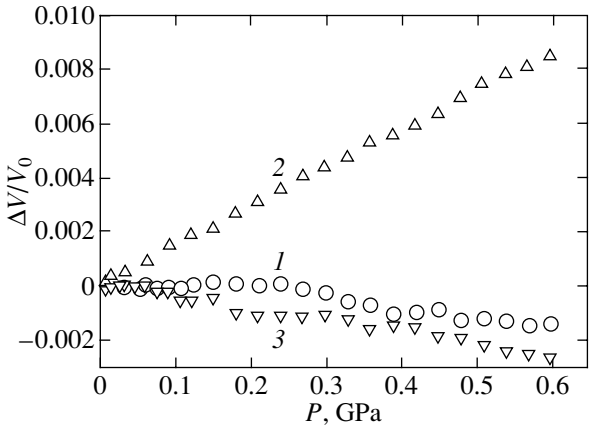

Fig. 4. Dependences of the relative change in the velocity of (*1*) longitudinal ultrasonic waves and (*2*, *3*) transverse ultrasonic waves with a polarization vector directed (*2*) parallel and (*3*) perpendicular to the loading axis on the compressive stress in the $Pd_{40}Cu_{30}Ni_{10}P_{20}$ bulk amorphous alloy.

The ultrasonic velocities obtained for different samples of each alloy coincide to within the experimental error of the velocity measurement and are as follows: $V_l = (4.80 \pm 0.05) \times 10^3$ m/s and $V_t = (2.170 \pm 0.005) \times 10^3$ m/s for the $Zr_{52.5}Ti_5Cu_{17.9}Ni_{14.6}Al_{10}$ alloy and $V_l = (4.70 \pm 0.03) \times 10^3$ m/s and $V_t = (1.920 \pm 0.005) \times 10^3$ m/s for the $Pd_{40}Cu_{30}Ni_{10}P_{20}$ alloy. Figure 1 shows the dependences of the relative changes in the resonant frequencies of longitudinal and transverse ultrasonic vibrations on the uniaxial compressive stress for one of the zirconium-based metallic glass samples measured in the loading and unloading cycles. It can be seen from this figure that the dependences of the resonant frequency on the stress do not exhibit hysteresis. The dependences of the relative changes in the ultrasonic velocities averaged over several samples (or several cycles of measurement) and calculated from relationship (8) for the same alloy are plotted in Fig. 2. The dependences thus obtained were used to calculate the third-order elastic moduli *A*, *B*, and *C* according to relationships (5)–(8) (see table). Since we were unaware of any experimental values of the isothermal bulk modulus for this alloy, the calculations were performed under the assumption that the isothermal bulk modulus is equal to the adiabatic bulk modulus: $K_T = K_S$. The table also presents the probable errors introduced by assuming that the maximum difference between the quantities K_T and K_S did not exceed 10%. These errors were calculated for the third-order elastic moduli *C* and *B*. (Note that the isothermal bulk modulus K_T is not required to calculate the third-order elastic modulus *A*.) For the $Pd_{40}Cu_{30}Ni_{10}P_{20}$ bulk metallic glass, we obtained similar dependences, which are shown in Figs. 3 and 4. It can be seen that, in the range of weak stresses, the resonant frequency of transverse ultrasonic vibrations in this amorphous alloy exhibits an insignificant hysteresis (Fig. 3, dependence *2*), which slightly exceeds the measurement error. The third-order elastic moduli calculated from the experimental data for the palladium-based metallic glass are also given in the table. As is seen from the table, all the third-order elastic moduli are negative in sign and their relative and absolute values for the $Pd_{40}Cu_{30}Ni_{10}P_{20}$ glass are larger than those for the $Zr_{52.5}Ti_5Cu_{17.9}Ni_{14.6}Al_{10}$ glass. It should be noted that the experimental dependences are

Third-order elastic moduli of the $Zr_{52.5}Ti_5Cu_{17.9}Ni_{14.6}Al_{10}$ and $Pd_{40}Cu_{30}Ni_{10}P_{20}$ bulk metallic glasses (relative and absolute values) and the possible corrections Δ for the change (by 10%) in the isothermal bulk modulus

Alloy	A/μ	*A*, GPa	B/μ	*B*, GPa	Δ	C/C_l	*C*, GPa	Δ
$Zr_{52.5}Ti_5Cu_{17.9}Ni_{14.6}Al_{10}$	–4.74 ± 0.03	–149 ± 3	–4.79 ± 0.03	–150 ± 3	–0.3*B*	–0.75 ± 0.07	–115 ± 15	–0.5*C*
$Pd_{40}Cu_{30}Ni_{10}P_{20}$	–9.0 ± 0.2	–307 ± 12	–6.5 ± 0.2	222 ± 11	–0.15*B*	–3.6 ± 0.2	–737 ± 60	–0.3*C*

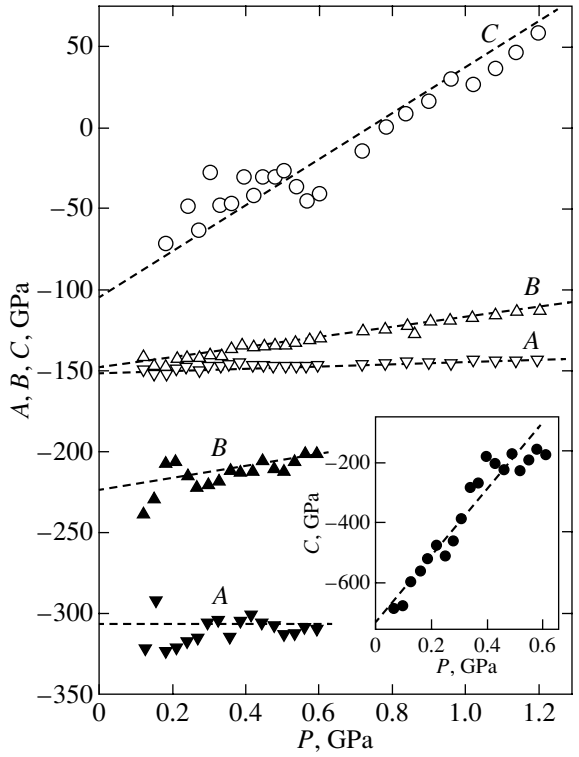

Fig. 5. Dependences of the third-order elastic moduli on the compressive stress in the bulk amorphous alloys $Zr_{52.5}Ti_5Cu_{17.9}Ni_{14.6}Al_{10}$ (open symbols) and $Pd_{40}Cu_{30}Ni_{10}P_{20}$ (closed symbols).

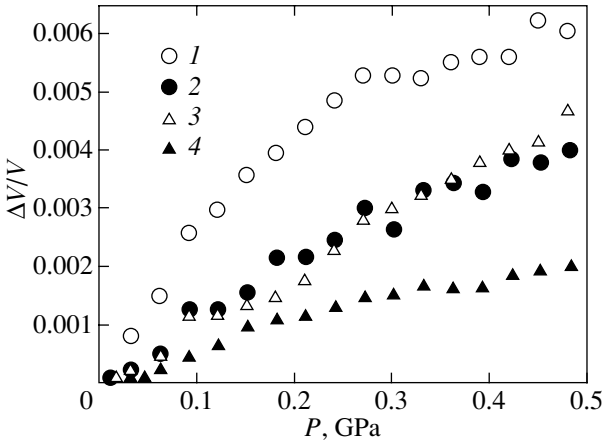

Fig. 6. Dependences of the relative change in the velocity of (*1*, *2*) longitudinal and (*3*, *4*) transverse ultrasonic waves on the hydrostatic pressure for (*1*, *3*) $Pd_{40}Cu_{30}Ni_{10}P_{20}$ and (*2*, *4*) $Zr_{52.5}Ti_5Cu_{17.9}Ni_{14.6}Al_{10}$ bulk amorphous alloys according to the data calculated from the third-order elastic moduli determined in this work.

characterized by a pronounced (higher order) nonlinearity (Figs. 1, 2). As an illustration, Fig. 5 shows the dependences of the third-order elastic moduli *A*, *B*, and *C* on the compressive stress for both alloys in the range of strong stresses, which were constructed from the experimental data. It can be seen from Fig. 5 that the dependences of the elastic moduli *B* and *C* on the compressive stress exhibit a linear behavior (the dependence of the modulus *C* on the compressive stress is substantially stronger than that of the modulus *B*), whereas the elastic modulus *A* remains constant to within the experimental error.

It was of interest to compare our results with the data obtained by other authors [2–5], who investigated the influence of hydrostatic pressure on the velocity of sound in a number of bulk metallic glasses. For this purpose, the dependences of the velocities of longitudinal and transverse ultrasonic waves on the hydrostatic pressure (Fig. 6) were calculated from the third-order elastic moduli determined in the present work. It turned out that the dependences thus calculated for the $Pd_{40}Cu_{30}Ni_{10}P_{20}$ bulk amorphous alloy are very similar (in both character and the velocity magnitude) to those given in [3, 5] for the $Pd_{39}Cu_{30}Ni_{10}P_{21}$ alloy. Moreover, the dependences calculated for the $Zr_{52.5}Ti_5Cu_{17.9}Ni_{14.6}Al_{10}$ alloy correlate closely with the dependences obtained in [5] for several zirconium-based bulk metallic glasses. Thus, our results are in good qualitative agreement with the data on the influence of hydrostatic pressure on the velocity of ultrasonic waves. However, it remains unclear whether the third-order elastic moduli obtained in this study are "true" moduli, i.e., elastic moduli determined only by a change in the mean interatomic distance under elastic stresses, or the reversible microstructural transformations occurring in metallic glasses under load can also contribute to their magnitudes. For example, the stress field can bring about an ordering of elastic dipoles (the appearance of a preferred dipole orientation) and, hence, can induce additional strains in the material. In our opinion, solving this problem calls for experimental investigations into the influence of heat treatment on the nonlinear elastic characteristics of metallic glasses. These studies will be performed in the immediate future.

ACKNOWLEDGMENTS

This work was supported by the US Civilian Research and Development Foundation for the Independent States of the Former Soviet Union (grant no. RP1-2320-VO-02) and the Ministry of Industry and Science of the Russian Federation (project no. NSh-2169.2003.2).

REFERENCES

1. A. Inoue, Acta Mater. **48**, 279 (2000).
2. W. H. Wang, R. J. Wang, F. Y. Li, D. Q. Zhao, and M. X. Pan, Appl. Phys. Lett. **74** (13), 1803 (1999).

3. L. M. Wang, L. L. Sun, W. H. Wang, R. J. Wang, Z. J. Zhan, D. Y. Dai, and W. K. Wang, Appl. Phys. Lett. **77** (23), 3734 (2000).
4. W. K. Wang, Mater. Trans., JIM **42** (4), 606 (2001).
5. W. H. Wang, P. Wen, L. M. Wang, Y. Zhang, M. X. Pan, D. Q. Zhao, and R. J. Wang, Appl. Phys. Lett. **79** (24), 3947 (2001).
6. A. E. Berlev, O. P. Bobrov, V. A. Khonik, K. Csach, A. Juríková, J. Miškuf, H. Neuhäuser, and M. Yu. Yazvitsky, Phys. Rev. B **68**, 132303 (2003).
7. N. P. Kobelev and Ya. M. Soĭfer, Fiz. Tverd. Tela (Leningrad) **21**, 1362 (1979) [Sov. Phys. Solid State **21**, 787 (1979)].
8. D. S. Hughes and J. L. Kelly, Phys. Rev. **92**, 1145 (1953).
9. R. Thurston, in *Physical Acoustics*, Ed. by W. P. Mason (Academic, New York, 1964; Mir, Moscow, 1966), Vol. 1, Part A.

Translated by O. Borovik-Romanova

Physics of the Solid State, Vol. 47, No. 3, 2005, pp. 411–415. Translated from Fizika Tverdogo Tela, Vol. 47, No. 3, 2005, pp. 400–403.

METALS AND SUPERCONDUCTORS

Time and Amplitude Dependences of the Damping Decrement and Shear Modulus upon Irreversible Structural Relaxation in a Zr–Cu–Ni–Al–Ti Bulk Metallic Glass

N. P. Kobelev*, E. L. Kolyvanov*, and V. A. Khonik**

** Institute of Solid-State Physics, Russian Academy of Sciences, Chernogolovka, Moscow oblast, 142432 Russia*
e-mail: kobelev@issp.ac.ru

*** Voronezh State Pedagogical University, ul. Lenina 86, Voronezh, 394043 Russia*

Received May 12, 2004; in final form, July 7, 2004

Abstract—The time dependences of the irreversible relaxation of the damping decrement and the shear modulus of a $Zr_{52.5}Ti_5Cu_{17.9}Ni_{14.6}Al_{10}$ bulk metallic glass are investigated using an inverse torsion pendulum in the range from room temperature to ~650 K. The spectrum of activation energies of irreversible structural relaxation is evaluated from the results obtained. Analysis of the amplitude dependences of the damping decrement and the shear modulus allows the conclusion that the relaxation centers responsible for the amplitude dependence differ from those associated with the irreversible structural relaxation at temperatures below and in the vicinity of the glass transition point. © *2005 Pleiades Publishing, Inc.*

1. INTRODUCTION

Bulk metallic glasses [1, 2] have been a subject of intensive experimental investigations in recent years. This is associated with the fact that these materials are very promising for practical applications. Moreover, since the discovery of bulk metallic glasses, the range of instruments and experimental techniques used for studying the physical characteristics of these interesting objects has been extended significantly. However, to date, the processes of irreversible structural relaxation occurring in metallic glasses at temperatures below the glass transition point have not been adequately investigated. Acoustical measurements are among the most efficient tools for examining the relaxation processes proceeding in solids. In our recent papers [3, 4], we reported on the results of investigations into the temperature dependences of the low-frequency internal friction and the shear modulus in a $Zr_{52.5}Ti_5Cu_{17.9}Ni_{14.6}Al_{10}$ bulk metallic glass. In those works, we separated the contributions made by the processes of reversible and irreversible structural relaxation to the temperature dependences of the damping decrement and the shear modulus, evaluated the spectra of activation energies for these relaxation processes, and proposed a phenomenological model based on relaxation centers with a double-well energy potential. This model has provided a satisfactory qualitative explanation of all the dependences observed in the experiments. The present work is a continuation of our previous investigations. The purpose of this work was to examine the time parameters of the irreversible structural relaxation at different temperatures and to elucidate how the acoustic strain amplitude affects the damping decrement and the shear modulus of a Zr–Cu–Ni–Al–Ti bulk metallic glass.

2. SAMPLE PREPARATION AND EXPERIMENTAL TECHNIQUE

As in our previous studies [3, 4], the damping decrement and the shear modulus were measured with an inverse torsion pendulum at frequencies ranging from 10 to 25 Hz. A master alloy of the composition $Zr_{52.5}Ti_5Cu_{17.9}Ni_{14.6}Al_{10}$ (at. %) was prepared by induction levitation melting under vacuum. Samples of the $Zr_{52.5}Ti_5Cu_{17.9}Ni_{14.6}Al_{10}$ bulk metallic glass were produced by quenching the melt into an evacuated copper mold at room temperature. The quenching rate in the vicinity of the glass transition temperature was approximately equal to 10^2 K/s [3, 5]. The structural state (amorphicity) of the alloy was checked using x-ray diffraction analysis. The procedure for preparing glass samples and their parameters were identical to those described in [3, 4]. In order to measure the time dependences of the damping decrement and the shear modulus, the sample was heated to a specified temperature at a rate of approximately 2 K/min and the time characteristics were measured after the five minutes required to stabilize the temperature, which was maintained constant to within 1 K in the course of each measurement. The strain amplitude was varied in the range from $\sim 1 \times 10^{-5}$ to 3×10^{-4}. The amplitude dependences presented in this paper were measured upon changing over from small strain amplitudes to large strain amplitudes. Upon the reverse changeover from maximum strain amplitudes, the damping decrement and the shear modulus exhibited insignificant hystereses. At room tem-

1063-7834/05/4703-0411$26.00

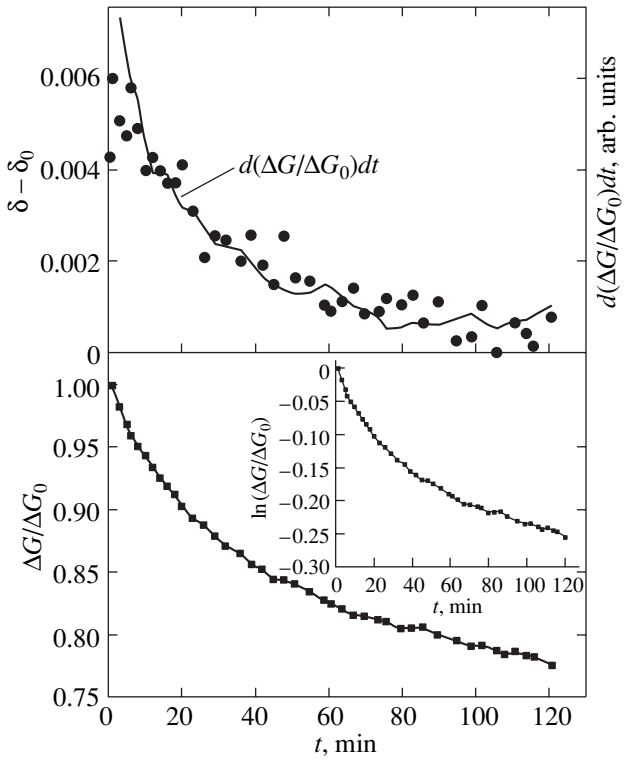

Fig. 1. Time dependences of the irreversible contribution to the damping decrement $\delta - \delta_0$, the relative change in the irreversible contribution to the shear modulus $\Delta G/\Delta G_0$, and the time derivative of the relative change in the irreversible contribution to the shear modulus $d(\Delta G/\Delta G_0)dt$ for the $Zr_{52.5}Ti_5Cu_{17.9}Ni_{14.6}Al_{10}$ bulk amorphous alloy at a temperature of 580 K. The inset shows the time dependence of $\ln(\Delta G/\Delta G_0)$.

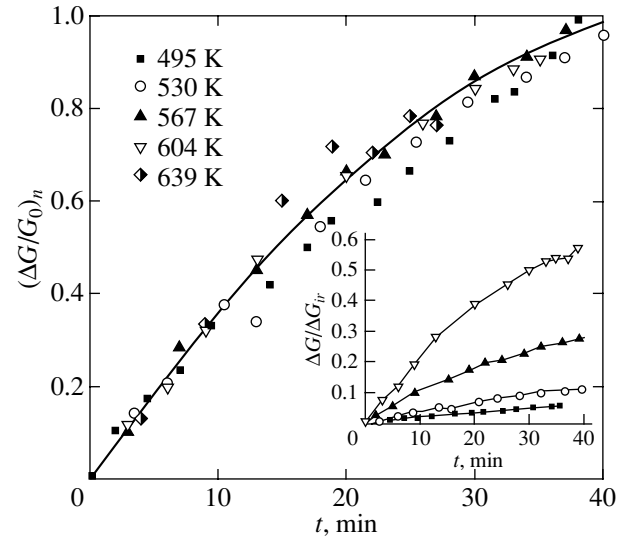

Fig. 2. Time dependences of the relative change in the irreversible contribution to the shear modulus normalized to the maximum change in the shear modulus of the Zr–Cu–Ni–Al–Ti alloy at different temperatures. The inset shows the magnitude of the relative relaxation of the irreversible contribution to the shear modulus as a function of the measurement time at different temperatures.

perature, these hystereses disappeared within approximately 5 min of the return to the minimum strain amplitudes (this time decreased with increasing temperature). This finding indicated that the material did not undergo multiple irreversible structural transformations in the course of measurements at large strain amplitudes. The experiments were performed in the range from room temperature to a temperature of 640 to 650 K, which is close to the glass transition point at the specified heating rate [3, 4].

3. RESULTS AND DISCUSSION

3.1. Time Dependences of the Damping Decrement and Shear Modulus

Figure 1 shows the characteristic time dependences of the irreversible contribution to the damping decrement $\delta - \delta_0$ (δ_0 is the reversible contribution to the damping decrement) and the relative change in the irreversible contribution to the shear modulus $\Delta G/\Delta G_0 = [G(t) - G_0]/[G(0) - G_0]$ (G_0 is the modulus of the material in a relaxed state at a specified temperature, i.e., after annealing at temperatures of 640–650 K). It was shown in [3, 4] that, according to the model of relaxation centers with an asymmetric double-well potential, the irreversible contribution to the shear modulus is proportional to the density of nonequilibrium energy states n_{ir} and the irreversible component of the damping decrement is proportional to $n_{ir}/\omega\tau \sim \partial n_{ir}/\partial t$, where ω is the circular frequency and τ is the relaxation time. Actually, as can be seen from Fig. 1, the time dependences of the irreversible contribution to the damping decrement and the time derivative of the relative change in the irreversible contribution to the shear modulus correlate with each other. However, the time dependences obtained have defied description in terms of only one relaxation time. The inset to Fig. 1 shows the dependence of $\ln(\Delta G/\Delta G_0)$ on the time t. It is clearly seen that this dependence exhibits a nonlinear behavior and that the characteristic relaxation times at the beginning and the end of the measurement differ by approximately one order of magnitude. This is quite consistent with the data available in the literature, according to which the relaxation processes in metallic glasses are characterized by a broad spectrum of activation energies and, correspondingly, relaxation times.

The time dependences of the irreversible contribution to the shear modulus, which were measured sequentially in regular temperature intervals for nearly identical times of exposure to each temperature, are depicted in Fig. 2. It can be seen from the inset to Fig. 2 that an increase in the temperature leads to an increase in the magnitude of the relative relaxation of the irreversible contribution to the shear modulus $\Delta G/\Delta G_{ir} = [G(0) - G(t)]/[G(0) - G_0]$ for the time of measurement. This suggests a higher density ($\partial n_{ir}/\partial E$) of nonequilibrium states with higher activation energies E. It should be noted that the time dependences of the relative

change in the irreversible contribution to the shear modulus normalized to the maximum change in the shear modulus for the total time of measurement, i.e., $(\Delta G/G)_n = \Delta G(t)/\Delta G(t_{max})$, are nearly identical for different temperatures. Consequently, the processes of irreversible relaxation due to such a stepwise change in the temperature are described by the same set of characteristic times for all the isotherms under investigation. This is associated with the fact that, in the case where $E/T \gg 1$ and the initial spectrum of activation energies of irreversible relaxation is sufficiently broad, even a short-term isothermal treatment results in a sharp, virtually stepwise cutoff of the low-energy portion of the spectrum (see, for example, [6]) and each subsequent annealing leads only to a shift of this step toward the high-energy range (by the same energy, provided the times of isothermal treatments and the temperature intervals between them remain unchanged). Therefore, in each cycle of annealing, the activation energies of irreversible relaxation lie in a narrow range with a characteristic energy proportional to the temperature, because $\tau = \tau_0 \exp(E/T)$ [7, 8]. In this case, the depth of modulus relaxation for the time of isothermal treatment, i.e., $\Delta G/G_{ir} = \Delta G(t_{max})/(\Delta G)_{ir}$ [where $(\Delta G)_{ir}$ is the total change in the shear modulus due to irreversible structural relaxation], should be proportional to the mean density of nonequilibrium energy states in the aforementioned narrow range of activation energies. This makes it possible to estimate the characteristic relaxation times from the time dependence of the relative change in the shear modulus at a specified temperature and then to reconstruct the spectrum of activation energies of irreversible structural relaxation from similar experiments. (According to our estimates, isothermal treatment for the first five uncontrollable minutes required to stabilize the temperature can lead to a decrease in the measured depths of relaxation by approximately 10–15% at each temperature but cannot affect their ratio at different temperatures.)

The calculated spectrum of activation energies of irreversible structural relaxation in the alloy under investigation is shown in Fig. 3. This spectrum was calculated from the experimental data obtained upon 30-min isothermal treatment in 30-degree intervals. The magnitudes of the activation energies were estimated under the assumption that $\tau_0 \approx 10^{-13}$ s [7, 8]. It should be noted that the calculated characteristics of the spectrum of activation energies virtually coincide with the results obtained in our previous works [3, 4], in which the spectrum of activation energies was evaluated from the temperature dependence of the irreversible contribution to the damping decrement.

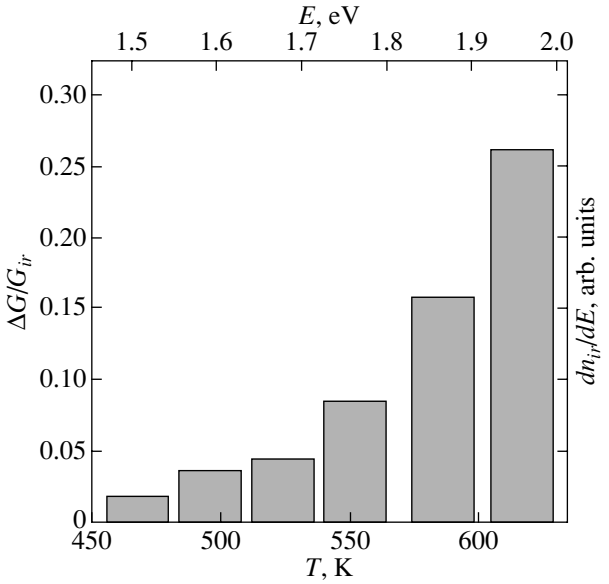

Fig. 3. Depth of irreversible relaxation of the shear modulus as a function of the temperature upon sequential isothermal treatments and the corresponding spectrum of activation energies of irreversible relaxation in the alloy under investigation.

3.2. Amplitude Dependences of the Damping Decrement and Shear Modulus

The investigation into the influence of the amplitude of torsional vibrations on both the damping decrement and the relative change in the shear modulus for as-quenched samples of the Zr–Cu–Ni–Al–Ti amorphous alloy revealed that the damping decrement and the shear modulus substantially depend on the amplitude. Figure 4 presents the amplitude-dependent contributions to the damping decrement $\Delta\delta_{ad} = \delta(\varepsilon) - \delta(0)$ and to the relative change in the shear modulus $(\Delta G/G)_{ad} = [G(\varepsilon) - G(0)]/G(0)$ as functions of the strain amplitude ε at room temperature for one of the samples. (Note that the quantities $\delta(0)$ and $G(0)$ were determined by extrapolating the amplitude dependences of the damping decrement and the shear modulus to zero amplitude, respectively.) These amplitude-dependent contributions are not related to instrumental effects. From analyzing the amplitude dependences measured for a hardened steel sample of the same shape and size (Fig. 4, curves *2*), it follows that the possible instrumental contribution to the amplitude dependence is at least one order of magnitude smaller than the experimentally observed contribution. It can be seen from Fig. 4 that, at small strain amplitudes, the amplitude-dependent contributions to the damping decrement and to the relative change in the shear modulus are proportional to the strain amplitude and are equal in magnitude; i.e., their ratio is equal to unity. At large strain amplitudes, the ratio of the damping decrement to the relative change in the shear modulus decreases with an increase in the strain amplitude.

The dependences of the amplitude-dependent contribution to the relative change in the shear modulus on the strain amplitude at several temperatures are plotted in Fig. 5. These dependences were measured during

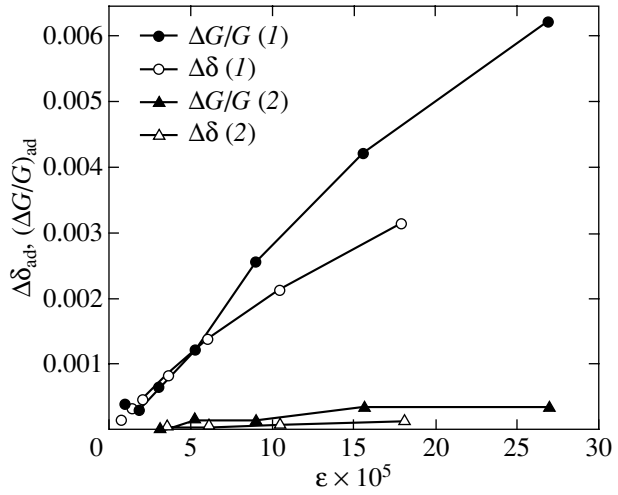

Fig. 4. Dependences of the amplitude-dependent contributions to the damping decrement $\Delta\delta_{ad}$ and to the relative change in the shear modulus $(\Delta G/G)_{ad}$ on the strain amplitude for (*1*) the $Zr_{52.5}Ti_5Cu_{17.9}Ni_{14.6}Al_{10}$ alloy and (*2*) hardened steel at room temperature.

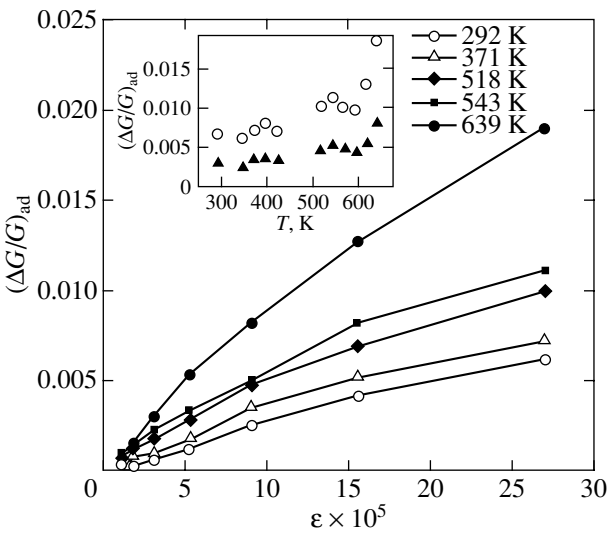

Fig. 5. Dependences of the amplitude-dependent contribution to the relative change in the shear modulus on the strain amplitude for the Zr–Cu–Ni–Al–Ti alloy at different temperatures. The inset shows the temperature dependences of the amplitude-dependent contribution to the relative change in the shear modulus for two strain amplitudes $\varepsilon = (1)\ 2.7 \times 10^{-4}$ and (*2*) 8×10^{-5}.

continuous heating of the sample at a rate of 2 K/min. The inset to Fig. 5 shows the temperature dependences of the amplitude-dependent contribution to the relative change in the shear modulus for two strain amplitudes. It can be seen from Fig. 5 that, as the temperature increases to approximately 600 K, the amplitude dependences of the studied quantity gradually become more pronounced (the amplitude-dependent contribution to the relative change in the shear modulus is approximately proportional to the temperature). At higher temperatures, the amplitude-dependent contribution to the relative change in the shear modulus increases drastically. After cooling to room temperature, the amplitude dependences of the amplitude-dependent contributions to both the damping decrement and the relative change in the shear modulus, as a rule, coincide with (or lie slightly below) the dependences measured prior to annealing. Therefore, we can assume that the amplitude-dependent contributions of these quantities are reversible (at least, upon annealing at temperatures below 600–640 K). In order to verify this assumption, we investigated the influence of the strain amplitude on the damping decrement and the relative change in the shear modulus in the course of isothermal treatments. Figure 6 depicts the time dependences of the relative change in the shear modulus G/G_{in} (where G_{in} is the shear modulus of the alloy in the initial state at room temperature) for two temperatures of isothermal treatment. In the course of measurements, the strain amplitude was increased by one order of magnitude (from a minimum amplitude of 1×10^{-5} to a maximum amplitude of 1×10^{-4}). At both temperatures, the alloy underwent irreversible structural relaxation

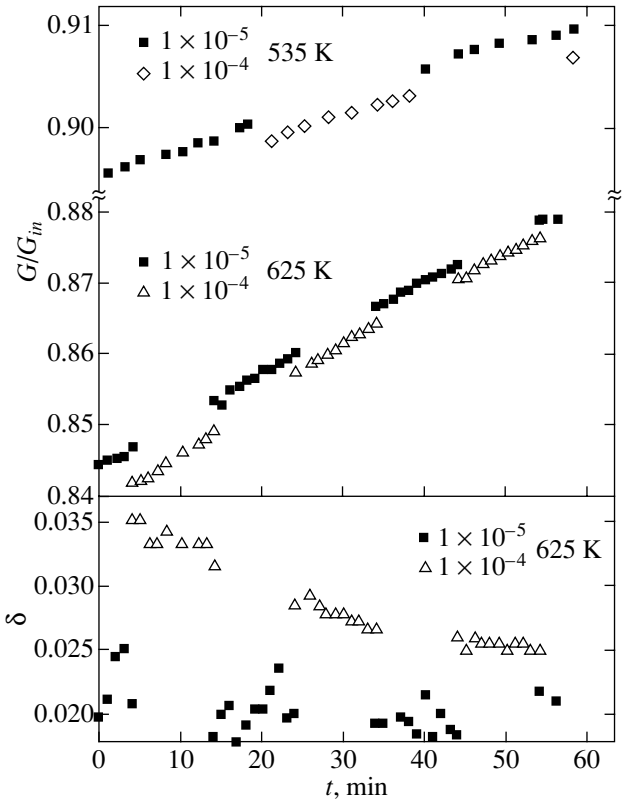

Fig. 6. Time dependences of the relative change in the shear modulus (at temperatures of 535 and 625 K) and of the damping decrement (at a temperature of 625 K) in the course of relaxation in the Zr–Cu–Ni–Al–Ti alloy for two acoustic strain amplitudes $\varepsilon = 1 \times 10^{-5}$ (closed squares) and 1×10^{-4} (open triangles and rhombuses).

(the shear modulus increased with time). As can be seen from Fig. 6, the strain amplitude has no effect on the relaxation process for all the temperatures used (after the reverse changeover from the large amplitude to the small amplitude, the time dependence of the relative change in the shear modulus follows the time dependence observed before the changeover to the large amplitude). It is worth noting that the relaxation process occurring at a lower temperature is not accompanied by a change in the amplitude-dependent contribution (the time dependences at small and large amplitudes are aligned parallel to each other). The same situation is observed at other temperatures below 600 K. Only at temperatures higher than 600 K is the relaxation process attended by a decrease in the amplitude-dependent contribution to both the damping decrement and the relative change in the shear modulus (Fig. 6).

Thus, we can draw the conclusion that the irreversible relaxation of the amplitude-dependent contribution begins only at temperatures above 600 K; i.e., it is characterized by activation energies that are substantially higher than those for relaxation of the amplitude-independent contributions to the damping decrement and the shear modulus. This implies that the structural units responsible for the amplitude-dependent internal friction in a bulk metallic glass, most likely, differ from the relaxation centers associated with the irreversible relaxation of the amplitude-independent contributions to the damping decrement and the shear modulus.

ACKNOWLEDGMENTS

This work was supported by the US Civilian Research and Development Foundation for the Independent States of the Former Soviet Union (grant no. RP1-2320-VO-02) and the Ministry of Industry and Science of the Russian Federation (project no. NSh-2169.2003.2).

REFERENCES

1. W. L. Johnson, MRS Bull. **24**, 42 (1999).
2. A. Inoue, Acta Mater. **48**, 279 (2000).
3. N. P. Kobelev, E. L. Kolyvanov, and V. A. Khonik, Fiz. Tverd. Tela (St. Petersburg) **45** (12), 2124 (2003) [Phys. Solid State **45**, 2225 (2003)].
4. N. P. Kobelev, E. L. Kolyvanov, and V. A. Khonik, Vest. Tambov. Univ. **8** (4), 545 (2003).
5. A. E. Berlev, O. P. Bobrov, V. A. Khonik, K. Csach, A. Juríková, J. Mi¡kuf, H. Neuhäuser, and M. Yu. Yazvitsky, Phys. Rev. B **68**, 132303 (2003).
6. V. A. Khonik, Phys. Status Solidi A **177**, 173 (2000).
7. V. A. Khonik, K. Kitagawa, and H. Morii, J. Appl. Phys. **87** (12), 8440 (2000).
8. Yu. V. Fursova and V. A. Khonik, Philos. Mag. Lett. **82** (10), 567 (2002).

Translated by O. Borovik-Romanova

Physics of the Solid State, Vol. 47, No. 3, 2005, pp. 416–423. Translated from Fizika Tverdogo Tela, Vol. 47, No. 3, 2005, pp. 404–411.

METALS AND SUPERCONDUCTORS

Low-Temperature Thermal Conductivity of Tellurium-Doped Bismuth

N. A. Red'ko, V. D. Kagan, and N. A. Rodionov

Ioffe Physicotechnical Institute, Russian Academy of Sciences, Politekhnicheskaya ul. 26, St. Petersburg, 194021 Russia
e-mail: nikolaj.a.redko@mail.ioffe.ru

Received July 12, 2004

Abstract—Phonon thermal conductivities κ_{22} ($\nabla T \parallel C_1$) and κ_{33} ($\nabla T \parallel C_3$) of tellurium-doped bismuth with an electron concentration in the range $1.8 \times 10^{19} \le n_L \le 1.4 \times 10^{20}$ cm^{-3} were studied in the temperature interval $2 < T < 300$ K. The temperature dependence of the phonon thermal conductivity obtained on doped bismuth samples of both orientations exhibits two maxima, one at a low temperature and the other at a high temperature. The effect of various phonon relaxation mechanisms on the dependence of both phonon thermal conductivity maxima on temperature, impurity concentration, and electron density is studied. © *2005 Pleiades Publishing, Inc.*

1. INTRODUCTION

In bismuth, which is a compensated semimetal, heat is transported by phonons, as well as by electrons and holes with concentration $n = p = 3 \times 10^{17}$ cm^{-3}. The electronic component of the thermal conductivity of bismuth, κ_e, in the temperature interval 1–20 K is small as compared to the phonon component, κ_{ph}. Only one bismuth isotope occurs in nature; therefore, with no isotopic scattering present, phonons scatter only from one another as a result of lattice vibration anharmonicity. At low temperatures, boundary scattering of phonons is also of importance. The temperature dependence of the thermal conductivity of pure bismuth exhibits a maximum at $T_{max} \cong 3.5$ K. At temperatures above this maximum, Umklapp (U) processes are responsible for the bismuth thermal conductivity exhibiting exponential behavior [1]. By approximating the phonon thermal conductivity with a simple relation $\kappa = (1/3)Csl$, we can assume the exponential growth of thermal conductivity with decreasing temperature to be due to the exponential increase in the phonon mean free path ($l \sim e^{\Theta/bT}$). Here, $\Theta \cong 120$ K is the Debye temperature, C is the phonon specific heat, and s is the velocity of sound for bismuth. Below $T = 15$ K, the phonon mean free path grows exponentially only until it becomes equal to the transverse dimension of the sample. Boundary scattering of phonons sets a limit on the growth of the phonon mean free path length, with a maximum appearing in the temperature dependence of the thermal conductivity at $T = 3.5$ K. A further decrease in temperature brings about a decrease in the thermal conductivity, which scales with temperature as does the phonon specific heat, $C \sim T^3$. This fast decrease in the phonon thermal conductivity of bismuth with decreasing temperature brings it close in magnitude to the electronic component of thermal conductivity for $T < 1$ K, and then, at $T \cong 0.2$ K, κ_e becomes larger than κ_{ph} [2].

As already mentioned, the phonon component of bismuth thermal conductivity falls off exponentially above the temperature of the maximum. As a result, at temperatures above $T = 20$ K, the phonon component of thermal conductivity is complemented by the electronic component, which grows with increasing temperature, and at $T \ge 100$ K the two components of bismuth thermal conductivity become equal [3].

Doping bismuth with the tellurium donor impurity gives rise to a growth in the electron density from 3×10^{17} to ~1×10^{20} cm^{-3}. As a result, the phonon component of thermal conductivity in doped bismuth decreases due to phonons being scattered from the electrons and the dopant [4, 5]. The temperature dependence of the phonon component of thermal conductivity of doped bismuth with an electron density in the range $1.8 \times 10^{19} \le n_L < 1 \times 10^{20}$ cm^{-3} revealed two maxima, whose origin has remained undetermined [5]. This communication reports on a study of the effects various phonon relaxation mechanisms exert on the dependences of both maxima in the phonon component of thermal conductivity on temperature, impurity concentration, and electron density.

2. SAMPLES AND EXPERIMENTAL TECHNIQUES

The temperature dependences of thermal conductivity and electrical resistivity were studied on single-crystal samples of bismuth doped with the tellurium donor impurity. The impurity electron concentration in doped bismuth ranged from 1.8×10^{19} to 1.4×10^{20} cm^{-3}.

1063-7834/05/4703-0416$26.00

Table 1. Parameters of doped bismuth samples: electron density n_L, Fermi electron energy ε_F, Debye electron temperatures $\Theta_{e\perp}$ and $\Theta_{e\parallel}$, and main maximum temperature T_{max} for phonon thermal conductivity κ_{22} and κ_{33}

No.	n_L, 10^{19} cm^{-3}	ε_F, meV	$\Theta_{e\perp}$, K	$\Theta_{e\parallel}$, K	$T_{max}(\kappa_{22})$, K	$T_{max}(\kappa_{33})$, K
1	1.8	133.6	5	59	5.5	5.6
2	5.3	193.4	7	84	8	7
3	7	212.6	7.7	93	8.4	8
4	11	248.6	9	108	10.8	9.3
5	14	270	10	117	11.8	13

The samples were spark eroded from the central part of a single-crystal ingot grown by horizontal zone leveling. The samples were rectangular parallelepipeds measuring $2.5 \times 2.5 \times 30$ mm, and their faces were perpendicular to the C_1, C_2, and C_3 crystallographic axes, respectively. The largest dimension of a sample coincided with either the bisector axis C_1 or the trigonal C_3 axis. The samples were etched in a C_2H_5OH–HNO_3 (1 : 1) solution. The main parameters of the samples are listed in Table 1.

A sample with heaters attached to its end faces was soldered to the bottom of a vacuum chamber (18 mm in diameter) immersed in a thermostatting liquid (helium, hydrogen, or nitrogen). The heater near the chamber bottom served to maintain the average temperature, while the heater at the other end of the sample produced a temperature gradient along the sample. The temperature was measured at two cross sections of the sample spaced $l_T \cong 15$ mm apart under a constant heat flux with carbon resistance thermometers in the temperature interval $1.5 < T < 40$ K and with copper–constantan thermocouples in the range $30 < T < 80$ K.

3. EXPERIMENTAL RESULTS

Thermal conductivity measurements were conducted on single-crystal tellurium-doped bismuth samples, with the heat flux propagating along the bisector or trigonal axis, which corresponds to the κ_{22} ($\nabla T \parallel C_1$) or κ_{33} ($\nabla T \parallel C_3$) thermal conductivity components. The phonon thermal conductivity component was isolated by suppressing the electronic component in a classically strong magnetic field. According to our data and the data from [4, 5], an increase in the bismuth electron concentration from 3×10^{17} to 1.4×10^{20} cm^{-3} due to tellurium doping causes the maximum thermal conductivity to decrease by ~100 times, but the electronic component of bismuth thermal conductivity remains small as compared to the phonon component, just as in pure bismuth. The phonon thermal conductivity component, as in pure bismuth, is dominant in the temperature interval 2–20 K. The electronic component of thermal conductivity in doped bismuth is small due to the mobility of electrons decreasing as a result of their scattering from the ionized tellurium impurity. Indeed, the increase in the electron concentration by nearly three orders of magnitude under bismuth doping brought about a decrease in the low-temperature electrical resistivity by a factor of approximately 100 as compared to the resistivity of pure bismuth.

The temperature dependences of the phonon thermal conductivities κ_{22} and κ_{33} of bismuth samples doped by tellurium to electron concentrations in the range $1.8 \times 10^{19} \le n_L \le 1.4 \times 10^{20}$ cm^{-3} are shown in Figs. 1 and 2, respectively. The temperature depen-

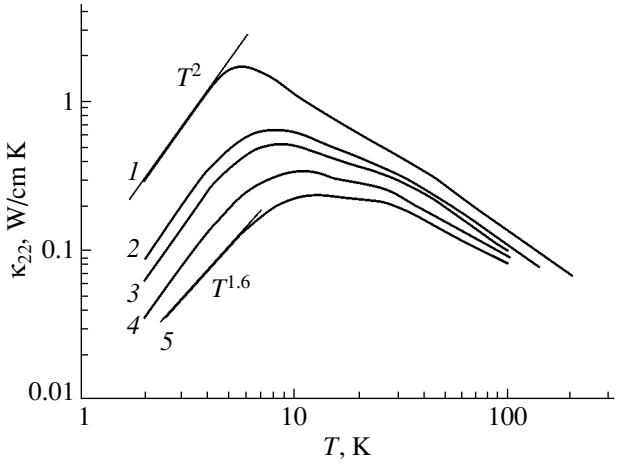

Fig. 1. Temperature dependence of the phonon thermal conductivity κ_{22} ($\nabla T \parallel C_1$) for tellurium-doped bismuth samples with various electron concentrations: (*1*) 1.8×10^{19}, (*2*) 5.3×10^{19}, (*3*) 7×10^{19}, (*4*) 1.1×10^{20}, and (*5*) 1.4×10^{20} cm^{-3}.

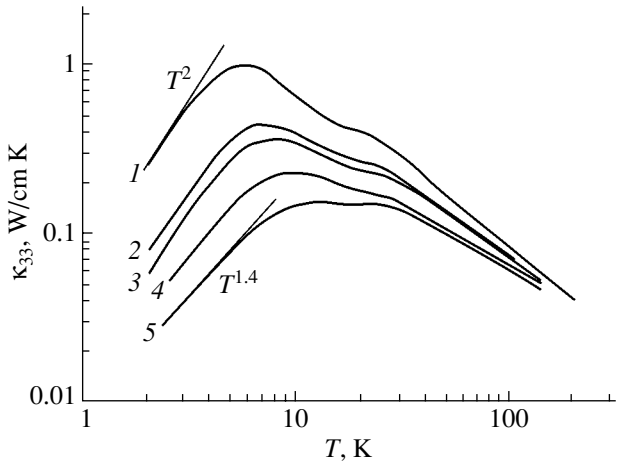

Fig. 2. Temperature dependences of the phonon thermal conductivity κ_{33} ($\nabla T \parallel C_3$) for tellurium-doped bismuth samples with various electron concentrations: (*1*) 1.8×10^{19}, (*2*) 5.3×10^{19}, (*3*) 7×10^{19}, (*4*) 1.1×10^{20}, and (*5*) 1.4×10^{20} cm^{-3}.

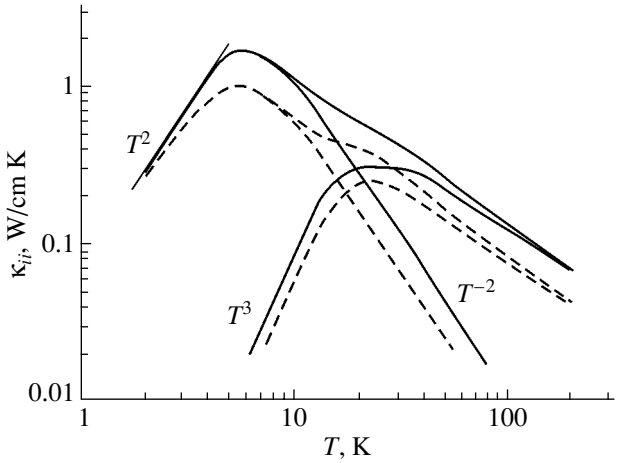

Fig. 3. Temperature dependences of the phonon thermal conductivity κ_{22} (solid lines) and κ_{33} (dashed lines) with isolated first and second maxima obtained on a tellurium-doped bismuth sample with an electron concentration $n_L = 1.8 \times 10^{19}$ cm^{-3}.

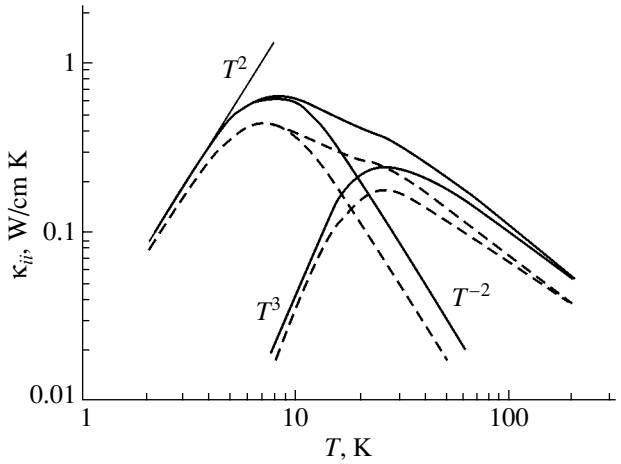

Fig. 4. Temperature dependences of the phonon thermal conductivity κ_{22} (solid lines) and κ_{33} (dashed lines) with isolated first and second maxima obtained on a tellurium-doped bismuth sample with an electron concentration $n_L = 5.3 \times 10^{19}$ cm^{-3}.

dence of the phonon thermal conductivity of all doped bismuth samples exhibits two maxima, one of which is observed at a low temperature (and will be referred to as the main or first maximum) and the other at a high temperature (referred to as the second maximum). The amplitude of the main maximum of the phonon thermal conductivity decreases with increasing electron concentration in doped bismuth samples of both orientations as approximately the inverse of electron concentration ($\kappa_{ii(\max)} \sim n_L^{-1}$). This concentration dependence of the phonon thermal conductivity suggests strong phonon–electron scattering. This conclusion is supported by the fact that the phonon thermal conductivity obeys a quadratic temperature dependence [$\kappa_{ii}(T) \sim T^2$] below the temperature of the maximum. Note that the phonon specific heat in bismuth scales for $T < 15$ K as $C \sim T^3$ [6], which, according to [7], is also one of the conditions for the $\kappa_{ii} \sim T^2$ relation to hold. All these data argue for the main maximum in the phonon thermal conductivity being due primarily to scattering of thermal phonons from electrons for $T < T_{\max}$ and to phonon scattering from phonons and impurities for $T > T_{\max}$.

The comparatively small electron Fermi momentum in pure and doped bismuth suggests that, according to the energy and momentum conservation laws, the L electrons of bismuth, in contrast to the case of metals, do not interact with all acoustic phonons. It turns out that electrons in bismuth interact only with the phonons for which the following condition is met (with due account of the dispersion law for the L electrons) [8]:

$$\frac{\hbar^2 q_1^2}{m_1} + \frac{\hbar^2 q_2^2}{m_2} + \frac{\hbar^2 q_3^2}{m_3} \le 8\zeta\left(1 + \frac{\zeta}{\mathscr{E}_g}\right). \qquad (1)$$

Here, ζ is the electron chemical potential of the samples studied, $\mathscr{E}_g$ is the energy band gap, m_i are the effective electron masses in the ellipsoids, and q_i are the momenta of the phonons interacting with electrons.

By approximating the electron Fermi surface of bismuth by ellipsoids of revolution with effective masses $m_1 \cong m_3$ and m_2, we can restrict ourselves, when using Eq. (1), to two different electronic Debye temperatures $\Theta_{1e} = s[8m_1\zeta(1 + \zeta/\mathscr{E}_g)]^{1/2}/k$ and $\Theta_{2e} = s[8m_2\zeta(1 + \zeta/\mathscr{E}_g)]^{1/2}/k$ [8]. With this simplified anisotropic electronic spectrum, we obtain for pure bismuth $\Theta_{1e} \cong 1$ K and $\Theta_{2e} \cong 15$ K. The values of Θ_{ie} for the doped bismuth samples are listed in Table 1. Calculations showed that the lowest electronic Debye temperature Θ_{1e} approximately coincides with the temperature of the main maximum in the phonon thermal conductivity (see Table 1). This implies that, below this temperature, all phonons interact with electrons. At temperatures below that of the second maximum in the phonon thermal conductivity, there is a small number of phonons capable of interacting with electrons. One may therefore safely assume that the second maximum in the phonon thermal conductivity derives primarily from phonon scattering on the sample boundaries at $T < T_{2\max}$ and from phonon scattering by phonons and impurities above the temperature of the second maximum. It is these considerations that are used to isolate both maxima from the temperature dependence of the phonon thermal conductivity for samples with different electron concentrations (Figs. 3–7). In this approach, we assume that certain acoustic branches of bismuth (quasi-longitudinal or quasi-transverse) are responsible for the first maximum in the phonon thermal conductivity and the others, for the formation of the second maximum.

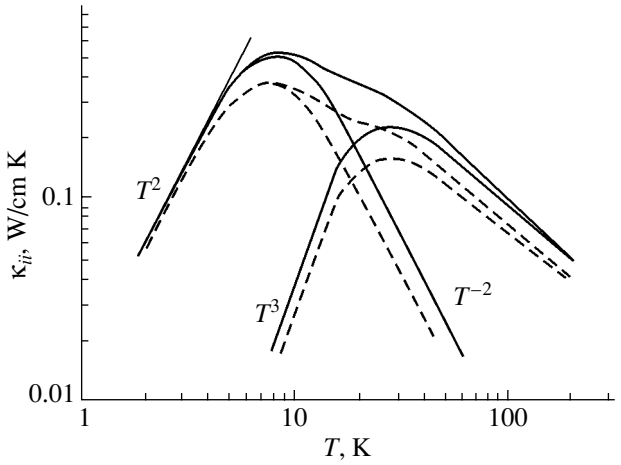

Fig. 5. Temperature dependences of the phonon thermal conductivity κ_{22} (solid lines) and κ_{33} (dashed lines) with isolated first and second maxima obtained on a tellurium-doped bismuth sample with an electron concentration $n_L = 7 \times 10^{19}$ cm^{-3}.

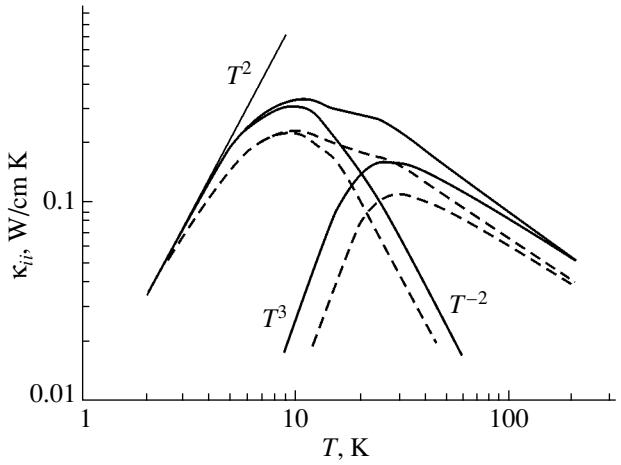

Fig. 6. Temperature dependences of the phonon thermal conductivity κ_{22} (solid lines) and κ_{33} (dashed lines) with isolated first and second maxima obtained on a tellurium-doped bismuth sample with an electron concentration $n_L = 1.1 \times 10^{20}$ cm^{-3}.

These maxima in the phonon thermal conductivity exhibit the following concentration dependence. As the electron concentration increases to 7×10^{19} cm^{-3}, the phonon thermal conductivity at the main maximum falls off as $\kappa_{ii(1\max)} \sim n_L^{-0.9}$. A further increase in electron concentration above $n_L > 7 \times 10^{19}$ cm^{-3} brings about a faster decrease in the phonon thermal conductivity at the maximum ($\kappa_{22(1\max)} \sim n_L^{-1.4}$, $\kappa_{33(1\max)} \sim n_L^{-2}$). The amplitude of the second maximum of the phonon thermal conductivity decreases with increasing electron concentration in doped bismuth in the same way for samples of both orientations, $\kappa_{ii(2\max)} \sim n_L^{-1/2}$. Note that the temperature of the main maximum in the phonon thermal conductivity shifts toward higher temperatures with increasing electron concentration in doped bismuth samples as $T_{1\max(\kappa)} \sim n_L^{1/3}$. The temperature of the second maximum shifts only slightly with increasing electron concentration.

The experimental dependence of the phonon thermal conductivity on temperature deviates from the quadratic course at temperatures below $T_{1\max}$ for doped bismuth samples with electron concentrations in excess of 7×10^{19} cm^{-3}. Heavy doping of bismuth with tellurium for $n_L > 7 \times 10^{19}$ cm^{-3} apparently results in the formation of defects and dislocations in a sample. This may account for the decreased exponent $m < 2$ of the temperature dependence of the phonon thermal conductivity.

Next, we analyze our experimental data on the phonon thermal conductivity obtained on samples of doped bismuth.

4. THEORETICAL ANALYSIS OF THE EXPERIMENTAL DATA

By solving the kinetic equation for the phonon distribution function, one can determine the phonon thermal conductivity

$$\kappa_{ik} = \sum_s \int \frac{d\mathbf{q}}{(2\pi)^3} \hbar \omega_{\mathbf{q}}^{(s)} v_i^{(s)} v_k^{(s)} \tau_{\text{ph}}(q) \frac{\partial N_0}{\partial T}, \qquad (2)$$

where $\mathbf{q}$ is the phonon wave vector, $\omega_{\mathbf{q}}^{(s)}$ is the phonon frequency of the sth branch, $\mathbf{v}^{(s)} = \partial\omega_{\mathbf{q}}^{(s)}/\partial\mathbf{q}$ is the

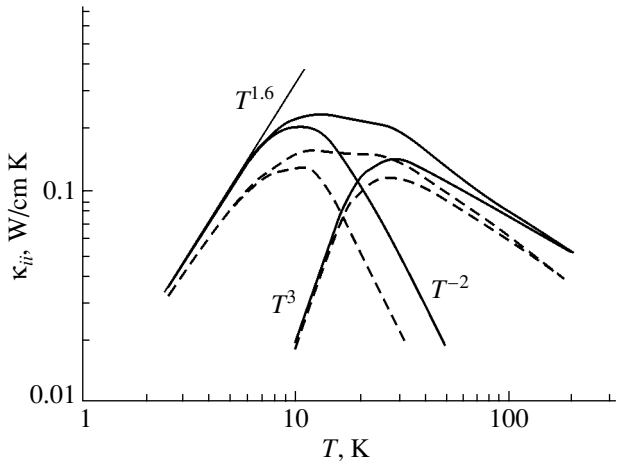

Fig. 7. Temperature dependences of the phonon thermal conductivity κ_{22} (solid lines) and κ_{33} (dashed lines) with isolated first and second maxima obtained on a tellurium-doped bismuth sample with an electron concentration $n_L = 1.4 \times 10^{20}$ cm^{-3}.

phonon velocity vector, $N_0 = [\exp(\hbar\omega_{\mathbf{q}}^{(s)}/kT) - 1]^{-1}$ is Planck's equilibrium distribution function, and $\tau_{ph}(q)$ is the total phonon relaxation time. At low temperatures, we take into account only the contribution of the three acoustic branches, for which the frequencies corresponding to wave vectors far less than the limiting values are small and therefore depend linearly on the wave vector. Integration over the phonon frequency for each branch is limited by a finite quantity called the Debye phonon frequency ω_D. The Debye temperature of a phonon branch is $\Theta = \hbar\omega_D/k$. In this way, the presence of limiting wave vectors at the Brillouin zone edge of the crystal is taken into account. For temperatures much lower than the Debye temperature, this limitation can be disregarded and extend integration to infinity.

The total phonon relaxation time includes all possible relaxation mechanisms, namely, phonon scattering from impurities and electrons, phonon–phonon scattering, and scattering of phonons from the sample boundaries:

$$\frac{1}{\tau_{ph}(q)} = \frac{1}{\tau_{ph-im}(q)} + \frac{1}{\tau_{ph-e}(q)} + \frac{1}{\tau_{ph-ph}(q)} + \frac{1}{\tau_{ph-b}(q)}. \quad (3)$$

In the phonon–phonon scattering, only normal processes are included. We disregard Umklapp processes, which are essential only in pure bismuth. Since normal processes conserve the total momentum of the phonon system, this factor must be taken into account by introducing an additional term into Eq. (2) (see [9, Eq. (6.1)]). Inclusion of the second term into Eq. (2), while not involving any change in the temperature and concentration dependences of the thermal conductivity, improves the accuracy of determination of the numerical value of κ_{ik}.

According to Eq. (2), the quantity $\tau_{ph}(q)$ undergoes averaging, so the numerical value of the integral is determined by the thermal wave vectors $q_T \cong 3kT/\hbar\bar{v}^{(s)}$, where $\bar{v}^{(s)}$ is the average phonon velocity for the *s*th branch. The wave-vector dependences of different phonon relaxation mechanisms result in different temperature dependences. As a result of averaging, the phonon relaxation times can be recast as

$$\frac{1}{\tau_{ph-im}} = a_1T^4, \quad \ldots\frac{1}{\tau_{ph-ph}} = a_2T^5;$$
$$\ldots\frac{1}{\tau_{ph-e}} = a_3T; \quad \ldots\frac{1}{\tau_{ph-b}} = \frac{\bar{v}^{(s)}}{L}, \quad (4)$$

where L is the smallest sample dimension. Taking these phonon relaxation mechanisms into account, one can write the temperature dependence of the phonon thermal conductivity in the form

$$\kappa = \frac{a_0T^3}{a_1T^4 + a_2T^5 + a_3T + a_4}, \quad (5)$$

where factor T^3 derives from integration over the magnitude of wave vectors in Eq. (2) and reflects the temperature dependence of the phonon specific heat.

In the low-temperature domain, the temperature dependence of the phonon thermal conductivity of doped bismuth exhibits a maximum (Figs. 1, 2). It appears as a result of interplay between the counteracting trends introduced by the different phonon relaxation mechanisms into the temperature dependence of thermal conductivity in Eq. (5). In pure bismuth, these mechanisms are boundary scattering at temperatures below the temperature of the maximum in thermal conductivity and Umklapp processes above this temperature. Phonon Umklapp processes in pure bismuth bring about an exponential growth in thermal conductivity with a decrease in temperature and account for the sharpness of its peak.

In doped bismuth, the contributions from phonon scattering are power-law functions of temperature and the maximum is not as steep. Equations (4) and (5) define the following simple rule for the temperature dependence of the thermal conductivity on both sides of the maximum. The increase (decrease) in thermal conductivity in Eq. (5) with an increase in temperature is associated with those phonon relaxation processes for which the power of temperature in Eqs. (4) is less than or greater than three, respectively. As a result, a maximum in the thermal conductivity arises at the temperature at which the variations due to different phonon relaxation mechanisms cancel each other. The external parameters (sample size, impurity and electron concentrations, etc.) governing the phonon relaxation mechanisms influence the characteristics of the maximum in the temperature dependence of the thermal conductivity. Investigating the dependence of the temperature of the maximum in the phonon thermal conductivity and of its amplitude on the sample dimensions, impurity concentration, and electron density offers the possibility of understanding the contributions provided by each of the phonon relaxation mechanisms to the phonon thermal conductivity.

Determination of the concentration dependence of the thermal conductivity for doped bismuth is complicated by the fact that phonons are scattered from the same tellurium donor impurities that donate electrons to the L band. In the doped bismuth samples used in this investigation, the concentration of electrons can be assumed to coincide with that of impurities, because the electron concentration in the samples exceeds the intrinsic value (i.e., the original electron concentration $n_0 = 3 \times 10^{17}$ cm^{-3} in the L band of pure bismuth) by two orders of magnitude.

As seen from Eq. (4), the phonon–impurity and phonon–electron relaxation times depend on the impurity concentration c. Since phonon scattering from impurities is proportional to the impurity concentration, the constant a_1 is proportional to c. Phonon–electron scattering depends on electron concentration only

in the nonparabolic approximation, so the constant a_3 is proportional to $(1 + 2\zeta/E_{g\mathrm{L}})^2$ [10], where ζ is the chemical potential of electrons in the L_s band and $E_{g\mathrm{L}}$ is the energy gap between the L_a and L_s bismuth bands. The relation between the electron concentration in the three ellipsoids of the L_s band of doped bismuth and the chemical potential can be expressed in the form [8]

$$n_0 + c = \frac{\sqrt{m_1 m_2 m_3}}{\pi^2 \hbar^3}(2\zeta)^{3/2}\left(1 + \frac{\zeta}{E_{g\mathrm{L}}}\right)^{3/2}, \qquad (6)$$

where m_i are the effective electron masses at the bottom of the L_s conduction band. The L band of bismuth is known to be strongly nonparabolic, so $\zeta/E_g \gg 1$. Neglecting the small initial electron concentration n_0 in bismuth in comparison with the high electron concentration in the doped bismuth samples studied, we obtain the following concentration dependence for the phonon relaxation time due to phonons scattering from electrons: $1/\tau_{\mathrm{ph-e}} \sim c^{2/3}$.

Simple concentration dependences of $T_{\max}$ and $\kappa_{\max}$ can be obtained in the cases where the phonon scattering mechanisms for which the power of the temperature is higher than three are dominated by phonon–impurity or phonon–phonon scattering and the phonon scattering mechanisms for which the power of the temperature is less than three are dominated by phonon–electron and phonon–boundary scattering. Theoretical estimates of $T_{\max}(c)$ and $\kappa_{\max}(c)$ made for doped bismuth samples with different combinations of phonon relaxation mechanisms are listed in Table 2. Only the fourth row of Table 2 is seen to fit our experimental data qualitatively, because in this case the amplitude of the thermal conductivity maximum decreases and the temperature of the maximum increases with increasing concentration. However, the power-law concentration dependences of these quantities are substantially weaker than those observed in the experiment.

Note the following very essential feature of phonon relaxation due to the interaction with degenerate electrons, because of which the relation for $1/\tau_{\mathrm{ph-e}}$ in Eq. (4) is valid only for temperatures lower than the electronic Debye temperature $\Theta_{\mathrm{e}} = (2\bar{v}p_{\mathrm{F}})/k$, where p_{F} is the Fermi electron momentum and $\bar{v}$ is the average phonon velocity. In an elementary event of phonon emission or absorption by an electron, energy and momentum are conserved [10]. The velocity of a phonon is much less than that of an electron, and the energy of a phonon is much less than that of an electron and can be neglected. In these conditions, an elementary scattering event for degenerate electrons with an isotropic energy spectrum reduces to an electron transfer from one point to another on the Fermi sphere, with the distance between these two points being equal to the phonon momentum. If the phonon momentum exceeds the diameter of the Fermi sphere, elementary events of emission or absorption of a phonon by an electron are impossible [11]. This analysis can be generalized to the case of a Fermi surface with an anisotropic (including ellipsoidal) electron spectrum, as is the case with bismuth. Therefore, for $q > 2p_{\mathrm{F}}$, phonons can no longer scatter off electrons of doped bismuth and we have

$$\frac{1}{\tau_{\mathrm{ph-e}}} = 0. \qquad (7)$$

In the earlier consideration, we neglected this sharp dependence of the electron–phonon relaxation. Nevertheless, our analysis remains valid as long as the temperatures, including the temperature of the maximum, are much lower than Θ_{e} (see Table 1). Therefore, Eq. (5) also holds for temperatures substantially lower than Θ_{e}.

If the relative magnitude of the scattering parameters is such that the estimated value $\check{T}_{\max}$ is greater than Θ_{e}, the temperature dependence of the phonon thermal conductivity determined above turns out to be incorrect. Indeed, there was assumed to be phonon–electron scattering at temperatures above Θ_{e} following Eq. (4). In actual fact, as seen from Eq. (7), there is no phonon–electron scattering at these temperatures. The only process remaining is phonon–phonon scattering, for which the phonon thermal conductivity is given by

$$\kappa = \frac{a_0}{a_2 T^2}. \qquad (8)$$

There is no maximum at $T = \check{T}_{\max}$, and the phonon thermal conductivity varies according to Eq. (8) as the temperature decreases to Θ_{e}. Below this temperature, the phonon–electron scattering becomes significant. As a result, the increase in the phonon thermal conductivity is replaced by a fairly steep falloff. Thus, in actual fact, $T_{\max}$ is of the order of Θ_{e}, i.e., of the order of $p_{\mathrm{F}} \sim c^{1/3}$, and the phonon thermal conductivity at the maximum turns out to scale as

$$\kappa_{\max} \approx \frac{a_0}{a_2 \Theta_{\mathrm{e}}^2} \sim c^{-2/3}. \qquad (9)$$

This consideration seems to suggest that the phonon thermal conductivity should decrease as soon as

Table 2. Theoretical estimates of the dependence of the temperature ($T_{\max}$) and amplitude ($\kappa_{\max}$) of the phonon thermal conductivity maximum on impurity concentration c in bismuth calculated for different phonon relaxation mechanisms characterized by relaxation time $\tau_{\mathrm{ph-i(j)}}$

No.	$\tau_{\mathrm{ph-i}}$	$\tau_{\mathrm{ph-j}}$	$T_{\max}(c)$	$\kappa_{\max}(c)$
1	$\tau_{\mathrm{ph-b}}$	$\tau_{\mathrm{ph-ph}}$	c^0	c^0
2	$\tau_{\mathrm{ph-b}}$	$\tau_{\mathrm{ph-im}}$	$c^{-1/4}$	$c^{-3/4}$
3	$\tau_{\mathrm{ph-e}}$	$\tau_{\mathrm{ph-im}}$	$c^{-1/9}$	$c^{-8/9}$
4	$\tau_{\mathrm{ph-e}}$	$\tau_{\mathrm{ph-ph}}$	$c^{1/6}$	$c^{-1/3}$

phonon–electron scattering becomes operative. However, taking into account the variation of the integrand in Eq. (2) smears this sharp temperature dependence and smoothes out the temperature maximum of the phonon thermal conductivity. The concentration dependence of Θ_{1e} for doped bismuth is close to that of the temperature of the first maximum in the phonon thermal conductivity. The behavior of the maximum in the phonon thermal conductivity following Eq. (9) is in qualitative agreement with the experimental data.

The presence of two maxima with a dip in between is an interesting feature of the temperature dependence of the phonon thermal conductivity. This dip is usually attributed to possible phonon resonant scattering from a system of impurity levels or localized vibrations [9]. No such levels have thus far been observed in the tellurium impurity, nor has anyone reported the appearance of localized vibrations in tellurium-doped bismuth. The temperature of the dip corresponds to energies that are small as compared to the energies of atomic levels and phonons with limiting momenta. One has, therefore, to look for another reason to account for the presence of two maxima in the temperature dependence of the phonon thermal conductivity.

Although Eq. (2) includes the three acoustic phonon branches, our subsequent consideration disregarded this point and was conducted as if the interaction constants in Eq. (5) were the same for the different branches, which is not the case. Equation (5) should actually have a sum of three terms of this kind, with different constants a_i for each phonon branch. Thus, the total phonon thermal conductivity represents, in actual fact, a sum of three functions whose maxima lie at different temperatures. If the two transverse branches have similar interaction constants, only two different terms will remain in the sum. Accordingly, one can in no case be sure that the total curve describing the phonon thermal conductivity will have only one maximum. One should rather expect the total phonon thermal conductivity curve to be double-humped, with a dip between the two maxima.

The first maximum in the phonon thermal conductivity is determined by the temperatures at which phonon–electron scattering is cut off (except for a small number of electrons with large momenta oriented along the ellipsoids, from which the contribution is small). Therefore, one can safely assume that phonon–electron scattering makes almost no contribution to the formation of the second maximum in the phonon thermal conductivity. To isolate the second maximum in the phonon thermal conductivity, we assume that the low-temperature dependence of the phonon thermal conductivity is determined by phonon scattering from boundaries, i.e., $\kappa_{ii} \sim T^3$. The amplitude of the second maximum substantially depends on the impurity concentration; therefore, phonon–impurity and phonon–boundary scattering contribute to its formation. The dependences of both the temperature and the amplitude of the maximum in the phonon thermal conductivity on the electron (impurity) concentration for these types of phonon scattering are listed in Table 2 (second row). The absence of experimental support for the relations presented in Table 2 is possibly due to their being power-law concentration dependences with a small exponent. An argument for the above explanation of the nature of the second maximum in the phonon thermal conductivity could be given, however, by experimental observation of its dependence on the transverse dimensions of a sample.

Experiments conducted on doped bismuth samples with electron concentrations above 7×10^{19} cm^{-3} revealed the existence of regions intermediate between the quadratic and linear behavior in the temperature dependence of the phonon thermal conductivity for $T < T_{1\max}$ (Figs. 1, 2, 6, 7). Heavy doping of bismuth with tellurium to electron concentrations in excess of 7×10^{19} cm^{-3} initiates the formation of defects and dislocations in a sample. Therefore, in the case of heavily doped bismuth, we should add phonon scattering from dislocations to the above-mentioned mechanisms. Scattering of phonons from dislocations [9] is usually assumed to coincide in its dependence on phonon frequency with the phonon–electron scattering.

For a more detailed review of phonon scattering from dislocations in semiconductors, the reader is referred to monograph [12]. Phonon scattering from one dislocation is the sum of two terms, one of which is governed by long-range forces and depends linearly on frequency and the other is due to short-range forces of the dislocation core and depends on the frequency squared. On averaging over the thermal distribution of phonons, these terms yield different temperature dependences:

$$\frac{1}{\tau_{\text{disl}}} = a_5 T + a_6 T^2. \tag{10}$$

This relation assumes the dislocations to be small as compared to the large distance separating them. The contribution from scattering of phonons by all dislocations in the crystal is equal to the contribution from phonon scattering on one dislocation multiplied by the number of dislocations. The second power of the temperature corresponds to the thermal phonon wave vector multiplied by the small size of the dislocation core, which is a small parameter. Therefore, the second term is usually dropped, after which Eq. (10) will coincide with the phonon–electron scattering relation in Eqs. (4).

The case of phonon scattering from large dislocations was treated in [12]. In this case, for short wavelengths smaller than a dislocation, the scattering determined by long-range forces is frequency-independent. The magnitude and temperature dependence of the first term in Eq. (10) depends on the product of the thermal phonon wave vector multiplied by the dislocation size.

As this product increases, the first term ceases to depend on temperature and decreases in magnitude [12].

In the case of a system of coupled dislocations, Eq. (10) has to be modified, because the long-range dislocation fields overlap and phonon scattering from them cannot be taken into account independently. It is difficult to calculate the first term, but we can estimate it by considering independent scattering of phonons from dislocations of a macroscopic size equal to the distance between the dislocation cores. Effectively, this increases the dimensions of the dislocations involved in the first term of Eq. (10), thus reducing this term.

As for the second term, it remains the same for a system of dislocations. A decrease in the first term changes the relative magnitude of the terms. For very low temperatures, the first term remains naturally larger than the second; in other words, phonon scattering from dislocations varies linearly with temperature. Note that monograph [12] reports on experiments that suggest a quadratic dependence of the phonon thermal conductivity on temperature; we believe, however, that those experiments were not given an adequate interpretation. We can assume that, at higher temperatures (but still below the temperature of the maximum in the phonon thermal conductivity), scattering from a system of dislocations is dominated by dislocation cores, to which the second term in Eq. (10) corresponds. This type of phonon scattering gives rise to a linear temperature dependence of the phonon thermal conductivity. It is a behavior close to this relation that is observed in phonon thermal conductivity experiments conducted on heavily tellurium-doped bismuth.

In concluding this section, we note that summation of the contributions due to the different phonon branches to the phonon thermal conductivity may provide a logical explanation for the existence of two maxima in the temperature dependence of the phonon thermal conductivity. Investigation of the variation in these maxima with impurity concentration offers the possibility of identifying the contributions from different phonon scattering mechanisms to the formation of these maxima. We should finally add that the theoretically predicted cutoff of phonon–electron scattering at the phonon momentum equal to twice the Fermi momentum has not been confirmed experimentally thus far. The above analysis suggests that this cutoff could determine the concentration dependence of the main temperature maximum in the phonon thermal conductivity. This may be considered an indirect argument for the existence of this feature of electron–phonon interaction.

The variation in the temperature dependence in question for bismuth samples doped heavily with tellurium is associated with the existence of a system of coupled dislocations and with the specific character of phonon scattering from this system. The temperature dependence of the phonon thermal conductivity suggests that phonons scatter on dislocation cores, whereas scattering caused by long-range forces turns out to be suppressed.

Thus, investigation of the temperature dependence of the phonon thermal conductivity at low temperatures permits one to obtain valuable information on the mechanisms of relaxation in a phonon system.

ACKNOWLEDGMENTS

This study was supported in part by the Foundation for Support of Leading Scientific Schools (project no. NSh-2200.2003.2).

REFERENCES

1. V. N. Kopylov and L. P. Mezhov-Deglin, Zh. Éksp. Teor. Fiz. **65** (8), 720 (1973) [Sov. Phys. JETP **38**, 357 (1973)].
2. W. P. Pratt and C. Uher, Phys. Lett. A **68** (1), 74 (1978).
3. C. Gallo, B. C. Chandrasekhar, and P. H. Sutter, J. Appl. Phys. **34** (1), 144 (1963).
4. M. E. Kuznetsov, V. S. Oskotskiĭ, V. I. Pol'shin, and S. S. Shalyt, Zh. Éksp. Teor. Fiz. **57** (10), 1112 (1969) [Sov. Phys. JETP **30**, 607 (1969)].
5. N. A. Red'ko, M. P. Boĭko, N. A. Rodionov, and V. I. Pol'shin, Fiz. Tverd. Tela (Leningrad) **29** (9), 2830 (1987) [Sov. Phys. Solid State **29**, 1627 (1987)].
6. T. C. Cetas, J. C. Holste, and C. A. Swenson, Phys. Rev. **182** (3), 679 (1969).
7. J. M. Ziman, *Electrons and Phonons* (Clarendon, Oxford, 1960; Inostrannaya Literatura, Moscow, 1962).
8. V. D. Kagan, N. A. Red'ko, N. A. Rodionov, V. I. Pol'shin, and O. V. Zotova, Fiz. Tverd. Tela (St. Petersburg) **46** (8), 1372 (2004) [Phys. Solid State **46**, 1410 (2004)].
9. R. Berman, *Thermal Conduction in Solids* (Clarendon, Oxford, 1976; Mir, Moscow, 1979).
10. N. A. Red'ko and V. D. Kagan, Fiz. Tverd. Tela (St. Petersburg) **36** (7), 1978 (1994) [Phys. Solid State **36**, 1081 (1994)].
11. A. A. Abrikosov, L. P. Gor'kov, and I. E. Dzyaloshinskiĭ, *Methods of Quantum Field Theory in Statistical Physics* (Fizmatgiz, Moscow, 1962; Prentice Hall, Englewood Cliffs, N.J., 1963).
12. B. M. Mogilevskiĭ and A. F. Chudnovskiĭ, *Thermal Conductivity of Semiconductors* (Nauka, Moscow, 1972) [in Russian].

Translated by G. Skrebtsov

Physics of the Solid State, Vol. 47, No. 3, 2005, pp. 424–428. Translated from Fizika Tverdogo Tela, Vol. 47, No. 3, 2005, pp. 412–416.

METALS AND SUPERCONDUCTORS

Praseodymium Valence State in $PrFe_{10}Mo_2$, $PrNi_5$, and $PrNi_4M$ Intermetallic Compounds (M = Cu, Al, Ga)

N. N. Efremova, E. V. Shcherbakova, A. G. Kuchin, L. D. Finkel'shtein, D. V. Vilisov, and A. S. Shkvarin

Institute of Metal Physics, Ural Division, Russian Academy of Sciences, ul. S. Kovalevskoĭ 18, Yekaterinburg, 620219 Russia
e-mail: scherbakova@imp.uran.ru

Received April 27, 2004; in final form, July 22, 2004

Abstract—X-ray L_3 absorption spectra of Pr and the crystallochemical characteristics of the $PrFe_{10}Mo_2$ and $PrNi_5$ intermetallic compounds have been studied. It has been shown for the first time that atoms of Pr, similar to those of Ce, can reside in a mixed valence state. The valency of praseodymium is $+3.08 \pm 0.03$ and $+3.10 \pm 0.03$ in $PrFe_{10}Mo_2$ and $PrNi_5$, respectively. The mixed valence state of Pr disappears when one Ni atom in $PrNi_5$ is replaced by Al or Ga. The nature of the quadrivalent state of Pr in intermetallic compounds is discussed.

1. INTRODUCTION

A characteristic feature of Ce and Pr is the instability of the 4*f* configuration, which may initiate electron fluctuations between two configurations with different numbers of *f* electrons, thus realizing a mixed valence state. The valency of Ce in R_xT_y intermetallic compounds (*R* stands here for a rare-earth element, and *T*, for a 3*d* transition element) was shown long ago by direct spectroscopic measurements to vary from +3.4 to +3.1 depending on the actual composition (see, e.g., [1]). The anomalies in the behavior of the magnetic and structural parameters with a variation in the atomic number *Z* of the rare-earth element in R_xT_y compounds observed for *R* = Ce [2, 3] are accounted for by cerium having mixed valency. There has been no success thus far, however, in revealing a mixed valence state in intermetallic compounds with praseodymium, although some authors [4] have invoked such concepts to interpret the magnetic properties of Pr compounds. We report here on a study of the Pr valency using x-ray L_3 absorption spectroscopy performed on the $PrFe_{10}Mo_2$, $PrNi_5$, and $PrNi_4M$ compounds, where M = Al, Cu, or Ga.

2. EXPERIMENTAL TECHNIQUES

$PrFe_{10}Mo_2$, $PrNi_5$, and $PrNi_4M$ alloys, with M = Cu, Ga, or Al, were prepared by rf melting in alundum crucibles in a pure argon environment. The $PrFe_{10}Mo_2$ alloy was subjected to homogenization annealing at 1100°C for two days, and the $PrNi_5$ and $PrNi_4M$ alloys, at 1000°C for eight days in vacuum with subsequent quenching in water. X-ray structural measurements showed the $PrFe_{10}Mo_2$ alloy to contain a compound with a $ThMn_{12}$-type tetragonal structure and a small amount of α-Fe (less than 2 wt %), while the $PrNi_5$ and $PrNi_4M$ alloys were single-phase and contained compounds with a $CaCu_5$-type hexagonal crystal structure.

The x-ray L_3 absorption spectra were measured with an ARS-KD-2 vacuum x-ray spectrometer equipped with a coordinate-sensitive detector. The analyzer was a $(10\bar{1}1)$-bent quartz single crystal with a radius of curvature of 1.940 m. The spectra were obtained in the second order of reflection with a linear dispersion of 15.8 eV/mm and $E/\Delta E \sim 8500$. The valence state was derived by traditional unfolding of a complex spectrum into a combination of Lorentzians and arctan functions to model the transition of the electron after absorption of an x-ray photon to bound and continuum states, respectively [1]. Spectra were measured three times on each sample. On account of the problem being ill posed, each spectrum was independently unfolded no less than three times. The areas bounded by the Lorentzians are proportional to the number of atoms in different valence states. The valence state of praseodymium was calculated from the relation

$$V_{\mathrm{Pr}} = 3 + S_{\mathrm{Pr}}^{+4}/(S_{\mathrm{Pr}}^{+3} + S_{\mathrm{Pr}}^{+4}),$$

where S_{Pr}^{+3} and S_{Pr}^{+4} are the areas under the Lorentzians modeling the signals from Pr^{+3} and Pr^{+4}, respectively.

3. EXPERIMENTAL RESULTS AND DISCUSSION

Figures 1 and 2 plot x-ray L_3 absorption spectra of praseodymium in $PrFe_{10}Mo_2$, $PrNi_5$, and $PrNi_4M$ and in reference compounds of trivalent praseodymium, Pr_2O_3 (peak *B*), and quadrivalent praseodymium, $Ce_2Pr_2O_8$ (peaks *C*, *D*, *E*), whose complex structure is similar in origin to that of the Ce^{+4} in CeO_2. The complex struc-

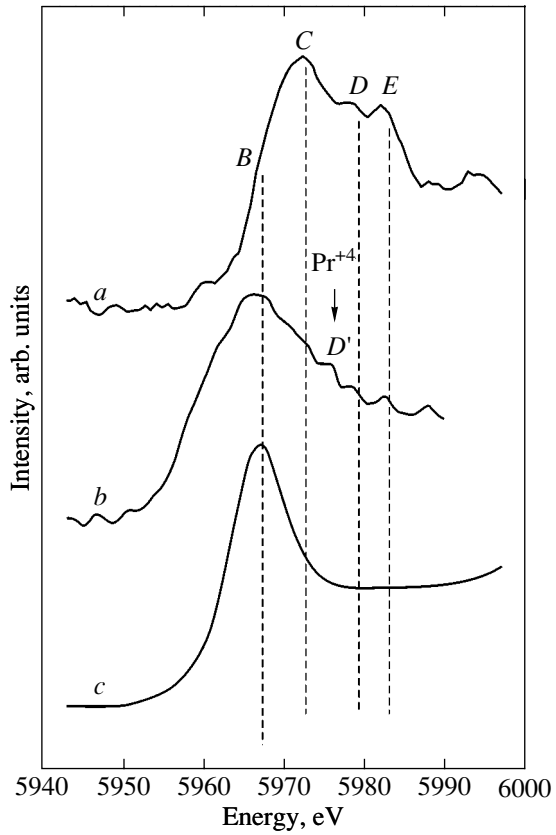

Fig. 1. X-ray L_3 absorption spectra of praseodymium measured in (*a*) $Ce_2Pr_2O_8$, (*b*) $PrFe_{10}Mo_2$, and (*c*) Pr_2O_3. Dashed lines identify the energy positions of the Pr^{+3} and Pr^{+4} peaks for the oxide compounds.

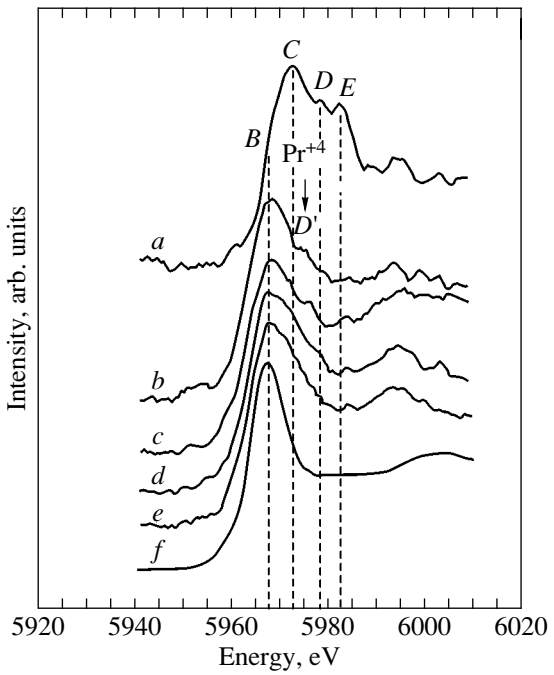

Fig. 2. X-ray L_3 absorption spectra of praseodymium measured in (*a*) $Ce_2Pr_2O_8$, (*b*) $PrNi_5$, (*c*) $PrNi_4Cu$, (*d*) $PrNi_4Al$, (*e*) $PrNi_4Ga$, and (*f*) Pr_2O_3. Dashed lines identify the energy positions of the Pr^{+3} and Pr^{+4} peaks for the oxide compounds.

ture of cerium L_3 absorption spectra has been repeatedly discussed in various approaches taking into account the variation in the character of the Ce 4*f*–O 2*p* interaction in the final state of the absorption process (see, e.g., [5–7]).

As follows from a comparison of the Pr L_3 absorption spectra obtained on the compounds under study and reference compounds, praseodymium is primarily trivalent in the compounds studied. In addition to the *C*, *D*, and *E* signals due to partial oxidation of praseodymium in the sample, however, one can clearly see a bend *D*' at a distance $\Delta E \sim 8$ eV from the *B* signal originating from Pr^{+3}. To reveal its nature, Fig. 3 presents L_3 absorption spectra of the rare-earth element in $CeNi_5$, where the cerium valency is $V_{Ce} = 3.23$ [8], and in $PrNi_5$ plotted in the same energy scale (matching was performed using the $R^{+3}L_3$ absorption maximum, whose position was taken as $E = 0$). We see that peak *D*' in the spectrum for $PrNi_5$ coincides in energy position with the peak *D*' in the $CeNi_5$ spectrum that is associated with Ce^{+4}. By analogy with $CeNi_5$, this peak may signify the presence of a small amount of Pr^{+4} in $PrNi_5$.

Deconvolution of the Pr L_3 absorption spectrum into constituents yielded a value of $+3.08 \pm 0.03$ for the praseodymium valency in $PrFe_{10}Mo_2$ and $V_{Pr} = +3.10 \pm 0.03$ in $PrNi_5$. As seen from Fig. 2, the intensity of peak *D*' in $PrNi_4Cu$ remains the same as in $PrNi_5$, i.e., $V_{Pr} = +3.10 \pm 0.03$, whereas in $PrNi_4Al$ and $PrNi_4Ga$ the *D*' peak is not seen at all, which means that the praseodymium valency here is close to three ($V_{Pr} = 3.00 \pm 0.03$). Note that the technique employed in the treatment of the spectra permits one to determine the valence state while neglecting the signals associated with sample oxidation, because these signals differ in energy position from the *B* and *D*' maxima by more than 2 eV.

Figures 4 and 5 plot the dependences of the lattice parameters on the atomic number *Z* of the rare-earth element for the compounds $RFe_{10}Mo_2$ [3, 9] and RNi_5 [2]. We see that these parameters deviate from the extrapolated values of $a(Z)$ and $c(Z)$ for the Ce compounds, which is usually associated with the presence of the Ce^{+4} ion. However, no noticeable deviations of the lattice parameters from the monotonic $a(Z)$ and $c(Z)$ relations are observed for Pr compounds.

In discussing the relation between the crystallochemical characteristics and the valency of *R* ions, we presume that, in addition to the main metallic bonding, there is an ionic covalent component of interatomic coupling in intermetallic compounds that is dependent on the actual relationship between the electronegativi-

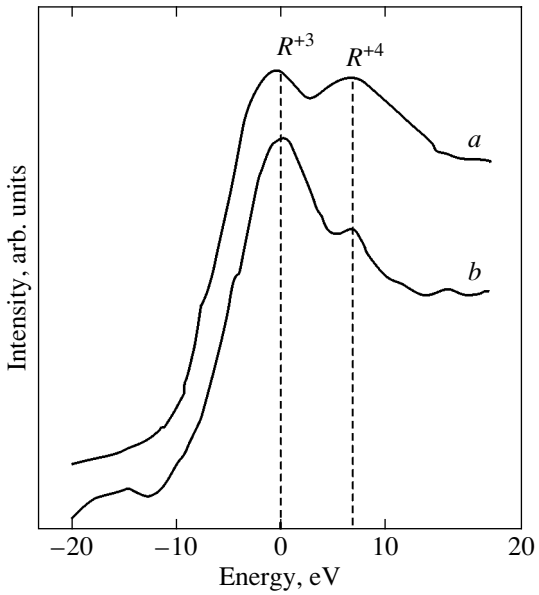

Fig. 3. X-ray L_3 absorption spectra of cerium and praseodymium measured in (*a*) $CeNi_5$ and (*b*) $PrNi_5$.

ties of the components and on the structural features of the compounds, such as different numbers of unlike neighbors and different lengths of the bonds they are connected by. In compounds with the same type of crystal structure, the lattice parameters decrease with increasing atomic number of the *R* element due to a decrease in the ionic radii (the so-called lanthanide compression).

Against the background of this pattern, which is typical of trivalent *R* elements, the ionic–covalent bond component in intermetallic compounds with valence-unstable Ce and Pr may increase due to the interatomic interaction involving not only the $5d^16s^2$ valence electrons, as is the case with the other *R* elements, but also the 4*f* electrons. It is known that Ce becomes quadrivalent in intermetallic compounds only in the presence of *nd* elements in the middle and at the end of the transition period. This suggests that the reason for the involvement of 4*f* electrons in chemical bonding should be searched for in the acceptor property of the unfilled *d* shell. Therefore, the number of *nd* ions in the immediate environment of the *R* ion with an unstable 4*f* configuration and their proximity to the *R* ion play a decisive part in the formation of the mixed valence state in an *R* ion and in the appearance of lattice parameter deviations toward smaller values (negative deviations) as a result of the ionic radius of R^{+4} being smaller than that of R^{+3}.

With these concepts in mind, we turn to an analysis of the dependence of the lattice parameters on the atomic number of the rare-earth element for the chosen compounds. As seen from Fig. 4, the parameter *c* of the $RFe_{10}Mo_2$ compounds with a $ThMn_{12}$-type tetragonal structure (Fig. 6) is only weakly dependent on the atomic number of the *R* element, a behavior resembling that of atomic radii, whereas the parameter *a* depends strongly on *Z*, a feature characteristic of ionic radii. This suggests that the ionic–covalent bond between *R* and 3*d* elements, which makes it possible to reveal lanthanide compression, takes place in this structure along the *a* direction while being practically nonexistent along *c*.

Indeed, in $RFe_{10}Mo_2$, the *R* atoms occupy one crystallographic position, 2*a*, whereas the iron atoms occupy three nonequivalent positions: 8*i*, 8*j*, and 8*f*. As follows from neutron diffraction studies of $YFe_{10}Mo_2$ [10], the shortest distances are $Y–Fe_{8i}$ and $Y–Fe_{8j}$; more specifically, $d(Y–Fe_{8f})$ = 0.323 nm, $d(Y–Fe_{8i})$ = 0.306 nm, and $d(Y–Fe_{8j})$ = 0.303 nm. One may reasonably assume that, in other $RFe_{10}Mo_2$ compounds, the relative bond lengths would be the same. The $R–Fe_{8i}$ bond is directed along the *a* axis, which accounts for the fact that the parameter *a* exhibits lanthanide compres-

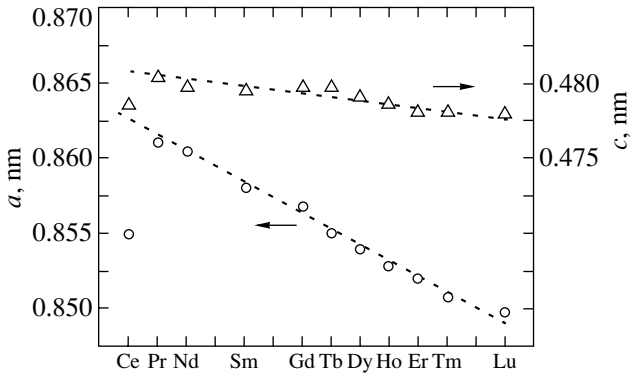

Fig. 4. Lattice parameters of $RFe_{10}Mo_2$ compounds. Dashed lines are extrapolated dependences of the lattice parameters on the atomic number of the *R* element, which reflect lanthanide compression.

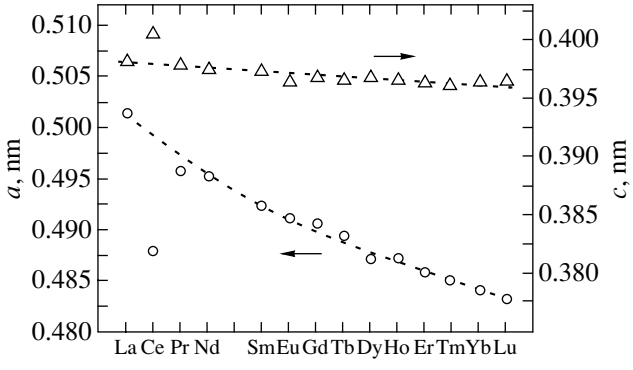

Fig. 5. Lattice parameters of RNi_5 compounds. Dashed lines are extrapolated dependences of the lattice parameters on the atomic number of the *R* element, which reflect lanthanide compression.

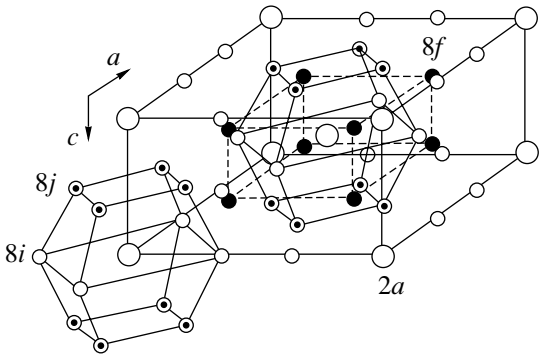

Fig. 6. $ThMn_{12}$-type crystal structure.

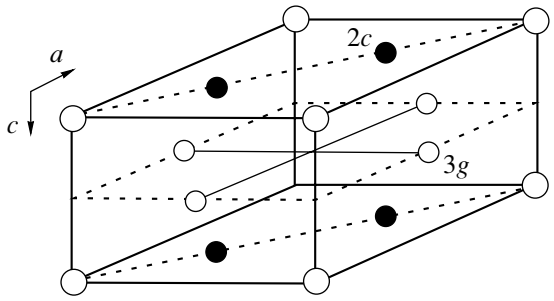

Fig. 7. $CaCu_5$-type crystal structure

sion and a deviation from the extrapolated course in the Ce compound due to the appearance of an additional ionic–covalent component caused by the 4*f* electrons becoming involved in the bonding. The *c* direction is dominated by the *R*–*R* interaction, with only the projection of the *R*–Fe_{8j} bond contributing; this accounts for the weak *c*(*Z*) dependence and the fact that the deviation of the parameter *c* from its extrapolated value for the Ce compound is less than that of the parameter *a*.

For the Pr compound, the deviation of the parameter *a* from the extrapolated *a*(*Z*) line toward smaller values was found to be only slightly in excess of the measurement error. This should be attributed primarily to the increase in the valency of Pr being considerably smaller than that for Ce. Furthermore, the positive contribution from the so-called "tetrad" effect [11] to the ionic radius increases as one crosses over from Ce to Pr, and this contribution is capable of compensating for the negative deviation of the parameter *a* caused by the presence of quadrivalent Pr.

$PrNi_5$ has a hexagonal crystal structure of the $CaCu_5$ type (Fig. 7). In this compound, the *R* atoms occupy one crystallographic position, 1*a*, and the Ni atoms occupy two nonequivalent positions, 2*c* and 3*g*. The bond lengths in this structure can be easily calculated and are listed in the table.

As follows from Fig. 7 and the table, the behavior of the parameter *a* reveals the effect of the Pr–Ni_{2c} bonds, for which the Pr–Ni bond length is the shortest. Therefore, the *a*(*Z*) dependence exhibits lanthanide compression and a deviation from the extrapolated behavior for Ce. For $PrNi_5$, the deviation of the parameter *a* is small, like that for $PrFe_{10}Mo_2$. In the *c* direction, the Pr–Pr interaction takes place in combination with the projected Pr–Ni_{3g} bond, which is weaker than the Pr–Ni_{2c} bond; this accounts for the absence of lanthanide compression and of negative deviations from the extrapolated course in this case (Fig. 5). Note that in $CeNi_5$ the parameter *c* deviates from the monotonic *c*(*Z*) behavior toward larger values. Apparently, the Ce–Ni_{2c} bond in this compound is substantially stronger than the interactions in the *c* direction, as a result of which the lattice is compressed along the *a* direction only, with the parameter *c* increasing.

Copper substituting for nickel in $PrNi_5$ occupies predominantly the 2*c* positions [12]. The Pr–$(Ni,Cu)_{2c}$ bond length increases from 0.2862 nm in $PrNi_5$ to 0.2875 nm in the Cu alloy, but the interaction remains sufficiently strong, so the praseodymium valency does not change for this copper concentration. In the substituted $PrNi_4Al$ and $PrNi_4Ga$ alloys, the praseodymium valence state decreases to +3. Neutron diffusion studies [13] have shown that Al and Ga replace Ni in the 3*g* positions only; however, as is evident from the table, this increases both the Pr–Ni_{3g} and Pr–Ni_{2c} bond lengths; i.e., the Pr–Ni interaction weakens, which becomes manifest in the praseodymium valence state decreasing to +3.

According to current concepts, the mixed valence state of Ce in metal alloys and compounds with *nd* metals is caused not by the $4f \longrightarrow 5d$ electronic transition, as is the case with other lanthanides with unstable

Lattice parameters (*a*, *c*), interatomic distance (*d*), and valence of Pr (V_{Pr}) in $PrNi_5$ and $PrNi_4M$ (*M* = Cu, Al, Ga)

Compound	*a*, nm	*c*, nm	$d_1 = a/\sqrt{3}$ Pr–Ni_{2c}	$d_2 = 0.5\sqrt{(a^2 + c^2)}$ Pr–Ni_{3g}	$d_3 = c$ Pr–Pr	$d_4 = 0.5\sqrt{(a^2 + 3c^2)}/3$ Ni–Ni	$V_{Pr} \pm 0.03$
$PrNi_5$	0.4957	0.3980	0.2862	0.3179	0.3980	0.2451	3.10
$PrNi_4Cu$	0.4980	0.4001	0.2875	0.3194	0.4001	0.2464	3.10
$PrNi_4Ga$	0.5009	0.4048	0.2892	0.3220	0.4048	0.2488	3.00
$PrNi_4Al$	0.5029	0.4066	0.2904	0.3234	0.4066	0.2498	3.00

valence states, but rather by delocalization of the 4*f* states as they become involved in atomic interaction. We conjectured that the quadrivalent cerium in a metal originates from the $(\in 4f^2)6s^2$ atomic configuration (the symbol $\in$ refers to a delocalized orbital) rather than from $4f^05d^26s^2$, as is the case, for instance, in CeO_2, and that delocalization of the 4*f* electron occurring as one crosses over from the $4f^15d^16s^2$ configuration to $(\in 4f^2)6s^2$ should be attributed to the well-known effect of *f*-electron penetration through the centrifugal barrier [14]. For this reason, a small perturbation of the atomic parameters causes a sharp change in the radius and energy of the 4*f* states [15].

This conjecture is substantiated by band structure calculations for the intermetallic compounds $CeFe_2$ [16] and $CeCo_5$ [17] with inclusion of 4*f*–3*d* hybridization, which yield a 4*f* band ~1-eV wide with a population of 1.13 electrons per atom. Indeed, if Ce^{+4} had the $4f^05d^26s^2$ configuration, the population of the *f* band would be less than 1. For the case of Pr, a theoretical analysis of the possible electron penetration was made in [15]. The transition from the $4f^25d^16s^2$ to $(\in 4f^3)6s^2$ configuration was considered, and it was concluded that the *f* bandwidth in the case of praseodymium is too small to permit *f*-electron delocalization. As can be seen from Fig. 3, however, the energy difference between the positions of the R^{+3} and R^{+4} L_3 absorption spectra for Ce and Pr is the same, $\Delta E \sim 7$ eV. This suggests that, in actual fact, two (rather than three, as in [15]) *f* electrons became delocalized. We believe that Pr^{+4} has the $4f^1(\in 4f^2)6s^2$ rather than $(\in 4f^3)6s^2$ configuration, as maintained in [15].

The appearance of delocalized 4*f* electrons in a 3*d* metal does certainly affect indirect exchange coupling, but this mechanism has not been studied thus far. Earlier [18], we reported the observation of a shoulder in the temperature dependence of the initial susceptibility measured along the easy magnetization axis of a $PrNi_4Cu$ alloy at $T \sim 2.2$ K, which can be tentatively assigned to a change in the degree of *f*-electron localization.

4. CONCLUSIONS

We have studied x-ray L_3 absorption spectra of Pr and the crystallochemical characteristics of intermetallic compounds $PrFe_{10}Mo_2$ and $PrNi_5$. It has been established that Pr atoms, like atoms of Ce, can exist in a mixed valence state. The valency of praseodymium is $+3.08 \pm 0.03$ and $+3.10 \pm 0.03$ in $PrFe_{10}Mo_2$ and $PrNi_5$, respectively. The values of the valency and of the deviations of the lattice parameters from their monotonic course governed by lanthanide compression are substantially smaller for Pr than those for Ce. Replacement of one Ni atom in $PrNi_5$ by Al or Ga suppresses the mixed valence state effect in the Pr atoms. It has been conjectured that the quadrivalent state of Pr originates from the delocalization of two *f* electrons and that Pr^{+4} ions have the $4f^1(\in 4f^2)6s^2$ electronic configuration.

The difference in behavior between the lattice parameters *a* and *c* in $RFe_{10}Mo_2$ and RNi_5 with *R* = Ce or Pr has been discussed. The parameter *a* is more sensitive to the *R*–*T* interaction, which is dominant in the *a* direction. The *R*–*R* interaction plays a decisive role in the behavior of the parameter *c*. The anisotropy in the *R*–*T* bond manifests itself in the fact that, in certain compounds (e.g., $CeFe_{10}Mo_2$), an increase in the Ce valence brings about lattice compression along both the *a* and *c* directions, whereas in others (for example, in $CeNi_5$) the lattice undergoes unilateral compression (with *a* decreasing and *c* increasing).

REFERENCES

1. J. Rühler, *Handbook on the Physics and Chemistry of Rare Earths*, Ed. by K. A. Gshneidner and L. Eyring (North-Holland, Amsterdam, 1987), p. 454.
2. K. H. J. Buschow, Rep. Prog. Phys. **40**, 1179 (1977).
3. A. S. Ermolenko, Ye. V. Shcherbakova, G. V. Ivanova, and E. V. Beloserov, Phys. Met. Metallogr. **70**, 52 (1990).
4. J. P. Gavigan, H. S. Li, J. M. D. Coey, T. Viadieu, L. Pareti, O. Moze, and F. Bolzoni, J. Phys. Colloq. **40**, C8 (1988).
5. A. Bianconi, A. Marcelli, R. Karnatak, A. Kotani, T. Jo, and J. Petiau, Phys. Rev. B **35**, 806 (1987).
6. L. D. Finkel'shtein, A. V. Postnikov, N. N. Efremova, and E. Z. Kurmaev, Mater. Lett. **14**, 115 (1992).
7. A. V. Soldatov, T. S. Ivanchenko, S. Della Longa, A. Kotani, Y. Iwamoto, and A. Bianconi, Phys. Rev. B **50**, 5074 (1994).
8. P. A. Alekseev, E. S. Klement'ev, V. N. Lazukov, E. V. Nefedova, I. P. Sadikov, N. N. Efremova, L. D. Finkel'shtein, N. B. Kalchugina, and O. D. Chistyakov, Phys. Met. Metallogr. **77** (6), 611 (1994).
9. X. C. Kou, R. Grössinger, G. Wiesinger, J. P. Liu, F. R. de Boer, I. Kleinschroth, and H. Kronmüller, Phys. Rev. B **51**, 8254 (1995).
10. R. B. Hemholdt, J. J. M. Vleggaar, and K. H. J. Buschow, J. Less-Common Met. **138**, L11 (1988).
11. S. J. Siekiersky, J. Inorg. Nucl. Chem. **33**, 377 (1971).
12. A. Percheron-Guegan, C. L. Lartigue, and J. C. Ahard, J. Less-Common Met. **109**, 287 (1985).
13. J. S. Cantrell, T. A. Beiter, and R. C. Bowman, J. Alloys Compd. **207/208**, 372 (1994).
14. L. D. Finkel'shtein, Phys. Met. Metallogr. **57** (2), 170 (1984).
15. S. V. Vonsovskii, M. I. Katsnel'son, and A. V. Trefilov, Phys. Met. Metallogr. **76** (3), 27 (1993).
16. O. Eriksson, L. Nordstrom, M. S. S. Brooks, and B. Johansson, Phys. Rev. Lett. **60**, 2523 (1988).
17. L. Nordstrom, O. Eriksson, M. S. S. Brooks, and B. Johansson, Phys. Rev. B **41**, 9111 (1990).
18. A. G. Kuchin, A. S. Ermolenko, V. I. Khrabrov, G. M. Makarova, and E. V. Belozerov, J. Magn. Magn. Mater. **159**, L309 (1996).

Translated by G. Skrebtsov

Physics of the Solid State, Vol. 47, No. 3, 2005, pp. 429–433. Translated from Fizika Tverdogo Tela, Vol. 47, No. 3, 2005, pp. 417–421.

METALS AND SUPERCONDUCTORS

Growth and Conductivity of Calcium Cuprate Films

G. A. Ovsyannikov[1, 3], S. A. Denisyuk[1], and I. K. Bdikin[2]

[1] *Institute of Radio Engineering and Electronics, Russian Academy of Sciences, Mokhovaya ul. 11, Moscow, 125009 Russia*
e-mail: gena@hitech.cplire.ru

[2] *Institute of Solid State Physics, Russian Academy of Sciences, Chernogolovka, Moscow oblast, 142432 Russia*

[3] *Chalmers University of Technology, Göteborg, SE-412 96 Sweden*

Received May 20, 2004

Abstract—Crystal and transport properties of epitaxial $CaCuO_2$ (CCO) films are studied for samples grown on (110)$NdGaO_3$, (001)$SrTiO_3$, and (001)$LaAlO_3$ substrates using the laser ablation technique. The resistivity is found to be dependent on the crystal quality of the films. The conductivity type varies depending on the doping. For lightly doped films with a resistance higher than 0.1 Ω cm, 3D hopping conductivity is observed. For low-resistance CCO films doped with Sr, a power law temperature dependence is found, which is inconsistent with the hopping conductivity. The influence of substrate tilting on the subsequent growth of $CaCuO_2$ films is studied. YBCO/CCO heterostructures preserve high critical temperatures and small widths of superconducting transitions, which is of special importance for growing Josephson heterostructures for superconducting electronics.

1. INTRODUCTION

Soon after the discovery of high-temperature superconductivity in metal oxide compounds, it was found that it is the CuO_2 planes that are responsible for the unusually high superconducting transition temperature [1]. $CaCuO_2$ (CCO) is one of the simple cuprate compounds with a perovskite crystal structure wherein the CuO_2 planes are separated by Ca atoms. The low-temperature electronic states of cuprates vary from antiferromagnetic (insulator) to superconducting (metal) as the doping level of charge carriers (electrons or holes) increases [1–3]. The CCO cuprate falls into the low-doping region on the phase diagram. Its antiferromagnetic transition temperature (the Néel temperature) reaches as high as 540 K. CCO is a Mott insulator [4]. Synthesis of this material in pure form requires high pressures, so most of the studies were performed using Sr-doped compounds $Ca_{1-x}Sr_xCuO_2$ (CSCO), which are more stable and can be obtained under normal conditions [4].

Another reason for the interest in CCO-based compounds is that the CuO_2 layers in these materials are equally spaced both inside the unit cells and between them. This is quite different from other cuprates, for example, $YBa_2Cu_3O_x$ (YBCO), where the CuO_2 layers are separated by nonsuperconducting CuO planes. What makes CCO especially interesting is the experimentally found growth in the critical temperature of cuprate superconductors with an increasing number of CuO_2 layers taking part in the conductivity. Due to its crystal structure, CCO can be regarded as an infinite-layer compound; hence, its critical temperature may reach very high values [5]. Indeed, there have been reports of critical temperatures of higher than 80 K observed for polycrystalline samples of CSCO obtained using the high-pressure technique [6, 7]. However, those results, obtained for granular samples, were not confirmed in later studies of CSCO thin films [8–10]. Most of the publications on CSCO thin films with various Sr doping levels report an increase in resistance with a decrease in temperature and do not report observation of the superconducting transition [8–10]. So far, it has been assumed that the superconductivity of CCO found in several studies was due to structure defects, which are difficult to reproduce [10].

Though the phase diagram of cuprates was established long ago, it is still not clear how the conductivity of the system changes as the doping increases. It is not known whether there is an intermediate phase between the antiferromagnetic and superconducting states. In the present paper, we report on a method developed for growing epitaxial films. The crystal structure of the grown films is determined, and the evolution of the temperature dependence of conductivity with varying doping level is studied.

2. FILM GROWTH

Epitaxial CCO films were deposited on (110)$NdGaO_3$ (NGO), (001)$SrTiO_3$ (STO), and (001)$LaAlO_3$ (LAO) substrates and also on CeO_2/Al_2O_3 heterostructures created on the *r*-planes of sapphire. CSCO films were deposited on (110)NGO substrates only. We used the laser ablation technique at substrate temperatures of 700 to 750°C and an oxygen pressure of 0.3 to 0.6 mbar, with the pressure in the chamber prior to ablation being 10^{-6} mbar. An excimer laser was

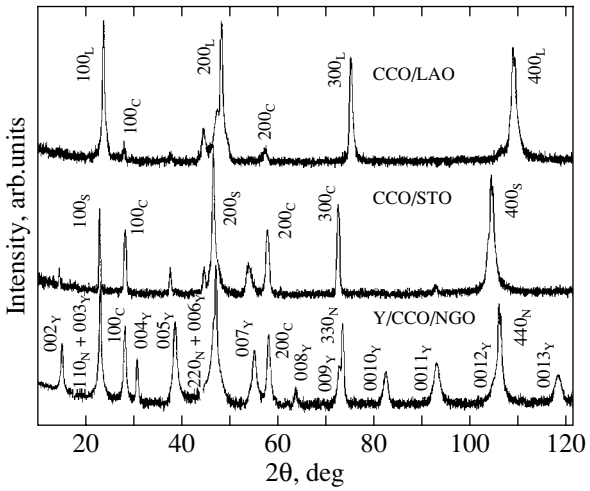

Fig. 1. Diffraction patterns of $CaCuO_2$ films grown on (001)$LaAlO_3$ (CCO/LAO) and (001)$SrTiO_3$ (CCO/STO) substrates. The lowest graph is for the $YBa_2Cu_3O_x/CaCuO_2$/(110)$NdGaO_3$ heterostructure (Y/CCO/NGO).

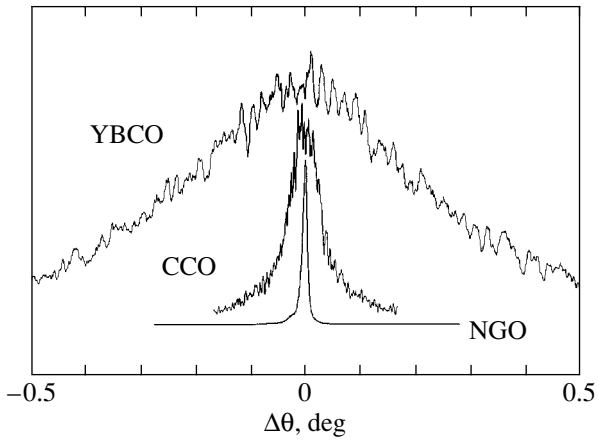

Fig. 2. Rocking curves of heterostructure $YBa_2Cu_3O_x/CaCuO_2$/(110)$NdGaO_3$ for reflections (005)$YBa_2Cu_3O_x$, (001)$CaCuO_2$, and (220)$NdGaO_3$. The widths of the peaks are cited in the text.

utilized (target energy density, 1.2–1.5 J/cm^2; repetition rate, 3–10 Hz). Targets were stoichiometric; they were made by pressure molding of a powder of appropriate composition. During the ablation process, the target was rotated to ensure uniform dispersion of the material. After deposition, the sample was slowly cooled in the chamber, first at the operational pressure down to 550°C and then at 700 mbar at a rate of 10–15° per minute. Overall, the technique of growing CCO films is similar to growing superconducting $YBa_2Cu_3O_x$ films [11]. The typical film thickness was 100–200 nm. The crystallographic constants of the films were measured by x-ray analysis, the surface morphology was studied by atomic-force microscopy, and the resistance was measured by the ac four-probe technique at 1 kHz.

3. CRYSTAL STRUCTURE

X-ray spectra (2θ–θ scans) for several substrates measured in the standard configuration of the source and detector (ψ = 0) are shown in Fig. 1. It is seen that the crystal quality of the films changes drastically with a switch from LAO substrates to NGO. The (00*L*)CCO peaks in CCO/LAO films are barely visible, while in YBCO/CCO/NGO heterostructures the amplitudes of the (00*L*)CCO peaks are close to the amplitudes of the substrate peaks. The crystal parameters determined by 2θ–θ scans at several substrate angles (ψ) are $a = b =$ 0.3855 nm and $c = 0.318$ nm. The lattice constant increases when Ca is substituted by Sr in CSCO films and reaches $c = 0.32$ and 0.33 nm for 15 and 50 at. % substitution, respectively. We did not succeed in growing epitaxial $CaCuO_2$ films on top of CeO_2/Al_2O_3 heterostructures, probably due to the chemical interaction between $CaCuO_2$ and CeO_2.

The width of the rocking curve of a $CaCuO_2$ film on the NGO substrate (0.05°) is significantly smaller than that of the best epitaxial $YBa_2Cu_3O_x$ films (0.2°) and only one order of magnitude higher than the rocking-curve width for the peaks of the single-crystal (110)$NdGaO_3$ substrate (0.006°) (Fig. 2).

As we established previously [11], in the case where the substrate surface deviates from the exact crystal

Table 1. Orientations of the YBCO and CCO films in heterostructures grown on straight and tilted planes of (110)NGO substrates

NGO substrate orientation	Grown heterostructure	Deviation of [110]NGO from the normal, deg	CCO film lattice constants, Å	Deviation of [001]CCO from the normal, deg	YBCO film lattice constants, Å	Deviation of [001]YBCO from the normal, deg
(110)	$YBa_2Cu_3O_x/Ca_{0.85}Sr_{0.15}CuO_2$	0	$c = 3.230$	0	$c = 11.709$	0
(7102)	$YBa_2Cu_3O_x/CaCuO_2$	7.9	$c = 3.179$	1.35	$c = 11.679$	1.35
(130)	$YBa_2Cu_3O_x/CaCuO_2$	26	$a = 3.843$	4.5	$a = 3.818$	3.8
			$b = 3.860$		$b = 3.878$	
			$c = 3.195$		$c = 11.707$	

plane direction, the orientation of the film may be different from either the geometric substrate surface or the exact crystallographic directions of the substrate. For example, when the substrate surface was oriented as (130)NGO, the angle between the planes (100)CeO_2 and (130)NGO was about 3°. For smaller substrate tilt angles, the epitaxial relation (100)CeO_2 || (110)NGO was preserved. It can be assumed that this is a peculiarity of CeO_2, but the present study of the CCO film also shows deviations from the exact epitaxial relation (001)CCO || (110)NGO if the substrate surface is tilted relative to the (110)NGO plane even at a small angle (Table 1). We determined the orientation relationships of [001]CCO, [001]YBCO and [110]NGO from rocking curves taken with wide-bandwidth x-ray radiation. The results are presented in Table 1. The deviation of the CCO axes from those of the substrate increases as the (110)NGO plane deviates from the substrate surface normal. In the case of the (130)NGO substrate orientation, the deviation reaches as high as 22° and a slight distortion of the CCO structure into orthorhombic is observed: $a = 3.84$, $b = 3.86$, and $c = 3.20$ Å. The epitaxial growth of YBCO on top of the CCO film is determined by the CCO, though a small deviation is observed nevertheless. Thus, the CCO film that deviated from the exact crystal directions of the substrate defines a new basis, which governs the orientation of subsequently deposited films. It is important that a CCO film also affects the domain structure of the subsequent YBCO film. In particular, we found that, even if the substrate is oriented as (130)NGO, other orientations of YBCO (*a* orientation) do not appear [11].

4. TEMPERATURE DEPENDENCES OF RESISTIVITY

In our experiments, we observed a correlation between the resistivity and the crystal quality of $CaCuO_2$ films [12]. As the width of the rocking curve decreases, the room temperature resistivity ρ goes down from 10^4 to 10 Ω cm. The decrease in ρ with an increase in crystal quality does not contradict the Mott insulator theory, according to which the metal–insulator transition takes place as the disorder grows [13]. In our experiments (Figs. 3, 4), the hopping conductivity is observed for ρ values much higher than $\rho_{max} = ha/(0.0262\pi e^2) \approx 6 \times 10^{-3}$ Ω cm (where $a = 3.8$ Å is the interatomic distance), which is characteristic of the Mott metal–insulator transition [13]. The quantity ρ_{max} obtained by Mott coincides in order of magnitude with the saturation resistance (the Ioffe–Regel limit) calculated for a 2D metal,

$$\rho_{2d} = ha/(k_F l e^2) \quad (1)$$

for $k_F l \approx 1$, where k_F is the Fermi momentum and l is the mean free path [14].

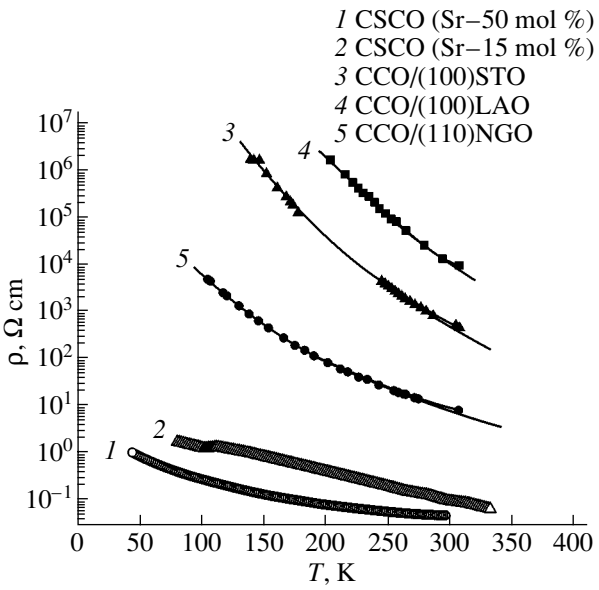

Fig. 3. Temperature dependences of resistivity of all the $CaCuO_2$-based films.

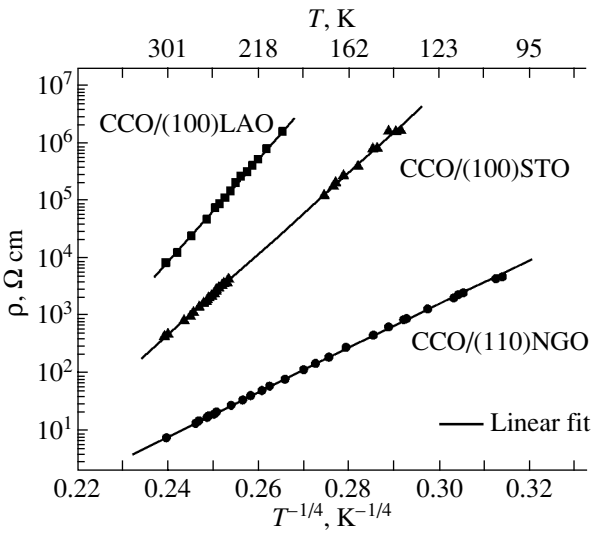

Fig. 4. Hopping conductivity. Solid lines are fits to Eq. (2).

The temperature dependences of resistivity of high-resistance samples (Fig. 4) are described well by the expression

$$\ln(\rho) = \ln(\rho_0) + (T_0/T)^{1/4}, \quad (2)$$

$$T_0 = c(k_B N(E_F)\lambda^3), \quad (3)$$

which is characteristic of the hopping conductivity [13] (here, c is a constant, k_B is the Boltzmann constant, $N(E_F)$ is the density of states on the Fermi level, and λ is the localization length). The temperature exponent

Table 2. Temperature dependences of the resistivity of films

Film composition	Substrate	Resistivity at T = 300 K, Ω cm	Lattice constant c, Å	Temperature dependence of resistivity
$CaCuO_2$	(001)$LaAlO_3$	9040	3.18	3D hopping $\rho = \rho_0 \exp(T_0/T)^{1/4}$
$CaCuO_2$	(001)$SrTiO_3$	510	3.18	
$CaCuO_2$	(110)$NdGaO_3$	8	3.18	Neither hopping nor power law
$Ca_{0.85}Sr_{0.15}CuO_2$	(110)$NdGaO_3$	0.10	–	
$Ca_{0.5}Sr_{0.5}CuO_2$	(110)$NdGaO_3$	0.05	3.30	Power law $\rho \sim T^{-S}$ (S = 1.6)

depends on the system dimensionality and, in our case, corresponds to the variable-range hopping. We can estimate the localization length λ for samples with hopping conductivity from the experimental value of the characteristic temperature T_0 by assuming that $N(E_F) = 10^{21}$ and $c = 18$. Using Eq. (3), we obtain $\lambda = c/(kN(E_F)T_0)^{1/3} =$ (0.5–2) Å for $T_0 = (2–60) \times 10^6$ K. The hopping activation energy $E_{hop} = k_B T(T_0/T)^{1/4} =$ (0.2–0.5) eV at $T =$ 300 K is somewhat lower than the gap $E = 1.5$ eV determined by optical methods [15]. Unlike ordinary insulators with activation conductivity, where the gap is created by the crystal field, the gap of the Mott insulators is due to strong electron correlations. The resistivity of the Mott insulator increases with decreasing temperature even if its conductivity band is half-filled. In our experiment, the activation type of conductivity is not achieved even at $\rho > 10^4$ Ω cm.

The resistivity decreases further as the Sr content in CCO films grows. This decrease is due to the growth of carrier concentration in CCO because of the higher doping, in accordance with the cuprate phase diagram. The resistivity of all CSCO films studied grows with decreasing temperature (Fig. 3). According to Table 2, at high doping ($\rho \lesssim 0.1$ Ω cm), the type of temperature dependence of conductivity changes from a hopping dependence to $\rho \sim T^{-S}$ with $S = 1.6$. Previously, this type of temperature dependence was observed in less resistive CSCO films with a Sr content of 30–40 at. % [10]. This temperature dependence is typical of disordered electronic systems with high values of low-temperature resistance [15, 16]. However, even at sufficiently high doping (CSCO films with $x = 0.5$), we did not observe the metallic resistivity temperature dependence typical of superconducting films.

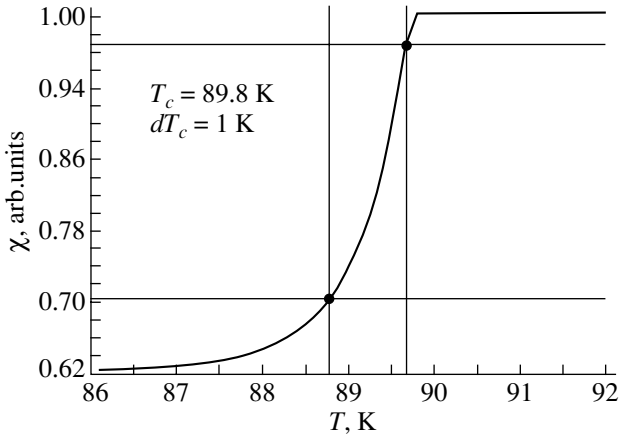

Fig. 5. Temperature dependence of the susceptibility of YBCO/CCO heterostructures grown on (110)NGO substrates.

We did not find any change in the susceptibility of the films associated with the antiferromagnetic transition during the measurements in the temperature range 20–100 K. The Néel temperature T_N of CCO is rather high [4] and is above the temperature range of our measurements. However, for Sr-doped CSCO, T_N can decrease drastically and be below our range. Insufficient sensitivity of the measurements also cannot be ruled out.

It is important that the superconducting transition was observed in YBCO/CCO heterojunctions and that suppression of the critical temperature for the superconducting transition of YBCO because of Ca doping [17] did not occur (Fig. 5). Therefore, CCO thin films can be used in heterostructures based on YBCO.

ACKNOWLEDGMENTS

The authors are grateful to T. Claeson, F.V. Komissinskiĭ, and Yu.A. Boĭkov for helpful discussions and their assistance in the experiments.

This work was supported in part by the Russian Foundation of Basic Research (project no. 04-02-16818a), INTAS (grants nos. 01-0809, 01-0249), the International Science and Technology Center (grant no. 2369), and the President of the Russian Federation (grant no. NSh-1344.2003.2).

REFERENCES

1. P. W. Anderson, Science **235**, 1196 (1987).
2. J. Orenstein and A. J. Millis, Science **288**, 468 (2000).
3. N.-C. Yeh, Bull. Assoc. Asia Pacific Phys. Soc. **12** (2), 2 (2002).
4. D. Vaknin, E. Caignol, P. K. Davis, J. E. Fischer, D. C. Johnston, and D. P. Goshorn, Phys. Rev. B **39** (13), 9122 (1989).

5. T. Siegrist, S. M. Zahurak, D. W. Murphy, and R. S. Roth, Nature **334**, 231 (1988).
6. M. Azuma, Z. Hiroi, M. Takano, Y. Bando, and Y. Takeda, Nature **356**, 775 (1992).
7. S. Adachi, H. Yamauchi, S. Tanaka, and N. Mori, Physica C (Amsterdam) **208**, 226 (1993).
8. D. P. Norton, B. C. Chakomokos, J. D. Budai, and D. H. Lowndes, Appl. Phys. Lett. **62** (14), 1679 (1993).
9. Q. Y. Mai, P. Dosanjh, I. Entin, R. Liang, J. F. Carolan, and W. N. Hardy, J. Appl. Phys. **75** (6), 3089 (1994).
10. X. M. Xie, C. Hattere, V. Mairet, C. F. Beuran, C. Coussot, C. D. Cavellin, B. Eustache, P. Laffez, X. Z. Xu, and M. Lagues, Appl. Phys. Lett. **67** (12), 1671 (1995).
11. I. K. Bdikin, P. B. Mozhaev, G. A. Ovsyannikov, F. V. Komissinskiĭ, I. M. Kotelyanskiĭ, and E. I. Raksha, Fiz. Tverd. Tela (St. Petersburg) **43** (9), 1543 (2001) [Phys. Solid State **43**, 1611 (2001)].
12. G. A. Ovsyannikov, S. A. Denisiuk, I. K. Bdikin, Z. G. Ivanov, and T. Claeson, Physica C (Amsterdam) **408–410**, 616 (2004).
13. N. F. Mott and E. A. Davis, *Electronic Processes in Non-Crystalline Materials* (Clarendon, Oxford, 1971; Mir, Moscow, 1974).
14. O. Gunnarsson, M. Caladra, and J. E. Han, Rev. Mod. Phys. **75**, 1085 (2003).
15. Y. Tokura, S. Koshihara, and T. Arima, Phys. Rev. B **41** (6), 11657 (1990).
16. P. A. Lee and T. V. Ramakrishman, Rev. Mod. Phys. **57**, 287 (1985).
17. G. Hammerl, A. Schnehl, R. R. Shulz, B. Goetz, H. Bielefeldt, C. W. Scheider, H. Hilgenkamp, and J. Manhart, Nature **407**, 162 (2000).

Translated by G. Tsydynzhapov

Physics of the Solid State, Vol. 47, No. 3, 2005, pp. 434–438. Translated from Fizika Tverdogo Tela, Vol. 47, No. 3, 2005, pp. 422–426.

METALS AND SUPERCONDUCTORS

Band Spectrum Modification and Dynamics of Superconducting Properties in the $Y_{1-x}Ca_xBa_2Cu_{3-x}Zn_xO_y$ System

M. V. Elizarova*, O. A. Martynova*, D. V. Potapov*, V. É. Gasumyants*, and L. P. Mezentseva**

**St. Petersburg State Polytechnic University, Politekhnicheskaya ul. 25, St. Petersburg, 195251 Russia*
e-mail: mariel@rphf.spbstu.ru

***Institute of Silicate Chemistry, Russian Academy of Sciences, ul. Odoevskogo 24/2, St. Petersburg, 199155 Russia*

Received July 7, 2004

Abstract—Temperature dependences of the electrical resistivity and Seebeck coefficient have been studied on a series of samples of the $Y_{1-x}Ca_xBa_2Cu_{3-x}Zn_xO_y$ system (x = 0–0.25). The effect exerted by a combination of the impurities under study on the properties of the normal phase was established. The experimental data obtained were analyzed quantitatively in terms of a phenomenological model of electron transport. The parameters of the band responsible for conduction in the normal phase and of the carrier system were calculated for all the samples studied. A mechanism of zinc doping–induced band structure modification in the yttrium system is proposed that accounts for the transformation of the temperature dependence of the Seebeck coefficient and the dynamics of superconducting properties in this compound. © *2005 Pleiades Publishing, Inc.*

1. INTRODUCTION

Publications dealing with the properties of yttrium-based superconductors discuss, in considerable detail, a number of substituents that, while not noticeably affecting the state of the oxygen subsystem, nevertheless exert a substantial influence on superconductivity and on the properties of the normal state. A remarkable example of such substituents is the zinc impurity on sheet copper sites. Being isovalent, the zinc impurity does not affect the hole doping level [1]. Some researchers believe, however, that zinc substitution in the sheet copper sites may bring about a nonuniform distribution of charge density in the copper–oxygen sheets [2] or localization of mobile carriers [3], which is essential for superconducting properties. Experiments have shown convincingly that substitution of zinc for sheet copper brings about a gradual suppression of the superconducting properties [1, 3–6]. Most researchers believe that this impurity acts directly on the mechanism of formation of superconducting pairs by initiating their breaking. Of particular interest is the finding [2] that zinc also exerts a noticeable effect on the band structure of $YBa_2Cu_3O_y$ in the normal phase through interaction with the sheet oxygen.

Note that, in contrast to other impurities, doping $YBa_2Cu_3O_y$ with zinc, while bringing about a strong suppression of superconductivity with increasing doping level, leaves the linear pattern of the temperature dependence of electrical resistivity unchanged and does not have a marked effect on the absolute values of the Seebeck coefficient S [1].

There is also considerable interest in the effect that a calcium impurity occupying yttrium sites has on superconductivity and on the properties of the normal phase of $YBa_2Cu_3O_y$. In this case, in contrast to the case of zinc substituting for sheet copper, the superconducting properties of the system are dominated by the state of the oxygen subsystem, which is influenced by the introduction of a nonisovalent calcium impurity [7–9]. Some aspects of the effect of calcium on the formation of oxygen vacancies and, hence, on the mechanism of superconductivity suppression have been given considerable attention in the literature [10, 11]. Not less intriguing is, however, the effect of both single doping of calcium into yttrium positions and of calcium codoped with other impurities on the properties of the normal state of $YBa_2Cu_3O_y$, in particular, on the temperature dependences of the Seebeck coefficient [7, 8, 12]. As shown by us earlier [7, 8, 13, 14], as the calcium content increases, an extended linear section appears in the $S(T)$ graphs and their slopes gradually increase, which should be assigned to a modification of the band structure of the compound.

Because calcium in yttrium sites and zinc occupying the sheet copper positions act on the superconducting properties of $YBa_2Cu_3O_y$ through different mechanisms, it is of interest to study the effect of simultaneous Ca $\longrightarrow$ Y and Zn $\longrightarrow$ Cu double doping in the yttrium system.

This communication reports on the specific effects of this dopant combination on the superconductivity, transport properties, and band spectrum in the normal phase of $YBa_2Cu_3O_y$. The band structure modification is analyzed in terms of a phenomenological model of electronic transport, more specifically, the narrow-band model, which allows one to determine the main band

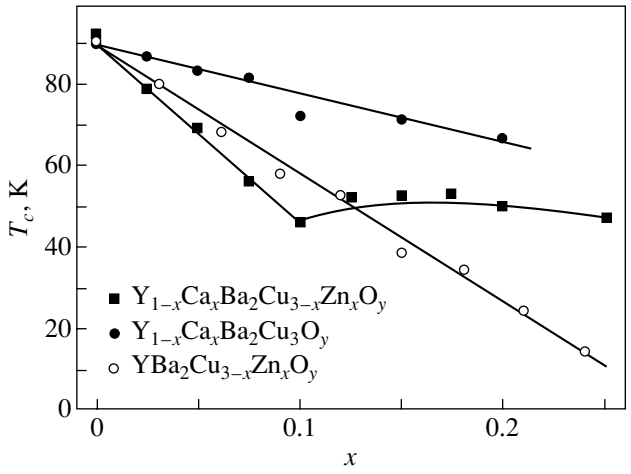

Fig. 1. Concentration dependence of the critical temperature for the $Y_{1-x}Ca_xBa_2Cu_{3-x}Zn_xO_y$ system plotted together with data obtained for the cases of Ca ⟶ Y [8] and Zn ⟶ Cu [4, 15] single substitutions.

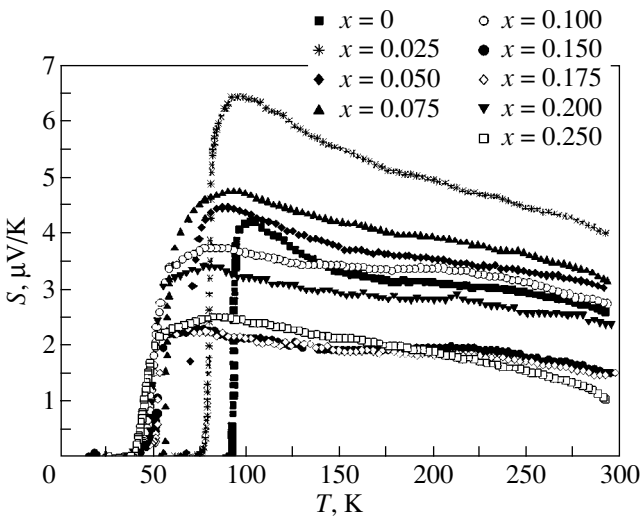

Fig. 2. Temperature dependence of the Seebeck coefficient for the $Y_{1-x}Ca_xBa_2Cu_{3-x}Zn_xO_y$ system.

spectrum parameters of the normal phase and follow their changes with increasing doping level and, hence, unravel the effect of specific impurities on the parameters of the band spectrum and of the carrier system.

2. EXPERIMENTAL RESULTS

We studied ceramic samples of composition $Y_{1-x}Ca_xBa_2Cu_{3-x}Zn_xO_y$ (x = 0.0, 0.025, 0.05, 0.075, 0.10, 0.15, 0.175, 0.20, 0.25) prepared by standard solid-phase techniques. The procedure culminated in annealing in an oxygen flow at T = 500°C, with subsequent gradual cooling to room temperature. The single-phase state of the samples was established by x-ray analysis to within 1–2%. All samples were subjected to measurements of the temperature dependences of the electrical resistivity and Seebeck coefficient.

Figure 1 displays the critical temperatures T_c for all samples derived from resistive measurements together with data obtained for the cases of single calcium doping into the yttrium positions [8] and of zinc doped into the sheet copper positions [4, 15]. The concentration dependence of the critical temperature is seen to be nonmonotonic for the $Y_{1-x}Ca_xBa_2Cu_{3-x}Zn_xO_y$ system. For small x, the superconductivity undergoes a gradual suppression with increasing doping level, whereas for x = 0.125 a certain recovery of the superconducting properties is seen. As x continues to increase, the magnitude of T_c remains practically constant. For $x \le 0.10$, T_c drops with increasing x in $Y_{1-x}Ca_xBa_2Cu_{3-x}Zn_xO_y$ faster than is the case with $Y_{1-x}Ca_xBa_2Cu_3O_y$ and $YBa_2Cu_{3-x}Zn_xO_y$.

Figure 2 shows the temperature dependence of the Seebeck coefficient obtained for the $Y_{1-x}Ca_xBa_2Cu_{3-x}Zn_xO_y$ system. An increase in the doping level is seen to give rise in this case to only a slight change in the absolute value of S (at room temperature, the Seebeck coefficient changes from 1.5 to 3.5 μV/K) and to a certain decrease in the magnitude of the maximum in the $S(T)$ graph. No linearization of the $S(T)$ relations and no gradual increase in their slope, which are characteristic of the calcium impurity [7, 8, 11–13], are observed in the case of the $Y_{1-x}Ca_xBa_2Cu_{3-x}Zn_xO_y$ system.

3. ANALYSIS OF THE EXPERIMENTAL DATA AND INTERPRETATION OF THE RESULTS

The experimental data were analyzed in terms of the phenomenological narrow-band model described in detail in [7]. The model assumes the existence of a narrow density-of-states peak near the Fermi level in the band spectrum of an HTSC and allows one to derive analytical expressions for the temperature dependences of the kinetic coefficients using four model parameters, namely, band filling by electrons F (which is the ratio of the total number of electrons to the total number of states in the band), the effective width of the conduction band W_D, the effective width of the interval of delocalized states W_σ, and the degree of band asymmetry b. Through quantitative comparison of the results of calculations with the experimental data on $S(T)$, we can determine the model parameters for each of the compositions studied and, hence, follow the modification of the band spectrum and carrier system with increasing doping level.

Figures 3 and 4 plot the calculated concentration dependences of the band filling by electrons and of the total effective conduction bandwidth, respectively, for all samples of the $Y_{1-x}Ca_xBa_2Cu_{3-x}Zn_xO_y$ system investigated together with the data on the $Y_{1-x}Ca_xBa_2Cu_{3-x}Co_xO_y$ system studied by us earlier [13]. The values of F and W_D for the $Y_{1-x}Ca_xBa_2Cu_{3-x}Zn_xO_y$

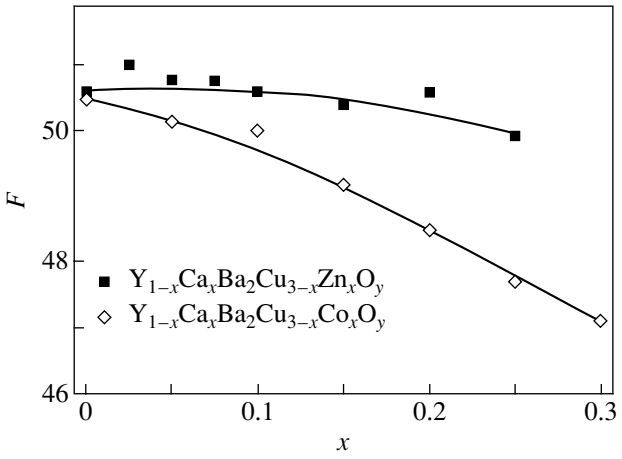

Fig. 3. Concentration dependences of the band filling by electrons, *F*, plotted together with data for Ca ⟶ Y and Co ⟶ Cu double substitutions [13].

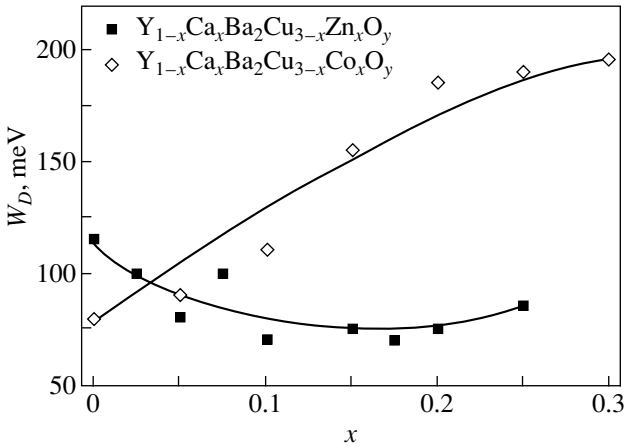

Fig. 4. Concentration dependences of the total effective conduction bandwidth, W_D, plotted together with data for Ca ⟶ Y and Co ⟶ Cu double substitutions [13].

system vary very little with increasing *x*, which becomes particularly revealing when compared with the respective results obtained for $Y_{1-x}Ca_xBa_2Cu_{3-x}Co_xO_y$. The effective bandwidth exhibits a weak tendency to decrease (Fig. 4). According to our previous results, the decrease in the band filling by electrons with an increase in *x* in $Y_{1-x}Ca_xBa_2Cu_{3-x}Co_xO_y$ may be explained if it is assumed that calcium introduces additional states into the band responsible for conduction; simultaneously, the effects produced by the two impurities are mutually charge compensated ($Co^{3+} \longrightarrow Cu^{2+}$, $Ca^{2+} \longrightarrow Y^{3+}$) [13]. The broadening of the conduction band in the $Y_{1-x}Ca_xBa_2Cu_{3-x}Co_xO_y$ system is associated only with the gradual disorder caused directly by the impurity cations (because the state of the oxygen subsystem remains unchanged with increasing *x* due to the charge compensation) [7, 13, 14] in accordance with the Anderson localization model. The constancy of *F* in the case of simultaneous isovalent ($Zn^{2+} \longrightarrow Cu^{2+}$) and nonisovalent ($Ca^{2+} \longrightarrow Y^{3+}$) substitutions observed in $Y_{1-x}Ca_xBa_2Cu_{3-x}Zn_xO_y$, as well as the weak decrease in the conduction bandwidth paralleled by the disorder introduced by the impurity ions and by the disorder forming on the oxygen subsystem, requires additional analysis. Obviously enough, a mechanism should arise in the $Y_{1-x}Ca_xBa_2Cu_{3-x}Zn_xO_y$ system that would, first, counteract the growth in the number of band states caused by the increasing calcium concentration (which should bring about a decrease in the degree of band filling) and, second, give rise to a relative narrowing of the band responsible for conduction. This mechanism can operate only if the zinc substituting into the sheet copper positions has an effect on the band structure in the normal phase.

As follows from our analysis, the best fit between the calculated and experimental *S*(*T*) dependences for $Y_{1-x}Ca_xBa_2Cu_{3-x}Zn_xO_y$ samples can be attained only in the case of zero conduction band asymmetry ($b = 0$) for the compositions with $x = 0$–0.075 and 0.2 and in the case of a slight asymmetry, not in excess of 0.5%, positive or negative, for samples with $x = 0.10$–0.175 and $x = 0.25$, respectively. Thus, we can assume, on the whole, that an increase in the doping level in the $Y_{1-x}Ca_xBa_2Cu_{3-x}Zn_xO_y$ system does not generate conduction band asymmetry of either sign. As for the degree of localization of the states, it exhibits slight variations with increasing *x* without showing any distinct trend.

The calculations made in [2] may be instructive for interpreting our findings. It is suggested in [2] that zinc doping in the copper–oxygen sheets causes the states of the oxygen atoms surrounding the impurity to transfer out of the conduction band toward lower energies. This means that a single zinc impurity may cause conduction band asymmetry, which, in turn, should give rise to the appearance of additional features in the temperature dependences of the Seebeck coefficient. Experimental data [1, 16, 17] indicate that substitution of zinc for sheet copper does indeed bring about a transformation of the *S*(*T*) dependence; namely, this causes a decrease in the amplitude of the peak and a shift in the peak toward lower temperatures. The calcium impurity also produces specific features in the *S*(*T*) graphs, both in the case of single substitution of calcium for yttrium and in combination with other impurities [7, 8, 11–13]. For samples doped heavily with calcium, an extended linear portion in the *S*(*T*) dependence is observed and, most remarkably, an increase in the calcium content initiates a gradual increase in the slope of the *S*(*T*) graphs. According to our previous results [13, 14], this transformation in the pattern of the temperature dependences of the Seebeck coefficient originates from the conduction band becoming asymmetric due to calcium introducing additional states into the band, i.e., from the appearance of an additional peak in the density of

states in the conduction band. In this connection, it appears instructive to note that codoping with calcium and zinc in the $Y_{1-x}Ca_xBa_2Cu_{3-x}Zn_xO_y$ system does not result in any specific transformation of the $S(T)$ dependence. As already mentioned, the band responsible for conduction is practically symmetric throughout the x range covered. This implies that zinc doping into the sheet copper sites compensates the band asymmetry generated by the calcium impurity. This can be possible only if the rearrangement of the zinc-induced band brings about a band asymmetry that is opposite in sign to the asymmetry due to calcium. Thus, in the $Y_{1-x}Ca_xBa_2Cu_{3-x}Zn_xO_y$ system, we encounter not only a modification of the conduction band in shape but also its rearrangement involving the states from which it derives. In our opinion, we witness here interplay between the effects of different impurities on the asymmetry, namely, on the one hand, a calcium-induced donation of states into the upper half of the band and, on the other hand, a transfer of states from the band to lower energies under the action of zinc.

The assumption that the states are transferred out of the band under the action of zinc also provides an explanation for the fact that W_D and F remain practically unchanged as the doping level is increased. Indeed, an increase in the doping level in the $Y_{1-x}Ca_xBa_2Cu_{3-x}Zn_xO_y$ system causes the density-of-states peak, on the one hand, to broaden as a result of growing disorder (according to the Anderson localization mechanism) and, on the other hand, to decrease in amplitude and, hence, narrow because some of the states are pushed out of the peak to lower energies. It is the parallel operation of these two mechanisms that accounts for the total effective bandwidth remaining, on the whole, unchanged. Note that, as shown in [13] in an analysis of the correlation between the total effective conduction bandwidth and the critical temperature for a number of substitutions in the yttrium system, the calcium peak is only a small feature in the total band density of states. In other words, the appearance of additional states in the vicinity of the Fermi level does not bring about an effective broadening of the conduction band considered in terms of a rectangular approximation of the $D(\varepsilon)$ function. Thus, in the case of simultaneous double doping of $Y_{1-x}Ca_xBa_2Cu_{3-x}Zn_xO_y$, the effects the two impurities exert on the degree of conduction band asymmetry cancel each other, whereas the variation in the effective bandwidth is governed by the interplay of two counteracting mechanisms, more specifically, of the zinc-induced decrease in the number of band states and of the band broadening by the Anderson mechanism through the calcium-initiated disordering of the oxygen subsystem.

The practically unchanging values of band filling by electrons, which is equal to the ratio of the total number of electrons in the band to the total number of band states, can be accounted for as follows. Doping by the calcium acceptor impurity (which is not completely compensated by the increasing oxygen deficiency [8]) gives rise to a decrease in the number of electrons in the band. The observed constancy of the parameter F in the $Y_{1-x}Ca_xBa_2Cu_{3-x}Zn_xO_y$ system demonstrates that there is a decrease in the number of band states with an increase in x and suggests the effect of the zinc impurity on the number of band states to be stronger than that of calcium. Note that calculations do not reveal the appearance of a dominant zinc-induced asymmetry but rather only compensation of the asymmetry due to calcium, which may be attributed to the limitations of the model, as it is not capable of taking into account minor features in the band structure, as well as to the rather simplified method employed for asymmetry modeling.

Now, we invoke the data obtained on the band structure transformation to discuss the variation in the superconducting properties of the system under study. As already mentioned, an increase in x in the $Y_{1-x}Ca_xBa_2Cu_{3-x}Zn_xO_y$ system gives rise to an unusual dynamics of the critical temperature (Fig. 1). There are two impurity concentration ranges over which the superconducting properties are modified differently. In one range (x = 0–0.10), T_c exhibits a decrease, which is stronger than that observed in the case of single doping by calcium or zinc. We believe that we are witnessing here interplay between two mechanisms of suppression of superconductivity. First, doping of zinc into the copper sheets, which are directly responsible for the superconducting properties, brings about a breaking of the superconducting pairs and, accordingly, a decrease in the critical temperature. Second, T_c is additionally lowered by the decrease in the density of states at the Fermi level, $D(\varepsilon_F)$, caused by the strong modification of the band spectrum. The reasons underlying this modification are, first, the onset of general lattice disorder, which brings about, in accordance with the Anderson localization mechanism, a decrease in the density of states in the band as a whole, and, second, a transfer of states from the conduction band to lower energies; this latter process is initiated by zinc and results in a general decrease in the density-of-states peak.

In the other range (x = 0.15–0.25), T_c remains practically constant. Note that all the trends in the variation of the band parameters with increasing x persist in this concentration range. Hence, the observed change in the $T_c(x)$ pattern for $x > 0.1$ cannot be attributed to a pronounced band structure rearrangement. The improvement in the superconducting properties (as compared with the general trend of T_c decreasing with increasing x) may stem from an increase in the density of states at the Fermi level. In our opinion, a possible reason for the growth of $D(\varepsilon_F)$ is that the appreciable band structure rearrangement initiated by zinc, on the one hand, and by calcium, on the other, drives the Fermi level to a local peak of the $D(\varepsilon)$ function generated by calcium states and becomes pinned at it. In this case, the growth of $D(\varepsilon_F)$ may partially compensate the zinc-induced

breaking of superconducting pairs and thus give rise to a certain recovery of the superconducting properties. Note that constancy of the critical temperature in the $Y_{1-x}Ca_xBa_2Cu_{3-x}Zn_xO_y$ system for $x > 0.10$ was also observed in [18] but was not given adequate explanation. This experimental finding certainly merits comprehensive study.

The results presented here suggest that, despite the large number of publications dealing with the effect of a zinc impurity occupying sheet copper positions on the properties of yttrium-based HTSCs, this substitution continues to be an intriguing object for further studies, both in the case of single doping and, particularly, in combination with other dopants.

4. CONCLUSIONS

We have experimentally studied the temperature dependence of the Seebeck coefficient in the $Y_{1-x}Ca_xBa_2Cu_{3-x}Zn_xO_y$ system and analyzed the results in terms of the narrow-band model. The main conclusions are as follows.

(1) The concentration dependence of the critical temperature in $Y_{1-x}Ca_xBa_2Cu_{3-x}Zn_xO_y$ exhibits two areas with different T_c dynamics; namely, for $x < 0.125$, superconductivity suffers gradual suppression and then remains practically unchanged with a further increase in x. The Seebeck coefficient varies very weakly with increasing doping level, and its temperature dependence does not exhibit the extended linear portion characteristic of a calcium impurity in $YBa_2Cu_3O_y$.

(2) Unlike other calcium-doped systems, the degree of filling of the band responsible for the conductivity, as well as the degree of its asymmetry, remains unchanged in $Y_{1-x}Ca_xBa_2Cu_{3-x}Zn_xO_y$ throughout the x range covered. In addition to direct suppression of superconductivity, doping of zinc into the sheet copper positions has a substantial effect on the band structure in the normal phase. Introducing zinc into the $YBa_2Cu_3O_y$ lattice brings about a transfer of states from the conduction band toward lower energies, which practically cancels the band asymmetry originating from the calcium impurity.

(3) The weak variation in the critical temperature in $Y_{1-x}Ca_xBa_2Cu_{3-x}Zn_xO_y$ observed to occur for $x > 0.10$ may be traced to a relative increase in the density of states at the Fermi level, which takes place in this doping interval due to the Fermi level being pinned at a local peak of the calcium states.

ACKNOWLEDGMENTS

This study was supported by the Russian Foundation for Basic Research (project no. 02-02-16841a), the Ministry of Education of the Russian Federation (project no. E02-3.4-120), and the St. Petersburg Administration (project no. M04-2.4D-426).

REFERENCES

1. V. Radhakrishnan, C. K. Subramaniam, V. Sankaranarayanan, G. V. S. Rao, and R. Shrivastan, Phys. Rev. B **40** (10), 6850 (1989).
2. R. Gupta and M. Gupta, Phys. Rev. B **59** (5), 3381 (1999).
3. Y. Xu, W. Guan, S. S. Ata-Allah, and Ch. Heiden, Physica C (Amsterdam) **235–240**, 823 (1994).
4. R. Liang, T. Nakamura, H. Kawaji, M. Itoh, and T. Nakamura, Physica C (Amsterdam) **170** (3–4), 307 (1990).
5. C. Bernhard, J. L. Tallon, C. Bucci, R. de Renzi, G. Guidi, G. V. M. Williams, and Ch. Niedermayer, Phys. Rev. Lett. **77** (11), 2304 (1996).
6. J. L. Tallon, C. Bernhard, G. V. M. Williams, and J. W. Loram, Phys. Rev. Lett. **79** (26), 5294 (1997).
7. V. E. Gasumyants, in *Advances in Condensed Matter and Materials Research*, Ed. by F. Gerard (Nova Sci., New York, 2001), Vol. 1, p. 135.
8. V. E. Gasumyants, M. V. Elizarova, E. V. Vladimirskaya, and I. B. Patrina, Physica C (Amsterdam) **341–348**, 585 (2000).
9. A. Gupta, A. Sedky, A. V. Narlikar, and D. P. Singh, J. Mater. Sci. **37** (8), 1557 (2002).
10. A. Sedky, A. Gupta, V. P. S. Awana, and A. V. Narlikar, Phys. Rev. B **58** (18), 12495 (1998).
11. J. L. Tallons and G. V. M. Williams, Phys. Rev. B **61** (14), 9820 (2000).
12. V. E. Gasumyants, M. V. Elizarova, and I. B. Patrina, Phys. Rev. B **59** (9), 6550 (1999).
13. M. V. Elizarova and V. É. Gasumyants, Fiz. Tverd. Tela (St. Petersburg) **41** (8), 1363 (1999) [Phys. Solid State **41**, 1248 (1999)].
14. V. E. Gasumyants, M. V. Elizarova, and I. B. Patrina, Supercond. Sci. Technol. **13** (12), 16000 (2000).
15. S. Zagoulaev, P. Monod, and J. Jegoudez, Phys. Rev. B **52** (14), 10474 (1995).
16. J. L. Tallon, J. R. Cooper, P. S. I. P. N. de Silva, G. V. M. Williams, and J. W. Loram, Phys. Rev. Lett. **75** (22), 4114 (1995).
17. M. Sera, T. Nishikava, and M. Sato, J. Phys. Soc. Jpn. **62** (1), 281 (1993).
18. R. A. Gunasekaran, R. Ganduly, and J. V. Yakhmi, Physica C (Amsterdam) **234** (1–2), 160 (1995).

Translated by G. Skrebtsov

Physics of the Solid State, Vol. 47, No. 3, 2005, pp. 439–445. Translated from Fizika Tverdogo Tela, Vol. 47, No. 3, 2005, pp. 427–432.

SEMICONDUCTORS AND DIELECTRICS

Instabilities with *S*- and *N*-Shaped Current–Voltage Characteristics and Phase Transitions in Chalcogenide Vitreous Semiconductors and Polymers

K. D. Tséndin, É. A. Lebedev, and A. B. Shmel'kin

Ioffe Physicotechnical Institute, Russian Academy of Sciences, Politekhnicheskaya ul. 26, St. Petersburg, 194021 Russia
e-mail: Tsendin@mail.ioffe.ru

Received July 5, 2004

Abstract—The conditions necessary for electric current instabilities to arise in strong electric fields are considered for disordered media, such as chalcogenide vitreous semiconductors and organic polymers. The thermal and electronic–thermal mechanisms of instabilities with *S*- and *N*-shaped current–voltage characteristics are discussed. The influence of phase transitions from one conduction state to another conduction state on the development of electrical instabilities is analyzed. © *2005 Pleiades Publishing, Inc.*

1. INTRODUCTION

Phenomena associated with electrical instabilities in disordered media have attracted particular research attention for a long time. Originally, this interest stemmed from the necessity of predicting the electric strength of dielectrics. The instability in these materials manifests itself as an irreversible breakdown resulting in the disruption of an insulation in a strong electric field.

The situation has changed significantly since the discovery and subsequent investigation of the switching effect in chalcogenide vitreous semiconductors [1–3]. This effect involves a rapid reversible transition from a high-resistance state to a low-resistance state. In chalcogenide vitreous semiconductors, the number of switching cycles from a high-resistance state to a low-resistance state and then from the low-resistance state to the high-resistance state could be as large as 10^8, which made these switches promising for advantageous use in microelectronics.

For chalcogenide vitreous semiconductors, the temperature dependence of the electrical resistance in a high-resistance state exhibits a pronounced semiconducting behavior, whereas the resistance in a low-resistance state is virtually independent of temperature. This circumstance suggests that the switching effect is caused by the reversible conductivity transition from the semiconductor state to the metal state and the reverse transition from the metal state to the semiconductor state after switching off the voltage. However, a number of chalcogenide vitreous semiconductors, after being in a low-resistance state for a certain amount of time, undergo a glass–crystal structural phase transition and the new state in which part of the film is crystallized is retained after the voltage is switched off (the memory effect).

The problem regarding the mechanism of the switching effect has been heatedly debated. It is believed that the switching effect is the first stage of the memory effect. It should also be noted that, by the time the switching effect was discovered, many general regularities of the electrical instabilities had been established in the course of their study in crystalline materials.

In particular, it has been established that the *S*-shaped current–voltage characteristic is associated with the formation of electric current filaments, whereas the *N*-shaped current–voltage characteristic is due to the appearance of high-field domains [4]. Moreover, it is known that there are instabilities in the form of trap recharging waves and recombination waves.

This information provides a deeper insight into the nature of the switching effect in chalcogenide vitreous semiconductors, but its mechanism is not completely understood. The main problem concerns the role played by the thermal mechanism in the first stage (initiation) of the process. A number of authors have believed that the switching effect is initiated by the electronic processes responsible for the *S*-shaped current–voltage characteristic (electronic theories) and that the considerable heat release is a side effect occurring only in the final stage, predominantly, in the region of the formation of electric current filaments [5]. According to other authors, the heat release is of fundamental importance and contributes substantially to the initiation of the switching effect. In this respect, it should be noted that proponents of this viewpoint do not deny the significance of electronic processes, which affect the semiconducting temperature dependence of the conductivity. This approach served as the basis for the electronic–thermal theory, which has offered satisfactory explanations for many characteristics of the switching effect in chalcogenide vitreous semiconductors [6].

1063-7834/05/4703-0439$26.00

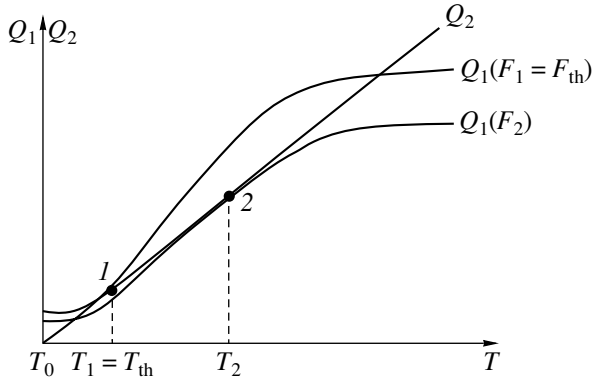

Fig. 1. Schematic representation of the left-hand (Q_1) and right-hand (Q_2) sides of Eq. (1a). Points *1* and *2* correspond to two solutions of the system of equations (1a) and (1b).

At present, the particular interest expressed by researchers in the problem regarding the electrical instabilities in disordered materials has been associated with two circumstances, namely, the real boom in the use of chalcogenide vitreous semiconductors for optical and electrical recording of information and the investigation of the switching effect in organic polymers for which not only *S*-shaped current–voltage characteristics but also *N*-shaped current–voltage characteristics indicating the transition from a low-resistance state to a high-resistance state are observed upon switching [7].

In this paper, the mechanisms of switching effects with the *S*- and *N*-shaped current–voltage characteristics observed in disordered organic polymers and chalcogenide vitreous semiconductors in strong electric fields are interpreted within a unified approach based on the electronic–thermal theory. As is known, materials of both these classes have a similar low-coordinated atomic structure. For this reason, chalcogenide vitreous semiconductors are often referred to as inorganic polymers. Moreover, preliminary results demonstrate that, in a number of cases, disordered polymers and chalcogenide vitreous semiconductors in strong electric fields exhibit similar behavior. In this respect, the results of the comparison and analysis of the data obtained for materials of these classes are of considerable interest both for the physics of polymers and chalcogenide vitreous semiconductors and for their practical application.

2. NECESSARY CONDITIONS FOR THERMAL AND ELECTRONIC–THERMAL ELECTRICAL INSTABILITIES WITH AN *S*-SHAPED CURRENT–VOLTAGE CHARACTERISTIC

Thermal instability is the simplest type of electrical instability in solids. The key condition for this instability to arise in electric fields is the semiconducting-type dependence of the electrical conductivity on the temperature. The positive feedback required to initiate the electrical instability with an *S*-shaped current–voltage characteristic occurs between the processes of heating and increase in the electric current passing through the sample. The passage of the electric current leads to heating of the sample; in turn, an increase in the temperature is accompanied by an increase in the conductivity. This results in a further increase in the electric current and the development of the instability.

Let us consider the conditions necessary for the thermal electrical instability to arise in a thin film within the approximation that the temperature does not depend on the coordinates. The field and temperature at which the instability arises are determined by the following system of equations:

$$Q_1 = Q_2, \tag{1a}$$

$$\frac{dQ_1}{dT} = \frac{dQ_2}{dT}, \tag{1b}$$

where $Q_1 = SL\sigma_0 F^2 \exp(-\Delta E/kT)$ and $Q_2 = \lambda S(T - T_0)$ are the terms describing the heat release and heat removal, respectively; S is the surface area of an active region; L is the film thickness; F is the field strength; T is the temperature of the sample; T_0 is the environment temperature; λ is the coefficient of external heat removal; and ΔE is the activation energy for conduction.

The system of equations (1a) and (1b) has a simple physical meaning, which is illustrated in Fig. 1.

Point *1* indicates the solution to the system of equations (1a) and (1b) and corresponds to an insignificant stationary heating to the temperature $T_{th}(= T_1)$ in the field $F_{th}(= F_1)$. A small increase in the field strength $F > F_{th}$ is accompanied by a drastic increase in the temperature (the thermal mechanism of electrical instability). By solving the system of equations (1a) and (1b), we obtain the following relationships for the threshold temperature T_{th} and the threshold field F_{th}:

$$T_1 = T_{th} = \frac{\Delta E}{2k}\left(1 - \sqrt{1 - \frac{4kT_0}{\Delta E}}\right) \approx T_0 + \frac{kT_0^2}{\Delta E}, \tag{2a}$$

$$F_{th} = \sqrt{\frac{\lambda k T_0}{L\sigma_0 \Delta E}} \exp\left(\frac{\Delta E}{2kT_0} - \frac{1}{2}\right). \tag{2b}$$

Here, it is assumed that $kT_0 \ll \Delta E$.

When analyzing the necessary conditions for electrical instability, it should be remembered that the system of equations (1a) and (1b) has not only solutions (2a) and (2b) but also solutions defined by the expressions

$$T_2 = \frac{\Delta E}{2k}\left(1 + \sqrt{1 - \frac{4kT_0}{\Delta E}}\right), \tag{3a}$$

$$F_2 = F_2(T_2). \tag{3b}$$

The two solutions to the system of equations under consideration are represented by points *1* and *2* in Fig. 1

and by the fields F_{th} and F_2 in the *S*-shaped current–voltage characteristic in Fig. 2. In the threshold field F_{th}, the sample in the high-resistance state prior to the onset of an avalanche-like development of thermal instability is heated only to the threshold temperature T_{th}. In the field F_2, the sample in the low-resistance state is heated to the temperature T_2, which is determined by the activation energy for conduction. The instability can arise at point *1* only when the radicands in relationships (2a) and (3a) are larger than zero, i.e., when the condition $4kT_0 < \Delta E$ is satisfied. The opposite condition $4kT_0 \geq \Delta E$ formulated in [8] means that the system of equations (1) has a stable solution only and the *S*-shaped current–voltage characteristic associated with the thermal mechanism of electrical instability disappears; i.e., the current–voltage characteristic becomes monotonic.

Another factor responsible for the disappearance of the *S*-shaped current–voltage characteristic is associated with the conditions for heat removal. In the case of intense heat removal, the electrical instability due to the Joule heating does not develop, because, under these conditions, the sharp increase in the temperature necessary for the instability to arise in the sample does not occur.

The range of parameters at which the sample exhibits an *S*-shaped current–voltage characteristic due to the Joule heating is shown in Fig. 3. According to the results presented in Fig. 3, the *S*-shaped current–voltage characteristic can be observed in the case where the temperature dependence of the conductivity is sufficiently strong (the values of $t_0 = kT_0/\Delta E$ are small) and the heat removal is not very intense [i.e., the parameters $\gamma = \lambda L/2\kappa_s(1 + \lambda\delta/2\kappa_c)$ are small]. Here, λ is the coefficient of external heat removal; L and δ are the thicknesses of the chalcogenide vitreous semiconductor film and the electrode, respectively; and κ_s and κ_c are the heat conductivity coefficients of the chalcogenide vitreous semiconductor and the electrode material, respectively. For small parameters γ, the values of $t_0(\gamma)$ at which the *S*-shaped current–voltage characteristics transform into monotonic current–voltage characteristics are close to 1/4. This corresponds to the uniform-temperature approximation [i.e., to the system of equations (1a) and (1b)] and the results obtained in [8]. As the parameter γ increases, the coordinate dependence of the temperature should be taken into account. This dependence leads to a monotonic decrease in the values of $t_0(\gamma)$. Therefore, the dependence $t_0(\gamma)$ shown in Fig. 3 permits one to predict the possible development of electrical instability with an *S*-shaped current–voltage characteristic due to the Joule heating for specific experimental situations (i.e., for particular values of t_0 and γ) [9].

Let us analyze how the phase transition from one conduction state to another conduction state, which can occur at the temperature $T_f > T_0$, affects the results

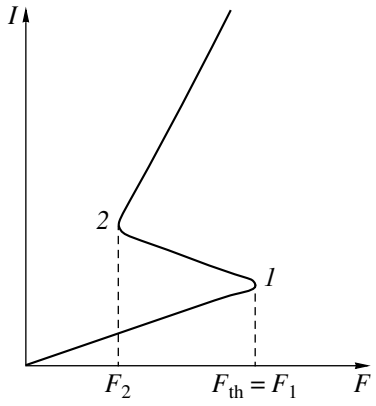

Fig. 2. Schematic representation of the *S*-shaped current–voltage characteristic. Points *1* and *2* correspond to points *1* and *2* in Fig. 1. The fields and temperatures at these points are determined from relationships (2a), (2b), (3a), and (3b).

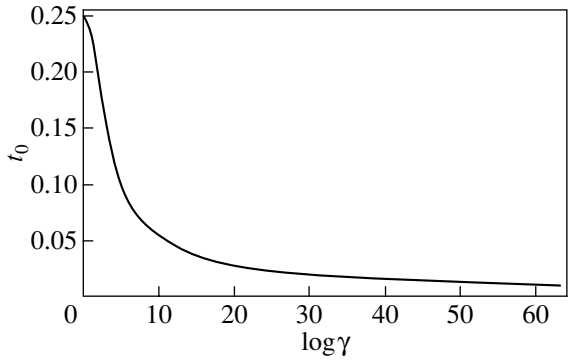

Fig. 3. Boundary of the existence region of the *S*-shaped current–voltage characteristic.

obtained. The analysis will be performed for small parameters γ, i.e., in the uniform-temperature approximation. It should be emphasized that the case in point is a semiconductor–metal phase transition that is not necessarily associated with structural ordering. As can be seen from Fig. 4, the conductivity transition manifests itself in the temperature independence from the heat release (curves Q_{1f}) in the range above the phase transition temperature T_f.

The condition $4kT_0 = \Delta E$ (see above) means that the temperatures $T_1 = T_{th}$ and T_2 become equal to each other and, moreover, the slope of the curve $Q_1(T)$ at the point $T_1 = T_2$ coincides with the slope of the curve $Q_2(T)$. This takes place at the inflection point of the curve $Q_1(T)$ (Fig. 1). In the case of the phase transition from one conduction state to another conduction state at the temperature T_f, the dependence $Q_1(T)$ can be approximated by the curve $Q_{1f}(T)$ (Fig. 4). For simplicity, we assume that the curve $Q_{1f}(T)$ at the temperature T_f varies smoothly, even if sharply, but does not have a kink.

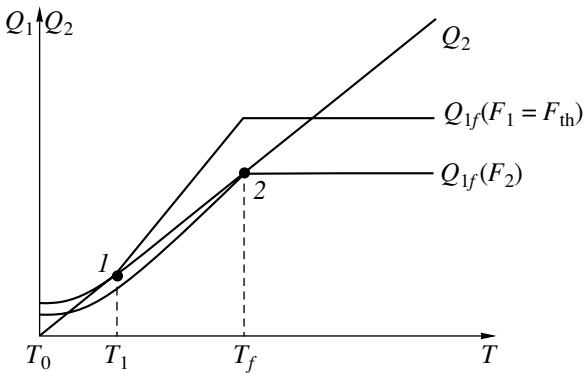

Fig. 4. Schematic representation of the left-hand (Q_1) and right-hand (Q_2) sides of Eq. (1a) in the case of a phase transition from one conduction state to another conduction state at a temperature T_f.

Therefore, the derivative dQ_{1f}/dT exists at all temperatures. In this case, the system of equations (1a) and (1b) describes the thermal mechanism of electrical instability with allowance made for the conductivity transition at the temperature T_f. Solutions (2a) and (2b) remain valid for $kT_0 \ll \Delta E$, whereas solutions (3a) and (3b) take the form

$$T_2 \approx T_f, \tag{4a}$$

$$F_2 \approx F_2(T_f). \tag{4b}$$

Assuming that the dependences $Q_{1f}(T)$ and $Q_1(T)$ differ from each other only in the immediate vicinity of the temperature T_{1f}, the inflection point of the curve $Q_{1f}(T)$ also lies in the vicinity of this temperature. Hence, the condition for the disappearance of the *S*-shaped current–voltage characteristic can be written in the following form:

$$Q_1 = Q_2|_{T_f}, \tag{5a}$$

$$\frac{dQ_1}{dT} = \left.\frac{dQ_2}{dT}\right|_{T_f}, \tag{5b}$$

$$\left.\frac{d^2Q_1}{dT^2}\right|_{T_f} = 0. \tag{5c}$$

As a result, we have $T_1 \approx T_2 \approx T_f$ or

$$\frac{kT_f^2}{\Delta E} = T_f - T_0. \tag{6}$$

Hence, the environment temperature has the form

$$T_0 = T_f\left(1 - \frac{kT_f}{\Delta E}\right) \equiv T_0(T_f). \tag{7}$$

The last relationship for the environment temperature T_0 replaces the condition $4kT_0 = \Delta E$ (or $t_0 = 1/4$). Therefore, the phase transition from one conduction state to another conduction state leads to a considerable decrease in the environment temperature T_0 [from the value of $\Delta E/4k$ to the value determined by relationship (7)] at which the *S*-shaped current–voltage characteristic associated with the thermal mechanism of electrical instability can be observed. For example, the ratio $\Delta E/4k$ at $\Delta E = 0.5$ eV is equal to 1450 K and the environment temperature $T_0(T_f)$ determined from relationship (7) at $T_f \approx 500$ K is 450 K. It is evident that an increase in the parameter γ results in a monotonic decrease in the environment temperature $T_0(\gamma)$, which corresponds to the disappearance of the *S*-shaped current–voltage characteristic in the case of the conductivity transition. For large parameters γ, the dependences calculated with and without regard for the conductivity transition should be very similar to each other. Therefore, the inclusion of the phase transition from one conduction state to another conduction state not only leads to a change in the range of parameters at which the material can exhibit an *S*-shaped current–voltage characteristic but also decreases the temperature of the transition to the low-resistance state.

Let us now consider our problem for the electronic–thermal mechanism of initiation of electrical instability. In the simplest approximation, the contribution of the electronic processes occurring in a strong electric field (with uniform strength F at temperature T) can be taken into account by introducing the conductivity $\sigma(T, F)$, which is dependent on both the temperature and the field strength. As a rule, the dependence of the conductivity σ on the field strength F for chalcogenide vitreous semiconductors can be written in explicit form

$$\sigma = \sigma_0 \exp\left(-\frac{\Delta E}{kT} + \frac{F}{F_0(T)}\right), \tag{8}$$

where $F_0(T)$ is the characteristic field whose strength and temperature dependence are governed by the specific electronic mechanism responsible for the change in the conductivity in a strong electric field. For simplicity, we assume that $F_0 = akT$, where a is a constant.

Then, the solutions to the system of equations (1a) and (1b) are the temperature and the field

$$T_{1,2} = \frac{1}{2k}\left(\Delta E - \frac{F_{1,2}}{a}\right)\left(1 \mp \sqrt{1 - \frac{4kT_0}{\Delta E - F_{1,2}/a}}\right), \tag{9a}$$

$$SL\sigma_0 F_{1,2}^2 \exp\left(-\frac{\Delta E}{kT_{1,2}} + \frac{F}{akT_{1,2}}\right) = \lambda S(T_{1,2} - T_0). \tag{9b}$$

The condition for the disappearance of the *S*-shaped current–voltage characteristic can be found from the equality of the radicand in relationship (9a) to zero:

$$T_{1,2} = 2T_0, \tag{10a}$$

$$4kT_0 = \Delta E(1 - F_1/a\Delta E), \quad V_{th} = F_{th}L. \tag{10b}$$

It can be seen from these expressions that the environment temperature corresponding to the disappearance of the *S*-shaped current–voltage characteristic also decreases significantly in the case of the electronic–thermal mechanism. The *S*-shaped current–voltage characteristic can disappear at any environment temperature T_0. In this case, we have $T_{1,2} = 2T_0$ and the critical parameters of the sample are determined from relationships (9a), (9b), (10a), and (10b) and obey the equation

$$\gamma_1 t_0 = (1 - 4t_0)^2, \quad (11)$$

where $\gamma_1 = \lambda e^2/L\sigma_0 a^2 k\Delta E$. This quantity and the parameter γ are proportional to the coefficient of external heat removal λ. However, since we use the uniform-temperature approximation, the quantity γ_1 does not depend on the heat conductivity coefficients. The different dependences of the quantities γ and γ_1 on the thickness L can be explained by the fact that the parameter γ depends on the thickness L due to a nonuniform heating, whereas the quantity γ_1 depends on the thickness because of the decrease in the effective activation energy in expression (8) with an increase in the field strength. Figure 5 depicts the dependence $t_0(\gamma_1)$ calculated from relationship (11). This dependence bounds the range of parameters at which the material can exhibit an *S*-shaped current–voltage characteristic due to the electronic–thermal mechanism of initiation of the instability.

Now, we analyze the influence of the semiconductor–metal conductivity transition at the temperature T_f on the development of the electrical instability. It is clear that, if the inequality $T_f > 2T_0$ is satisfied, the results obtained hold true on a qualitative level. At $T_f < 2T_0$, it is necessary to use the approach based on relationships (5a)–(5c).

Among the chalcogenide vitreous semiconductors, the $Si_{12}Te_{48}As_{30}Ge_{10}$ compound has been investigated most extensively. For this compound, the temperature dependence of the characteristic field F_0 is described by the expression

$$F_0 = akT(1 - T/T_s), \quad (12)$$

where the temperature T_s lies in the range 450–500 K and corresponds to an unknown phase transition. The temperature T_f of the phase transition from one conduction state to another conduction state is close to the temperature T_s. By assuming that, at this temperature, the exponent becomes equal to zero, the temperature T_f of the conductivity transition can be determined from the equation

$$\frac{\Delta E}{kT_f} = \frac{F}{akT_f(1 - T_f/T_s)}. \quad (13)$$

For $T_0 > T_s/2$, the dependence $\sigma(T)$ with the characteristic field F_0 represented by relationship (12) has no inflection point and the solution corresponding to the instability formally exists in all cases. Then, the approximate equality $T_0 \approx T_f$ can be treated as the condition for the disappearance of the *S*-shaped current–voltage characteristic.

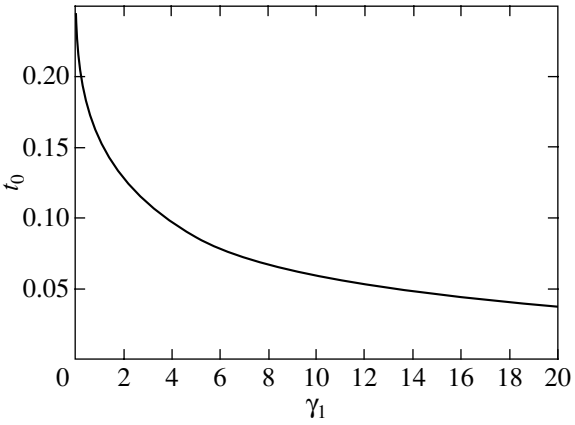

Fig. 5. Boundary of the existence region of the *S*-shaped current–voltage characteristic in the case of the electronic–thermal mechanism of electrical instability. The conductivity is described by relationship (8).

It should be noted that, for the thermal and electronic–thermal mechanisms with the characteristic field $F_0 = akT$, the exponent at the inflection point of the dependence $\sigma(T)$ is equal to –2; i.e., the conductivity is determined by the expression $\sigma = \sigma_0 \exp(-2)$. As a result, we have $-\Delta E/2kT_0 + F/F_0 = -2$ in the case of the electronic–thermal mechanism. For $\Delta E = 0.5$ eV and $T_0 = 300$ K, we obtain $-5800/600 + F/F_0 = -2$ and, hence, $F/F_0 \sim 8$. Note also that the heating associated with the electronic–thermal switching for the characteristic field F_0 given by expression (12) at $T_0 < T_s/2$ is less than the quantity $kT_0^2/\Delta E$ and decreases with an increase in the field strength *F*. In our opinion, this indicates the possible crossover to a purely electronic mechanism of the switching effect.

3. NECESSARY CONDITIONS FOR THERMAL ELECTRICAL INSTABILITY WITH AN *N*-SHAPED CURRENT–VOLTAGE CHARACTERISTIC

In the general case, the *N*-shaped current–voltage characteristic corresponds to the transition from a low-resistance state to a high-resistance state. Therefore, the negative feedback required to initiate the thermal electrical instability should occur between the processes of heating and change in the electric current passing through the sample; i.e., the heating of the sample should lead to a decrease in the electric current. It is obvious that the thermal electrical instability with an *N*-shaped current–voltage characteristic cannot be observed for the semiconducting-type temperature dependence of the conductivity $\sigma(T) = \sigma_0 \exp(-\Delta E/kT)$ with a positive derivative $d\sigma/dT > 0$. For an *N*-shaped

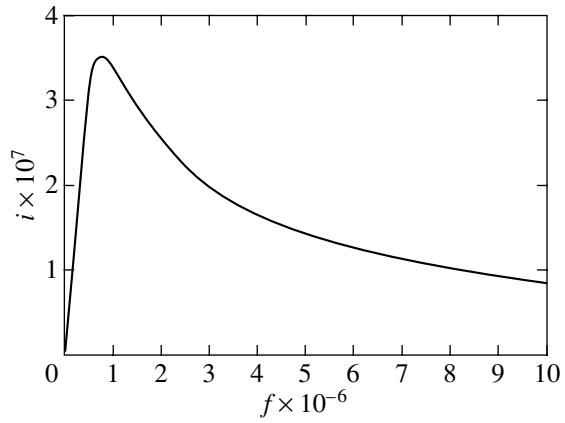

Fig. 6. *N*-shaped current–voltage characteristic in the case of thermal electrical instability. The conductivity is described by relationship (14).

current–voltage characteristic to be observed, the dependence $\sigma(T)$ must contain a portion with a negative derivative $d\sigma/dT < 0$, i.e., in which the conductivity decreases with an increase in the temperature. In a more general form, this situation can be considered as a metal–semiconductor conductivity transition at the temperature T_f when the resistance R_1 of the metal is less than the resistance R_2 of the semiconductor. When this transition occurs as a result of the Joule heating I^2R, the appreciably higher voltage is necessary to maintain the new state at the temperature T_f. If such a voltage is not applied to the sample, the sample undergoes relaxation oscillations with transitions from the state with resistance R_2 to and from the state with resistance R_1.

In the framework of the phenomenological electronic–thermal theory, the origin of an *N*-shaped current–voltage characteristic has not been considered in the literature. It is not evident whether the electronic–thermal theory can explain the existence of an *N*-shaped current–voltage characteristic, because the transition from a low-resistance state to a high-resistance state can be accompanied by a decrease in the released power. This leads to a decrease in the temperature of the sample, which seemingly should transform into the initial low-resistance state.

Below, we will demonstrate that the *N*-shaped current–voltage characteristic can be obtained with due regard for the dependence $\sigma(T)$ involving a portion with a negative derivative $d\sigma/dT < 0$. For this purpose, the dependence $\sigma(T)$ is approximated by the function

$$\sigma(T) = \sigma_0 \exp(-\Delta E/kT - T/T_p). \quad (14)$$

This dependence exhibits a maximum at a temperature $T_{\max} = (T_p \Delta E/k)^{1/2}$, which approximates the temperature of the phase transition from one conduction state to another conduction state. The dependence has a positive derivative $d\sigma/dT > 0$ at $T < T_p$ and a negative derivative $d\sigma/dT < 0$ at $T > T_p$. Therefore, the temperature $T_{\max}$ simulates the temperature T_f of the phase transition from the state with a semiconducting-type temperature dependence of the conductivity to the state with a metallic-type temperature dependence of the conductivity. The current–voltage characteristic can be determined from the following relationships:

$$Q_1 = Q_2 \quad \text{or} \quad L\sigma F^2 = \lambda(T - T_0), \quad (15a)$$

$$J(F) = \sigma(T(F))F = \sigma_0 \exp(-\Delta E/kT(F) - T(F)/T_p)F. \quad (15b)$$

The temperature $T(F)$, which is dependent on the mean electric field $F = V/L$, is the solution of Eq. (15a). Here, we used the simplest approximation of the uniform temperature T and field F, which are independent of the coordinates. Substitution of the temperature $T(F)$ into expression (15b) gives the current–voltage characteristic. Since Eq. (15a) is transcendental, it is more convenient to use the temperature T as a parameter and to calculate the quantities $F(T)$ and $J(T)$ and the current–voltage characteristic at a specified temperature T. Then, the final equations describing the current–voltage characteristic can be written in the form

$$i = J/J_0 = ((\tau - 1)\exp(-1/t_0\tau - \tau/t_p))^{1/2}, \quad (16a)$$

$$f = F/F_0 = ((\tau - 1)\exp(1/t_0\tau + \tau/t_p))^{1/2}, \quad (16b)$$

where $\sigma(\tau) = \sigma_0 \exp(-1/t_0\tau - \tau/t_p)$, $J_0 = (\lambda\sigma_0 T_0/L)^{1/2}$, $F_0 = J_0/\sigma_0$, $\tau = T/T_0$, $1/t_0 = \Delta E/kT_0$, and $t_p = T_p/T_0$.

Relationships (16a) and (16b) describe the current–voltage characteristic associated with the Joule heating of the layer for which the temperature dependence of the conductivity $\sigma(T)$ is given by expression (14). The current–voltage characteristics were calculated for several parameters (t_0, t_p). One of these current–voltage characteristics at $1/t_0 = 15$ and $t_p = 0.0765$ ($T_{\max} \approx T_f \approx$ 300 K) is plotted in Fig. 6.

It can be seen from Fig. 6 that the phenomenological electronic–thermal theory provides a correct description of the *N*-shaped current–voltage characteristic when the dependence $\sigma(T)$ exhibits a portion in which the conductivity decreases with an increase in the temperature ($d\sigma/dT < 0$). This inference does not hold for all parameters. Actually, condition (15a) is satisfied only in the case where the conductivity decreases rather smoothly and the released Joule heat ensures the temperature higher than the phase transition temperature T_f in the range of the descending portion of the *N*-shaped current–voltage characteristic.

The transition from a low-resistance state to a high-resistance state with an *N*-shaped current–voltage characteristic was observed in poly(ethylene) with additives of graphite [10]. The switching effect has been used in devices that prevent electric circuits from overloading. The *N*-shaped current–voltage characteristic in these devices is explained by the sharp decrease in the con-

ductivity of the material at a temperature of approximately 400 K. This temperature can be identified with the aforementioned temperature T_f of the phase transition from one conduction state to another conduction state. In our earlier work [7], we experimentally observed an *N*-shaped current–voltage characteristic in the poly(phenylvinylene) organic semiconductor and made the assumption that this characteristic is related to the portion with a negative derivative $d\sigma/dT < 0$ in the temperature dependence of the conductivity $\sigma(T)$.

4. CONCLUSIONS

Thus, it has been demonstrated that the origin of *S*-shaped and *N*-shaped current–voltage characteristics can be described in terms of the phenomenological electronic–thermal theory.

The key condition for the existence of an *S*-shaped current–voltage characteristic is a strong activation dependence of the conductivity on the temperature (i.e., small ratios $kT/\Delta E$) and a heat removal that is not too large (i.e., not overly large parameters γ and γ_1).

It has been shown that the phenomenological electronic–thermal theory provides a correct description of the *N*-shaped current–voltage characteristic when the temperature dependence of the conductivity $\sigma(T)$ exhibits a portion with a negative derivative $d\sigma/dT < 0$.

REFERENCES

1. B. T. Kolomiets and É. A. Lebedev, Radiotekh. Élektron. (Moscow) **8**, 2097 (1963).
2. S. R. Ovshinsky, Phys. Rev. Lett. **21**, 1450 (1968).
3. B. T. Kolomiets, É. A. Lebedev, and I. A. Taksami, Fiz. Tekh. Poluprovodn. (Leningrad) **3**, 731 (1969) [Sov. Phys. Semicond. **3**, 621 (1969)].
4. B. K. Ridley, Proc. Phys. Soc. **32**, 954 (1963).
5. D. Adler, H. K. Henisch, and N. Mott, Rev. Mod. Phys. **50**, 209 (1978).
6. B. T. Kolomiets, É. A. Lebedev, and K. D. Tséndin, Fiz. Tekh. Poluprovodn. (Leningrad) **5**, 1568 (1971) [Sov. Phys. Semicond. **5**, 1369 (1972)].
7. E. Lebedev, S. Ferero, W. Brutting, and M. Schwoerer, Synth. Met. **111–112**, 345 (2000).
8. B. Yu. Lototskiĭ and L. K. Chirkin, Fiz. Tverd. Tela (Leningrad) **6**, 1967 (1964) [Sov. Phys. Solid State **6**, 1553 (1965)].
9. B. L. Gel'mont and K. D. Tséndin, in *Electronic Phenomena in Noncrystalline Semiconductors* (Nauka, Leningrad, 1976), p. 177 [in Russian].
10. A. R. Duggal and L. M. Levinson, Appl. Phys. Lett. **71**, 1939 (1997).

Translated by O. Borovik-Romanova

Physics of the Solid State, Vol. 47, No. 3, 2005, pp. 446–450. Translated from Fizika Tverdogo Tela, Vol. 47, No. 3, 2005, pp. 433–436.

SEMICONDUCTORS AND DIELECTRICS

Electron Capture by Charged Impurities in Semiconductors under Conditions of Spatial Diffusion

V. D. Kagan

Ioffe Physicotechnical Institute, Russian Academy of Sciences, Politekhnicheskaya ul. 26, St. Petersburg, 194021 Russia

e-mail: victor.kagan@mail.ioffe.ru

Received July 12, 2004

Abstract—The capture of electrons by charged impurities in semiconductors due to spatial diffusion is investigated theoretically. In a semiconductor, an electron either can be captured by the field of a charged impurity if this electron loses energy by emitting phonons or can be ionized from the trapping state if it acquires energy by absorbing phonons. The electron trapping is governed by a change in the distribution function of electrons in both coordinate and momentum space. The trapping coefficient is calculated under the condition where it is determined by the diffusion redistribution of the electron density in the field of a charged impurity. © *2005 Pleiades Publishing, Inc.*

1. STATEMENT OF THE PROBLEM

In a semiconductor, impurities lose electrons to the conduction band and the density of conduction electrons is determined by a balance between the trapping of electrons by impurities into a bound state and the release of electrons from this state. The balance equation describing the evolution of the electron density n_e can be written in the form

$$\frac{dn_e}{dt} = k_i n_{\text{im}} - k_r n_{\text{im}} n_e + G. \quad (1)$$

Equation (1) for the electron balance includes the terms describing the ionization and trapping of electrons in a semiconductor containing impurities with a concentration n_{im} (where k_i and k_r are the coefficients of ionization and trapping of electrons, respectively) and the term G characterizing the generation of nonequilibrium electrons. The coefficients involved in this phenomenological equation can be determined within the microscopic kinetic theory. The self-consistent variant of the microscopic kinetic theory was elaborated in my recent paper [1], in which the kinetic equation allowing for the transitions between free and bound states of electrons in impurities was obtained for the first time and the electron balance equation (1) was derived from this kinetic equation. In turn, this made it possible to calculate the coefficients k_i and k_r in the framework of the microscopic kinetic theory.

However, in [1], the theoretical treatment was carried out under the important assumption that the distribution functions $f^{(1, 2)}$ of free and trapped electrons depend only on the total electron energy E. If the motion of an electron is described in terms of classical mechanics, the total electron energy is the sum of the kinetic energy $\varepsilon_{\mathbf{p}}$, which is a function of the electron momentum $\mathbf{p}$, and the potential energy $U(\mathbf{r})$, which is a function of the coordinate $\mathbf{r}$; that is,

$$E = \varepsilon_{\mathbf{p}} + U(\mathbf{r}), \quad \varepsilon_{\mathbf{p}} = \frac{\mathbf{p}^2}{2m}. \quad (2)$$

Here, m is the effective electron mass. For a charged impurity, the potential energy is defined by the relationship $U(\mathbf{r}) = -e_1^2/r$, where $e_1^2 = \frac{ze^2}{\kappa}$, z is the impurity charge expressed in terms of an elementary charge, and κ is the static permittivity of the lattice. The total energy is positive for free electrons and negative for bound electrons. Hence, in what follows, the total energy of trapped electrons will be designated as $-E$.

The transitions between the states of free and trapped electrons are governed by a change in the electron distribution function in both momentum and coordinate space. In coordinate space, the change in the electron distribution function is treated as a spatial diffusion. In this paper, we will determine the conditions under which the spatial diffusion can be ignored and will then calculate the coefficients of ionization and trapping of electrons under the condition where the spatial diffusion and the energy relaxation play equally important roles.

2. THEORETICAL TREATMENT

Energy relaxation in semiconductors occurs in the course of electron–phonon collisions. Let us consider a situation in which the temperatures are high enough to satisfy the inequality $T \gg 3ms^2$, where T is the temperature expressed in terms of energy and s is the velocity

of sound. For both free and trapped electrons, the coordinate dependence should be taken into account when the particles are characterized by thermal energies. Therefore, the motion of these particles can be described in terms of standard kinetic equations without inclusion of the terms accounting for the transitions between the states of free and trapped particles. It should be noted, however, that these terms will be needed in subsequent calculations of the ionization and trapping coefficients.

For free electrons subjected to a force field induced by an impurity located at the origin of the coordinates, the principal component of the distribution function $f(r, E)$ depends on both the total energy of an electron and the radius r, which is equal to the distance between the electron and the impurity. Moreover, the distribution function of free electrons has an insignificant component associated with the electric current:

$$f_1(r, E) = \tau(\varepsilon_\mathbf{p})\frac{\mathbf{p}}{m}(\nabla f(r, E) - \nabla U(\mathbf{r})\partial f(r, E)/\partial E), \quad (3)$$

where $\tau(\varepsilon_\mathbf{p})$ is the relaxation time of the electron momentum $\mathbf{p}$. For the distribution function $f(r, E)$, we obtain the following kinetic equation, which is averaged over the angular variables:

$$D(E + e_1^2/r)\sqrt{(E + e_1^2/r)} \times\left[\partial^2 f/\partial^2 r + \frac{(2E + e_1^2/r)}{(E + e_1^2/r)}\partial f/r\partial r\right] + \partial/\partial E\left[\frac{\sqrt{2}(E + e_1^2/r)^2}{l\sqrt{m}}(T\partial f/\partial E + f)\right] = 0, \quad (4)$$

where $D(\varepsilon_\mathbf{p}) = \frac{2\varepsilon_\mathbf{p}}{3m}\tau(\varepsilon_\mathbf{p})$, $\varepsilon_\mathbf{p} = E + e_1^2/r$, and l is the energy mean free path. In kinetic equation (4), the term describing the energy relaxation is transformed into a differential form, because the energy transfer due to electron–phonon collisions is insignificant [2]. Let us assume that $D \sim \sqrt{E + e_1^2/r}$. This relationship is satisfied under the condition where the electron momentum relaxation is provided by phonons or point impurities. The solutions we are interested in should decrease for long distances. It is necessary to note that the Boltzmann function $f(r, E) = A\exp(-E/T)$, which is independent of the distance, is always a solution to kinetic equation (4). Therefore, the spatial diffusion can come into effect only when the electron distribution is a nonequilibrium function of the energy for short distances.

For energies $E \gg e_1^2/r$, the variables involved in kinetic equation (4) can be separated and the general solution can be written in the following form:

$$f(r, E) = a_0\exp(-E/T) + \frac{1}{r}\sum_{n=0}^{\infty} c_n L_n^{(1)}(E/T)\exp(-(E/T + \sqrt{n}r/l_d)), \quad (5)$$

where $L_n^{(1)}$ is the generalized Laguerre polynomial and $l_d^2 = D(T)l\sqrt{m}/\sqrt{T}$. The expansion coefficients can be determined from the energy dependence of the electron distribution function for distances shorter than the mean free path l_d. In the function $f(r, E)$ [solution (5)], the dominant contribution is made by the component that does not decrease with an increase in the distance and is an equilibrium function of the energy.

For energies $E \ll e_1^2/r$, we obtain quite a different solution to the kinetic equation. The variables involved in this equation can also be separated. As a result, the function $f(r, E)$ and its approximation $\varphi(E)$ for short distances r_0 can be related by the integral expression

$$f(r, E) = \int_0^\infty \varphi(E')dE' \int_{-\infty}^{\infty} dt e^{it(E'-E)}\frac{K_0(\sqrt{\gamma rt(Tt - i)})}{K_0(\sqrt{\gamma r_0 t(Tt - i)})}, \quad \gamma = \frac{4e_1^2}{l_d^2}. \quad (6)$$

In expression (6), K_0 is the Macdonald function, which provides a decrease in the function $f(r, E)$ [solution (6)] as the distance r increases, and the square root is determined in such a way that it is positive for large values of the variable. By virtue of the singularity of the Macdonald function K_0 at the origin of the coordinates, the distance r_0 should be set very short but finite.

For $\varphi(E) = A\exp(-E/T_e)$, where T_e is the electron temperature ($T_e \neq T$), the solution to the kinetic equation can be represented in a simpler form, that is,

$$f(r, E) = Ae^{-E/T_e}\frac{K_0(\sqrt{\gamma r T_e^{-2}(T_e - T)})}{K_0(\sqrt{\gamma r_0 T_e^{-2}(T_e - T)})}. \quad (7)$$

Let us now assume that the electron temperature T_e tends to a temperature T. As a consequence, the function $f(r, E)$ described by relationship (7) is transformed into an equilibrium function. This transformation can be illustrated as follows. It is assumed that $r \gg r_0$. The difference between the distances r and r_0 should decrease as the electron temperature T_e tends to the temperature T; as a result, the numerator and denominator in relationship (7) cancel each other out. Therefore, the solution to the kinetic equation does not decrease with an increase in the distance and is an equilibrium

function of the energy only in the case when the boundary condition is specified in the form of an energy function that is very similar to the equilibrium function.

Since the distance r_0 is very short, the Macdonald function K_0 in the denominator of expression (6) can be replaced by the quantity $L = \ln(l_d T/e_1\sqrt{r_0})$. Then, expression (6) can be rewritten in the simplified form

$$f(r, E) = \int_0^\infty \frac{dE'}{TL}\frac{\varphi(E')}{R}\exp\left(\frac{E-E'}{2T} - \frac{1}{2}R\right),$$
$$R = \sqrt{\frac{\gamma r}{T} + \frac{(E-E')^2}{T^2}}. \quad (8)$$

It turned out that, under an arbitrary boundary condition, the function $f(r, E)$ described by expression (8) decreases for distances greater than the quantity $l_d^2 E/e_1^2$, as is the case with relationship (7).

Kinetic equation (4) becomes applicable to trapped electrons after the energy E is replaced by the quantity $-E$. Since the kinetic energy is positive, we have $E < e_1^2/r$. Therefore, for trapped electrons, there exist only solutions of the type given by expression (6).

The ionization and trapping coefficients k_i and k_r can be calculated from the expression obtained in [1] for the collision integral describing electron–phonon collisions that are responsible for transitions between the states of free and trapped particles. After integrating this expression over the entire phase space, we derive electron balance equation (1). In turn, the electron balance equation makes it possible to obtain expressions for the ionization and trapping coefficients k_i and k_r in terms of the distribution functions of free and trapped particles $f^{(1, 2)}(\mathbf{r}, \mathbf{p})$:

$$k_r = \frac{1}{16\pi^5\hbar^4 n_e}\int d\mathbf{p}d\mathbf{r}d\mathbf{q}\delta(\varepsilon_\mathbf{p} - \varepsilon_{\mathbf{p}-\hbar\mathbf{q}} - \hbar\omega_\mathbf{q})|c_\mathbf{q}|^2$$
$$\times f^{(1)}(\mathbf{r}, \mathbf{p})(n_q + 1)\Theta\left(\varepsilon_\mathbf{p} - \frac{e_1^2}{r}\right)\Theta\left(\frac{e_1^2}{r} - \varepsilon_{\mathbf{p}-\hbar\mathbf{q}}\right),$$
$$k_i = \frac{1}{16\pi^5\hbar^4}\int d\mathbf{p}d\mathbf{r}d\mathbf{q}\delta(\varepsilon_\mathbf{p} - \varepsilon_{\mathbf{p}-\hbar\mathbf{q}} - \hbar\omega_\mathbf{q})|c_\mathbf{q}|^2 \quad (9)$$
$$\times f^{(2)}(\mathbf{r}, \mathbf{p})n_\mathbf{q}\Theta\left(\varepsilon_\mathbf{p} - \frac{e_1^2}{r}\right)\Theta\left(\frac{e_1^2}{r} - \varepsilon_{\mathbf{p}-\hbar\mathbf{q}}\right).$$

Here, $\mathbf{q}$ and $\omega_\mathbf{q} = sq$ are the wave vector and the frequency of a phonon, respectively; $c_\mathbf{q}$ is the electron–phonon coupling constant; and $n_\mathbf{q} = (e^{\hbar\omega_\mathbf{q}/T} - 1)^{-1}$ is the Planck distribution function for phonons. Mathematically, the functions $\Theta(x) = 1$ $(x > 0)$ and $\Theta(x) = 0$ $(x < 0)$ entering into relationships (9) correspond to the conditions that an electron with momentum $\mathbf{p}$ be free and its energy be positive and that an electron with momentum $\mathbf{p} - \hbar\mathbf{q}$ be trapped and its energy be negative. When deriving relationships (9), it was assumed that the transitions between the states of free and trapped electrons occur in the vicinity of each impurity independently of one another. This becomes possible only when the impurity concentration satisfies the following conditions:

$$\frac{e_1^2}{3ms^2} \gg n_{\text{im}}^{-\frac{1}{3}} \gg \frac{e_1^2}{T}. \quad (10)$$

By simplifying relationships (9), we obtain

$$k_r = \frac{1}{2\pi l\hbar^3 n_e ms^4}\int_0^\infty dE\int_E^\infty dE'\frac{E'^2}{1 - e^{-E'/T}}$$
$$\times \int_0^{8e_1^2 ms^2/E'^2} r^2 dr f^{(1)}(r, E),$$
$$k_i = \frac{1}{2\pi l\hbar^3 ms^4}\int_0^\infty dE\int_E^\infty dE'\frac{E'^2}{e^{-E'/T} - 1} \quad (11)$$
$$\times \int_0^{8e_1^2 ms^2/E'^2} r^2 dr f^{(2)}(r, E' - E).$$

Substitution of the solutions to kinetic equation (4) into integrals (11) demonstrates that the parameter $e_1^2/l_d T$ is of fundamental importance in solving our problem. In the case when this parameter is small, it is necessary to use the solution given by expression (5). However, the principal function involved in this solution is independent of the coordinates; hence, we are led to the kinetic theory considered in [1].

When the parameter $e_1^2/l_d T$ is large, the spatial diffusion plays a significant role in the process of electron trapping. Therefore, it is necessary to use solutions of the type given by expression (6). Among these solutions, for simplicity, we will restrict our consideration to the solution given by relationship (7). The basic inequality can be written in the form

$$e_1^2(T_e - T)/l_d T_e^2 \gg 1. \quad (12)$$

In order to calculate the trapping coefficient k_r, we use the nonequilibrium function $\varphi(E) = [n_e\hbar^3\sqrt{2\pi^3}/(mT_e)^{3/2}]\exp(-E/T_e)$. In this case, the electron temperature T_e is not anomalously close to the temperature T. Upon substituting the nonequilibrium func-

tion into relationship (11) for the trapping coefficient k_r, we obtain

$$k_r = \frac{4\sqrt{\pi}l_d^3 T_e^{5/2}}{3Llms(T_e - T)^{3/2}}\int_0^\infty x^2 K_0(x)dx. \quad (13)$$

This relationship differs from the formula $k_r^{(L)} = 4\pi e_1^2 D(T)/T$ proposed by Langevin [2, 3]. The main reason for this difference is that the Langevin coefficient is not a trapping coefficient. The trapping coefficient is the quantity k_r involved in electron balance equation (1). It is this quantity that can be measured in the experiment. We calculated this quantity theoretically. Relationship (11) defines the trapping coefficient and is universal in all the cases under consideration. In [1], this relationship was used under the conditions opposite to those specified by inequality (12). In the present work, the same relationship is used in the situation where inequality (12) is satisfied. The Langevin coefficient is the ratio of the electron flux through a sphere surrounding a charged impurity to the electron concentration. The identification of the Langevin coefficient with the trapping coefficient is an arbitrary and unreasonable assumption. The Langevin theory was outlined by Abakumov *et al.* [2, ch. 7]. Moreover, these authors made some attempts to generalize this theory. However, in all the cases analyzed in [2], the trapping coefficient was defined as the normalized flux of particles through a sphere surrounding a charged impurity. Since this quantity is not a trapping coefficient, all the inferences drawn in [2] cannot be considered satisfactory.

We assume that the degree of nonequilibrium of the electron distribution function is not anomalously small: $(T_e - T)/T_e \sim 1$. Consequently, the ratio of the Langevin coefficient to the trapping coefficient given by formula (13) is equal to $e_1^2 s\sqrt{m}/l_d T_e^{3/2}$. This ratio involves the product of the large quantity $e_1^2/l_d T_e$ multiplied by the small quantity $\sqrt{ms^2/T_e}$ and, hence, can be of any order of magnitude.

The calculation of the ionization coefficient k_i is performed in the same manner as for the trapping coefficient k_r. However, in this case, the electron density n_{e0} involved in the function $\varphi(E)$ is assumed to be equilibrium and the electron temperature T_e is taken to be anomalously close to the temperature T: $T_e = T + 3ms^2$. Moreover, the difference between the temperatures is disregarded for energies higher than the energy E_1 ($E_1 \sim T$) and is taken into account for lower energies. The final expression for the ionization coefficient contains two terms:

$$k_i = \frac{4n_{e0}}{9l}\left(\frac{64\sqrt{2\pi m}e_1^6 s^2}{E_1^3\sqrt{T}} + \frac{\sqrt{3\pi}l_d^3 T^{5/2}}{3Lm^{5/2}s^4}\int_0^Q x^2 K_0(x)dx\right),$$
$$Q = 96\left(\frac{e_1 ms^2}{l_d E_1 T}\right)^2. \quad (14)$$

It should be noted that the expressions for the ionization coefficient can be different depending on the parameter that involves the diffusion length and accounts for the degree of nonequilibrium of the distribution function at low energies. Under the condition $e_1^2/l_d T \gg T/3ms^2 \gg 1$, we have

$$k_i = \frac{256\sqrt{2\pi m}n_{e0}e_1^6 s^2}{9E_1^3 l\sqrt{T}}. \quad (15)$$

This relationship is valid at high energies and does not involve quantities characterizing the degree of nonequilibrium of the distribution function. However, under the condition $T/3ms^2 \gg e_1^2/l_d T \gg 1$, we obtain

$$k_i = \frac{4\sqrt{3\pi}n_{e0}l_d^3 T^{5/2}}{27Llm^{5/2}s^4}\int_0^\infty x^2 K_0(x)dx. \quad (16)$$

Expression (16) is similar to relationship (13) with allowance made for the difference in the degrees of nonequilibrium of the distribution functions for free and trapped electrons.

3. CONCLUSIONS

The trapping coefficient controlled by the spatial diffusion was calculated in the framework of the theories proposed earlier in [2]. However, this coefficient does not coincide with the trapping coefficient entering into the balance equation; i.e., it is not an experimentally measured trapping coefficient. In this paper, the influence of the spatial diffusion on the capture of electrons by a charged impurity and their release from the trapping state was analyzed within the kinetic theory developed in [1]. It was demonstrated that the influence of the spatial diffusion on the processes of ionization and trapping of electrons by charged impurities manifests itself only when specific conditions are satisfied. These conditions include the degree of nonequilibrium of the distribution functions for free and trapped electrons. Expressions were derived for the ionization and

trapping coefficients involved in the balance equations for the electron density.

ACKNOWLEDGMENTS

The author would like to thank S.V. Gantsevich and M.I. Muradov for their participation in discussions of the results and for helpful remarks.

This work was supported by the Ministry of Industry and Science of the Russian Federation, project no. NSh-2242.2003.2.

REFERENCES

1. V. D. Kagan, Fiz. Tverd. Tela (St. Petersburg) **47** (2), 210 (2005) [Phys. Solid State **47** (2), 217 (2005)].
2. V. N. Abakumov, V. I. Perel', and I. N. Yassievich, *Nonradiative Recombination in Semiconductors* (S.-Peterb. Inst. Yad. Fiz. Ross. Akad. Nauk, St. Petersburg, 1997) [in Russian].
3. M. P. Langevin, Ann. Chim. Phys. **28**, 289 (1903); Ann. Chim. Phys. **28**, 433 (1903).

Translated by O. Borovik-Romanova

Physics of the Solid State, Vol. 47, No. 3, 2005, pp. 451–458. Translated from Fizika Tverdogo Tela, Vol. 47, No. 3, 2005, pp. 437–444.

SEMICONDUCTORS AND DIELECTRICS

Charge-Transfer Transitions and Optical Spectra of Vanadates

A. V. Zenkov

Ural State Technical University, ul. Mira 19, Yekaterinburg, 620002 Russia

e-mail: andreas@r66.ru

Received May 27, 2004; in final form, July 26, 2004

Abstract—Specific features of the charge-transfer states and O2*p* ⟶ V3*d* transitions in the $(VO_6)^{9-}$ octahedral complex are studied using the cluster approach. The reduced matrix elements of the electric-dipole transition operator are calculated for many-electron wave functions corresponding to the initial and final states of a charge-transfer transition. Using a parameterization of the results, the relative intensities of the allowed charge-transfer transitions are calculated disregarding the mixing of different configurations of the same symmetry. The Tanabe–Sugano theory is used with inclusion of this mixing to calculate the energies of many-electron charge-transfer transitions and their actual intensities. Modeling of the optical spectrum of $LaVO_3$ reveals a complicated charge-transfer transition band consisting of 81 lines. The main maxima of the band are in the range 6.3–7.3 eV. There are also additional maxima in the regions of ≈3 and ≈8–9 eV. The bandwidth is ≈10 eV. The results of model calculations are in agreement with experiments and demonstrate the weakness of the widely used assumption that the spectrum of charge-transfer transitions has a simple structure. © *2005 Pleiades Publishing, Inc.*

1. INTRODUCTION

One of the current problems in the physics of strongly correlated systems is uncovering the nature of the electronic structure and energy spectrum of oxides of 3*d* elements, which are very promising for the creation of new important materials, from high-temperature superconductors to materials with colossal magnetoresistance and highly nonlinear optical properties. Optical and magnetooptical methods have proven very effective in studying the electronic structure and energy spectrum of these compounds. However, the nature of the low-energy electron-hole excitations is still under discussion. First proposed in [1] for yttrium iron garnet and developed further in [2] for a wider class of iron-based oxides, the idea that the optical and magnetooptical properties in the near-ultraviolet range and the fundamental optical absorption edge are determined by the charge-transfer (CT) transitions from the oxygen anion to the 3*d*-metal cation is obtaining general recognition at the present time [3, 4]. The ligand–metal and metal–ligand CT processes are well-established concepts in theoretical chemistry and spectrochemistry [5].

However, there is no consistent theory of CT states and transitions in 3*d*-metal oxides, and this has held back progress in understanding the nature of the optical spectra, the interpretation of experiments, and the development of the appropriate theory of the electronic structure of strongly correlated systems. Most studies have used the very primitive idea of CT without much modification since its introduction. Attempts have been made to link the specific features of the optical spectra of 3*d*-metal oxides to certain 2*p*–3*d* CT transitions [6] (as though mentioning an electron shell is enough to precisely define the wave function) or, at best, the t_{2g} and e_g symmetry classification of 3*d* electrons in a crystal field has been drawn from and then, going back to the original source [2], 2*p* ⟶ 3*d* t_{2g} and 2*p* ⟶ 3*d* e_g CT transitions have been used [7–9]. This kind of "one-electron" approach to CT transitions and states is entirely insufficient not only for quantitative but even for qualitative description of the observed optical and magnetooptical properties of 3*d*-metal oxides.

One-electron band models, including modern modifications like LDA + *U* [10], do not resolve the issue, because they are unable to reproduce the important effects of intra-atomic correlations, which shape the structures of the ground and excited CT states.

The goal of the present work is to study CT transitions and states and the optical spectra of vanadates using the cluster model of charge-transfer transitions, which has been successfully employed to describe the optical and magnetooptical spectra of orthoferrites, iron garnets, and a number of insulating cuprates and manganites [11–14]. The model has a clear physical meaning and makes it possible to correctly include electron–electron correlations and the crystal-field and variable-valence effects. In a later paper, we will extend our analysis to strongly correlated oxides of other transition 3*d* metals.

1063-7834/05/4703-0451$26.00

2. CHARGE-TRANSFER STATES AND TRANSITIONS IN VANADATES

Slightly distorted $(VO_6)^{9-}$ octahedral complexes are the main optical and magnetooptical centers in V_2O_3-type oxides with the corundum structure and in RVO_3 compounds with the perovskite structure (R stands for a trivalent ion of yttrium or a rare-earth metal). The configuration of the ground state of the $(VO_6)^{9-}$ complex consists of predominantly anion-type occupied molecular orbitals (MOs) $O_{1s,\,2s,\,2p}$, predominantly cation-type occupied molecular orbitals $V_{1s,\,2s,\,2p,\,3s,\,3p}$, and partly occupied MOs of the 3d type. The ground state of the complex is the orbital triplet $|\kappa_0\gamma_{2p}^6 t_{2g}^2\,{}^3T_{1g}\rangle$, where κ_0 denotes the internal MOs (which are invariable in our case) and is omitted in what follows. The excited states of the electron configuration are $|\gamma_{2p}^6 3d^{2^{2s+1}}\Gamma_g\rangle$. A transition between the ground and any of the excited states is a so-called d–d transition, which does not involve anion states.

A charge-transfer excited state of the complex is formed if an electron is transferred from a predominantly anion MO to a 3d-type MO (either t_{2g} or e_g) of the central V^{3+} ion of the complex. This configuration is conventionally described as $\tilde{\gamma}_{2p}^1 3d^3$, where $\tilde{\gamma}_{2p}^1$ denotes a "hole" in the anion-MO core. A transition between the ground and an excited configuration is a CT transition $\gamma_{2p} \longrightarrow 3d$ (t_{2g} or e_g).

A charge-transfer configuration has two unfilled shells: the "ligand" γ_{2p} and 3d shells. Many-electron states of the CT configuration can be written as $|\tilde{\gamma}_{2p}^1\,{}^2\Gamma_u;\ 3d^{3^{2s'+1}}\Gamma_g'\rangle$ disregarding the interactions between the 2p hole and 3d electrons. The interaction between the 2p hole and 3d shell splits these states into $|\tilde{\gamma}_{2p}^1\,{}^2\Gamma_u;\ 3d^{3^{2s'+1}}\Gamma_g' :\ {}^{2s+1}\tilde{\Gamma}_u\rangle$ terms. The splitting can reach as high as several tenths of an electronvolt, according to the estimates made in [15].

According to the parity, spin, and quasimomentum selection rules, electric-dipole transitions are allowed from the ground state ${}^3T_{1g}$ of the $(VO_6)^{9-}$ complex to the terms of ${}^3\mathfrak{G}_u$ type ($\mathfrak{G} = T_1 \times T_1 = A_1 + E + T_1 + T_2$) of the CT configurations $\tilde{\gamma}_{2p}^1 t_{2g}^3$ (CT into the t_{2g} shell) and $\tilde{\gamma}_{2p}^1 t_{2g}^2 e_g$ (CT into the e_g shell). Among the highest energy MOs of the 2p type, there are two with the t_{1u} symmetry ($t_{1u}(\sigma)$, $t_{1u}(\pi)$) and one MO of the $t_{2u}(\pi)$ type. Thus, six one-electron CT transitions, denoted as ${}^3T_{1g} \longrightarrow {}^3\mathfrak{G}_u$ in the symmetry notation, have the lowest energies. These transitions are $t_{2u}(\pi)$, $t_{1u}(\pi)$, and $t_{1u}(\sigma) \longrightarrow t_{2g}$ with predicted energies of 3.1, 3.9, and 5.1 eV, respectively (here and henceforth, the data are presented for the $(FeO_6)^{9-}$ complex in the "orthoferrite" environment), and $t_{2u}(\pi)$, $t_{1u}(\pi)$, and $t_{1u}(\sigma) \longrightarrow e_g$ with predicted energies of 4.4, 5.3, and 6.4 eV, respectively [16].

These one-electron transitions generate the following many-electron CT transitions of the ${}^3T_{1g}$–${}^3\mathfrak{G}_u$ type allowed in the electric-dipole approximation:

$$\gamma_u^{61}A_{1g};\ t_{2g}^2\,{}^3T_{1g} :\ {}^3T_{1g} \longrightarrow \gamma_u^{52}\gamma_u;\ t_{2g}^{3\ 2\sigma+1}\mathfrak{F} :\ {}^3\mathfrak{G}_u$$

(the one-electron $\gamma_u \longrightarrow t_{2g}$ transition) and

$$\gamma_u^{61}A_{1g};\ t_{2g}^2\,{}^3T_{1g} :\ {}^3T_{1g} \longrightarrow \gamma_u^{52}\gamma_u;\ t_{2g}^2\,{}^3T_{1g};$$
$$e_g^{12}E_g({}^{2\sigma'+1}\mathfrak{F}) :\ {}^3\mathfrak{G}_u$$

(the one-electron $\gamma_u \longrightarrow e_g$ transition). Here, ${}^{2\sigma+1}\mathfrak{F} = {}^4A_2, {}^2E, {}^2T_1$, and ${}^2T_2$; $\mathfrak{F} = T_1 \times E = T_1 + T_2$; and $\sigma' = 1/2$ or 3/2. The limitations are due to the Pauli exclusion principle and the triangle rules for spins and quasimomenta.

The transition intensity is characterized by the so-called line strength, which is the square of the modulus of the reduced matrix element (RME) for the transition between states. The RME of the electric-dipole operator between the many-electron wave functions of the initial and final configurations corresponding to the one-electron CT transition $\gamma_u \longrightarrow t_{2g}$ is given by

$$\begin{aligned}\langle\gamma_u^{52}\gamma_u;\ t_{2g}^{3\ 2\sigma+1}\mathfrak{F} :\ {}^3\mathfrak{G}_u\|\hat{\mathbf{d}}\|\gamma_u^{61}A_{1g};\ t_{2g}^2\,{}^3T_{1g} :\ {}^3T_{1g}\rangle \\ = (-1)^{j(\gamma)+j(\mathfrak{G})-\sigma+\frac{1}{2}}\sqrt{[\mathfrak{F}](2\sigma+1)[\mathfrak{G}]} \\ \times\begin{Bmatrix} T_1 & T_2 & \gamma \\ \mathfrak{F} & \mathfrak{G} & T_1 \end{Bmatrix}\langle t_{2g}^{3\ 2\sigma+1}\mathfrak{F}|t_{2g}^2\,{}^3T_{1g}\rangle\langle t_{2g}\|\hat{\mathbf{d}}\|\gamma_u\rangle.\end{aligned} \tag{1}$$

The RME of the electric-dipole operator between the many-electron wave functions of the initial and final configurations corresponding to the one-electron CT transition $\gamma_u \longrightarrow e_g$ is given by

$$\begin{aligned}\langle\gamma_u^{52}\gamma_u;\ t_{2g}^2\,{}^3T_{1g};\ e_g^{12}E_g({}^{2\sigma'+1}\mathfrak{F}) :\ {}^3\mathfrak{G}_u\|\hat{\mathbf{d}}\|\gamma_u^{61}A_{1g}; \\ t_{2g}^2\,{}^3T_{1g};\ e_g^{01}A_{1g}({}^3T_{1g}) :\ {}^3T_{1g}\rangle = (-1)^{j(\gamma)+j(\mathfrak{G})+3\sigma'+\frac{1}{2}} \\ \times\sqrt{3[\mathfrak{G}](2\sigma'+1)/2}\begin{Bmatrix} E & \mathfrak{F} & T_1 \\ \mathfrak{G} & T_1 & \gamma \end{Bmatrix}\langle e_g\|\hat{\mathbf{d}}\|\gamma_u\rangle.\end{aligned} \tag{2}$$

In Eqs. (1) and (2), $j(\Gamma)$ is a phase factor equal to an even number for the cubic-group representations $\Gamma = A_1$, E, and T_2 and to an odd number for the representations $\Gamma = A_2$ and T_1; $[\Gamma]$ is the dimensionality of the corresponding representation; $\begin{Bmatrix}\cdots\\ \cdots\end{Bmatrix}$ is a 6Γ symbol; and $\langle\ldots|\ldots\rangle$ is the genealogy factor. The calculation technique is discussed in more detail, for example, in [17].

The RMEs that are allowed according to Eq. (1) are shown in Table 1.

Table 1. Many-electron CT transitions generated by the one-electron transitions $t_{2u}(\pi)$, $t_{1u}(\pi)$, and $t_{1u}(\sigma) \longrightarrow 3d\ t_{2g}$

No.	$\mathfrak{G}$	γ	$\mathfrak{F}$	RME	No.	$\mathfrak{G}$	γ	$\mathfrak{F}$	RME
1	A_1	T_1	T_1	$-\frac{1}{\sqrt{3}}\langle t_{2g}\|\|\hat{\mathbf{d}}\|\|t_{1u}\rangle$	11	T_1	T_2	E	$\frac{1}{\sqrt{6}}\langle t_{2g}\|\|\hat{\mathbf{d}}\|\|t_{2u}\rangle$
2	A_1	T_2	T_2	$\frac{1}{\sqrt{3}}\langle t_{2g}\|\|\hat{\mathbf{d}}\|\|t_{2u}\rangle$	12	T_1	T_2	T_1	$\frac{1}{2}\langle t_{2g}\|\|\hat{\mathbf{d}}\|\|t_{2u}\rangle$
3	E	T_1	T_1	$\frac{1}{\sqrt{6}}\langle t_{2g}\|\|\hat{\mathbf{d}}\|\|t_{1u}\rangle$	13	T_1	T_2	T_2	$-\frac{1}{2}\langle t_{2g}\|\|\hat{\mathbf{d}}\|\|t_{2u}\rangle$
4	E	T_1	T_2	$-\frac{1}{\sqrt{2}}\langle t_{2g}\|\|\hat{\mathbf{d}}\|\|t_{1u}\rangle$	14	T_2	T_1	A_2	$\frac{2}{\sqrt{3}}\langle t_{2g}\|\|\hat{\mathbf{d}}\|\|t_{1u}\rangle$
5	E	T_2	T_1	$-\frac{1}{\sqrt{2}}\langle t_{2g}\|\|\hat{\mathbf{d}}\|\|t_{2u}\rangle$	15	T_2	T_1	E	$-\frac{1}{\sqrt{6}}\langle t_{2g}\|\|\hat{\mathbf{d}}\|\|t_{1u}\rangle$
6	E	T_2	T_2	$\frac{1}{\sqrt{6}}\langle t_{2g}\|\|\hat{\mathbf{d}}\|\|t_{2u}\rangle$	16	T_2	T_1	T_1	$-\frac{1}{2}\langle t_{2g}\|\|\hat{\mathbf{d}}\|\|t_{1u}\rangle$
7	T_1	T_1	E	$\frac{1}{\sqrt{2}}\langle t_{2g}\|\|\hat{\mathbf{d}}\|\|t_{1u}\rangle$	17	T_2	T_1	T_2	$\frac{1}{2}\langle t_{2g}\|\|\hat{\mathbf{d}}\|\|t_{1u}\rangle$
8	T_1	T_1	T_1	$\frac{1}{2}\langle t_{2g}\|\|\hat{\mathbf{d}}\|\|t_{1u}\rangle$	18	T_2	T_2	E	$-\sqrt{\frac{3}{2}}\langle t_{2g}\|\|\hat{\mathbf{d}}\|\|t_{2u}\rangle$
9	T_1	T_1	T_2	$\frac{1}{2}\langle t_{2g}\|\|\hat{\mathbf{d}}\|\|t_{1u}\rangle$	19	T_2	T_2	T_1	$\frac{1}{2}\langle t_{2g}\|\|\hat{\mathbf{d}}\|\|t_{2u}\rangle$
10	T_1	T_2	A_2	$\frac{2}{\sqrt{3}}\langle t_{2g}\|\|\hat{\mathbf{d}}\|\|t_{2u}\rangle$	20	T_2	T_2	T_2	$-\frac{1}{2}\langle t_{2g}\|\|\hat{\mathbf{d}}\|\|t_{2u}\rangle$

The three one-electron CT transitions $t_{2u}(\pi)$, $t_{1u}(\pi)$, and $t_{1u}(\sigma) \longrightarrow 3d\ t_{2g}$ generate thirty many-electron CT transitions in the electric-dipole approximation: three ${}^3T_{1g} \longrightarrow {}^3A_{1u}$ transitions, six ${}^3T_{1g} \longrightarrow {}^3E_u$ transitions, ten ${}^3T_{1g} \longrightarrow {}^3T_{1u}$ transitions, and eleven ${}^3T_{1g} \longrightarrow {}^3T_{2u}$ transitions.

The RMEs that are allowed according to Eq. (2) are shown in Table 2.

The three one-electron CT transitions $t_{2u}(\pi)$, $t_{1u}(\pi)$, and $t_{1u}(\sigma) \longrightarrow 3d\ e_g$ generate thirty-six many-electron CT transitions in the electric-dipole approximation: six ${}^3T_{1g} \longrightarrow {}^3A_{1u}$ transitions, six ${}^3T_{1g} \longrightarrow {}^3E_u$ transitions, twelve ${}^3T_{1g} \longrightarrow {}^3T_{1u}$ transitions, and twelve ${}^3T_{1g} \longrightarrow {}^3T_{2u}$ transitions.

3. PARAMETERIZATION OF THE RESULTS

Further parameterization of the results is possible in the framework of a so-called local approximation [11], where many-center integrals are completely neglected in calculating the RMEs of the dipole moment. In this case, all the dipole RMEs from Tables 1 and 2 can be expressed in terms of the effective covalence parameters λ_σ and λ_π for σ and π bonds, respectively, and the dipole moment of the cation–anion bond $d = eR_0$, where R_0 is the distance between the ions.

In this approximation, the RMEs $\langle t_{2u}(\pi)\|\hat{\mathbf{d}}\|e_g\rangle$, $\langle t_{1u}(\pi)\|\hat{\mathbf{d}}\|e_g\rangle$, and $\langle t_{1u}(\sigma)\|\hat{\mathbf{d}}\|t_{2g}\rangle$ are zero. Therefore, this approximation manifests itself as an additional selection rule that forbids the $\pi \longrightarrow \sigma$ transitions [$t_{2u}(\pi)$, $t_{1u}(\pi) \longrightarrow e_g$] and the $\sigma \longrightarrow \pi$ transitions [$t_{1u}(\sigma) \longrightarrow t_{2g}$] even if they are allowed by the electric-dipole selection rules. Only the CT transitions σ–σ [$t_{1u}(\sigma) \longrightarrow e_g$] and π–π [$t_{1,\,2u}(\pi) \longrightarrow t_{2g}$] are allowed. In what follows, we use the terms strong (for σ–σ and π–π) and weak CT transitions (for π–σ and σ–π).

The local approximation (if it produces a nonzero result) takes into account the main contribution to the transition matrix elements. This approximation contains first-order corrections in the cation–anion overlap integrals [11].

Among the thirty many-electron transitions in Table 1, there are twenty strong π–π transitions [$t_{2u}(\pi)$, $t_{1u}(\pi) \longrightarrow 3d\ t_{2g}$] and ten weak σ–π transitions [$t_{1u}(\sigma) \longrightarrow 3d\ t_{2g}$].

Among the thirty-six many-electron transitions in Table 2, there are twelve strong σ–σ transitions [$t_{1u}(\sigma) \longrightarrow 3d\ e_g$] and twenty-four weak π–σ transitions [$t_{2u}(\pi)$, $t_{1u}(\pi) \longrightarrow 3d\ e_g$].

The integrated line strength of the $\gamma_u \longrightarrow t_{2g}$ (π–π) transitions is $I_{\pi\pi} = \frac{27}{2}\lambda_\pi^2 d^2$, and that of the $\gamma_u \longrightarrow e_g$ (σ–

Table 2. Many-electron CT transitions generated by the one-electron transitions $t_{2u}(\pi)$, $t_{1u}(\pi)$, and $t_{1u}(\sigma) \longrightarrow 3d\ e_g$

No.	$\mathfrak{G}$	γ	$\mathfrak{F}$	σ'	RME	No.	$\mathfrak{G}$	γ	$\mathfrak{F}$	σ'	RME
1	A_1	T_1	T_1	$\frac{3}{2}$	$\frac{\sqrt{6}}{3}\langle e_g\|\|\hat{\mathbf{d}}\|\|t_{1u}\rangle$	15	T_1	T_1	T_2	$\frac{3}{2}$	$\frac{\sqrt{6}}{2}\langle e_g\|\|\hat{\mathbf{d}}\|\|t_{1u}\rangle$
2	A_1	T_1	T_1	$\frac{1}{2}$	$-\frac{1}{\sqrt{3}}\langle e_g\|\|\hat{\mathbf{d}}\|\|t_{1u}\rangle$	16	T_1	T_1	T_2	$\frac{1}{2}$	$-\frac{\sqrt{3}}{2}\langle e_g\|\|\hat{\mathbf{d}}\|\|t_{1u}\rangle$
3	A_1	T_2	T_2	$\frac{3}{2}$	$\frac{\sqrt{6}}{3}\langle e_g\|\|\hat{\mathbf{d}}\|\|t_{2u}\rangle$	17	T_1	T_2	T_1	$\frac{3}{2}$	$-\frac{\sqrt{6}}{2}\langle e_g\|\|\hat{\mathbf{d}}\|\|t_{2u}\rangle$
4	A_1	T_2	T_2	$\frac{1}{2}$	$-\frac{1}{\sqrt{3}}\langle e_g\|\|\hat{\mathbf{d}}\|\|t_{2u}\rangle$	18	T_1	T_2	T_1	$\frac{1}{2}$	$\frac{\sqrt{3}}{2}\langle e_g\|\|\hat{\mathbf{d}}\|\|t_{2u}\rangle$
5	E	T_1	T_1	$\frac{3}{2}$	$\frac{2}{\sqrt{3}}\langle e_g\|\|\hat{\mathbf{d}}\|\|t_{1u}\rangle$	19	T_1	T_2	T_2	$\frac{3}{2}$	$\frac{1}{\sqrt{2}}\langle e_g\|\|\hat{\mathbf{d}}\|\|t_{2u}\rangle$
6	E	T_1	T_1	$\frac{1}{2}$	$-\frac{\sqrt{6}}{3}\langle e_g\|\|\hat{\mathbf{d}}\|\|t_{1u}\rangle$	20	T_1	T_2	T_2	$\frac{1}{2}$	$-\frac{1}{2}\langle e_g\|\|\hat{\mathbf{d}}\|\|t_{2u}\rangle$
7	E	T_1	T_2	$\frac{3}{2}$	0	21	T_2	T_1	T_1	$\frac{3}{2}$	$-\frac{1}{\sqrt{2}}\langle e_g\|\|\hat{\mathbf{d}}\|\|t_{1u}\rangle$
8	E	T_1	T_2	$\frac{1}{2}$	0	22	T_2	T_1	T_1	$\frac{1}{2}$	$\frac{1}{2}\langle e_g\|\|\hat{\mathbf{d}}\|\|t_{1u}\rangle$
9	E	T_2	T_1	$\frac{3}{2}$	0	23	T_2	T_1	T_2	$\frac{3}{2}$	$-\frac{\sqrt{6}}{2}\langle e_g\|\|\hat{\mathbf{d}}\|\|t_{1u}\rangle$
10	E	T_2	T_1	$\frac{1}{2}$	0	24	T_2	T_1	T_2	$\frac{1}{2}$	$\frac{\sqrt{3}}{2}\langle e_g\|\|\hat{\mathbf{d}}\|\|t_{1u}\rangle$
11	E	T_2	T_2	$\frac{3}{2}$	$-\frac{2}{\sqrt{3}}\langle e_g\|\|\hat{\mathbf{d}}\|\|t_{2u}\rangle$	25	T_2	T_2	T_1	$\frac{3}{2}$	$\frac{\sqrt{6}}{2}\langle e_g\|\|\hat{\mathbf{d}}\|\|t_{2u}\rangle$
12	E	T_2	T_2	$\frac{1}{2}$	$\frac{\sqrt{6}}{3}\langle e_g\|\|\hat{\mathbf{d}}\|\|t_{2u}\rangle$	26	T_2	T_2	T_1	$\frac{1}{2}$	$-\frac{\sqrt{3}}{2}\langle e_g\|\|\hat{\mathbf{d}}\|\|t_{2u}\rangle$
13	T_1	T_1	T_1	$\frac{3}{2}$	$-\frac{1}{\sqrt{2}}\langle e_g\|\|\hat{\mathbf{d}}\|\|t_{1u}\rangle$	27	T_2	T_2	T_2	$\frac{3}{2}$	$-\frac{1}{\sqrt{2}}\langle e_g\|\|\hat{\mathbf{d}}\|\|t_{2u}\rangle$
14	T_1	T_1	T_1	$\frac{1}{2}$	$\frac{1}{2}\langle e_g\|\|\hat{\mathbf{d}}\|\|t_{1u}\rangle$	28	T_2	T_2	T_2	$\frac{1}{2}$	$\frac{1}{2}\langle e_g\|\|\hat{\mathbf{d}}\|\|t_{2u}\rangle$

σ) transitions is $I_{\sigma\sigma} = 12\lambda_\sigma^2 d^2$. Their ratio is $\frac{I_{\pi\pi}}{I_{\sigma\sigma}} = \frac{9}{8}\frac{\lambda_\pi^2}{\lambda_\sigma^2}$. Since $\lambda_\sigma^2 > \lambda_\pi^2$ [11], the integrated intensities of these two types of transitions are comparable in magnitude.

4. MODELING THE CHARGE-TRANSFER TRANSITION BAND IN VANADATES

Let us apply the theoretical approach discussed above to the modeling of optical properties of perovskite vanadates $R\mathrm{VO}_3$.

It should be noted that these compounds (like all other oxides of transition 3*d* elements in the beginning of the row) are usually considered to be Mott–Hubbard systems rather than CT systems; i.e., the Coulomb energy U is considered to be lower than the CT energy Δ [3]. However, this conclusion is usually based on experimental spectra (typically, the reflection spectra influenced by surface effects, which complicate calculations on the basis of the Kramers–Kronig relation), which are not always unambiguous. Paper [18] contains a typical example of this sort of erroneous argumentation as concerns the optical-conductivity spectrum $\sigma(\omega)$ of LaTiO_3, while the same line of reasoning is used for the spectra of other 3*d* metal oxides, including vanadates. The peak at $\hbar\omega \approx 0.1$ eV in the $\sigma(\omega)$ spectrum is assigned to the transition between the occupied and vacant Hubbard subbands, and the peak at $\hbar\omega \approx 4$ eV is assigned to the O 2*p*–Ti $3d(t_{2g})$ CT transition. In this case, the O 2*p*–Ti $3d(e_g)$ CT transition has to be assigned to the peak at $\hbar\omega \approx 9$ eV and the energy

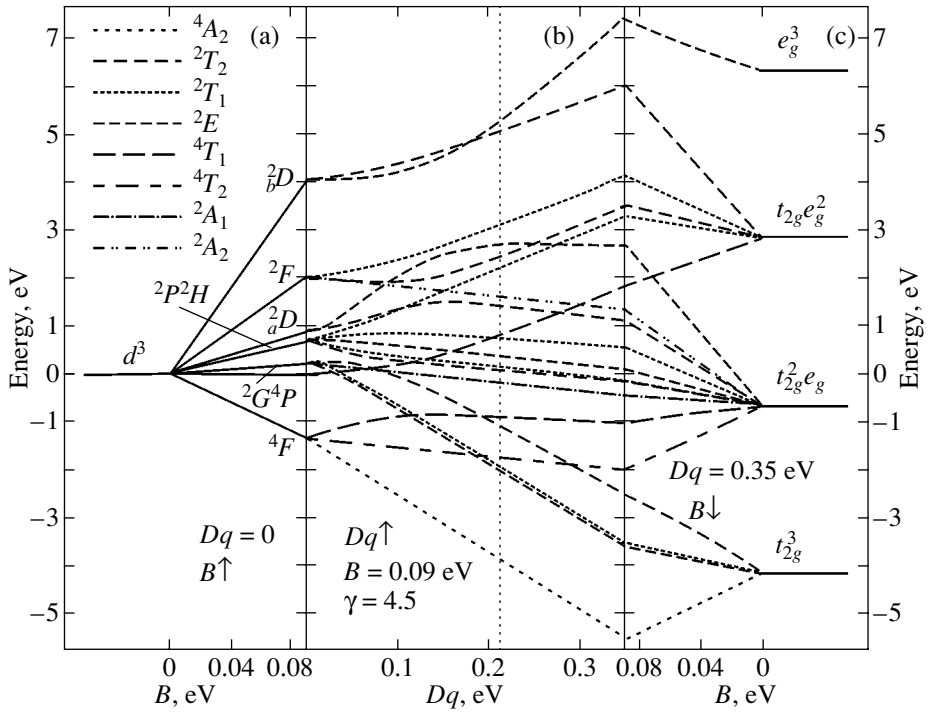

Fig. 1. Correlation diagram of the excited CT configuration $3d^3$ in the octahedral crystal field. The degeneracy of the free-ion d^3 level is removed (a) by the Coulomb interaction between electrons and (b) by the crystal field. A Tanabe–Sugano diagram calculated for the Racah parameters $B = 0.09$ eV and $\gamma = C/B = 4.5$ is shown in the center of the figure. The vertical line indicates the value of the crystal-field parameter $Dq = 0.21$ eV used in the calculations. (c) The level splitting by the crystal field as the parameters B and C decrease to zero.

difference between these transitions is unrealistically large. It is much better to assume that the energy of the O 2*p*–Ti 3*d*(t_{2g}) transition is smaller than 4 eV. The intensity of this transition is relatively low [compared to O 2*p*–Ti 3*d*(e_g)], so the corresponding peak is not visible on the background of the plateau in the range 1–4 eV. In this case, the peak at 4 eV is assigned to the stronger O 2*p*–Ti 3*d*(e_g) transition. It is this approach that we used for the modeling of optical spectra of titanates in [19].

We will make the following assumptions as the basis for our analysis.

(1) The highest (in energy) oxygen orbital is the nonbonding $t_{1g}(\pi)$ (O_{2p}) orbital [20], which is a characteristic feature of MeO_6 octahedral complexes, where *Me* is a 3*d* metal.

(2) The energies of nonbonding oxygen states in the $(VO_6)^{9-}$ complex are assumed to be equal to the energies of the respective states in the $(FeO_6)^{9-}$ complex [16]. In this case, the energy differences are (in electronvolts)

$$E_{t_{1g}(\pi)} - E_{t_{2u}(\pi)} \approx 0.8, \quad E_{t_{1g}(\pi)} - E_{t_{1u}(\pi)} \approx 1.8,$$

$$E_{t_{1g}(\pi)} - E_{t_{1u}(\sigma)} \approx 3.0.$$

This assumption is reasonable, because the energies of purely oxygen states are mainly determined by the crystal environment.

(3) A charge-transfer transition results in the formation of the $3d^3$ configuration of the central atom, which formally corresponds to the Cr^{3+} ion. Therefore, the electron–electron interaction parameters *B* and *C* (Racah parameters) used in the Tanabe–Sugano diagram (see below) for the excited $3d^3$ CT configuration are taken to be the same as those for the ground state of the Cr^{3+} ion [21] in the octahedral oxygen environment.

(4) The optical-conductivity spectrum feature at ≈1.1 eV [22] is taken as the reference point for the energies of the CT levels and transitions in $LaVO_3$. We suppose that this feature is related to the lowest energy CT transition $t_{1g}(\pi) \longrightarrow 3d\ t_{2g}$, which is parity-forbidden in the electric dipole approximation.

(5) We do not take into account the interaction between the 2*p* hole and 3*d* shell.

Assumptions 2 and 4 allow us to determine the energies of the following one-electron CT transitions (in electronvolts): $E_{t_{2u}(\pi)\to t_{2g}} = 1.1 + 0.8 = 1.9$, $E_{t_{1u}(\pi)\to t_{2g}} = 1.1 + 1.8 = 2.9$, and $E_{t_{1u}(\sigma)\to t_{2g}} = 1.1 + 3.0 = 4.1$. Using the value $E_{e_g} - E_{t_{2g}} \equiv 10Dq \approx 2.1$ eV [21], we find the energies of the $t_{2u}(\pi) \longrightarrow e_g$, $t_{1u}(\pi) \longrightarrow e_g$, and

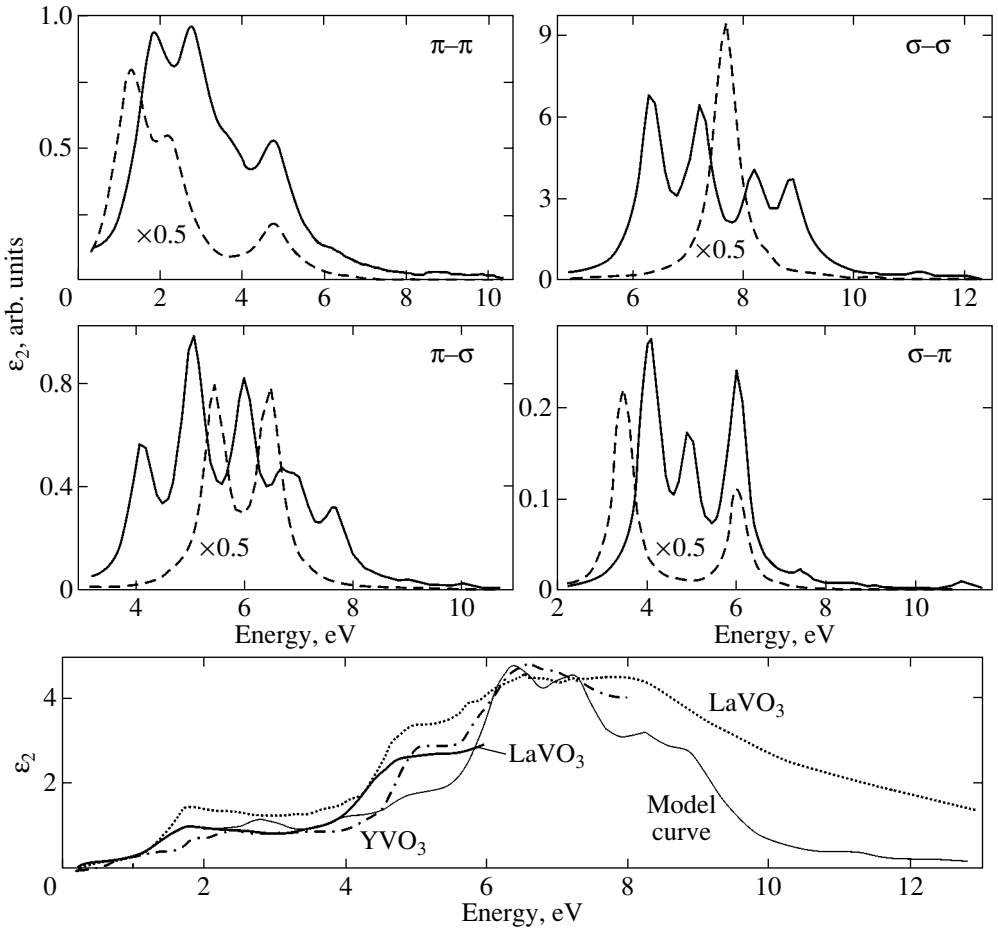

Fig. 2. Results of theoretical modeling of the O2*p*–V3*d* CT transition band in a vanadate. The upper part of the figure gives the partial contributions to Imε from the strong and weak CT transitions in the presence (solid lines) and in the absence (dash lines) of electron–electron interaction. The lower part of the figure presents the sum of all partial contributions (thin solid line) and experimental data for $LaVO_3$ [22] (thick solid line), $LaVO_3$ [18] (dotted line), and YVO_3 [18] (dash-dotted line).

$t_{1u}(\sigma) \longrightarrow e_g$ transitions to be 4.0, 5.0, and 6.2 eV, respectively.

In order to find the energies of the many-electron CT transitions generated by these one-electron transitions and the transition intensities including the mixing of the t_{2g}^3 and t_{2g}^2 e_g states in Eqs. (1) and (2), we calculate the Tanabe–Sugano diagram for the $3d^3$ configuration using parameters $B = 0.09$ eV and $\gamma = C/B = 4.5$ [21] (Fig. 1b). The vertical line in Fig. 1b indicates the value of the crystal-field parameter $Dq = 0.21$ eV used in our calculations.

The degeneracy of the d^3 level of a free ion is removed by the Coulomb interaction between electrons (Fig. 1a) and by the crystal field (Fig. 1b). The level splitting by the crystal field as the parameters *B*, *C* decrease to zero (i.e., for decreasing electron correlations) is shown in Fig. 1c.

Analysis of the spectra in terms of one-electron band models (based on the $2p \longrightarrow 3d\ t_{2g}$ and $2p \longrightarrow 3d\ e_g$ CT transitions) is equivalent to using the simplified level diagram shown in Fig. 1c instead of the actual diagram shown in Fig. 1b.

Employing the Tanabe–Sugano diagram, we obtain a series of strong bands of total span ≈10 eV (from ≈2 to ≈12 eV) for $Dq = 0.21$ eV. Each of the six one-electron CT transitions $t_{2u}(\pi)$, $t_{1u}(\pi)$, $t_{1u}(\sigma) \longrightarrow t_{2g}$, e_g generates a multitude (from 13 to 15) many-electron transition with close and often coinciding energies. The entire spectrum consists of 81 lines.

Let us attempt to model the allowed electric-dipole CT transition band in the optical spectrum of $LaVO_3$-like vanadates.

Since the contributions of the transitions $t_{2u}(\pi) \longrightarrow e_g$, $t_{1u}(\pi) \longrightarrow e_g$, and $t_{1u}(\sigma) \longrightarrow t_{2g}$ cannot be taken into account in the local approximation, we manually introduce the corresponding covalence parameter $\lambda_{\pi\sigma} \equiv \lambda_{\sigma\pi}$. Based on the concept of strong and weak CT transitions, we assume the following model relations: $\lambda_\pi^2 =$

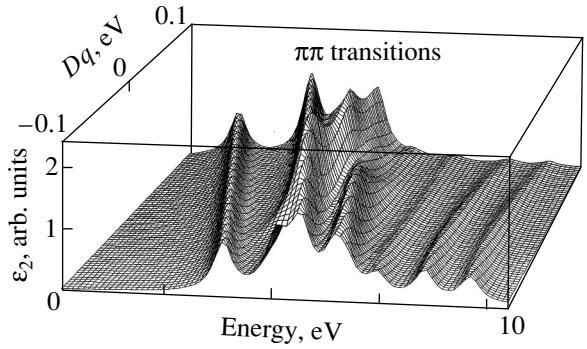

Fig. 3. Results of theoretical modeling of the O2*p*–V3*d* CT transition band in a vanadate. Spectral dependence of the partial contribution to Imε from the strong π–π CT transitions for different values of the crystal-field magnitude (parameter *Dq*).

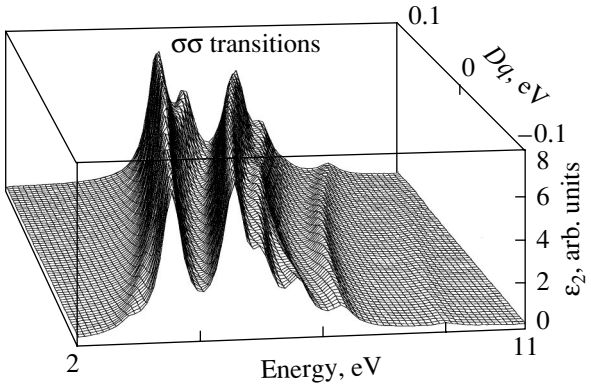

Fig. 4. Results of theoretical modeling of the O2*p*–V3*d* CT transition band in a vanadate. Partial contribution to Imε(ω) from the strong σ–σ CT transitions as a function of *Dq*.

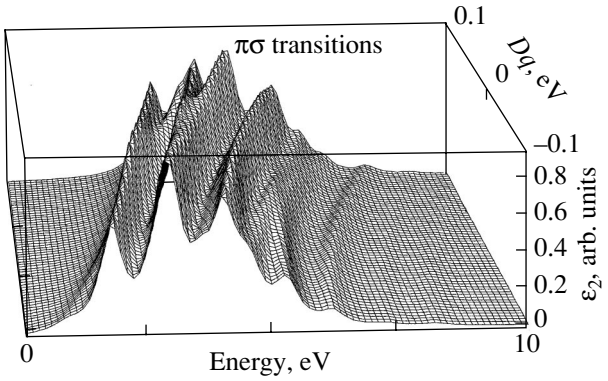

Fig. 5. Results of theoretical modeling of the O2*p*–V3*d* CT transition band in a vanadate. Partial contribution to Imε(ω) from the weak π–σ CT transitions as a function of *Dq*.

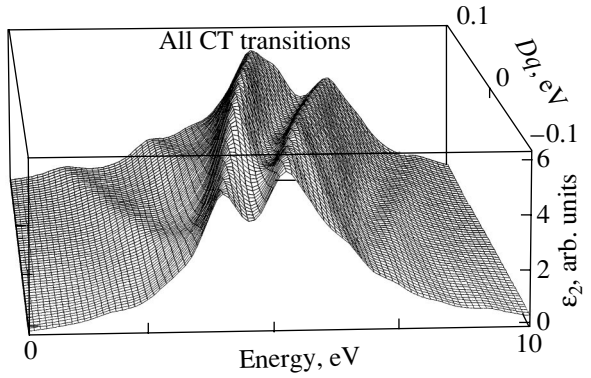

Fig. 6. Results of theoretical modeling of the O2*p*–V3*d* CT transition band in a vanadate. Sum of the partial contributions to Imε(ω) from all CT transitions (strong and weak) as a function of *Dq*.

$\frac{1}{4}\lambda_\sigma^2$ and $\lambda_{\pi\sigma}^2 = \lambda_{\sigma\pi}^2 = 0.07\lambda_\sigma^2$. The line half-width Γ_r is assumed to be the same for all Lorentzian-shaped CT transition lines.

The results of the calculation are shown in Fig. 2. In order to better represent the spectrum structure, the partial contributions to the imaginary part ε_2 of the diagonal permittivity tensor component $\varepsilon = \varepsilon_1 + i\varepsilon_2$ coming from the π–π and σ–σ strong transitions and the π–σ and σ–π weak transitions (the upper part of Fig. 2) are calculated for $\Gamma_r = 0.25$ eV. The sum of all contributions (thin solid line in the lower part of Fig. 2) is calculated using a more realistic value, $\Gamma_r = 0.5$ eV. All spectra are shown in the same relative units. The lower part of Fig. 2 also gives the experimental optical spectrum of $LaVO_3$ taken from [22] (thick solid line) and the experimental spectra of $LaVO_3$ and YVO_3 taken from [18] (dotted and dash-dotted lines, respectively). We convert all experimental data from the optical conductivity σ(ω) into permittivity. The results of model calculations are in good agreement with experiments [18, 22, 23]. In the range $\hbar\omega < 2.5$ eV, the calculated curve coincides exactly with the experimental curve taken from [22].

The upper part of Fig. 2 also presents simple model spectra for the limiting case of zero values of the Racah parameters *B* and *C* (dash lines). The electron–electron interaction causes splitting of lines and their displacement, so the resulting spectrum bears no resemblance to the picture with one peak (due to the 2*p*–3*d* transition) or, in the best case, two peaks (due to the $2p \longrightarrow 3d\ t_{2g}$ and $2p \longrightarrow 3d\ e_g$ transitions), which is often implied when spectra are analyzed in terms of CT transitions.

The dependences of the optical spectra on the crystal-field parameter *Dq* are shown in Figs. 3–6. The calculations of the partial contributions (Figs. 3–5) and the integrated CT transition spectrum (Fig. 6) are performed using the values of parameter Γ_r cited above. The value of *Dq* can be negative for the excited CT states, which is taken into account in our calculations. Variations in *Dq* cause not only relative changes in the

peaks heights but also qualitative transformations of the entire spectrum.

5. CONCLUSIONS

The specific features of the charge-transfer states and O $2p \longrightarrow$ V $3d$ transitions in the $(VO_6)^{9-}$ octahedral complex have been studied in the cluster approach, which successfully combines the concepts in crystal-field theory and the molecular-orbitals method. We have not considered an alternative to these (intracenter) CT transitions, so-called intercenter transitions (involving adjacent complexes), which are similar to the disproportionation reactions

$$(VO_6)^{9-} + (VO_6)^{9-} \longrightarrow (VO_6)^{10-} + (VO_6)^{8-}$$

(note that the intercenter CT transitions in the cluster approximation are nothing other than Mott–Hubbard interband transitions).

Using the Racah algebra for the rotation and cubic groups, we have calculated the reduced matrix elements of the electric-dipole transition operator for many-electron wave functions corresponding to the initial and final states of a CT transition.

Based on a parameterization of the results, we have calculated the relative intensities of the allowed π–π and σ–σ CT transitions disregarding the mixing of different configurations of the same symmetry. The Tanabe–Sugano theory was used with inclusion of the configuration mixing to calculate the energies of many-electron CT transitions and their actual intensities.

Modeling of the optical spectrum of vanadates has revealed a complex CT transition band consisting of 81 lines. The band has main maxima in the range 6.3–7.3 eV and supplementary maxima in the regions ≈2–3 and ≈8–9 eV with an overall bandwidth of ≈10 eV. The dependence of the spectrum structure on the magnitude of the crystal field and on the electron–electron interaction has been discussed. The model calculation results are in good agreement with experiments in spite of the roughness of the model used.

The results make evident the weakness of the widespread assumption that the CT transition spectrum has a simple structure consisting of only one or two peaks. Consequently, the traditional theoretical interpretation of many features of the optical spectra of vanadates and (taking into account the results of [11, 19]) other $3d$-metal oxides has to be refined.

ACKNOWLEDGMENTS

The author is grateful to A.S. Moskvin for discussions of the work.

This work was supported by the Russian Foundation for Basic Research, project no 04-02-96068.

REFERENCES

1. A. M. Clogston, J. Phys. Radium **20** (2–3), 151 (1959).
2. F. J. Kahn, P. S. Pershan, and J. P. Remeika, Phys. Rev. **186** (3), 891 (1969).
3. M. Imada, A. Fujimori, and Y. Tokura, Rev. Mod. Phys. **70** (4), 1039 (1998).
4. K. Shinagawa, in *Magnetooptics*, Ed. by S. Sugano and N. Kojima (Springer, Berlin, 1999).
5. A. Lever, *Inorganic Electronic Spectroscopy* (Elsevier, Amsterdam, 1984; Mir, Moscow, 1987).
6. T. Ido, K. Magoshi, H. Eisaki, and S. Uchida, Phys. Rev. B **44** (18), 12094 (1991).
7. S. Yamaguchi, Y. Okimoto, and Y. Tokura, Phys. Rev. B **54** (16), R11022 (1996).
8. S. Yamaguchi, Y. Okimoto, K. Ishibashi, and Y. Tokura, Phys. Rev. B **58** (11), 6862 (1998).
9. N. N. Kovaleva, J. L. Gavartin, A. L. Shluger, A. V. Boris, and A. M. Stoneham, Zh. Éksp. Teor. Fiz. **121** (1), 210 (2002) [JETP **94**, 178 (2002)].
10. V. I. Anisimov, J. Zaanen, and O. Andersen, Phys. Rev. B **44** (2), 943 (1991).
11. A. S. Moskvin, Phys. Rev. B **65** (20), 205 113 (2002).
12. A. V. Zenkov, B. B. Krichevtsov, A. S. Moskvin, K. M. Mukimov, R. V. Pisarev, and M. M. Ruvinshteĭn, Zh. Éksp. Teor. Fiz. **96** (4), 1397 (1989) [Sov. Phys. JETP **69**, 792 (1989)].
13. Yu. P. Gaĭdukov, A. V. Zenkov, S. V. Koptsik, G. S. Krinchik, and A. S. Moskvin, Pis'ma Zh. Éksp. Teor. Fiz. **51** (4), 201 (1990) [JETP Lett. **51**, 228 (1990)].
14. A. S. Moskvin, A. V. Zenkov, E. A. Ganshina, G. S. Krinchik, and M. M. Nishanova, J. Phys. Chem. Solids **54** (1), 101 (1993).
15. A. V. Zenkov, Candidate's Dissertation (Ural State Univ., Sverdlovsk, 1990).
16. A. I. Likhtenshteĭn, A. S. Moskvin, and V. A. Gubanov, Fiz. Tverd. Tela (Leningrad) **24** (12), 3596 (1982) [Sov. Phys. Solid State **24**, 2049 (1982)].
17. D. T. Sviridov, Yu. F. Smirnov, and V. N. Tolstoĭ, in *Spectroscopy of Crystals* (Nauka, Moscow, 1975), p. 24 [in Russian].
18. T. Arima and Y. Tokura, J. Phys. Soc. Jpn. **64** (7), 2488 (1995).
19. A. V. Zenkov, Phys. Status Solidi B **241** (11), 2508 (2004); DOI 10.1002/pssb.200402043 (2004).
20. D. J. Lam, B. W. Veal, and D. E. Ellis, Phys. Rev. B **22** (12), 5730 (1980).
21. I. B. Bersuker, *Electronic Structure and Properties of Coordination Compounds* (Khimiya, Leningrad, 1986) [in Russian].
22. F. Inaba, T. Arima, T. Ishikawa, T. Katsufuji, and Y. Tokura, Phys. Rev. B **52** (4), R2221 (1995).
23. M. Kasuya, Y. Tokura, T. Arima, H. Eisaki, and S. Uchida, Phys. Rev. B **47** (11), 6197 (1993).

Translated by G. Tsydynzhapov

Physics of the Solid State, Vol. 47, No. 3, 2005, pp. 459–465. Translated from Fizika Tverdogo Tela, Vol. 47, No. 3, 2005, pp. 445–451.

SEMICONDUCTORS AND DIELECTRICS

Theory of the Microstructure of Disordered $AA'BO_3$ and $ABB'O_3$ Perovskite-Structure Solid Solutions

K. Yu. Gufan

Research Institute of Physics, Rostov State University, pr. Stachki 194, Rostov-on-Don, 344090 Russia
e-mail: Gufan_gufan@mail.ru

Received March 16, 2004; in final form, June 10, 2004

Abstract—A model is considered in which atoms A and A' or B and B' of disordered solid solutions $A_xA'_{1-x}BO_3$ and $AB_xB'_{1-x}O_3$ are distributed over a regular system of points 1(a) and 1(b) of the symmetry group O_h^1 characterizing the ideal perovskite structure. The probabilities $P(G_i|x)$ of unit cells having crystal-field symmetry at their center lowered to $G_i = T_d$, D_{3d}, C_{3v}, C_{4v}, D_{2h}, C_{2v}, C_s, or C_2 are calculated as a function of the concentration x. The limits for x in which the Jahn–Teller and/or dipole ordering mechanism is probable are determined. In the approximation taking into account only effective pair interactions, the scattering amplitude F_{hkl} is found to depend on a single parameter r_0. The theory predicts that the dependence of the intensities of even and odd reflections on $\sin\theta/\lambda$ is nonmonotonic and that the distributions of nonuniform strains and of values of the lattice parameters in solid solutions are discrete. © *2005 Pleiades Publishing, Inc.*

1. INTRODUCTION

The problem of determining the probability distribution of the symmetry of the nearest neighbor cation arrangement of certain types at sublattices A and B in the perovskite structure arose in discussing the possible Jahn–Teller or pseudo-Jahn–Teller mechanisms of structural transformations in solid solutions of rare-earth manganates [1–4]. It is believed that the Mn ion in $LaMnO_3$ is trivalent (Mn^{3+}) and that its four d electrons (in the zeroth approximation) form the ground state $^5D(3d)^4$ of the free ion, which is split by the weak crystal field of symmetry O_h into two terms, $^5T_{2g}$ and ^5E_g, separated by an energy barrier of 2.2×10^4 cm^{-1} [5]. Studies of the nuclear spin resonance in MnF_3 have shown [6] that the degenerate ground orbital state E_g of Mn^{3+} results in an appreciable distortion of the cuboctahedron of anions due to the Jahn–Teller effect. In turn, this fact suggests that at least a few of the low-symmetry $LaMnO_3$ phases are caused by the collective Jahn–Teller effect [7–9].

However, rather than the pure compound, $La_{1-x}Me_x^{2+}MnO_3$ solid solutions with heterovalent substitution for cations in the A position are attracting considerable attention. The interest in these solutions stems from the fact that $La_{1-x}Me_x^{2+}MnO_3$ solid solutions exhibit appreciable magnetoresistance [10]. Assuming that the model of purely ionic bonds is also valid for conducting solid solutions, the magnetoresistance can be associated with non-Jahn–Teller Mn^{4+} ions in $La_{1-x}Me_x^{2+}MnO_3$. It is clear that Mn^{4+} ions should lower the transition temperatures and the probabilities of the transitions to phases whose symmetry results from the collective Jahn–Teller effect.

In this paper, we discuss another mechanism that should suppress the collective Jahn–Teller effect in $\alpha_{1-x}\beta_xMnO_3$ solid solutions during heterovalent and isovalent substitutions for α and β ions on the A sublattice of the perovskite structure (i.e., on the regular system of points 1(b) in the O_h^1 group).

This mechanism is based on the fact that the nearest neighborhood of the Jahn–Teller Mn^{3+} ion (positioned at one of the B-sublattice sites, i.e., in one of the positions belonging to the regular system of points 1(a) of group O_h^1) violates the cubic crystal-field symmetry characteristic of the ideal perovskite structure due to a random distribution of α and β ions in the disordered $\alpha_{1-x}\beta_xMnO_3$ solid solution. The goal of this study is to determine the probabilities of the crystal field having various symmetries in the B sublattice as a function of the concentration x of the element β in solid solutions with an average composition $\alpha_{1-x}\beta_x$.

2. MODEL

The perovskite sublattice A is assumed to be ideal cubic without subjection to deformations. This assumption allows us to identify the mechanism under study, which is associated only with the symmetry of the ion distribution over the sites of the perovskite A sublattice. The ions on the B and C sublattices of the perovskite structure move and change their charges to accommodate themselves to the symmetry of the reduced perovs-

kite cell [11], which is dictated by the distribution of α and β ions over the *A* sublattice.[1]

According to the accepted model, the crystal-field symmetry at each site of the *B* sublattice of ideal perovskite is mainly controlled by the nearest neighbor α and β ions arranged over the vertices of the ideal cube (i.e., over the sites of the reduced perovskite cell [11]), with each vertex containing only one ion. Hence, the arrangement of α and β ions obeys the Fermi statistics [12].

When calculating the probability of the $\alpha_{1-x}\beta_x$ solid solution being in a certain state, the geometrical correlation of the cell structure should be taken into account. For example, only 1/8 of the ions located at the vertices of a reduced perovskite cell belong to this cell. Hence, if one β ion is at a vertex of a fixed reduced cell and its other vertices are occupied by α ions, then the crystal-field symmetry at the center of the ideal cube (with the ideal spatial arrangement of its vertices) lowers to C_{3v}. The field symmetry at the centers of seven more cells to which this β ion belongs also lowers to C_{3v}. If two β ions are arranged at vertices belonging to the same edge of a given reduced cell, then the field symmetry in the three neighboring cells decreases to C_{2v}, the field symmetry in the eight cells that share one of the two β ions with the given cell is lowered to C_{3v}, and so on.

In this paper, we disregard the possibility of influence from temperature-dependent dynamic correlations of symmetries of neighboring cells. The inclusion of dynamic correlations requires consideration of the interactions between deformations of the unit cells [7–9] and between displacements of the ions arranged on the *B* sublattices. This inclusion can produce small corrections to the results obtained below if the interactions are weak. In the case where the dynamic interactions cannot be considered weak, we have a fundamentally different problem, which has been repeatedly discussed in the literature [13–15] and is beyond the scope of this study.

3. RESULTS OF STATISTICAL CALCULATIONS

According to the problem posed, we calculate (in terms of the Fermi statistics) the dependence of the probability $P(G_i|x)$ of the formation of perovskite cells whose crystal-field symmetry at the center is lowered to $G_i \subset O_h$ on the β-component concentration in the $\alpha_{1-x}\beta_x MnO_3$ solid solution.[2]

Above all, let us distinguish the symmetries of those crystal fields at *B*-sublattice sites in which the E_g level splits into two nondegenerate levels. The possible distributions of α cations over sublattice *A* provide the crystal-field symmetries D_{2h}, C_{4v}, C_{2v}, C_s, and C_2, to which the initial symmetry O_h can be lowered and at which the double degeneracy of the E_g level is removed. In this case, the total probability of the formation of cells in which the ground state of the Mn^{3+} ion is nondegenerate is given by

$$\begin{aligned} &P(D_{2h};\, C_{4v};\, C_{2v};\, C_s;\, C_2|x) \\ &\equiv P(D_{2h}|x) + \ldots + P(C_2|x) \\ &= 12x^2(x-1)^2(x^4 - 2x^3 + 5x^2 - 4x + 2). \end{aligned} \tag{1}$$

In the case of a rather symmetric distribution of α ions over the *A*-sublattice sites positioned at the eight cube vertices surrounding a fixed Mn ion, the crystal-field symmetry at the Mn^{3+}-ion site can be O_h, T_d, D_{3d}, or C_{3v}. The Mn^{3+}-ion ground state remains degenerate in these fields. The total probability of the formation of cells with these increased symmetries is equal to the probability of their formation in the solid solution:

$$\begin{aligned} P(O_h;\, T_d;\, D_{3d};\, C_{3v}|x) &= 1 - 24x^2 + 96x^3 - 180x^4 \\ &+ 192x^5 - 120x^6 + 48x^7 - 12x^8. \end{aligned} \tag{2}$$

It is noteworthy that the probability of the formation of reduced cells with increased symmetries at the β-ion concentrations *x* of most interest is low. For example, for $x = 1/3$ and $1/2$, we have

$$\begin{aligned} &P(O_h|1/3) < 4\%, \quad P(O_h|1/2) < 0.8\%, \\ &P(T_d|1/3) < 0.5\%, \quad P(T_d|1/2) < 0.8\%, \\ &P(D_{3d}|1/3) < 4.2\%, \quad P(D_{3d}|1/2) < 3.2\%, \\ &P(D_{2h}|1/3) < 1.5\%, \quad P(D_{2h}|1/2) < 2.4\%, \\ &P(C_{4v}|1/3) < 1.5\%, \quad P(C_{4v}|1/2) < 2.4\%. \end{aligned} \tag{3}$$

We also note that the probability of the existence of rhombohedral ferroelectric cells with symmetry C_{3v} possessing an intrinsic dipole moment is equal to

$$\begin{aligned} P(C_{3v}|x) &= 8x(1-x)(3x^2 - 3x + 1) \\ &\times (x^4 - 2x^3 + 4x^2 - 3x + 1) \end{aligned} \tag{4}$$

and is rather high at these values of *x*: $P(C_{3v}|1/3) \approx 0.227$ and $P(C_{3v}|1/2) \approx 0.156$. The probabilities of the formation of dipole-polarized cells with symmetries C_{2v} and C_s are $P(C_{2v}|1/3) \approx 0.249$, $P(C_{2v}|1/2) \approx 0.1875$, $P(C_s|1/3) \approx 0.351$, and $P(C_s|1/2) \approx 0.469$.

The values of *x* at which $P(C_{3v}|x)$ and $P(C_s|x)$ are maximum exceed the percolation threshold over sites of a simple cubic lattice [16] (perovskite sublattice *B* in our case). The spatial distributions of dipole fields and

[1] In the above assumption, the *C* sublattice corresponds to a regular system of points 3(*d*) of group O_h^1 and is occupied by oxygen ions.

[2] Since each cell site can be occupied by an α or a β atom, the probability of *m* a atoms and *n* – *m* b atoms being arranged over *n* sites is defined by the binomial distribution. The other coefficients in the probabilities of the symmetry distributions of cells are defined by the ratio of the point group orders $|O_h|/|G_i|$, where G_i is the local symmetry group of the cell at a given *m*.

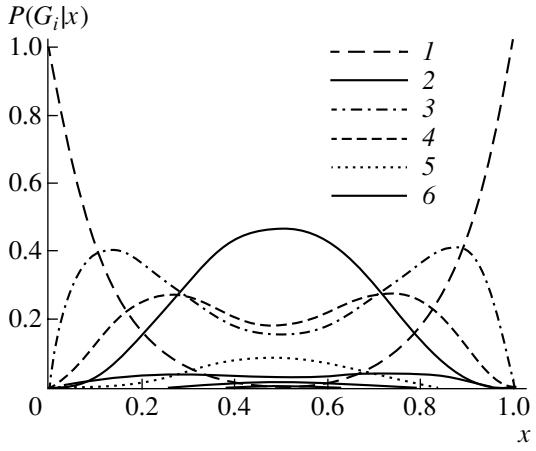

Fig. 1. Probability $P(G_i|x)$ of finding a unit cell in which the crystal-field symmetry at the center is decreased to $G_i(G_i \subset O_h)$ as a function of the α-element concentration in an $\alpha_{1-x}\beta_x$ binary solid solution. The α and β elements are considered to be randomly distributed over the sites of the simple cubic lattice. (*1*) $G_1 = O_h$, (*2*) $G_2 = C_s$, (*3*) $G_3 = C_{3v}$, (*4*) $G_4 = C_{2v}$, (*5*) $G_5 = C_2$, and (*6*) $P(G_i|x) \le 0.03$ and $G_6 = T_d$, D_{3d}, C_{4v}, and D_{2h}.

of spontaneous cell polarizations caused by them can produce dipole ordering of solid solutions in this case [13, 14, 16].

Figure 1 shows the $P(G_i|x)$ dependences for the following nine possible symmetries of crystal fields at the center of the reduced perovskite cell that can arise in a binary solid solution of α and β cations distributed over the *A* sublattice: $G_i = O_h$, T_d, D_{3d}, C_{3v}, D_{2h}, C_{4v}, C_{2v}, C_s, and C_2.

We note that Jahn–Teller transitions in piezoelectric crystals exhibit quite different properties [17]. Figure 2 shows the dependences $P(T_d; D_{3d}; C_{3v}|x) = 2x(1 - x)(7x^6 - 21x^5 + 53x^4 - 71x^3 + 54x^2 - 22x + 4)$ and the total probability of the formation of cells with symmetries that allow the piezoelectric effect. Figure 3 shows the β ion–concentration dependences of the total probabilities of the formation of cells in which the E_g level splits and cells in which spontaneous polarization arises and Mn ions are displaced from centrosymmetric sites. For comparison, Figs. 1–3 show the dependence of the probability of the formation of cells with symmetry O_h on the β-element concentration (dashed curve).

4. DISCUSSION

The mechanism of structural phase transitions based on the interaction of symmetric unit cells deformed due to the Jahn–Teller effect or pseudo-Jahn–Teller interactions was primarily investigated for phase transitions in binary oxides with the ABO_3 perovskite structure [7–9]. In those studies, it was assumed that the crystal microstructure is homogeneous and that all unit cells have symmetry O_h. However, these assumptions are not valid for solid solutions, as follows from the above considerations.

This circumstance results from the fact that the probability of finding an undistorted unit cell of ideal perovskite (e.g., at $x = 1/3$) in the crystal is so small [$P(O_h|1/3) < 4\%$] that collective interaction between them is unlikely. At the same time, even at the β-ele-

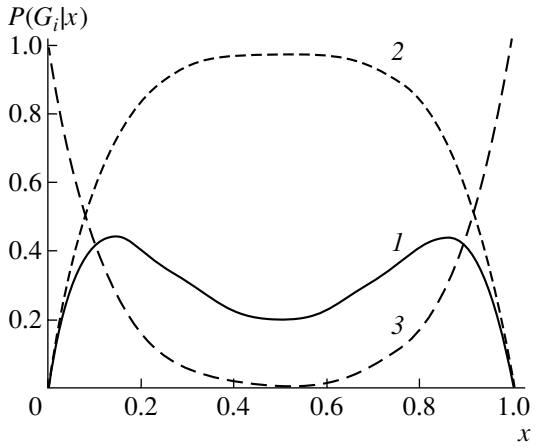

Fig. 2. Total probabilities of the formation of unit cells in which the crystal-field symmetry at the center allows for the piezoelectric effect plotted as a function of concentration *x* in a disordered quasi-binary $\alpha_{1-x}\beta_x MnO_3$ solid solution: (*1*) $P(T_d; D_{3d}; C_{3v}|x)$ and (*2*) $P(T_d; D_{3d}; C_{3v}; C_{4v}; C_{2v}; C_s; C_2|x)$. The notation is the same as in Eq. (1). For comparison, curve *3* shows $P(O_h|x)$.

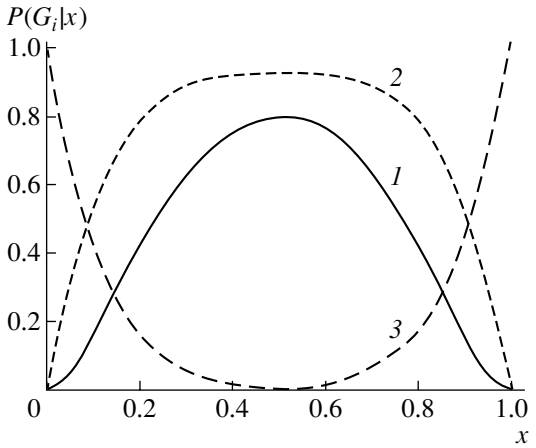

Fig. 3. Total probabilities of the formation of unit cells in which the crystal-field symmetry does not allow degenerate electronic states of Mn^{3+} ions plotted as a function of concentration *x*: (*1*) $P(D_{2h}; C_{4v}; C_s; C_2|x)$ (the Mn^{3+} ion is displaced from the unit cell center) and (*2*) $P(C_{4v}; C_{3v}; C_{2v}, C_s; C_2|x)$. For comparison, curve *3* shows $P(O_h|x)$.

ment concentration $x \approx 13.2\%$, the probability of finding a cell of symmetry C_{3v}, $P(C_{3v}|0.1322) \approx 0.403$, significantly exceeds the percolation threshold [16]. The value of $P(C_{3v}|0.1322)$ shows that almost each cell whose crystal field at its center has rhombohedral symmetry and a dipole component ($G_i = C_{3v}$) most probably has three spontaneously polarized cells with field symmetry C_{3v} among its nearest neighbors. The solid-solution microstructure with dipoles that are oriented along threefold axes and randomly distributed over the Mn^{3+} sublattice promotes ferroelectric or antiferroelectric ordering of dipoles. The possible ordering mechanism is associated with direct interactions between dipoles rather than with the pseudo-Jahn–Teller effect [4, 8, 9].

According to [13, 14], the dipole interaction mechanism can result in the phase transition to a ferroelectric state when only nearest neighbors interact [13, 18, 19] or to antiferroelectric ordering [19] when the interaction extends to several coordination shells.[3] Moreover, by calculating the probability of two cells with a dipole moment being nearest neighbors, $P(C_{3v}; C_{4v}; C_{2v}; C_s; C_2|x) = 2x(1-x)(9x^6 - 27x^5 + 43x^4 - 41x^3 + 28x^2 - 12x + 4)$, it can be shown that the threshold concentration at which the existence of infinite clusters of ferroelectric (dipole-polarized) cells is highly probable is reached even at $x \geq 4.8\%$ (Fig. 3).

We note that the total probability of the existence of cells in which the degeneracy of the E_g ground term (characteristic of cells with symmetry O_h) is retained, $P(O_h; T_d; D_{3d}; C_{3v}|x)$, is also high at small x.[4] The probability of finding high-symmetry cells $P(O_h; T_d; D_{3d}; C_{3v}|x)$ exceeds the percolation threshold for these cells up to concentrations of the β element $x \leq 0.327$ in the quasi-binary $\alpha_{1-x}\beta_x MnO_3$ solid solution (Fig. 2). Therefore, in the range $0.048 < x < 0.327$, there is competition between two fundamentally different mechanisms of structural transitions. One mechanism is associated with dipole–dipole interactions [13], and the other (Jahn–Teller) is caused by deformation interactions [7–9]. These mechanisms result in ordered phases with different symmetries, which makes it possible to determine the actual phase transition mechanism experimentally. We note that we have $P(O_h; T_d; D_{3d}; C_{3v}|0.153) = P(C_{3v}; C_{4v}; C_{2v}; C_s; C_2|0.153) \approx 0.698$.

[3] If only the effective pair interactions of cells with symmetry C_{3v} are considerable, then it can be shown, using the self-consistent-field approximation (as in [14, 18, 20]), that only rhombohedral phases will be stable.

[4] If the symmetry of the field exerted on an atom with one, four, six, or nine 3*d* electrons is described by the T_d group (the orbital state of the free ion is *D* and the weak crystal field approximation is valid), then the ion ground state in the crystal is T_1 [5]. However, in the case under study, there exists a rather strong field of symmetry O_h, which is slightly distorted to T_d by isovalent or heterovalent substitution of ions on the regular system of points 1(*a*) of the O_h symmetry group.

5. EXTENSION OF THE THEORETICAL RESULTS TO OTHER OBJECTS

Assuming, as was done above, that oxygen ions play a passive role in lowering the crystal-field symmetry at the center of unit cells, all the considerations and conclusions concerning the *B*-sublattice field symmetry in a disordered quasi-binary $AA'BO_3$ solid solution are applied with no change to the *A*-sublattice field symmetry caused by the random distribution of *B*-sublattice cations in disordered $ABB'O_3$ solid solutions. These solid solutions have been extensively studied since the discovery of relaxors, a new type of electrostriction materials.

Studies of the strongest (Bragg) reflections in $PbMg_{1/3}Nb_{2/3}O_3$ [21–24], $PbFe_{1/2}Nb_{1/2}O_3$ [25], $PbZn_{1/2}Nb_{1/2}O_3$ [26], $PbSc_{1/2}Nb_{1/2}O_3$ [27], and other solid solutions have established unambiguously that their macroscopic averaged symmetry O_h^1 and structure correspond to the cubic structure of ideal perovskite.

Refinement of the average structure by considering the reflection intensity has shown the following. First, in order to obtain acceptable values of the *R* factor, an anomalously large Debye–Waller factor for Pb ions should be assumed [21–27], which cannot be understood under the assumption of purely thermal random displacements of cations [24–27]. Moreover, the nonmonotonic temperature dependence of the Debye–Waller factor in lead magnesium niobate (PMN) indicates that its value is controlled by at least two factors [21]: mostly by (presumably) static displacements at temperatures below the Burns temperature T_B and thermal vibrations at $T > T_B$ [21]. Second, the dependence of the integrated intensities of Bragg reflections of various parities on the angle at which they are observed is nonmonotonic [23] and exhibits many other features, which can be understood only by assuming a random (as in [23–27]) or regular (as follows from our model) displacement of lead ions from the ideal position on the cubic perovskite sublattice *B* [23].

Various models have been used to refine the atomic positions in solid solutions with the perovskite structure. In [21], it was assumed that Pb and $Mg_{1/3}Nb_{2/3}$ cations are displaced with equal probability along the body diagonals and twelve (110)-type directions of cubes surrounding cations in the perovskite structure. The symmetry axes of these cubes coincide in direction with the crystal symmetry axes. The displacement values are controlled by cube edges; according to [21], $a_c(Pb) > a_c(Mg_{1/3}Nb_{2/3})$. Moreover, it was assumed in [21] that the oxygen in the crystal is randomly distributed over a circular cylinder whose axis is directed along one of the fourfold axes of the crystal. In [23], it was shown that the model considered in [21] adequately describes only the positions and intensities of diffraction peaks corresponding to small scattering angles. Based on a complete set of diffraction reflection data, the authors of [23] discarded the symmetric-dis-

placement model proposed in [21] and instead assumed that Pb ions are displaced randomly over the surface of a sphere of radius r_0 [23].

The results calculated in [23] show that oxygen and cation displacements in the *A* sublattice affect the *R* factor only slightly. This conclusion also follows from the results of studies of various models [24, 26]. These facts justify the model accepted above, in which the ions that induce randomly distributed lower symmetry fields exerted on ions of another sublattice are themselves considered to occupy an ideal averaged high-symmetry position.

In [23], it is also argued that an experiment with partially ordered perovskite $PbSc_{1/2}Ta_{1/2}O_3$ shows that the degree of ordering has no effect on the interpretation of x-ray diffraction patterns in terms of the model that assumes a random distribution of Pb displacements. This statement justifies the application of the model developed above to relaxors, whose structure contains partially ordered nanometer regions.

Since there is a variety of objects that could be used to verify the model, including the calculation scheme, let us consider the structure factor for an averaged crystal and take into account the probabilities of possible ion displacements in the *A* sublattice of the $AB_xB'_{1-x}O_3$ solid solution in the case where *B* and *B*' ions are distributed randomly over the *B* sublattice. The *B* and *B*' ions distributed randomly over the *B* sublattice of the ideal cubic perovskite have the coordinates

$$\begin{aligned}&(a/2, a/2, a/2);\ (\bar{a}/2, a/2, a/2);\ (\bar{a}/2, a/2, a/2);\\ &(\bar{a}/2, \bar{a}/2, a/2);\ (a/2, a/2, \bar{a}/2);\ (\bar{a}/2, a/2, \bar{a}/2);\\ &(a/2, \bar{a}/2, \bar{a}/2);\ (\bar{a}/2, \bar{a}/2, \bar{a}/2),\end{aligned} \quad (5)$$

In this case, their contribution to the scattering amplitude can easily be found to be

$$\begin{aligned}F_{hkl}(B, B') &= 8[xf_B + (1-x)f_B]\\ &\times \cos\left(h\frac{a}{2}\right)\cos\left(k\frac{a}{2}\right)\cos\left(l\frac{a}{2}\right).\end{aligned} \quad (6)$$

A similar expression can also be written for the contribution of undisplaced Pb ions to F_{hkl}.

According to our model, at any *B*-ion concentration, there are fourteen types of *B*- and *B*'-ion distributions over the regular system of points 1(*a*) in the nearest neighborhood of a fixed *A* ion. The crystal fields at the *A*-ion position will remain centrosymmetric if the nearest neighborhood has symmetry O_h, T_d, D_{3d}, or D_{2h}. The contribution from the *A* ions in this symmetric neighborhood to the total scattering amplitude is proportional to the probability of the formation of such cells:

$$\begin{aligned}&F_{hkl}(O_h; T_d; D_{3d}; D_{2h}|x)\\ &= f_A\{[x^8 + (1-x)^8] + 4x^2(1-x)^2[x^2 + (1-x)^2]^2\}.\end{aligned} \quad (7)$$

In the ten other types of *B*- and *B*'-ion distributions over the sites in the nearest neighborhood of the *A* ion, this ion is displaced. The direction and magnitude of the displacement depend on the neighborhood symmetry and *B*-ion concentration. In the case of crystal-field symmetries C_{3v}, C_{4v}, and C_{2v}, the *A* ion in the equilibrium state is displaced along one of the eight (111)-type directions, six (001)-type directions, and twelve (110)-type directions, respectively. For symmetry C_s, the *A*-ion is displaced in the [110] plane. However, there are three different structures for which crystal-field symmetry C_s arises. Two of the structures correspond to the case where three of the eight sites of the nearest neighborhood are occupied by ions of one species (e.g., *B*) and the other five sites are occupied by ions of the other species (*B*'). The third structure corresponds to an equal number of *B* and *B*' ions. It is convenient to characterize the first two structures using the distance between the *B* ions. In the $C_s^{(1)}$ structure, these three distances are *a*, *a*, and $a\sqrt{2}$. In the $C_s^{(2)}$ structure, they are *a*, $a\sqrt{2}$, and $a\sqrt{3}$. There are also three types of arrangement of cations in the nearest neighborhood of the *A* ion in the case of the C_{3v} symmetry.

In general, the *A*-ion displacements will be different in magnitude if the symmetry of the nearest neighborhood is G_0 but the chemical composition is $B_mB'_{8-m}$ in one case and $B_{8-m}B'_m$ in another (m = 1, 2, 3).

Thus, it follows that the structure amplitude within the accepted model will depend on 21 independent parameters (*A*-ion displacements) if the analysis is restricted to only symmetry considerations. It is reasonable to discuss this general result only in relation to a specific experiment.

6. HYPOTHESIS OF THE DOMINANT ROLE PLAYED BY EFFECTIVE PAIR INTERACTIONS

In this study, we restrict our analysis to calculating the component of the scattering amplitude structure associated with Pb-ion displacement under the assumption that only effective pair interactions between ions are of importance. In this case, the total structure amplitude F_{hkl} depends on only one parameter r_0, the displacement of the *A* (Pb) ion along (111), if the nearest neighborhood of this ion contains one *B*' (or *B*) ion at the site $(\bar{a}/2, \bar{a}/2, \bar{a}/2)$ and seven *B* (*B*') ions at the other 1(*b*) sites, defined by Eq. (5), in the nearest neighborhood of the Pb ion. Designating the Pb-ion displacement along a fourfold axis as $u_0 = r_0/\sqrt{3}$, the contribu-

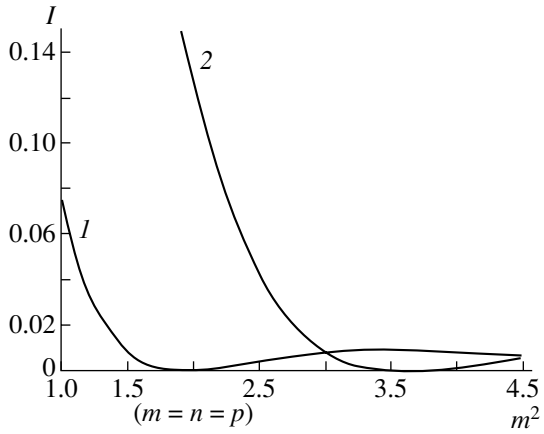

Fig. 4. Dependence of the intensity of Bragg reflections caused by a superposition of Pb displacements at $x = 1/3$ ($u_0 = 0.035a$) on m^2 (see text for details).

tion to the total scattering amplitude that corresponds to displaced *A* ions can be found to be

$$\begin{aligned} &F_{hkl}(C_{3v};\, C_{4v};\, C_{2v};\, C_s;\, C_2|x) \\ &= f_A\{8x(1-x)[x^2-(1-x)^2]^{-1}[x^8-(1-x)^8] \\ &\quad\times\cos(hu_0)\cos(ku_0)\cos(lu_0) \\ &+4x^2(1-x)^2[x^2+(1-x)^2][\cos(2hu_0)+\cos(2ku_0) \\ &\quad+\cos(2lu_0)+\cos(2hu_0)\cos(2ku_0) \\ &\quad+\cos(2ku_0)\cos(2lu_0)+\cos(2hu_0)\cos(2lu_0)] \\ &+2x^4(1-x)^4[4\cos(2hu_0)\cos(2ku_0)\cos(2lu_0) \\ &\quad+\cos(4hu_0)+\cos(4ku_0)+\cos(4lu_0)] \\ &+16x^3(1-x)^3[x^2+(1-x)^2]\cos(hu_0)\cos(ku_0) \\ &\quad\times\cos(lu_0)[2\cos^2(hu_0)+2\cos^2(ku_0) \\ &\quad+2\cos^2(lu_0)-3]\}. \end{aligned} \tag{8}$$

The notation $F_{hkl}(C_{3v}; C_{4v}; C_{2v}; C_s; C_2)$ means that only the nontrivial component of the structure amplitude is given, which is due to the lead ions displaced from positions 1(*a*). The point groups entering into Eq. (8) as the argument of F_{hkl} describe the crystal-field symmetry at the center of the cells in which the lead ion is displaced from position 1(*a*). We recall that this model includes only symmetry lowering due to nonuniform distributions of *B* and *B*' ions over positions 1(*b*) in the perovskite structure on a scale comparable to the unit cell size. For preliminary analysis of Eq. (8), we roughly assume that $x = 1/3$ and $u_0 = r_0\sqrt{3} = 0.035a$, as follows from the data obtained by averaging Pb displacements over the various directions determined using the "best" of the models considered in [25]. In this case, Eq. (8) makes it possible to compare the intensities of even and odd Bragg reflections caused by *A*-ion displacements at an arbitrary x-ray wavelength. We have $h = 2m$, $k = 2n$, and $l = 2p$ for even reflections and $h = 2m + 1$, $k = 2n + 1$, and $l = 2p + 1$ for odd reflections (m, n, and p are integers). For qualitative comparison with experiment [23], we set $m = n = p$ and calculate the reflection intensities in units of f_A^2 as a function of the "continuous" parameter $m^2 \sim (\sin\theta/\lambda)^2$. The result is shown in Fig. 4. We can see that the model predicts a nonmonotonic behavior of the intensity, which is in qualitative agreement with the experimental data from [22]. For quantitative comparison, modification of the model is required to take into account the dependence of the atomic scattering amplitudes on θ, on the Debye–Waller factor, etc.

7. ANOTHER HYPOTHESIS

Based on the model at hand and taking into account the giant electrostriction of many relaxors, we can assume that the *A*-ion displacements according to the crystal-field symmetry cause spontaneous polarization and, hence, changes in the unit cell parameters. In the accepted model, the unit cells should remain cubic. Thus, remaining within the accepted model, we can take into account only volume striction of the reduced cells. In this case, at a given *B*-ion concentration in the $AB_xB'_{1-x}O_3$ solid solution and under the assumption that the crystal retains its integrity, according to experiment, we can make the following two conclusions.

(1) The elastic energy arises only when cubic cells differing in volume are in contact (according to the accepted model, the crystal fields at the centers of these cells differ in symmetry in this case). Hence, a disordered single-crystal solid solution should contain "large" (in comparison with the unit cell volume) regions with different lattice parameters (different symmetries of the crystal field at the unit cell center).

(2) Since the most probable symmetries of the crystal field at the center of unit cells are finite in number at a fixed concentration *x*, the experimentally determined lattice parameters in a single-crystal solid solution should take on discrete values. Certainly, this discreteness will be somewhat spread out by nonuniform deformations at the contact surfaces of volumes each of which consists of unit cells with the same crystal-field symmetry.

The calculations carried out predict that the intensities of Bragg reflections at a given β-ion concentration *x* will depend on the values of the lattice parameters. Therefore, the model at hand makes it possible to determine which lead ion displacements initiate a decrease or, alternatively, an increase in the initial volume of the reduced cells [11] of the perovskite structure in solid solutions.

ACKNOWLEDGMENTS

The author is grateful to M.F. Kupriyanov for the literature put at his disposal and helpful advice regarding the interpretation of x-ray diffraction data and to S.B. Vakhrushev for information on the properties of the PMN compound.

This study was supported by the Russian Foundation for Basic Research and the National Natural Science Foundation (China), project no. 02-02-039016.

REFERENCES

1. J. B. Goodenough, *Magnetism and the Chemical Bond* (Interscience, New York, 1963; Metallurgiya, Moscow, 1968).
2. I. O. Troyanchuk, Zh. Éksp. Teor. Fiz. **102** (1), 251 (1992) [Sov. Phys. JETP **75**, 132 (1992)].
3. J. N. Song, J. H. Park, K.-B. Lee, and Y. H. Jeong, cond-mat/0110587.
4. I. B. Bersuker, V. G. Vekhter, and I. Ya. Ogurtsov, Usp. Fiz. Nauk **116** (4), 605 (1975) [Sov. Phys. Usp. **18**, 569 (1975)].
5. C. J. Ballhausen, *Introduction to Ligand Field Theory* (McGraw-Hill, New York, 1962; Mir, Moscow, 1964).
6. R. G. Shulman and Y. Jakarino, Phys. Rev. **109** (4), 1084 (1958).
7. I. B. Bersuker, Phys. Lett. **20** (6), 589 (1966).
8. N. Kristoffel and P. Konsin, Phys. Status Solidi **21** (1), K39 (1967).
9. B. Halperin and R. Englman, Phys. Rev. B **3** (5), 1698 (1971).
10. M. B. Salamon, Rev. Mod. Phys. **73**, 583 (2001).
11. E. G. Fesenko, V. S. Filip'ev, and M. F. Kupriyanov, Fiz. Tverd. Tela **11** (2), 466 (1969) [Sov. Phys. Solid State **11**, 366 (1969)].
12. L. D. Landau and E. M. Lifshitz, *Course of Theoretical Physics*, Vol. 5: *Statistical Physics*, 2nd ed. (Nauka, Moscow, 1964; Pergamon, Oxford, 1980).
13. V. G. Vaks, *Introduction to the Microscopic Theory of Ferroelectrics* (Nauka, Moscow, 1973) [in Russian].
14. G. A. Smolenskiĭ, A. V. Bokov, V. A. Isupov, N. N. Kraĭnik, R. E. Pasynkov, and M. S. Shur, *Ferroelectrics and Antiferroelectrics* (Nauka, Leningrad, 1971) [in Russian].
15. A. I. Gusev and A. A. Rempel', *Nonstoichiometry, Disorder, and Order in Solids* (Ural. Otd. Ross. Akad. Nauk, Yekaterinburg, 2001) [in Russian].
16. B. I. Shklovskiĭ and A. L. Éfros, Usp. Fiz. Nauk **117**, 401 (1975) [Sov. Phys. Usp. **18**, 845 (1975)]; A. L. Éfros, *Physics and Geometry of Disorder* (Nauka, Moscow, 1982) [in Russian].
17. B. G. Vekhter, Fiz. Tverd. Tela (Leningrad) **15** (2), 509 (1973) [Sov. Phys. Solid State **15**, 354 (1973)].
18. Yu. M. Gufan, *Structural Phase Transitions* (Nauka, Moscow, 1982) [in Russian].
19. A. Yu. Gufan, E. N. Klimova, Yu. V. Prus, and M. B. Stryukov, Izv. Ross. Akad. Nauk, Ser. Fiz. **65** (6), 788 (2001).
20. J. S. Smart, *Effective Field Theories of Magnetism* (Saunders, London, 1966; Mir, Moscow, 1968).
21. P. Bonneau, P. Garnier, E. Husson, and A. Morell, Mater. Res. Bull. **24** (2), 201 (1989); P. Bounneau, P. Garnier, G. Calvarin, E. Husson, J. R. Cavarri, A. W. Hewat, and A. Morrell, J. Solid State Chem. **91** (2), 350 (1991).
22. A. Verbaere, Y. Piffard, Z. G. Ye, and E. Husson, Mater. Res. Bull. **27** (10), 1227 (1992).
23. S. Vakhrushev, S. Zhukov, G. Fetisov, and V. Chernyshov, J. Phys.: Condens. Matter **6** (22), 4021 (1994).
24. A. R. Lebedinskaya, M. F. Kupriyanov, and R. Skulski, Mater. Sci. Eng. B **83**, 119 (2001); Phase Transit. **75** (3), 289 (2002).
25. R. V. Kolesova, V. V. Kolesov, M. F. Kupriyanov, and R. Skulski, Phase Transit. **68**, 621 (1999).
26. R. V. Kolesova, V. V. Kolesov, M. F. Kupriyanov, and O. A. Lavrova, Izv. Ross. Akad. Nauk, Ser. Fiz. **64** (6), 1097 (2000).
27. M. F. Kupriyanov and V. Kogan, Ferroelectrics **124**, 213 (1991).

Translated by A. Kazantsev

Physics of the Solid State, Vol. 47, No. 3, 2005, pp. 466–473. Translated from Fizika Tverdogo Tela, Vol. 47, No. 3, 2005, pp. 452–459.

SEMICONDUCTORS AND DIELECTRICS

Electronic Excitations in $BeAl_2O_4$, Be_2SiO_4, and $Be_3Al_2Si_6O_{18}$ Crystals

V. Yu. Ivanov, V. A. Pustovarov, E. S. Shlygin, A. V. Korotaev, and A. V. Kruzhalov

Ural State Technical University, ul. Mira 19, Yekaterinburg, 620002 Russia

e-mail: ivy@dpt.ustu.ru

Received June 16, 2004

Abstract—Low-temperature (T = 7 K) time-resolved selectively photoexcited luminescence spectra (2–6 eV) and luminescence excitation spectra (8–35 eV) of wide-bandgap chrysoberyl $BeAl_2O_4$, phenacite Be_2SiO_4, and beryl $Be_3Al_2Si_6O_{18}$ crystals have been studied using time-resolved VUV spectroscopy. Both the intrinsic luminescence of the crystals and the luminescence associated with structural defects were assigned. Energy transfer to impurity luminescence centers in alexandrite and emerald was investigated. Luminescence characteristics of stable crystal lattice defects were probed by 3.6-MeV accelerated helium ion beams. © *2005 Pleiades Publishing, Inc.*

1. INTRODUCTION

Models of the relaxation of electronic excitations in inorganic dielectrics have been developed on the basis of studies of the energy dissipation processes in alkali halide crystals (AHCs). Self-trapped excitons (STEs), which have been found to exist in AHCs and govern basic relaxation processes, such as below-threshold defect formation, are of fundamental interest in solid-state physics. The ideas developed for AHCs underlie the intense interest in the specific features of nonequilibrium processes involving intrinsic and impurity electronic excitations in other classes of wide-bandgap dielectrics, including binary and complex oxides.

STE luminescence is excited in AHCs both under optical selective generation of excitons and, in the interband transition region, in recombination of electrons with low-mobility self-trapped holes. In oxide crystals, the various states (configurations) of STEs appear in alternate mechanisms of electronic-excitation relaxation, namely, free-exciton localization or the recombination scenario giving rise to STE formation through summation of the deformation potentials of both carriers. The luminescence bands corresponding to different STE configurations differ in terms of their excitation spectra [1–4]. By properly analyzing the luminescence and luminescence excitation spectra obtained using time-resolved VUV spectroscopy and the x-ray and cathodoluminescence spectra, one can isolate intrinsic luminescence bands in the wide-bandgap oxide crystals and determine their nature.

In oxides irradiated by beams of neutrons or accelerated ions, luminescence spectra exhibit additional bands, which typically form when anion vacancies in the crystal capture one (F^+ center) or two electrons (F center). In these cases, information on defect formation can be gained by studying the optical characteristics of neutron-irradiated crystals or by measuring the ion luminescence spectra created by accelerated ions [5].

Model objects for wide-bandgap oxides (E_g > 9 eV) with lowered crystal symmetry are binary oxides BeO, α-Al_2O_3, and SiO_2, which are of considerable importance for both fundamental and applied physics. Table 1 presents the positions of the maxima of STE intrinsic luminescence bands (E_m) for a number of crystals. Bands of type I are produced by the excitonic mechanism of STE luminescence excitation, and bands of type II, by the recombination mechanism.

The crystal lattices of the complex oxides $BeAl_2O_4$ (chrysoberyl), Be_2SiO_4 (phenacite), and $Be_3Al_2Si_6O_{18}$ (beryl) exhibit motifs (weakly distorted BeO_4 and SiO_4 tetrahedra and AlO_6 octahedra) that are typical of the parent crystal-forming compounds, namely, beryllium, aluminum, and silicon oxides. As a result, the scenarios of formation and the structure of the relaxed electronic excitations (associated with local lattice fragments) may turn out to be similar for binary and complex oxides.

Table 1. Parameters of intrinsic luminescence bands in several oxides

Crystal	Band I (E_m, eV)	Band II (E_m, eV)	E_g, eV	Reference
BeO	6.7	4.9	10.63	[4]
α-Al_2O_3	7.5	3.8	9.4	[1]
α-SiO_2	2.8	–	10.2	[6]
$YAlO_3$	5.9	4.2	7.5	[1]
$Y_3Al_5O_{12}$	4.9	4.2	6.7	[1]

1063-7834/05/4703-0466$26.00

Table 2. Band assignment in luminescence spectra of $BeAl_2O_4$, Be_2SiO_4, and $Be_3Al_2Si_6O_{18}$ recorded at T = 12 K

Crystal	Bandgap width (E_g, eV) T = 300 K	Defect luminescence bands (E_m, eV)	Intrinsic luminescence bands of the crystal (E_m, eV)	
			exciton mechanism	recombination mechanism
$BeAl_2O_4$	9.0	Several bands in the range 2.0–3.8	3.5, 4.3	5.2
Be_2SiO_4	8.5	2.6, 3.0, 4.0	3.5	2.7, 4.1
$Be_3Al_2Si_6O_{18}$	8.9	2.5, 2.9, 3.1	3.5	4.2 (**C** ∥ **E**); 4.9 (**C** ⊥ **E**)

Our preliminary studies of $BeAl_2O_4$, Be_2SiO_4, and $Be_3Al_2Si_6O_{18}$ crystals [7–9] revealed complex intrinsic luminescence bands characteristic of oxide crystals with lowered lattice symmetry. An analysis of the reflectance and luminescence excitation spectra of these crystals yielded an estimate of the bandgap width at 300 K (Table 2).

We report here on a coordinated study of low-temperature (T = 7 K) time-resolved luminescence (2–6 eV) and luminescence excitation (4–35 eV) spectra, obtained with the use of VUV synchrotron radiation, and of x-ray and ion luminescence spectra of $BeAl_2O_4$, Be_2SiO_4, and $Be_3Al_2Si_6O_{18}$ crystals. The study was aimed at identifying the origin of intrinsic luminescence of the regular lattice and of stable defects. The energy transfer to impurity luminescence centers in the crystals of interest was investigated using time-resolved luminescence spectroscopy of Cr^{3+} impurity ions, which serve as luminescence probes in alexandrite ($BeAl_2O_4$–Cr) and emerald ($Be_3Al_2Si_6O_{18}$–Cr).

2. CHARACTERIZATION OF SAMPLES

Chrysoberyl ($BeAl_2O_4$) has orthorhombic symmetry (*Pmnb*) and contains 19.8 wt % BeO and 80.2 wt % Al_2O_3 [10]. Due to the small ionic radius of Be^{2+}, the crystal structure of chrysoberyl has a lower symmetry than minerals of the spinel group with similar formulas. This structure consists of oxygen ions which form a hexagonal close-packed arrangement with four-coordinated beryllium ions and six-coordinated aluminum ions. The arrangement of the oxygen ions in this hexagonal close-packed lattice accounts for the pseudohexagonal cell and the corresponding angles and twinning.

Crystals of phenacite (Be_2SiO_4) have trigonal symmetry (*R*3) and contain 45.5 wt % BeO and 54.5 wt % SiO_2 [10]. The lattice structure is formed by SiO_4 and BeO_4 tetrahedra, with each oxygen ion being linked with two beryllium ions and one silicon ion located at the corners of an equilateral triangle. Phenacite crystals have a threefold $\mathbf{C}_3$ crystallographic axis.

Crystals of beryl ($Be_3Al_2Si_6O_{18}$) have hexagonal symmetry (P_6/mmc) and contain 14.0 wt % BeO, 19.0 wt % Al_2O_3, and 67 wt % SiO_2 [10]. The basic units of the structure are closed ring configurations of SiO_4 tetrahedra. The layers of beryllium and aluminum ions are sandwiched between "silicate" rings. The four-coordinated beryllium ion and the six-coordinated aluminum ion provide vertical and horizontal links with these rings, respectively. The $\mathbf{C}_6$ axis of the beryl crystal is perpendicular to the silicate ring plane.

Thus, the beryl and phenacite crystals have a preferred symmetry axis, which makes it possible to carry out experiments with the samples properly oriented with respect to the electric vector of the synchrotron radiation (SR) field or the direction of the accelerated ion beam.

The crystals used in the study were optically perfect single crystals grown by V.A. Maslov at different times at the Institute of Geology and Geophysics, SD RAS (Novosibirsk), and by L.I. Isaenko at the Institute of Single Crystals, SD RAS.

3. EXPERIMENTAL TECHNIQUES

Measurements were performed using time-resolved VUV spectroscopy at the SUPERLUMI station (HASYLAB laboratory, DESY, Hamburg) [11]. Luminescence excitation in the 4- to 35-eV region was effected with the use of a 2-m vacuum monochromator with interchangeable gratings (spectral resolution 3.2 Å or 25×10^{-3} eV for energies ~10 eV). The luminescence excitation spectra are normalized against equal numbers of photons striking the crystal by means of sodium salicylate. The luminescence spectra measured in the range 2.0–6.0-eV were analyzed with a B&M monochromator in a Czerny–Turner configuration and an R2059 PM tube (Hamamatsu). The luminescence and luminescence excitation spectra were obtained both in the time-integrated mode and in time windows (of width Δ_t) gated relative to the SR exciting pulse (with a time delay δ_t with respect to the SR signal onset). The time window parameters (δt_1 = 2.1 ns, Δt_1 = 14.1 ns, δt_2 = 46 ns, Δt_2 = 155.1 ns) were set in accordance with the luminescence decay kinetics and allowed us to measure luminescence and luminescence excitation spectra in the so-called fast and slow time windows. The parameters of the fast luminescence decay kinetics were calculated by deconvolution. The impurity luminescence spectra of chromium-doped crystals were obtained with a resolution better than 1 Å using a cooled CCD camera and an ARC Spectro Pro-380i monochromator.

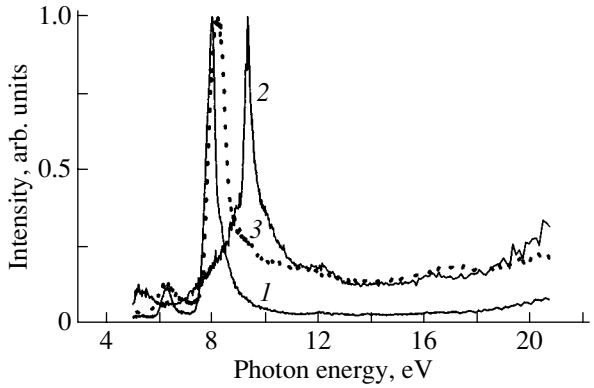

Fig. 1. Luminescence excitation spectra (E_{em} = 3.5 eV) of (*1*) $Be_3Al_2Si_6O_{18}$ (**E** ∥ **C**), (*2*) $BeAl_2O_4$, and (*3*) Be_2SiO_4 (**E** ∥ **C**) recorded at 9.6 K.

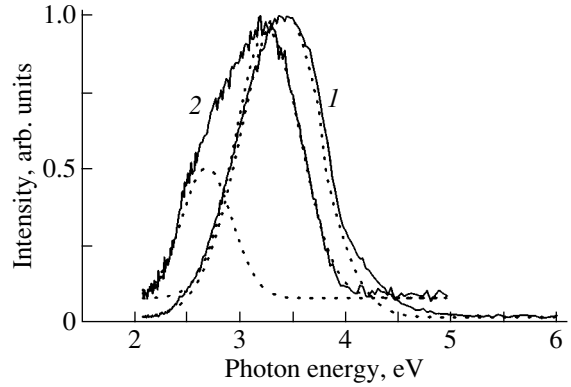

Fig. 2. Luminescence spectra of $Be_3Al_2Si_6O_{18}$ (**E** ∥ **C**) recorded at T = 9.6 K at excitation energy E_{exc} equal to (*1*) 8.0 and (*2*) 6.2 eV and their decomposition into Gaussians.

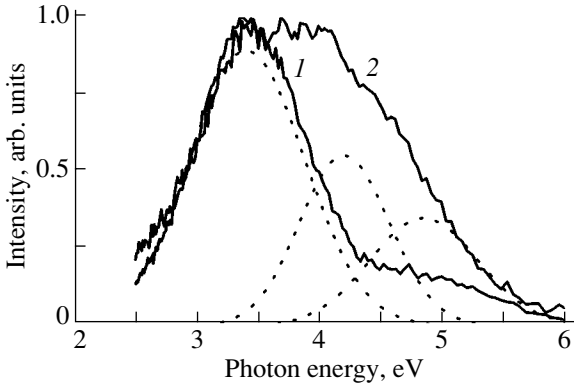

Fig. 3. Luminescence spectra of $Be_3Al_2Si_6O_{18}$ (**E** ⊥ **C**) recorded at T = 9.6 K at excitation energy E_{exc} equal to (*1*) 8.0 and (*2*) 10.8 eV and their deconvolution into Gaussians.

The ion luminescence and the defect formation at 80–300 K were studied on an R-7M cyclotron from the Ural State Technical University in a beam of accelerated He^+ ions (E = 3.6 MeV) [12]. The ion luminescence spectra were measured continuously with an Oriel Instruments 77441 spectrograph in the course of crystal irradiation. The ion fluence was monitored with a Faraday cylinder.

4. EXPERIMENTAL RESULTS

A combined analysis of time-resolved luminescence and luminescence excitation spectra and of the luminescence decay kinetics in all the compounds studied allowed us to isolate two luminescence band types for each compound. The spectral luminescence excitation profiles of $BeAl_2O_4$, Be_2SiO_4, and $Be_3Al_2Si_6O_{18}$ (Fig. 1) agree well with the estimated bandgap widths E_g derived earlier in [7]: E_g = 9.0, 8.5, and 8.9 eV at 300 K, respectively.

4.1. Beryl $Be_3Al_2Si_6O_{18}$

The luminescence spectra excited in the transmission region by photons with energy $E_{exc} < E_g$ are dominated by a complex band peaking at about 3.0 eV (Fig. 2). Unfolding it into constituent Gaussians isolates bands with maxima at 2.6 eV (FWHM = 0.55 eV) and 3.1 eV (FWHM = 0.7 eV). Because these luminescence bands are excited in the crystal transmission region, their nature can be associated with radiative decay of electronic excitations near native or impurity defects. When excited near the fundamental absorption edge, i.e., under selective creation of excitons, the maximum in the luminescence spectrum shifts toward higher energies to yield E_m = 3.5 eV and FWHM = 0.9 eV. The luminescence spectra also exhibit a weak shoulder at 4.2 eV. The luminescence decay kinetics in beryl has a microsecond-range component. The properties of the 3.5-eV luminescence are characteristic, in particular, of STE luminescence in oxide crystals; hence, this luminescence can be assumed to be intrinsic.

The luminescence spectra of crystals excited in the region of the fundamental absorption edge in the **E** ⊥ **C** geometry exhibit an additional band peaking at 4.9 eV (curve *1* in Fig. 3). The 3.5-eV band contains both fast ($\tau_1 \sim 6$ ns, $\tau_2 \sim 52$ ns) and slow ($\tau > 1$ μs) components in the decay kinetics. The 4.9-eV luminescence is excited most efficiently in the electron–hole pair generation region, E_{exc} = 10.8 eV (Figs. 3, 4); in these conditions, the luminescence spectra have another distinct band located at 4.2 eV (curve *2* in Fig. 3), which is seen as a weak shoulder in the **E** ∥ **C** geometry. The decay kinetics of the 4.2- and 4.9-eV bands contains fast components ($\tau_1 \sim 3$ ns, $\tau_2 \sim 64$ ns) and a slow ($\tau > 1$ μs) component.

The luminescence spectra obtained at 80–300 K under irradiation of the crystal by helium ions are dominated only by low-energy bands (their deconvolution into Gaussians yields E_m = 2.5, 2.9, and 3.1 eV in Fig. 5), which were assigned earlier to the luminescence of lattice defects. Increasing the beryl irradiation dose enhances the 2.5-eV band intensity, which can be traced to a buildup of radiation-induced defects. The decay kinetics of the 2.5-eV luminescence was established to have only a slow component in the millisecond range.

Thus, an analysis of low-temperature luminescence spectra of pure beryl reveals groups of defect-associated bands at E_m = 2.5, 2.9, and 3.1 eV and bands deriving from intrinsic crystal luminescence at E_m = 3.5, 4.2, and 4.9 eV, whose relative intensity depends on both excitation energy and crystal orientation.

4.2. Chrysoberyl $BeAl_2O_4$

The luminescence spectra obtained under excitation in the crystal transmission region (E_{exc} = 4.6, 5.5, 8.2 eV) reveal only a 2.6-eV band (FWHM = 0.6 eV) due to lattice defects. When excited in the region of the fundamental absorption edge (E_{exc} = 9.3 eV), the luminescence spectra become complex and consist of at least two bands of comparable intensity with maxima at 3.5 and 4.3 eV and a weaker band located at 2.6 eV (Fig. 6). The short-wavelength luminescence bands at 3.5 and 4.3 eV (FWHM = 0.85, 0.9 eV, respectively), as well as the similar luminescence bands of beryl, can be assigned to the intrinsic crystal luminescence. The decay kinetics of the 3.5- and 4.3-eV luminescence contains a fast and a slow component ($\tau_1 \sim 25$ ns, $\tau_2 >$ 1 μs), and that of the 2.6-eV luminescence contains a slow component only ($t > 1$ μs).

The ion luminescence spectrum of chrysoberyl at 80–300 K exhibits a number of bands in the range 2–6 eV (Fig. 7). The short-wavelength part of the spectrum has bands at 5.2 and 4.3 eV, whose intensities fall off with irradiation (i.e., with increasing dose). Note that the 5.2-eV band is present, albeit as a weak shoulder, in the luminescence spectra excited near the fundamental absorption edge (Fig. 6), whereas this luminescence is dominant in the low-temperature spectrum obtained under selective core-level excitation in the soft-x-ray domain (curve *4* in Fig. 7).

By contrast, the intensity of the long-wavelength part of the spectra (the series of bands in the range 2.0–3.8 eV) grows with irradiation dose and is dominated by the luminescence peaking at 3.5 eV. Although this luminescence coincides in position with the luminescence band excited near the fundamental absorption edge, its halfwidth is substantially smaller. This becomes particularly evident when comparing spectra obtained in different irradiation stages. As the dose and the 3.5-eV luminescence intensity grow, the half-width of this spectral band decreases to FWHM = 0.5 eV. The same phenomenon is observed in ion luminescence spectra under cooling to T = 80 K in the initial irradiation stages. As a whole, these observations suggest that

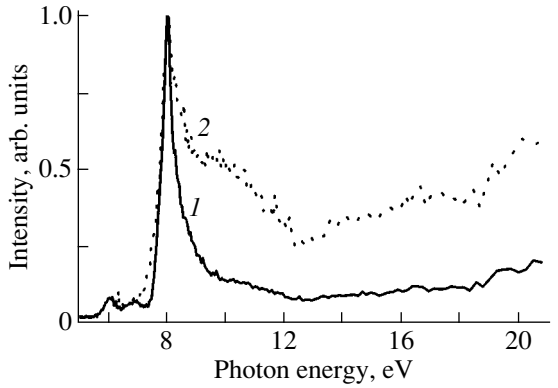

Fig. 4. Luminescence excitation spectra for (*1*) E_m = 3.5 and (*2*) 4.9 eV of $Be_3Al_2Si_6O_{18}$ crystals (**E** ⊥ **C**) recorded at T = 9.6 K.

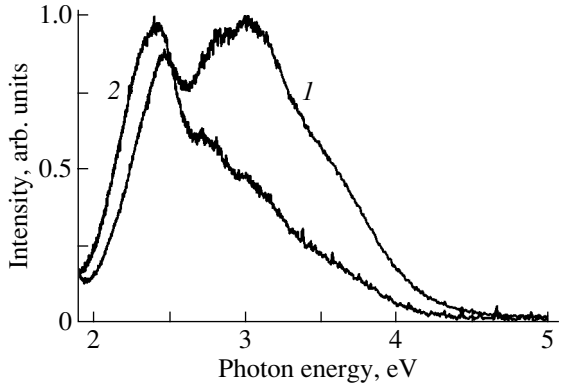

Fig. 5. Ion luminescence spectra of $Be_3Al_2Si_6O_{18}$ (He beam **He** ⊥ **C**) recorded at fluences of (*1*) 8.8×10^{13} and (*2*) 1.7×10^{15} cm^{-2}. T = 300 K.

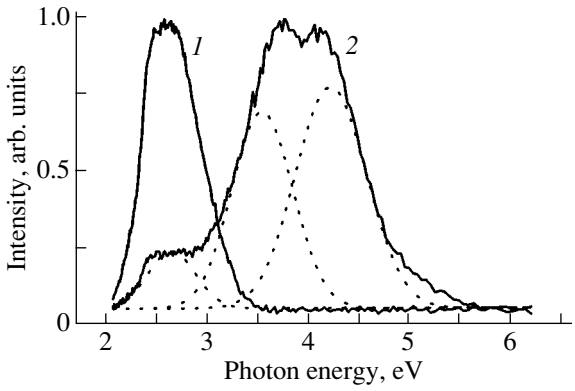

Fig. 6. Luminescence spectra of $BeAl_2O_4$ recorded under excitation with (*1*) E_{exc} = 5.5 and (*2*) 9.3 eV and their deconvolution into Gaussians. T = 9.6 K.

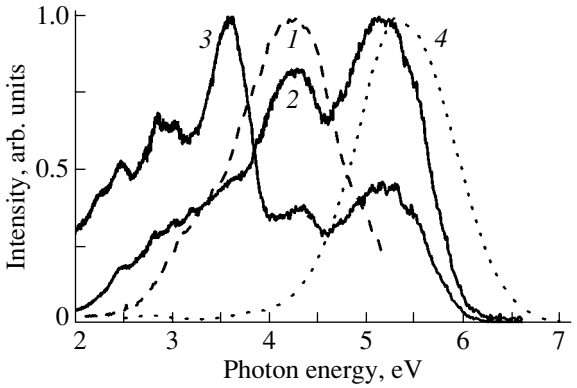

Fig. 7. X-ray-induced luminescence of $BeAl_2O_4$ recorded under (*1*) integrated (3–60 keV) and (*4*) selective (E_{exc} = 140 eV) excitation and compared with ion luminescence spectra of $BeAl_2O_4$ measured at fluences of (*2*) 4.0×10^{14} and (*3*) 1.8×10^{15} cm^{-2}. Spectra *1–3* were measured at 300 K, and spectrum *4*, at 12 K.

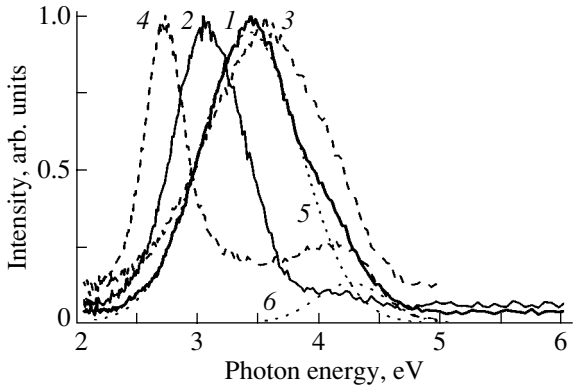

Fig. 8. Luminescence spectra of Be_2SiO_4 recorded under excitation with (*1*) E_{exc} = 8.1, (*2*) 6.2, and (*3*) 25.8 eV at T = 9.6 K and (*4*) an x-ray-induced luminescence spectrum measured at T = 300 K; (*5*, *6*) constituent Gaussians of peak *1*.

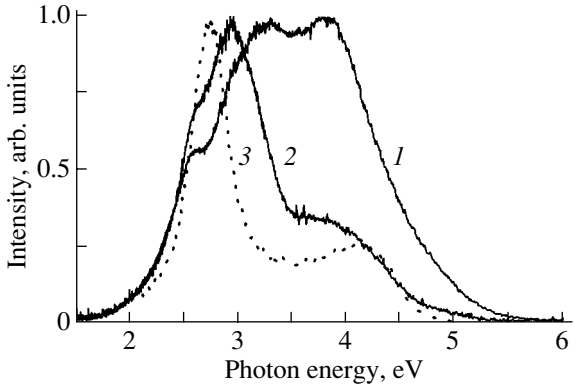

Fig. 9. Ion luminescence spectra of Be_2SiO_4 recorded at a fluence of (*1*) 1.1×10^{14} and (*2*) 2.2×10^{15} cm^{-2} and (*3*) an x-ray-induced luminescence spectrum. T = 300 K.

two different centers radiate in the same luminescence region of chrysoberyl. One center is excited in the region of the fundamental absorption edge and is characteristic of the regular lattice, while the other operates for $E_{exc} < E_g$ and should be associated rather with a lattice defect. Note that a similar situation is realized in one of the compounds that form chrysoberyl, namely, α-Al_2O_3, where the luminescence near 3.8 eV is due to STEs [1] and F^+ centers [13].

The x-ray-induced luminescence spectra of $BeAl_2O_4$ crystals recorded at 300 K contain two bands at 3.5 and 4.3 eV (curve *1* in Fig. 7). At 80 K, the 3.5-eV luminescence is quenched but the luminescence at 5.2 eV appears, so the spectrum then has two bands, at 4.3 and 5.2 eV.

Thus, the luminescence spectra of chrysoberyl exhibit two groups of bands, more specifically, intrinsic luminescence bands at 3.5, 4.3, and 5.2 eV and a number of bands in the range 2.0–3.8 eV associated with the relaxation of electronic excitations near defects.

4.3. Phenacite Be_2SiO_4

Similar to beryl and chrysoberyl, the luminescence spectra of phenacite are associated with two types of luminescence centers (Fig. 8). A defect-associated luminescence band (E_m = 3.0 eV, FWHM = 0.65 eV) is observed under excitation in the transmission region of the crystal (E_{exc} < 7 eV). The intrinsic luminescence (E_m = 3.5, 4.1 eV and FWHM = 0.9, 0.8 eV, respectively) is excited in the region where free excitons (E_{exc} = 8.1 eV) and isolated electron–hole pairs for $E_{exc} > E_g$ are created (Figs. 1, 8). The decay kinetics of the 3.5-eV luminescence contains fast components ($\tau_1 \sim 1$ ns, $\tau_2 \sim 15$ ns) and a slow ($\tau_3 > 1$ μs) component. Significantly, the band at E_m = 4.1 eV is more pronounced in the luminescence spectra excited by photons in the region where secondary electron–hole pairs are created ($E_{exc} \geq 25.8$ eV) than in the luminescence spectra excited near the fundamental absorption edge. The luminescence band at 4.1 eV is observed simultaneously with the 2.7-eV band in the x-ray-induced luminescence of phenacite.

The spectrum of ion luminescence of phenacite (Fig. 9) resembles the luminescence spectrum measured under high-energy photoexcitation (e.g., for $E_{exc} \geq 25.8$ eV) and, in the initial stages of ion irradiation, consists of bands located at 2.6, 3.0, and 4.1 eV. The fraction of the low-energy bands in the spectrum grows with increasing irradiation dose.

An analysis of the luminescence properties of phenacite showed that its luminescence spectrum has bands due to intrinsic luminescence with E_m = 2.7, 3.5, and 4.1 eV and bands associated with native lattice defects with λ_m = 2.6 and 3.0 eV. The 3.5-eV luminescence is excited primarily in the free-exciton generation

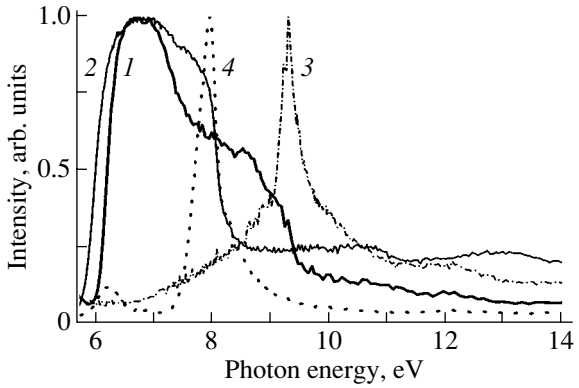

Fig. 10. Luminescence excitation spectra of (*1*) $BeAl_2O_4$–Cr, (*2*) $Be_3Al_2Si_6O_{18}$–Cr, (*3*) $BeAl_2O_4$, and (*4*) $Be_3Al_2Si_6O_{18}$ recorded at (*1*, *2*) E_{em} = 1.82 and (*3*, *4*) 3.44 eV.

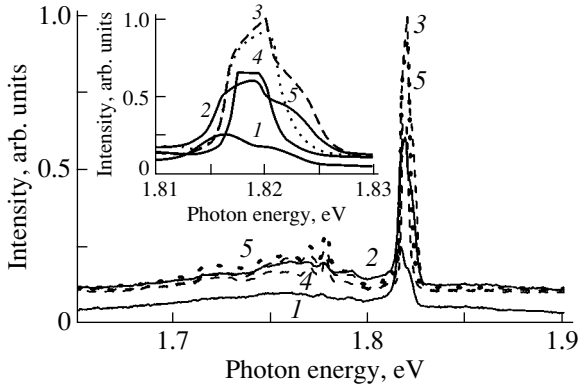

Fig. 11. Luminescence spectra of $BeAl_2O_4$–Cr recorded at E_{exc} = 6.8 eV at different temperatures *T*: (*1*) 300, (*2*) 200, (*3*) 100, (*4*) 17, and (*5*) 16 K.

region, whereas the bands at 2.7 and 4.1 eV are produced in the creation of electron–hole pairs.

4.4. Alexandrite ($BeAl_2O_4$–Cr) and Emerald ($Be_3Al_2Si_6O_{18}$–Cr)

The Cr^{3+} *R*-line luminescence excitation spectra of alexandrite and emerald recorded at 300 K reveal a broad band peaking at about 6.8 eV, as well as less pronounced features in the region of the fundamental absorption edge of the matrix (Fig. 10). The slight broadening of the 6.8-eV band in $Be_3Al_2Si_6O_{18}$–Cr crystals is due to the proximity of another band, which is seen as a shoulder at 7.8 eV and lies closer to the fundamental absorption edge of the crystal. A similar shoulder in the luminescence excitation spectra of $BeAl_2O_4$–Cr is shifted, just as the fundamental absorption edge, toward higher energies and is observed at about 9 eV.

The luminescence spectra of alexandrite (Fig. 11) recorded in the temperature region 100–300 K reveal a well-resolved chromium *R*-line doublet. Both doublet lines grow in intensity with crystal cooling and shift toward higher energies. For $T < 100$ K, one of the lines (at a higher energy) is not seen. The *R*-line doublet in the luminescence spectra of a number of crystals is known [14] to derive from crystal-field splitting of the radiating ground-state level of the Cr^{3+} ion substituting for the aluminum ion in the mirror-symmetry (C_s) plane. The fact that only one doublet line is observed at low temperatures is accounted for by the existence of an energy barrier that prevents population of the higher lying state. The origin of the lines in the range 1.75–1.8 eV is still a subject for debate. Their possible relation to chromium ions substituting for aluminum in the inverse symmetry (C_i) plane or to phonon replicas of the *R* lines has been discussed [14]. At high chromium ion concentrations and with noticeable exchange coupling, the so-called *N* lines appear in this energy region [14]. There are also the so-called *S* and *B* lines in this region, which are associated with transitions to the $^4A_{2g}$ ground state from states located higher in energy than ^2E_g (*R* lines), namely, from the $^2T_{1g}$ (*S* lines) and $^2T_{2g}$ states (*B* lines) [15].

5. DISCUSSION OF THE RESULTS

The crystals studied by us emit several characteristic types of luminescence.

(1) All pure crystals produce luminescence excited only in the region of or above the fundamental absorption edge, which forms the shorter-wavelength section of the spectra. Luminescence of this type has been described for wide-bandgap oxides in terms of the STE model [1–4]. The low symmetry of the crystal not only accounts for the self-trapping of electronic excitations themselves but also explains why they have various configurations. For instance, in BeO, α-Al_2O_3, $YAlO_3$, and $Y_3Al_5O_{12}$, two types of luminescence originating from the radiative decay of STEs have been observed to exist [1, 3]. This luminescence is characterized by a large half-width and a large Stokes shift, as well as by the absence of excitation bands in the transmission region of the crystal. There are two alternate mechanisms of STE formation. One of them is photoexcitation of the exciton (the excitonic mechanism) followed by its relaxation to the self-trapped state. The other mechanism involves creation of the STE through relaxation of the electronic excitations in the recombination of electron–hole pairs. The reasons underlying the formation of different STE configurations in complex oxides are connected with the pronounced nonuniformity of the electronic valence-band structure. It is known that low-symmetry crystal fields initiate complete splitting of the oxygen 2*p* states forming the upper valence band state [16]. The nonbonding (π-type) orbitals form the top of the valence band. In the upper, narrow low-dispersion subband, the hole translational

mass is comparatively large, which favors hole self-trapping. Self-trapping of holes in complex oxides accounts for the formation of STEs by the recombination mechanism, in which an electron recombines with a self-trapped hole. The lower valence-band subband has a large width and dispersion, and the translational mass of holes in this subband is small. It is this lower subband that is involved in the creation of free excitons. However, self-trapping of the hole component of the exciton is unlikely because of the small translational mass. According to the STE level diagram proposed by Sumi [17] and validated by experiments performed on some oxides [1–4], in the case where an electron or a hole cannot become self-trapped separately, the self-trapped state can form when the lattice strains generated by the electron and the hole are added.

Because the exciton–phonon coupling in low-symmetry wide-bandgap oxides is stronger than that in alkali halide crystals, free excitons usually do not manifest themselves in optical spectra. They have a small range and become localized directly at the point of their formation. Thus, a local fragment of the crystal structure plays an important role in the self-trapping process. As already mentioned, crystal lattices of complex oxides $BeAl_2O_4$, Be_2SiO_4, and $Be_3Al_2Si_6O_{18}$ and of binary oxides BeO, Al_2O_3, and SiO_2 contain identical local lattice fragments; therefore, the exciton self-trapping processes in the complex and binary oxides should be similar. This gives us grounds to assert that the intrinsic luminescence bands of the complex oxides observed in the short-wavelength region of the luminescence spectra derive from radiative STE decay. The two bands observed in this luminescence may be due to two different mechanisms of formation of a localized state (of the exciton and recombination types) or be associated with the existence of different local lattice fragments in the complex crystals. To substantiate the above conclusions concerning the mechanisms of STE formation, additional studies of the luminescence excited directly in the region of the fundamental absorption edge and at shorter wavelengths where free carriers are produced, as well as of thermally stimulated luminescence, are needed.

(2) In crystals with defects, luminescence associated with the relaxation of electronic excitations near defects is excited in the crystal transmission region. Ions and neutrons bombarding the binary oxides produce primarily anion vacancies, because the binding energy of oxygen is less than that of a cation. Therefore, the main bands observed in these crystals that have a distorted stoichiometry and are excited in the transmission region of the crystals are *F*-like centers (in particular, *F* and F^+ centers and their aggregates). Investigation of the dynamics of luminescence initiated by helium ions suggests that similar lattice defects probably form in complex oxides as well. These defects account for the appearance and growth in intensity of additional bands in the long-wavelength region of the spectrum. The appearance of these bands is accompanied by the observation of luminescence kinetics components with decay times in the millisecond range. This situation is characteristic, in particular, of *F*-center generation in BeO [5]. Thus, the observed situation can be assigned to the formation of stable *F*-like lattice defects in our crystals.

The assignment of defect and intrinsic luminescence bands of $BeAl_2O_4$, Be_2SiO_4, and $Be_3Al_2Si_6O_{18}$ is presented in Table 2.

(3) Chromium-activated crystals (alexandrite, emerald) exhibit a similar pattern of excitation of the impurity luminescence. Figure 10 compares the luminescence excitation spectra of pure and chromium-activated crystals. The fact that the dominant band in the luminescence excitation spectra of both crystals has the same position in the VUV region and a similar half-width suggests that this band is associated with intracenter chromium-ion excitation and that the nearest neighbor environment of the impurity ion in both crystals is the same. The specific features in the luminescence excitation spectra at 7.8 eV (for emerald) and at 9.0 eV (for alexandrite), which are located a few tenths of an electronvolt below the fundamental absorption edge, are customarily interpreted as a manifestation of impurity-bound large-radius excitons in wide-bandgap oxides. Finally, chromium *R* lines can also appear by the recombination mechanism when photons with $E_{exc} > E_g$ produce free electron–hole pairs. This conclusion is supported by the observed spectral composition of the high-temperature peaks (T = 360, 550 K for $BeAl_2O_4$ and T = 480 K for $Be_3Al_2Si_6O_{18}$) of thermally stimulated luminescence (TSL) in crystals irradiated by x rays. The TSL spectrum exhibits a peak at 1.8 eV in the region of impurity chromium ion luminescence.

ACKNOWLEDGMENTS

The authors are indebted to G. Zimmerer and M. Kirm (Hamburg University) for their assistance in the experiments and to V.A. Maslov and L.A. Isaenko for providing the samples.

This study was supported by the Russian Foundation for Basic Research (project no. 02-02-16322), the Ministry of Education and Science of the Russian Federation (project no. E02-3.4-362), and CRDF ("Promising Materials" science and education center).

REFERENCES

1. A. I. Kuznetsov, V. N. Abramov, V. V. Myurk, and B. R. Namozov, Fiz. Tverd. Tela (Leningrad) **33** (7), 2000 (1991) [Sov. Phys. Solid State **33**, 1126 (1991)].
2. V. Mürk, B. Namozov, and N. Yaroshevich, Radiat. Meas. **24** (4), 371 (1995).
3. V. A. Pustovarov, V. Yu. Ivanov, M. Kirm, A. V. Kruzhalov, A. V. Korotaev, and G. Zimmerer, Fiz. Tverd. Tela (St. Petersburg) **43** (7), 1189 (2001) [Phys. Solid State **43**, 1233 (2001)].

4. I. N. Ogorodnikov, V. A. Pustovarov, M. Kirm, A. V. Kruzhalov, and L. I. Isaenko, Fiz. Tverd. Tela (St. Petersburg) **43** (8), 1396 (2001) [Phys. Solid State **43**, 1454 (2001)].
5. O. V. Ryaboukhin, V. Yu. Ivanov, A. V. Korotaev, A. V. Kruzhalov, and F. G. Neshov, in *Proceedings of 1st International Congress on Radiation Physics. High Current Electronics and Modification of Materials* (Tomsk, 2000), p. 318.
6. A. R. Silin' and A. N. Trukhin, *Point Defects and Elementary Excitations in Crystalline and Vitreous SiO_2* (Zinatne, Riga, 1985) [in Russian].
7. V. Yu. Ivanov, A. V. Kruzhalov, V. L. Petrov, T. I. Polupanova, and V. A. Pustovarov, in *Proceedings of VI All-Union Meeting on Use of the Synchrotron Radiation* (Inst. Yad. Fiz. Sib. Otd. Akad. Nauk SSSR, Novosibirsk, 1984), p. 291.
8. A. V. Korotaev, V. Yu. Ivanov, D. V. Permyakov, and V. A. Pustovarov, DESY, HASYLAB, Annual Report-2001 (Hamburg, Germany, 2001), p. 321.
9. A. V. Korotaev, V. Yu. Ivanov, V. A. Pustovarov, A. V. Kruzhalov, and B. V. Shulgin, Nucl. Instrum. Methods Phys. Res. A **486**, 417 (2002).
10. C. Klein and C. S. Hurlbut, Jr., *Manual of Mineralogy (after James D. Dana)*, 20th ed. (Wiley, New York, 1985; Nedra, Moscow, 1982).
11. G. Zimmerer, Nucl. Instrum. Methods Phys. Res. A **308**, 178 (1991).
12. O. V. Ryabukhin, V. Yu. Ivanov, A. V. Korotaev, A. V. Kruzhalov, F. G. Neshov, and S. Yu. Sokovnin, in *Proceedings of International Meeting on Radiation Physics of Solids* (Sevastopol, 1999), p. 343.
13. B. D. Evans and M. Stapelbroek, Phys. Rev. B **18**, 7089 (1978).
14. C. P. Powell, L. Xi, X. Gang, G. J. Quarles, and J. C. Walling, Phys. Rev. B **32** (5), 2788 (1985).
15. R. M. Fernandes Scalvi, M. S. Li, and L. V. A. Scalvi, J. Phys.: Condens. Matter **15**, 7437 (2003).
16. S. Ciraci and I. P. Batra, Phys. Rev. B **28** (2), 982 (1983).
17. H. Sumi, J. Phys. Soc. Jpn. **43** (4), 1286 (1977).

Translated by G. Skrebtsov

Physics of the Solid State, Vol. 47, No. 3, 2005, pp. 474–476. Translated from Fizika Tverdogo Tela, Vol. 47, No. 3, 2005, pp. 460–462.

SEMICONDUCTORS AND DIELECTRICS

Absorption Spectrum of Thin K_2CdI_4 Films

O. N. Yunakova*, V. K. Miloslavskiĭ*, and E. N. Kovalenko**

**Kharkov National University, pl. Svobody 4, Kharkov, 61077 Ukraine*

e-mail: Vladimir.K.Miloslavsky@univer.kharkov.ua

***Kharkov National University of Radioelectronics, Kharkov, 61166 Ukraine*

Received July 7, 2004

Abstract—The absorption spectrum of thin films of a new compound, K_2CdI_4, was studied. It was established that this compound belongs to direct-bandgap dielectrics and that its low-frequency electronic and excitonic excitations are localized in CdI_4^{2-} structural blocks of the crystal lattice. It was found that, in M_2CdI_4 compounds (M = K, Rb, Cs), the bandgap width E_g grows and the spin–orbit splitting of the valence band top decreases with increasing ionic radius of the alkali metal. *© 2005 Pleiades Publishing, Inc.*

1. INTRODUCTION

Thermographic studies [1] suggest the formation of a K_4CdI_6 compound with a low melting point (210°C) in the KI–CdI_2 system, whereas in the isomorphic RbI– and CsI–CdI_2 systems M_2CdI_4 (M = Rb, Cs) compounds form with similar melting points (216°C for Rb_2CdI_4 and 210°C for Cs_2CdI_4 [1]). X-ray diffraction studies of melted powders of stoichiometric composition K_4CdI_6 [2] do not corroborate the formation of this compound in the KI–CdI_2 system. It appeared reasonable that K_2CdI_4 does form in the KI–CdI_2 system, as is the case with RbI– and CsI–CdI_2. Based on this assumption, we synthesized a new compound, K_2CdI_4. Investigation of the absorption spectrum of this compound promises to throw light both on the formation of excitons in M_2CdI_4 and on possible ferroelastic properties of these compounds.

This communication reports on a study of the absorption spectrum of K_2CdI_4 in the range 2–6 eV carried out at 90 and 290 K.

2. EXPERIMENT

K_2CdI_4 thin films were prepared by vacuum deposition using the technique employed in [3, 4] to synthesize Rb_2CdI_4 and Cs_2CdI_4 films. A mixture of pure KI and CdI_2 powders of the assumed stoichiometric composition was preliminarily melted in vacuum under a screen. The liquid fraction of the melt was evaporated onto the screen, and the crystalline sediment was deposited at a higher temperature onto quartz substrates heated to 100°C. The sample was annealed for one hour at 120°C.

The films thus prepared are hygroscopic and, when exposed to air and cooled to room temperature, exhibit strong light scattering. To prevent this effect, while still warm, the samples were transferred to a vacuum cryostat, whose copper finger was preliminarily heated to 70°C. After evacuation of the cryostat and charging it with nitrogen, the films remain transparent.

The film thickness was determined from transmission spectra (in the region of transparency) with due account of light interference in the film as described in [5]. The absorption spectra were measured on an SF-46 spectrophotometer in the energy region 2–6 eV. The parameters of the long-wavelength excitonic bands (position E_m, half-width Γ, value of the imaginary part of permittivity at the band maximum ε_{2m}) were determined [6] by fitting the experimental relation with a symmetric two-oscillator linear combination of a Lorentzian and a Gaussian.

3. ABSORPTION SPECTRUM OF THIN K_2CdI_4 FILMS

The absorption spectrum of the thin films under study exhibits a strong long-wavelength band A_0 at 4.612 eV and a weaker band A_1 at 4.97 eV; a shorter wavelength region contains bands C_1 (5.46 eV) and C_2 (5.82 eV) (see figure). As the temperature is increased, the A bands shift to longer wavelengths, broaden, and grow weaker, which suggests their relation to excitonic excitations. We assign the broader, less temperature-sensitive C bands to interband absorption.

The spectral position of the A_0 band (4.612 eV) as plotted in the $E_m(x)$ coordinates, where x is the molar concentration in the $(2KI)_{1-x}(Cd_{0.5}I)_x$ system, lies on a straight line connecting the energies E_m of the excitonic peak for KI and of the X_1 peak for CdI_2 at $x = 2/3$, which shows the band to originate from the K_2CdI_4 compound (see inset to figure). The alternate compound K_4CdI_6 (x = 0.5) would feature a long-wavelength peak at 4.88 eV. The assignment of the spectrum to K_2CdI_4 is

1063-7834/05/4703-0474$26.00 © 2005 Pleiades Publishing, Inc.

supported by the proximity of the A_0 band to the corresponding bands of Rb_2CdI_4 and Cs_2CdI_4 (see table).

The sharp long-wavelength edge and the high intensity of the A_0 band suggest that K_2CdI_4 belongs to direct bandgap dielectrics.

For proper assignment of the main absorption bands observed in the spectrum of thin K_2CdI_4 films, it is reasonable to compare it with the spectra of the starting binary components CdI_2 and KI (see figure) and of the corresponding isostructural compounds Rb_2CdI_4 and Cs_2CdI_4 [3, 4].

The absorption edge of CdI_2 derives from indirect transitions with a bandgap E_g = 3.437 eV. The long-wavelength bands X_1 and X_2 originate from direct transitions between the valence band formed by the I 5*p* states and the conduction band arising from the Cd 4*s* states [7]. The separation between the X_1 and X_2 bands (ΔE = 0.59 eV) is determined by the spin–orbit splitting of the upper valence band in CdI_2.

Our measurements show the long-wavelength *A* band in KI to lie at 5.84 eV at 90 K (see figure), which agrees with the data from [8].

The A_0 band in K_2CdI_4 occupies an intermediate position between the X_1 band in CdI_2 and the *A* band in KI. According to the concept put forward in [9] for multicomponent compounds, the linear variation in the position of long-wavelength exciton bands in the KI, K_2CdI_4, and CdI_2 series (see inset to figure) indicates exciton creation in the volume of the crystal involving both sublattices of the compound. Nevertheless, we believe that excitonic excitations are localized in the CdI_4^{2-} structural blocks of the compound. This assumption is argued for by the positions of the main absorption bands in the spectra of K_2CdI_4, Rb_2CdI_4, and Cs_2CdI_4 being close together (see table), as well as by some features in the absorption spectra of these compounds, which will be discussed later.

If excitonic excitations are localized in CdI_4^{2-} structural blocks of the K_2CdI_4 crystal lattice, then the A_0 and A_1 bands originate from direct allowed transitions from the top of the valence band arising from the I 5*p* states to the conduction band deriving from the Cd 4*s* states and the distance between these bands $\Delta E_A = E_{A1} - E_{A0}$ is determined by the spin–orbit splitting of the upper valence band, as in CdI_2.

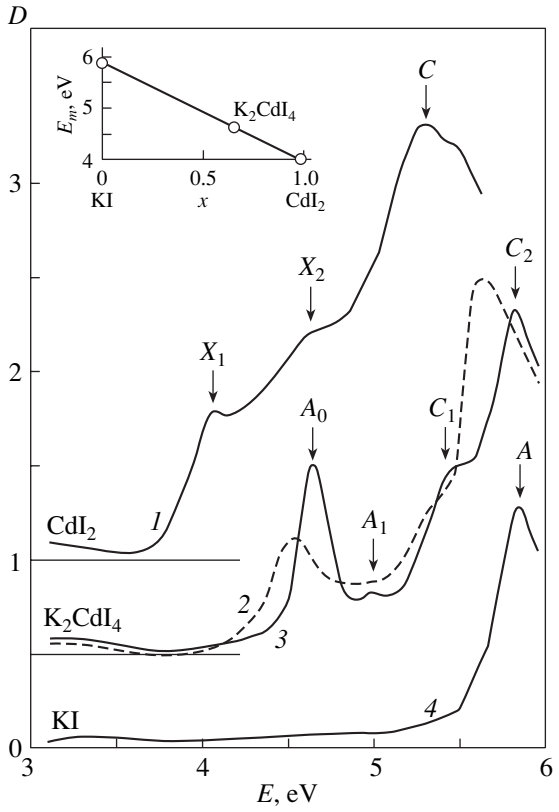

Absorption spectrum of thin films of (*1*) CdI_2 (T = 90 K, t = 60 nm), (*2*) K_2CdI_4 (T = 290 K, t = 145 nm), (*3*) K_2CdI_4 (T = 90 K, t = 145 nm), and (*4*) KI (T = 90 K, t = 150 nm). Inset: E_m vs. molar concentration x for the $(2KI)_{1-x}(Cd_{0.5}I)_x$ system.

As already mentioned, while the absorption spectra of thin M_2CdI_4 films (M = K, Rb, Cs) are similar in structure and in the position of the main absorption bands, the absorption edge in the series K_2CdI_4, Rb_2CdI_4, and Cs_2CdI_4 shifts slightly shortward, with an attendant increase in the bandgap E_g (see table). In K_2CdI_4, the bandgap width E_g was estimated from the bend in the absorption edge after isolation of the A_0 and A_1 bands; from the value E_g^1 = 5.18 eV thus obtained,

Positions and splittings of the main absorption bands and the bandgap width

Compound	E_{A0}, eV	E_{A1}, eV	ΔE_A, eV	E_{C1}, eV	E_{C2}, eV	ΔE_C, eV	E_g, eV	r_i, Å
K_2CdI_4	4.612	4.97	0.358	5.46	5.82	0.36	4.82	1.33 (K^+)
Rb_2CdI_4	4.63	4.92	0.29	5.34	5.62	0.28	4.89	1.48 (Rb^+)
Cs_2CdI_4	4.65	4.89	0.24	5.35	5.6	0.25	4.96	1.69 (Cs^+)
CdI_2	4.04 (X_1)	4.58 (X_2)	0.54 (ΔE_X)					
KI	5.84						6.33	

the distance between the subbands ΔE_A should be subtracted, which yields $E_g = 4.82$ eV.

The short-wavelength shift of the absorption edge and the growth of E_g is customarily assigned to the higher ionicity of the compound [10]. However, in the K_2CdI_4, Rb_2CdI_4, and Cs_2CdI_4 series, the ionicity decreases, so the cause of the short-wavelength shift should apparently be looked for in the specific features of the crystal structure of these compounds.

The M_2CdI_4 lattice is built of CdI_4^{2-} tetrahedra surrounded by alkali metal ions M^- forming a hendecagon [11, 12]. Note that the alkali-metal–iodine bond lengths greatly exceed d_{Cd-I} (for instance, in Cs_2CdI_4, we have $d_{Cs-I} = 3.825$–4.499 Å, $d_{Cd-I} = 2.76$–2.91 Å [12]). The lattice parameters and the unit cell volumes are similar ($a = 10.6$, 10.7 Å; $b = 8.4$, 8.46 Å; $c = 14.9$, 14.85 Å; and $\Omega = 1327$, 1349 Å^3 for Rb_2CdI_4 and Cs_2CdI_4, respectively [4, 11, 12]). The ionic radius of alkali metals r_i increases in the series K^-, Rb^-, and Cs^- [13] (see table), which, in view of the above data, apparently gives rise to an increasing compression of the CdI_4^{2-} tetrahedra in M_2CdI_4 by the alkali-metal environment and, accordingly, to the short-wavelength absorption edge shift. According to [14], hydrostatic compression of thin CdI_2 films causes the absorption edge to shift to shorter wavelengths. Because the shift coefficients are different for the X_1 and X_2 bands, the separation between the X_1 and X_2 bands decreases with increasing pressure. The separation between the A_0 and A_1 bands in the M_2CdI_4 series (M = K, Rb, Cs) decreases (see table), which is in qualitative agreement with the results from [14] in the case of excitonic excitations localized in CdI_4^{2-} tetrahedra and substantiates the assumption that the splitting of the A band in M_2CdI_4, as in CdI_2, is indeed caused by spin–orbit splitting of the upper valence band. This assumption is further supported by the splittings of the C bands, $\Delta E_C = E_{C2} - E_{C1}$, being similar (see table).

4. CONCLUSIONS

The above suggests that excitonic and electronic excitations in K_2CdI_4 are localized in CdI_4^{2-} structural blocks of the crystal lattice. The absorption edge in K_2CdI_4 derives from direct allowed transitions from the top of the valence band arising from I 5*p* states to the conduction band deriving from Cd 4*s* states. The splitting of the A and C bands is caused by the spin–orbit splitting of the valence band top.

The smaller spin–orbit splitting in M_2CdI_4 as compared to pure CdI_2 should be attributed to the effect of alkali metal ions on structural blocks of the CdI_4^{2-} crystal lattice; indeed, as the ionic radius r_i increases, the compression of the CdI_4^{2-} tetrahedra by the alkali ion environment increases, which gives rise to an increase in the bandgap width E_g and to a decrease in the spin–orbit splitting of the upper valence band in the compounds under study.

REFERENCES

1. I. N. Belyaev, E. A. Shurginov, and N. S. Kudryashov, Zh. Neorg. Khim. **17** (10), 2812 (1972).
2. H. P. Beck and W. Milius, Z. Anorg. Allg. Chem. **562**, 102 (1988).
3. O. N. Yunakova, V. K. Miloslavskiĭ, and E. N. Kovalenko, Fiz. Tverd. Tela (St. Petersburg) **45** (5), 888 (2003) [Phys. Solid State **45**, 932 (2003)].
4. O. N. Yunakova, V. K. Miloslavskiĭ, and E. N. Kovalenko, Fiz. Nizk. Temp. **29**, 922 (2003) [Low Temp. Phys. **29**, 691 (2003)].
5. V. K. Miloslavskiĭ, A. I. Rybalka, and V. M. Shmandiĭ, Opt. Spektrosk. **48** (3), 619 (1980) [Opt. Spectrosc. **48**, 341 (1980)].
6. V. K. Miloslavskiĭ, O. N. Yunakova, and Sun Tsya-Lin, Opt. Spektrosk. **78** (3), 436 (1995) [Opt. Spectrosc. **78**, 391 (1995)].
7. I. Pollini, J. Thomas, R. Coehoorn, and C. Haas, Phys. Rev. B **33** (8), 5747 (1986).
8. K. Teegarden and G. Baldini, Phys. Rev. **155** (3), 896 (1966).
9. Y. Onodera and Y. Toyozawa, J. Phys. Soc. Jpn. **22** (3), 833 (1967).
10. R. S. Bauer and B. A. Huberman, Phys. Rev. B **13** (9), 3344 (1976).
11. K. S. Aleksandrov, S. V. Melnikova, I. N. Flerov, A. D. Vasilev, A. I. Kruglik, and I. T. Kokov, Phys. Status Solidi A **105**, 441 (1988).
12. V. Touchard, V. Louer, J. P. Auffredic, and D. Louer, Rev. Chim. Miner. **24**, 414 (1987).
13. I. T. Goronovskiĭ, Yu. P. Nazarenko, and E. F. Nekryach, *A Brief Handbook on Chemistry* (Naukova Dumka, Kiev, 1987) [in Russian].
14. A. D. Brothers and J. T. Pajor, Phys. Rev. B **14** (10), 4570 (1976).

Translated by G. Skrebtsov

Physics of the Solid State, Vol. 47, No. 3, 2005, pp. 477–483. Translated from Fizika Tverdogo Tela, Vol. 47, No. 3, 2005, pp. 463–468.

DEFECTS, DISLOCATIONS, AND PHYSICS OF STRENGTH

Evolution of a Microstructure of Materials under Irradiation

V. V. Slezov[1], A. V. Subbotin[2], and O. A. Osmaev[1, 3]

[1] *Akhiezer Institute of Theoretical Physics, "Kharkov Institute of Physics and Technology" National Science Center, ul. Akademicheskaya 1, Kharkov, 61108 Ukraine*

[2] *Dollezhal Research and Design Institute of Power Engineering, Moscow, 101000 Russia*

e-mail: subbotin@nikiet.ru

[3] *Ukrainian State Academy of Railway Transport, Kharkov, 61050 Ukraine*

e-mail: oleg_osmayev@kipt.kharkov.ua

Received June 16, 2004

Abstract—The evolution of a microstructure of metals (or alloys) under irradiation resulting in swelling of the material is considered for the case with the formation of Frenkel pairs. A closed system of equations describing the evolution of the microstructure of the material exposed to irradiation is obtained, and relationships for the swelling rate are derived. It is shown that the swelling rate varies linearly with time for a stationary source of point defects (the number of Frenkel pairs per lattice site). An expression for the swelling rate is deduced for a radiation source operating in a more realistic pulsed mode. © *2005 Pleiades Publishing, Inc.*

1. INTRODUCTION

It is well known that prolonged exposure of crystalline solids to irradiation by neutrons and ions with energies high enough for pairs of point defects ("interstitial atom–vacant lattice site" pairs) to be generated in the crystal lattice leads to the evolution of the microstructure and, consequently, the physical and mechanical properties of the material. The evolution of the microstructure is governed by the porosity and the dislocation subsystem arising in the material. Of course, the rate of formation of the microstructure depends on the type of irradiation and its characteristics (such as the energy and charge spectra, cross sections for nuclear reactions, etc.). In turn, these characteristics determine the rates of generation of vacancies and interstitial atoms, i.e., Frenkel pairs, and impurities of different types, including gaseous impurities.

When the material is heated to temperatures above the temperature at which point defects become mobile ($T \geq 0.3T_{\text{melt}}$), their recombination is less pronounced and the decomposition of the supersaturated solid solution predominantly occurs through the nucleation and growth of two- and three-dimensional complexes (such as vacancy pores, precipitates of new phases, and dislocation loops of the interstitial and vacancy types) and the development of the already existing dislocation structure. Eventually, these processes lead to the evolution of the microstructure of the material.

In this paper, we consider the types of irradiation of a material that are responsible only for the formation of Frenkel pairs per lattice site in a unit time ($k = k_V = k_i$, where the subscripts V and i refer to the vacancies and interstitial atoms, respectively). The evolution of the microstructure of the material under irradiation results in its swelling.

The physical reason for this phenomenon under the given conditions is the difference between the sink strengths of interstitial atoms and vacancies at the dislocations. In turn, this difference is determined by the difference between the energies of interactions of point defects (namely, vacancies V and interstitial atoms i) with an elastic field of dislocations.

In this study, the evolution of a microstructure of materials exposed to irradiation is analyzed by using the example of a pure metal under conditions of prolonged formation and decomposition of a two-component solid solution of vacancies and interstitial atoms with the formation of vacancy pores and dislocation loops, as well as with the climb of elements of the already existing dislocation system. We disregard the difference between dislocation loops and elements of the dislocation structure with different orientations.

The evolution of a microstructure of a pure metal is examined at the stage preceding the coalescence (or Ostwald ripening) stage under conditions of both continuous and pulsed irradiation.

2. THE BASIC SYSTEM OF EQUATIONS

Let us write a system of equations describing the evolution of a microstructure of a material under irradiation. For this purpose, it is necessary to know the fluxes of point defects incident on pores and dislocations. It is these fluxes that determine the rates of their development. In order to calculate the fluxes under the conditions of the formation of point defects, we use initial equations, namely, non-steady-state diffusion equations that account for both the sources of point defects

(in the bulk of the material) and sinks. In the system under consideration, the surfaces of macrodefects act as sinks. The annihilation (recombination) of point defects in the bulk of the material is insignificant and, as a rule, can be ignored [1, 2]. In this exact formulation, the problem is very complicated and has defied analytical solution.

However, as a rule, the time required to attain a quasi-steady state (or, in other words, the time taken to adjust the spatial distribution of point defects to new environmental conditions) is substantially shorter than the characteristic time of change in the environmental conditions. Taking into account this circumstance, the above problem can be analytically solved with a high degree of accuracy (of the order of the ratio between these times as compared to unity) [1, 2]. In what follows, we will assume that this condition is satisfied. The appropriate criterion will be formulated below, because it is determined by the coefficients involved in the equations under consideration. One important remark needs to be made. Since we analyze the diffusion processes occurring in an ensemble of macrodefects with sources of point defects, the flux of point defects incident on a particular macrodefect should be determined with due regard for the entire ensemble [1, 2]. It was shown earlier in [1, 2] that, at a sufficiently small volume fraction of macrodefects (at a virtually arbitrary fraction), the many-particle problem can be reduced to a single-particle problem. Therefore, each macrodefect can be considered in an effective medium that is determined by averaging over the positions of all macrodefects, except for a specified "range of influence" outside the given macrodefect [1, 2].

3. FLUXES OF POINT DEFECTS INCIDENT ON MACRODEFECTS

As was shown in [1, 2], the fluxes of vacancies and interstitial atoms can be determined (with a high degree of accuracy for calculating mean quantities) from the following expressions:

$$j_V^p = -\frac{D_V}{R}\left(\Delta_V - \frac{\alpha^V}{R}\right),$$
$$j_i^p = -\frac{D_i}{R}\left(\Delta_i + \frac{\alpha^i}{R}\right) \quad (1)$$

per unit area of a pore;

$$j_V^D = -A_V D_V \Delta_V, \quad A_V = \frac{2\pi}{\ln(L/r_V)},$$
$$j_i^D = -A_i D_i \Delta_i, \quad A_i = \frac{2\pi}{\ln(L/r_i)} \quad (2)$$

per unit length of a dislocation line of a rectilinear dislocation; and

$$\tilde{j}_V^D = -\tilde{A}_V D_V\left(\Delta_V \mp \frac{\alpha_D^V}{R_D}\right), \quad \tilde{A}_V = \frac{2\pi}{\ln\frac{8R_D}{r_V}} \approx A_V,$$
$$\tilde{j}_i^D = -\tilde{A}_i D_i\left(\Delta_i \pm \frac{\alpha_D^i}{R_D}\right), \quad \tilde{A}_i = \frac{2\pi}{\ln\frac{8R_D}{r_i}} \approx A_i \quad (3)$$

per unit length of a circular dislocation loop.

In expressions (1)–(3), Δ_V and Δ_i are the supersaturations of the material with vacancies and interstitial atoms, respectively ($\Delta_V = c_V - c_\infty^V$, $\Delta_i = c_i - c_\infty^i$); c_V and c_i are the concentrations of vacancies and interstitial atoms, respectively; c_∞^V and c_∞^i are the equilibrium concentrations of vacancies and interstitial atoms at a planar interface, respectively; D_V and D_i are the diffusion coefficients of vacancies and interstitial atoms in the material, respectively; R is the pore radius; R_D is the radius of the dislocation loop;

$$\alpha^V = c_\infty^V \frac{2\sigma\omega}{T}, \quad \alpha^i = c_\infty^i \frac{2\sigma\omega}{T},$$

where σ is the surface tension, ω is the volume per atom in the material, and T is the temperature expressed in terms of energy; and

$$\alpha_D^V = c_\infty^V \frac{a}{2\pi}\frac{\omega G}{(1-\nu)T}\ln\frac{R_D}{a},$$
$$\alpha_D^i = c_\infty^i \frac{a}{2\pi}\frac{\omega G}{(1-\nu)T}\ln\frac{R_D}{a},$$

where a is the lattice parameter of the material, G is the shear modulus of the lattice, and ν is the Poisson ratio.

In the above expressions, the upper and lower signs in parentheses refer to the vacancy and interstitial dislocation loops, respectively; L is the length of the dislocation cell in the material; r_V is the radius of capture of a vacancy by a dislocation; and r_i is the radius of capture of an interstitial atom by a dislocation ($r_i \gg r_V$).

In relationships (2) and (3), the radius of interaction of point defects with dislocations is replaced by the effective radius of capture. This replacement is fairly justified because of the weak logarithmic dependences of all the quantities on the interaction radius. Relationships (2) and (3) describe the well-known fluxes of point defects incident on macrodefects (rectilinear dislocations, dislocation loops) in the absence of sources of points defects in the bulk of the material.

According to the results obtained in [1, 2], this approximation is valid because the sources play an important role in the balance of point defects and lead only to small corrections to fluxes. In a zeroth-order

approximation, these corrections can be ignored. The recombination of point defects can be disregarded in virtually all cases [1, 2], because the additional terms that appear in the fluxes due to the recombination are small as compared to unity. These terms are of the order of the following quantities:

$\frac{1}{2}\left(\frac{R}{R_{0V}}\right) \ll 1$ (where R_{0V} is the radius of influence of the pore: $R_{0V} \gg R$)

for pores,

$$\left(\ln\frac{L}{a}\right)^{-1} \ll 1$$

for rectilinear dislocations, and

$$\frac{k_0(R_V^D/l_V)}{R_V^D\frac{d}{dr}k_0(r/l_V)\big|_{r=R_V^D}\ln\frac{R_V^D}{r_V}} \approx \left(\ln\frac{L}{r_V}\right)^{-1} \ll 1$$

for ring dislocations.

Here, k_0 is the zeroth-order Bessel function of the imaginary argument. For this function, we can write

$$\frac{k_0(R_V^D/l_V)}{R_V^D\frac{d}{dr}k_0(r/l_V)\big|_{r=R_V^D}} \approx -\frac{2}{3},$$

where $R_V^D \approx l_V$ is the radius of influence of dislocations and l_V is the length of screening of the diffusion field (induced by point defects of a particular macrodefect) by other macrodefects (elements of the microstructure) [1, 2].

The balance equations for point defects in materials under irradiation have the form

$$\begin{aligned}\frac{d\Delta_V}{dt} &= -A_V D_V \Delta_V F + K - \int_0^\infty f_p 4\pi R^2 \left(\frac{dR}{dt}\right)_p^V dR,\\ \frac{d\Delta_i}{dt} &= -A_i D_i \Delta_i F + K + \int_0^\infty f_p 4\pi R^2 \left(\frac{dR}{dt}\right)_p^i dR.\end{aligned} \tag{4}$$

Here, $F = \rho + \int_0^\infty 2\pi R f^D dR$ is the perimeter of dislocation lines per unit volume, $\rho \approx 1/L^2$ is the density of dislocations capable of absorbing and emitting points defects, f^D is the radius distribution function of dislocation loops per unit volume (in cm^{-4}), f_p is the size distribution function of pores per unit volume (in cm^{-4}), $\left(\frac{dR}{dt}\right)_p^V = -j_V$ is the change in the radius of a pore due to the flux of vacancies, K is the number of Frenkel pairs generated in a unit time per lattice site, $\left(\frac{dR}{dt}\right)_p^i = +j_i$ is the change in the radius of the pore due to the flux of interstitial atoms, and

$$\left(\frac{dR}{dt}\right)_p = -j_V + j_i = \left(\frac{dR}{dt}\right)_p^V - \left(\frac{dR}{dt}\right)_p^i. \tag{5}$$

A flux of point defects that is incident normal to the pore surface is conventionally treated as positive.

In order to obtain a closed system of equations describing the evolution of a microstructure of the material under irradiation, the system of equations (1)–(5) should be complemented by relationships for the time evolution of the size distribution functions of an ensemble of pores and dislocation loops and the relevant initial data.

Our primary interest here is in the evolution of the microstructure of the material at the stage of clearly pronounced swelling when the dislocation subsystem is stabilized and the number of pores varies rather slowly. In this situation, the dislocation perimeter and the slowly varying number of pores per unit volume can be treated as quasi-steady-state to a good approximation.

Moreover, in the case where the inequality $K^{-1} \gg (\rho D_V)^{-1}$ or $\rho D_V \gg K$ is satisfied, we assume that Eqs. (1) and (2) on the time scale K^{-1} are quasi-steady-state equations.

To put it differently, the quantities Δ_V and Δ_i have managed to "follow" the slow variation in the sinks and the sources of point defects. This implies that equations of system (4) on the time scale $\Delta t \gg K^{-1}$ can be considered quasi-steady-state equations:

$$\begin{aligned}-A_V D_V \Delta_V F + K - \int_0^\infty f_p 4\pi R^2 \left(\frac{dR}{dt}\right)_p^V dR &= 0,\\ -A_i D_i \Delta_i F + K + \int_0^\infty f_p 4\pi R^2 \left(\frac{dR}{dt}\right)_p^i dR &= 0.\end{aligned} \tag{6}$$

By subtracting the second expression from the first expression in this system and making allowance for the equalities

$$\int_0^\infty f_p 4\pi R^2 \left(\frac{dR}{dt}\right)_p^V dR = 4\pi N \bar{R} D_V \left(\Delta_V - \frac{\alpha^V}{\bar{R}}\right),$$

$$\int_0^\infty f_p 4\pi R^2 \left(\frac{dR}{dt}\right)_p^i dR = -4\pi N \bar{R} D_i \left(\Delta_i + \frac{\alpha^i}{\bar{R}}\right),$$

we obtain

$$\begin{aligned}&-A_V F(D_V\Delta_V - D_i\Delta_i(1+\eta))\\ &-4\pi N\bar{R}\left[(D_V\Delta_V - D_i\Delta_i) - D^*\frac{2\sigma\omega}{\bar{R}T}\right] = 0,\end{aligned} \tag{7}$$

where N is the number of pores per unit volume. In this relationship, we took into account that $A_i = A_V(1 + \eta)$, $\eta = \left(\ln\frac{r_i}{r_V}\right)\left(\ln\frac{L}{r_V}\right)^{-1} \ll 1$, and $D^* = D_V c_\infty^V + D_i c_\infty^i$. Actually, we have $A_i = A_V\frac{1}{1-\eta} \cong A_V(1 + \eta)$ and $\bar{R} \approx \frac{1}{N}\int fRdR$, where $\bar{R}$ is the mean pore size. By introducing the designations $D^*\Delta^* = D^V\Delta^V - D^i\Delta^i$ or $\Delta^* = \frac{D^V\Delta^V - D^i\Delta^i}{D^*}$, relationship (7) can be rewritten in the form

$$-A_V F D^*\Delta^* + A_V F D_i\Delta_i\eta - 4\pi N\bar{R}D^*\Delta^* + 4\pi N D^*\frac{2\sigma\omega}{T} = 0. \quad (8)$$

From expression (6) for $D_i\Delta_i$, we obtain

$$-A_i D_i\Delta_i F + K - 4\pi N\bar{R}D_i\left(\Delta_i + \frac{\alpha^i}{\bar{R}}\right) = 0. \quad (9)$$

The first two terms in relationship (8) determine the excess of interstitial atoms that are captured by the dislocation subsystem of the material in a unit time and form additional atomic planes; in other words, these terms describe the swelling of the material.

The second two terms in relationship (8) describe the porosity that arises in a unit time per unit volume. These terms are exactly equal to the first two terms. This is evident because the porosity of the material is governed by the additional lattice sites and, accordingly, by the absence of sites from which atoms "pass" into additional atomic planes.

The degree of swelling of the material is conveniently judged from its porosity. This is associated with the fact that, in the dislocation subsystem, the growing atomic planes merge together and form complete atomic planes with virtually no change in the perimeter of dislocations per unit volume in an already sufficiently stabilized dislocation subsystem [3].

As a result, the swelling rate ε'_{ii} can be written in the form

$$\varepsilon'^D_{ii} = -2\pi A_V F D^*\Delta^* + 2\pi A_V F D_i\Delta_i\eta = \varepsilon'^p_{ii} = 4\pi N\bar{R}D^*\Delta^* - 4\pi N D^*\frac{2\sigma\omega}{T} = \varepsilon'_{ii}, \quad (10)$$

where the prime sign indicates the derivative with respect to time. After substituting the expression $\frac{\alpha^i}{\bar{R}} = c_\infty^i\frac{2\sigma\omega}{T\bar{R}}$ into formula (9), the quantities $D^*\Delta^*$ and $D_i\Delta_i$ can be calculated from relationships (8) and (9) in the following form:

$$D^*\Delta^* = \frac{2\pi A_V F D_i\Delta_i}{2\pi A_V F + 4\pi N\bar{R}}\eta + \frac{4\pi N D^*\frac{2\sigma\omega}{T}}{2\pi A_V F + 4\pi N\bar{R}}, \quad (11)$$

$$D_i\Delta_i = \frac{K - 4\pi N\bar{R}D_i c_\infty^i\frac{2\sigma\omega}{T\bar{R}}}{A_i F + 4\pi N\bar{R}}. \quad (12)$$

4. SWELLING OF A MATERIAL EXPOSED TO IRRADIATION

Upon substituting expressions (11) and (12) into relationship (10), we obtain the following formula for the swelling rate $\varepsilon'_{ii} = \varepsilon'^D_{ii} = \varepsilon'^p_{ii}$:

$$\varepsilon'_{ii} = \frac{A_V F 4\pi N\bar{R}}{P^2}\left(K - 4\pi N\bar{R}D_i c_\infty^i\frac{2\sigma\omega}{t\bar{R}}\right)\eta - \frac{A_V F 4\pi N\bar{R}}{P}D^*\frac{2\sigma\omega}{T\bar{R}}, \quad (13)$$

where $P = A_V F + 4\pi N\bar{R}$ is the total perimeter of dislocations and pores per unit volume ($[P] = [\text{cm}^{-2}]$).

Relationship (13) can be simplified as follows. Taking into account that, in this case, the inequalities $\frac{4\pi N\bar{R}}{P} < 1$, $D_i c_\infty^i < D^*$, and $\eta \ll 1$ are satisfied, we obtain a simpler expression without regard for the small term in parentheses, that is,

$$\varepsilon'_{ii} = \frac{A_V F 4\pi N\bar{R}}{P^2}K\eta - \frac{A_V F 4\pi N\bar{R}}{P}D^*\frac{2\sigma\omega}{T\bar{R}} \quad (14)$$

or

$$\varepsilon'_{ii} = \frac{A_V F 4\pi N\bar{R}}{P^2}\left[K\eta - PD^*\frac{2\sigma\omega}{T\bar{R}}\right]. \quad (15)$$

By introducing the designations $A_V F = a > 0$, $4\pi N\bar{R} = b > 0$, and $P = a + b$, we find that the factor $\frac{ab}{(a+b)^2} \le \frac{1}{4}$ ahead of the brackets in expression (15) has a maximum value under the conditions $0 < a < \infty$ and $0 < b < \infty$. As a result, we obtain $\left.\frac{ab}{(a+b)^2}\right|_{a=b} = \frac{1}{4}$, which is the maximum value taken by this function. It is worth noting that this function slowly varies in the vicinity of its maximum over a sufficiently prolonged period of time.

Let us consider in more detail the behavior of the factor ahead of the brackets in expression (15), namely,

$$\frac{A_V F 4\pi N\bar{R}}{(A_V F + 4\pi N\bar{R})^2},$$

with due regard for the following.

The scenario of the evolution of the microstructure can be divided, with a high accuracy, into three stages.

(1) Irradiation of the material initiates the onset of the incubation stage. This stage involves slow nucleation of an ensemble of vacancy pores. An increase in the supersaturation of solid solutions formed by point defects leads to a drastic increase in the nucleation rate. This is accompanied by a rapid increase in the number of vacancy pores per unit volume $N_V(t)$ and a rather slow increase in the mean pore size $\bar{R}$. For cold-deformed materials, we can write the following inequality:

$$A_V F \gg 4\pi N\bar{R}(t).$$

It can be seen from expression (15) that, at the first stage of the evolution of the microstructure, the power Q of the "effective source" $(\frac{4\pi N\bar{R}}{A_V F}K\eta)$ increases.

(2) The onset of the second stage is specified by the condition

$$A_V F \propto 4\pi N\bar{R}(t).$$

The same condition determines the duration of the first stage.

The evolution of the microstructure at the second stage is characterized by a maximum power of the effective source. This can be judged from the condition specifying the onset of the second stage. The power of the effective source at this stage is determined by the relationship

$$Q \propto \frac{1}{4}K\eta.$$

(3) The onset of the third stage, during which the power Q of the effective source decreases with time, is governed by the condition

$$A_V F \ll 4\pi N\bar{R}(t).$$

This condition also determines the duration of the second stage. Indeed, it follows from expression (15) that, within the time intervals for which the inequality $4\pi N\bar{R}(t) \gg A_V F$ holds, we have

$$\varepsilon'_{ii} \approx \frac{A_V F}{4\pi N\bar{R}}K\eta,$$
$$\varepsilon_{ii} \approx \frac{A_V F}{4\pi N\bar{R}}K\eta t \propto t^n, \quad n < 1. \tag{16}$$

Therefore, beginning from this stage, the swelling is governed by the effective vacancy source decaying with time [4], because the factor $4\pi N\bar{R}$ increases with time. It was shown earlier in [4] that, at sufficiently long times, the relationship $\bar{R} \propto t^{1/3}$ is satisfied not only in the case where the total number of excess vacancies (volume) or impurity atoms remains unchanged but also under the condition where sources of these defects exist. According to the results obtained in [4], the sources responsible for the appearance of an excess volume can be separated into three groups, namely, decaying ($n < 1$), stationary ($n = 1$), and growing ($1 < n < \alpha$) sources. The parameter α is determined by the mechanism of mass transfer. The excess vacancies (or the material) have had time to be absorbed by growing particles of the new phase. This process is accompanied by a decrease in the supersaturation of the system and, accordingly, in the number of new-phase particles [4]. For decaying sources, we obtain $N \propto t^{n-1}$, $\bar{R} \propto t^{1/3}$, and $\varepsilon_{ii} \propto t^n$, where $n < 1$. Moreover, we have $N\bar{R} \propto t^{n-2/3}$; that is,

$$N \propto t^{n-1}, \quad N\bar{R} \propto t^{n-2/3}. \tag{17}$$

It can be seen from relationships (16) that the self-consistent source $(\varepsilon_{ii} \propto \frac{t}{N\bar{R}} \propto t^n)$ is characterized by $n = 5/6$ [5]. As a consequence, expressions (17) take the form

$$N \propto t^{-1/6}, \quad N\bar{R} \propto t^{1/6}. \tag{18}$$

Hence, it follows that the factor $\frac{A_V F 4\pi N\bar{R}}{(A_V F + 4\pi N\bar{R})^2}$ varies very slowly with time in the range of its maximum (a change in the time interval by several orders of magnitude leads to only an insignificant variation in this factor). It is also evident that the exposure of the material to irradiation over the period of time corresponding to the most efficient operation of the source makes the main contribution to the swelling.

Therefore, beginning from the instant at which $A_V F \approx 4\pi N\bar{R}$, the factor $\frac{A_V F 4\pi N\bar{R}}{(A_V F + 4\pi N\bar{R})^2}$ in expression (15) can be taken equal to its maximum value of 1/4. Hence, in this time interval, which is most important for the swelling of the material, relationship (14) can be represented in the very simple form

$$\varepsilon'_{ii}\big|_{t>t_0} = \frac{1}{4}\left[K\eta - 8\pi N D^* \frac{2\sigma\omega}{T}\right]. \tag{19}$$

As can be seen from relationship (19), the swelling rate for a stationary source is linear in time:

$$\varepsilon_{ii}\big|_{t>t_0} = \frac{1}{4}\left[K\eta - 8\pi ND^*\frac{2\sigma\omega}{T}\right]t. \qquad (20)$$

5. PULSED IRRADIATION

As was noted above, the quasi-steady-state approximation can be used under the conditions of so-called rapid adjustment when the concentration profiles of the supersaturated solid solutions formed by vacancies and interstitial atoms have had time to adjust to the varying conditions of irradiation in a cycle. These conditions are specified by the following relationships:

for an ensemble of vacancy pores,

$$\tau^i_{\text{pore}} \ll \tau^V_{\text{pore}} \ll \Delta t_1, \Delta t_2,$$

where

$$\tau^i_{\text{pore}} \propto \frac{(3/4\pi)^{2/3}}{4N^{2/3}D_i} \approx \frac{\bar{R}^2}{D_i}, \quad \tau^V_{\text{pore}} \propto \frac{(3/4\pi)^{2/3}}{4N^{2/3}D_V} \approx \frac{\bar{R}^2}{D_V};$$

for dislocations

$$\tau^i_{\text{disl}} \ll \tau^V_{\text{disl}} \ll \Delta t_1, \Delta t_2,$$

where

$$\tau^i_{\text{disl}} \propto \frac{1}{\rho D_i}, \quad \tau^V_{\text{disl}} \propto \frac{1}{\rho D_V}.$$

Here, Δt_1 is the duration of irradiation in one cycle and Δt_2 is the pulse separation in one cycle.

The second type of conditions that offer the possibility of averaging over cycles in the framework of the proposed approach can be formulated as follows: the changes in the parameters of the ensembles of pores and dislocations for a time Δt_2 in one cycle should be small. Quantitatively, these conditions can be written in the following form:

for pores,

$$\Delta t_2 \ll \frac{\bar{R}_V^3}{D_V c_0^V \frac{2\sigma\omega}{KT}} \equiv \tau^{eV}_{\text{pore}},$$

for interstitial dislocation loops,

$$\Delta t_2 \ll \frac{\ln\left(\frac{2\bar{R}}{R_{0V}}\right)\bar{R}_e^2(1-\nu)KT}{D_V c_0^V \omega G} \equiv \tau^{eV}_{\text{loop},\,i}.$$

Here, τ^{eV}_{pore} and $\tau^{eV}_{\text{loop},\,i}$ are the times of evaporation of a pore and a dislocation loop, respectively, with sizes averaged over the ensemble in the absence of irradiation.

For pulsed operation of the source K, when the source operates for a time Δt_1 and does not operate for a time Δt_2, we have

$$\begin{aligned}\varepsilon_{ii} &= \left[\frac{1}{4}K\eta\Delta t_1 - 2\pi ND^*\frac{2\sigma\omega}{T}(\Delta t_1 + \Delta t_2)\right]n \\ &= \left[\frac{1}{4}K\eta\frac{\Delta t_1}{\Delta t_1 + \Delta t_2} - 2\pi ND^*\frac{2\sigma\omega}{T}\right]t,\end{aligned} \qquad (21)$$

where $t = (\Delta t_1 + \Delta t_2)n$ is the duration of n cycles of pulses from the point-defect source. Note that, in relationship (21), the term associated with the solid solution contributes to the swelling rate throughout the source-operation period.

As follows from relationship (21), in order to increase this term, it is necessary that the number of nucleated pores at the nucleation stage for the given K be as large as possible.

It should be remembered that relationship (21) was derived from the expressions describing the fluxes of vacancies incident on pores in the quasi-steady-state approximation. This holds true for the inequality $\Delta t_1 \gg \bar{R}^2/D_V$. Here, $\bar{R}$ is the mean size of pores formed in the course of the preceding cycles and D_V is the diffusion coefficient of vacancies.

Moreover, the condition for a small change in the parameters of the system during one cycle of the source operation should be satisfied; that is,

$$\frac{d\bar{R}}{dt} = \frac{D_V}{\bar{R}}\left(\Delta - \frac{\alpha}{\bar{R}}\right), \quad \Delta t_2 \gg \frac{\bar{R}^3}{D_V\alpha} \approx \frac{\bar{R}^3}{D_V c_\infty^V \frac{2\sigma\omega}{T}}.$$

6. CONCLUSIONS

It should be noted that, when irradiation leads to nuclear reactions with the formation of an atomic gas, this factor proves to be very important for the source of atoms per lattice site:

$$I_{\text{gas}} > \frac{1}{4}\eta K = \frac{1}{4}\frac{\ln\frac{r_i}{r_V}}{\ln\frac{L}{r_V}}K.$$

This can be explained by the fact that the fluxes of gas atoms incident on pores bring about separation of the fluxes of point defects. In this case, vacancies predominantly pass into pores with the gas, whereas interstitial atoms are involved in the dislocation subsystem.

The mechanical load acting on the material results in an asymmetric distribution of pores in the grain

boundaries and thus substantially affects the material structure. The initial stage of the evolution of the microstructure (nucleation of pores filled with a gas under irradiation) plays an important role in the swelling of materials. All these problems will be considered in future publications.

ACKNOWLEDGMENTS

V.V. Slezov acknowledges the partial support of the US Civilian Research and Development Foundation for the New Independent States of the Former Soviet Union (CRDF), grant no. UE1-2523-CK-03.

REFERENCES

1. V. V. Slesov and P. A. Bereznyok, in *Physics of Radiation Effects in Crystals: Irradiation Creep in Metals*, Ed. by N. A. Johnson and A. N. Orlov (1986), pp. 575–621.
2. V. V. Slezov, Fiz. Tverd. Tela (Leningrad) **31** (8), 20 (1989) [Sov. Phys. Solid State **31**, 1289 (1989)].
3. V. V. Slezov, Zh. Éksp. Teor. Fiz. **53** (9), 912 (1967) [Sov. Phys. JETP **26**, 552 (1968)].
4. V. V. Slezov and V. B. Shikin, Fiz. Tverd. Tela (Leningrad) **6** (1), 7 (1964) [Sov. Phys. Solid State **6**, 5 (1964)].
5. A. V. Subbotin, At. Énerg. **43** (2), 100 (1977).

Translated by O. Borovik-Romanova

Physics of the Solid State, Vol. 47, No. 3, 2005, pp. 484–488. Translated from Fizika Tverdogo Tela, Vol. 47, No. 3, 2005, pp. 469–473.

DEFECTS, DISLOCATIONS, AND PHYSICS OF STRENGTH

Elastic-Strain Field Soliton in a Structurally Unstable Crystal

E. E. Slyadnikov

Tomsk Scientific Center, Siberian Division, Russian Academy of Sciences, Tomsk, 634021 Russia
e-mail: slyad@cc.tpu.edu.ru

Received June 24, 2004

Abstract—It is shown that a spatially localized collective excitation of the crystal lattice (soliton) can form and propagate in a structurally unstable crystal. This soliton is a structural defect consisting of two interphase boundaries separated by another phase and can be considered a pulse of the elastic-strain field with a characteristic length $l \approx 10^{-8}$–10^{-4} cm and a duration $\tau_p \approx 10^{-13}$–10^{-9} s. © *2005 Pleiades Publishing, Inc.*

1. INTRODUCTION

In continuum mechanics, it is postulated that the local topology of a medium does not change under deformation, i.e., that the particles located in the immediate vicinity of a material particle remain the same. In other words, the structure and interparticle links are not rearranged. Based on this smooth-manifold model, an elegant phenomenological theory of elastic continuum has been developed [1]. At the present time, however, it has become clear that many phenomena associated with structural phase transformations, the formation of defects, plasticity, and fracture of crystals cannot be treated in terms of a model of a medium with invariable local topology. Changes in the structure of real solids must be taken into account.

In [2], it was proposed that, in a crystal subjected to an external mechanical force, there appear structural states of another lattice in the space of interstitial sites in addition to the structural states of the original crystal lattice. Therefore, in a loaded crystal lattice, the atoms have additional degrees of freedom; the crystal transfers to a state with low shear stability, and its behavior becomes nonlinear.

In crystals undergoing a martensitic transformation under an external influence, the low shear stability and crystal lattice nonlinearity can be simply taken into account using the model of double-well crystal potential for atoms and the pseudospin representation [3]. By combining the ideas put forward in [2, 3], we assume that, in a loaded crystal, the structural instability and, hence, the double-well crystal potential for atoms arise even at the nonlinear-elasticity stage.

In the course of loading a crystal, according to the experimental stress–strain curve, the stage of linear elastic strains is followed by a stage of nonlinear elastic strains [1]. The latter stage is characterized by various anomalous effects, e.g., an experimentally observed increase in the velocity of sound [4]. At the nonlinear-elasticity stage, nonlinear collective excitations appear in the crystal lattice, which determine the nonlinear behavior of the crystal. It is convenient to study localized collective excitations in a crystal in terms of a quantum system of pseudospins [3], which interacts with pulses of the elastic-strain field.

A few recent experimental and theoretical studies have been devoted to the interaction of an elastic-strain field with matter [5–7]. It is of particular interest to consider the case where elastic-strain pulses are several oscillation periods long (ultrashort pulses). Lasers make it possible to generate nanosecond and picosecond pulses [6, 7]. Solutions for ultrashort pulses in the form of unipolar (half-wave) solitons and dissipative structures were found in [8, 9]. In a structurally unstable crystal, two energy levels interacting strongly with the elastic-strain field are considered and treated as an even and an odd state of an atom moving in a double-well crystal potential. These states differ in energy due to quantum tunneling of the atom between the two wells of the crystal potential. The frequency separation ω_0 between these states in a structurally unstable crystal is typically 10^9–10^{13} s^{-1} [3], which is a few orders of magnitude less than the electron transition frequencies. Therefore, at frequencies much lower than the optical electron transition frequencies, an elastic-strain pulse will interact predominantly with two energy levels of an atomic system. The probability of optical transitions between these levels will be small. In this paper, we study the interaction of an ultrashort elastic-strain pulse with a structurally unstable crystal.

2. THE HAMILTONIAN AND BASIC EQUATIONS

We write the Hamiltonian of the system in question in a semiclassical approximation in which the structurally unstable crystal is described quantum mechanically and the elastic-strain field is treated classically. The length of an ultrashort pulse is assumed to be $l = c\tau_p \approx 10^{-8}$–$10^{-4}$ cm $\gg a$, where c is the velocity of sound, $\tau_p \approx 10^{-13}$–10^{-9} s is the pulse duration, and

1063-7834/05/4703-0484$26.00

$a \approx 10^{-9}$ cm is the characteristic length scale of the double-well potential. For the sake of simplicity, we use the molecular-field approximation (MFA) [10], in which each atom is assumed to move in a mean field produced by the other atoms. This approximation makes it possible to describe a structural transition from the initial to the final phase via a pretransition state under an external influence [3].

The Hamiltonian of a pseudospin quantum system interacting with the internal molecular field can be written in the MFA in the form

$$H_0 = \hbar\sum_a [-\omega_0 S_a^x - J_0\langle S_a^z\rangle S_a^z - I_0\langle S_a^z\rangle^2 S_a^z], \quad (1)$$

where $\hbar$ is the Planck constant; $\hbar\omega_0$ is the energy difference between the even and odd states of an atom; $\hbar J_0$ and $\hbar I_0$ are the two- and three-particle interaction constants of pseudospins, respectively, characterizing the asymmetry of the double-well potential; the angular brackets signify the quantum averaging; S^x, S^y, and S^z are the Pauli operators; and summation over a is carried out over all atoms on the crystal lattice.

An elastic-strain pulse is assumed to propagate through a three-dimensional structurally unstable crystal and cause a change in the asymmetry of the double-well potential. This change is described by the Hamiltonian

$$H_{\text{int}} = -\sum_a\sum_{p,q} F_{pq}\varepsilon_a^{pq} S_a^z, \quad (2)$$

where ε_a^{pq} is the elastic-strain tensor of the crystal at the atomic lattice site a, related to the atomic displacements $U_a = (U_a^x, U_a^y, Y_a^z)$ through the equation

$$\varepsilon_a^{pq} = (1/2)[\partial U_a^p/\partial x_q + \partial U_a^q/\partial x_p], \quad (3)$$

and F_{pq} are the pseudospin–phonon coupling constants.

In addition to Hamiltonians (1) and (2), we use the Hamiltonian of the elastic-strain field

$$H_{\text{ph}} = \int\Bigg[(1/2\rho)\sum_j P_j^2 + (1/2)\sum_{j,k,l,m}\lambda_{jklm}(\partial U^j/\partial x_k)(\partial U^l/\partial x_m)\Bigg]d\mathbf{r}, \quad (4)$$

where ρ is the average density of the crystal, P_j ($j = x, y, z$) is the elastic-strain field momentum associated with dynamic displacements, and λ_{jklm} is the elastic-modulus tensor of the crystal [1]. Integration in Eq. (4) is performed over the entire volume of the crystal. Here, the semiclassical approximation is used in which the pseudospin dynamics is described quantum mechanically and the elastic-strain field is treated classically.

Thus, the total Hamiltonian of the system is

$$H = H_0 + H_{\text{int}} + H_{\text{ph}}. \quad (5)$$

In the semiclassical approximation, the evolution of the spin operator is governed by the Heisenberg equation

$$i\hbar\partial S_a^k/\partial t = [S_a^k, H], \quad (6)$$

and the elastic-strain field is described by the classical Hamilton equations for a continuum,

$$\partial U^q/\partial t = \delta\langle H\rangle/\delta P_q, \quad \partial P_q/\partial t = -\delta\langle H\rangle/\delta U^q. \quad (7)$$

With Eqs. (7), the classical interaction Hamiltonian $\langle H_{\text{int}}\rangle$ can be written as

$$\langle H_{\text{int}}\rangle = -\int\sum_{q,p}\hbar F_{pq}\varepsilon^{pq}(\mathbf{r})\langle S^z(\mathbf{r})\rangle n(\mathbf{r})d\mathbf{r}. \quad (8)$$

Here, $n(\mathbf{r}) = \sum_a \delta(\mathbf{r} - \mathbf{r}_a)$ is the atomic density distribution function and $\delta(\mathbf{r} - \mathbf{r}_a)$ is the Dirac delta function.

Let a longitudinal–transverse elastic-strain pulse be propagated in a cubic crystal parallel to one of the fourfold axes (taken to be the z axis). We consider the one-dimensional case where all dynamic variables depend only on z and t. The symmetry operations of the system under study in this case are rotations through 90° about the z axis ($x \longrightarrow y$, $y \longrightarrow -x$, $z \longrightarrow z$) and reflections $x \longrightarrow -x$ and $y \longrightarrow -y$. Taking into account that the vector **S** is axial, i.e., that, under reversal of one of the coordinate axes, the corresponding component of this vector remains unchanged and the other two change sign, the Hamiltonian H_{int} can be rewritten as

$$H_{\text{int}} = -\sum_a \hbar[F_1\varepsilon_a^{zz}S_a^z + F_2(\varepsilon_a^{xz}S_a^x + \varepsilon_a^{yz}S_a^y)], \quad (9)$$

where $F_1 = F_{zz}$ and $F_2/2 = F_{xz} = F_{zx} = F_{yz} = F_{zy}$.

Under the above assumptions, the Hamiltonian H_{ph} takes the form

$$H_{\text{ph}} = (1/2)\int\{[P_x^2 + P_y^2 + P_z^2/\rho] + \lambda_{11}(\partial U_z/\partial z)^2 + \lambda_{44}[(\partial U_x/\partial z)^2 + (\partial U_y/\partial z)^2]\}d\mathbf{r}. \quad (10)$$

In Eq. (10), we use the Voigt notation for fourth-rank tensors: $\lambda_{11} = \lambda_{zzzz}$ and $\lambda_{44} = \lambda_{xzxz} = \lambda_{yzyz}$ From Eqs. (7)–(10), we obtain

$$\partial^2\varepsilon_{zz}/\partial t^2 - a_\parallel^2\partial^2\varepsilon_{zz}/\partial z^2 = -(F_1/\rho)\partial^2 R/\partial z^2, \quad (11)$$

$$\partial^2\varepsilon_{xz}/\partial t^2 - a_\perp^2\partial^2\varepsilon_{xz}/\partial z^2 = -(F_2/2\rho)\partial^2 R/\partial z^2, \quad (12)$$

$$\partial^2\varepsilon_{yz}/\partial t^2 - a_\perp^2\partial^2\varepsilon_{yz}/\partial z^2 = -(F_2/2\rho)\partial^2 R/\partial z^2, \quad (13)$$

where $a_\parallel = \sqrt{\lambda_{11}/\rho}$, $a_\perp = \sqrt{\lambda_{44}/\rho}$, $U = \langle S_x\rangle$, $W = \langle S_y\rangle$, and $R = \langle S_z\rangle$.

Taking the quantum average of the Heisenberg equations (6), we obtain a set of equations for U, W, and R. By putting the derivatives equal to zero in the left-hand side of Eq. (6), we find the equilibrium values U_0, $W_0 = 0$, and R_0. Introducing the notation $U = U_0 + u$, $W = w$, and $R = R_0 + r$, we obtain the following set of equations for the deviations of the quantum values of the components of the pseudospin $\mathbf{S} = (S_x, S_y, S_z)$ from their equilibrium values in the case where the shear component of the elastic-strain pulse $\Omega = F_2(\varepsilon_{xz} + \varepsilon_{yz})$ is nonzero and $\varepsilon_{zz} = 0$:

$$\partial u/\partial t = \omega_1 w + (\Omega + \tilde{J}r)w, \tag{14}$$

$$\partial w/\partial t = \omega_2 r - \omega_1 u - U_0\Omega - (\Omega + \tilde{J}r)u, \tag{15}$$

$$\partial r/\partial t = -\omega_0 w. \tag{16}$$

Here, $\omega_1 = J_0R_0 + I_0R_0^2$, $\omega_2 = \omega_0 - U_0\tilde{J}$, and $\tilde{J} = J_0 + 2I_0R_0$. The set of equations (14)–(16) should be solved in combination with Eq. (13) for the shear component of the elastic-strain field, which can be rewritten in the new notation in the form

$$\partial^2\Omega/\partial t^2 - c^2\partial^2\Omega/\partial z^2 = -(F_2^2/\rho)\partial^2 r/\partial z^2. \tag{17}$$

The set of equations (14)–(17) is closed and self-consistently describes the dynamics of both the structurally unstable crystal and an elastic-strain pulse propagating in it.

In general, the nonlinear set of equations (14)–(17) is very difficult to analyze. Therefore, following [8, 9], we consider the case where

$$\begin{aligned} \omega_\pm\tau_p &\gg 1, \\ \omega_+^2 &= \omega_0(\omega_0 - J_0U_0) = \omega_0\omega_2, \\ \omega_-^2 &= (J_0R_0 + I_0R_0^2)^2 + \omega_0(\omega_0 - J_0U_0 - 2I_0U_0R_0) \\ &= \omega_1^2 + \omega_0\omega_2. \end{aligned} \tag{18}$$

Here, ω_+ and ω_- are the frequencies of the soft pseudospin mode in the pretransition state and in the initial (or final) phase, respectively. The spectral width of an ultrashort pulse is $\Delta\omega \approx \tau_p^{-1} \approx 10^{12}$–$10^9$ s^{-1}. Therefore, for the low-frequency mode, we have $\omega_\pm\tau_p > 1$. Putting $\omega_\pm \approx 10^{12}$–$10^9$ s^{-1}, we obtain $\tau_p > 10^{-12}$–10^{-9} s.

Condition (18) is more stringent than the restriction to low frequencies under which the MFA does not distort the real pattern of the interaction between an ultrashort pulse and the structurally unstable crystal. Under condition (18), the dynamic parameters of an elastic-strain pulse vary fairly slowly, which indicates that the interaction of the pulse with the crystal is weak and the crystal is excited insignificantly. Therefore, we can assume that the nonlinear effects in the process under study are weak.

3. SOLITON IN A CRYSTAL IN THE PRETRANSITION STATE

In the pretransition state [3], the order parameter R_0 is zero and $U_0 = (1/2)\tanh(\omega_0/2k_BT)$; therefore, we have $\omega_1 = 0$ and $\omega_2 \neq 0$. By differentiating Eq. (16) with respect to time and substituting Eq. (15) into it, we obtain

$$\partial^2 r/\partial t^2 = -\omega_0\omega_2 r + \omega_0 U_0 + \omega_0(\Omega + J_0 r)u. \tag{19}$$

Using inequality (18), it can be found that the left-hand side and the last term in the right-hand side of Eq. (19) are of a higher order of smallness than the first two terms in the right-hand side. Therefore, we can solve Eq. (19) for r using an iterative method. Taking into account the relation between r and Ω, we reduce Eq. (17) to a close nonlinear equation for Ω:

$$\begin{aligned} \partial^2\Omega/\partial t^2 - \tilde{c}^2\partial^2\Omega/\partial z^2 &= (F_1^2U_0/\rho\omega_0\omega_2^2)\partial^2/\partial z^2 \\ &\times\{(1 + \omega_2^{-1}J_0U_0)^2\Omega^3 + \partial^2\Omega/\partial t^2\}, \end{aligned} \tag{20}$$

where

$$\tilde{c}^2 = c^2 - (F_1^2U_0/\rho\omega_2).$$

The right-hand side of Eq. (20) contains a nonlinear and a dispersion term and, hence, is of a higher order of smallness than the terms in the left-hand side. Therefore, we can use the approximation of unidirectional propagation along the tunneling axis (parallel to the z axis) in much the same manner as was done in [8, 9]. As a result, we obtain

$$\begin{aligned} 2\tilde{c}\partial\Omega/\partial z &= (F_1^2U_0/\tilde{c}^2\rho\omega_0\omega_2^2)\partial/\partial\tau \\ &\times\{(1 + \omega_2^{-1}J_0U_0)^2\Omega^3 + \partial^2\Omega/\partial\tau^2\}, \end{aligned} \tag{21}$$

where $\tau = t - z/\tilde{c}$. Equation (21) is a modified Korteweg–de Vries equation,

$$\partial\Omega/\partial z - \alpha_+\Omega^2\partial\Omega/\partial\tau - \beta_+\partial^3\Omega/\partial\tau^3 = 0, \tag{22}$$

where

$$\alpha_+ = (F_1^2U_0/2\tilde{c}^3\omega_0\omega_2^2)[1 + \omega_2^{-1}J_0U_0]^2,$$

$$\beta_+ = F_1^2U_0/2\tilde{c}^3\omega_0\omega_2^2.$$

A single-soliton solution to Eq. (22) has the form

$$\Omega = \Omega_+\mathrm{sech}[(t - z/\tilde{c}_+)\tau_p], \tag{23}$$

where

$$\tilde{c}_+^{-1} = \tilde{c}^{-1} - \beta_+/\tau_p^2, \quad \Omega_+ = \tau_p^{-1}\sqrt{6\beta_+/\alpha_+}.$$

Solution (23) describes a unipolar (half-wave) soliton. Unlike the envelope soliton, this soliton does not contain high-frequency oscillations. If the interaction of the elastic-strain pulse with the crystal in the pretransition state stimulates the appearance of the initial phase $\varepsilon_{xz} + \varepsilon_{yz} > 0$ (or, alternatively, the final phase $\varepsilon_{xz} + \varepsilon_{yz} <$

0), then the initial phase with $r > 0$ (or the final phase with $r < 0$) arises inside the soliton.

It follows from Eq. (23) that the velocity of this soliton exceeds the phase velocity $\tilde{c}$ of a low-frequency plane wave. It should be stressed, however, that the constitutive equations (14)–(16) do not include relaxation. This approximation is valid with the proviso that

$$\omega_\pm > \tau_p^{-1} \gg \gamma, \tag{24}$$

where γ is a relaxation parameter characterizing the soft-mode damping. To make an estimate, let us assume that $\gamma \approx 10^8$ s^{-1} and is practically independent of temperature for the structurally unstable crystal in the pretransition state. Putting also $\omega_0 \approx 10^{13}$ s^{-1}, $\omega_\pm \approx \omega_0(T^\pm)^{-1/2}|T - T^\pm|^{1/2}$, $T^\pm \approx 10^2$ K, $|T - T^\pm| = 10$ K, and $|T - T^\pm|/T^\pm \approx 10^{-1}$, we find that $\omega_\pm \approx 10^{-1/2}\omega_0 = 3 \times 10^{12}$ s^{-1} and inequality (24) is not satisfied for $\tau_p^{-1} = 10^{13}$ s^{-1}. Therefore, solitons 10^{-13}–10^{-9} s long of the type considered here are not excited at temperatures close to the stability limits $T^\pm$.

4. SOLITON IN THE INITIAL OR FINAL PHASE OF THE CRYSTAL

Let us consider the crystal in the initial state with $R_0 > 0$ (or the final state with $R_0 < 0$), where $R_0 \neq 0$ and, hence, $\omega_1 \neq 0$. By differentiating Eq. (16) and substituting Eq. (15) into it, we find

$$\begin{aligned}&\partial^2 r/\partial t^2 \\ &= -\omega_0\omega_2 r + \omega_0\omega_1 u + \omega_0 U_0\Omega + \omega_0(\Omega + \tilde{J}r)u.\end{aligned} \tag{25}$$

We solve Eq. (25) for r using an iterative method and then, taking into account the relation between r and Ω, reduce Eq. (17) to a close nonlinear equation for Ω,

$$\begin{aligned}&\partial^2\Omega/\partial t^2 - \tilde{c}^2\partial^2\Omega/\partial z^2 \\ &= (F_1^2 U_0\omega_0/\rho[\omega_0\omega_2 + \omega_1^2]^2)\partial^2/\partial z^2 \\ &\times\{\omega_1(2 + (3/2)\tilde{J}U_0\omega_0[\omega_0\omega_2 + \omega_1^2]^{-1})\Omega^2 + \partial^2\Omega/\partial t^2\},\end{aligned} \tag{26}$$

where

$$\tilde{c}^2 = c^2 - (F_1^2 U_0\omega_0/\rho[\omega_0\omega_2 + \omega_1^2]).$$

The right-hand side of Eq. (26) contains a nonlinear and a dispersion term and, hence, is of a higher order of smallness than the terms in the left-hand side. Therefore, we can use the approximation of unidirectional propagation along the tunneling axis parallel to the z axis. As a result, we find

$$\begin{aligned}2\tilde{c}\partial\Omega/\partial z &= (F_1^2 U_0\omega_0/\tilde{c}^2\rho[\omega_0\omega_2 + \omega_1^2]^2)\partial/\partial\tau \\ &\times\{\omega_1(2 + (3/2)\tilde{J}U_0\omega_0[\omega_0\omega_2 + \omega_1^2]^{-1})\Omega^2 \\ &+ \partial^2\Omega/\partial\tau^2\},\end{aligned} \tag{27}$$

where $\tau = t - z/\tilde{c}$. Equation (27) is the Korteweg–de Vries equation

$$\partial\Omega/\partial z - \alpha_-\Omega\partial\Omega/\partial\tau - \beta_-\partial^3\Omega/\partial\tau^3 = 0, \tag{28}$$

where

$$\begin{aligned}\alpha_- &= (F_1^2 U_0\omega_0/\tilde{c}^3\rho[\omega_0\omega_2 + \omega_1^2]^2)\omega_1 \\ &\times(2 + (3/2)\tilde{J}U_0\omega_0[\omega_0\omega_2 + \omega_1^2]^{-1}), \\ \beta_- &= F_1^2 U_0\omega_0/\tilde{c}^3\rho[\omega_0\omega_2 + \omega_1^2]^2.\end{aligned}$$

A single-soliton solution to Eq. (28) has the form

$$\Omega = \Omega_- \sec h^2[(t - z/\tilde{c}_-)/2\tau_p], \tag{29}$$

where

$$\tilde{c}_-^{-1} = \tilde{c}^{-1} - \beta_-/\tau_p^2, \quad \Omega_- = \tau_p^{-2}(3\beta_-/\alpha_-).$$

The velocity of the soliton exceeds the phase velocity $\tilde{c}$ of a low-frequency plane wave, as is the case in the pretransition state. If the crystal in the initial (or final) state interacts with an elastic-strain pulse stimulating the appearance of the final phase $\varepsilon_{xz} + \varepsilon_{yz} < 0$ (or the initial phase $\varepsilon_{xz} + \varepsilon_{yz} > 0$), then the final phase with $r < 0$ (or the initial phase with $r > 0$) arises inside the soliton.

In the immediate vicinity of the stability limits $T^\pm$, the soliton described by Eq. (29) cannot form due to high damping of the soft mode. Indeed, at $|T - T^\pm| = 1$ K and $|T - T^\pm|/T^\pm \approx 10^{-2}$, where the critical-oscillation frequency is $\omega_- \approx J_0(T^\pm)^{-1/2}|T - T^\pm|^{1/2} \approx 10^{13}$ s^{-1}, $J_0 \approx 10^{14}$ s^{-1}, and $T_c \approx 10^2$ K, the soliton with a duration of less than $\tau_p \approx 10^{-12}$ s is not excited. Therefore, solitons 10^{-13}–10^{-9} s long of the type considered here cannot be excited at temperatures close to the stability limits $T^\pm$.

5. DISCUSSION OF THE RESULTS

From the results described above, we can draw the important conclusion that a spatially localized collective excitation of the atomic lattice—a soliton—can be excited and propagated in a structurally unstable crystal. This soliton is, on the one hand, a structural defect consisting of two interphase boundaries with another phase between them and, on the other hand, an elastic-strain pulse with a characteristic length $l \approx 10^{-8}$–10^{-4} cm and a duration $\tau_p \approx 10^{-13}$–10^{-9} s. The soliton velocity slightly exceeds the velocity of a plane acoustic wave, which is likely the reason why the velocity of sound is experimentally observed to increase at the stage of nonlinear elastic strains [4].

It is reasonable to assume that the soliton found theoretically to arise in a structurally unstable crystal is the collective nonlinear excitation responsible for the behavior of the lattice at the stage of nonlinear elastic strains.

The elastic-strain soliton can arise in a structurally unstable crystal system only if a soft undamped mode exists. However, as the crystal stability limit is approached, the frequency of the corresponding soft mode tends to zero, whereas the relaxation parameter γ remains practically unchanged. Therefore, in the immediate vicinity of the stability limits $T^{\pm}$, the soft mode in a structurally unstable crystal is generally overdamped and the elastic-strain soliton cannot arise in this case.

REFERENCES

1. L. D. Landau and E. M. Lifshitz, *Course of Theoretical Physics*, Vol. 7: *Theory of Elasticity*, 4th ed. (Nauka, Moscow, 1987; Pergamon, New York, 1986).
2. V. E. Panin, V. E. Egorushkin, Yu. A. Khon, and T. F. Elsukova, Izv. Vyssh. Uchebn. Zaved., Fiz. **12**, 5 (1982).
3. E. E. Slyadnikov, Fiz. Tverd. Tela (St. Petersburg) **46** (6), 1065 (2004) [Phys. Solid State **46**, 1095 (2004)].
4. L. B. Zuev, B. S. Semukhin, K. I. Bushmelyova, and N. V. Zarikovskay, Mater. Lett. **42**, 97 (2000).
5. V. E. Panin, V. A. Klimenov, V. P. Bezborodov, O. B. Perevalova, V. P. Podkovka, N. P. Kolomeets, P. A. Gorodishchenskiĭ, and É. V. Kozlov, Fiz. Khim. Obrab. Mater. **6**, 77 (1993).
6. D. H. Auston and K. P. Cheung, Phys. Rev. Lett. **53** (16), 1555 (1984).
7. J. T. Darrow, B. B. Hu, X. C. Zhang, and D. H. Auston, Opt. Lett. **15**, 323 (1990).
8. É. M. Belenov, A. V. Nazarkin, and V. A. Ushchapovskiĭ, Zh. Éksp. Teor. Fiz. **100** (3), 762 (1991) [Sov. Phys. JETP **73**, 422 (1991)].
9. S. V. Sazonov, Fiz. Tverd. Tela (St. Petersburg) **37** (6), 1612 (1995) [Phys. Solid State **37**, 875 (1995)].
10. L. Allen and J. H. Eberly, *Optical Resonance and Two-Level Atoms* (Wiley, New York, 1975; Mir, Moscow, 1978).

Translated by Yu. Epifanov

Physics of the Solid State, Vol. 47, No. 3, 2005, pp. 489–494. Translated from Fizika Tverdogo Tela, Vol. 47, No. 3, 2005, pp. 474–479.

MAGNETISM AND FERROELECTRICITY

Optical Properties and Electronic Structure of Rare-Earth Ferroborates

V. N. Zabluda, S. G. Ovchinnikov, A. M. Potseluĭko, and S. A. Kharlamova

Kirensky Institute of Physics, Siberian Division, Russian Academy of Sciences, Akademgorodok, Krasnoyarsk, 660036 Russia

e-mail: stais@iph.krasn.ru, sgo@iph.krasn.ru

Received May 17, 2004

Abstract—The optical absorption spectra of single-crystal ferroborate $GdFe_3(BO_3)_4$ and $GdFe_{2.1}Ga_{0.9}(BO_3)_4$ are measured and interpreted. It is found that the absorption edge and the absorption bands *A*, *B*, and *C* observed below the edge are close to those for $FeBO_3$. A many-electron model of the band structure of $GdFe_3(BO_3)_4$ is suggested including strong electron correlations between the iron *d* states. It is shown that $GdFe_3(BO_3)_4$ has a charge-transfer dielectric gap. A rise in pressure is predicted to result in a crossover between the high-spin and low-spin states of the Fe^{3+} ion, collapse of the magnetic moment, a weakening of Coulomb correlations, an abrupt reduction in the energy gap, and an insulator–semiconductor transition. *© 2005 Pleiades Publishing, Inc.*

1. INTRODUCTION

For more than 30 years, studies of the rare-earth oxiborates with the huntite structure $RM_3(BO_3)_4$ have been carried out in order to fabricate high-efficiency functional materials for laser, piezoelectric, and acoustic devices. These crystals, along with the high-temperature superconductor cuprates and manganites exhibiting colossal magnetoresistance, are examples of systems with strong electron correlation (SEC). SEC determines their electronic structure and magnetic, optical, and electrical properties.

The rare-earth ferroborate $GdFe_3(BO_3)_4$ has the huntite structure belonging to space group $R32(D_{3h}^7)$, with $Z = 3$. The rare-earth Gd^{3+} ions have a prismatic environment, and the Fe^{3+} ions have an octahedral environment [1]. $GdFe_3(BO_3)_4$ is known to be an easy-plane antiferromagnet with a Néel temperature $T_N = 38$ K [2, 3]. At 10 K, all the sublattices are subjected to the spin-flop reorientation transition into the easy-axis antiferromagnetic (AFM) phase. This material is an insulator at room temperature.

Of the entire collection of oxiborates of transition metals, $FeBO_3$ ferroborate is the most interesting and most similar for comparison with the single-crystal $GdFe_3(BO_3)_4$ studied in the present work. This compound has been studied for a long time, and its magnetic [4, 5], optical [6], and dielectric properties are well known. Recently, optically induced disordering of the magnetic order was observed to occur in this compound under pulsed optical pumping [7]. At normal pressure, this material is a charge-transfer insulator with an optical gap of 2.9 eV [6, 8]. $FeBO_3$ is a typical representative of the systems with SEC [9]. Recent studies of this compound under high pressure have shown dramatic changes in its magnetic and electrical properties associated with the insulator–semiconductor transition [10–12].

This work is devoted to the optical absorption spectra and the electronic structure of $GdFe_3(BO_3)_4$, which have not yet been studied. Section 2 describes the specimens and experimental techniques used. In Section 3, we present the measured optical absorption spectra of $GdFe_3(BO_3)_4$ and $GdFe_{2.1}Ga_{0.9}(BO_3)_4$. In Section 4, the optical properties are analyzed in the terms of the multiband model of the electronic structure of $GdFe_3(BO_3)_4$ and are compared with those of $FeBO_3$. Section 5 is concerned with predictions of the influence of an increase in pressure on the optical properties and electronic structure.

2. SPECIMENS AND EXPERIMENTAL TECHNIQUE

$GdFe_3(BO_3)_4$ and $GdFe_{2.1}Ga_{0.9}(BO_3)_4$ single crystals were grown from a solution in melt using the group technique with a seed [13]. The obtained single crystals were dark green ($GdFe_3(BO_3)_4$), green ($GdFe_{2.1}Ga_{0.9}(BO_3)_4$), or transparent in the visible region. To carry out optical measurements, specimens from bulk isometric crystals were prepared in the form of thin plates with their planes either parallel or normal to the threefold axis C_3. The thickness of the plates intended for optical measurements was about 53 μm for the first crystallographic orientation of plates and about 42(37) μm for the second orientation, with the area of plates in both cases being about 2 mm^2. The spectra of optical absorption $D = \ln(I_0/I)$ for both $GdFe_3(BO_3)_4$ and $GdFe_{2.1}Ga_{0.9}(BO_3)_4$ were obtained using a double-beam spectrometer (designed at the Institute of Physics,

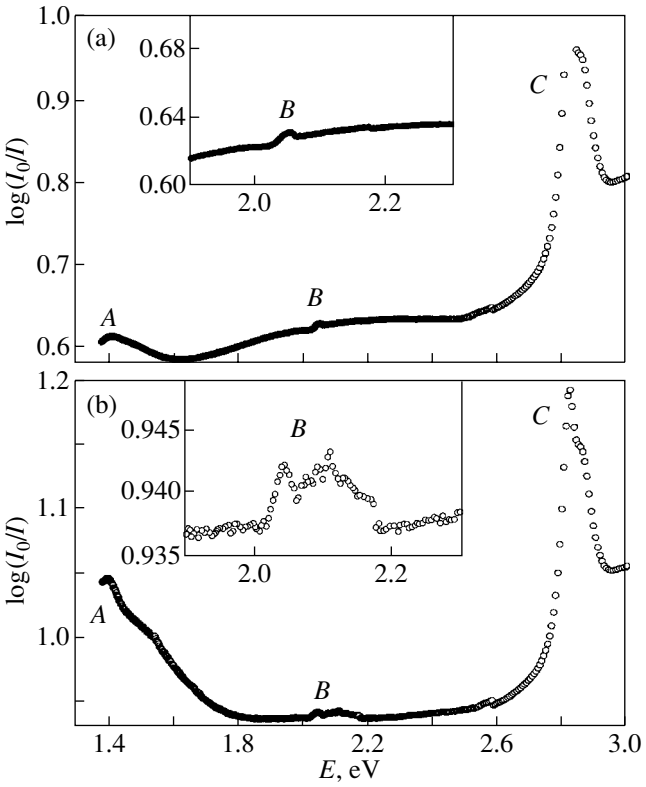

Fig. 1. Optical absorption spectra at T = 300 K for (a) $GdFe_3(BO_3)_4$ and (b) $GdFe_{2.1}Ga_{0.9}(BO_3)_4$.

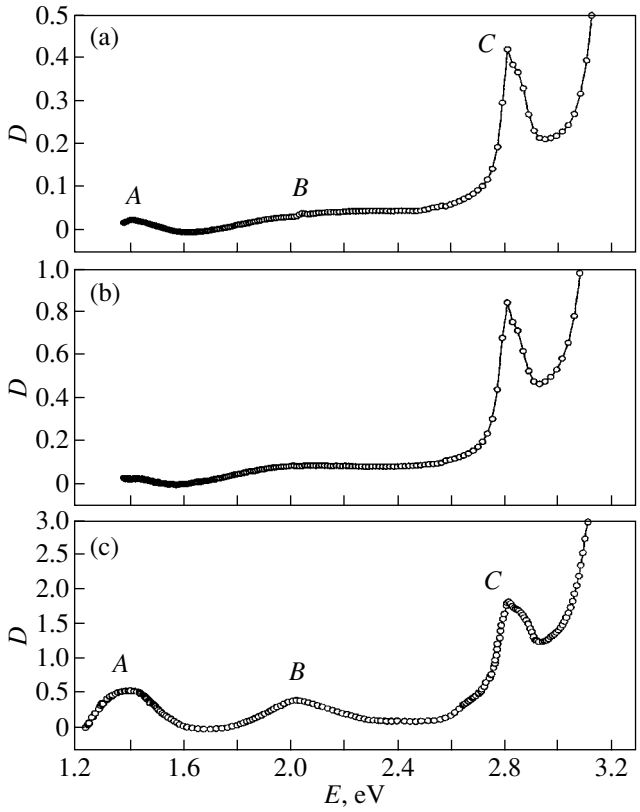

Fig. 2. Optical absorption spectra (a, b) of $GdFe_3(BO_3)_4$ for the *c* and *a* directions, respectively, and (c) of $FeBO_3$.

Siberian Division, Russian Academy of Sciences) in the range 10000–40000 cm^{-1} (1.24–4.96 eV) at 300 K. The slit spectral width of the grating monochromator used was 10 cm^{-1}. The absorption was measured with an accuracy of 3%.

3. OPTICAL ABSORPTION SPECTRA OF $GdFe_3(BO_3)_4$ AND $GdFe_{2.1}Ga_{0.9}(BO_3)_4$

The measured optical absorption spectra of $GdFe_3(BO_3)_4$ and $GdFe_{2.1}Ga_{0.9}(BO_3)_4$ are shown in Fig. 1. In the spectrum of $GdFe_{2.1}Ga_{0.9}(BO_3)_4$, the *B* peak is clearly observed to split. In Fig. 2, the $GdFe_3(BO_3)_4$ absorption spectra for two directions of the incident light beam with respect to the crystallographic C_3 axis are shown in comparison with the spectrum of the well-known compound $FeBO_3$ [6, 8].

B–O and Fe–O lengths and the energy gaps in $FeBO_3$ and $GdFe_3(BO_3)_4$

	B–O, Å	Fe–O, Å	E_g, eV
$FeBO_3$	1.3790	2.028	2.9
$GdFe_3(BO_3)_4$	1.3676	2.029	3.1

The energy band gap, which determines the fundamental absorption edge in $GdFe_3(BO_3)_4$, is equal to E_g = 3.1 eV, which is slightly higher than the corresponding value in $FeBO_3$ (E_g = 2.9 eV). Three groups of bands were observed (at E = 1.4, 2.0, 2.8 eV), which were the same for both crystallographic orientations. It was found that the bands in the spectra of $GdFe_3(BO_3)_4$ and $FeBO_3$ have similar energies to within an accuracy of several tenths of an electronvolt. Based on this similarity, we assumed that the optical properties of $FeBO_3$ and $GdFe_3(BO_3)_4$ are identical in the range 1.0–3.5 eV.

The influence of the rare-earth Gd^{3+} ion on the optical spectrum was clarified by studying high-resolution Fourier spectra. It was established that the Gd^{3+} ion does not have any fundamental absorption bands up to 32264 cm^{-1} (4 eV) [14]; therefore, the *A*, *B*, *C* bands can be associated with absorption of Fe^{3+} ions. Thus, all transitions are related to the Fe^{3+} ion and its nearest environment.

The difference between the local crystal structures of $GdFe_3(BO_3)_4$ and $FeBO_3$ is as follows: the single-crystal $GdFe_3(BO_3)_4$, unlike $FeBO_3$, has a slightly distorted coordination oxygen octahedron FeO_6 and three pairs of equal Fe–O lengths that are fairly close in value (the table shows the mean lengths for $GdFe_3(BO_3)_4$).

Therefore, along with the cubic component, the crystal field also has a low-symmetry component. However, this component is small and we will neglect it in our further discussion.

Thus, the band groups *A*, *B*, and *C* observed in $GdFe_3(BO_3)_4$ (as well as in $FeBO_3$; Fig. 2c) can be interpreted as *d–d* transitions from the ground state of iron ions with spin $S = 5/2$ to an excited state with spin $S = 3/2$, more specifically, ${}^6A_{1g}({}^6S) \longrightarrow {}^4T_{1g}({}^4G)$ for the *A* group of bands, ${}^6A_{1g}({}^6S) \longrightarrow {}^4T_{2g}({}^4G)$ for the *B* group, and ${}^6A_{1g}({}^6S) \longrightarrow {}^4A_{1g}, {}^4E_g({}^4G)$ for the *C* group. Furthermore, the Fe–O and B–O lengths (see table) for $GdFe_3(BO_3)_4$ and for $FeBO_3$ are virtually identical, which allows one to infer that the electronic structures of these two crystals are similar in the energy range up to 4 eV in the vicinity of the Fermi level.

4. ANALYSIS OF THE OPTICAL PROPERTIES OF $GdFe_3(BO_3)_4$ IN TERMS OF A MULTIELECTRON MODEL OF THE BAND STRUCTURE OF OXIBORATES: COMPARISON WITH $FeBO_3$

This section contains an analysis of the properties of $GdFe_3(BO_3)_4$ in the terms of the multielectron model used in [15] to calculate the $FeBO_3$ band structure. This model is also valid for $GdFe_3(BO_3)_4$ in the energy range up to 4 eV.

In insulator $GdFe_3(BO_3)_4$, there are localized Fe^{3+} *d* electrons in FeO_6 octahedra and localized Gd^{3+} *f* electrons in the GdO_6 triangle prism. Within the BO_3 group, strong *sp* hybridization occurs between the boron and oxygen orbitals. According to calculations of the $FeBO_3$ band structure, the hybridization of the Fe *d* electrons with the *sp* electrons of the BO_3 group is negligibly small. The top of the filled valence band E_v and the bottom of the empty conduction band E_c are formed by the *sp* orbitals of the BO_3 group, which, therefore, determine the band gap $E_g = E_c - E_v$.

According to one-electron first-principles calculations, in the case where the Fe^{3+} d^5 terms and Gd^{3+} f^7 terms are partly occupied, there will be partly filled bands, which corresponds to the metal state. However, owing to SEC, both the *d* and *f* electrons are in the Mott–Hubbard insulator regime. Therefore, in order to adequately describe the electronic structure and the optical properties of $GdFe_3(BO_3)_4$, the multielectron approach should be used with inclusion of SEC. Since the bond lengths within the BO_3 group are close to the corresponding lengths in $FeBO_3$ (see table), we can assume that the band gaps $E_g = E_c - E_v$ are also similar for these crystals. A certain decrease in the B–O bond length in $GdFe_3(BO_3)_4$ results in strengthening of the B–O hybridization and in E_g increasing to 3.1 eV as compared to 2.9 eV in $FeBO_3$. The one-electron scheme of the valence and conduction bands is superimposed by one-particle *d*- and *f*-electron resonances at energies

$$\Omega_d = E(d^{n+1}) - E(d^n), \quad \Omega_f = E(f^{n+1}) - E(f^n), \tag{1}$$

where $E(d^n)$ and $E(f^n)$ are the energies of the many-electron terms of iron and gadolinium. These energies are calculated with inclusion of SEC effects. Since Fe–O and Gd–O hybridization is weak, the Ω levels interact with *sp* bands of the BO_3 group only weakly.

The absence of absorption for the Gd^{3+} ion within the energy range $\hbar\omega \le 4$ eV indicates that the filled level $\Omega_{fv} = E(f^7) - E(f^6)$ is very low, while the empty level $\Omega_{fc} = E(f^8) - E(f^7)$ is very high. Therefore, only iron *d* states fall into the band gap E_g and we can conclude that the electronic structures of $FeBO_3$ and $GdFe_3(BO_3)_4$ in the energy range studied are similar. Moreover, because the Fe–O lengths of the FeO_6 octahedra are similar in $FeBO_3$ and in $GdFe_3(BO_3)_4$, we may also expect that the same will be true for both the Racah parameters *A*, *B*, and *C* and the cubic crystal-field component $\Delta = \varepsilon_d(e_g) - \varepsilon_d(t_{2g})$ for the iron ion. Taking SEC into account, the energies of the fundamental terms of the d^n configurations can be expressed in terms of these parameters as follows [15, 16]:

$$\begin{aligned} E({}^5E_1, d^4) &= 4\varepsilon_d + 6A - 21B - 0.6\Delta, \\ E({}^6A_1, d^5) &= 5\varepsilon_d + 10A - 35B, \\ E({}^5T_2, d^6) &= 6\varepsilon_d + 15A - 21B - 0.4\Delta. \end{aligned} \tag{2}$$

Here, ε_d is the one-electron energy of a *d* electron in the atom. In the cubic crystal field, this level splits: $\varepsilon_d(t_{2g}) = \varepsilon_d - 0.4\Delta$ and $\varepsilon_d(e_g) = \varepsilon_d + 0.6\Delta$. The Racah parameters and the crystal field depend on the number of *d* electrons in the d^n configuration; however, this dependence is weak and we neglect it for the sake of simplicity. In the $GdFe_3(BO_3)_4$ compound, as in $FeBO_3$, the *d–d* transitions in Fe^{3+} with the energies

$$\begin{aligned} \varepsilon_A = E({}^4T_1) - E({}^6A_1), \quad \varepsilon_B = E({}^4T_2) - E({}^6A_1), \\ \varepsilon_C = E({}^4E_1) - E({}^6A_1) \end{aligned} \tag{3}$$

determine the absorption spectrum at $\hbar\omega < E_g$. Using the experimental energies of *d–d* transitions and the Tanabe–Sugano diagrams, the Racah parameters are determined to be $B = 0.084$ eV, $C = 0.39$ eV, and $\Delta = 1.57$ eV; these parameters are similar to the Racah parameters for $FeBO_3$. The parameter *A* and the one-electron energies ε_d are determined by the Fe^{3+} ion and are taken to be the same as in $FeBO_3$ [15], namely, $A = 3.42$ eV and $\varepsilon_d = -14.84$ eV.

The high intensity of absorption band *C* in the spectrum of $GdFe_3(BO_3)_4$ is explained, as in $FeBO_3$, by the superposition of an additional charge-transfer absorp-

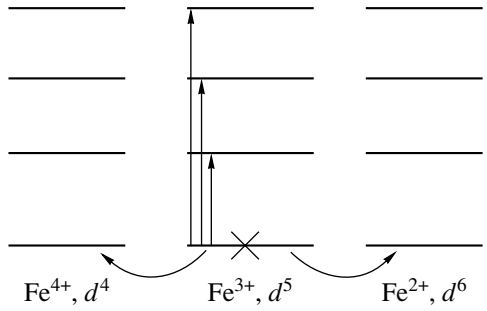

Fig. 3. Diagram of the Fe^{4+}, Fe^{3+}, and Fe^{2+} terms; the cross indicates the ground term $^6A_{1g}$, which is filled at $T = 0$.

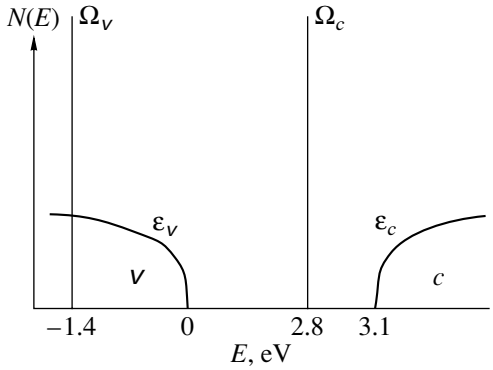

Fig. 4. Density of states of $GdFe_3(BO_3)_4$. The Fermi level lies above the valence band top ε_v.

tion mechanism, i.e., by the p^6d^5–p^5d^6 process. The creation of an excess electron due to the $Fe^{3+} \longrightarrow Fe^{2+}$ transition (Fig. 3) requires an energy

$$\Omega_c = E(^5T_2, d^6) - E(^6A_1, d^5). \quad (4)$$

Similarly, the annihilation of an electron is associated with the $Fe^{3+} \longrightarrow Fe^{4+}$ transition and requires an energy

$$\Omega_v = E(^6A_1, d^5) - E(^5E_1, d^4). \quad (5)$$

The levels Ω_c and Ω_v are expressed in terms of the Racah parameters as

$$\Omega_c = \varepsilon_d + 5A + 14B - 0.4\Delta, \quad (6)$$

$$\Omega_v = \varepsilon_d + 4A - 14B + 0.6\Delta; \quad (7)$$

and can be interpreted as the top and bottom Hubbard subbands. The difference between them determines the effective Hubbard parameter

$$U_{\text{eff}} = \Omega_c - \Omega_v = A + 28B - \Delta = 4.2 \text{ eV}. \quad (8)$$

This value of U_{eff} is typical of d ions in the middle of the 3d series. For example, this value of U_{eff} can be compared to the correlation energy $kT^* = 4.92$ eV, which was determined for crystal $Fe_{1.91}V_{0.09}BO_4$ from the temperature dependence of resistance using the Éfros–Shklovskiĭ law [17].

It should be noted that borates have different magnetic ordering temperatures ($T_{N1} = 38$ K for $GdFe_3(BO_3)_4$ and $T_{N2} = 348$ K for $FeBO_3$). The effect of magnetic order on the optical properties is different in the three temperature ranges: (i) below the magnetic ordering temperature, $T < T_{N1}$, the electronic structures of both borates are qualitatively similar but differ quantitatively due to the splitting of the A, B, and C bands in the molecular field, because their temperatures T_N differ by a factor of 10; (ii) in the range $T_{N1} < T < T_{N2}$, the electronic structures of borates should differ due to their magnetic properties being different; (iii) and in the paramagnetic phase, namely, at $T > T_{N2}$, the electronic structures of both borates are similar both qualitatively and quantitatively. The last conclusion is valid if there is no contribution from the Gd^{3+} f electrons, which appears only if the exciting energies are $\hbar\omega \approx 4$ eV or higher. For the same reason, substitution of neodymium for gadolinium causes additional lines to appear in the absorption spectrum and results in a more complicated electronic structure of the substituted crystals $Gd_{1-x}Nd_xFe_3(BO_3)_4$.

Taking into account all these considerations and the experimental data, we come to the model of the electronic structure of $GdFe_3(BO_3)_4$ shown in Fig. 4.

5. PROPERTIES OF $GdFe_3(BO_3)_4$ UNDER HIGH PRESSURES PREDICTED FROM THE MANY-ELECTRON MODEL

From the above discussion and calculations, as well as from the similarity between the electronic structures of $GdFe_3(BO_3)_4$ and $FeBO_3$, it follows that $GdFe_3(BO_3)_4$ will exhibit the following behavior: a crossover from the high-spin to low-spin state of the Fe^{3+} ion, collapse of the magnetic moment, a weakening of Coulomb correlations, an abrupt reduction in the energy gap, and an insulator–semiconductor transition.

According to [18], the effect of an increased pressure on the electronic structure is mainly due to an increase in the crystal field Δ:

$$\Delta(P) = \Delta(0) + \alpha P. \quad (9)$$

As a result, as can be seen from the Tanabe–Sugano diagrams for Fe^{3+} [19], the high-spin $^6A_1(S = 5/2)$ term and the low-spin $^2T_2(S = 1/2)$ term approach each other (Fig. 5a).

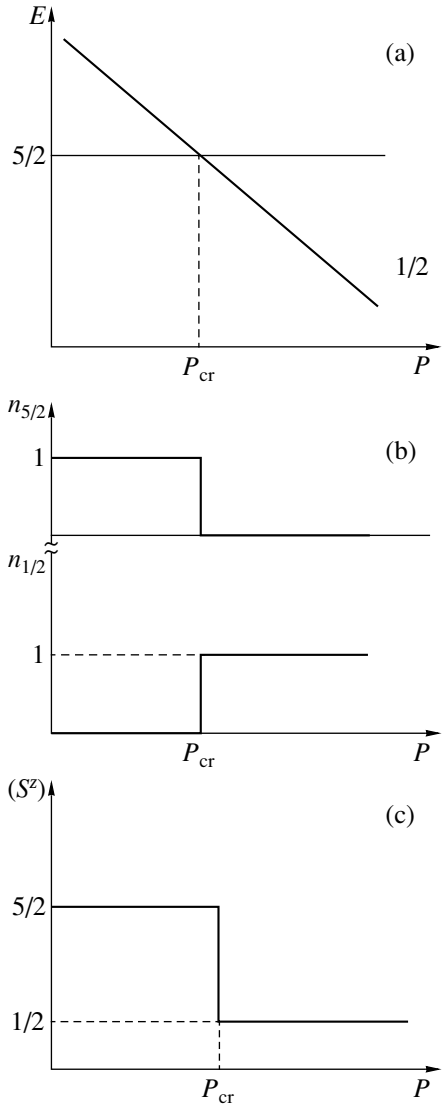

Fig. 5. (a) Fragment of the Tanabe–Sugano diagram for the crossover from the high-spin $^6A_1(S = 5/2)$ to low-spin $^2T_2(S = 1/2)$ iron terms, (b) the probability of an Fe^{3+} ion being in the $S = 5/2$ and 1/2 states, and (c) the collapse of the magnetic moment.

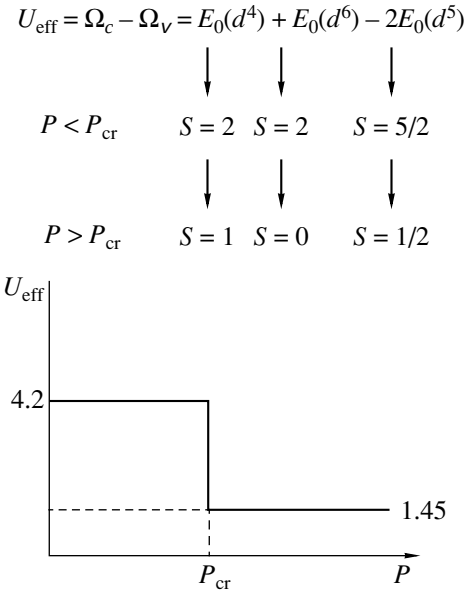

Fig. 6. Crossovers of terms for the d^4, d^5, and d^6 configurations and the jump in the effective Hubbard parameter.

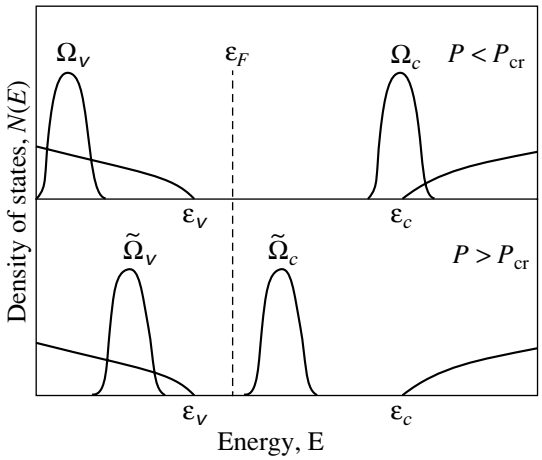

Fig. 7. $GdFe_3(BO_3)_4$ density of states under low and high pressure in the many-electron *p–d* model.

Therefore, at $P = P_{cr}$, the crossover can also occur in $GdFe_3(BO_3)_4$, which results in a collapse of the magnetic moment (Fig. 5b):

$$\langle S^z \rangle = 5/2 n_{5/2} + 1/2 n_{1/2}, \quad (10)$$

where $n_{5/2}$ and $n_{1/2}$ are the probabilities of the Fe^{3+} ion being in the $S = 5/2$ and $S = 1/2$ states, respectively. At $T = 0$, we have $n_{5/2} = 1$ up to the crossover point, and then this probability becomes zero above P_{cr}; the probability is $n_{1/2} = 0$ at $P < P_{cr}$ and $n_{1/2} = 1$ at $P > P_{cr}$.

For $FeBO_3$, the critical pressure P_{cr} is about 47 GPa [11]. For $GdFe_3(BO_3)_4$, a similar crossover can be expected and the critical pressure should have a similar value, because the Fe–O length and the critical field Δ are close to the respective values for $FeBO_3$. Under high pressure, the energies of the lower and the upper edges of Hubbard bands change due to the crossover [18]. We thus get for Fe^{3+}

$$\tilde{\Omega}_c = E(^1A_1, d^6) - E(^2T_2, d^5), \quad (11)$$

$$\tilde{\Omega}_v = E(^2T_2, d^5) - E(^3T_1, d^4). \quad (12)$$

As a result, the Hubbard effective correlation parameter decreases (Fig. 6), which means there is a decrease in the gap between the Hubbard subbands:

$$U_{eff} = \tilde{\Omega}_c - \tilde{\Omega}_v = A + 9B - 7C \approx 1.45 \text{ eV}. \quad (13)$$

A dramatic (almost threefold) decrease in SEC thus occurs, and instead of the Mott–Hubbard insulator we get the semiconductor state (Fig. 7).

A further increase in pressure can result in closure of the semiconductor gap (due to the increase in the small *d*-band width) and in the subsequent transition to the metal state.

6. CONCLUSIONS

The optical properties of the grown single crystals $GdFe_3(BO_3)_4$ and $GdFe_{2.1}Ga_{0.9}(BO_3)_4$ have been studied. It has been proved both theoretically and experimentally that, in the paramagnetic phase, the electronic structure and the optical spectra of $GdFe_3(BO_3)_4$ and $FeBO_3$ are similar to each other in the energy range below 4 eV in the vicinity of the Fermi energy. A many-electron model of the band structure of $GdFe_3(BO_3)_4$ has been suggested taking into account SEC of iron *d* states. It has been established that, under normal conditions, $GdFe_3(BO_3)_4$ is a charge-transfer insulator with SEC. In terms of the many-electron model, an increase in pressure was predicted to result in a crossover from the high-spin to low-spin state of the Fe^{3+} ion in $GdFe_3(BO_3)_4$, collapse of the magnetic moment, Coulomb correlation weakening, an abrupt reduction in the energy gap, and an insulator–semiconductor transition.

ACKNOWLEDGMENTS

This work was supported by the Russian Foundation for Basic Research (project no. 03-02-16268) and the program of the Department of Physical Sciences of the Russian Academy of Sciences “Strongly Correlated Electrons.”

REFERENCES

1. N. I. Leonyuk and L. I. Leonyuk, Prog. Cryst. Growth Charact. **31**, 179 (1995).
2. A. D. Balaev, L. N. Bezmaternykh, I. A. Gudim, S. A. Kharlamova, S. G. Ovchinnikov, and V. L. Temerov, J. Magn. Magn. Mater. **258–259**, 532 (2003).
3. A. D. Balaev, L. N. Bezmaternykh, S. A. Kharlamova, V. L. Temerov, S. G. Ovchinnikov, and A. D. Vasi’ev, J. Magn. Magn. Mater. **286–287**, 332 (2003).
4. J. C. Joubert, T. Shirk, W. B. White, and R. Roy, Mater. Res. Bull. **3**, 671 (1968).
5. M. P. Petrov, G. A. Smolenskiĭ, A. P. Paugurt, S. A. Kizhaev, and M. K. Chizhov, Fiz. Tverd. Tela (Leningrad) **14**, 109 (1972) [Sov. Phys. Solid State **14**, 87 (1972)].
6. I. S. Édel’man, A. V. Malakhovskiĭ, T. I. Vasil’eva, and V. N. Seleznev, Fiz. Tverd. Tela (Leningrad) **14**, 2810 (1972) [Sov. Phys. Solid State **14**, 2442 (1972)].
7. A. V. Kimel, R. V. Pisarev, J. Hohlfeld, and Th. Rasing, Phys. Rev. Lett. **89**, 287401 (2002).
8. A. J. Kurtzig, R. Wolf, R. C. Le Graw, and J. W. Nielsen, Appl. Phys. Lett. **14**, 350 (1969).
9. N. F. Mott, Proc. Phys. Soc. A **62**, 416 (1949).
10. A. G. Gavriliuk, I. A. Trojan, R. Boehler, M. Eremets, A. Zerr, I. S. Lyubutin, and V. A. Sarkisyan, Pis’ma Zh. Éksp. Teor. Fiz. **75** (1), 25 (2002) [JETP Lett. **75**, 23 (2002)].
11. I. A. Troyan, M. I. Eremets, A. G. Gavrilyuk, I. S. Lyubutin, and V. A. Sarkisyan, Pis’ma Zh. Éksp. Teor. Fiz. **78** (1), 16 (2003) [JETP Lett. **78**, 13 (2003)].
12. V. A. Sarkisyan, I. A. Troyan, I. S. Lyubutin, A. G. Gavrilyuk, and A. F. Kashuba, Pis’ma Zh. Éksp. Teor. Fiz. **76** (11), 788 (2002) [JETP Lett. **76**, 664 (2002)].
13. L. N. Bezmaternykh, S. A. Kharlamova, and V. L. Temerov, Crystallogr. Rep. **49**, 855 (2004).
14. E. P. Chukalina, D. Yu. Kuritsin, M. N. Popova, L. N. Bezmaternyhk, S. A. Kharlamova, and V. L. Temerov, Phys. Lett. A **322**, 239 (2004).
15. S. G. Ovchinnikov and V. N. Zabluda, Zh. Éksp. Teor. Fiz. **125**, 198 (2004) [JETP **98**, 135 (2004)].
16. D. T. Sviridov, R. K. Sviridova, and Yu. F. Smirnov, *Optical Spectra of Transition Metal Ions in Crystals* (Nauka, Moscow, 1976) [in Russian].
17. A. D. Balaev, O. A. Bayukov, A. D. Vasil’ev, D. A. Velikanov, N. B. Ivanova, N. V. Kazak, S. G. Ovchinnikov, A. Abd-Elmeguid, and V. V. Rudenko, Zh. Éksp. Teor. Fiz. **124** (5), 1103 (2003) [JETP **97**, 989 (2003)].
18. S. G. Ovchinnikov, Pis’ma Zh. Éksp. Teor. Fiz. **77**, 808 (2003) [JETP Lett. **77**, 676 (2003)].
19. Y. Tanabe and S. Sugano, J. Phys. Soc. Jpn. **9**, 753 (1951).

Translated by E. Borisenko

Physics of the Solid State, Vol. 47, No. 3, 2005, pp. 495–501. Translated from Fizika Tverdogo Tela, Vol. 47, No. 3, 2005, pp. 480–486.

MAGNETISM AND FERROELECTRICITY

Magnetization Curve and Magnetic Correlations in a Nanochain of Ferromagnetic Grains with Random Anisotropy

S. V. Komogortsev and R. S. Iskhakov

Kirensky Institute of Physics, Siberian Division, Russian Academy of Sciences, Akademgorodok, Krasnoyarsk, 660036 Russia
e-mail: komogor@iph.krasn.ru

Received May 17, 2004

Abstract—The magnetization curve and magnetization correlation function are calculated for a ferromagnetic chain of single-domain nanoparticles with a randomly oriented anisotropy axis for different ratios between the exchange correlation and anisotropy energies. It is shown that the coercive force decreases as the exchange correlations increase. For strong exchange correlations, the magnetization curve is described by the following three successive magnetization processes as the applied field is increased: (i) nonuniform rotation of the magnetization of stochastic domains, (ii) collapse of the magnetic solitons, and (iii) nonuniform rotation of exchange-correlated magnetization vectors of the nanoparticles. For high fields, the calculated correlation function of the transverse magnetization components coincides with that predicted from linear theory. At low and zero fields, the main parameters of the correlation function (the variance and correlation radius) tend to certain finite values rather than diverge (as is the case in linear theory). The irreversible variation in the magnetization at low fields (the hysteresis loop) and the hysteresis of the main parameters of the correlation function are calculated. © *2005 Pleiades Publishing, Inc.*

1. INTRODUCTION

The interest in simulating model systems with randomly oriented magnetic anisotropy is related to gaining a detailed understanding of the mechanisms of formation of unique magnetic properties of amorphous and nanocrystalline magnets. One of the main reasons giving rise to these properties of amorphous and nanocrystalline magnetic alloys is the randomly oriented local magnetic anisotropy coexisting with a strong exchange correlation of magnetic moments [1, 2]. Orientational randomness of anisotropy in these materials generates a specific magnetic microstructure, which can be described as an ensemble of stochastic magnetic domains. It was found that the average self-consistent characteristics of these domains (anisotropy and size) determine the main integral properties (coercivity and permeability) of amorphous and nanocrystalline magnets [3]. The stochastic magnetic domain is defined as follows. In [4], it was shown that a randomly oriented local magnetic field destroys the long-range magnetic order in a disordered ferromagnet. However, ferromagnetic ordering (correlations) is still preserved on a finite scale: due to exchange interaction, the magnetic order extends over distances that are large in comparison with interatomic distances. This ferromagnetically ordered region is a stochastic domain. To describe the magnetic structure of such systems with "intermediate" magnetic order, it is necessary to study the magnetization correlation function $K_m(r)$ [5].

The correlation function $K_m(r)$ can be directly reconstructed from experimental studies of small-angle neutron scattering in nanostructured ferromagnets [6, 7]. One of the main parameters of this function, variance $K_m(0)$, can be determined from the magnetization curve near saturation [8]. Recent studies have shown that the correlation radius R_m can also be determined from the magnetization curve [9, 10]. However, in the low-field region, perturbation theory does not apply and a linear analytical theory of the magnetization curve cannot be developed. At the same time, this region has been intensively studied experimentally and the interest in applying simulation methods to the description of nanomagnets has increased. We note a general fact: the importance of simulation experiments increases in connection with the possible description of new physical effects.

The published micromagnetic simulations deal with some applied problems of magnetism [11–16] (numerical studies of magnetization curves of a specific narrow class of materials) and some fundamental problems [17–22]. Those studies have shown that both the shape of the magnetization curve and the form of the magnetization correlation function are determined by the grain size and the fundamental magnetic constants. We believe that, in those studies, insufficient attention was paid to establishing the relation of the magnetic structure in various fields and at different relative magnitudes of exchange correlations and anisotropy to the magnetization curve of a model system, i.e., to work aimed at solving the main problem in magnetic material science of nanomagnets. Indeed, it has now become clear that the form of the magnetization correlation function $K_m(r)$ (which characterizes the spin structure) is related to the shape of the magnetization curve, $M(H)$

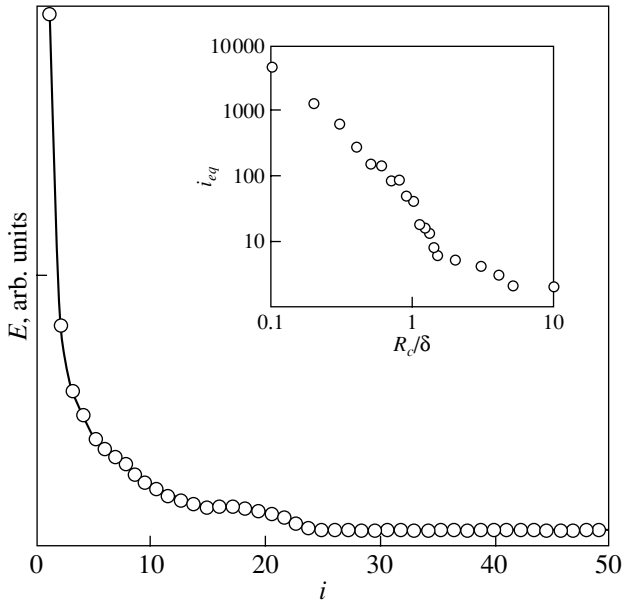

Fig. 1. Dependence of the calculated total energy of the chain on the number of iterations. The inset shows the dependence of the number of iterations required to attain the energy minimum on the parameter R_c/δ.

(which is a magnetic property of a nanomagnet). The aim of this study is to investigate simultaneously both the correlation function and the magnetization curve for a simple model system, namely, a chain of exchange-coupled nanoparticles with randomly oriented anisotropy. Our simulation is intended to provide answers to the following questions.

(1) How does the form of the magnetization curve change in the intermediate regime between weak (relative to the exchange correlation energy) and strong anisotropy?

(2) What are the features of the magnetization curve at low fields in the case of weak anisotropy?

(3) What is the character of the behavior of the correlation function of a nanostructured magnet at low fields?

The model considered is a special case of the model of a nanomagnet with one-dimensional inhomogeneities of magnetic anisotropy. However, it will be shown that this model exhibits the general laws characterizing nanomagnets. Furthermore, it is known that significant research attention has been recently turned to a new class of magnetic materials, one like magnetic nanowires. It was found that these materials are most often in the form of nanochains of exchange-bound nanoparticles [23, 24]. Therefore, our model can also be applied to describe experimental results on the magnetization of nanowires.

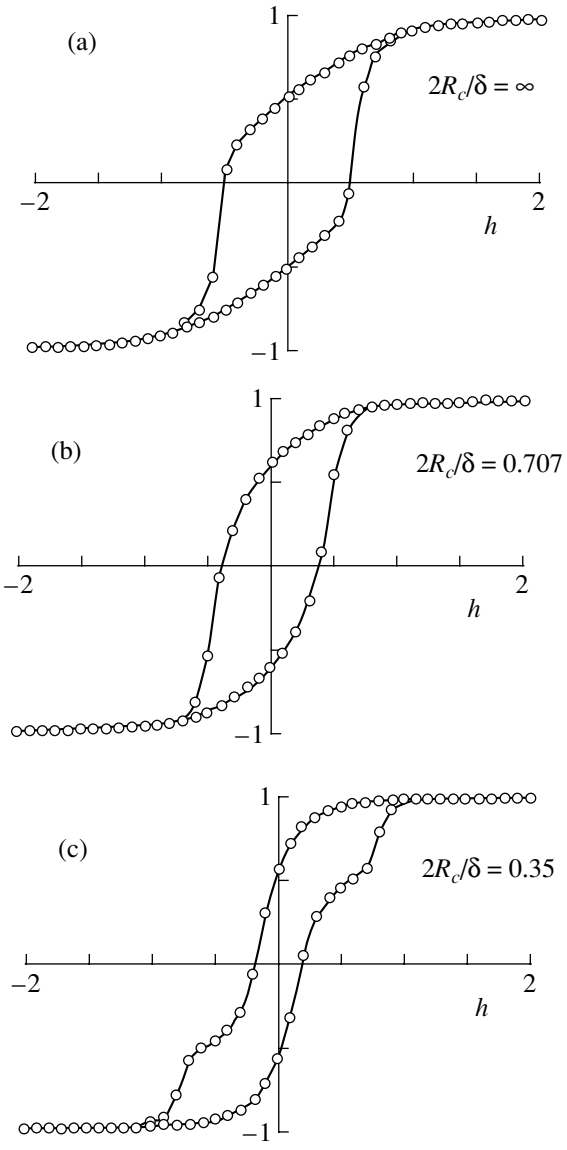

Fig. 2. Magnetization curves calculated at different values of the parameter $2R_c/\delta$.

2. METHOD AND MODEL

A discrete analog of our model is a one-dimensional chain of spins **s** with random anisotropy at each site *i* with a constant nearest neighbor exchange interaction *J*. It is known that the energy of such a chain can be written as a sum over the sites of the chain:

$$E = -\sum_i (J\mathbf{s}_i\mathbf{s}_{i+1} + K(\mathbf{s}_i\mathbf{n}_i)^2 + \mathbf{H}\mathbf{s}_i). \quad (1)$$

Likewise, for a nanochain of ferromagnetic grains, we can write the energy as

$$E = -\sum_i \left[\frac{1}{8}\frac{A}{R_c^2}(\cos(\theta_i - \theta_{i+1}) + \cos(\theta_i - \theta_{i-1})) + K\cos^2(\theta_i - \theta_i^a) + HM\cos\theta_i\right], \quad (2)$$

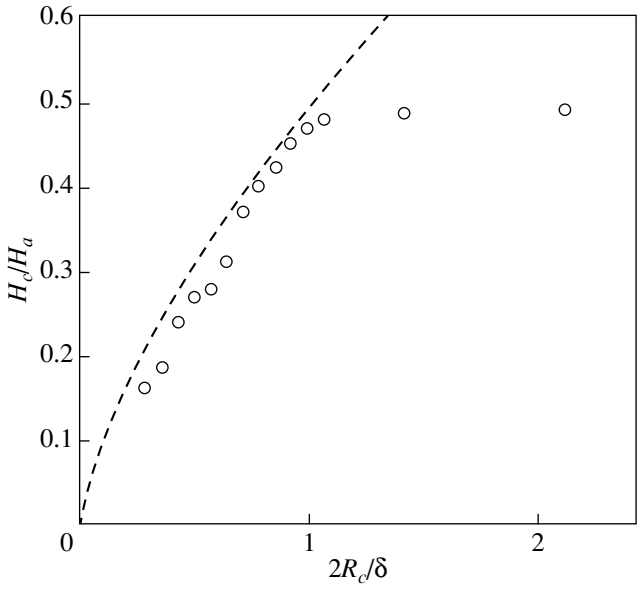

Fig. 3. The coercive force as a function of the reduced correlation radius of local anisotropy. The dashed line is the function $H_c = kH_a(2R_c/\delta)^{2/3}$.

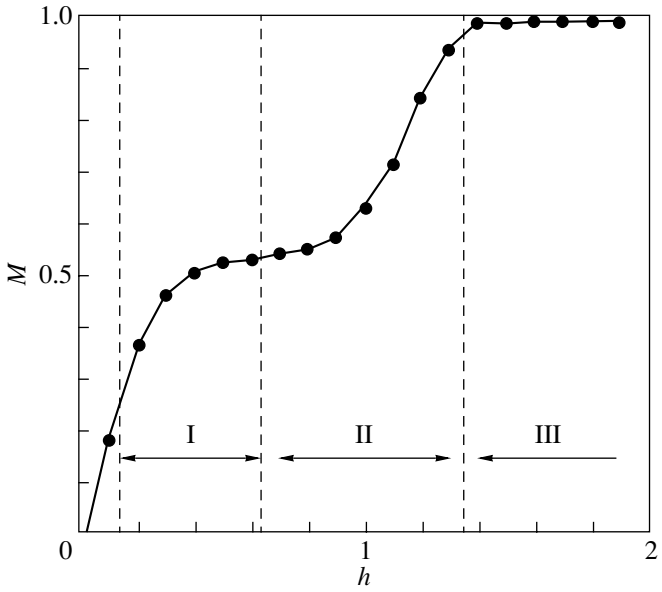

Fig. 4. Magnetization curve starting from the demagnetized state of the nanochain for the case of $R_c/\delta \approx 0.28$.

where the direction of the local magnetization vector is characterized by the angle θ_i measured from the direction of the field **H**; the distance between the neighboring sites is equal to the nanoparticle size $2R_c$ (in this case, R_c is the correlation radius of random anisotropy); $A \equiv J(2R_c)^2$ is the exchange interaction constant; M_s is the saturation magnetization; $K = H_aM_s/2$ is the local magnetic anisotropy energy density, related to the anisotropy field H_a; θ_i^a is the angle of the easy magnetization axis (a random function); and H is the external magnetic field. Since we are interested only in the states corresponding to the minimum energy, it is convenient to write Eq. (2) as

$$E = -K\sum_i \left[\frac{1}{8}\left(\frac{\delta}{R_c}\right)^2 (\cos(\theta_i - \theta_{i+1}) + \cos(\theta_i - \theta_{i-1})) + \cos^2(\theta_i - \theta_i^a) + 2h\cos\theta_i\right], \quad (3)$$

where $\delta/R_c = \sqrt{A/KR_c^2}$ is a dimensionless parameter characterizing the ratio between the exchange correlation and anisotropy energies and $h = H/H_a$. In our case (the anisotropy is random at each site), we have $R_c = 1/2$ (see, e.g., [20]). We intentionally retained the quantity R_c in Eqs. (2) and (3) in order to use, when interpreting the results, the important concept of scaling (the direct dependence of the minima of the total energy on the dimensionless parameters δ/R_c and h) in systems with random anisotropy.

In this study, we disregard the contribution of dipole–dipole interaction to the total energy for several reasons. First, in earlier simulations of similar systems [11, 12], it has been shown that the magnetic structure and the magnetization curve of nanomagnets only weakly depend on the magnetic dipole interactions, in contrast to those of large-grain and single-crystal ferromagnets. This result is qualitatively clear, since only exchange correlations and magnetic anisotropy participate in the formation of the basic unit of the spin structure, the stochastic magnetic domain. Second, the inclusion of long-range magnetic dipole forces

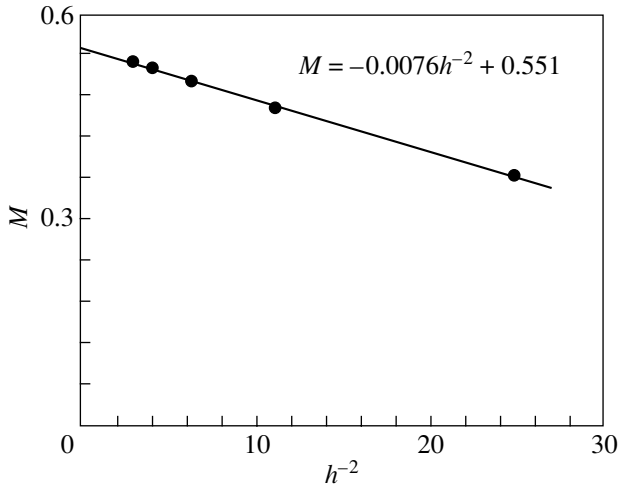

Fig. 5. Magnetization curve in the first field range ($R_c/\delta \approx 0.28$).

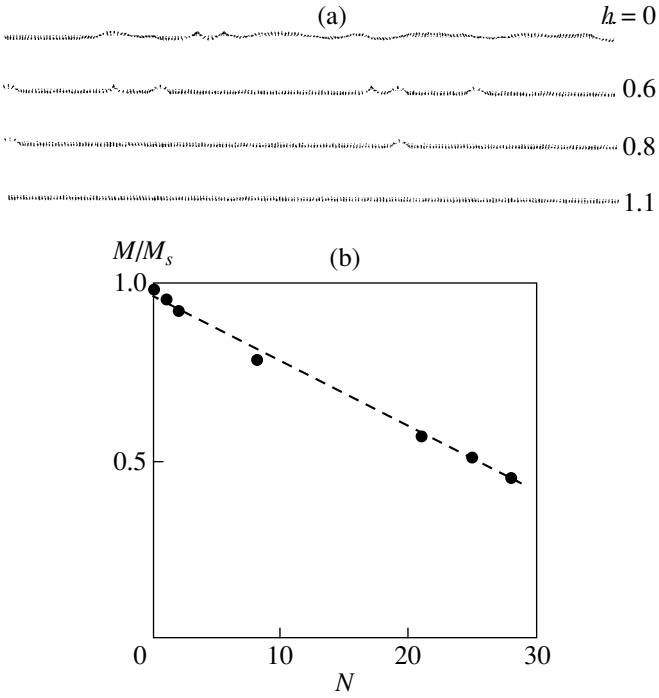

Fig. 6. (a) Magnetic structure of a fragment of the chain at different values of the external field in the second range. (b) Dependence of magnetization on the number of magnetic solitons in the second field range.

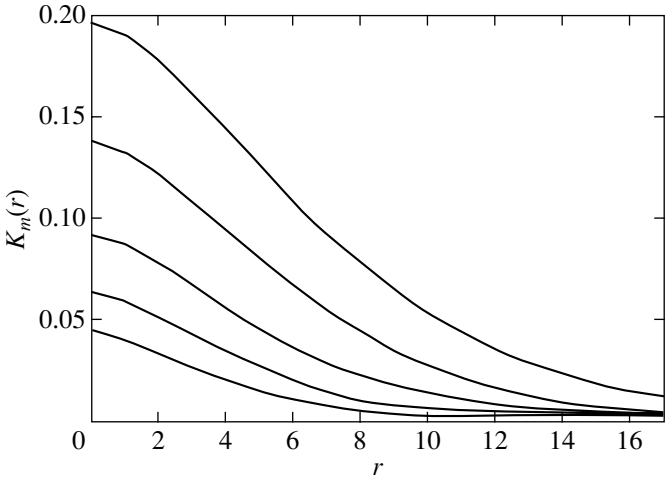

Fig. 7. Dependence of the correlation function for the transverse magnetization components on the external field (from top to bottom: $h = 0, 0.1, 0.2, 0.3, 0.4$) for $2R_c/\delta = 0.35$.

increases the amount of computational time required (which is long even if we disregard these forces) by orders of magnitude.

There are two different methods for solving our problem numerically: (i) numerical solution of the differential equation obtained by minimizing functional (2) or (3) [18–20] and (ii) a straightforward choice of the spin distribution corresponding to the minimum of total energy (2) or (3) (see, e.g., [17]). The advantage of the first method in the case of $R_c/\delta \ll 1$ (strong exchange correlations, weak anisotropy) is that the computation speed is high, in contrast to the second method, where the computation time increases sharply with decreasing ratio R_c/δ (see inset to Fig. 1). In the case where R_c/δ is of the order of unity or larger (strong anisotropy, weak exchange correlations), the first method fails, since the system becomes strongly nonlinear and divergences appear when the differential equation is solved numerically. Moreover, the solution to the differential equation is assumed to be unique and, therefore, cannot be used at low fields, where hysteresis arises. In this case, the problem is solved using the second method.

A procedure for calculating the magnetization curve using the first method was suggested and described in [18, 19]. With the second method, the magnetization curve can be found as follows: for a certain field (e.g., $H = 0$), "relaxation" of the system is performed (by choosing the magnetization distribution that corresponds to the minimum energy), then the field is varied slightly and relaxation from the previous state is performed. We assume that this procedure allows one to reach the local energy minima responsible for hysteresis.

The relaxation is performed as follows. The angle θ_i at site i is changed by Δ, and the energy at this site is calculated. If the energy increases as compared to the previous state, the state is not stored in memory and the angle is changed by $-\Delta$; this procedure is repeated with a subsequent decrease in the step to ± 0.0001 rad. This procedure is performed successively for each site.

Due to the coupling between the nearest neighbors, the state at site i is changed when minimizing the energy at site $i + 1$. Therefore, to minimize the energy, we have to come back and perform the relaxation at site i again. By performing such iterations for the entire chain, we found that the total energy first decreases and then ceases to vary at a certain stage (Fig. 1). We assume that this state corresponds to the energy minimum. We note that the choice of another sequence of step-by-step spin relaxation can result in a different random distribution of magnetization; however, for a sufficiently long chain, the average characteristics do not change. In the calculations, we used chains 1000- to 5000-spins long and periodic boundary conditions. Since the energy of a nanochain is invariant under rotations in the plane normal to the external field, we averaged over the angle in this plane when averaging the projection of the magnetization onto the field axis.

3. RESULTS AND DISCUSSION

Figure 2 shows the magnetization curves calculated for different values of the parameter $2R_c/\delta$ characterizing the ratio between the anisotropy and exchange correlation energies. The curve in Fig. 2a corresponds to

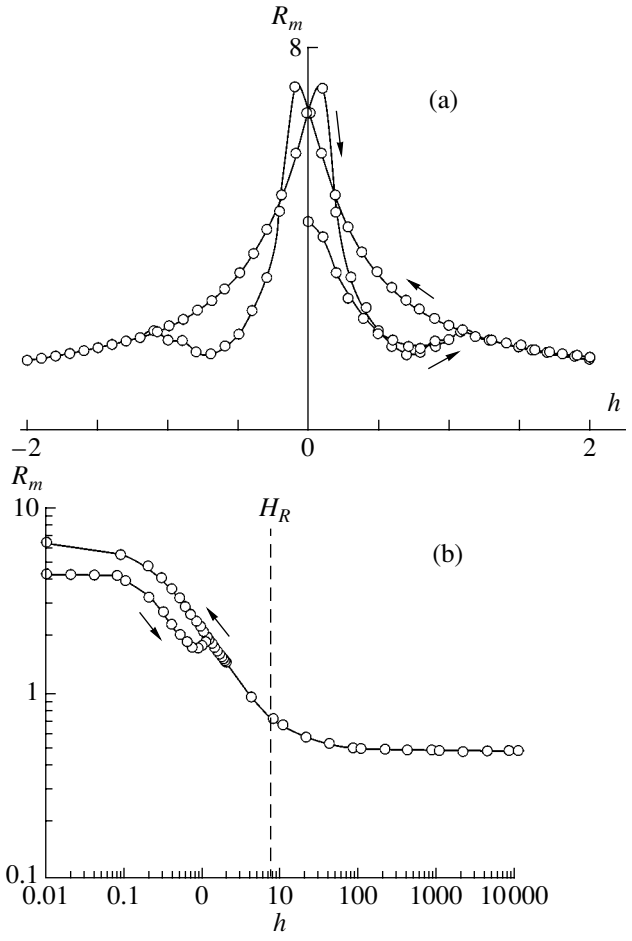

Fig. 8. Field dependence of the magnetization correlation radius R_m on (a) a linear and (b) a logarithmic scale (for $2R_c/\delta = 0.35$).

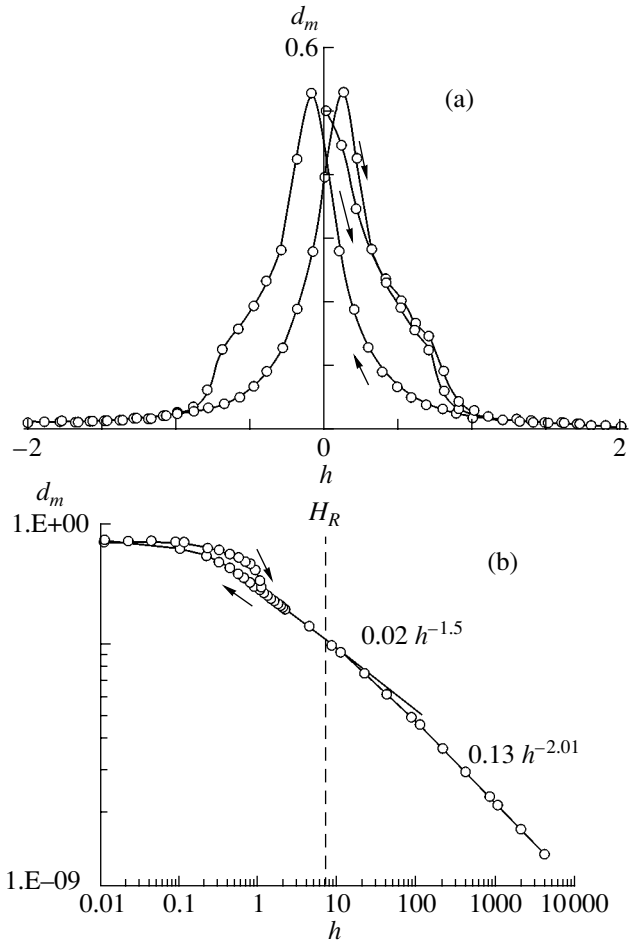

Fig. 9. Field dependence of the magnetization variance $d_m = K_m(0)$ on (a) a linear and (b) a logarithmic scale (for $2R_c/\delta = 0.35$).

zero exchange correlation energy and reproduces the classical result of Stoner and Wohlfarth for a system of noninteracting single-domain particles (or very large crystallites, with $R_c \gg \delta$) with random easy-axis anisotropy [25]. In this case, the coercive field is $h_c = 1/2$ ($H_c = H_a/2$) and the residual magnetization is $M_r = (1/2)M_s$. The coercive force decreases with decreasing $2R_c/\delta$, i.e., as exchange correlations are included (Figs. 2b, 2c). The dependence of H_c on $2R_c/\delta$ obtained from the calculated magnetization curves is plotted in Fig. 3. In the region of $2R_c/\delta < 1$, the calculated dependence of the coercive force becomes close to the analytical dependence of the average anisotropy field of a one-dimensional magnetic block (stochastic magnetic domain) [18, 26, 27]:

$$\langle H_a \rangle = H_a(2R_c/\delta)^{2/3}. \quad (4)$$

By comparing the curves in Fig. 3, we see that H_c as a function of $2R_c/\delta$ follows the same power law as does $\langle H_a \rangle$ and that these quantities differ by a constant factor, $H_c = k\langle H_a \rangle$. In our case, $k \approx 0.48$. This correlation between the dependences of H_c and $\langle H_a \rangle$ corresponds to a model in which the magnetic structure of the nanochain is considered a system of exchange-uncoupled magnetic blocks with randomly oriented anisotropy axes averaged over each block.

For strong exchange correlations, a steplike feature arises on the magnetization curve (Figs. 2c, 4). This feature appears at $2R_c/\delta \approx 0.4$ and becomes more pronounced at stronger exchange correlations ($2R_c/\delta \ll 1$). In Fig. 4, we show the calculated magnetization curve starting from the demagnetized state of the nanochain for the case of $2R_c/\delta \approx 0.28$. We see that this magnetization curve can be divided into three parts, corresponding to three field ranges.

In the first range, the magnetization increases with field due to nonuniform rotation of the magnetizations of stochastic domains. This interpretation is confirmed by the fact that the $M \sim H^{-2}$ dependence is satisfied in this region (Fig. 5). We note that this dependence was predicted and observed experimentally in [10]. The average anisotropy field $\langle H_a \rangle$ of a block determined from the Akulov low-field dependence agrees well with the value of $\langle H_a \rangle$ calculated from Eq. (3).

In the second field range of the $M(h)$ curve, the magnetic structure proves to be an ensemble of magnetic blocks with the average magnetizations oriented along the field and an additional ensemble of localized regions in which the magnetization is not reversed; these regions are topological magnetic solitons whose structure and size do not depend on the external field within the second range (Fig. 6a). As the field increases, the magnetization of magnetic solitons is reversed in a jumplike manner and the solitons decrease in number and disappear in fields above H_a ($h > 1$). Figure 6b shows the dependence of the magnetization on the number of magnetic solitons in the second field range. The linear dependence indicates that the magnetization reversal in each soliton provides an equal contribution to the increase in magnetization. Since the solitons do not differ in size or magnetization in the second range, we may consider them as a sort of magnetization quanta.

The magnetic structure of the nanochain in the third field range of the reversible $M(h)$ dependence is a stochastic magnetic structure or "magnetization ripples" (see, e.g., [28]). This structure is described well by the one-dimensional linear theory of reversible processes of inhomogeneous magnetization rotation [29].

We calculated the correlation function for the transverse components of magnetization for each magnetic state of the nanochain corresponding to a point on the calculated hysteresis loop (for $2R_c/\delta \approx 0.35$). Figure 7 shows the $K_m(r)$ dependence calculated for different fields. The main parameters of the function $K_m(r)$ are the variance $d_m = K_m(0)$ and the correlation radius R_m. We see that both the variance $K_m(0)$ and the magnetic correlation length $2R_m$ decrease with increasing external field. For our simple model, the field dependences of $d_m = K_m(0)$ and $R_m(h)$ can be calculated in the entire field range.

Figures 8 and 9 show the calculated field dependences of the correlation radius $R_m(h)$ and the variance of the transverse components of magnetization $d_m(h)$ plotted on both linear and logarithmic scales. We see that the h dependences of the main parameters of the correlation function $K_m(r)$, as well as the $M(h)$ dependence, are characterized by a region of reversible variation and a region of irreversible changes (hysteresis). The reversible variations in $R_m(h)$ and $d_m(h)$ are the simplest to explain. At high fields, the calculated R_m and d_m are identical to those predicted from linear theory (Figs. 8b, 9b). Indeed, according to linear theory [29], in fields below $H_R = 2A/M_s R_c^2$, we have $R_m = \sqrt{2A/M_s H} \equiv \delta h^{-1/2}$ and $d_m = (aH_a)^2 H_R^{-1/2} H^{-3/2} = a^2(R_c/\delta)h^{-3/2}$. In fields above H_R, R_m tends to a constant value, which is approximately equal to the correlation radius of random magnetic anisotropy ($R_c = 1/2$ in our case), and the variance of magnetization behaves as $d_m = (aH_a)^2 H^{-2} = a^2 h^{-2}$. It is seen in Figs. 8b and 9b that the calculated functions $R_m(h)$ and $d_m(h)$ exhibit similar behavior. We note that these results were obtained both by directly minimizing the total energy (in the present work) and by solving the corresponding differential equation (in [30]).

The irreversible variations in $R_m(h)$ and $d_m(h)$ are most difficult to explain. We see that, as the field approaches zero, the quantities R_m and d_m do not diverge (contrary to the predictions from linear theory) but rather tend to finite values. The variations in $R_m(h)$ and $d_m(h)$ with field are hysteretic. We point out specific features of this hysteresis. First, we see that $R_m(0)$ in the demagnetized state is smaller than $R_m(0)$ in the state with residual magnetization (the opposite is true for $d_m(0)$). Second, we see that there is a field range (close to $h = 1$) where $R_m(h)$ increases with H, in disagreement with the prediction from linear theory. We note that this field range coincides with the region where magnetic solitons exist and a specific feature arises on the magnetization curve (the second range).

The behavior of $R_m(h)$ and $d_m(h)$ in the field range $h < 1$ ($H < H_a$) allows us to assert that the quantitative characteristics of a stochastic domain (its size and average anisotropy) are fairly arbitrary in many respects (at least, in the one-dimensional case). Therefore, these quantities can only be evaluated by order of magnitude.

Thus, in our simulation we succeeded in providing answers to all three questions stated in Section 1.

ACKNOWLEDGMENTS

This study was supported by the Krasnoyarsk Regional Science Foundation (grant no.12F0011C), the Russian Foundation for Basic Research (grant no. 04-02-16230), and the Governmental Support Foundation (grant no. MK-1684.2004.2).

REFERENCES

1. V. A. Ignatchenko and R. S. Iskhakov, Zh. Éksp. Teor. Fiz. **72**, 1005 (1977) [Sov. Phys. JETP **45**, 526 (1977)].
2. R. Alben, J. J. Becker, and M. C. Chi, J. Appl. Phys. **49**, 1653 (1978).
3. G. Herzer, IEEE Trans. Magn. **26**, 1397 (1990).
4. Y. Imry and S.-K. Ma, Phys. Rev. Lett. **35**, 1399 (1975).
5. J. M. Ziman, *Models of Disorder: The Theoretical Physics of Homogeneously Disordered Systems* (Cambridge Univ. Press, London, 1979; Mir, Moscow, 1982).
6. J. Weissmuller, A. Michels, J. G. Barker, A. Wiedenmann, U. Erb, and R. D. Shull, Phys. Rev. B **63**, 214414 (2001).
7. A. Michels, R. N. Viswanath, J. G. Barker, R. Birringer, and J. Weissmuller, Phys. Rev. Lett. **91**, 267204 (2003).
8. V. A. Ignatchenko, R. S. Iskhakov, and G. V. Popov, Zh. Éksp. Teor. Fiz. **82**, 1518 (1982) [Sov. Phys. JETP **55**, 878 (1982)].
9. R. S. Iskhakov, S. V. Komogortsev, Zh. M. Moroz, and E. E. Shalygina, Pis'ma Zh. Éksp. Teor. Fiz. **72**, 872 (2000) [JETP Lett. **72**, 603 (2000)].

10. R. S. Iskhakov, V. A. Ignatchenko, S. V. Komogortsev, and A. D. Balaev, Pis'ma Zh. Éksp. Teor. Fiz. **78**, 1142 (2003) [JETP Lett. **78**, 646 (2003)].
11. H. Kronmuller, R. Fischer, M. Seeger, and A. Zern, J. Phys. D: Appl. Phys. **29**, 2274 (1996).
12. R. Fischer and H. Kronmuller, J. Magn. Magn. Mater. **184**, 166 (1998).
13. J. Fidler and T. Schrefl, J. Magn. Magn. Mater. **203**, 28 (1999).
14. W. M. Saslow and N. C. Koon, Phys. Rev. B **49**, 3386 (1994).
15. O. Nedelko, P. Dikukh, and A. Slawska-Waniewska, J. Magn. Magn. Mater. **254–255**, 281 (2003).
16. I. R. McFadyen and I. A. Beardsley, J. Appl. Phys. **67**, 5540 (1990); I. A. Beardsley and J. S. Zhu, J. Appl. Phys. **67**, 5352 (1990).
17. R. Dickmann and E. M. Chudnovsky, Phys. Rev. B **44**, 4397 (1991).
18. A. A. Ivanov, V. A. Orlov, and G. O. Patrushev, Fiz. Met. Metalloved. **84** (2), 47 (1997) [Phys. Met. Metallogr. **84**, 125 (1997)].
19. A. A. Ivanov and G. O. Patrushev, Fiz. Met. Metalloved. **86** (4), 1 (1998) [Phys. Met. Metallogr. **86**, 331 (1998)].
20. A. A. Ivanov, V. A. Orlov, and G. O. Patrushev, Fiz. Tverd. Tela (St. Petersburg) **41**, 1432 (1999) [Phys. Solid State **41**, 1311 (1999)].
21. B. Dieny and B. Barbara, Phys. Rev. B **41**, 11549 (1990).
22. D. R. Denholm and T. J. Sluckin, Phys. Rev. B **48**, 901 (1993).
23. H. Zeng, R. Skomski, L. Menon, Y. Liu, S. Bandyopadhyay, and D. J. Sellmyer, Phys. Rev. B **65**, 134426 (2002).
24. R. S. Iskhakov, S. V. Komogortsev, A. D. Balaev, A. V. Okotrub, A. G. Kudashov, V. L. Kuznetsov, and Yu. V. Butenko, Pis'ma Zh. Éksp. Teor. Fiz. **78**, 271 (2003) [JETP Lett. **78**, 236 (2003)].
25. E. C. Stoner and E. P. Wohlfarth, Philos. Trans. R. Soc. London, Ser. A **240**, 599 (1948).
26. R. S. Iskhakov, S. V. Komogortsev, A. D. Balaev, and L. A. Chekanova, Pis'ma Zh. Éksp. Teor. Fiz. **72**, 440 (2000) [JETP Lett. **72**, 304 (2000)].
27. R. Skomski, J. Phys.: Condens. Matter **15**, R841 (2003).
28. V. A. Ignatchenko, Zh. Éksp. Teor. Fiz. **54**, 303 (1968) [Sov. Phys. JETP **27**, 162 (1968)].
29. V. A. Ignatchenko and R. S. Iskhakov, Fiz. Met. Metalloved., No. 6, 75 (1992).
30. A. V. Luk'yanenko and S. V. Komogortsev, in *Proceedings of the II Baikal International Conference on Magnetic Materials* (Irkutsk, 2003), p. 72.

Translated by I. Zvyagin

Physics of the Solid State, Vol. 47, No. 3, 2005, pp. 502–507. Translated from Fizika Tverdogo Tela, Vol. 47, No. 3, 2005, pp. 487–492.

MAGNETISM AND FERROELECTRICITY

Nuclear Spin Resonance of ^{53}Cr in Ferromagnetic $CuCr_2S_4 : Sb$

V. N. Berzhanskiĭ, A. I. Gorbovanov, and S. N. Polulyakh

Taurida National University, ul. Yaltinskaya 4, Simferopol, 95007 Ukraine

e-mail: roton@crimea.edu

Received May 27, 2004

Abstract—The influence of variable valence on NSR spectra of ^{53}Cr nuclei in ferromagnetic $CuCr_{2-x}Sb_xS_4$ ($x = 0, 0.02, 0.07$) at $T = 77$ K is considered. For quadrupole nuclei in locally anisotropic positions, the effects of variable valence result in averaging of not only the resonance frequency but also of the quadrupole and magnetic anisotropy constants. The significant difference between the experimental and calculated values of these constants indicates the important role of the intrinsic electronic contribution to the anisotropy of hyperfine fields of compounds containing Cr^{4+} ions. Additional lines caused by intrinsic and induced defects in the structure are observed in the spectra of doped and undoped compounds. *© 2005 Pleiades Publishing, Inc.*

1. INTRODUCTION

Ferromagnets based on chromium chalcogenide spinels ACr_2X_4 (where A = Cd, Hg, Cu, and others; X = S, Se, Te) form an important class of magnetically ordered materials. Most of them are semiconductors. Of these compounds, copper spinels $CuCr_2X_4$ stand out due to their metal conductivity and high temperatures of magnetic ordering [1]. When analyzing the physical properties of these compounds, it is important to determine the cation valence state. This can be done using the NSR method.

In magnetically ordered materials, the NSR frequency is controlled by the local hyperfine field at nucleus sites [2]. This field is directly proportional to the ion magnetic moment. A change in the valence state results in a changed magnetic moment, so the hyperfine field, to a first approximation, is directly proportional to the number of unpaired electrons.

The variable-valence effect consists in the ion valence that fluctuates in time taking on one of two possible values. These fluctuations in a paramagnetic nuclear-spin system result in a switching between two frequencies, an effect well-known in the theory of electron spin resonance (ESR) [3, 4]. If the fluctuation frequency is lower than the difference between the resonance frequencies in each state (slow switching), the magnetic resonance spectrum is a superposition of spectral lines. In the case of rapid switching, a single line at an averaged frequency is observed.

The influence of variable valence on the NSR spectra of ^{53}Cr nuclei in ferromagnetic $CuCr_2S_4$ was experimentally observed in [5, 6]. An analysis of the frequency position of spectral lines showed that both tri- and tetravalent chromium ions coexist at low temperatures. As the temperature increases, an additional line appears whose frequency position corresponds to a state with fractional valence $Cr^{3.5+}$. A further temperature increase strengthens this line, and, at $T = 77$ K, the chromium ions are observed to be predominantly in the $Cr^{3.5+}$ state.

Chromium ions in the spinel structure occupy tetrahedral sites with local symmetry $\bar{3}m$. In this case, the anisotropy of the local magnetic field and the electric quadrupole interactions have a significant effect on the spectral line shape. However, the spectral line shape was not discussed in [5, 6]. However, analysis of the NSR line shape yields information on the influence of vacancies and different-valence impurities on the physical properties of these compounds. As a rule, actual samples are nonstoichiometric and contain anion vacancies. In contrast to oxygen spinels, anion vacancies in chalcogenide spinels do not cause a change in the interatomic distances. For example, the $CuCr_2S_{4-y}$ structure remains homogeneous over the range $0 \le y \le 0.17$ [1].

When studying copper NSR in $CuCr_2S_4$, quadrupole broadening of spectral lines was established in [7] from the existence of multiphoton spin-echo signals, despite the fact that copper ions occupy tetrahedral sites, at which there should be no electric field gradient. This indicates local distortions of tetrahedral sites.

Impurity ions, as well as anion vacancies, have a significant effect on the physical properties of chalcogenide spinels. For example, when studying the magnetic properties of $CuCr_{2-x}Sb_xS_4$, the transition to the spin-glass phase was observed in [8] at high dopant concentrations, which indicates the strong influence of these impurities on exchange interactions.

This study is devoted to the influence of the variable valence, anion vacancies, and doping with antimony on the ^{53}Cr NSR line shape in copper sulfochromite.

1063-7834/05/4703-0502$26.00

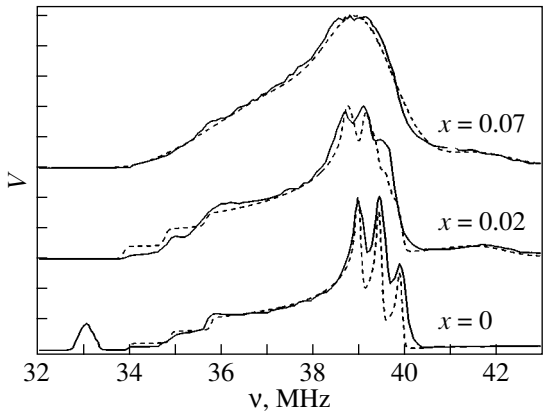

Fig. 1. Experimental and calculated ^{53}Cr NSR spectra (solid and dashed curves, respectively) in $CuCr_{2-x}Sb_xS_4$ at T = 77 K.

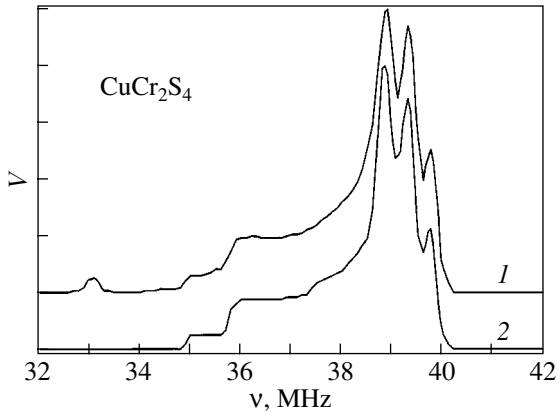

Fig. 2. ^{53}Cr NSR spectrum (*1*) before and (*2*) after sample annealing.

2. EXPERIMENTAL

NSR signals were studied using a pulsed incoherent NSR spectrometer. NSR spectra were measured from the dependence of the amplitude V of the two-pulsed echo signal on the oscillation frequency of the ac magnetic field of exciting pulses. Polycrystalline $CuCr_{2-x}Sb_xS_4$ samples with various degrees of Sb substitution (x = 0, 0.02, 0.07) at T = 77 K were studied. The ^{53}Cr NSR spectra of these samples are shown in Fig. 1 (solid curves).

It was experimentally found that the NSR spectrum of an undoped compound depends on the time interval between exciting pulses and consists of a main portion and an additional line at a frequency of 33 MHz, which is observed only at short (10–30 μs) intervals between exciting pulses. In doped compounds (Fig. 1), this line disappears and another additional, fast-relaxing line arises at high-frequencies, with its maximum being at approximately 41.5 MHz.

We assumed that the low-frequency line in the undoped compound is caused by chromium ions arranged near anion vacancies. To verify this assumption, a sample was annealed in chalcogen (sulfur) vapor (in a preliminarily evacuated quartz cell) for 9 h at 600°C. The masses of the sample and of the added sulfur were 585 and 50 mg, respectively. Figure 2 shows the ^{53}Cr NSR spectra for the sample before (curve *1*) and after annealing (curve *2*). We can see that annealing in sulfur vapor does indeed entail the disappearance of the additional spectral line.

3. DISCUSSION OF THE EXPERIMENTAL RESULTS

3.1. Main Portion of the Spectrum

When analyzing the main portion of the spectrum, we assume uniaxial local symmetry of B positions. The ^{53}Cr nucleus is a quadrupole with spin I = 3/2. The NSR spectrum of this nucleus is a triplet consisting of a central line (corresponding to the magnetic spectroscopic transition $\pm 1/2 \rightleftharpoons \mp 1/2$) and two quadrupole satellites. The resonance frequency ν depends on the angle θ between the electronic magnetization vector and the $\langle 111 \rangle$ crystallographic direction. The NSR frequency is given by

$$\nu = \nu_0 + (\nu_A \pm \nu_q)(3\cos^2\theta - 1 + \eta \sin^2\theta \cos 2\varphi), \quad (1)$$

where ν_0 is an isotropic constant, ν_A is the anisotropy constant, ν_q is the quadrupole constant, and η is the asymmetry parameter. This formula defines the resonance frequencies of the quadrupole satellites. For the central line, we have $\nu_q = 0$.

In [9], it was assumed that the angle θ takes on two fixed values (0, $\pi/2$) and the numerical constant values were taken as ν_0 = 38.47 MHz, $\nu_A \approx 0.34$ MHz, and $\nu_q \approx$ 0.6 MHz. In this case, major disagreement between theory and experiment is observed at low frequencies; this part of the spectrum was not observed in [9].

When analyzing the inhomogeneously broadened spectral line, we assume that the angle θ takes on any value with equal probability. In this case, a powder spectrum is observed [10] and the spectral line for a quadrupole nucleus with spin I = 3/2 can be described by a model spectrum consisting of three peaks,

$$g_1(\nu) = \frac{1}{8\pi\Delta\nu} \times \int_0^{2\pi} \frac{d\varphi}{\sqrt{(3-\eta\cos 2\varphi)(1-\eta\cos 2\varphi + (\nu_0 - \nu)/\Delta\nu)}} \quad (2)$$

in the range $\nu_0 - 2\Delta\nu < \nu < \nu_0 + \Delta\nu(1 - \eta\cos 2\varphi)$ and $g_1(\nu) = 0$ at other frequencies ν. For the central line and quadrupole satellites, $\Delta\nu$ is equal to ν_A and $\nu_A \pm \nu_q$, respectively. We also assume that the inhomogeneous broadening of the spectral line at a fixed angle θ is described by a Gaussian with standard deviation σ,

Table 1. Fitting constants for echo spectra of ^{53}Cr nuclei

x	ν_0, MHz	ν_A, MHz	ν_q, MHz	η	σ
0	37.95 ± 0.01	1.54 ± 0.01	0.45 ± 0.01	0	0.04 ± 0.01
0.02	37.80 ± 0.01	1.52 ± 0.01	0.45 ± 0.01	0.095 ± 0.005	0.06 ± 0.01
	40.32 ± 0.01*				0.30 ± 0.05*
0.07	38.10 ± 0.01	1.30 ± 0.01	0.46 ± 0.01	0.200 ± 0.005	0.46 ± 0.01
	40.64 ± 0.01*				0.46 ± 0.05*

* The values correspond to the high-frequency line at 41.5 MHz.

$$g_2(\nu - \nu') = \frac{1}{\sigma\sqrt{2\pi}}\exp\left(-\frac{(\nu-\nu')^2}{2\sigma^2}\right). \quad (3)$$

The observed line shape $g(\nu)$ can be written as [11]

$$g(\nu) = \int_{-\infty}^{\infty} g_1(\nu')g_2(\nu-\nu')d\nu'. \quad (4)$$

Expression (4) was used for numerical approximation of the main portion of the experimental spectra. Constants ν_0, ν_A, ν_q, and η were varied so as to minimize the root-mean-square deviation between calculated and experimental data. The high-frequency lines in doped samples were also fitted by Eq. (4). The fits are shown in Fig. 1 by dashed curves, and the corresponding parameters are listed in Table 1.

As follows from Table 1, doping with antimony increases the inhomogeneous broadening σ, which is typical of NSR in magnetically ordered materials. Moreover, the asymmetry parameter η also increases. This is due to the fact that both the anisotropy and quadrupole constants are sensitive to the charges and magnetic moments localized at lattice sites. The increase in the asymmetry parameter is indicative of a decrease in the local neighborhood symmetry caused by antimony ions substituted for chromium ions.

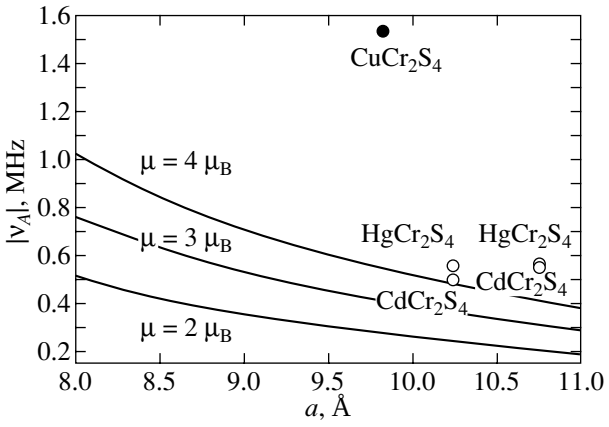

Fig. 3. Calculated lattice contribution to the anisotropy constant.

3.2. Anisotropy Constant

The anisotropy constant includes intrinsic and lattice contributions. To estimate the lattice contribution, we use the model of point magnetic dipoles, within which the fields exerted on nuclei by the magnetic moments of lattice ions are calculated.

In the case of chromium chalcogenide spinels, it is sufficient to consider only the magnetic moments of chromium ions. We assume that the magnetic moments of all ions are oriented along the same crystallographic direction due to exchange coupling. Since the dipole field decreases rather slowly with distance, calculations cannot be restricted to only the first coordination shell; the contributions of more distant ions should also be included, which improves the field calculation accuracy. Calculations show that, with inclusion of ions separated from a given ion by a distance no longer than six cell parameters (14460 ions), the dipole field is calculated with an accuracy of better than 0.5%.

In Fig. 3, the solid curves correspond to the lattice contributions to the anisotropy constant calculated as a function of the cell parameter at various values of the magnetic moments of ions occupying *B* positions in the spinel structure.

It is of interest to compare the calculated and experimental data for a number of chalcogenide spinels. In Fig. 3, open circles are experimental values of the anisotropy constant at $T = 4.2$ K, taken from [12]. The numerical values of the unit cell parameter are taken from [1]. In these compounds, chromium is in the trivalent state and we can assume with good accuracy that there are three Bohr magnetons per ion. As follows from Fig. 3, the lattice contribution is insufficient for describing the experimental values and, therefore, the contribution from the electron shell of an ion to the anisotropy of the local magnetic field exerted on its own nucleus should be included. Most likely, this contribution is from covalent effects, which result in an electron density transfer to the e_g orbital of the chromium ion.

The closed circle in Fig. 3 corresponds to the experimental value of the anisotropy constant in $CuCr_2S_4$ cal-

culated using Eq. (1). The $CuCr_2S_4$ cell parameter is also taken from [1]. As follows from Fig. 3, the deviation of the experimental value from the value calculated within the model of point dipoles for copper spinel is significantly higher than that calculated for cadmium and mercury spinels. This difference is explained by the chromium valence state in $CuCr_2S_4$.

Indeed, at $T = 77$ K, chromium can be in the Cr^{3+} and Cr^{4+} states with equal probability. The Cr^{4+} state exhibits strong spin–orbit coupling, which is indicative of a significant deviation of the electron shell symmetry from spherical; therefore, the contribution from this electron shell to the anisotropy constant is substantial.

Based on the experimental value of the anisotropy constant in $CuCr_2S_4$, we can estimate this constant for the Cr^{4+} state. Since rapid exchange takes place in the case under consideration, the experimental value of the anisotropy constant in $CuCr_2S_4$ is its average over the Cr^{3+} and Cr^{4+} states:

$$\nu_A(Cr^{3.5+}) = [\nu_A(Cr^{3+}) + \nu_A(Cr^{4+})]/2. \quad (5)$$

Assuming that the anisotropy constant of the Cr^{3+} ion in $CuCr_2S_4$ is of the same order of magnitude as in other chalcogenide spinels, namely, $\nu_A(Cr^{3+}) \approx 0.5$–$0.6$ MHz, we obtain $\nu_A(Cr^{4+}) \approx 2.3$–$2.4$ MHz.

Substitution of Sb^{5+} for chromium ions in spinel octahedral sites should decrease the fraction of tetravalent chromium ions, which, in turn, should vary the anisotropy constant away from the value of $\nu_A(Cr^{4+})$. As follows from Table 1, an increase in the dopant concentration indeed causes ν_A to decrease.

3.3. Quadrupole Constant

The quadrupole constant ν_q in a uniaxial crystallographic position is defined by the nucleus quadrupole moment Q and the electric field gradient (EFG) V_{zz} at the nucleus site: $\nu_q = eQV_{zz}/4h$ (in the case of spin $I = 3/2$). The EFG tensor component V_{zz} can be written as the sum of the lattice contribution V_{zz}^l and the intrinsic (or valence) contribution V_{zz}^e [13]:

$$V_{zz} = (1 - \gamma_\infty)V_{zz}^l + (1 - R)V_{zz}^e, \quad (6)$$

where R and γ_∞ are the screening and antiscreening constants, respectively.

The lattice contribution can be estimated in terms of the model in which every ion is a point charge of a corresponding value. Moreover, the local symmetry of the anion positions in the spinel structure allows the existence of an electric dipole moment; therefore, the dipole contribution to the quadrupole constant can be more significant than the contribution of only point charges [14].

The necessity of considering electric dipole moments of anions entails a two-stage calculation of the quadrupole constant; we calculate the dipole moments first and then the lattice contribution itself.

Table 2. Electric field gradient at the chromium nucleus sites

Compound	Cell parameter, Å	Anion parameter u	ν_q, MHz		
			calculation		experiment
			model of point charges	model of point charges and dipoles	
$CdCr_2S_4$	10.240	0.3901	0.047	0.594	0.95
$CdCr_2Se_4$	10.755	0.3894	0.027	0.568	0.98
$CuCr_2S_4$	9.814	0.3841	–0.09	0.740	0.45
$CuCr_2Se_4$	10.334	0.38	–0.149	0.589	0.097
$HgCr_2S_4$	10.237	0.391	0.067	0.649	0.95
$HgCr_2Se_4$	10.753	0.389	0.019	0.568	0.99

The dipole moments are calculated using an iterative procedure. Initially, the electric field at the anion site is assumed to be due to only the point electric charges (of both cations and anions). Based on the calculated field, the electric dipole moments of the anions are calculated, and then the procedure is repeated again with inclusion of the dipole fields of the anions. The calculation is complete when the new value of the dipole moment is identical to the preceding value to within a specified accuracy.

The lattice contribution ν_q^l is calculated with an accuracy of better than 1% for a number of chromium chalcogenide spinels with inclusion of ions within a sphere six cell parameters in radius. The results are shown in Table 2. The numerical values of the anion polarizabilities are taken from [15], and the structural data are taken from [1].

In contrast to the anisotropy constant, the calculated quadrupole constants ν_q^l cannot be used for direct comparison with the experimental values, because the experimentally observed value of ν_q differs from the calculated value of ν_q^l by a factor of $1 - \gamma_\infty$, where γ_∞ is the antiscreening factor [13].

Table 2 lists the experimental values of the quadrupole constant for cadmium and mercury spinels taken from [12]. In these compounds, the chromium ion is in the Cr^{3+} state at 4.2 K. Assuming the Cr^{3+} electron shell to be spherically symmetric to a first approximation, we disregard the contribution from the valence electrons to the field gradient at the nucleus site. Then, by comparing the calculated and experimental values of the quadrupole constant, we find that $1 - \gamma_\infty = 1.46$–1.73. To a first approximation, due to the rather narrow range of numerical values of the factor $1 - \gamma_\infty$, we can restrict our consideration to only the lattice contribution in the case of Cr^{3+} ions.

In copper sulfochromite, the $Cr^{3+} \rightleftharpoons Cr^{4+}$ exchange frequency is higher than the difference between the quadrupole splittings of the NSR spectra in

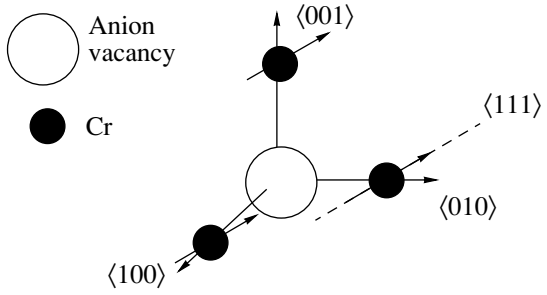

Fig. 4. Anion vacancy–based impurity center.

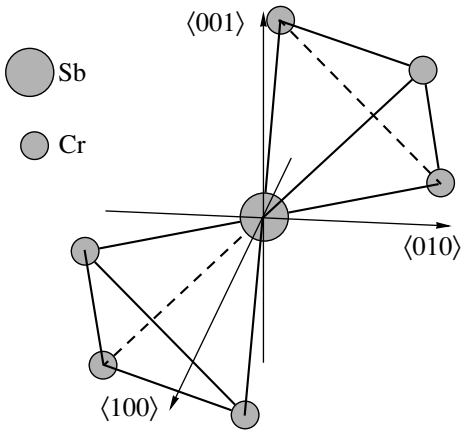

Fig. 5. Antimony ion arrangement in the spinel structure.

each state. Therefore, we can calculate ν_q^l for copper sulfochromite under the assumption that the copper ion is monovalent and that the chromium valence is +3.5 (Table 2). When comparing the calculated and experimental results, we assume that the experimentally observed value of the quadrupole constant is equal to its average over the Cr^{3+} and Cr^{4+} states,

$$\nu_q(Cr^{3.5+}) = [\nu_q(Cr^{3+}) + \nu_q(Cr^{4+})]/2.$$

Moreover, we assume that "defreezing" of the orbital angular momentum for the Cr^{4+} ion is so small that the contribution from the valence electrons to the field gradient at the nucleus site can be neglected to a first approximation. In this case, we obtain $1 - \gamma_\infty = 2.87$–3.14 for Cr^{4+}. This value of the antiscreening factor for tetravalent chromium is larger than that for trivalent chromium, which is in good agreement with the lowering of the electron shell symmetry in the Cr^{4+} state and with the results obtained for the anisotropy constant. The rather close antiscreening factors for the Cr^{3+} and Cr^{4+} ions result in the fact that doping with antimony does not have a significant effect on the quadrupole splitting of the NSR spectrum (Table 1).

3.4. Additional Spectral Lines

In the low-frequency region of the ^{53}Cr NSR spectrum, an additional fast-relaxing line is observed in undoped spinel. We assume that this line is caused by anion vacancies in $CuCr_2S_4$. It is known that the formation of anion vacancies in chromium chalcogenide spinels results in only local distortions in the lattice and does not change the general symmetry or cell parameter of $CuCr_2S_{4-y}$ in the range $0 \le y \le 0.17$.

Chromium ions occupy octahedral sites in the spinel structure. The nearest neighbors to the chromium ion are six anions. The lines connecting a chromium ion with its nearest neighbor anions are parallel to the ⟨100⟩-type directions of the spinel crystal structure. If an anion vacancy arises in the nearest neighborhood, then one of the ⟨100⟩ directions becomes symmetrically distinguished and the angle θ in Eq. (1) is measured from this axis (Fig. 4).

The anion vacancy charge at the impurity center is compensated due to a decrease in the chromium valence ($2Cr^{4+} \longrightarrow 2Cr^{3+}$). The anion vacancy in the nearest neighborhood of a chromium ion weakens the electron density transfer to the chromium ion. It seems that the decrease in the electron density transfer results in the local electron magnetization vector being fixed along a ⟨111⟩-type direction. In this case, the angle θ in Eq. (1) takes on the "magic" value at which the spectrum degenerates into a single line. The decrease in the transferred electron density also weakens the hyperfine magnetic field at the chromium nucleus site, which is observed experimentally.

Faster relaxation of the additional line in undoped $CuCr_2S_4$ also agrees well with the proposed mechanism, since the vacancy formation provides an additional channel for coupling between the nuclear-spin system and the lattice, which acts as a thermodynamic reservoir in relaxation processes.

Doping with antimony (even in small amounts) causes the additional low-frequency line to disappear. Apparently, in the presence of Sb^{5+} ions, whose positive charge is higher than that of major chromium ions, anion defects disappear.

We assume that the influence of the antimony impurity on the chromium NSR spectra is similar to that of anion vacancies; namely, the direction from the chromium ion to the nearest neighbor antimony ion (one of the ⟨110⟩ directions) becomes symmetrically distinguished (Fig. 5). However, the Sb^{5+} impurity defect does not fix the direction of the electron magnetization vector, so we assume that the angle θ can take on any value with equal probability, just as is the case for the main portion of the spectrum (Table 1).

When chromium ions are substituted for by antimony ions, the cation sublattice valence is compensated due to an increase in the number of Cr^{3+} ions at the impurity center (with the result that, e.g., at $x = 0.5$, only Cr^{3+} remains in the compound). Therefore, the impurity line frequency is observed in the high-frequency range in this case.

The presence of a high-frequency line in doped samples indicates the appearance of chromium ions (or their clusters) with high spin densities. In other words, substituting for Cr^{4+} ions with ions of a higher valence (Sb^{5+}) results in the formation of complexes that consist of two Cr^{3+} ions and one Cr^{4+} ion, between which fast electron exchange takes place. Since the magnetic moment of chromium ions is dictated by the number of unpaired 3*d* electrons, a complex of three crystallographically equivalent ions ($Cr^{3+} \rightleftharpoons Cr^{4+} \rightleftharpoons Cr^{3+}$) exchanging through one 3*d* electron will have a magnetic moment of $(8/3)\mu_B$ per ion. The frequency position of the high-frequency line (Table 1) corresponds to ions of these complexes.

4. CONCLUSIONS

An analysis of the ^{53}Cr NSR spectra in $CuCr_{2-x}Sb_xS_4$ at $T = 77$ K has shown that the effects of variable valence of quadrupole nuclei in locally anisotropic positions result in averaging of not only the resonance frequency but also of the quadrupole and magnetic anisotropy constants.

The equilibrium concentration of anion vacancies causes the formation of an additional low-frequency line in the ^{53}Cr NSR spectrum. This indicates weakening of exchange coupling of Cr ions at defect centers based on anion vacancies.

Sb^{5+}-based impurity centers yield an additional spectral line in the high-frequency region. The formation of this line is associated with a change in the ratio of the Cr^{3+} to Cr^{4+} ion concentration due to valence compensation.

The lattice model for calculating the dipole magnetic and electric fields is not capable of explaining the experimental values of the anisotropy of these fields. This necessitates inclusion of the contribution from the electron shell of ions. The determined values of the anisotropic and quadrupole constants of the Cr^{4+} ion are significantly higher than those for the Cr^{3+} ion due to the electronic configuration of the Cr^{4+} ion. The asymmetry of the electron cloud of the Cr^{4+} ion is caused by the spin–orbit coupling, which is much stronger for Cr^{4+} ions than for Cr^{3+} ions in $CdCr_2S_4$.

ACKNOWLEDGMENTS

The authors are grateful to T.G. Aminov and G.G. Shabunina for preparing the samples and to S.V. Yagupov, N.S. Nepevnaya, and N.E. Polekhin for their assistance in annealing the samples.

REFERENCES

1. K. P. Belov, Yu. D. Tret'yakov, I. V. Gordeev, L. I. Koroleva, and Ya. A. Kesler, *Magnetic Semiconductors—Chalcogenide Spinels* (Mosk. Gos. Univ., Moscow, 1981) [in Russian].
2. M. I. Kurkin and E. A. Turov, *Nuclear Magnetic Resonance in Magnetoordered Substances and Its Applications* (Nauka, Moscow, 1990) [in Russian].
3. K. M. Salikhov, A. G. Semenov, and Yu. D. Tsvetkov, *Electron Spin Echo and Its Application* (Nauka, Novosibirsk, 1976) [in Russian].
4. N. M. Bazhin and K. M. Salikhov, *EPR Relaxation of Free Radicals in Liquids* (Nauka, Novosibirisk, 1973) [in Russian].
5. N. M. Kovtun, V. K. Prokopenko, and A. A. Shemyakov, Solid State Commun. **26**, 877 (1978).
6. N. M. Kovtun, V. K. Prokopenko, A. A. Shemyakov, T. G. Aminov, and G. G. Shabunina, Fiz. Tverd. Tela (Leningrad) **24** (9), 2814 (1982) [Sov. Phys. Solid State **24**, 1593 (1982)].
7. V. N. Berzhanskiĭ, A. I. Gorbovanov, and S. N. Polulyakh, Zh. Éksp. Teor. Fiz. **115** (6), 2106 (1999) [JETP **88**, 1151 (1999)].
8. T. G. Aminov, T. I. Arbuzova, G. G. Shabunina, and V. M. Novotvortsev, in *NMMM-2000* (Mosk. Gos. Univ., Moscow, 2000), p. 188 [in Russian].
9. H. Figiel, J. Kukucz, and A. Bombik, J. Magn. Magn. Mater. **15–18**, 701 (1980).
10. M. Mehring, *High-Resolution NMR Spectroscopy of Solids* (Springer, Berlin, 1976; [U. Haeberlen and M. Mehring], Mir, Moscow, 1980).
11. I. V. Aleksandrov, *Theory of Magnetic Relaxation. Relaxation in Liquids and Solid Nonmetallic Paramagnets* (Nauka, Moscow, 1975) [in Russian].
12. G. H. Stauss, Phys. Rev. **181**, 636 (1969).
13. R. E. Watson and A. J. Freeman, in *Hyperfine Interactions*, Ed. by A. J. Freeman and R. B. Frankel (Academic, New York, 1967).
14. R. Kirsch, A. Gerard, and M. Wautelet, J. Phys. C **7**, 3633 (1974).
15. C. Kittel, *Introduction to Solid State Physics*, 5th ed. (Wiley, New York, 1976; Nauka, Moscow, 1978).

Translated by A. Kazantsev

Physics of the Solid State, Vol. 47, No. 3, 2005, pp. 508–512. Translated from Fizika Tverdogo Tela, Vol. 47, No. 3, 2005, pp. 493–497.

MAGNETISM AND FERROELECTRICITY

Dependence of the Structure and Magnetic Properties of FeTaN Films on Nitrogen Concentration

A. S. Kamzin*, F. Wei, Z. Yang**, and S. A. Kamzin***

**Ioffe Physicotechnical Institute, Russian Academy of Sciences, Politekhnicheskaya ul. 26, St. Petersburg, 194021 Russia*
e-mail: Kamzin@pop.ioffe.rssi.ru
***Research Institute of Magnetic Materials, Lanzhou University, Lanzhou, 730000 China*
Received May 27, 2004

Abstract—The structural morphology and magnetic properties of thin FeTaN films with a high Ta content (10 wt %) prepared by annealing compounds deposited by reactive rf magnetron sputtering in an Ar + N gas mixture are studied. The dependence of the properties of FeTaN films on their nitrogen content and annealing temperature were established. The deposition and thermal treatment regimes favoring the preparation of thin nanostructural FeTaN films with high soft magnetic characteristics [B_s = 1.6 T, H_c = 0.2 Oe, and μ_1 (1 MHz) = 3400] were determined. © *2005 Pleiades Publishing, Inc.*

1. INTRODUCTION

Thin ferrite films are currently attracting intense research interest because they offer considerable application potential for use, for instance, in high-density magnetic-recording media, magnetic sensors, microwave applications, etc. [1–3]. The advantages of ferrites in the form of thin films lie in the rich diversity of their magnetic and electrical properties, high chemical stability, and mechanical strength. An important application of magnetic films is associated with devices developed for superhigh-density information recording and reading. Indeed, films of Ba–*M*-type hexagonal ferrites are very promising as carriers in this case due to their high coercivity. In turn, the use of such information carriers imposes stringent requirements on recording devices. To achieve superdense information recording on such carriers, the saturation field in the core of a write head should be as high as ~20 kG or even higher [4, 5]. Nanostructural Fe*X*N films, where *X* = Hf, Nb, Zr, Si, B, or Al, satisfy these requirements (see, e.g., [6] and references therein). However, each of these ions introduced as a third element affects the magnetic properties of the synthesized material differently. It was suggested in [7] that doping with Ta could substantially improve the soft magnetic characteristics of Fe–N films due to the relatively strong interaction of Ta with nitrogen ions [8], which enhances the solubility of N atoms in FeTaN films and improves their soft magnetic properties. FeTaN films 0.6 μm thick and with a high (12.5 wt %) tantalum content were prepared [9] and found to be amorphous after deposition. Annealing of amorphous FeTaN compounds deposited at a nitrogen partial pressure of 7.5% yielded films with sufficient soft magnetic characteristics [9]. It was revealed in [10] that the magnetic properties of FeTaN films have the best thermal stability. The technology of preparation of FeTaN films with fairly high soft magnetic characteristics is described in [11].

As is evident from available publications, there is still much to refine in the technology of preparation of magnetic films with preset properties. Thin magnetic films are prepared using a variety of methods, among them sol-gel technology, magnetron sputtering, laser ablation, molecular beam epitaxy, etc. (see, e.g., [11–13]). The ratio of components in the compound and the technological regime employed (sputtering conditions, gas pressure at sputtering, substrate temperature) affect the properties of Fe*X*N films very strongly. Annealing of deposited compounds is a process essential to the formation of these properties. The annealing temperature can be varied within a broad range, which makes it possible to purposefully control the film properties. Hence, film annealing requires thorough study. This communication reports on a study of the effect of the preparation conditions and concentration of N ions on the microstructure and magnetic properties of thin (~1000 nm) Fe*X*N films for *X* = Ta.

2. EXPERIMENTAL CONDITIONS

Thin FeTaN films were prepared by rf reactive magnetron sputtering from a composite target in a mixture of Ar and N_2 gases onto glass plate substrates. The composite targets were pure iron platelets, with part of them screened by a foil of highly purified Ta. The content of Ta ions in sputtered films can be controlled by properly varying the area of the Fe plate screened by a Ta foil. Experiments showed that, by screening 20% of the iron plate area by a Ta foil, an FeTaN compound can be prepared in which 10 wt % of Fe ions are replaced by Ta ions. The number of N ions in FeTaN was determined by the partial pressure of nitrogen in the Ar + N_2 gas

mixture in the sputtering chamber during the film deposition. The conditions of FeTaN film preparation are listed in the table. The films were annealed in a vacuum furnace at a pressure of ~1×10^{-5} Torr.

Structural characterization of the films was carried out with an x-ray diffractometer. Phase analysis was performed by x-ray diffractometry and Mössbauer spectroscopy (MS) with detection of conversion and Auger electrons (conversion electron MS). The film morphology was studied using electron transmission and atomic-force microscopy (AFM). The saturation magnetization M_s and the coercivity H_c of films were measured with a high-sensitivity (10^{-3} emu) vibrating-sample magnetometer. The anisotropy energy was derived from *B–H* hysteresis loops as described in [14].

Conditions of FeTaN film preparation

Pressure in chamber	5×10^{-7} Torr
Pressure at sputtering	2×10^{-3} Torr
Partial nitrogen pressure in the Ar + N mixture	0–10%
RF sputtering voltage	2.8 kV
Substrate temperature	20°C
Film thickness	400 nm
Deposition rate	20–28 nm/min

3. EXPERIMENTAL RESULTS AND DISCUSSION

Figure 1a presents x-ray diffraction patterns obtained after deposition of FeTaN films at different partial nitrogen pressures $P(N_2)$ by sputtering in an Ar + N_2 gas mixture. As follows from the diffractograms in Fig. 1a, nitrogen-free FeTa films consist of α-Fe crystallites in which the interplanar spacing $d(110) = 2.073$ Å exceeds that for pure α-Fe (2.026 Å). This suggests that Ta ions substitute for Fe ions in the α-Fe lattice to form an α-Fe(Ta) substitutional solid solution. The (110) diffraction line of the α-Fe state broadens with increasing partial pressure $P(N_2)$ and shifts toward smaller angles. These changes can be explained by assuming that nitrogen atoms enter the α-Fe lattice interstitially and stretch it. Films deposited at pressures $P(N_2) \geq 3\%$ do not have a crystalline structure; i.e., they are practically amorphous. This conclusion is corroborated by direct measurements (below room temperature) of the magnetic characteristics of films deposited at $P(N_2) = 5\%$ (Fig. 2). If a film were to consist only of nanosized α-Fe crystallites, the coercivity H_c would be lower than its room-temperature value or remain constant, because H_c depends on the exchange coupling between grains and should be inversely proportional to the magnetization M_s [15]. However, as is evident from Fig. 2, both M_s and H_c grow monotonically as the temperature decreases to –173°C.

Figure 3 displays the dependence of the saturation induction B_s and coercivity H_c of as-deposited films on the partial nitrogen pressure. As seen from Fig. 3, unannealed films do not have the properties needed for the development of magnetoresistive heads. As shown in [15], the main condition for the formation of the required soft magnetic characteristics in such materials

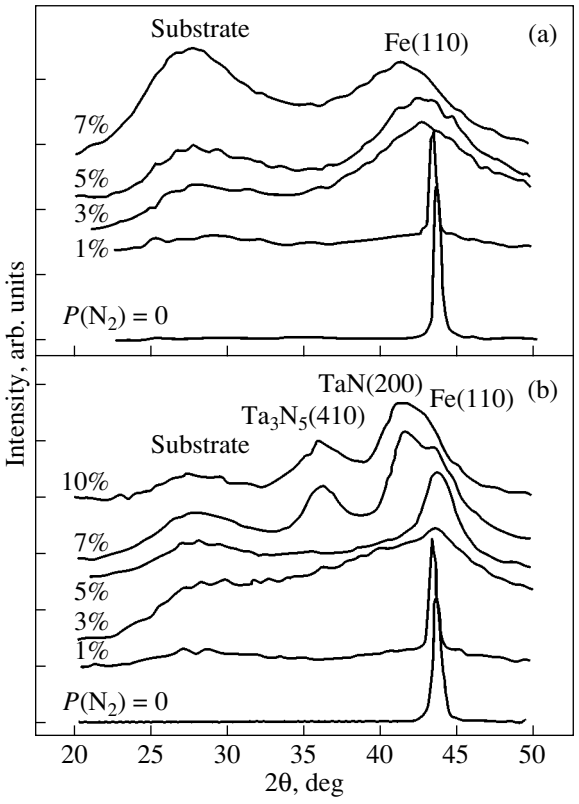

Fig. 1. X-ray diffractograms (a) of as-deposited films and (b) after their annealing at 450°C plotted vs. partial nitrogen pressure $P(N_2)$ in the sputtering chamber.

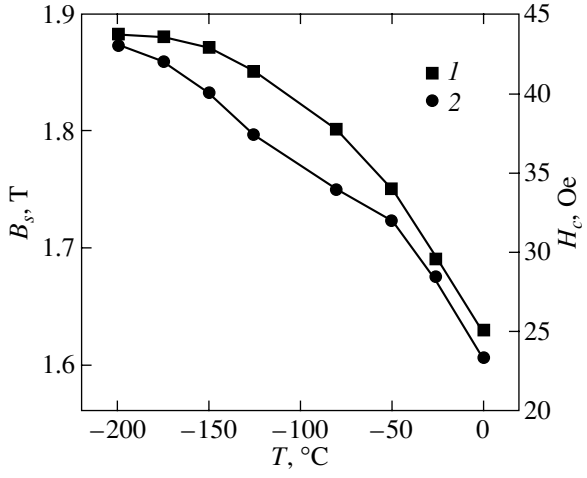

Fig. 2. (*1*) Saturation induction B_s and (*2*) coercivity H_c (measured below room temperature) of films deposited at $P(N_2) = 5\%$.

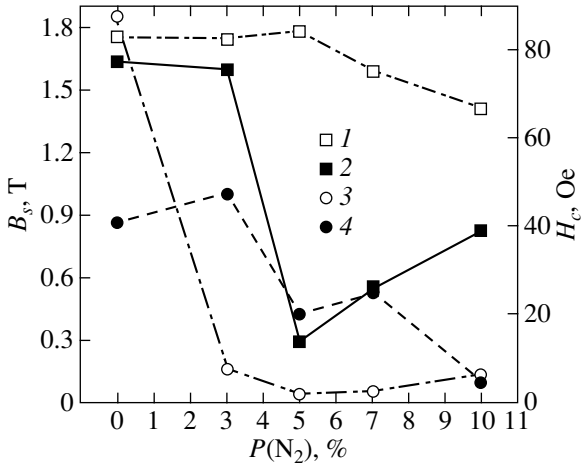

Fig. 3. (*1*, *2*) Saturation induction B_s and (*3*, *4*) coercivity H_c measured (*2*, *4*) after deposition of the films and (*1*, *3*) following their annealing at 450°C and plotted vs. partial nitrogen pressure $P(N_2)$.

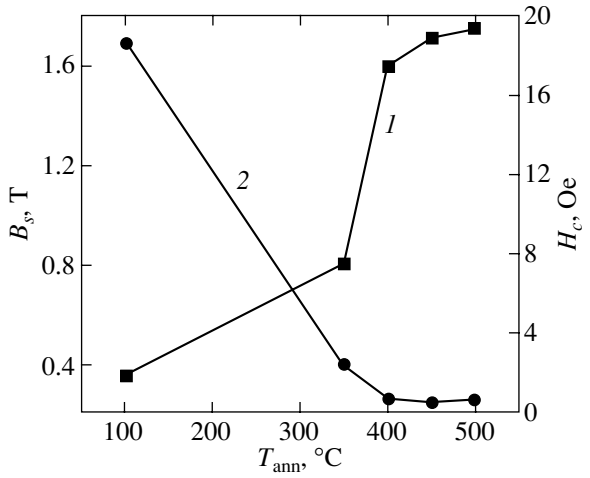

Fig. 4. (*1*) Saturation induction B_s and (*2*) coercivity H_c of films deposited at $P(N_2)$ = 5% as a function of annealing temperature T_{ann}.

is a small or very low magnetic anisotropy (a few joules per cubic meter). In α-Fe with grains of the order of 10 nm in size, the magnetic anisotropy is a few joules per cubic meter because the nanosized α-Fe crystallites are coupled by exchange interaction. In polycrystalline nitrogen-free films, the size of the α-Fe particles exceeds the exchange coupling length between them. In this case, the magnetization process depends on the magnetocrystalline anisotropy of these grains, as is the case with bulk iron samples (H_c = ~50 Oe).

As already mentioned, the most efficient method of preparing nanostructural alloys involves thermally controlled crystallization of amorphous compounds. Therefore, we studied the dependence of the magnetic characteristics on the annealing temperature T_{ann} on films deposited at $P(N_2)$ = 5%. The experimental data thus obtained are presented in Fig. 4. For films annealed at low temperatures, the saturation induction B_s is seen to be low, whereas the coercivity H_c is high and coincides with that measured on amorphous films. Increasing the annealing temperature brings about a monotonic increase in the saturation induction B_s and a smooth falloff of the coercivity H_c. The quantities B_s and H_c are observed to undergo sharp changes in the temperature range T_{ann} = 350–400°C. As the annealing temperature is increased still further, B_s and H_c do not change, which indicates termination of the crystallization of α-Fe nanoparticles in the film. Thus, the optimum temperature for film crystallization lies in the region 400–450°C. This is why the deposited amorphous compounds were annealed in a vacuum furnace at 450°C.

Figure 1b shows x-ray diffractograms of films taken after annealing for different partial nitrogen pressures $P(N_2)$. The diffractograms in Fig. 1b taken before and after annealing do not exhibit any pronounced differences for films deposited at pressures $P(N_2) < 3\%$. However, deposition at pressures $P(N_2) \geq 3\%$ produces nanosized crystallites, which become embedded in the amorphous matrix. The products of crystallization in films deposited at different $P(N_2)$ are different.

Figure 3 plots the saturation induction B_s and coercivity H_c of annealed films as a function of partial nitrogen pressure $P(N_2)$. It can be seen that annealing increases the saturation induction B_s of the films, with the enhancement of B_s being the largest in films deposited at high pressures $P(N_2)$. In films deposited at pressures $P(N_2) < 5\%$, the value of B_s remains practically unchanged. Films prepared at $P(N_2) \geq 5\%$ exhibit a monotonic decrease in B_s. The dependence of the film coercivity H_c on $P(N_2)$ is somewhat different, as is evident from Fig. 3. As $P(N_2)$ increases, H_c decreases rapidly to reach its lowest value at $P(N_2) = 5\%$, after which it grows smoothly. Such changes in magnetic properties can be assigned to the crystallization of compounds that differently affect the coercivity of the films. Indeed, in films deposited at pressures $P(N_2) \leq 5\%$, the enhancement of B_s should be ascribed to annealing-induced crystallization of predominantly nanosized α-Fe particles. Annealing of films deposited at pressures $P(N_2) > 5\%$ initiates simultaneous crystallization of α-Fe nanoparticles and of the TaN compound. Figure 5 shows Mössbauer spectra of films deposited at a partial nitrogen pressure $P(N_2) = 5\%$ (Fig. 5a) and subsequently annealed at 450°C (Fig. 5b), as well as of a film deposited at $P(N_2) = 7\%$ and annealed at 450°C (Fig. 5c). The spectrum of the film deposited at $P(N_2) = 5\%$ (Fig. 5a) does not have a Zeeman line structure and consists of broad lines, which indicates that this compound is amorphous.

The Mössbauer spectra of films deposited at $P(N_2) = 5\%$ and annealed at 450°C (Fig. 5b) demonstrate a Zeeman sextuplet with linewidths of 0.30 ± 0.03 mm/s and an effective magnetic field at the iron-ion nucleus sites

of 333.8 ± 0.4 kOe. The areas of the Zeeman sextuplet lines are in the ratio 3 : 4 : 1 : 1 : 4 : 3. This means that the magnetic moments of iron ions in the film are perpendicular to the wave vector of the γ radiation striking the film surface along the normal. Therefore, the magnetic moments of iron ions are confined to the film plane. In the region of zero velocity of the Mössbauer source, the spectrum exhibits lines suggesting that the films have a small amount of a compound in which iron is in the paramagnetic state. The parabolic shape of the background spectral line also implies the presence of a small amount of iron in the amorphous state. Atomic force microscopy of a film obtained at $P(N_2)$ = 5% and T_{ann} = 450°C reveals α-Fe grains ~5–10 nm in size, which is less than the ferromagnetic-exchange length. The fraction of nanocrystallites in the volume of these films is the largest. Thus, AFM, x-ray diffraction (Fig. 1b), and Mössbauer spectroscopy measurements (Fig. 5b) suggest that annealing of films deposited at $P(N_2)$ = 5% causes primarily α-Fe nanoparticles to crystallize in the amorphous matrix, with the (110) plane of these α-Fe grains being oriented predominantly parallel to the film surface.

As seen from Fig. 5c, the Mössbauer spectrum of a film deposited at $P(N_2)$ = 7% and then annealed at 450°C consists of broad lines (~2 mm/s) of the Zeeman sextuplet. An analysis of this spectrum revealed it to be actually a superposition of lines belonging to the α-Fe state and Ta_xN_y-type compounds. The total sextuplet line areas are approximately in the ratio 3 : 4 : 1 : 1 : 4 : 3, which indicates that the magnetic moments of the iron ions are confined to the film plane. In the region of zero velocity, the spectrum contains lines indicating the presence of a small amount of iron compounds in the paramagnetic state in the films. Hence, the data obtained using Mössbauer spectroscopy may be considered direct evidence supporting the validity of the results obtained in AFM and x-ray diffraction studies, which suggest simultaneous annealing-induced crystallization of α-Fe nanoparticles and compounds of the TaN type in films deposited at pressures $P(N_2) > 5\%$.

It was conjectured in [16] that, if a segregated TaN compound is dense enough, it blocks the exchange coupling between α-Fe particles, thus destroying the soft magnetic properties of the films. This conjecture is borne out by measurements of the magnetic characteristics of these films, which are presented in Fig. 3.

Films in which only nanosized α-Fe particles crystallize have high soft magnetic characteristics, because the effective anisotropy in this case is substantially suppressed by exchange coupling among the α-Fe nanoparticles [14]. Note that, as follows from experiments, annealing of films deposited at $P(N_2)$ = 5% brings about the formation primarily of α-Fe nanoparticles crystallizing in the amorphous matrix, with the (110) plane of these α-Fe grains being oriented predominantly parallel to the film surface.

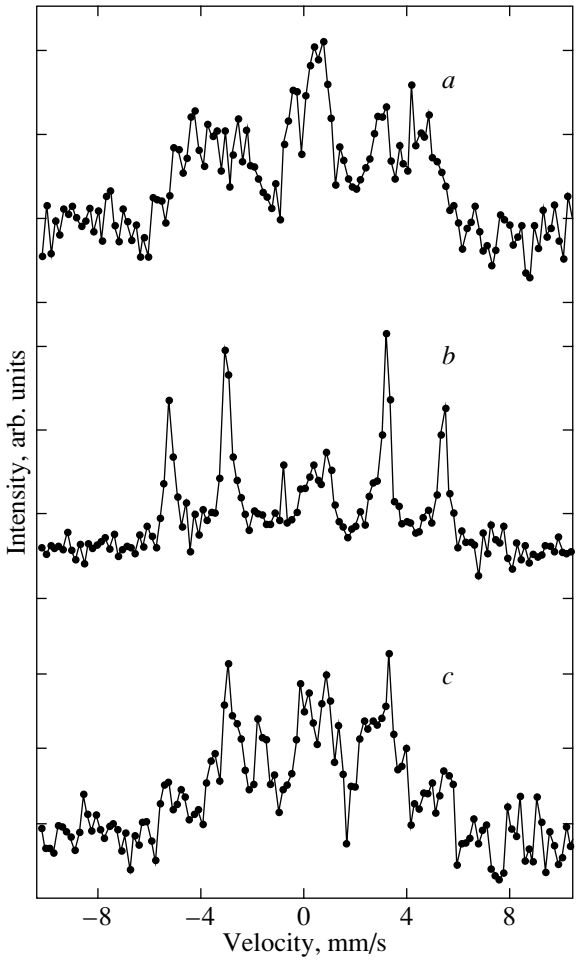

Fig. 5. Conversion electron Mössbauer spectra of films (a) deposited at $P(N_2)$ = 5%, (b) deposited at $P(N_2)$ = 5% and then annealed at 450°C, and (c) deposited at $P(N_2)$ = 7% and annealed at 450°C.

4. CONCLUSIONS

Our studies have established the conditions favorable for the preparation of thin soft magnetic FeTaN films with a tantalum content of 10 wt % by using controlled crystallization of deposited amorphous compounds. The dependences of the microstructure and magnetic properties on partial nitrogen pressure in the sputtering chamber have been determined. It was shown that Ta ions in nitrogen-free films substitute for Fe ions in the α-Fe lattice to form a crystallizable α-Fe(Ta) solid solution. The films deposited at higher partial nitrogen pressures are practically amorphous in structure. Annealing gives rise to the formation of nanocrystalline α-Fe and other TaN-type phases, which are embedded in the amorphous matrix of the films. It was established that films deposited at a partial nitrogen pressure $P(N_2)$ = 5% have high soft magnetic characteristics. This is accounted for by the fact that the films thus prepared are made up primarily of nanosized α-Fe crystallites distributed over an amorphous matrix, with

the α-Fe grains being less than 10 nm in size. The films have a cluster structure and possess induced uniaxial anisotropy, which originates from N ions occupying octahedral positions in the α-Fe lattice.

ACKNOWLEDGMENTS

This study was supported by the Russian Foundation for Basic Research (project no. 02-02-39006) and the National Science Foundation of China.

REFERENCES

1. X. Sui and M. H. Kryder, Appl. Phys. Lett. **63**, 1582 (1993).
2. T. Kiyomura, Y. Maruo, and M. Gomi, J. Appl. Phys. **88**, 4768 (2000).
3. B. Y. Wong, X. Sui, D. E. Laughlin, and M. H. Kryder, J. Appl. Phys. **75**, 5966 (1994).
4. O. Kohomoto, IEEE Trans. Magn. **27**, 3640 (1991).
5. S. Wang and M. H. Kryder, J. Appl. Phys. **69**, 5625 (1991).
6. D. Zheng, Y. Ma, D. Wu, T. Xie, F. Wei, and Z. Yang, Phys. Status Solidi A **193**, 61 (2002); B. Ma, F. L. Wei, X. X. Liu, C. T. Xiao, and Z. Yang, Mater. Sci. Eng. B **57**, 96 (1999).
7. R. D. Pehkle and F. Elliott, Trans. AIME **218**, 1088 (1960).
8. K. Nakauishi, O. Shimiz, and S. Yoshida, IEEE Trans. Magn. **28**, 7128 (1992).
9. W. C. Chang, D. C. Wu, J. C. Lin, and C. J. Chen, J. Appl. Phys. **79**, 5159 (1996).
10. M. K. Minor, B. Viala, and J. A. Barnard, J. Appl. Phys. **79**, 5005 (1996).
11. Y. Ma, X. Li, T. Xie, F. Wei, and Z. Yang, Mater. Sci. Eng. B **103**, 233 (2003).
12. F. Chen, Z. Zhigan, Z. Xu, C. Liao, and C. Yan, Thin Solid Films **339**, 109 (1999).
13. S. A. Chambers, R. F. C. Farrow, S. Maat, M. F. Toney, L. Folks, J. G. Catalano, T. P. Trainor, and G. E. Brown, Jr., J. Magn. Magn. Mater. **246**, 124 (2002).
14. K. H. J. Buschow, *Handbook of Magnetic Materials* (North-Holland, Amsterdam, 1997), Vol. 10, p. 433.
15. G. Herzer, IEEE Trans. Magn. **26**, 1937 (1990).
16. N. Hasegawa and M. Saito, IEEE Trans. Magn. Jpn. **6**, 91 (1991).

Translated by G. Skrebtsov

Physics of the Solid State, Vol. 47, No. 3, 2005, pp. 513–516. Translated from Fizika Tverdogo Tela, Vol. 47, No. 3, 2005, pp. 498–500.

MAGNETISM AND FERROELECTRICITY

^{55}Mn Spin Relaxation with the Participation of Mobile Carriers in Doped Perovskites

N. P. Fokina and M. O. Élizbarashvili

Tbilisi State University, Tbilisi, 380028 Georgia

e-mail: n_ fokina@caucasus.net

Received May 31, 2004

Abstract—Analytical expressions are derived for the rates of longitudinal and transverse nuclear spin relaxation under conditions of fast modulation of the magnitude and direction of a hyperfine field induced by unpaired electrons of an ion. The results obtained are used to explain the data available in the literature on the ^{55}Mn spin relaxation in the ferromagnetic metallic phase of doped perovskites, in which the modulation of the hyperfine field is caused by the hopping of e_g electrons between Mn^{3+} and Mn^{4+} ions. It is demonstrated that, within this model, the rates of longitudinal and transverse relaxation are characterized by the same temperature dependence and their ratio is independent of temperature, which is in agreement with the experimental data. © *2005 Pleiades Publishing, Inc.*

1. INTRODUCTION

In recent years, increased interest has been expressed by researchers in manganites of the general formula $La_{1-x}A_xMnO_3$ (A = Ca, Sr, Pb). This is explained by the fact that these materials exhibit unusual magnetic and transport properties, which are controlled primarily by the content x of Mn^{4+} ions. According to the model of double exchange, which was proposed by Zener [1], the e_g electrons can easily execute hoppings (with a frequency f_{hop}) from Mn^{3+} to Mn^{4+} ions, provided the spins at both sites have parallel orientations. Consequently, ferromagnetic ordering of manganites has often been accompanied (especially in the case of doping at a level $x = 0.3$) by the formation of a ferromagnetic metallic phase with a drastically decreased electrical resistance.

Manganite compounds have been intensively studied using nuclear magnetic resonance (NMR) and, in particular, ^{55}Mn NMR [2–7]. Owing to the hyperfine interaction, the frequency f_{NMR} of ^{55}Mn NMR depends on the charge state of the ion; hence, at temperatures above the ordering temperature, the NMR lines of Mn^{3+} and Mn^{4+} ions are recorded individually. However, at temperatures below T_C, at which the manganite undergoes a transition from the paramagnetic insulating phase to the ferromagnetic metallic phase, these lines merge into a single line, because, in this temperature range, the hopping frequency exceeds the NMR frequency: $f_{hop} > f_{NMR}$ [2–7]. Savosta *et al.* [3–5] investigated the temperature dependences of the rates of longitudinal (T_1^{-1}) and transverse (T_2^{-1}) ^{55}Mn nuclear spin relaxation for this averaged spectrum. It was found that the temperature dependences of the relaxation rates T_1^{-1} and T_2^{-1} are identical to each other and that the ratio T_1/T_2 falls in the range from 10 to 60 and does not depend on temperature. This behavior is observed not only in the ferromagnetic metallic phase but, sometimes, also in the ferromagnetic insulating phase ($d\rho/dT < 0$, where ρ is the electrical resistivity), which indicates the presence of ferromagnetic metallic clusters in this phase [5].

The aforementioned similarity between the temperature dependences of the rates of longitudinal and transverse nuclear spin relaxation was qualitatively explained in [3]. The purpose of this work was to perform an analytical investigation of the ^{55}Mn nuclear spin relaxation occurring in samples with mobile carriers through the mechanism proposed in [3].

2. ANALYTICAL TREATMENT

Manganese ions in doped manganites are located in a crystal field, which is usually treated as the sum of the basic term of cubic symmetry and a small addition of crystal fields of lower symmetry. Following Section 3 in the paper by Kubo *et al.* [8], we will restrict our consideration to the specific case in which a Mn^{4+} ion resides in an octahedral cubic crystal field and a Mn^{3+} ion additionally experiences a relatively weak tetragonal crystal field due to the Jahn–Teller distortion; i.e., we will disregard crystal fields of lower (for example, orthorhombic) symmetry.

Let us consider nuclear spin relaxation in a zero external magnetic field. In a Mn^{4+} ion, the ^{55}Mn nucleus with a gyromagnetic ratio γ_n undergoes a contact hyperfine interaction with the electron shell. For a ferromagnetic phase with a preferred direction z (the easy mag-

1063-7834/05/4703-0513$26.00 © 2005 Pleiades Publishing, Inc.

netization axis), the effective nuclear spin Hamiltonian can be written in the form

$$\mathcal{H}_0(\mathrm{Mn}^{4+}) = -\gamma_n\hbar H_F^{4+} I^z = -\gamma_n\hbar H_{\mathrm{loc}}^z \mathrm{Mn}^{4+} I^z, \quad (1)$$

where H_F^{4+} is the effective contact hyperfine field in the Mn^{4+} ion in ferromagnetic manganite. This field differs from the effective hyperfine field in a free ion, which can be calculated, for example, by the Hartree–Fock method [9].

The symmetry of the environment of the nuclear spin in Mn^{3+} ions is lower than cubic symmetry; in this case, the tensor describing the electron–nuclear interaction is not reduced to a scalar [10]. In [8], the ^{55}Mn nuclear Hamiltonian for a Mn^{3+} ion with a tetragonal distortion of the environment was calculated in the following form:

$$\begin{aligned}\mathcal{H}_0(\mathrm{Mn}^{3+}) &= -\gamma_n\hbar\{[H_F^{3+} + (1/2)(3\cos^2\theta - 1)H']I^z \\ &\quad + I^x(3/4)H'\sin 2\theta\} \\ &\equiv -\gamma_n\hbar\{H_{\mathrm{loc}}^z(\mathrm{Mn}^{3+})I^z + H_{\mathrm{loc}}^x(\mathrm{Mn}^{3+})I^z\},\end{aligned} \quad (2)$$

where θ is the angle between the direction z and the tetragonal axis Z, the x axis lies in the plane containing the axes z and Z, and H' is the parameter of the dipole field induced by an e_g electron at the site of the nucleus removed over a distance r and averaged over the d wave functions. The absolute value of this parameter for a free Mn^{3+} ion can be determined from the expression [8]

$$|H'| = (4/7)|\mu_B|\langle r^{-3}\rangle,$$

where μ_B is the Bohr magneton. For the compounds under consideration, H_F^{4+}, H_F^{3+}, and H' are adjustable parameters.

The Hamiltonian of ^{55}Mn nuclei in manganites doped at a level x, which is averaged by e_g electron hoppings and corresponds to a single NMR line, has the form

$$\begin{aligned}\mathcal{H}_0(x) &= x\mathcal{H}_0(\mathrm{Mn}^{4+}) + (1-x)\mathcal{H}_0(\mathrm{Mn}^{3+}) \\ &= -\gamma_n\hbar\{\overline{H_{\mathrm{loc}}^z} I^z + \overline{H_{\mathrm{loc}}^x} I^x\}.\end{aligned} \quad (3)$$

Here, the averaging is performed over the distribution of Mn^{3+} and Mn^{4+} ions in accordance with the doping level:

$$\begin{aligned}\overline{H_{\mathrm{loc}}^{z,x}} &= (1-x)H_{\mathrm{loc}}^{z,x}(\mathrm{Mn}^{3+}) + xH_{\mathrm{loc}}^{z,x}(\mathrm{Mn}^{4+}), \\ \overline{H_{\mathrm{loc}}^z} &= xH_F^{4+} + (1-x)H_F^{3+} \\ &\quad + (1-x)H'(1/2)(3\cos^2\theta - 1), \\ \overline{H_{\mathrm{loc}}^x} &= (1-x)H'(3/4)\sin 2\theta.\end{aligned} \quad (4)$$

It follows from expression (3) that the ^{55}Mn nucleus, on average, "sees" the field aligned along the direction deviated from the electronic quantization axis z; namely, it is quantized in the system of coordinates (ξ, η, ζ), which is related to the system of coordinates (x, y, z) through the transformation

$$\begin{aligned}I^x &= I_\xi\cos\Theta + I_\zeta\sin\Theta, \\ I^z &= -I_\xi\sin\Theta + I_\zeta\cos\Theta, \quad I^y = I_\eta,\end{aligned}$$

where $\tan\Theta = \overline{H_{\mathrm{loc}}^x}/\overline{H_{\mathrm{loc}}^z}$. In the system of coordinates (ξ, η, ζ), we have

$$\mathcal{H}_0(x) = -\hbar\omega_{\mathrm{eff}} I_\zeta, \quad (5)$$

$$\omega_{\mathrm{eff}} = \gamma_n\sqrt{\left(\overline{H_{\mathrm{loc}}^z}\right)^2 + \left(\overline{H_{\mathrm{loc}}^x}\right)^2}. \quad (6)$$

According to the mechanism proposed in [3], the relaxation of a nuclear system with Hamiltonian (5) is associated with the fluctuations of the local fields on the nucleus due to hoppings of the e_g electrons between Mn^{3+} and Mn^{4+} ions; i.e., in the terminology used by Abragam [10], the first-order relaxation takes place. In the system of coordinates (x, y, z), the interaction responsible for the relaxation can be represented as

$$\mathcal{H}'(t) = -\gamma_n\hbar\{I^z\delta H_{\mathrm{loc}}^z(t) + I^x\delta H_{\mathrm{loc}}^x(t)\}, \quad (7)$$

$$\delta H_{\mathrm{loc}}^{z,x}(t) = H_{\mathrm{loc}}^{z,x}(t) - \overline{H_{\mathrm{loc}}^{z,x}}. \quad (8)$$

In the "nuclear" system of coordinates (ξ, η, ζ), the relaxation Hamiltonian (7) takes the form

$$\mathcal{H}'(t) = -\gamma_n\hbar\{I_\zeta\delta H_{\mathrm{loc}}^\zeta(t) + I_\xi\delta H_{\mathrm{loc}}^\xi(t)\}, \quad (9)$$

$$\begin{aligned}\delta H_{\mathrm{loc}}^\zeta(t) &= \delta H_{\mathrm{loc}}^z(t)\cos\Theta + \delta H_{\mathrm{loc}}^x(t)\sin\Theta, \\ \delta H_{\mathrm{loc}}^\xi(t) &= -\delta H_{\mathrm{loc}}^z(t)\sin\Theta + \delta H_{\mathrm{loc}}^x(t)\cos\Theta.\end{aligned} \quad (10)$$

By analogy with the case of chemical exchange [10], the correlation function of the z component of the local field with respect to the hopping electron spins is taken to be an exponential function [3],

$$\overline{\delta H_{\mathrm{loc}}^z(t)\delta H_{\mathrm{loc}}^z} = \overline{(\delta H_{\mathrm{loc}}^z)^2}\exp(-|t|/\tau_e). \quad (11)$$

The time dependence $\delta H_{\mathrm{loc}}^x(t)$ also includes a fast exponential function describing the precession of the e_g electron with a frequency ω_e in the exchange field of a ferromagnetic metal:[1]

$$\overline{(\delta H_{\mathrm{loc}}^{z,x})^2} = x(1-x)[H_{\mathrm{loc}}^{z,x}(\mathrm{Mn}^{3+}) - H_{\mathrm{loc}}^{z,x}(\mathrm{Mn}^{4+})]^2. \quad (12)$$

[1] In the case when the estimates are made using an exchange field of 81.2 T in manganite [4] and taking into account that the correlation times τ_e calculated in [3] should be multiplied by the coefficient $[4x(1-x)]^{-1} > 1$ (see, below, expression (19)), the frequency of the fast exponential function, according to the data presented in [3, Fig. 8], exceeds the rate of hopping of an e_g electron at a temperature $T > 200$ K. Then, the terms with $\delta H_{\mathrm{loc}}^x(t)$ can be disregarded.

The correlation time corresponding to hoppings of electron holes is given by the expression

$$\tau_e = \tau_\infty \exp(E/k_B T), \quad (13)$$

where E is the hopping activation energy.

Then, we use the expressions derived by Moriya [11] (see also the monograph by Turov and Petrov [12]) for the rates of nuclear spin relaxation due to fluctuations of the local fields at the nucleus under consideration:

$$T_1^{-1} = (\gamma_n^2/2)\int_{-\infty}^{\infty} dt \langle \{\delta H_{\rm loc}^{\xi}(t)\delta H_{\rm loc}^{\xi}\}\rangle \cos(\omega_{\rm eff} t), \quad (14)$$

$$T_2^{-1} = (1/2)T_1^{-1} + \gamma_n^2 \int_0^{\infty} dt \langle \{\delta H_{\rm loc}^{\zeta}(t)\delta H_{\rm loc}^{\zeta}\}\rangle. \quad (15)$$

It should be noted that expressions (14) and (15) hold in the approximation of small correlation times, i.e., times that are shorter than the inverse root-mean-square fluctuation of the local field in frequency units; the braces in these expressions designate the symmetrized product.

Upon substituting the fluctuations of the local fields described by formula (10) into expressions (14) and (15), we obtain the following relationships for the rates of the longitudinal and transverse ^{55}Mn nuclear relaxation:

$$T_2^{-1} = \gamma_n^2 \tau_e \Big\{ \overline{(\delta H_{\rm loc}^z)^2}[\cos^2\Theta + (1/2)\sin^2\Theta] + \overline{(\delta H_{\rm loc}^x)^2}[1+\omega_e^2\tau_e^2]^{-1}[\sin^2\Theta + (1/2)\cos^2\Theta]\Big\}, \quad (16)$$

$$T_1^{-1} = \gamma_n^2 \tau_e \Big\{ \overline{(\delta H_{\rm loc}^z)^2}\sin^2\Theta + \overline{(\delta H_{\rm loc}^x)^2}[1+\omega_e^2\tau_e^2]^{-1}\cos^2\Theta\Big\}. \quad (17)$$

By assuming that $\omega_e^2\tau_e^2 \gg 1$, replacing the corresponding designations, and changing over from the first-order relaxation to the second-order relaxation [10], relationships (16) and (17) can be transformed in such a way that they become consistent with the results obtained by Moriya [11] (expressions (2.26), (2.27)), who also assumed that the nuclear quantization axis deviates from the electronic quantization axis.

Let us now consider the temperature range in which the inequality $\omega_e^2\tau_e^2 \gg 1$ holds true. If the anisotropic contribution to the electron–nuclear interaction is altogether absent or is considerably smaller than the isotropic contribution, it can be assumed that $\sin\Theta \approx 0$ and $\cos\Theta \approx 1$. Taking into account that, in this case,

$$\gamma_n^2(1/4)(3\cos^2\Theta - 1)^2 (H')^2 \approx [\omega_{\rm eff}(Mn^{3+}) - \omega_{\rm eff}(Mn^{4+})]^2, \quad (18)$$

we obtain the following relationships for the rates of the longitudinal and transverse ^{55}Mn nuclear relaxation: $T_1^{-1} \approx 0$ and

$$T_2^{-1} \approx x(1-x)\tau_e[\omega_{\rm eff}(Mn^{3+}) - \omega_{\rm eff}(Mn^{4+})]^2. \quad (19)$$

As could be expected, expression (19) at $x = 1/2$ is transformed into the Anderson formula for the effect of narrowing due to fast motion (see, for example, expression (21) in the paper by Mizoguchi and Inoue [13]).

For localized Mn^{3+} ions that are characterized by a nonzero orbital moment and serve as relaxation centers with a strongly anisotropic fluctuation spectrum, in the limiting case, we have $\Theta \longrightarrow \pi/2$ and, hence, $T_1^{-1} = 2T_2^{-1}$. Note that this relationship was not observed for doped perovskites [6].

In the intermediate case of the relationship between the parameters H_F^{4+}, H_F^{3+}, and H', the ratio of the rate of transverse relaxation to the rate of longitudinal relaxation is given by the formula

$$T_2^{-1}/T_1^{-1} = \frac{\cos^2\Theta + (1/2)\sin^2\Theta}{\sin^2\Theta}. \quad (20)$$

In order to estimate ratio (20), it can be averaged over the angle θ with due regard for relationships (4). As a result, we obtain the expression

$$T_2^{-1}/T_1^{-1} \sim \frac{([xH_F^{4+} + (1-x)H_F^{3+}]/H')^2 + 0.35}{0.3}. \quad (21)$$

By assuming that $H_F^{4+} \approx H_F^{3+}$ and using the estimates obtained by Papavassiliou *et al.* [7], we find $T_2^{-1}/T_1^{-1} \sim 30$, which is in agreement with the experimental data [3, 5, 6]. It is necessary to note that the experimental temperature dependences of the relaxation rates T_1^{-1} and T_2^{-1} turn out to be entirely similar to each other (this similarity is described by expression (20)) and that these rates increase exponentially with an increase in the temperature T [3, 5]. Savosta *et al.* [3] explained this behavior in terms of the quadratic temperature dependence of the activation energy, which is characteristic of spin polarons. It should also be noted that, if the nuclear relaxation were to be associated with the scattering of conduction electrons by nuclear spins (i.e., with the Korringa mechanism), its temperature dependence, with any form of electron–nucleus interaction, would be linear [12]. Hence, there is good reason

to believe [3] that the ferromagnetic metallic phase of doped manganites is not a common metal.

Note that some researchers [4, 14] have observed two different ferromagnetic metallic phases in manganites. In particular, Savosta and Novák [4] revealed that the coexistence of these two phases manifests itself in asymmetry of the ^{55}Mn NMR line, which can be decomposed into two lines. According to the assumption made in [4], the broader line (the correlation time τ_e is longer) corresponds to more insulating regions, whereas the narrower line (the correlation time τ_e is shorter) is attributed to more metallic regions. Heffner *et al.* [14] noted spatially inhomogeneous spin–lattice relaxation in ferromagnetic metallic phase samples of doped manganites, which can also be explained by the coexistence of two different ferromagnetic metallic phases.

3. CONCLUSIONS

Thus, we derived analytical expressions for the rates of longitudinal and transverse ^{55}Mn nuclear spin relaxation under conditions of fast thermally activated motion of charge carriers (holes), which modulate the hyperfine interaction in the Mn^{3+}–Mn^{4+} system. These formulas are consistent with the experimental data obtained earlier in [3, 5, 6] for the ferromagnetic metallic phase of manganites of different compositions.

ACKNOWLEDGMENTS

We would like to thank V.A. Atsarkin for his participation in discussions of the results and for helpful remarks.

This work was supported by the Tbilisi State University and the Institute of Cybernetics of the Academy of Sciences of Georgia.

REFERENCES

1. C. Zener, Phys. Rev. **82** (3), 403 (1951).
2. M. M. Savosta, P. Novák, Z. Jirák, J. Heitmánek, and M. Marysko, Phys. Rev. Lett. **79** (21), 4278 (1997).
3. M. M. Savosta, V. A. Borodin, and P. Novák, Phys. Rev. B **59** (13), 8778 (1999).
4. M. M. Savosta and P. Novák, Phys. Rev. Lett. **87** (13), 137204 (2001).
5. M. M. Savosta, V. I. Kamenev, V. A. Borodin, P. Novák, M. Marysko, J. Heitmánek, K. Dörr, and M. Sahana, Phys. Rev. B **67** (10), 094403 (2003).
6. M. M. Savosta, V. D. Doroshev, V. I. Kamenev, V. A. Borodin, T. N. Tarasenko, and A. S. Mazur, Zh. Éksp. Teor. Fiz. **124** (3), 633 (2003) [JETP **97**, 573 (2003)].
7. G. Papavassiliou, M. Fardis, M. Belesi, T. G. Maris, G. Kallias, M. Pissas, and D. Niarchos, Phys. Rev. Lett. **84** (4), 761 (2000).
8. T. Kubo, A. Hirai, and H. Abe, J. Phys. Soc. Jpn. **26** (5), 1095 (1969).
9. A. J. Freeman and R. E. Watson, in *Magnetism*, Ed. by G. T. Rado and H. Suhl (Academic, New York, 1965), Vol. 2A.
10. A. Abragam, *The Principles of Nuclear Magnetism* (Clarendon, Oxford, 1961; Inostrannaya Literatura, Moscow, 1963).
11. T. Moriya, Prog. Theor. Phys. **16** (6), 641 (1956).
12. E. A. Turov and M. P. Petrov, *Nuclear Magnetic Resonance in Ferro- and Antiferromagnets* (Nauka, Moscow, 1969; Wiley, New York, 1972), Chap. 5.
13. T. Mizoguchi and M. Inoue, J. Phys. Soc. Jpn. **21** (7), 1310 (1966).
14. R. H. Heffner, J. E. Sonier, D. E. MacLaughlin, G. J. Nieuwenhuys, G. Ehlers, F. Mezei, S.-W. Cheong, J. S. Gardner, and H. Röder, Phys. Rev. Lett. **85** (15), 3285 (2000).

Translated by O. Moskalev

Physics of the Solid State, Vol. 47, No. 3, 2005, pp. 517–522. Translated from Fizika Tverdogo Tela, Vol. 47, No. 3, 2005, pp. 501–505.

MAGNETISM AND FERROELECTRICITY

Spin-Reorientation Transitions and Domain Structure in $TbFe_{11-x}Co_xTi$ Single Crystals

S. A. Nikitin[1,3], T. I. Ivanova[1,3], N. Yu. Pankratov[1,3], Yu. G. Pastushenkov[2], and K. P. Skokov[2]

[1]*Moscow State University, Leninskie gory, Moscow, 119899 Russia*

e-mail: ivanova@phys.msu.ru

[2]*Tver State University, ul. Zhelyabova 3, Tver, 170000 Russia*

[3]*International Laboratory of Strong Magnetic Fields and Low Temperatures, Wroclaw, 53421 Poland*

Received June 22, 2004

Abstract—The magnetic structure of single-crystal $TbFe_{11-x}Co_xTi$ compounds has been studied over a broad temperature range and in strong magnetic fields (up to 14 T). Measurements of magnetization and magnetostriction and a study of the domain structure revealed that spin-reorientation transitions (SRTs) in $TbFe_{11-x}Co_xTi$ single crystals depend substantially on the cobalt concentration. It was established that the SRT temperatures and threshold magnetic fields are governed by the interplay between the magnetic anisotropies of the 3*d* and terbium sublattices. It is shown that, in these compounds, the low-temperature phase with planar anisotropy is separated in temperature from the high-temperature phase with uniaxial anisotropy by an intermediate metastable phase containing domains of the uniaxial or planar phase. *© 2005 Pleiades Publishing, Inc.*

1. INTRODUCTION

The materials used to fabricate modern high-efficiency permanent magnets include intermetallic compounds of 3*d* and 4*f* metals. Rare-earth (RE) 4*f* metals provide a high saturation magnetization and giant anisotropy, while 3*d* elements (iron or cobalt) account for the high values of the magnetic-ordering temperature and coercivity, as well as for the high remanent and saturation magnetizations [1]. Among these compounds is $Nd_2Fe_{14}B$, which has recently been enjoying wide application. Magnetic materials based on RE intermetallic compounds, $R(Fe,Co)_{11}Ti$, with the $ThMn_{12}$ crystal structure are also promising [2–8].

The magnetic sublattices of the RE and 3*d* transition metals in these intermetallics are coupled by strong exchange interaction. The interplay between the magnetic anisotropies of the 3*d* and RE sublattices gives rise to spin-reorientation phase transitions (SRTs). Substitution of cobalt for iron on the 3*d* sublattice in $RFe_{11}Ti$ compounds has a significant effect on the structure of the 3*d* band, which makes $R(Fe,Co)_{11}Ti$ RE intermetallic compounds particularly interesting for investigating the effect the electronic structure exerts on the magnetic properties, phase transitions, and exchange coupling [9–12].

The present communication reports on a study of the effect of substitution (of cobalt for iron) on the 3*d* sublattice on the character of exchange coupling, magnetic ordering, and domain structure in $Tb(Fe,Co)_{11}Ti$ intermetallic compounds with the $ThMn_{12}$ tetragonal crystal structure. Coordinated experimental investigations of the magnetic properties and domain structure of single crystals of $TbFe_{11-x}Co_xTi$ compounds were carried out over a broad range of temperatures and magnetic fields.

2. EXPERIMENTAL TECHNIQUES AND SAMPLES

The $TbFe_{11-x}Co_xTi$ alloys to be studied were prepared by rf melting in alundum crucibles in an argon environment on a Donets-1-type setup. The alloy components were high-purity metals Tb and Ti, as well as 99.9%-pure Fe. The alloys thus prepared were subjected to high-temperature annealing in an SShVL-type resistance furnace. To improve homogeneity, the ingots were crushed again and remelted in vacuum. The single-phase state of the alloys was established from x-ray diffraction patterns of powder samples of the compounds. All of the $TbFe_{11-x}Co_xTi$ compounds thus prepared ($x = 0, 1, 2, 3, 4, 5$) crystallize in the $ThMn_{12}$ tetragonal structure (space group $I4/mmm$). It was found that heating of the alloys to 1800 K followed by rapid cooling to 1500 K with subsequent slow cooling to 1400 K over 3–8 h produces single crystals of the main phase in the form of (110) plates and [001]-oriented needles. Single crystals of the $TbFe_{11-x}Co_xTi$ compounds were prepared from these ingots. The quality of the single crystals was checked by Laue diffraction.

The temperature and field dependences of the magnetization of the $TbFe_{11-x}Co_xTi$ compounds were measured (i) in magnetic fields of up to 3 T at temperatures

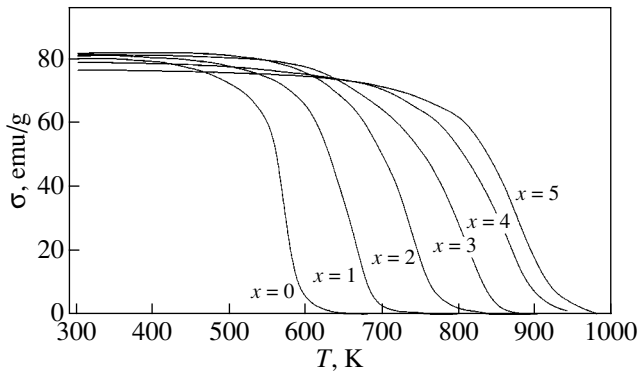

Fig. 1. Temperature dependence of magnetization of $TbFe_{11-x}Co_xTi$ compounds plotted for different cobalt concentrations.

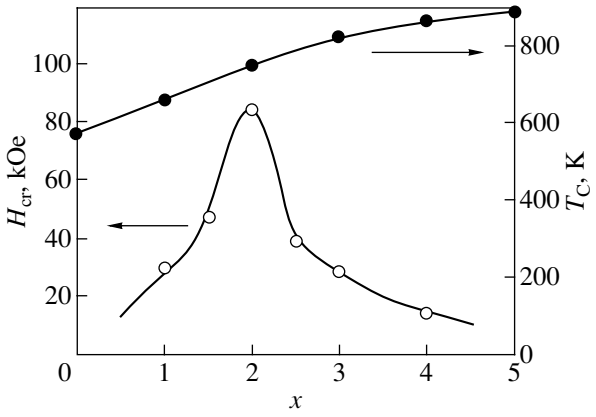

Fig. 2. Concentration dependences of the critical magnetic field and Curie temperature for $TbFe_{11-x}Co_xTi$ single crystals.

from 300 K to the Curie point with a vibrating sample magnetometer, (ii) within the temperature range 77–300 K in fields of up to 1.2 T with a pendulum magnetometer, and (iii) at temperatures ranging from 4.2 to 250 K and in magnetic fields of up to 14 T with a capacitor magnetometer in a superconducting coil at the International Laboratory of Strong Magnetic Fields and Low Temperatures (Wrocław, Poland). The Curie temperatures (T_C) of the compounds were derived from the temperature dependences of the magnetization measured in a field $\mu_0 H = 5 \times 10^{-2}$ T. The domain structure of $TbFe_{11-x}Co_xTi$ single crystals on differently oriented surfaces and in a broad temperature range, 4.2–370 K, was studied using the magnetooptical Kerr method at the Max Planck Institute of Physics (Stuttgart, Germany).

3. EXPERIMENTAL RESULTS AND DISCUSSION

3.1. Magnetic Properties

The Curie temperature of the $TbFe_{11-x}Co_xTi$ compounds was defined as the point of fast falloff of the specific magnetization measured in a field of 500 Oe (Fig. 1). Our studies showed that substitution of cobalt for iron in the $TbFe_{11-x}Co_xTi$ system gives rise to a monotonic growth of the Curie temperature T_C (Fig. 1). As the cobalt concentration increases, T_C varies at a rate of ~90 K/atom in the range from $x = 1$ to 2 and at a rate of 20 K/atom in the range from $x = 4$ to 5 (Fig. 2). The Curie temperature is determined primarily by the exchange coupling on the 3*d* sublattice, which contains atoms of iron and cobalt. As follows from neutron diffraction measurements [13], Co atoms in compounds with the $ThMn_{12}$ structure occupy primarily the 8*f* and 8*j* positions, where the distance between Fe atoms is less than a critical value of ~0.24 nm and the exchange coupling integral between Fe atoms is negative. Co atoms have a positive exchange integral; therefore, substitution of Co for Fe enhances the positive exchange coupling on the 3*d* sublattice, with the result that the Curie temperature also increases. It should be pointed out that the difference in the Curie temperatures between the $TbFe_{11-x}Co_xTi$ and $YFe_{11-x}Co_xTi$ compounds (the Y magnetic moment is zero) does not exceed 10%.

As the Co concentration increases, the saturation magnetization σ_S for $TbFe_{11-x}Co_xTi$ single crystals first grows weakly to reach a small maximum at $x = 2$ and then decreases, which correlates with the behavior of magnetization in other RE intermetallic compounds under substitution of Co for Fe, as well as in Fe–Co binary alloys. This phenomenon can be explained in terms of the band theory of magnetism as a result of successive filling of the 3*d* bands with positive and negative spin orientation under replacement of iron with cobalt (the number of 3*d* electrons per atom in Co is larger by one than that in Fe) [14].

The magnetization isotherms $\sigma(H)$ of single-crystal $TbFe_{11-x}Co_xTi$ have a complex pattern indicating the occurrence of spin-reorientation phase transitions in these compositions, with the temperature and character of the transitions depending substantially on the cobalt concentration. It is of particular interest that sharp jumps are observed to occur in $\sigma(H)$ curves of $TbFe_{11-x}Co_xTi$ single crystals at critical values of the magnetic field H_{cr}. Let us consider the magnetic properties of the $TbFe_9Co_2Ti$ compound in more detail. Figure 3 presents magnetization isotherms along the [001], [110], and [100] crystallographic directions of a $TbFe_9Co_2Ti$ single crystal measured at 4.2 K in magnetic fields of up to 140 kOe. We see that the [100] axis, along which the magnetization rapidly reaches saturation, is the easy magnetization axis (EMA) and that the [001] axis, where the magnetization field is the strongest, is the hard magnetization axis (HMA). Hence, the

basal plane is an easy plane at $T = 4.2$ K. Figure 4 displays magnetization isotherms measured along the [001] axis of a $TbFe_9Co_2Ti$ single crystal in the temperature interval 80–300 K and at magnetic fields of up to 12 kOe. In the low-temperature region, the $\sigma(H)$ curves follow a practically linear course typical of the case where [001] is the hard magnetization axis. As the temperature increases, a jump appears in the $\sigma(H)$ curves at a critical magnetic field $H = H_{cr}$, after which the curve rapidly reaches saturation. At high temperatures, $T >$ 275 K, the [001] axis becomes an easy axis, thus suggesting spin reorientation in the $TbFe_9Co_2Ti$ compound. Near the spin-reorientation transition temperature (T_{SR} = 275 K), characteristic breaks take place in the magnetization isotherms (Fig. 4). This behavior of magnetization is evidence of a first-order magnetization process (FOMP), which is induced by a magnetic field. These phase transitions are associated with the spontaneous magnetization vector I_S transferring from one minimum of magnetocrystalline anisotropy (MCA) to another [15]. Hence, at low temperatures, $T < T_{SR}$, $TbFe_9Co_2Ti$ has planar anisotropy and becomes a uniaxial ferrimagnet at high temperatures. These two states are separated in temperature by an intermediate phase, which is metastable, because, as will be shown below, uniaxial-phase and planar-phase domains coexist in this state. In the $\sigma(H)$ curves (Figs. 3, 4), we clearly see that, in the vicinity of the FOMP, there is a field where $\partial^2\sigma/\partial H^2$ is maximum and positive ($H = H_{cr1}$) and a field where $\partial^2\sigma/\partial H^2$ is maximum in magnitude and negative ($H = H_{cr2}$). The field interval H_{cr1}–H_{cr2} defines the FOMP phase transition region. There is practically no hysteresis in this region. Figure 5 plots the temperature dependence of the average value of H_{cr} for a $TbFe_9Co_2Ti$ single crystal. The average value of H_{cr} was derived from the maximum of the first derivative of $\sigma(H)$, which corresponds to the inflection point in the magnetization curves. The critical field H_{cr} decreases with increasing temperature for all cobalt concentrations, with the $H_{cr}(T)$ curves becoming practically linear at high temperatures. Figure 2 shows the concentration dependence of H_{cr} obtained at $T = 4.2$ K for $TbFe_{11-x}Co_xTi$ single crystals. The maximum of this curve is seen to lie at $x = 2$.

An external magnetic field decreases the spin-reorientation transition temperature.

The SRT noticeably influences the dependences of magnetostriction on temperature and external magnetic field. Indeed, the temperature dependence of longitudinal magnetostriction $\lambda_{\parallel}(T)$ measured along the [001] axis of a $TbFe_9Co_2Ti$ single crystal in magnetic fields of up to 12 kOe reveals a clearly pronounced maximum at $T = 269$ K, a temperature close to T_{SR} (Fig. 6). Decreasing the magnetic field shifts the maximum in the $\lambda_{\parallel}(T)$

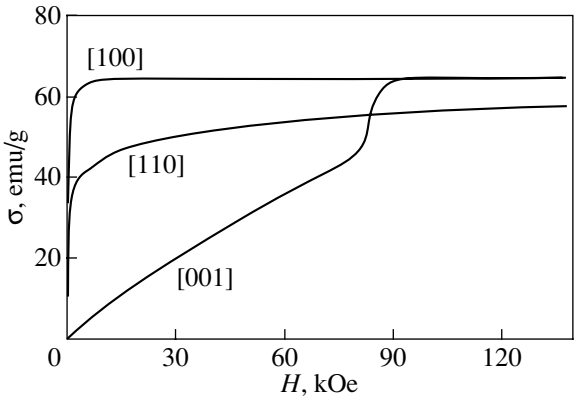

Fig. 3. Magnetization isotherms of a $TbFe_9Co_2Ti$ single crystal measured at 4.2 K along the [001], [110], and [100] crystallographic axes.

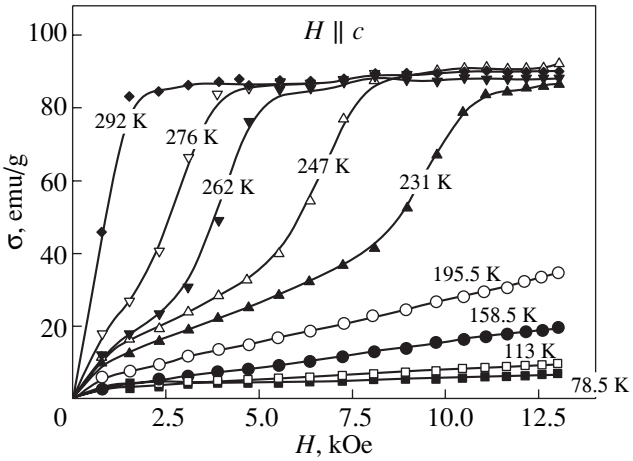

Fig. 4. Magnetization isotherms of a $TbFe_9Co_2Ti$ single crystal measured along the [001] axis in the temperature interval 80–300 K.

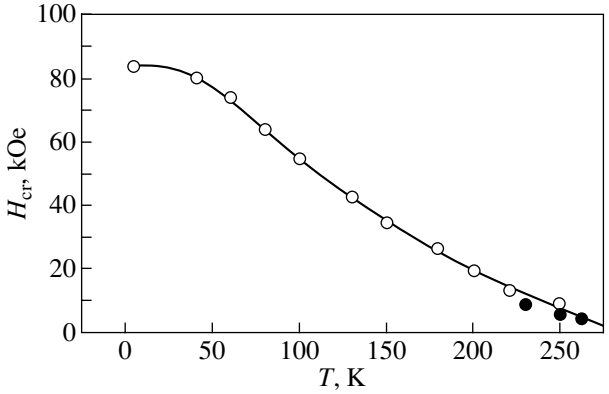

Fig. 5. Temperature dependence of H_{cr} for a $TbFe_9Co_2Ti$ single crystal.

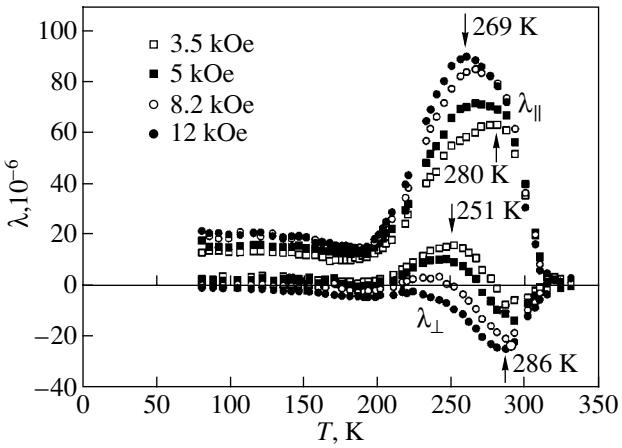

Fig. 6. Temperature dependence of the longitudinal and transverse magnetostriction of a $TbFe_9Co_2Ti$ single crystal measured at different magnetic fields.

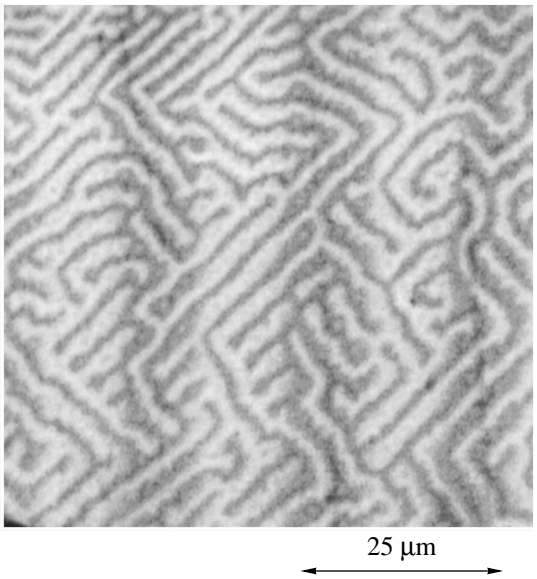

Fig. 7. Domain structure of the $TbFe_9Co_2Ti$ intermetallic compound in the EMA + EP intermediate state at T = 295 K.

curve toward lower temperatures; for instance, at H = 3.5 kOe, the maximum is seen at T = 251 K.

The observed behavior of $\lambda_{\parallel}(T)$ can be interpreted in the following way. For $T > T_{SR}$, magnetostriction along the [001] axis should be fairly small, because this effect has even parity and displacements of boundaries of antiparallel domains do not contribute to magnetostriction; furthermore, there is no rotation-induced magnetostriction, as the vector M_S does not rotate in a field $H \parallel$ [001]. When cooled below T_{SR}, the vector N_S rotates through an angle θ_0 relative to the [001] axis, while the application of a magnetic field restores M_S to align with [001]; therefore, rotation-induced magnetostriction takes place. The observed effect will be $\lambda = \lambda_c - \lambda_c \cos^2\theta_0$, where λ_c is the magnetostriction constant and θ_0 is the angle between the magnetization vector and the *c* axis.

3.2. Domain Structure

The domain structure (DS) of $TbFe_{11-x}Co_xTi$ single crystals was studied on differently oriented surfaces and over a broad temperature range, 4.2–370 K, by the magnetooptic Kerr method with a Polywar Met metallographic microscope (Reichner-Jung, Germany), on which a cryostat with the sample was mounted. The technique employed in these low-temperature studies was described in considerable detail in [16–18]. The DS transformation occurring during a spin-reorientation transition in $TbFe_{11-x}Co_xTi$ compounds was observed for two compositions, $TbFe_{11}Ti$ and $TbFe_9Co_2Ti$. In $TbFe_{11-x}Co_xTi$ compounds, the magnetostriction is high ($\lambda \sim 10^{-4}$) and the magnetoelastic contribution to magnetocrystalline anisotropy is quite large. Therefore, these compounds enable one to follow the effect of both substitution and the uniaxial magnetic anisotropy induced by the magnetoelastic contribution on the DS rearrangement pattern. Two cases were considered in this work: (i) transition from the magnetically uniaxial to a magnetically biaxial state (with easy-plane anisotropy) in $TbFe_{11}Ti$ and (ii) transition from the magnetically uniaxial to a magnetically biaxial state (with easy-plane anisotropy and the preferred easy axis induced by the magnetoelastic contribution) in $TbFe_9Co_2Ti$.

At high temperatures, the $TbFe_{11}Ti$ compound is magnetically uniaxial. As the temperature is lowered to T_{SR} = 310 K, the anisotropy type changes from the easy-axis to easy-plane MCA and an EMA–EP metastable state sets in. After this, a crossover to the easy-plane anisotropy takes place at T_{SR2} = 290 K, which is observed in the DS patterns.

The extreme case of the effect of stresses on the pattern of DS variation in the course of spin reorientation was studied on $TbFe_9Co_2Ti$. The magnetoelastic contribution to MCA in compounds of the $Tb(Fe,Co)_{11}Ti$ system is large. Therefore, in the easy-plane anisotropy region, $Tb(Fe,Co)_{11}Ti$ compounds quite frequently show a situation where one of the [110]-type EMAs is made preferred by the stresses present in the sample as the easiest axis of magnetization. This crystal is also magnetically quasi-uniaxial in the low-temperature region, where easy-plane anisotropy prevails. The magnetic phase diagram of $Tb(Fe,Co)_{11}Ti$ compounds was shown in [8] to have a transition region within which the energies of the high-temperature (I) and low-temperature (II) phases turn out to be equal. In this region, the $TbFe_9Co_2Ti$ compound exhibits two DS systems

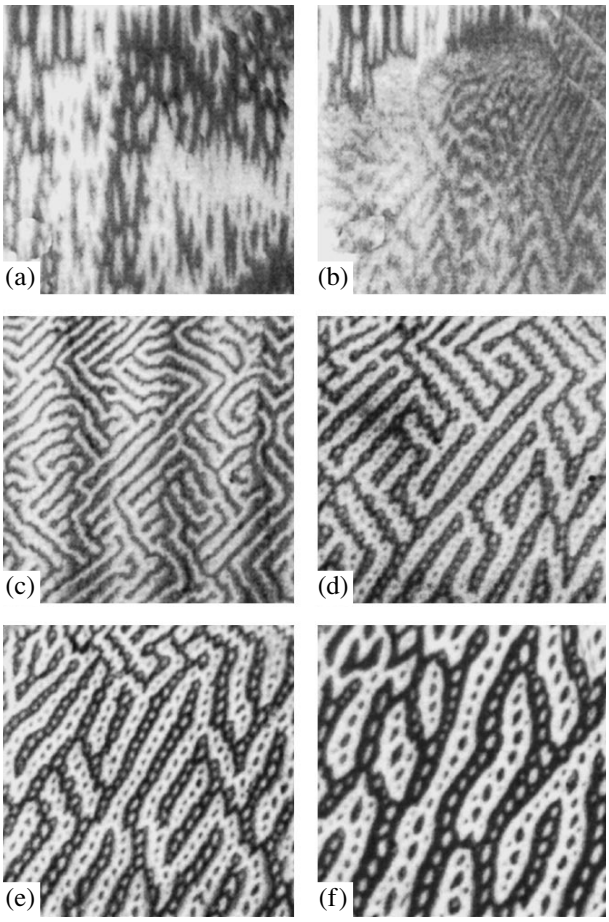

Fig. 8. DS rearrangement in a $TbFe_9Co_2Ti$ single crystal during the phase transition from (a) the EMA to (d–f) an EP state with a preferred EMA. The sample temperature is (a) 370, (b) 326, (c) 293, (d) 220, (e) 200, and (f) 80 K.

corresponding to the low- and high-temperature phases (Fig. 7).

Phase I has a stripe DS. In the case exemplified in Fig. 7, the phase with such domains lies directly under the plane of observation. The EMA of this domain system, which coincides with the [110] crystallographic axis of the tetragonal lattice, makes an angle of approximately 60° with the sample surface. Domain system I, representing a magnetic phase with EMA-type anisotropy, is located under phase-II domains. These are 180° stripe domains with the magnetization aligned with the [001] axis. DS I magnetizes system II, thus causing a periodic variation of domain width in the star system. Figure 8 illustrates the DS variation for the $TbFe_9Co_2Ti$ compound in the temperature interval corresponding to the crossover from the EMA to EP anisotropy with a preferred, easiest magnetization axis. Note that, in this case, phases I and II coexist in the temperature interval 220–360 K.

4. CONCLUSIONS

Spin-reorientation transitions in $TbFe_{11-x}Co_xTi$ compounds are driven by magnetocrystalline interactions with two major contributions.

In the low-temperature region, FOMP-type SRTs are driven primarily by the interplay between different crystal-field parameters that determine the anisotropy on the RE sublattice. The MCA energy reaches a minimum as a result of the MCA constants of the first and higher orders having opposite signs. As the temperature increases, mutual compensation of the MCAs of the 3*d* and 4*f* sublattices plays a substantial role. Single-ion MCA of terbium ions with a negative Stevens coefficient favors planar anisotropy, whereas that of Fe ions is favorable for uniaxial anisotropy. Substitution of cobalt for iron reduces the 3*d*-sublattice MCA, because the single-ion MCA constants of iron and cobalt have opposite signs. As a result, the SRT temperature decreases substantially with increasing cobalt concentration. In the vicinity of the MCA compensation point, a spontaneous SRT transition occurs, which is associated with the magnetization vector switching from the basal plane to the *c* axis. The coexistence of domains with a uniaxial and a planar phase in the SRT proximity substantiates the presence of a metastable phase in the transition region.

ACKNOWLEDGMENTS

This study was supported by the Russian Foundation for Basic Research (project no. 02-02-16523), the program "Universities of Russia" (project no. 01.01.054), and the federal program for support of leading scientific schools (project no. NSh-205.2003.02).

REFERENCES

1. K. H. J. Buschow, *Handbook of Ferromagnetic Materials* (North-Holland, Amsterdam, 1989), Vol. 4.
2. A. A. Kazakov, N. V. Kudrevatykh, and P. E. Markin, J. Magn. Magn. Mater. **146**, 208 (1995).
3. K. Yu. Guslienko, X. C. Kou, and R. Grössinger, J. Magn. Magn. Mater. **150**, 383 (1995).
4. S. A. Nikitin, T. I. Ivanova, I. S. Tereshina, V. I. Zubenko, and I. V. Telegina, Fiz. Tverd. Tela (St. Petersburg) **37** (2), 561 (1995) [Phys. Solid State **37**, 306 (1995)].
5. S. A. Nikitin, I. S. Tereshina, and T. I. Ivanova, Fiz. Tverd. Tela (St. Petersburg) **38** (2), 507 (1996) [Phys. Solid State **38**, 278 (1996)].
6. M. D. Kuzmin and A. K. Zvezdin, J. Appl. Phys. **83**, 3239 (1998).
7. I. S. Tereshina, S. A. Nikitin, I. V. Telegina, V. V. Zubenko, Yu. G. Pastushenkov, and K. P. Skokov, J. Alloys Compd. **283**, 45 (1999).

8. T. I. Ivanova, Yu. G. Pastushenkov, K. P. Skokov, I. V. Telegina, and I. A. Tskhadadze, J. Alloys Compd. **280**, 20 (1998).
9. V. K. Sinha, S. F. Cheng, W. E. Wallace, and S. G. Sankar, J. Magn. Magn. Mater. **81**, 227 (1989).
10. J. J. Bara, B. F. Bogacz, A. T. Pedziwiator, and R. Wielgosz, J. Alloys Compd. **307**, 45 (2000).
11. Z. F. Gu, D. C. Zeng, Z. Y. Liu, S. Z. Liang, J. C. P. Klaasse, E. Bruck, F. R. de Boer, and K. H. J. Buschow, J. Alloys Compd. **321**, 40 (2001).
12. T. I. Ivanova, S. A. Nikitin, D. V. Tokareva, I. V. Telegina, Yu. G. Pastushenkov, K. P. Skokov, W. Suski, and Yu. Skourski, J. Magn. Magn. Mater. **238**, 215 (2002).
13. Y. Yang, L. Kong, H. Song, J. Yang, Y. Ding, B. Zhang, C. Ye, and L. Jin, J. Appl. Phys. **67**, 4632 (1990).
14. K. N. R. Taylor and M. I. Darby, *Physics of Rare Earth Solids* (Chapman and Hall, London, 1972; Mir, Moscow, 1974).
15. G. Asti and F. Bolzoni, J. Appl. Phys. **58**, 1924 (1985).
16. Yu. G. Pastushenkov, K.-D. Durst, and H. Kronmüller, Phys. Status Solidi A **104**, 487 (1987).
17. A. Forkl, T. Dragon, and H. Kronmüller, J. Appl. Phys. **67** (6), 3047 (1990).
18. Yu. G. Pastushenkov, A. Forkl, and H. Kronmüller, J. Magn. Magn. Mater. **174**, 278 (1997).

Translated by G. Skrebtsov

Physics of the Solid State, Vol. 47, No. 3, 2005, pp. 523–526. Translated from Fizika Tverdogo Tela, Vol. 47, No. 3, 2005, pp. 506–508.

MAGNETISM AND FERROELECTRICITY

Manifestation of Basal-Plane Anisotropy and Mechanical Boundary Conditions in Magnetic Birefringence of Sound in Hematite

I. Sh. Akhmadullin, S. A. Migachev, M. F. Sadykov, and M. M. Shakirzyanov

Zavoiskiĭ Physicotechnical Institute, Kazan Scientific Center, Russian Academy of Sciences, Sibirskiĭ trakt 10/7, Kazan, 420029 Tatarstan, Russia

e-mail: shakirzyanov@kfti.knc.ru

Received July 8, 2004

Abstract—The angular dependence of the magnetic birefringence of sound in hematite is experimentally investigated as a function of the direction of a magnetic field applied in the basal plane of the hematite crystal. It is found that, at room temperature, the curve of magnetoacoustic oscillations in the magnetic field, i.e., the oscillatory dependence of the amplitude of an acoustic wave transmitted through the crystal on the magnetic field strength, is characterized by hexagonal and uniaxial anisotropy. It is shown that the hexagonal anisotropy is governed by the basal-plane anisotropy of higher orders. The appearance of the uniaxial magnetic anisotropy in the basal plane of the crystal is explained by the mechanical stresses arising in the sample when piezoelectric transducers are glued to the sample ends. This assumption is confirmed by the observed change in the direction of the uniaxial anisotropy axis under variations in the boundary conditions. © *2005 Pleiades Publishing, Inc.*

1. INTRODUCTION

Magnetic birefringence of a transverse acoustic wave propagating along the hard magnetization axis $\mathbf{C}_3$ in the easy-plane antiferromagnet α-Fe_2O_3 was observed experimentally in our recent work [1]. In accordance with the inferences made from the theory of birefringence [2], we revealed that the amplitude of an acoustic wave transmitted through the sample exhibits oscillations dependent on the magnetic field strength H (magnetoacoustic oscillations) and that the polarization of the acoustic wave changes from linear at the entry into the sample to elliptic at the exit from the sample. The nature of this phenomenon is associated with the lifting of the degeneracy in the spectrum of transverse acoustic waves with wave vector $\mathbf{k} \parallel \mathbf{C}_3$ due to the magnetoelastic interaction [3]. During propagation of the acoustic wave along the $\mathbf{C}_3$ axis, only one of the two normal modes of transverse vibrations efficiently interacts with the magnetic subsystem, specifically with vibrations of the antiferromagnetic vector $\mathbf{L}$ in the basal plane of the crystal. These vibrations correspond to the low-frequency quasi-ferromagnetic branch of the spectrum of spin waves in two-sublattice easy-plane antiferromagnets, including hematite α-Fe_2O_3 [2, 3]. Owing to the renormalization of the elastic moduli resulting from the magnetoelastic coupling, the velocity of the interacting mode (magnetoelastic mode) becomes different from that of the noninteracting mode and depends on the magnetic field $\mathbf{H}$ (due to the dependence of the antiferromagnetic resonance frequency ω_{f0} on the magnetic field $\mathbf{H}$). This leads to a phase shift between the normal modes of transverse vibrations $\Delta\varphi(H)$, whose magnitude at the exit from the sample of length d in the direction of propagation of the acoustic wave is determined by the expression $\Delta\varphi(H) = \Delta k(H)d/2$, where $\Delta k(H)$ is the difference between the wave vectors of the normal modes of transverse vibrations. Therefore, the amplitude of the resultant wave at the exit from the sample is an oscillating function that depends on the magnetic field strength [1, 2]. Investigation into the angular dependence of the birefringence has revealed that the curves of magnetoacoustic oscillations in a magnetic field substantially depend on the direction of the magnetic field in the basal plane of the crystal [1]. In particular, we observed a 60° periodic dependence of the amplitude of an acoustic wave on the magnetic field strength. This dependence can be explained in terms of the fields of the fourth- and sixth-order basal-plane anisotropy. It is worth noting that the hexagonal dependence overlaps with a 180° periodic dependence. The latter dependence indicates a strong uniaxial magnetic anisotropy in the basal plane of the crystal. However, this anisotropy has defied explanation in terms of crystalline or magnetic anisotropy [4] and can be associated with the generation of additional magnetostriction fields [5, 6]. In our experiments, there are two most probable factors responsible for the generation of these fields: (i) residual stresses in unannealed samples, which were sawed from a single-crystal boule grown along one of the twofold axes in the basal plane of the crystal sample, and (ii) mechanical stresses arising in the sample when piezoelectric transducers are glued to the sample ends parallel to the basal plane of the sample [5, 6]. According to [5, 6], the inhomogeneous strains

1063-7834/05/4703-0523$26.00

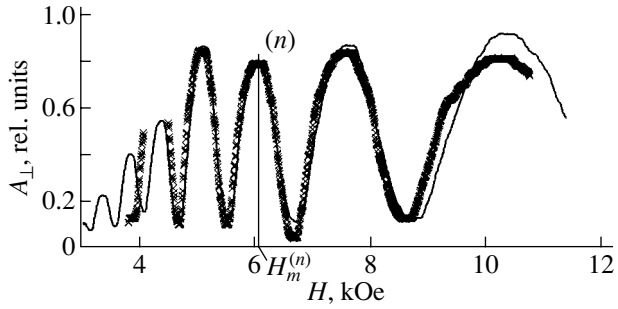

Fig. 1. Oscillations of the amplitude of the transmitted acoustic wave as a function of the magnetic field H ($\varphi_H \cong 0$) at angles $\xi \cong 30°$ ($\varphi_0 \cong 30°$) (solid line) and $\xi \cong 120°$ ($\varphi_0 \cong 120°$) (crossed line).

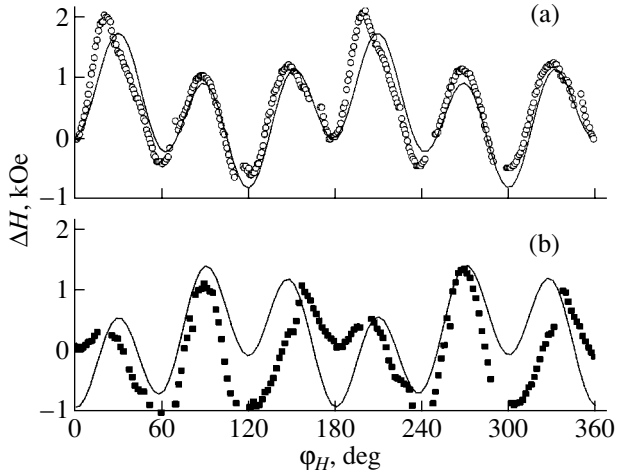

Fig. 2. Angular dependences of the magnetic field strength (corresponding to the maximum in the curve of magnetoacoustic oscillations) in the basal plane of the crystal at angles (a) $\xi \cong 30°$ and (b) $\xi \cong 120°$. The solid line indicates the approximation by functions of form (2).

induced by these stresses can be comparable in magnitude to the spontaneous striction in hematite [7]. The main objective of this work was to elucidate the origin of the periodicity in the angular dependence of the magnetic birefringence of sound. For this purpose, we carried out new experiments with annealed hematite samples. The results of these experiments are discussed in this paper.

2. EXPERIMENTAL TECHNIQUE

We measured the amplitude of a transverse ultrasonic wave (at a frequency $f \cong 91$ MHz) transmitted through a hematite sample ($\mathbf{k} \parallel \mathbf{C}_3$) as a function of the strength and direction of the magnetic field applied in the basal plane perpendicular to the $\mathbf{C}_3$ axis of the crystal. The measurement procedure and requirements for samples were described in detail in [1]. We note only that the ellipticity of the acoustic wave at the exit from the crystal sample allows one to specify the directions of polarization of the emitting and receiving piezoelectric transducers arranged at the plane-parallel ends of the sample at any angle to each other. It is most convenient (first of all, for comparison with theory) to arrange them either parallel or perpendicular to each other [1]. Below, we will present the results of measurements performed for their orthogonal orientation and two directions of polarization of the input piezoelectric transducer (emitter). In the first case, the direction of polarization of the emitter made an angle $\xi = 30°$ with the preferred twofold axis $\mathbf{C}_2$ (the growth axis of the single-crystal boule). In the second case, the angle ξ was equal to 120°. The receiving piezoelectric transducers were glued accordingly.

The measurements were carried out at room temperature in magnetic fields $3 \le H \le 20$ kOe, which were applied in the basal easy-magnetic plane of the sample. The sample was rotated in a magnetic field. The direction of the magnetic field in the basal plane of the crystal was specified by an angle φ_H measured from the same preferred twofold axis $\mathbf{C}_2$. The single crystals were annealed in air according to the standard procedure: the samples were uniformly heated to an annealing temperature of 1100°C for 3 h and were then annealed at this temperature for 6 h. After annealing, the samples were cooled in the furnace to room temperature over a period of 20 h.

3. EXPERIMENTAL RESULTS

Figure 1 shows the experimental curves of magnetoacoustic oscillations of the amplitude of the transverse ultrasonic wave $A_\perp(H)$ for these samples at an angle $\varphi_H = 0$ for orientations of the transducers at angles $\xi \cong 30°$ (solid line) and $\xi \cong 120°$ (crossed line). Figure 2 depicts the dependences of the magnetic field strength $\Delta H_m^{(n)}(\varphi_H) = H_m^{(n)}(\varphi_H) - H_m^{(n)}(0)$, which corresponds to the nth maximum in the curve $A_\perp(H)$, on the field direction for both orientations of the emitter. It can be seen from Fig. 2 that the magnetic field strength $\Delta H_m^{(n)}(\varphi_H)$ in both cases (i.e., at $\xi = 30°$ and 120°) is a periodic function with a period of 60°. In turn, this function overlaps with a 180° periodic function indicating an anisotropy with a considerable amplitude. A comparison of Figs. 2a and 2b (points) clearly demonstrates that the axis of this anisotropy is rotated through an angle of 90°. It should be noted that the results of the experiments performed with annealed samples for orientation of the emitter at an angle $\xi \cong 30°$ differ very insignificantly from the results obtained for unannealed samples under the same conditions [1]; hence, the latter results are not presented in these figures to avoid overcrowding. Therefore, we can assume that the residual strain associated with the single-crystal growth is small as compared to the strain caused by spontaneous striction and that the observed uniaxial anisotropy in the

basal plane of the crystal sample is related to the boundary conditions [6].

4. DISCUSSION

The experimentally observed magnetoacoustic oscillations (Fig. 1) can be described by the expression obtained in [2] (in relative units):

$$A_\perp(H) = \sqrt{\sin^2(2\varphi_0)\sin^2(\Delta k(H)d/2)}, \quad (1)$$

where φ_0 is the angle between the direction of polarization of the excited wave and the direction of polarization of the normal (transverse) magnetoelastic mode. Expression (1) allows us to obtain only qualitative agreement with the experimental data; however, there is a significant quantitative discrepancy between theory and experiment. A similar situation occurs with other easy-plane antiferromagnets, such as $MnCO_3$ [8] and $FeBO_3$ [9]. The possible reasons for the absence of a close quantitative agreement between theory and experiment were discussed in detail in [10]. One of the theoretical models that provides a good fit of the calculated data to the experimental dependence of the amplitude of the transverse ultrasonic wave $A_\perp$ on the magnetic field strength H was considered in [6].

The experimental angular dependence of the magnetic field $\Delta H_m^{(n)}(\varphi_H) = H_m^{(n)}(\varphi_H) - H_m^{(n)}(0)$, which corresponds to the nth maximum in the curve $A_\perp(H)$ (this is also true for any other point in the curve of magnetoacoustic oscillations), is approximated well by the function

$$\Delta H_m^{(n)}(\varphi_H) \equiv \Delta H_m^{(n)} \cong \beta\cos 2(2\varphi_H - \alpha) + \chi\cos(6\varphi_H). \quad (2)$$

This function can be interpreted as follows. According to expression (1), the amplitude of the acoustic wave at the exit from the sample is largest under the condition

$$\Delta k(H_m^{(n)}) = \pi(2n+1)/2, \quad H_m^{(n)} \equiv H_m^{(n)}(\varphi_H). \quad (3)$$

In the case of the sufficiently strong fields used in the experiment, for which the inequality $\Delta k/k \ll 1$ is satisfied, the difference between the wave vectors $\Delta k(H_m^{(n)})$ can be represented by the approximate expression [2]

$$\Delta k(H_m^{(n)}) \approx k\frac{\Delta}{\omega_{f0}^2(H_m^{(n)})}, \quad \Delta = \frac{H_E(2B_{14})^2}{M_0 C_{44}}, \quad k = 2\pi f/V_\eta, \quad V_\eta = C_{44}/\rho, \quad (4)$$

where V_η is the velocity of the noninteracting mode, C_{44} is the elastic modulus, ρ is the density of the crystal, B_{14} is the component of the tensor of the magnetoelastic coupling, H_E is the exchange magnetic field, and M_0 is the equilibrium magnetization of the sublattices. By assuming the uniaxial anisotropy and taking into account the fourth- and sixth-order basal-plane anisotropy, the antiferromagnetic resonance frequency of the quasi-ferromagnetic mode ω_{f0} has the form [5, 11]

$$\omega_{f0}^2(H_m^{(n)}) = \gamma^{-2}\{H_m^{(n)}(H_m^{(n)} + H_D) + 2H_E H_{ms}^{(0)} + 2H_E H_p\cos 2(\theta - \varphi_H) + 36H_E H_a\cos 6\varphi_H\}. \quad (5)$$

It follows from expressions (4) and (5) that the magnetic field strength $H_m^{(n)}$, at which condition (3) is satisfied, is a composite periodic function of the angle φ_H.

Relationship (5) includes the following magnetic fields: H_D is the Dzyaloshinski field, $H_{ms}^{(0)}$ is the isotropic part of the field of spontaneous magnetostriction, H_a is the effective field of the basal-plane anisotropy of higher orders [4], and H_p is the magnetostriction field induced by strains arising under the action of an arbitrary external force applied in the basal plane of the crystal at an angle θ to the preferred twofold axis $\mathbf{C}_2$ [5, 11]. An example of this force is pressure applied in the basal plane of the crystal, whose effect on the antiferromagnetic resonance frequency ω_{f0} was thoroughly investigated earlier. Following the conclusions drawn in [6], we can assume that, in the case under consideration, the nonzero additional magnetostriction field H_p induced in the basal plane of the crystal is determined by the mechanical boundary conditions. These conditions are created when piezoelectric transducers with a strong anisotropy of the thermal expansion coefficient (the X cut of lithium niobate) are glued to the sample ends parallel to the basal plane of the crystal. Hardening of the glued area (epoxy resin) is accompanied by the heat release. As a result, the transducer plate experiences strong tension in the preferred direction in the plane of the cut. In turn, this tension gives rise to inhomogeneous mechanical stresses at the sample ends. These stresses, like the magnetostriction fields induced by them, should possess axial symmetry. Apparently, the direction of the axis of this symmetry is determined by the direction of the maximum extension of the piezoelectric transducer. In our opinion, this assumption is confirmed by the experimentally observed change in the phase of the uniaxial anisotropy by an angle of 90° upon regluing of both piezoelectric transducers with a 90° rotation of the polarization vectors.

From the above consideration, it follows that the parameters α, β, and χ, which are involved in expression (2) for the approximating function $\Delta H_m^{(n)}$, are determined by the following factors: the parameter β is determined by the magnetostriction field H_p of external stresses, the angle α is governed by the orientation of the X axis in the cut plane of the piezoelectric transducer with respect to the $\mathbf{C}_2$ axis of the crystal in the basal plane, and the parameter χ depends on the magnetic field of the hexagonal basal-plane anisotropy H_a. The experimental angular dependences of the magnetic field strength corresponding to the maximum in the

curve of magnetoacoustic oscillations (Fig. 2) are approximated by functions of form (2) with the following parameters: $\beta \cong 0.5$, $\chi \cong 0.8$, and $\alpha \cong 17°$ in Fig. 2a and $\beta \cong 0.5$, $\chi \cong 0.8$, and $\alpha \cong 105°$ in Fig. 2b (solid lines). As can be seen from Fig. 2b, the approximating function describes the experimental curve satisfactorily. Moreover, this function entirely corresponds to the change in the anisotropy axis by an angle of 90° under variations in the boundary conditions and describes well the general trend of the observed dependence. Based on the experimental data, the exchange-strengthened values of these fields can be estimated as $\sqrt{36H_E H_a} \approx 4.6$ kOe and $\sqrt{2H_E H_p} \approx 1.8$ kOe. The basal-plane anisotropy field is comparable in magnitude to the published data [4].

5. CONCLUSIONS

The observed angular dependence of the magnetic birefringence of the transverse acoustic wave in easy-plane antiferromagnets is determined by the distribution of relatively weak magnetic fields in the basal plane of the crystal. This demonstrates a high sensitivity of the ultrasonic methods, which can be efficiently used to investigate not only the elastic and magnetoelastic properties of strong magnets but also their purely magnetic properties.

ACKNOWLEDGMENTS

This work was supported by the Russian Foundation for Basic Research, project no. 04-02-16025.

REFERENCES

1. I. Sh. Akhmadullin, S. A. Migachev, M. F. Sadykov, and M. M. Shakirzyanov, Fiz. Tverd. Tela (St. Petersburg) **46** (2), 305 (2004) [Phys. Solid State **46**, 312 (2004)].
2. E. A. Turov, Zh. Éksp. Teor. Fiz. **96** (6), 2140 (1989) [Sov. Phys. JETP **69**, 1211 (1989)].
3. V. I. Ozhogin and V. L. Preobrazhenskiĭ, Usp. Fiz. Nauk **155** (4), 593 (1988) [Sov. Phys. Usp. **31**, 713 (1988)].
4. E. A. Turov, A. V. Kolchanov, V. V. Men'shikov, I. F. Mirsaev, and V. V. Nikolaev, *Symmetry and Physical Properties of Antiferromagnets* (Fizmatlit, Moscow, 2001) [in Russian].
5. A. S. Borovik-Romanov and E. G. Rudashevskiĭ, Zh. Éksp. Teor. Fiz. **47** (6), 2095 (1964) [Sov. Phys. JETP **20**, 1407 (1964)].
6. Yu. N. Mitsaĭ, K. M. Skibinskiĭ, M. B. Strugatskiĭ, and V. V. Tarakanov, Fiz. Tverd. Tela (St. Petersburg) **39** (5), 901 (1997) [Phys. Solid State **39**, 803 (1997)].
7. M. A. Urguhart and J. E. Goldman, Phys. Rev. **101** (5), 1443 (1956).
8. V. R. Gakel', Pis'ma Zh. Éksp. Teor. Fiz. **9** (5), 590 (1969) [JETP Lett. **9**, 360 (1969)].
9. A. P. Korolyuk, V. V. Tarakanov, and V. I. Khizhnyĭ, Fiz. Nizk. Temp. **22** (8), 924 (1996) [Low Temp. Phys. **22**, 708 (1996)].
10. E. A. Turov, I. F. Mirsaev, and V. V. Nikolaev, Usp. Fiz. Nauk **172** (2), 193 (2002) [Phys. Usp. **45**, 185 (2002)].
11. E. A. Turov and V. G. Shavrov, Fiz. Tverd. Tela (Leningrad) **7** (1), 217 (1965) [Sov. Phys. Solid State **7**, 166 (1965)].

Translated by N. Korovin

Physics of the Solid State, Vol. 47, No. 3, 2005, pp. 527–530. Translated from Fizika Tverdogo Tela, Vol. 47, No. 3, 2005, pp. 509–511.

MAGNETISM AND FERROELECTRICITY

Electronic Structure and Magnetic States of Crystalline and Fullerene-Like Forms of Nickel Dichloride $NiCl_2$

A. N. Enyashin, N. I. Medvedeva, Yu. E. Medvedeva, and A. L. Ivanovskiĭ

Institute of Solid-State Chemistry, Ural Division, Russian Academy of Sciences, Pervomaĭskaya ul. 91, Yekaterinburg, 620219 Russia

e-mail: ivanovskii@ihim.uran.ru

Received July 12, 2004

Abstract—The electronic structure and magnetic properties of the crystalline and fullerene-like forms of nickel dichloride $NiCl_2$ are investigated in the framework of the local spin density functional theory. It is demonstrated that the band gap can be reproduced in the energy band spectrum of the $NiCl_2$ compound with inclusion of the magnetic ordering in the calculation of the band structure. The metamagnetic nature of the $NiCl_2$ dichloride (i.e., the transition from an antiferromagnetic phase to a ferromagnetic phase in a weak magnetic field) is explained in terms of a small difference (0.025 eV/cell) between the total energies of the ferromagnetic and antiferromagnetic phases. Polyhedral three-shell nanoparticles of the $NiCl_2$ compound exhibit magnetic properties (the magnetic moment of nickel lies in the range 2.0–2.3 μ_B). For isostructural nanoparticles of the $FeCl_2$ dichloride, the magnetic moment of iron is larger and falls in the range 4.2–4.5 μ_B, whereas nanoparticles of the $CdCl_2$ dichloride are found to be nonmagnetic. The results of analyzing the interatomic interactions indicate that the composition of fullerene-like nanoparticles of the dichlorides under investigation can deviate from the 1 : 2 stoichiometric composition. © *2005 Pleiades Publishing, Inc.*

1. INTRODUCTION

Among the magnetic materials suitable for a wide range of practical applications, quasi-two-dimensional metamagnetic systems are of particular interest. The best known representatives of these systems are nickel dichloride $NiCl_2$ and isostructural *d* metal dihalides of the $CdCl_2$ type. In the ground state, the $NiCl_2$ dichloride is an antiferromagnetic material. The $NiCl_2$ compound in the antiferromagnetic phase has a structure consisting of nickel ferromagnetic layers in which the adjacent layers are antiferromagnetically ordered [1, 2]. The $NiCl_2$ dichloride undergoes a transition from the antiferromagnetic phase to the ferromagnetic phase in weak magnetic fields.

The mechanism responsible for the formation of a band gap in the energy band spectrum of the $NiCl_2$ dichloride and a number of other crystalline nickel-containing compounds has been a matter of great discussion between different groups of researchers [3]. In particular, the one-electron spin-restricted calculations performed by Ackerman *et al*. [4] predicted that the $NiCl_2$ dichloride should possess metallic conductivity. However, Ronda *et al*. [3] carried out experimental investigations of the photoconductivity in nickel dichloride and revealed that the energy band spectrum of this compound is characterized by a band gap of ~4.6 eV. Antoci and Minich [5] and Zaanen *et al*. [6] assumed that the formation of a band gap in the band spectrum of nickel dichloride can be caused by transitions from a Ni 3*d*–Cl 3*p* occupied band to a Ni *d* empty energy band rather than by transitions between *d*–*d* states of nickel; i.e., the band gap in the band spectrum of this compound is associated with charge-transfer transitions and is not a Mott–Hubbard gap, in contrast to the case with nickel oxide NiO. The question regarding the role played by magnetism in the formation of a band gap in the energy band spectrum of the $NiCl_2$ dichloride remains open.

Quite recently, Hacohen *et al*. [7] synthesized unique quasi-one-dimensional and quasi-zero-dimensional nanostructures of nickel dichloride (namely, nanotubes and polyhedral fullerene-like nanoparticles, respectively) through reactive laser ablation [7]. Moreover, Hacohen *et al*. [8] and Popovitz-Biro *et al*. [9] prepared a number of fullerene-like nanoparticles from related metal dihalides, such as CdI_2, $CdCl_2$, and $FeCl_2$. However, there are no reliable data on the electronic and magnetic properties of these low-dimensional systems.

In this work, the electronic structure and magnetic states of the crystalline (two-dimensional) and fullerene-like (zero-dimensional) forms of the $NiCl_2$ dichloride were thoroughly investigated within the local spin density functional theory formalism for the first time. Moreover, we examined the magnetic properties of $FeCl_2$ and $CdCl_2$ fullerene-like nanoparticles.

2. COMPUTATIONAL TECHNIQUE, RESULTS, AND DISCUSSION

Nickel dichloride $NiCl_2$ has a layered structure (space group $R\bar{3}m$) consisting of molecular layers,

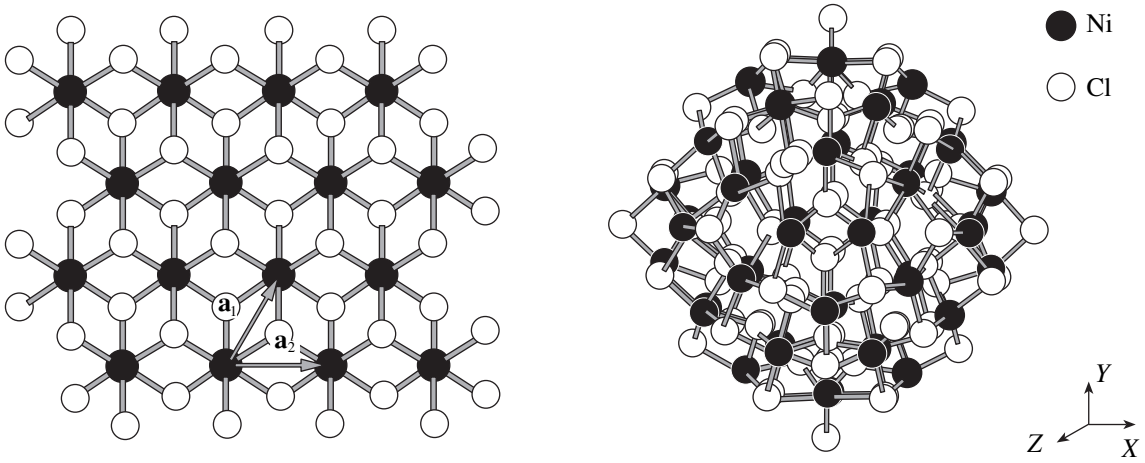

Fig. 1. Atomic structures of a fragment of the $NiCl_2$ molecular layer ($\mathbf{a}_1$ and $\mathbf{a}_2$ are translational vectors) and a polyhedral (fullerene-like) nanoparticle of the composition $(NiCl_2)_{48}$.

each composed of three Cl–Ni–Cl atomic networks (Fig. 1). The band structure of the $NiCl_2$ crystal was calculated using the linearized muffin-tin orbital method [10] for three phases, namely, the nonmagnetic, ferromagnetic, and real antiferromagnetic phases. The antiferromagnetic phase has a structure composed of nickel ferromagnetic layers in which the adjacent layers are antiferromagnetically ordered [1, 2]. For the nonmagnetic phase of the $NiCl_2$ compound, the energy at the Fermi level E_F coincides with the maximum of the density of nickel *d* states. Owing to the ferromagnetic ordering, the total energy of the system decreases by ~0.31 eV and the energy band spectrum is characterized by a band gap of ~0.35 eV (Fig. 2). Thus, the comparison of the results obtained for the nonmagnetic and ferromagnetic phases of the $NiCl_2$ dichloride shows that the band gap can be reproduced in the energy band spectrum of this compound with inclusion of the in-plane magnetic ordering in the band structure calculation performed in the framework of the local spin density functional theory.

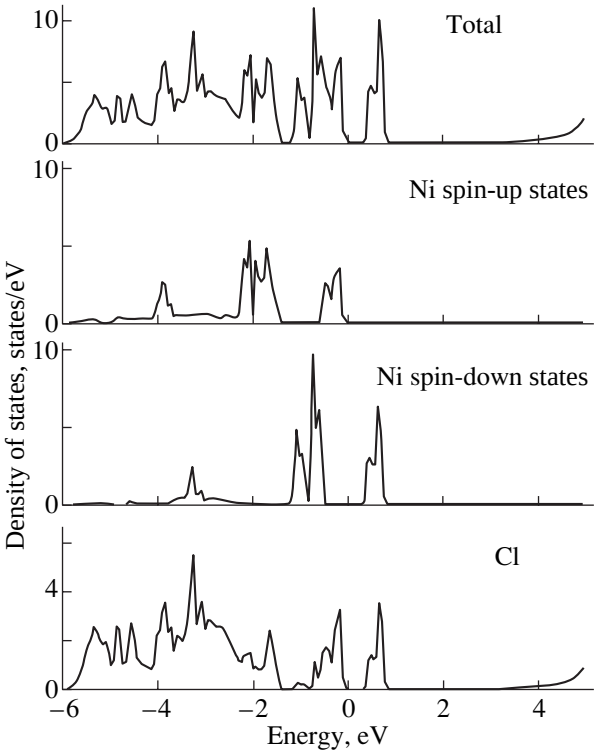

Fig. 2. Total and partial densities of states for the $NiCl_2$ ferromagnetic phase according to the linearized muffin-tin orbital calculations.

In the $NiCl_2$ compound, Ni^{2+} ions have a $3d^8$ configuration in which six electrons occupy the t_{2g} bands and two electrons are localized in the e_g bands. In the ferromagnetic phase of the $NiCl_2$ compound, electrons occupy the t_{2g} spin-up states, the e_g spin-up states, and the t_{2g} spin-down states. The top of the valence band is formed by the e_g bands overlapping with the Cl 3*p* states; i.e., the formation of the band gap is associated with transitions between the $e_g^{\uparrow}$ hybridized states and the $e_g^{\downarrow}$ unoccupied states (Fig. 2). The magnetic moment of nickel is equal to 1.3 μ_B.

The inclusion of the antiferromagnetic ordering between the nickel ferromagnetic layers leads to a lowering of the $e_g^{\uparrow}$ occupied band and to an increase in the band gap to 0.42 eV. It should be particularly emphasized that the total energy of the antiferromagnetic phase is 0.025 eV lower than the total energy of the ferromagnetic phase. In this case, the band structures of the antiferromagnetic and ferromagnetic phases differ insignificantly. Therefore, the electronic properties of

the $NiCl_2$ dichloride are only slightly affected by the antiferromagnetic ordering and the metamagnetic nature of this compound (i.e., the transition from the antiferromagnetic phase to the ferromagnetic phase in a weak magnetic field) can be explained in terms of the very small difference between the total energies of the ferromagnetic and antiferromagnetic phases.

Atomic models of the low-dimensional structures of the $NiCl_2$ compound were constructed on the basis of a Cl–Ni–Cl molecular layer. This layer can be described by the primitive translational vectors $\mathbf{a}_1$ and $\mathbf{a}_2$ (Fig. 1). Models of the chiral and achiral nanotubes were obtained by rolling "ribbons" cut from a layer of width $|c| = na_1 + ma_2$ [7, 11]. Fullerene-like nanoparticles were modeled with the use of $NiCl_2$ layer fragments serving as nanoparticle faces. In order to provide alternation of the Ni–Cl bonds, vertices of these fullerene-like nanoparticles, unlike carbon fullerenes, must be occupied by even numbers of atoms. With due regard for this requirement, it is possible to construct only one type of polyhedral particles in which the face walls are built of $NiCl_6$ octahedra shared by edges and each vertex is formed by two octahedra shared by faces (Fig. 1). In order to ensure the stoichiometric composition $NiCl_2$, it is necessary to remove two chlorine atoms, for example, from two vertices of the fullerene-like nanoparticles (Fig. 1). Such fullerenes of the stoichiometric composition $NiCl_2$ are three-shell nanoparticles of the cage type in which the outer and inner shells are composed of chlorine atoms and the middle shell consists of nickel atoms. These nanoparticles have octahedral morphology, which was experimentally observed by Hacohen *et al*. [7].

The electronic and magnetic properties of $NiCl_2$, $FeCl_2$, and $CdCl_2$ fullerene-like nanoparticles were investigated using the example of polyhedral nanoparticles of the composition $(MeCl_2)_{48}$. The particle geometry was optimized by the MM+ molecular mechanics method with allowance made for dipole interactions. The calculations were performed using the spin-polarized discrete-variational method [12]. The model densities of states are presented in Fig. 3. The Cl 3*p* states are localized in the energy range 8–2 eV below the Fermi level E_F. The near-Fermi states predominantly involve the Ni 3*d* orbitals. Fullerene-like nanoparticles of the composition $(NiCl_2)_{48}$ are characterized by a metal-like band spectrum. A similar band spectrum is obtained for $(FeCl_2)_{48}$ nanoparticles. For $(CdCl_2)_{48}$ nanoparticles, the upper valence band is primarily formed by the Cl 3*p* states and the lowest free energy states are of the mixed Cd 5*s*–Cl 3*p* type. The band gap is approximately equal to 0.5 eV. The atomic magnetic moments of the $(NiCl_2)_{48}$, $(FeCl_2)_{48}$, and $(CdCl_2)_{48}$ fullerene-like nanoparticles were calculated from the populations of the atomic spin orbitals. According to these calculations, the atomic magnetic moments are equal to 2.0–2.3 μ_B for the $(NiCl_2)_{48}$ nanoparticles and 4.2–4.5 μ_B for the $(FeCl_2)_{48}$ nanoparticles. The $(CdCl_2)_{48}$ nanoparticles are found to be nonmagnetic.

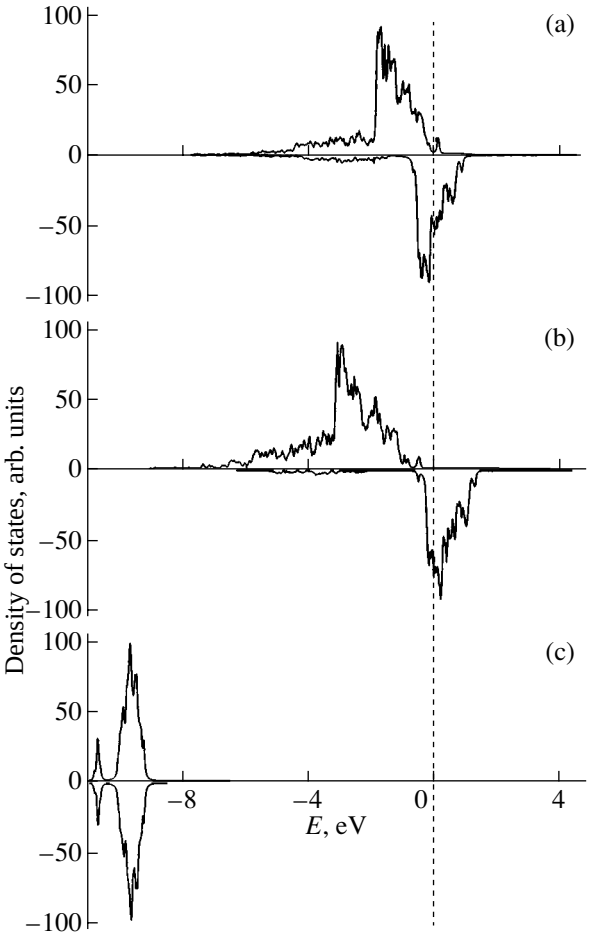

Fig. 3. Model densities of *d* states of metal atoms in (a) $(NiCl_2)_{48}$, (b) $(FeCl_2)_{48}$, and (c) $(CdCl_2)_{48}$ fullerene-like nanoparticles according to the spin-polarized discrete-variational calculations. The vertical line indicates the edge of the occupied band.

The calculations of the overlap integrals and the effective atomic charges *Q* demonstrated that the Coulomb interactions play a dominant role in the stabilization of the $(NiCl_2)_{48}$ and $(FeCl_2)_{48}$ fullerene-like nanoparticles, whereas the covalent component of the bond is small (the overlap integral is less than 0.1 e). The degree of ionicity of the bond is estimated from the Pauling formula and is approximately equal to 75%. The atomic charges of the metallic shell of the nanoparticles fall in the range +(0.33–0.41) for nickel and in the range +(0.35–0.46) for iron. Two groups of atoms can be clearly distinguished among the nonequivalent chlorine atoms involved in the outer and inner shells of the fullerene-like nanoparticles. For atoms of the first group, the effective atomic charges *Q* lie in the range –(0.19–0.36) for the $(NiCl_2)_{48}$ nanoparticles and in the range –(0.25–0.30) for the $(FeCl_2)_{48}$ nanoparticles. For atoms of the second group, the effective charges *Q* are considerably smaller and equal to ~–0.07 for the $(NiCl_2)_{48}$ nanoparticles and –(0.01–0.10) for the

$(FeCl_2)_{48}$ nanoparticles. This implies that chlorine atoms of the latter group are weakly bonded to metals atoms and can easily leave the nanoparticle cage. This group contains 36 chlorine atoms located in the inner shell of the nanoparticle. Therefore, the 1 : 2 stoichiometric composition of the fullerene-like nanoparticle can change to 1 : 1.25. This ratio is in good agreement with the results obtained in [7–9], according to which the composition of the dichloride fullerene-like nanoparticles synthesized is characterized by a ratio of 1 : 1.2 (or less).

3. CONCLUSIONS

Thus, the electronic structure and magnetic states of the crystalline and fullerene-like forms of the $NiCl_2$ dichloride were investigated using the linearized muffin-tin orbital and discrete-variational methods in the framework of the local spin density functional theory. It was demonstrated that the band gap can be reproduced in the energy band spectrum of the $NiCl_2$ crystal with inclusion of the magnetic ordering in the calculation of the band structure. The calculations of the total energies for three phases, namely, the nonmagnetic, ferromagnetic, and antiferromagnetic phases, showed that the antiferromagnetic phase is more stable. The metamagnetic nature of the $NiCl_2$ dichloride and the transition from the antiferromagnetic phase to the ferromagnetic phase in a weak magnetic field were explained in terms of the small difference between the total energies of the ferromagnetic and antiferromagnetic phases.

It was established that $NiCl_2$ polyhedral three-shell (fullerene-like) nanoparticles possess magnetic properties (the magnetic moment of nickel is equal to 2.0–2.3 μ_B). For isostructural fullerene-like nanoparticles of the $FeCl_2$ dichloride, the magnetic moment of iron is larger and falls in the range 4.2–4.5 μ_B, whereas nanoparticles of the $CdCl_2$ dichloride are found to be nonmagnetic. The results of analyzing the interatomic interactions indicate that the composition of dichloride fullerene-like nanoparticles can deviate from the 1 : 2 stoichiometric composition.

ACKNOWLEDGMENTS

This work was supported by the Russian Foundation for Basic Research, project nos. 04-03-32111 and 04-03-96117 (Ural).

REFERENCES

1. L. Landau, Phys. Z. Sowjetunion **4**, 675 (1933).
2. P. A. Lindgard, R. J. Birgeneau, J. Als-Nielsen, and H. J. Guggenheim, J. Phys. C **8** (7), 1059 (1975).
3. C. R. Ronda, G. J. Arends, and C. Haas, Phys. Rev. B **35** (8), 4038 (1987).
4. J. Ackerman, C. Fouassier, E. L. Holt, and S. L. Holt, Inorg. Chem. **11** (12), 3118 (1972).
5. S. Antoci and L. Minich, Phys. Rev. B **21** (8), 3383 (1980).
6. J. Zaanen, G. A. Sawatzky, and J. W. Allen, Phys. Rev. Lett. **55** (4), 418 (1985).
7. Y. R. Hacohen, R. Popovitz-Biro, Y. Prior, S. Gemming, G. Seifert, and R. Tenne, Phys. Chem. Chem. Phys. **5** (8), 1644 (2003).
8. Y. R. Hacohen, R. Popovitz-Biro, E. Grunbaum, Y. Prior, and R. Tenne, Adv. Mater. **14**, 1075 (2002).
9. R. Popovitz-Biro, N. Sallacan, and R. Tenne, J. Mater. Chem. **13** (7), 1631 (2003).
10. O. K. Andersen, Phys. Rev. B **12** (8), 3060 (1975).
11. V. V. Ivanovskaya, A. N. Enyashin, N. I. Medvedeva, and A. L. Ivanovskii, cond-mat/0304230 (2003).
12. M. R. Press and D. E. Ellis, Phys. Rev. B **35** (9), 4438 (1987).

Translated by O. Borovik-Romanova

Physics of the Solid State, Vol. 47, No. 3, 2005, pp. 531–538. Translated from Fizika Tverdogo Tela, Vol. 47, No. 3, 2005, pp. 512–518.

LATTICE DYNAMICS AND PHASE TRANSITIONS

Vibrational Spectrum and Elastic Properties of KPb_2Cl_5 Crystals

K. S. Aleksandrov*, A. N. Vtyurin*, A. P. Eliseev, N. G. Zamkova*, L. I. Isaenko**, S. N. Krylova*, V. M. Pashkov**, P. P. Turchin***, and A. P. Shebanin****

** Kirensky Institute of Physics, Siberian Division, Russian Academy of Sciences, Akademgorodok, Krasnoyarsk, 660036 Russia*

e-mail: vtyurin@iph.krasn.ru

*** Joint Institute of Geology, Geophysics, and Mineralogy, Siberian Division, Russian Academy of Sciences, pr. Nauki 3, Novosibirsk, 630090 Russia*

**** Krasnoyarsk State University, Krasnoyarsk, 660041 Russia*

Received June 22, 2004

Abstract— The Raman spectra and elastic moduli of KPb_2Cl_5 crystals were studied experimentally. The results are interpreted using a parameter-free model of the crystal lattice dynamics with inclusion of the multipole moments of the electron shells of ions. The calculated and experimental results are in good agreement. It is shown that not only the halogen ions but also the heavy cations make a significant contribution to the eigenvectors of high-frequency lattice vibration modes, which accounts for the relatively low frequencies of these modes. *© 2005 Pleiades Publishing, Inc.*

1. INTRODUCTION

The current development of solid-state systems of infrared nonlinear optics and photonics has stimulated a search for and the creation of new materials that have a broad spectral window in the IR region (the low-frequency boundary is 30 μm). Because of this trend, interest has recently arisen in studying the optical and spectral properties of complex halides containing heavy cations, which have a relatively short phonon spectrum in contrast to traditional oxide systems.

Crystals of the $Me^+Pb_2Hal_5$ family (where Me^+ is an alkali metal and Hal is a halogen) have the abovementioned spectral window in the IR region, and there exist techniques for growing relatively large single crystals of these compositions [1]. Unlike many other complex halides, these crystals are sufficiently resistant to the atmosphere. A rather loose packing of ions having large radii in the lattice opens up wide possibilities for varying the compositions and properties of these crystals and for their use as active laser media [2]. However, the physical properties of these crystals have not been studied in detail.

In this work, we study the vibrational spectrum and elastic properties of KPb_2Cl_5 crystals, which belong to this family. In this study, we intend to elucidate the nature of formation of the low-frequency boundary of the spectral window of the crystal and determine the structural blocks and interactions that control its position. This study also allows us to obtain information on the relation between the crystal structure and the crystal elastic moduli, which are of interest from both the standpoint of materials-science characterization of the material and its possible applications in acoustooptical IR devices.

To interpret the vibrational spectrum and to establish a relation between the lattice vibration frequencies and the lattice structure, we use the first-principles approach developed recently in [3–5]. It should be noted that, in the case of low-symmetry structures with a large number of atoms in a unit cell, the use of empirical methods (see, e.g., [6, 7]), which are traditionally employed for this purpose, requires a large number of fitting parameters, which cannot be determined using a limited amount of experimental data. Therefore, the application of parameter-free methods becomes very important.

2. EXPERIMENTAL

KPb_2Cl_5 crystals belong to the monoclinic space group $P2_1/c$ and have a = 8.854(2) Å, b = 7.927(2) Å, c = 12.485(3) Å, β = 90.05(3), V = 876.3(4) Å^3, Z = 4, and a density of 4.781 g/cm^3. The coordinates of the atoms are given in Table 1, and the projection of the structure on the *bc* plane is shown in Fig. 1 [8].

To fabricate optical-grade single crystals, the starting $PbCl_2$ and KCl reagents were repeatedly purified by resolidification. KPb_2Cl_5 crystals were grown using the Bridgman crystal growth technique in a two-zone furnace. The linear temperature gradient in the growth region of the furnace was about 20 K/cm, and the velocity of ampoule motion to the cold zone was 2–4 mm/day. The technique is described in more detail in [9]. The crystal structure was determined at room temperature using a STOE STADI4 single-crystal diffractometer and MoK_α radiation ($2\theta_{max}$ = 80°). The samples chosen had no inclusions or defects visible under a polarizing microscope and were subjected to a mechanical treat-

Table 1. Atomic coordinates ($\times 10^4$) in crystal KPb_2Cl_5

	X	*Y*	*Z*
K(1)	5092(5)	514(6)	1696(4)
Pb(1)	65(1)	58(1)	1742(1)
Pb(2)	2547(1)	4359(1)	9937(1)
Cl(1)	9585(4)	1655(5)	4023(3)
Cl(2)	2218(4)	405(4)	9986(3)
Cl(3)	5401(5)	1798(6)	4186(4)
Cl(4)	2355(5)	3117(5)	2204(3)
Cl(5)	7702(6)	3449(5)	1885(3)

ment followed by polishing in a solution of hydrochloric acid.

Raman spectra were excited with polarized 514.5-nm radiation from a 500-mW Ar^+ laser. The spectra were recorded on a U-1000 spectrometer (I.S.A. Jobin Yvon, France). For experiments, we used $2 \times 2 \times 4$-mm samples, with the edges orientated along the crystallographic axes.

The elastic moduli $C_{\lambda\mu}$ were determined by measuring the velocities of bulk acoustic waves (BAWs) followed by solving the inverse problem of crystal acoustics.

The BAW velocities were measured using four single-crystal samples in the form of a rectangular parallelepiped with linear dimensions of about 6 mm. The faces of the first sample were normal to the [100], [010], and [001] crystallographic axes. The faces of the other three samples were normal to the axes of the coordinate system that is obtained by rotating the initial system through 45° about one of the following three axes: axis X_1 ([100], $\left[0\frac{1}{\sqrt{2}}\frac{1}{\sqrt{2}}\right]$, $\left[0\frac{-1}{\sqrt{2}}\frac{1}{\sqrt{2}}\right]$ directions), X_2 ($\left[\frac{1}{\sqrt{2}}0\frac{1}{\sqrt{2}}\right]$, [010], $\left[\frac{-1}{\sqrt{2}}0\frac{1}{\sqrt{2}}\right]$ directions), or X_3 ($\left[\frac{1}{\sqrt{2}}\frac{1}{\sqrt{2}}0\right]$,$\left[\frac{-1}{\sqrt{2}}\frac{1}{\sqrt{2}}0\right]$, [001] directions). Using the crystal symmetry and this set of directions, we can perform two independent measurements in different crystallographic directions for each velocity to be measured. X-ray orientations of the samples were carried out to an accuracy of better than ±5'. The opposite faces of the samples were parallel to each other with an accuracy of better than ±2 μm/m.

The velocities of longitudinal and shear BAWs were measured using a pulse ultrasound method [10]; the block diagram of the setup employed is shown in Fig. 2. The operation of the setup is based on measuring the time of propagation of an ultrasound pulse in a sample. A short (10-ns) video pulse from generator *1* is supplied to piezoelectric transducer *2* (the BAW velocities are measured with piezoelectric transducers based on lithium niobate with a resonance frequency of 29.5 MHz); after multiple reflections in sample *3*, a pulse train is preliminarily amplified by amplifier *4* and then is visually recorded by oscilloscope *5*. The main pulse train of time-interval counter *6* activates generator *1*, and the delayed-pulse train synchronizes the sweep of oscillo-

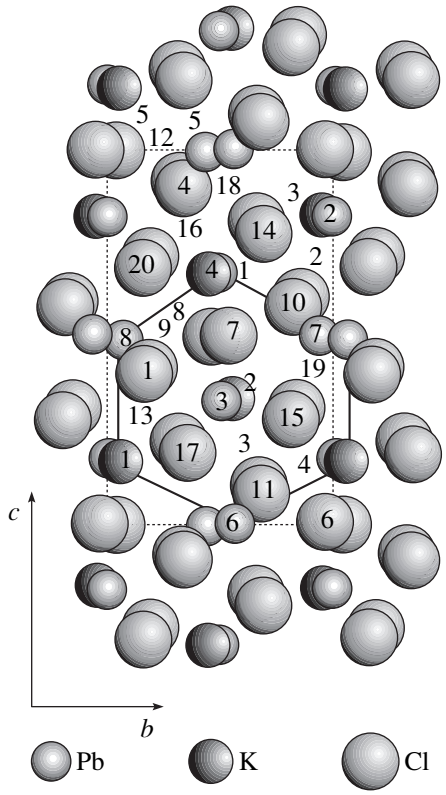

Fig. 1. Projection of the KPb_2Cl_5 structure on the *bc* plane. The pseudohexagonal packing of the channels that contain metal cations and are extended along the *a* direction is shown. Numerals are the ion numbers (identical to those in Fig. 4).

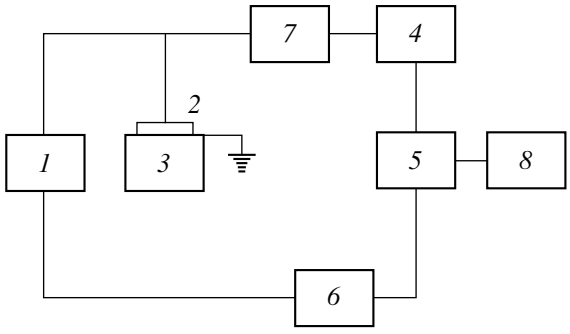

Fig. 2. Block diagram of the ultrasound experimental setup: (*1*) G5-11 video-pulse generator, (*2*) piezoelectric transducer, (*3*) sample, (*4*) U2-5 resonance amplifier (30 MHz), (*5*) S7-9 sampling oscilloscope, (*6*) I2-26 time-interval counter, (*7*) diode limiter of the probe-pulse amplitude, and (*8*) ATsP 1 analog-to-digital converter.

scope 5. The experimental procedure consists in measuring the time interval between two sequentially reflected radio pulses on the oscilloscope screen. This scheme gives an accuracy of 10^{-2} and 10^{-4}% for absolute and relative measurements of the BAW velocities, respectively.

3. RESULTS AND DISCUSSION

3.1. Vibrational Spectrum

The vibrational representation is reduced to the following irreducible representations at the center of the Brillouin zone:

$$\Gamma = 24A_g(xx, yy, zz, xy, yx) + 24B_g(xz, zx, yz, zy) + 24A_u + 24B_u, \quad (1)$$

where the parentheses contain the Raman tensor components for which the corresponding lattice vibrations are active. Note that, because of the low symmetry and the complex crystal structure, it is impossible to separate vibration modes related by individual atomic sublattices using group-theoretical considerations.

The experimental Raman spectra of KPb_2Cl_5 crystals recorded at room temperature are shown in Fig. 3. As expected, the spectra are restricted to low frequencies; indeed, all the lines are below 250 cm^{-1}. The spectra are strongly anisotropic, and the spectral lines are highly polarized. The number of well-resolved peaks is slightly smaller than the number of modes determined from Eq. (1); therefore, their interpretation requires comparison of the peaks with the results of model calculations.

The vibrational spectrum of the KPb_2Cl_5 crystal lattice was calculated in terms of the generalized Gordon–Kim model [3, 4], in which distortions of the electron densities of ions are included. Taking these distortions into account is especially important for low-symmetry structures, since the interactions of multipole moments of ions in them contribute substantially to the total lattice energy and the crystal vibration frequencies.

Following [3, 4], we calculated the electron-density distribution of each ion in the presence of an external field of the corresponding symmetry:

$$V_{\text{ext}}^{(l)} = r^{(l)}P_l(\cos\theta), \quad (2)$$

where $P_l(\cos\theta)$ are Legendre polynomials. The spherically symmetrical component of an external potential was taken to be the Watson sphere potential

$$V_W = \begin{cases} -Z_{\text{ion}}/R_W, & r < R_W \\ -Z_{\text{ion}}/r, & r > R_W. \end{cases} \quad (3)$$

In the calculations, we took into account dipole ($l = 1$) and quadrupole ($l = 2$) electron-density distortions.

The radii of the Watson spheres for each ion were determined by minimizing the total crystal energy

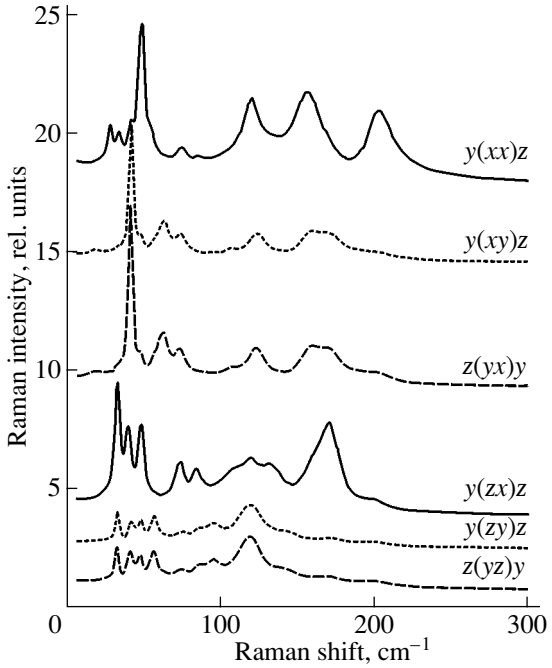

Fig. 3. Polarized Raman spectra of crystal KPb_2Cl_5.

(Table 2). Table 2 also contains the dipole (α_d) and quadrupole (α_q) ion polarizabilities calculated using a modified Steinheimer equation [3, 4]. The corresponding values of induced dipole (P) and quadrupole (Q) moments were found by minimizing the total crystal energy with respect to the corresponding moment: $\partial E/\partial P_\alpha = 0$ and $\partial E/\partial Q_{\alpha\beta} = 0$. The expressions used to calculate the total crystal energy, dipole and quadrupole moments, and the dynamical matrix can be found in [4, 5].

The equilibrium values of the lattice parameters were refined by minimizing the total crystal energy as a function of these parameters. For this purpose, we used the experimentally determined atomic coordinates in the unit cell (Table 1). The values obtained (a = 8.7 Å, b = 7.6 Å, c = 12.5 Å) agree well with the experimental data.

The eigenvectors obtained by diagonalizing the dynamical matrix were subjected to symmetry analysis. We constructed the complete vibrational representation

Table 2. Calculated parameters of the interionic interactions in crystal KPb_2Cl_5

Parameter	K^+	Pb^{2+}	Cl^-
R_W, Å	1.85	1.85	1.16
α_d, Å^3	0.7	1.6	3.3
α_q, Å^5	0.9	1.5	5.8

Table 3. Experimental and calculated frequencies of Raman-active lattice vibration modes in crystal KPb_2Cl_5

A_g, ω, cm^{-1}		B_g, ω, cm^{-1}	
calculation	experiment	calculation	experiment
34i		38i	
26i		28i	
25i		6	
21	18	28	33
34	27	39	40?
41	35	45	42
45	43	46	48
53	50	57	57
57	56	64	
58		67	
60	62	71	
67		74	75
73	73	80	85
76		84	
86	85	90	88
91		95	95
92		100	
101		103	108
106	108	107	119
110	120	115	132
123	124	120	144
129	127	129	158
134	132	140	173
159	200?	161	202

Table 4. BAW velocities in a KPb_2Cl_5 single crystal (experiment)

No.	Propagation direction	Wave type	Polarization	Velocity, m/s
1	[001]	*QL*	[001]	2766.2
2		*SS*	[010]	1520.8
3		*QSF*	[100]	1532.6
4	$\left[\frac{1}{\sqrt{2}}\ \frac{1}{\sqrt{2}}\ 0\right]$	*QL*	$\left[\frac{1}{\sqrt{2}}\ \frac{1}{\sqrt{2}}\ 0\right]$	3027.4
5		*QSS*	$\left[\frac{-1}{\sqrt{2}}\ \frac{1}{\sqrt{2}}\ 0\right]$	1442.5
6		*QSF*	[001]	1529.1
7	[010]	*L*	[010]	2717.8
8		*SF*	[001]	1731.3
9		*SS*	[100]	1521.0
10	$\left[\frac{1}{\sqrt{2}}\ 0\ \frac{1}{\sqrt{2}}\right]$	*QL*	$\left[\frac{1}{\sqrt{2}}\ 0\ \frac{1}{\sqrt{2}}\right]$	2894.0
11		*QSS*	$\left[\frac{-1}{\sqrt{2}}\ 0\ \frac{1}{\sqrt{2}}\right]$	1464.6
12		*SF*	[010]	1610.2
13	[100]	*QL*	[100]	3010.3
14		*QSS*	[001]	1532.8
15		*SF*	[010]	1730.6
16	$\left[0\ \frac{1}{\sqrt{2}}\ \frac{1}{\sqrt{2}}\right]$	*QL*	$\left[0\ \frac{1}{\sqrt{2}}\ \frac{1}{\sqrt{2}}\right]$	2778.9
17		*QSS*	$\left[0\ \frac{-1}{\sqrt{2}}\ \frac{1}{\sqrt{2}}\right]$	1471.5
18		*QSF*	[100]	1637.7

$P(g)$ of the crystal space group, which was used to calculate the projection operators [11]:

$$\Gamma_\rho = \frac{N(\rho)}{N(g)} \sum_{g \in G} \chi_\rho(g)\Gamma(g), \qquad (4)$$

where $N(\rho)$ is the dimension of the representation ρ of point symmetry operation, $N(g)$ is the dimension of the symmetry group, $\chi_\rho(g)$ is the character of the matrix of the irreducible representation ρ, $\Gamma(g)$ is the vibrational representation of the symmetry operation of the irreducible representation ρ of group G, and Γ_ρ is the projection operator. Summation is taken over all symmetry-group operations. A vibration eigenvector **f** is transformed according to the irreducible representation ρ of group G if it satisfies the criterion [11]

$$\Gamma_\rho \mathbf{f} = \frac{N(g)}{N(\rho)}\mathbf{f}. \qquad (5)$$

This algorithm of expansion of the eigenvectors of the dynamical matrix in terms of irreducible representations was realized using the Mathematica 4.2 software package.

The experimental and calculated frequencies of the Raman spectrum are given in Table 3. Note that these experimental and calculated frequencies agree well in the middle portion of the spectrum. For the lowest frequencies (below 20 cm^{-1}), the calculated frequencies depend strongly on small changes in the atomic coordinates; their variation within the experimental error can result in significant (up to 100%) changes in the vibration frequencies.

Figure 4 shows the relative contributions of the atomic displacements to the eigenvectors of the corresponding modes (the renormalization to ionic masses was taken into account). To check the correctness of the procedure, we calculated the atomic displacements for

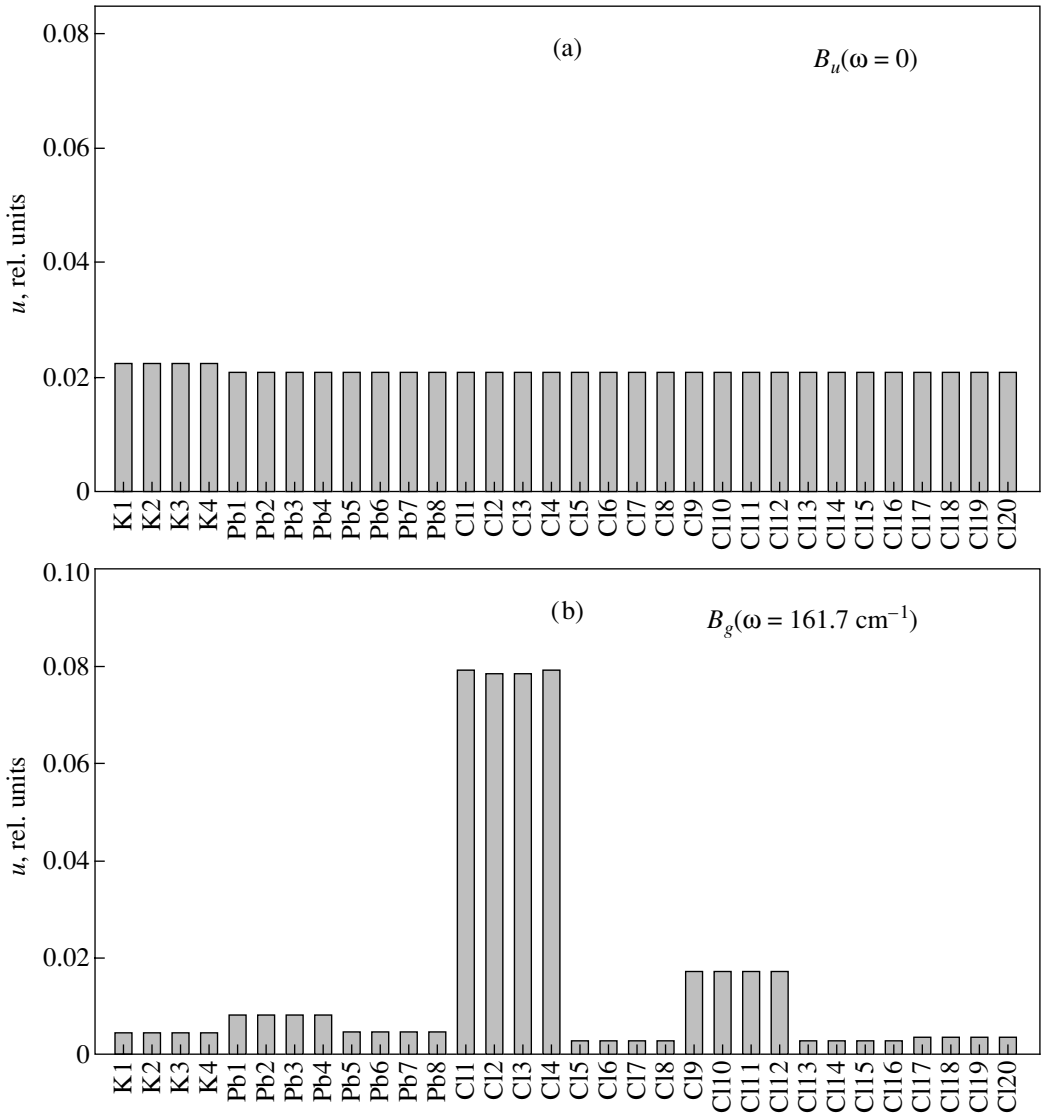

Fig. 4. Relative ion-vibration amplitudes of (a) the acoustic mode, (b) high-frequency mode, and (c) low-frequency mode. (d) The relative ion-vibration amplitude of a middle-range Raman-active mode. (e) The relative ion-vibration amplitude of a Raman-inactive polar mode.

the acoustic mode. The results support the correctness and are shown in Fig. 4a. Figure 4b shows the atomic displacements for the highest frequency spectrum mode, which corresponds to the spectral-window boundary of the crystal. It is seen that, although the maximum displacements correspond to chlorine ions, the contribution of heavy metal ions to the eigenvector of this vibration remains significant, which is likely to account for the relatively low value of the corresponding frequency (as compared, e.g., to the frequencies in high-symmetry perovskite-like chloride systems [15]).

As is seen in Figs. 4c–4e, the low symmetry of the structure leads to a strong interaction between the vibrations of atomic sublattices in virtually all vibration modes; in particular, even the lowest frequency modes contain a significant contribution from the displacements of light chlorine ions.

3.2. Elastic Moduli

The problem of determining the elastic moduli $C_{\lambda\mu}$ by measuring the BAW velocities for monoclinic media was solved in [12] and discussed in detail in [13]. In the chosen crystallographic setting, the elastic-modulus matrix of the crystal has the form [14]

$$\begin{pmatrix} C_{11} & C_{12} & C_{13} & 0 & C_{15} & 0 \\ C_{12} & C_{22} & C_{23} & 0 & C_{25} & 0 \\ C_{13} & C_{23} & C_{33} & 0 & C_{35} & 0 \\ 0 & 0 & 0 & C_{44} & 0 & C_{46} \\ C_{15} & C_{25} & C_{35} & 0 & C_{55} & 0 \\ 0 & 0 & 0 & C_{46} & 0 & C_{66} \end{pmatrix}. \quad (6)$$

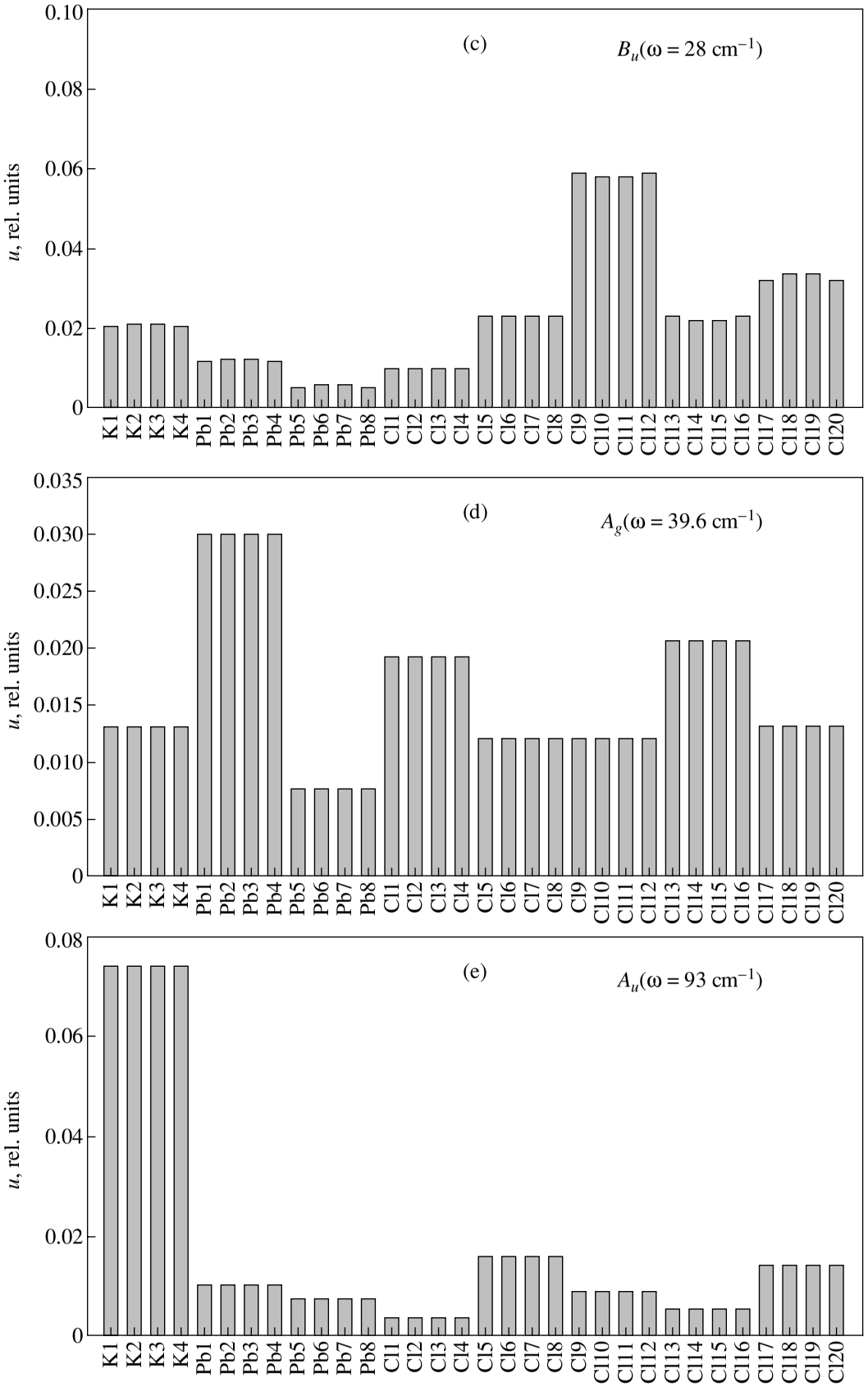
(c)
$B_u(\omega = 28\ \mathrm{cm}^{-1})$
(d)
$A_g(\omega = 39.6\ \mathrm{cm}^{-1})$
(e)
$A_u(\omega = 93\ \mathrm{cm}^{-1})$
u, rel. units
K1 K2 K3 K4 Pb1 Pb2 Pb3 Pb4 Pb5 Pb6 Pb7 Pb8 Cl1 Cl2 Cl3 Cl4 Cl5 Cl6 Cl7 Cl8 Cl9 Cl10 Cl11 Cl12 Cl13 Cl14 Cl15 Cl16 Cl17 Cl18 Cl19 Cl20

Fig. 4. (Contd.)

Table 5. Experimental and calculated elastic moduli of crystal KPb_2Cl_5 (in units of 10^{10} N/m^2)

Elastic modulus	C_{11}	C_{12}	C_{13}	C_{15}	C_{22}	C_{23}	C_{25}	C_{33}	C_{35}	C_{44}	C_{46}	C_{55}	C_{66}
Experiment	4.34	1.93	1.77	–0.55	3.53	1.52	0.05	3.62	0.06	1.11	0.03	1.10	1.43
Calculation	4.00	1.30	1.37	–0.03	3.87	1.42	0.01	3.47	0.01	1.30	0.03	1.30	1.24

The independent elastic moduli were separately determined using the method of special directions [12, 13]. The measured BAW velocities and the main BAW characteristics are given in Table 4. The experimental error in determining the BAW velocities was less than 0.5 m/s.

The elastic moduli $C_{\lambda\mu}$ are calculated from the known eigenvalues ρv^2 of the Green–Christoffel tensor [13] $\Gamma_{\alpha\gamma} = C_{\alpha\beta,\gamma\delta}n_\beta n_\delta$ by solving the Green–Christoffel equations $(\Gamma_{\alpha\gamma} - \rho v^2\delta_{\alpha\gamma})U_\delta = 0$ for each crystallographic direction. Here, $\rho = 4.780$ g/cm^3 is the density of the crystal under study; v is the velocity of BAW with polarization U_δ; n_α are the direction cosines of the wave normal; and $C_{\alpha\beta,\gamma\delta}$ is the elastic-modulus tensor, whose components are related to the elastic-modulus matrix $C_{\lambda\mu}$ by the well-known Voigt transformation [14].

The elastic moduli of the single crystal are calculated using the procedure described in [12, 13] and are given (in units of 10^{10} N/m^2) in Table 5, which also presents the elastic moduli calculated in the Gordon–Kim model. For centrosymmetric crystals, the elastic moduli are related to the dynamical matrix of a crystal by the expressions [6]

$$C_{\alpha\beta,\gamma\delta} = [\alpha\beta,\gamma\delta] + [\gamma\beta,\alpha\delta] - [\alpha\gamma,\beta\delta],$$
$$[\alpha\beta,\gamma\delta] = \frac{1}{2V}\sum_{k,k'=1}^{N_a}\sqrt{m_k m_{k'}}D^{\gamma\delta}_{kk',\alpha\beta}, \quad (7)$$

where V is the unit cell volume, k and k' are the ion indices, N_a is the number of ions in the unit cell, m_k is the ion mass, and

$$D^{\gamma\delta}_{kk',\alpha\beta} = \left.\frac{\partial^2 D_{kk',\alpha\beta}}{\partial q_\gamma \partial q_\delta}\right|_{q=0}$$

are the coefficients of expansion of the dynamical matrix D in powers of the wave vector **q** for the second-order term.

A comparison of the experimental and calculated values shows that they agree well with each other.

4. CONCLUSIONS

We have recorded the polarized Raman spectra of KPb_2Cl_5 crystals and interpreted them using a parameter-free model with inclusion of the higher multipole moments of ions of the crystal lattice. The model developed has been shown to provide good agreement between the calculated and experimental frequencies of the vibrational spectrum of the low-symmetry ionic crystal with a complex structure. The eigenvectors of lattice vibrations were determined and analyzed. It was found that the frequencies of the phonon spectrum are low due to the significant (although small) contribution of heavy cations even to the eigenvectors of the highest frequency vibration modes.

Using the same approach, we have experimentally and theoretically determined the elastic moduli of the crystal and achieved good agreement between the experimental and calculated values.

ACKNOWLEDGMENTS

The authors thank V.I. Zinenko for helpful discussions of the results.

This work was supported by the integration program of the Siberian Division, Russian Academy of Sciences (project no. 88), the program of support for leading scientific schools (project no. NSh-939.2003.2), and the programs of the Presidium of the RAS and of the Department of Physical Sciences of the RAS.

REFERENCES

1. K. Nitsch, M. Dusek, M. Nikl, K. Polak, and M. Rodova, Prog. Cryst. Growth Charact. Mater. **30**, 1 (1995).
2. R. Balda, J. Fernandez, A. Mendioroz, M. Voda, and M. Al-Saleh, Phys. Rev. B **68**, 165101 (2003).
3. O. V. Ivanov, D. A. Shport, and E. G. Maksimov, Zh. Éksp. Teor. Fiz. **114**, 333 (1998) [JETP **87**, 186 (1998)].
4. N. G. Zamkova, V. I. Zinenko, O. V. Ivanov, E. G. Maksimov, and S. N. Sofronova, Ferroelectrics **283**, 49 (2003).
5. A. N. Vtyurin, S. V. Goryaĭnov, N. G. Zamkova, V. I. Zinenko, A. S. Krylov, S. N. Krylova, and A. D. Shefer, Fiz. Tverd. Tela (St. Petersburg) **46**, 1261 (2004) [Phys. Solid State **46**, 1301 (2004)].
6. M. Born and K. Huang, *Dynamical Theory of Crystal Lattices* (Clarendon, Oxford, 1954; Inostrannaya Literatura, Moscow, 1958).
7. M. B. Smirnov, in *Dynamic Theory and Physical Properties of Crystals*, Ed. by A. N. Lazarev (Nauka, St. Petersburg, 1992), p. 41 [in Russian].

8. A. A. Merkulov and L. I. Isaenko, in *Proceedings of the V International Conference on Crystals: Growth, Properties, Real Structure, Application* (Aleksandrov, 2001), p. 83.
9. A. A. Merkulov and L. I. Isaenko, Zh. Strukt. Khim. **45**, 724 (2004).
10. B. P. Sorokin, P. P. Turchin, and D. A. Glushkov, Fiz. Tverd. Tela (St. Petersburg) **36**, 2907 (1994) [Phys. Solid State **36**, 1545 (1994)].
11. H. Streitwolf, *Gruppentheorie in der Festkörperphysik* (Teubner, Leipzig, 1967; Mir, Moscow, 1971).
12. K. S. Aleksandrov, Kristallografiya **3**, 639 (1959) [Sov. Phys. Crystallogr. **3**, 647 (1959)].
13. K. S. Aleksandrov and G. T. Prodaĭvoda, *Anisotropy of Elastic Properties of Minerals and Rocks* (Sib. Otd. Ross. Akad. Nauk, Novosibirsk, 2000) [in Russian].
14. Yu. I. Sirotin and M. P. Shaskolskaya, *Fundamentals of Crystal Physics* (Nauka, Moscow, 1975; Mir, Moscow, 1982).

Translated by K. Shakhlevich

Physics of the Solid State, Vol. 47, No. 3, 2005, pp. 539–546. Translated from Fizika Tverdogo Tela, Vol. 47, No. 3, 2005, pp. 519–526.

LATTICE DYNAMICS AND PHASE TRANSITIONS

Vibration Spectra and the Valence Force Field of the $LiCuVO_4$ Crystal

V. B. Shirokov*, Yu. I. Yuzyuk*, V. I. Torgashev*, and A. S. Prokhorov**

**Research Institute of Physics, Rostov State University, pr. Stachki 194, Rostov-on-Don, 344090 Russia*

***General Physics Institute, Russian Academy of Sciences, ul. Vavilova 38, Moscow, 117942 Russia*

e-mail: shirokov@ip.rsu.ru

Received June 22, 2004

Abstract—Polarized Raman spectra of single-crystal $LiCuVO_4$ containing quasi-one-dimensional cuprate chains are measured. The force constants of the valence force field are calculated for the phonon modes at the center of the Brillouin zone with an accuracy sufficient to describe the experiment. From the results, it follows that the crystal contains rigid Cu–O–V–Cu–O–V structural rings with a charge distributed along their bonds. © *2005 Pleiades Publishing, Inc.*

1. INTRODUCTION

Low-dimensional spin systems are attracting the attention of scientists because simple models with a small number of parameters can used to describe them over a wide temperature range. These systems are also highly topical because of their implications for high-temperature superconductivity.

The $LiCuVO_4$ crystal is a one-dimensional spin system with a distinctive geometric pattern of Cu^{2+} ions (spin 1/2), which are placed mainly along one axis [1]. Consequently, the intrachain interaction dominates over the interchain interaction [2–4]. NMR measurements of ^{65}Cu and ^{51}V [5] show that the magnetic properties of the $LiCuVO_4$ crystal are mainly determined by bivalent copper; however, vanadium, which is supposedly pentavalent, also carries a small magnetic moment. According to magnetic measurements, the susceptibility has a wide maximum at $T_M = 28$ K and its temperature dependence is described well by the Bonner–Fisher model of a one-dimensional antiferromagnetic chain with spin 1/2 [4]. At $T_N \sim 4$ K, the susceptibility has a narrow peak accompanying the antiferromagnetic transition, which is due to interaction in other dimensions [6, 7].

In the present paper, we report on Raman spectra measurements of the $LiCuVO_4$ single crystal in the range 50–1000 cm^{-1} for different scattering geometries at room temperature. Based on these measurements and the IR data from [8], we develop a dynamic model of the phonon subsystem at the center of the Brillouin zone.

2. $LiCuVO_4$ CRYSTAL STRUCTURE

The $LiCuVO_4$ crystal has space symmetry group *Imma* (D_{2h}^{28} no. 72) with two formula units per unit cell. The orthorhombic cell has the following parameters at room temperature: $a = 5.662$ Å, $b = 5.809$ Å, and $c = 8.758$ Å [1]. Atoms occupy the following positions: Cu (4*a*) at (0, 0, 0), Li (4*d*) at (1/4, 1/4, 3/4), V (4*e*) at (0, 1/4, 0.386), O1 (8*h*) at (0, 0.0164, 0.2748), and O2 (8*i*) at (0.2352, 1/4, 0.9993). The crystal structure is shown in Fig. 1. Atoms O1 and O2 are numbered as *7–10* and *11–14*, respectively. The origin in Fig. 1 is displaced by (0, 1/2, 0) relative to the standard position for the *Imma* group from the International Tables. The Cu–O2 chains along the *b* axis formed by copper atoms *1* and *2* and oxygen atoms O2 (*11–14*) are seen in Fig. 1. Each of the

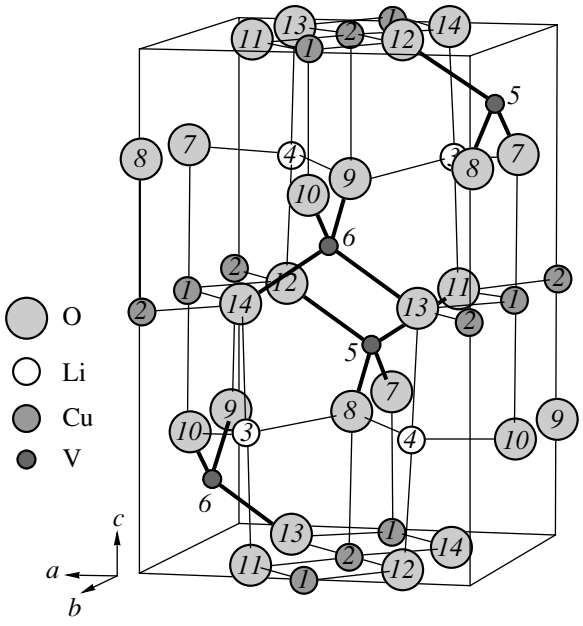

Fig. 1. $LiCuVO_4$ crystal lattice. Atoms are numbered as follows: (*1*, *2*) Cu, (*3*, *4*) Li, (*5*, *6*) V, (*7–10*) O1, and (*11–14*) O2.

1063-7834/05/4703-0539$26.00 © 2005 Pleiades Publishing, Inc.

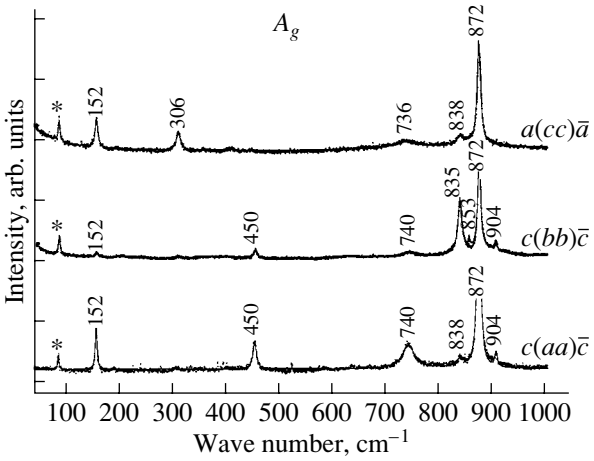

Fig. 2. Raman spectra of the $LiCuVO_4$ crystal for the diagonal scattering geometry corresponding to the A_g modes. Points are experimental data, and the solid line is a least squares fit by the additive-oscillator model. The star denotes the laser spontaneous emission line.

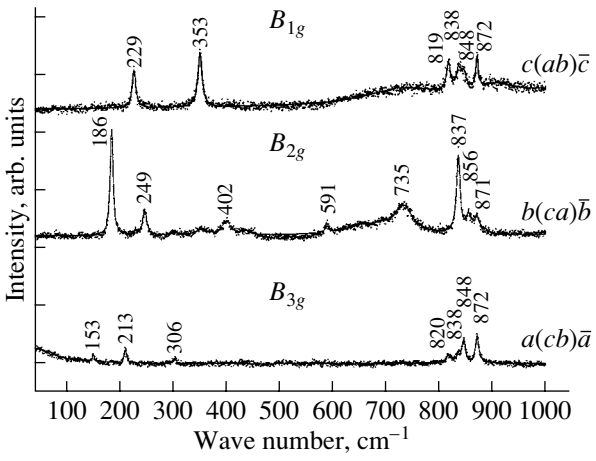

Fig. 3. Raman spectra of the $LiCuVO_4$ crystal corresponding to the B_{1g} modes. Points are experimental data, and the solid line is a least squares fit by the additive-oscillator model.

four Cu–O intervals in the chain is equal to 1.97 Å. The oxygen atoms of two adjacent copper chains belong simultaneously to two vertices of VO_4 tetrahedra, which interlink chains and form Cu–V layers in the *ab* plane. The two other oxygen atoms O1 in the VO_4 tetrahedra (numbers *7–10* in Fig. 1) are bonded to the copper atoms of adjacent Cu–V layers. The length of this Cu–O bond is 2.41 Å, which is 0.4 Å longer than the Cu–O bond inside a chain. Chains formed by Li atoms *3* and *4* and oxygen atoms O1 (*7*, *9* and *8*, *10*) are situated along the *a* axis (Fig. 1). The Li–O bonds in the chains are 2.11-Å long and are shorter than the Li–O bonds along the *c* axis, which are 2.18-Å long. Li atoms, which are in a slightly distorted octahedral environment, link Cu–V layers. Cu and Li atoms are situated in the inversion centers.

3. EXPERIMENTAL RESULTS

Raman spectra of single-crystal $LiCuVO_4$ were excited by an argon laser (λ = 515.5 nm) and recorded using a Jobin Yvon T64000 spectrometer in the backscattering geometry. Polarized Raman spectra were measured using samples precisely oriented relative to the crystallographic axes of the orthorhombic cell. We used samples in the form of $4 \times 1 \times 1$ mm prisms. The data obtained are shown in Figs. 2 and 3.

According to group theory analysis, the $LiCuVO_4$ crystal has the following set of phonon modes [8].

15 Raman-active modes, $5A_g + 2B_{1g} + 4B_{2g} + 4B_{3g}$;

20 IR-active modes, $8B_{1u} + 6B_{2u} + 6B_{3u}$; and

4 inactive modes, $4A_u$.

Three acoustic modes (B_{1u}, B_{2u}, B_{3u}) are excluded from the list.

IR reflection spectra of the $LiCuVO_4$ single crystal for the B_{2u} and B_{3u} phonons were measured and studied in [8], and the results are listed in Table 1.

The number of experimentally observed lines in the Raman spectra of the crystal exceeds the number of phonon modes at the Brillouin zone center given by the factor-group analysis. This discrepancy is especially evident in the high-frequency range (above 650 cm^{-1}). In this range, we expect stretching modes ν_1 and ν_3 of the distorted VO_4 groups (the notation for the VO_4-tetrahedron modes is taken from [8]). Triply degenerate vibration ν_3 is split into three modes: A_g, B_{2g}, and B_{3g}. Vibration ν_1 is not degenerate and transforms into the A_g mode in the crystal. Hence, in the high-frequency range, there should be four lines in the Raman spectrum ($2A_g + B_{2g} + B_{3g}$) and four lines in the IR spectrum ($2B_{1u} + B_{2u} + B_{3u}$). In the IR spectrum, the B_{2u} line corresponding to the stretching vibration V–O1 (r = 1.67 Å) has a frequency of 872 cm^{-1} and the B_{3u} line corresponding to the V–O2 vibration (r = 1.8 Å) has a frequency of 733 cm^{-1} [8]. Studies of the dynamical matrix of each of the V–O1 and V–O2 vibrations show

Table 1. Vibrations of the $LiCuVO_4$ crystal

Symmetry	Frequency, cm^{-1}	Note
$5A_g$ (R)	152 306 450 740 872	
$2B_{1g}$ (R)	229 353	
$4B_{2g}$ (R)	186 249 402 735	
$4B_{3g}$ (R)	152 213 305 848	
$6B_{2u}$ (IR)	113 182 236 325 466 872	[8]
$6B_{3u}$ (IR)	259 326 393 486 624 733	[8]
$4A_u$	110 303 388 591	Calculated
$8B_{1u}$ (IR)	101 178 301 362 463 513 817 904	Calculated

that the stretching V–O1 vibration contributes to spectra of A_g, B_{3g}, B_{2u}, and B_{1u} symmetries and that the V–O2 vibration contributes to A_g, B_{2g}, B_{3u}, and B_{1u}. Therefore, these vibrations correspond to lines 872 and 740 cm^{-1} in the A_g spectrum, 735 cm^{-1} in the B_{2g} spectrum, and 848 cm^{-1} in the B_{3g} spectrum (the most intense line in this region after exclusion of A_g-type lines) (Figs. 2, 3). This identification is based on the assumption that the 733 cm^{-1} line of the IR spectrum corresponds to the stretching V–O2 vibration. However, noticeable line 835 cm^{-1} in the (*bb*) scattering geometry is certainly related to the stretching V–O mode and the appearance of this mode (837 cm^{-1}) in the B_{2g} symmetry does not contradict the correlation analysis. The line frequencies assumed as the basis for the calculations below are set off in bold in Figs. 2 and 3.

4. DYNAMIC MODEL

We studied a simple dynamic model of lattice vibrations at wave vector $\mathbf{k} = 0$ in a $LiCuVO_4$ crystal within the harmonic approximation. The unit cell of the $LiCuVO_4$ crystal is made up of 14 atoms. The dynamical matrix is a 42×42 matrix. The symmetry permits 149 second-order invariants based on atom displacements. Hence, in general, the potential energy includes 149 constants. The requirement that the potential energy be invariant under infinitesimal translations reduces the number of constants by 23. Actually, this condition is equivalent to the requirement that the frequencies of acoustic modes be zero. The remaining 126 constants are independent. They completely determine the quadratic part of the energy. The phonon frequencies are found by diagonalizing the dynamical matrix. In our case, there are 39 frequencies. We assume that there is no accidental degeneracy of frequencies of the same symmetry. Then, according to the general theory of stability for parameter-dependent matrices [9], in order for the solution to the crystal dynamics problem to be stable near the given (experimental) frequencies it is sufficient to take into account 39 interaction constants. This means that there are 39 interaction constants that can be adjusted in such a way that they will produce dynamical-matrix frequencies that approximate experimental values with any predetermined accuracy.

Let us write the potential energy of the vibrating crystal in the form

$$2V = \sum f_{i,j} q_i q_j + c_{i,j} r_i r_j \alpha_i \alpha_j + h_{i,j} r_i \alpha_i q_j. \quad (1)$$

Here, q_i and α_i are variations in the bond coordinates and bond angles, respectively [10], and $r_i = \sqrt{r_{i,1} r_{i,2}}$, where $r_{i,1}$ and $r_{i,2}$ are the equilibrium distances used to determine the angle coordinate. Equation (1) is used only to introduce the force constants. After substituting the expressions for q_i and α_i according to [10] into Eq.(1), calculations are performed in the real coordinate space. The dynamical matrix is reduced to the quasi-diagonal form determined by the crystal symmetry by using the symmetry coordinates introduced in [8].

We estimate the upper bound of the V–O bond–stretching constant in the $LiCuVO_4$ crystal using the expression $4f = m\omega^2$, where the frequency is $\omega = 872$ cm^{-1}, m is the vanadium mass, and the factor 4 characterizes the tetrahedral environment: $f = 5.7$ mdyn/Å. An analogous estimation for the octahedral Cu–O bond using the frequency $\omega = 633$ cm^{-1}, taken from [11] for the CuO crystal, gives $f = 2.5$ mdyn/Å.

In order to obtain the force constants of the VO_4 group in a zero approximation, we performed calculations based on Eq. (1) and experimental values of the eigenfrequencies of the $[VO_4]^{3-}$ complex. The internal-vibration frequencies of $[VO_4]^{3-}$ are taken from [12]: $\omega_{A_1} = 818$ cm^{-1}, $\omega_E = 319$ cm^{-1}, $\omega_{F_2^1} = 780$ cm^{-1}, and $\omega_{F_2^2} = 368$ cm^{-1}. Here, the subscript denotes the symmetry of the corresponding vibration under the assumption that the equilibrium configuration of the $[VO_4]^{3-}$ complex has the symmetry of an ideal tetrahedron. As a result of the calculations, we obtained the following values: $f_{11} = 4.86$, $f_{12} = 0.76$, $c_{11} = 0.75$, and $c_{12} = 0.19$ in units of mdyn/Å. Here, f_{11} is the bond-stretching constant for V–O, f_{12} is the bond–bond interaction constant for $(V–O_1)(V–O_2)$, c_{11} is the bond–bending constant for O–V–O, and c_{12} is the angle–angle interaction constant for two angles with a common V–O bond. It is worth noting that the values of the constants f_{12} and c_{11} characterizing the extent of bond covalence are large.

The values of the force constants shown above are used as zero-approximation parameters, which are identical for both VO_4 groups contained in the unit cell of the $LiCuVO_4$ crystal. The values of the constants for cuprate chain are taken from [11]: the bond-stretching constant for Cu–O is 1.28 mdyn/Å, and the bond-bending constant for O–Cu–O is 0.32 mdyn/Å. The initial value for the Li–O bond is 0.4 mdyn/Å. The calculations are carried out using a perturbation theory algorithm [13] and the Maple 6 software package. All frequencies in Table 1 obtained from the Raman (Figs. 1, 2) and IR [8] experiments are fitted except for the A_u and B_{1u} symmetries. The resulting values of the force constants are shown in Table 2. The variations of the constants shown in the table are those caused by a change in any frequency from the full list (including A_u and B_{1u}) by 1 cm^{-1}. We note that the calculations are performed to the third or even fourth decimal place. This sensitivity of the constants is due to the strong nonlinearity of the secular equations for frequencies in the dynamic problem for the crystal under consideration. The calculations are performed until a precision $|\omega_{exp} - \omega|/\omega_{exp} = 0.01\%$ is achieved. The ion displacements for the calculated normal modes are shown in Fig. 4.

Table 2. Bond coordinates and calculated force constants, with their variations corresponding to a 1-cm^{-1} shift of any of the frequencies listed in Table 1

No.	Constant	Atoms	Interaction	Atom numbers according to Fig. 1	Bond length, Å Angle, deg	Constant value, mdyn/Å
1	*f*1	V–O1	$(q_1)^2$	*5–7*	1.67	5.48 ± 0.01
2	*f*2	V–O2	$(q_2)^2$	*5–11*	1.80	4.488 ± 0.006
3	*f*3	Cu–O2	$(q_3)^2$	*1–11*	1.97	1.355 ± 0.003
4	*f*4	Li–O1	$(q_4)^2$	*3–7*	2.11	0.329 ± 0.001
5	*f*5	Li–O2	$(q_5)^2$	*3–11*	2.18	0.5139 ± 0.0005
6	*f*6	Cu–O1	$(q_6)^2$	*1–7*	2.41	0.146 ± 0.006
7	*c*1	O1–V–O1	$(\alpha_1)^2$	*7–5–8*	108.7	0.273 ± 0.003
8	*c*2	O1–V–O2	$(\alpha_2)^2$	*7–5–11*	108.9	0.162 ± 0.001
9	*c*3	O2–V–O2	$(\alpha_3)^2$	*11–5–12*	112.3	0.708 ± 0.005
10	*c*4	O2–Cu–O2	$(\alpha_4)^2$	*11–1–12*	85.0	0.131 ± 0.001
11	*c*5	O2–Cu–O2	$(\alpha_5)^2$	*11–1–13*	95.0	0.313 ± 0.002
12	*c*6	O2–Cu–O1	$(\alpha_6)^2$	*11–1–7*	91.5	0.407 ± 0.007
13	*c*7	O2–Cu–O1	$(\alpha_7)^2$	*14–1–7*	88.5	0.488 ± 0.004
14	*c*8	Cu–O1–V	$(\alpha_9)^2$	*1–7–5*	127.9	−0.076 ± 0.001
15	*cc*1		$\alpha_2\alpha_3$	(*7–5–11*)/(*7–5–12*)		−0.178 ± 0.001
16	*cc*2		$\alpha_2\alpha_2'$	(*7–5–11*)/(*8–5–11*)		0.136 ± 0.001
17	*cc*3		$\alpha_4\alpha_5$	(*11–1–12*)/(*11–1–13*)		0.418 ± 0.001
18	*cc*4		$\alpha_5\alpha_5'$	(*11–1–13*)/(*12–1–14*)		0.033 ± 0.002
19	*cc*5		$\alpha_4\alpha_4'$	(*11–1–12*)/(*13–1–14*)		0.343 ± 0.001
20	*cc*6		$\alpha_2\alpha_2'$	(*7–5–11*)/(*9–6–14*)		−0.040 ± 0.001
21	*cc*7		$\alpha_2\alpha_2'$	(*7–5–11*)/(*9–6–13*)		−0.014 ± 0.001
22	*ff* 1		q_1q_1'	(*5–7*)/(*5–8*)		0.15 ± 0.01
23	*ff* 2		q_1q_2	(*5–7*)/(*5–11*)		0.794 ± 0.005
24	*ff* 3		q_2q_2'	(*5–11*)/(*5–12*)		1.585 ± 0.006
25	*ff* 4		q_3q_3'	(*1–13*)/(*1–11*)		0.235 ± 0.003
26	*ff* 5		q_3q_3'	(*1–13*)/(*1–12*)		0.111 ± 0.003
27	*ff* 6		q_3q_3'	(*1–13*)/(*1–14*)		−0.286 ± 0.003
28	*ff* 7		q_1q_1'	(*5–7*)/(*6–9*)		0.05 ± 0.01
29	*ff* 8		q_2q_2'	(*5–11*)/(*6–13*)		−0.235 ± 0.006
30	*ff* 9		q_2q_3	(*5–11*)/(*1–13*)		−0.349 ± 0.003
31	*ff*10		q_2q_3	(*5–11*)/(*1–11*)		0.927 ± 0.003
32	*ff*11		q_4q_5	(*3–10*)/(*4–12*)		0.0497 ± 0.0003
33	*ff*12		q_5q_5	(*3–11*)/(*4–12*)		−0.3374 ± 0.0005
34	*ff*13		q_3q_3'	(*1–13*)/(*2–11*)		−0.320 ± 0.003
35	*ff*14		q_3q_6	(*1–13*)/(*2–9*)		0.087 ± 0.001
36	*ff*15		q_2q_4	(*5–11*)/(*3–7*)		0.518 ± 0.003
37	*ff*16		q_2q_5	(*5–11*)/(*4–13*)		0.460 ± 0.001
38	*ff*17		q_4q_5	(*3–7*)/(*3–11*)		−0.0380 ± 0.0003
39	*ff*18		q_4q_4'	(*3–9*)/(*4–9*)		0.092 ± 0.001

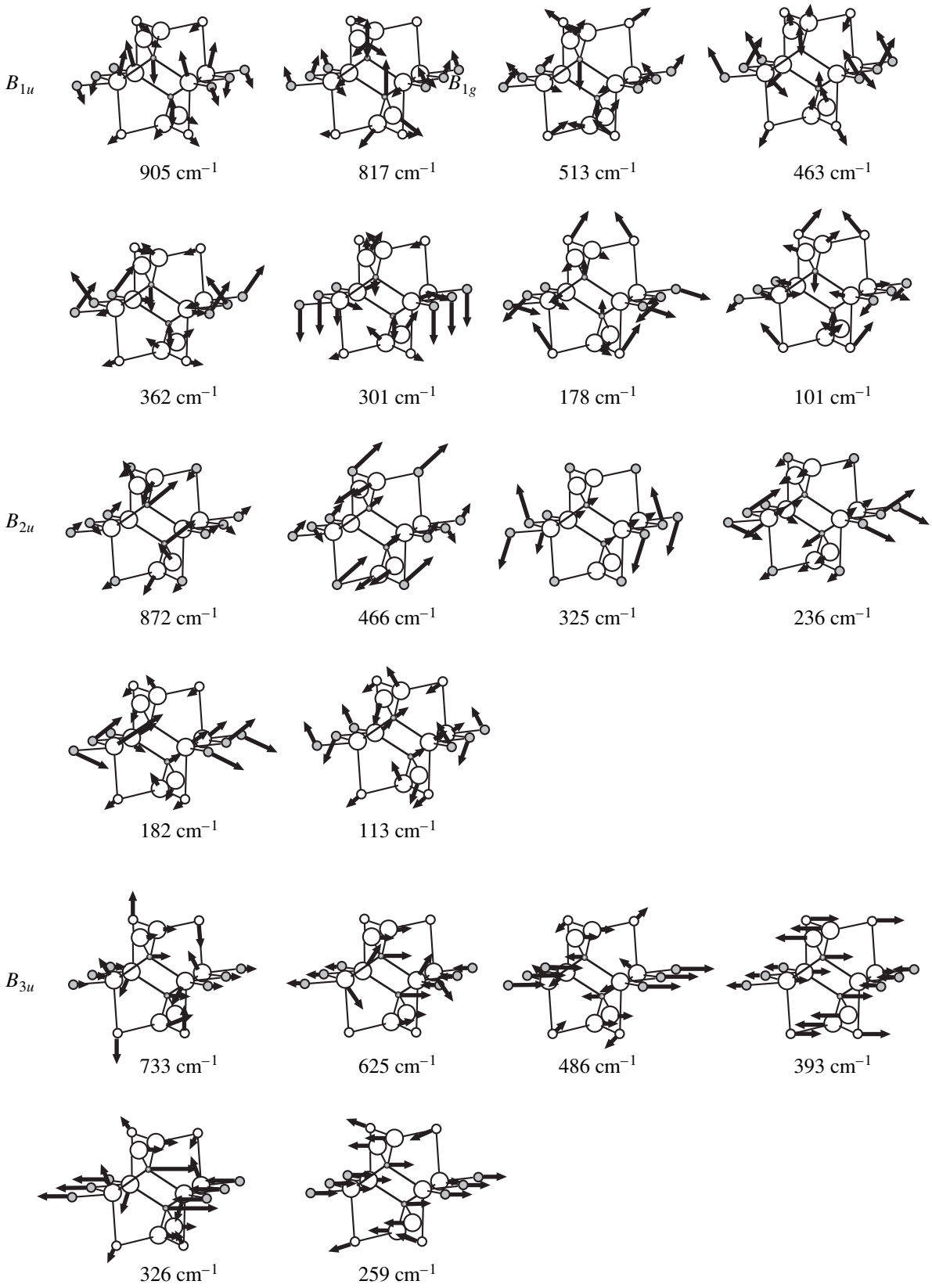

Fig. 4. Ion displacements in the normal phonon modes of the $LiCuVO_4$ crystal. Insert shows enlarged view of the lattice part used for graphical representation of the modes. Atoms are numbered according to Fig. 1.

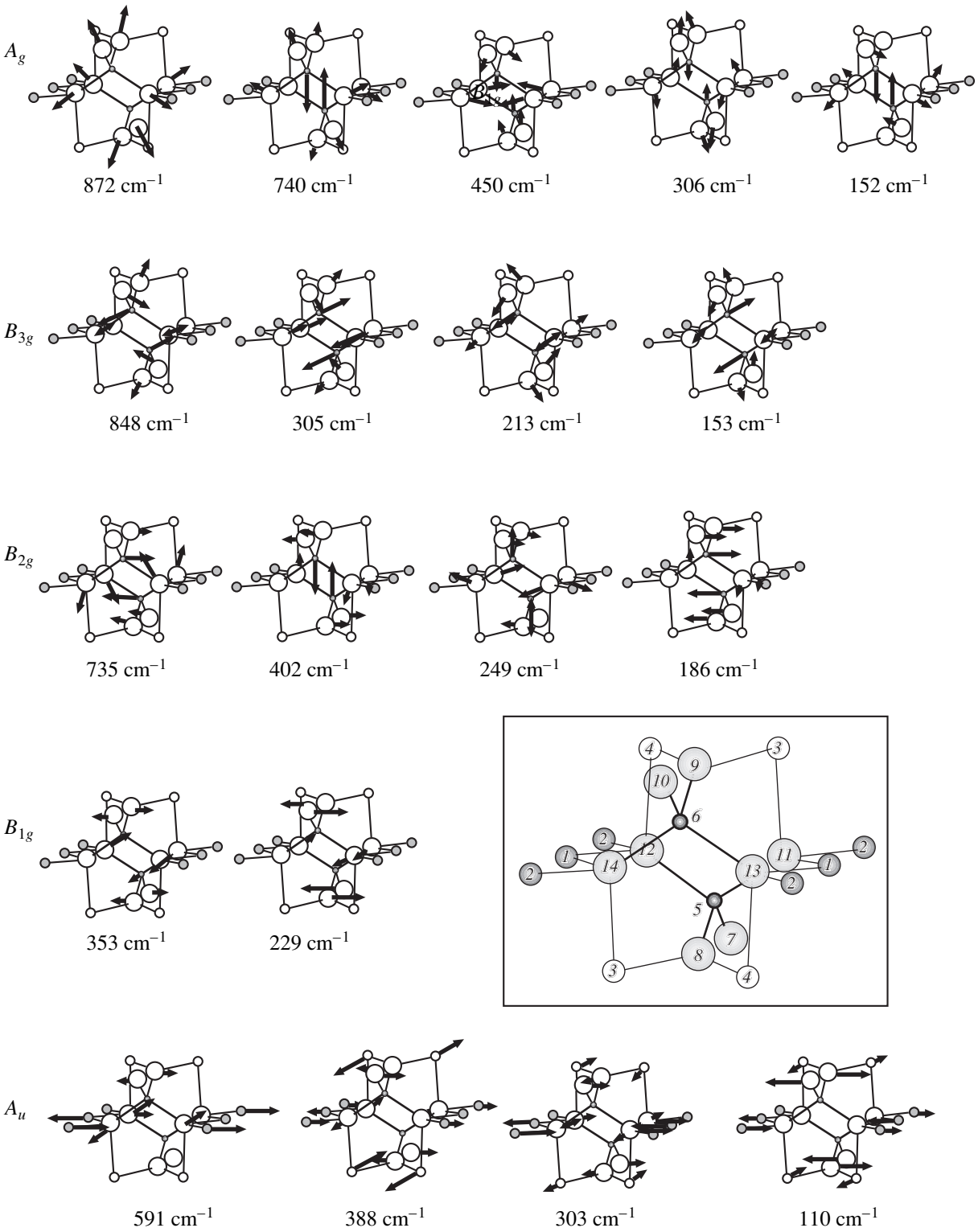

Fig. 4. (Contd.)

As mentioned previously, the solution to the dynamic problem in the nondegenerate case is single-valued and stable in some vicinity of the obtained solution. This is true in regard to the mathematical part of the problem. However, before proceeding to this part, we should identify the spectrum, set the dimensionality of the problem, and choose the interaction constants. The possibilities for spectrum identification were dis-

cussed above. The full dynamic problem for the center of the Brillouin zone of the $LiCuVO_4$ crystal should contain 39 frequencies except the acoustic modes.

The introduction of symmetry coordinates makes it possible to exclude four more equations for the A_u vibrations and eight equations for the B_{1u} vibrations, since their frequencies are unknown. However, this makes the full dynamic problem unstable.

Without constraints, the frequencies of the A_u and B_{1u} symmetries become complex values. For this reason, we constrained them in the following way: the lowest frequencies of the A_u and B_{1u} modes should not be any smaller than 100 cm^{-1}, and the highest frequency of the B_{1u} mode cannot exceed the maximum observed frequency in the spectrum range of stretching vibrations of the VO_4 group (904 cm^{-1}). According to the correlation analysis [8], the high-frequency lines ν_1 and ν_3 of the VO_4 group do not contribute to the A_u spectrum. Therefore, the upper bound of A_u frequencies should be determined by the maximum frequency of the Cu–O subsystem; i.e., it cannot exceed 630 cm^{-1}.

5. RESULTS AND DISCUSSION

First, let us verify our identification of the Raman spectra. As noted above, there is obvious ambiguity concerning lines 740 and 835 cm^{-1} of the A_g symmetry and lines 735 and 837 cm^{-1} of the B_{2g} symmetry. If the force constants are calculated using frequency pair 835 and 837 cm^{-1} for the given symmetries instead of 740 and 735 cm^{-1}, the constant $f3$ for the Cu–O bond in chains is reduced to the values typical for the Li–O bond. Therefore, we conclude that these frequencies in the Raman spectra are due to a structural transformation of the surface layer caused by the substitution of Cu by Li in cuprate chains. There are two reasons for this transformation. One reason is the high mobility of Li [14] and the way in which the Li–Cu sublattices are ordered during the crystal growth; indeed, highly mobile Li atoms predominantly fill vacancies at the surface. The other reason is the substitution of Cu^{2+} ions by Li^+ facilitated by hydrogen, which is readily adsorbed on the surface of the $LiCuVO_4$ crystal during its storage because the crystal contains oxygen.

Let us discuss the calculation results shown in Table 2. The difference between the constants for V–O1 ($f1$ = 5.48 mdyn/Å) and V–O2 ($f2$ = 4.488 mdyn/Å) is due to the difference in the bond lengths, 1.67 and 1.8 Å, respectively; the value n in the expression $f1/f2 = (r2/rl)^n$ is about 2.66. The values of the bond-stretching constants $f2$ for the V–O bond and $f3$ and $f6$ for the Cu–O bond are smaller than the upper boundaries estimated above. This fact suggests that there is a charge between these atoms, which screens the interaction between the ions. For the Cu atom, the constant $f6$ = 0.146 mdyn/Å is almost an order of magnitude smaller than the constant $f3$ = 1.355 mdyn/Å in a cuprate chain. The constant $f6$, together with the constant $f5$ of the Li–O2 bond, determines the coupling of Cu–V layers. The small values of the constants are in agreement with the layered structure of the crystal along the c axis. The small value of the constant $f6$, together with the large values of the bond-bending constants $c7$ and $c8$, is due to the distributed charge above the Cu chain.

The force constant $ff3$ has an unexpectedly large value, 1.585 mdyn/Å (Table 2). This constant determines the variation in the potential energy associated with a simultaneous change in the length of two V–O2 bonds between atoms *5–11* and *5–12*. In conjunction with the large value of the bond-bending constant for these atoms, this fact means that there is a large charge between V atoms belonging to adjacent tetrahedra (atoms *5*, *6* in Fig. 1) and along the appropriate V–O2 bonds. Taking into account the large value of the bond-bending constant $c5$ between atoms *11–1–13* of a Cu chain (see also the values of constants $c6$, $c7$), we can say that there is a rigid structural ring Cu–O–V–O–Cu formed by atoms *1* → *11* → *5* → *12* → *1* → *14* → *6* → *13* → *1* and that a significant electron charge is distributed along this ring.

The 740 and 735 cm^{-1} lines differ from all other lines of the spectrum in that they have a larger width. A possible reason for the broadening of the lines could be coupling to the magnetic subsystem of the crystal [8]. The magnetic atom Cu does not take part in the g-type vibrations because it resides at the inversion center. However, displacements of the adjacent oxygen atoms change the angle of the Cu–O2–Cu bond in the chain, thus modifying the exchange constant [15] and the ground state of the phonon subsystem. In addition, coupling is possible through the exchange interaction with the distributed charge of the Cu–O–V–O–Cu ring. Because of the large values of the constants $ff3$ and $ff2$, the variation in the V–O2 distance due to the displacement of oxygen atoms of the Cu chain causes a significant change in the potential energy, which cannot but modify the exchange constant (in the adiabatic approximation, the potential energy is the ground-state energy of the electron subsystem).

In concluding, let us indicate the possible reasons for the appearance of the extra lines. The $LiCuVO_4$ crystal is opaque in visible light; therefore, the penetration depth of the laser beam is small and the chance of interference from surface effects is high. One of the effects is modification of the surface-layer structure due to the atoms being implanted from air. Another surface effect is the change in the crystal symmetry due to the boundary, which leads to modification of the selection rules. This modification includes both a violation of the translational symmetry close to the surface (along the surface normal) and disappearance of the reflection plane parallel to the surface. Due to the latter, lines from the IR spectrum and lines that are absent in the Raman spectra of bulk samples appear in the Raman spectra. The larger beam penetration depth, the smaller these effects. The high concentration of radiation power during micro-Raman measurements in absorbing crys-

tals can lead to significant local heating of the measurement area. Due to the superionic properties of the $LiCuVO_4$ crystal [14], this can cause a depletion of Li in the measurement area. In addition, nonlinear effects due to many-phonon processes are possible. This is supported by the B_{1g} spectrum shown in Fig. 3, where lines in the region of the stretching vibrations of the VO_4 group are present on the background of a wide diffusion band. Finally, one more reason for the appearance of extra lines is the presence of magnetic atoms in the lattice. In this case, additional lines can appear in the region of the phonon excitation spectrum due to the magnon–magnon [16] and magnon–phonon [17] interactions in the paramagnetic phase. In order to confirm any of the reasons for the appearance of extra lines in the spectrum, further investigations are necessary.

6. CONCLUSIONS

For the first time, the polarized Raman spectra of the $LiCuVO_4$ crystal at room temperature have been measured. Full information about the components of the polarizability tensor α_{ij} is reported, and symmetry identification of the lines is performed. Comparison of the experimental spectra and predictions based on a factor-group analysis demonstrates good correlation, which confirms the $Imma$–D_{2h}^{28} (no. 72) symmetry group for the structure of the $LiCuVO_4$ crystal.

The interaction constants are determined precisely in the framework of the valence force field model by numerical calculations. The constants describe well the Raman spectra from the present work and the IR spectra obtained earlier in [8]. The analysis of the force field constants leads to the conclusion that the $LiCuVO_4$ crystal lattice contains a rigid structure ring Cu–O–V–Cu–O–V with a charge distributed over its bonds.

ACKNOWLEDGMENTS

This work was supported in part by the President of the Russian Federation (grant no. NSh-14-15.2003.2).

REFERENCES

1. M. A. Lafontaine, M. Leblanc, and G. Ferey, Acta Crystallogr. C **45**, 1205 (1989).
2. M. Yamaguchi, T. Furuta, and M. Ishikawa, J. Phys. Soc. Jpn. **65**, 2998 (1996).
3. A. N. Vasil'ev, Pis'ma Zh. Éksp. Teor. Fiz. **69**, 828 (1999) [JETP Lett. **69**, 876 (1999)].
4. A. N. Vasil'ev, L. A. Ponomarenko, H. Manaka, I. Yamada, M. Isobe, and Y. Ueda, Phys. Rev. B **64**, 024419 (2001).
5. T. Tanaka, H. Ishida, M. Matsumoto, and S. Wada, J. Phys. Soc. Jpn. **71**, 308 (2002).
6. H. Saji, J. Phys. Soc. Jpn. **33**, 671 (1972).
7. Ch. Kegler, N. Buttgen, H.-A. Krug von Nidda, A. Krimmel, L. Svistov, B. I. Kochelaev, A. Loidl, A. Prokofiev, and W. Assmus, Eur. Phys. J. B **22**, 321 (2001).
8. B. Gorshunov, P. Haas, M. Dressel, V. I. Torgashev, V. B. Shirokov, A. V. Prokofiev, and W. Assmus, Eur. Phys. J. B **23**, 427 (2001).
9. V. I. Arnol'd, *Additional Chapters to the Theory of Ordinary Differential Equations* (Nauka, Moscow, 1978) [in Russian].
10. E. B. Wilson, Jr., J. C. Decius, and P. C. Cross, *Molecular Vibrations: The Theory of Infrared and Raman Vibrational Spectra* (McGraw-Hill, New York, 1955; Inostrannaya Literatura, Moscow, 1960).
11. G. Kliche and Z. V. Popovic, Phys. Rev. B **42**, 10060 (1990).
12. K. Nakamoto, *Infrared Spectra of Inorganic and Coordination Compounds* (Wiley, New York, 1963; Mir, Moscow, 1966).
13. L. D. Landau and E. M. Lifshitz, *Course of Theoretical Physics*, Vol. 3: *Quantum Mechanics: Non-Relativistic Theory*, 4th ed. (Nauka, Moscow, 1989; Oxford Univ. Press, Oxford, 1980).
14. L. S. Parfen'eva, A. I. Shelykh, I. A. Smirnov, A. V. Prokof'ev, V. Assmus, Kh. Misiorek, Ya. Mukha, A. Ezhovskiĭ, and I. G. Vasil'eva, Fiz. Tverd. Tela (St. Petersburg) **45**, 1991 (2003) [Phys. Solid State **45**, 2093 (2003)].
15. Y. Mizuno, T. Tohyama, S. Maekava, T. Osafune, N. Motoyama, H. Eisaki, and S. Ushida, Phys. Rev. B **59**, 5326 (1998).
16. A. I. Akhiezer, V. G. Bar'yakhtar, and S. V. Peletminskiĭ, *Spin Waves* (Nauka, Moscow, 1967; North-Holland, Amsterdam, 1968).
17. G. Güntherodt and R. Zeyher, in *Light Scattering in Solids IV*, Ed. by M. Cardona and G. Güntherodt (Springer, Berlin, 1984; Mir, Moscow, 1986).

Translated by G. Tsydynzhapov

Physics of the Solid State, Vol. 47, No. 3, 2005, pp. 547–555. Translated from Fizika Tverdogo Tela, Vol. 47, No. 3, 2005, pp. 527–535.

LATTICE DYNAMICS AND PHASE TRANSITIONS

Polar Phonons and Specific Features of the Ferroelectric States in Cadmium Titanate

B. P. Gorshunov*, A. V. Pronin*, I. Kutskov*, A. A. Volkov*, V. V. Lemanov, and V. I. Torgashev*****

**Prokhorov General Physics Institute, Russian Academy of Sciences, ul. Vavilova 38, Moscow, 117942 Russia*
***Ioffe Physicotechnical Institute, Russian Academy of Sciences, Politekhnicheskaya ul. 26, St. Petersburg, 194021 Russia*
****Rostov State University, pr. Stachki 194, Rostov-on-Don, 344090 Russia*

Received June 22, 2004

Abstract—Polarized spectra of reflectance $R(\nu)$ and transmittance $\mathrm{Tr}(\nu)$ of single-crystal $CdTiO_3$ samples have been obtained in the frequency range $7 < \nu < 1000$ cm^{-1} and for temperatures from 5 to 300 K using IR Fourier spectroscopy and submillimeter-range techniques. Dispersion analysis was carried out in terms of the additive-oscillator model, and dielectric responses $\varepsilon'(\nu)$ and $\varepsilon''(\nu)$ were calculated. The polar modes were assigned to particular symmetry types, and their oscillator parameters (dielectric contributions, normal frequencies, damping constants) were determined. The numerical values of the components of the static permittivity tensor, ε_{11} and ε_{33}, are shown to be almost fully determined by the total dielectric contributions due to the B_{3u} and B_{1u} phonons, respectively. In the low-frequency domain, lines showing anomalous behavior of the oscillator parameters, which is characteristic of soft ferroelectric modes, were observed. It is shown that, in $CdTiO_3$ at cryogenic temperatures, there exist several different polar states with switching in the direction of the spontaneous polarization vector. © *2005 Pleiades Publishing, Inc.*

1. INTRODUCTION

The continuing interest in perovskite-type compounds stems from the rich variety of their properties (dielectric, optical, magnetic, etc.), which can be used to advantage in many applications [1]. In recent years, some doped and nonstoichiometric perovskite compositions have revealed new phenomena and characteristics, for instance, relaxor states [2], colossal magnetoresistance [3], and electrostriction [4]. This gives one grounds to consider the perovskite structural type to be one of the most promising in applied materials science, and investigating the properties of materials of this structural type is a problem of current, major significance.

The anomalous properties of the perovskites can be traced predominantly to the various instabilities in their crystal lattice, which give rise to structural distortions. One of the most widely encountered types of structural distortion of a perfect cubic perovskite (space group $Pm3m$) is associated with the lattice being unstable to two types of comparatively small tilts of the octahedra, namely, inphase and antiphase tilts for conjugate octahedra, which correspond to phonon modes at the Brillouin zone edge [5]. As a result of these dynamic instabilities, their interplay, and a sequence of structural phase transformations, the lattice symmetry lowers to orthorhombic [5], which corresponds to one of the most representative structural types ($GdFeO_3$ structural type) among distorted perovskites [6]. The perovskite mineral proper, $CaTiO_3$, belongs to this structural type below approximately 1380 K [7]. Similar distortions are also characteristic of cadmium titanate $CdTiO_3$ [5, 8].

Ferroelectricity in $CdTiO_3$ below 50 K was discovered by Smolenskiĭ [9]. The anomalous dielectric and optical behavior was later established to exist over a substantially broader temperature interval both in ceramic and single crystal samples [10–14] prepared by a variety of technologies.

X-ray studies of $CdTiO_3$ carried out on single crystals [8] at room temperature have shown this representative of the perovskite family to have a centrosymmetric structure belonging to space group $Pnma$. Structural measurements performed at cryogenic temperatures have recently been published [15]. It has been established that the $CdTiO_3$ structure at 20 K can be satisfactorily described in terms of the $P2_1ma$ polar space group, with the Ti atoms displaced toward the face center of the TiO_6 octahedron. Actually, this is inconsistent with the previous conclusion reached by the same authors [10, 11] that the $CdTiO_3$ symmetry is $Pn2_1a$ below about 88 K.

In view of the abovementioned structural uncertainties and of the lack of detailed spectroscopic studies of the lattice dynamics (with the exception of rather fragmentary remarks made in [10, 16]), we present here the results of investigating spectra of reflectance $R(\nu)$ and transmittance $\mathrm{Tr}(\nu)$ measured by us on a $CdTiO_3$ single crystal in the frequency range $\nu = 7$–1000 cm^{-1} and within the temperature interval $5 < T < 300$ K. Note that the Raman measurements reported in [10] did not

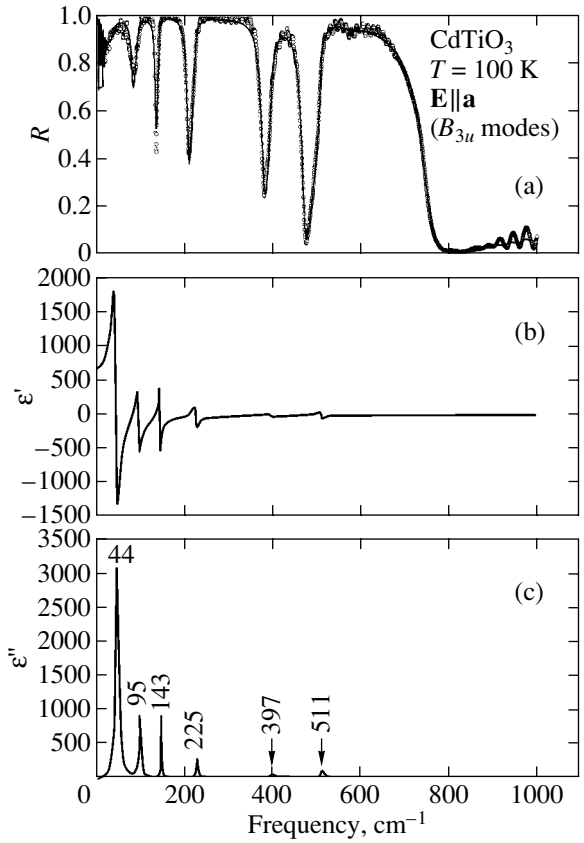

Fig. 1. Spectra (a) of IR reflectance $R(\nu)$ and (b) of the real, $\varepsilon'(\nu)$, and (c) imaginary, $\varepsilon''(\nu)$, parts of the permittivity of a $CdTiO_3$ single crystal obtained at 100 K in the **E** ∥ **a** geometry (B_{3u} modes). Points are experiment, and solid lines are fittings with the model of additive oscillators. The figures above the peaks in the dielectric loss spectrum $\varepsilon''(\nu)$ are numerical values of the normal frequencies of the B_{3u} phonon modes.

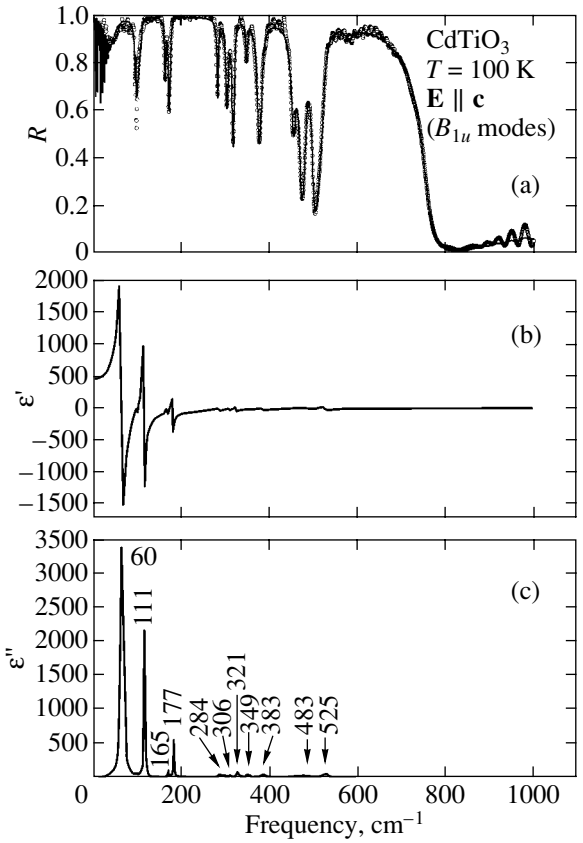

Fig. 2. Spectra (a) of reflectance $R(\nu)$ and (b) of the real, $\varepsilon'(\nu)$, and (c) imaginary, $\varepsilon''(\nu)$, parts of the permittivity of a $CdTiO_3$ single crystal obtained at 100 K in the **E** ∥ **c** geometry (B_{1u} modes). Points are experiment, and solid lines are fittings with the model of additive oscillators. The figures above the peaks in the dielectric loss spectrum $\varepsilon''(\nu)$ are numerical values of the normal frequencies of the B_{1u} phonon modes.

reveal any spectral anomalies associated with a phase transition and that the spectral IR studies reported in [16] were made only above the phase transition point.

2. EXPERIMENT

The $CdTiO_3$ samples on which submillimeter-range transmittance spectra in the frequency region 7–32 cm^{-1} and IR reflectance spectra in the range 30–1000 cm^{-1} were obtained were very thin plates of high optical quality measuring approximately 3×4 mm (for the growth technique used and characterization of the crystals, see [17]). The transmittance and reflectance spectra were measured with a BWT-based, laboratory-type Épsilon spectrometer [18] and a Bruker-113v IR Fourier spectrometer, respectively.

Quantitative information on the phonon-mode parameters was extracted from dispersion analysis made in terms of an additive-oscillator model [18] in which

$$\varepsilon(\nu, T) = \varepsilon_\infty(T) + \sum_i \frac{\Delta\varepsilon_i(T)\nu_i^2(T)}{\nu_i^2(T) - \nu^2 + i\gamma_i(T)\nu}, \quad (1)$$

$$R(\nu, T) = \left|\frac{\sqrt{\varepsilon(\nu, T)} - 1}{\sqrt{\varepsilon(\nu, T)} + 1}\right|^2. \quad (2)$$

Here, ε_∞ is the high-frequency dielectric contribution, ν_i is a normal frequency, γ_i is the damping constant, and $\Delta\varepsilon_i$ is the dielectric contribution for the ith mode.

3. EXPERIMENTAL

Since $CdTiO_3$ has a centrosymmetric structure at room temperature, one may expect that the IR spectra will exhibit 25 polar phonon modes of three symmetry types [17]:

$$\Gamma_{vib} = 9B_{1u} + 7B_{2u} + 9B_{3u}. \quad (3)$$

All light-reflectance measurements were carried out on 40-μm-thick single-crystal plates with the unit cell axis *b* perpendicular to the sample plane. Because of this geometric constraint, only the B_{1u} (**E** || **c**) and B_{3u} (**E** || **a**) phonon modes could be observed. Figures 1 and 2 display $CdTiO_3$ IR reflectance spectra obtained at T = 100 K for two orientations of the vector **E** of the exciting electromagnetic wave with respect to the unit cell basis. Both spectra are well polarized and correspond to the B_{3u} (Fig. 1) and B_{1u} (Fig. 2) phonon modes. The **E** || **a** spectrum (B_{3u} modes) clearly exhibits six lines (Fig. 1), whereas for **E** || **c** (B_{1u} modes) the number of observed resonance features (Fig. 1) is twice as large, exceeding the number of modes expected from Eq. (3). Note, however, that some lines are very weak. Because the normal mode frequencies in the two spectra are numerically different (see table), we believe that these very weak features in the **E** || **c** spectrum may actually be manifestations of the B_{2u} modes (not studied directly in our experiment), which could be observed due to the presence of small regions with domain structure in the sample resulting in a certain depolarization of the spectrum.

Below room temperature, the spectral resonances become narrower and their frequencies shift mostly toward higher values. Some of the low-frequency lines, however, exhibit a noticeable decrease in the normal frequency with decreasing temperature. These visual observations were corroborated by a numerical analysis.

Least squares fitting of Eqs. (1) and (2) to experimental spectra yields the numerical values of the dielectric contribution $\Delta\varepsilon_i$, normal frequency ν_i, and damping constant γ_i for each mode. The solid lines in Figs. 1 and 2 show the model reflectance spectra obtained using this procedure. The oscillator parameters for each mode are shown in the table. The model spectrum is seen to approximate the experimental one very well. Slight discrepancies are seen only close to the weak features, which have almost no influence on the numerical values of the oscillator parameters for the main resonances.

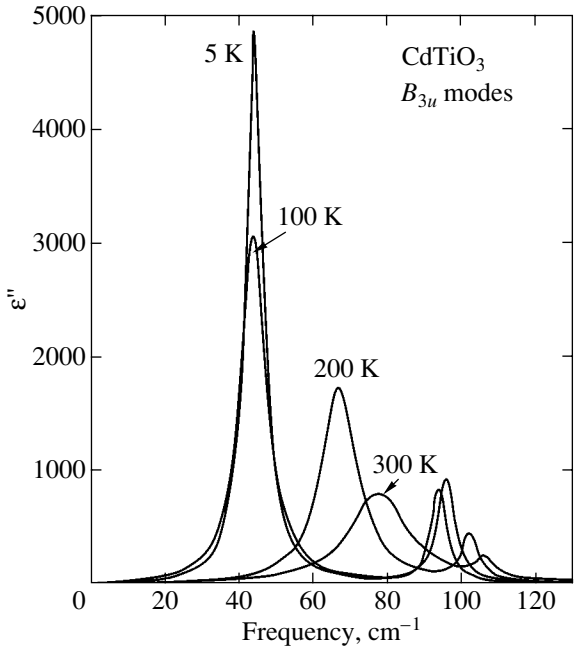

Fig. 3. Temperature dependence of the low-frequency part of the dielectric loss spectrum ε"(ν) obtained on $CdTiO_3$ in the **E** || **a** geometry (B_{3u} modes). The strong line at 40–80 cm^{-1} corresponds to a soft mode whose condensation drives the ferroelectric state with $\mathbf{P}_x$ || **a** and polar-phase symmetry $P2_1ma$–C_{2v}^2. The two higher frequency lines soften insignificantly.

We used the parameters obtained for each oscillator to reconstruct the dielectric functions ε'(ν) and ε"(ν) from Eqs. (1) and (2). Figures 1 and 2 show these functions at 100 K for the orientations **E** || **a** and **E** || **c**. These spectra clearly reveal the main difference between the low- and high-frequency modes; namely, the former

Polar-phonon parameters in $CdTiO_3$ at T = 100 K

B_{3u} modes (ε_∞ = 5.74)			B_{1u} modes (ε_∞ = 5.74)			B_{3u} modes (ε_∞ = 5.74)			B_{1u} modes (ε_∞ = 5.74)		
Δ_i	ν_i, cm^{-1}	γ_i, cm^{-1}	Δ_i	ν_i, cm^{-1}	γ_i, cm^{-1}	Δ_i	ν_i, cm^{-1}	γ_i, cm^{-1}	Δ_i	ν_i, cm^{-1}	γ_i, cm^{-1}
593.9	43.8	8.45							0.70	321.5	3.76
			396.6	60.6	7.08				0.09	349.5	4.81
55.1	95.5	5.77	0.4	95.8	0.50				0.57	383.4	9.23
			56.4	111.4	2.83	0.95	387.1	11.99			
14.4	143.2	2.27							0.07	458.0	10.34
			1.5	164.8	3.09				0.22	483.3	9.90
			7.2	177.1	2.43	1.2	511.0	7.18			
7.7	225.3	6.05							0.84	525.5	9.61
			0.26	283.9	3.23	0.01	579.7	33.32	0.02	582.3	21.6
			0.34	305.9	5.95						

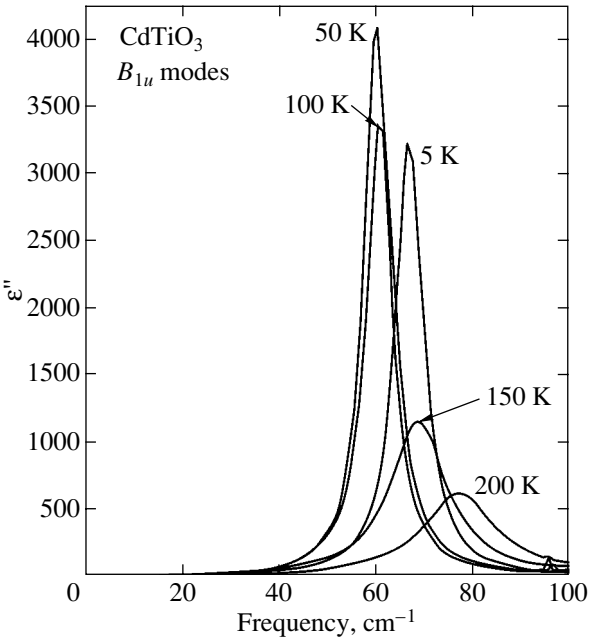

Fig. 4. Temperature dependence of the low-frequency part of the dielectric loss spectrum ε"(ν) obtained in the **E** ∥ **c** geometry (B_{1u} modes). The strong low-frequency line exhibits only quasi-soft behavior. The existence and condensation of this critical soft mode could bring about the formation of a polar phase of the $Pnm2_1$–C_{2v}^7 symmetry.

modes are substantially stronger than the latter and, hence, provide the dominant contribution to the static permittivity. Furthermore, it is primarily the low-frequency resonances that exhibit a marked enough variation in their oscillator parameters with temperature. Figures 3 and 4 illustrate the temperature-induced evolution of the spectra of the imaginary part of the permittivity in the low-frequency domain. The lowest frequency lines in both spectra undergo substantial softening down to about 80 K; below 50 K, however, the frequencies of these resonances start to grow. Note that the lowest frequency B_{3u} mode (Fig. 3) resembles a soft ferroelectric mode in many respects, whereas the analogous B_{1u} mode is markedly harder (Fig. 4).

The temperature dependence of the oscillator parameters of all modes obtained by fitting them to the IR reflectance spectra is displayed in Fig. 5. Above 200 cm^{-1}, the modes are seen to undergo only barely noticeable frequency shifts. Figure 5b also shows the temperature dependences of the total ($\Sigma_i \Delta\varepsilon_i$) dielectric contributions due to all modes of all symmetry types and of the contributions due to the lowest frequency modes only ($\Delta\varepsilon_1$). We clearly see that it is the lowest frequency modes that determine the behavior of these dependences. To make this conclusion still more revealing, Fig. 5c compares the inverse dielectric contribution $[\Delta\varepsilon_1(T)]^{-1}$ due to the lowest frequency B_{3u} soft

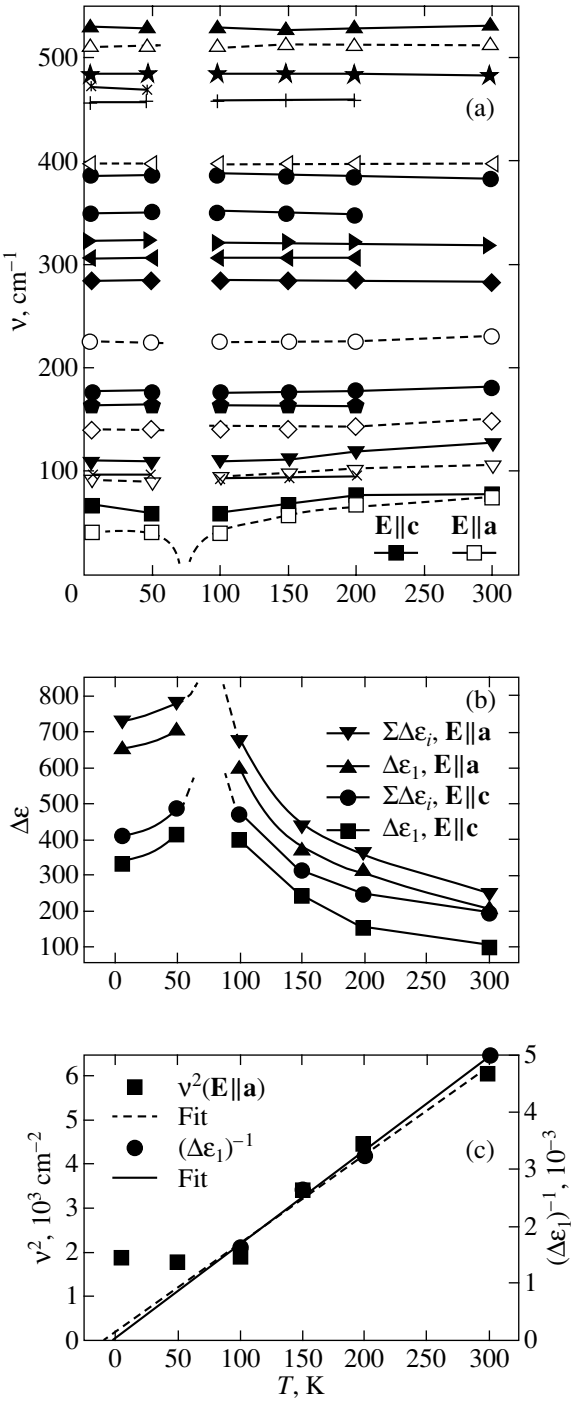

Fig. 5. Temperature dependences of the oscillator parameters of phonon modes in $CdTiO_3$ obtained from a dispersion analysis of IR reflectance spectra. (a) Temperature dependences of normal phonon mode frequencies: open symbols correspond to B_{3u} modes, and filled symbols correspond to B_{1u} modes; (b) temperature dependences of the total ($\Sigma_i \Delta\varepsilon_i$) and individual ($\Delta\varepsilon_1$, lowest-frequency) dielectric contributions due to the B_{3u} and B_{1u} phonon modes; and (c) temperature dependences of the square of the frequency of the soft B_{3u} mode (squares and the dashed line) and the inverse of the dielectric contribution from this mode, $(\Delta\varepsilon_1)^{-1}$ (circles and dashed line).

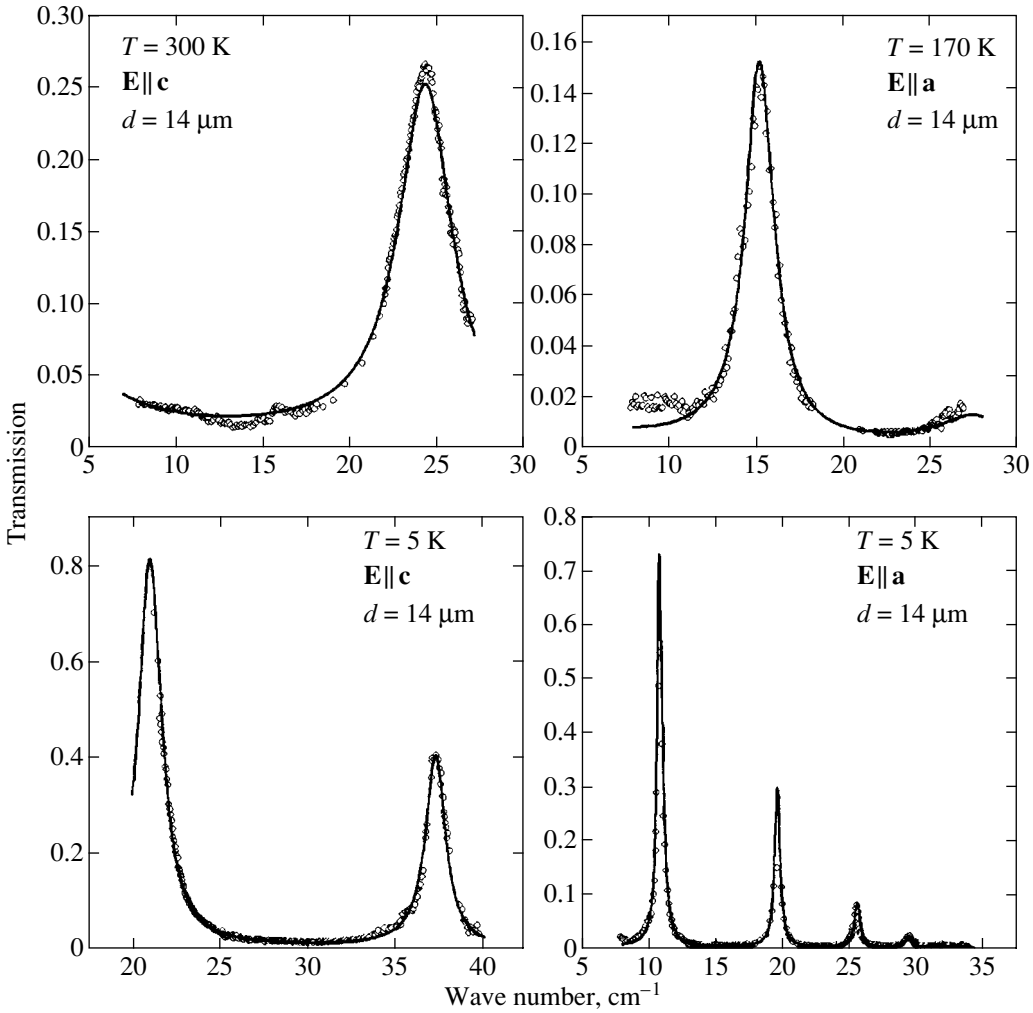

Fig. 6. Submillimeter-range transmittance spectra of a $CdTiO_3$ single-crystal plane-parallel plate (circles) d = 14 μm thick (along the unit cell b axis) obtained at different temperatures. In the **E** ∥ **a** geometry, the B_{3u} modes are active, and in the **E** ∥ **c** geometry, the B_{1u} modes are active. Spectral fitting (solid lines) was performed using the Fresnel relations for a dielectric layer with the values of ε' and ε" taken from Figs. 1 and 2. Note that the scales in all four panels are different.

mode and its normal frequency squared, $\nu_1^2(T)$. The almost exact coincidence of the two graphs suggests that the temperature dependence of the dielectric contribution is governed exclusively by the variation in the normal frequency of the mode rather than in its oscillator strength (which is $f_i = \Delta\varepsilon_i \nu_i^2$). In concluding the description of the FIR reflectance spectra, we stress that the behavior of the soft modes in the temperature interval 50–100 K was not determined to sufficient accuracy, because their frequencies dropped below the instrumental capabilities of the Bruker-113v Fourier spectrometer. This is why the temperature dependence graphs in Fig. 5 exhibit breaks.

More reliable quantitative information on the dynamic behavior of the soft mode in $CdTiO_3$ was derived from submillimeter-range transmittance spectra Tr(ν) measured at frequencies of 7 to 32 cm^{-1} on a very thin (d = 14 μm) plane-parallel plate. Figure 6 demonstrates typical spectra obtained for the two polarization directions that isolate B_{3u} and B_{1u} modes. The positions of the Tr(ν) transmittance peaks on the frequency scale and their separations are determined by the refractive index $n(\nu)$, and the peak values of Tr(ν) are determined by the extinction coefficient $k(\nu)$ (the imaginary part of the refractive index).

The solid lines in Fig. 6 are fits to the experimental Tr(ν) dependence obtained using the Fresnel relations for the transmittance of a plane dielectric layer. This fitting procedure allows one to derive the real and imaginary parts of the refractive index, $n(\nu, T)$ and $k(\nu, T)$; the real and imaginary parts of the permittivity, $\varepsilon'(\nu, T)$ and $\varepsilon''(\nu, T)$; and the reflectance $R(\nu, T)$ [18].

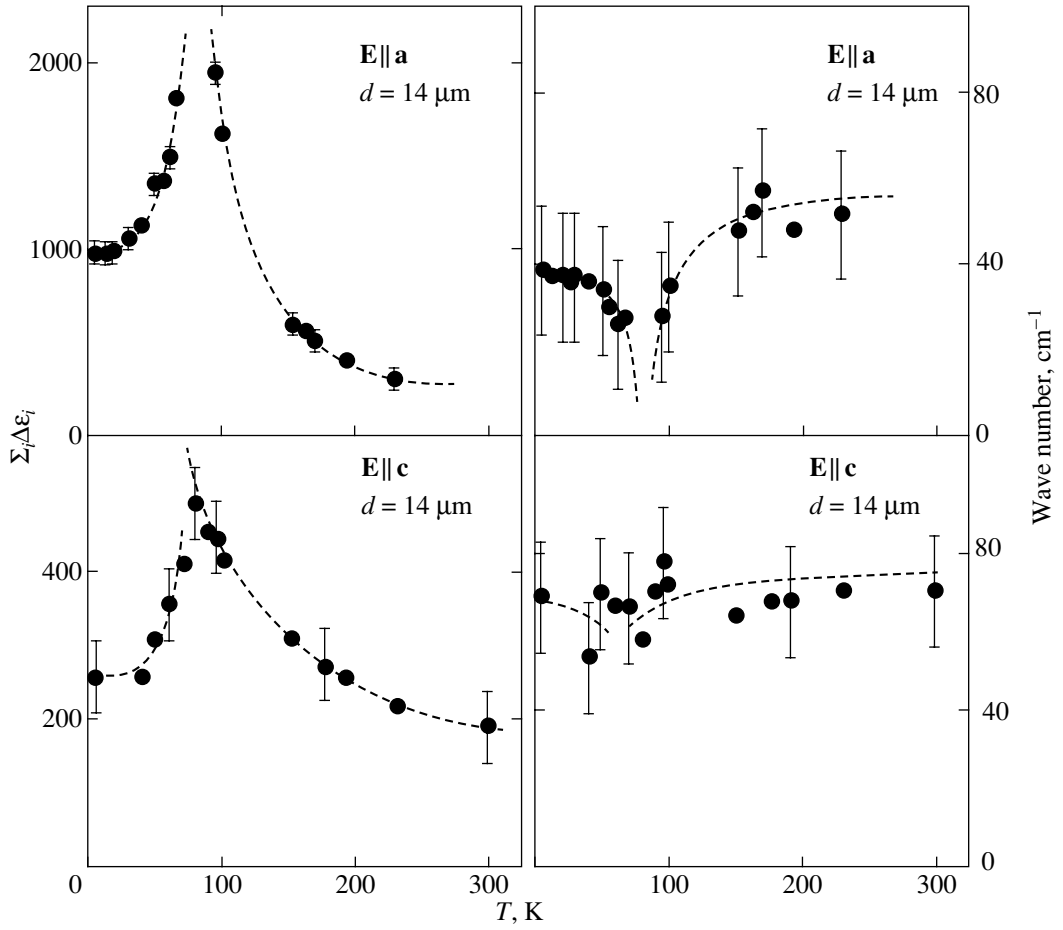

Fig. 7. Temperature dependences of the total ($\Sigma_i\Delta\varepsilon_i$) dielectric contributions in the frequency range 7–32 cm^{-1} and of the frequencies of the lowest frequency normal phonon modes in $CdTiO_3$ obtained by dispersion analysis of the submillimeter-range transmittance spectra. In the **E** || **a** geometry, the B_{3u} modes are active, and in the **E** || **c** geometry, the B_{1u} modes are active. The B_{1u} mode is seen to be only quasi-soft, with the values of its frequency and dielectric contribution being consistent with the respective values derived from reflectance spectra. The B_{3u} mode exhibits a temperature dependence typical of a soft ferroelectric mode in the vicinity of a first-order phase transition. Note that the frequency of this mode decreases to less than 20 cm^{-1} even at 90 K. We have not succeeded in approaching the Curie point closer because of the very strong absorption of radiation in the sample.

Figure 7 plots the temperature dependences of the normal mode frequencies and dielectric contributions obtained using the above procedure for submillimeter-range spectra in the **E** || **c** and **E** || **a** geometries. Although the low-temperature dielectric contribution for **E** || **a**, as estimated from the submillimeter-range spectra, is slightly larger than that derived from a similar estimate of the reflectance spectra ($\Sigma_i\Delta\varepsilon_i \approx 1000$ as obtained from the submillimeter-range spectra at 5 K and $\Sigma_i\Delta\varepsilon_i \approx 800$ as obtained from the reflectance measurements), they are clearly consistent if we take into account the large error involved in the derivation of the normal mode frequencies by extrapolating the reflectance tails to the low-frequency domain. This allows us to propose that there is an absence of "subphonon" excitations (central peaks or relaxations) in $CdTiO_3$ spectra within the temperature and spectral regions covered.

4. COMBINED EXPERIMENTAL RESULTS AND DISCUSSION

Recent IR spectroscopic studies of calcium titanate $CaTiO_3$ and calculations of its lattice dynamics [19] have established that the lowest frequency spectral lines are the three lines with symmetries B_{1u}, B_{2u}, and B_{3u} that originate from the polar, threefold-degenerate F_{1u} phonon at the Brillouin zone center of the cubic modification. Considering the close structural similarity between $CaTiO_3$ and $CdTiO_3$ [8], it appears only natural to assume that the situation should be the same for $CdTiO_3$.

If cadmium titanate undergoes phase transitions to polar states, then the IR active B_{1u}, B_{2u}, and B_{3u} modes should also become Raman active. This does occur in the $CdTiO_3$ crystal [17], in contrast to the conclusions drawn earlier in [10].

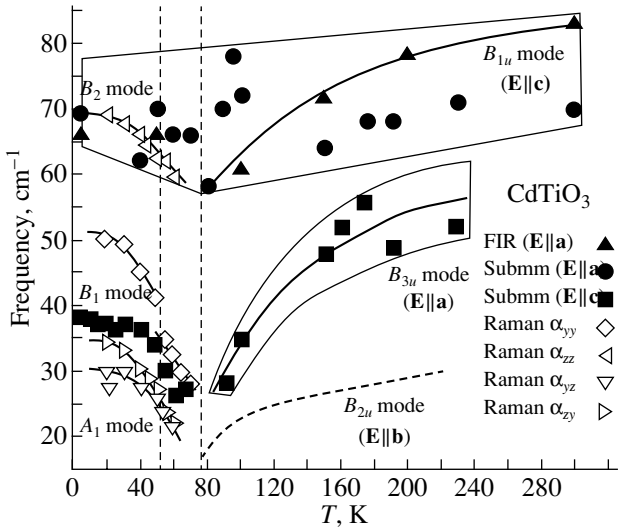

Fig. 8. Compilation of IR and Raman [17] data on the temperature dependence of the frequencies of the lowest frequency normal phonon modes in $CdTiO_3$. Dashed line plots the hypothetical temperature dependence of the frequency of the B_{2u} soft mode not studied here. Different symbols specify the type of experiment from which the data were derived. The broad stripes bound the maximum errors in the determination of the mode frequency for all experiments. At low temperatures, the IR and Raman modes reveal correlated behavior (within experimental error). Vertical dashed straight lines identify the temperatures at which the phonon modes exhibit singular behavior. The mode symmetry at 5 K corresponds to the C_{2v}^2 group of this polar phase.

Figure 8 combines data on the low-temperature dependence of soft mode frequencies in Raman and IR spectra. The low-frequency IR spectra were found to have two lines corresponding to B_{1u} and B_{3u} modes with an anomalous temperature dependence, while the Raman spectra have three such lines. We assume that these lines originate from the threefold-degenerate, lowest frequency F_{1u} polar mode of the cubic phase. All the lines undergo an anomalous temperature dependence in the range 50–80 K, where anomalies in the behavior of the optical and dielectric constants of $CdTiO_3$ have also been observed [10–14]. We attribute these anomalies to structural phase transitions to polar states with an attendant decrease in symmetry to at least the C_{2v} crystal class. Now the polar modes become Raman active, as is evident from the corresponding spectra [17]. The slight differences (5 cm^{-1} at most) between the frequencies of the 30 cm^{-1} line in the *yz* and *zy* spectra (Fig. 8) observed at temperatures below 50 K are probably due to the complex domain structure of the ferroelectric phases, to the sample not being single phase, or again to the manifestation of polariton effects. Due to purely geometric constraints on the sample shape (thin plates), we did not succeed in studying B_{2u} phonons in IR spectra. As follows convincingly from dielectric measurements [11], however, one of the phonon modes of this symmetry should be soft. The

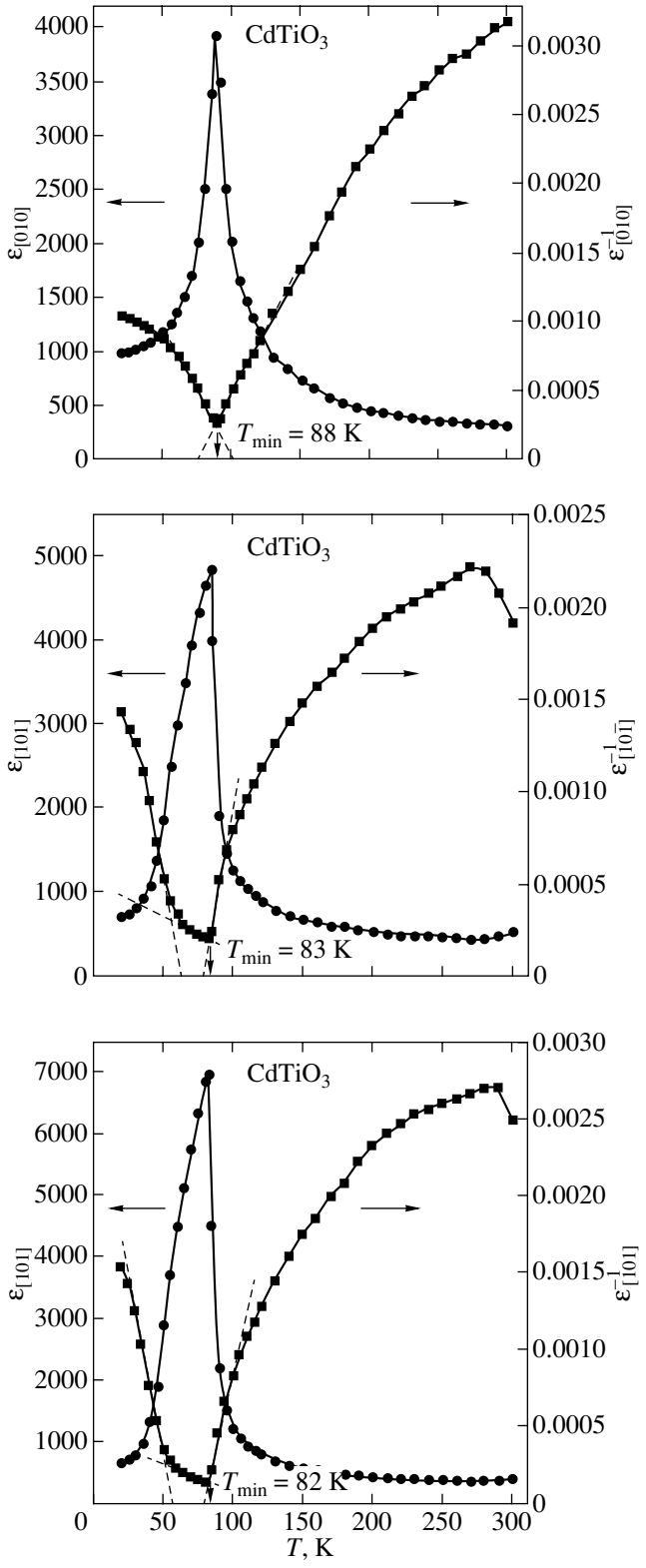

Fig. 9. Temperature dependences of $\varepsilon(T)$ and $\varepsilon^{-1}(T)$ of single-crystal $CdTiO_3$ along three orthogonal directions of the orthorhombic unit cell, extracted from dielectric measurements at 10 kHz [11]. Note the 5- to 6-K shift of the maximum of $\varepsilon_{[010]}$ relative to that of $\varepsilon_{[101]}$. Dashed lines plot the Curie–Weiss law fits.

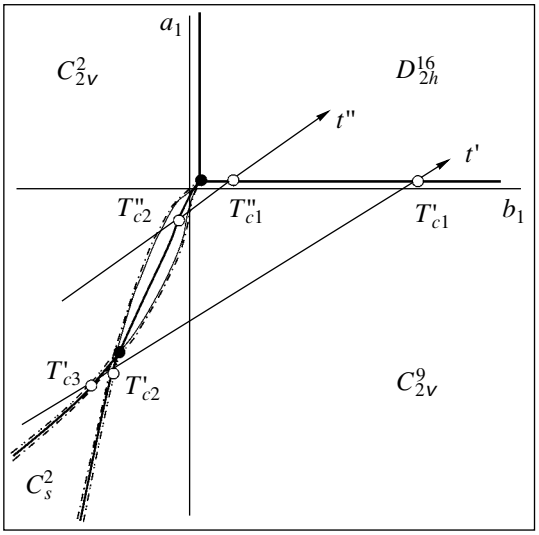

Fig. 10. Phase diagram corresponding to model (4) and two qualitatively different thermodynamic paths (t' and t'') illustrating different sequences of phase transitions to polar states. We have $a_1 \sim \nu_1^2$ for the soft B_{2u} mode and $b_1 \sim \nu_1^2$ for the soft B_{3u} mode. Along sloped paths, both modes are critical. The chosen arrangement of the paths corresponds to the situation where the B_{2u} mode is the first to condense.

dashed line in Fig. 8 specifies its tentative behavior in the *Pnma* phase.

To make our arguments more revealing, we conducted an analysis of the dielectric measurements reported in [11]. Figure 9 displays the temperature dependences of $\varepsilon(T)$ and $\varepsilon^{-1}(T)$ taken from [11]. First, we immediately see the inverse permittivity along the *b* axis, $\varepsilon_{[010]}^{-1}(T)$, to follow the Curie–Weiss law in the range 88–200 K. Second, the $\varepsilon_{[101]}(T)$ and $\varepsilon_{[\bar{1}01]}(T)$ permittivities along the *a* and *c* directions follow a more complex course (the Curie–Weiss law is satisfied only within a very narrow temperature interval), with the minimum in the $\varepsilon_{[\bar{1}01]}^{-1}(T)$ relation shifted by approximately 5–6 K toward lower temperatures as compared to that in $\varepsilon_{[010]}^{-1}(T)$. Third, both the $\varepsilon_{[101]}(T)$ and $\varepsilon_{[\bar{1}01]}(T)$ graphs exhibit a sharp break at about 60 K. This last observation correlates with Raman studies [17], which likewise revealed two singular points in this temperature interval. The fact that the positions of these singular points in our measurements and those derived from dielectric studies [11] differ somewhat can be attributed to the different technologies of crystal growth employed. Thus, the available experimental data suggest (see also [12, 13]) a multistage character of the transition to different polar states in $CdTiO_3$.

Because the B_{1u} mode softens very little indeed (Fig. 8), it may be considered noncritical. On the other hand, the B_{2u} and B_{3u} modes should be treated as critical degrees of freedom that are associated with phase transitions to polar states. In this case, local singularities near ferroelectric phase transitions in $CdTiO_3$ can be viewed in terms of models with two single-component order parameters. Condensation of the B_{2u} polar mode brings about a lowering of crystal symmetry down to the C_{2v}^9 group with an attendant onset of spontaneous polarization P_y ($\mathbf{P}_s \parallel \mathbf{b}$), whereas B_{3u}-mode condensation should provide the C_{2v}^2 symmetry of the ferroelectric phase with P_x ($\mathbf{P}_s \parallel \mathbf{a}$). The effective Landau potential in this case can be written as

$$\Phi_1 = a_1 P_y^2 + a_2 P_y^4 + a_3 P_y^6 + b_1 P_x^2 + b_2 P_x^4 + b_3 P_x^6 + \gamma P_y^2 P_x^2. \quad (4)$$

Here, a_i, b_i, and γ are renormalized constants of the true multicomponent potential of the cubic perovskite phase, whose properties will be considered in a later paper. By introducing sixth-order polarization terms in Eq. (4), we allow for the possibility of first-order phase transitions, which follows from both spectroscopic data [17] and dielectric measurements [11].

We refer the reader to [20] for a more detailed analysis of model (4) and display one of the phase diagrams applicable to our situation in Fig. 10. There are two ways to lower the crystal symmetry by transforming the orthorhombic D_{2h}^{16} phase into a phase with a changed direction of the polarization vector. As we go along the thermodynamic path t' shown in Fig. 10, the B_{2u} and B_{3u} modes are softened simultaneously and a first-order phase transition occurs at $T_{C1'}$ (set by our data at about 78 K); as a result, the C_{2v}^9 phase ($P_y \neq 0$) arises under condensation of displacements associated with the B_{2u} mode. Next, due to a cascade of two first-order phase transitions at $T_{C2'}$ and $T_{C3'}$ with an intermediate monoclinic phase of symmetry C_s^2 ($P_{xy} \neq 0$; here, both modes condense), the spontaneous polarization vector changes to $\mathbf{P}_x \parallel \mathbf{a}$ in the C_{2v}^2 phase ($P_x \neq 0$). Alternately, P_y can switch to P_x directly along the thermodynamic path t'' at the first-order phase transition point $T_{C2''}$; in this case, there is a fairly large region where both polar states (C_{2v}^9 and C_{2v}^2) coexist. Along the thermodynamic paths inclined to the coordinate axes in the phase diagram, both modes become soft, with the B_{2u} mode condensing first (this mode is softer than the B_{3u} mode).

Obviously enough, this model is consistent with all the experimental data available [11, 17], including the "contradictory" information derived from x-ray measurements [10, 15]. However, in order to unambiguously identify which of the t' and t'' paths is realized in $CdTiO_3$, a more comprehensive investigation of the temperature interval 50–90 K is certainly needed.

5. CONCLUSIONS

(1) First measurements of polarized IR spectra of crystalline $CdTiO_3$ made in the range 5–300 K have been performed. Symmetry assignment of the lines has been made in good agreement with factor group theory predictions and Raman spectra [17] assuming the $Pnma$–D_{2h}^{16} space group. This symmetry is suggested to hold for $CdTiO_3$ in the temperature range from 78 to 300 K.

(2) Dispersion analysis was employed to determine the oscillator parameters (dielectric contributions, frequencies, damping constants) for all experimentally observed polar modes, and their temperature dependence was established.

(3) IR spectroscopic study of the dynamic behavior of the $CdTiO_3$ crystal in the range 5–300 K has revealed a quantitative correlation with quasi-static measurements of $\varepsilon(\nu, T)$ in the kilohertz-frequency range [11–13], which substantiates the conclusion that there are no subphonon low-frequency excitations (central peak) in this crystal.

(4) Low-temperature studies of IR spectra revealed a soft B_{3u} mode whose condensation should result in the C_{2v}^2 polar state. This finding correlates with x-ray diffraction data [15] and, when considered together with Raman data [17] and dielectric measurements [11], suggests a multistage transformation of the $CdTiO_3$ structure into different polar states with $Pna2_1$–C_{2v}^9 and $Pmc2_1$–C_{2v}^2 symmetries involving switching in the direction of the spontaneous polarization vector.

(5) The temperature region between 50 and 90 K requires additional comprehensive investigation because there is an indirect evidence for complex dynamic behavior of $CdTiO_3$ in this temperature interval. At any rate, our preliminary analysis of experimental data conducted in terms of the model of two interacting polar modes allows the existence of one more intermediate polar phase of monoclinic symmetry Pb–C_s^2 between the $Pna2_1$–C_{2v}^9 and $Pmc2_1$–C_{2v}^2 phases in this narrow temperature interval.

ACKNOWLEDGMENTS

This study was supported by the Russian Foundation for Basic Research (project nos. 03-02-16720, 04-02-16228) and, in part, by the Foundation of the President of the Russian Federation (project nos. NSh-2168.2003.2, NSh-1415.2003.2).

REFERENCES

1. M. E. Lines and A. M. Glass, *Principles and Application of Ferroelectrics and Related Materials* (Clarendon, Oxford, 1977; Mir, Moscow, 1981).
2. G. A. Samara, J. Phys.: Condens. Matter **15**, R367 (2003).
3. A. P. Ramirez, J. Phys.: Condens. Matter **9**, 8171 (1997).
4. S. E. Park and T. R. Shrout, J. Appl. Phys. **82**, 1804 (1997).
5. V. B. Shirokov and V. I. Torgashev, Kristallografiya **49**, 25 (2004) [Crystallogr. Rep. **49**, 20 (2004)].
6. N. W. Thomas, Acta Crystallogr. B **52**, 16 (1996).
7. B. J. Kennedy, C. J. Howard, and B. C. Chakoumakos, J. Phys.: Condens. Matter **11**, 1479 (1999).
8. S. Sasaki, C. T. Prewitt, J. D. Bass, and W. A. Schulze, Acta Crystallogr. C **43**, 1668 (1987).
9. G. A. Smolenskiĭ, Dokl. Akad. Nauk SSSR **70**, 405 (1950).
10. P.-H. Sun, T. Nakamura, Y. J. Shan, Y. Inaguma, and M. Itoh, Ferroelectrics **217**, 137 (1998).
11. Y. J. Shan, H. Mori, H. Imoto, and M. Itoh, Ferroelectrics **270**, 381 (2002).
12. M. E. Guzhva, V. V. Lemanov, P. A. Markovin, and T. A. Shuplygina, Ferroelectrics **218**, 93 (1998).
13. M. E. Guzhva, V. V. Lemanov, and P. A. Markovin, Fiz. Tverd. Tela (St. Petersburg) **43**, 2058 (2001) [Phys. Solid State **43**, 2146 (2001)].
14. H. El-Mallah, B. E. Watts, and B. Wanklyn, Phase Transit. **9**, 235 (1987).
15. Y. J. Shan, H. Mori, K. Tezuka, H. Imoto, and M. Itoh, Ferroelectrics **284**, 107 (2003).
16. A. S. Knyazev, Yu. M. Poplavko, and V. P. Zakharov, Fiz. Tverd. Tela (Leningrad) **16**, 2215 (1974) [Sov. Phys. Solid State **16**, 1446 (1974)].
17. V. I. Torgashev, Yu. I. Yuzyuk, V. B. Shirokov, V. V. Lemanov, and I. E. Spektor, Fiz. Tverd. Tela (St. Petersburg) **47** (2), 324 (2005) [Phys. Solid State **47**, 337 (2005)].
18. A. A. Volkov, Yu. G. Goncharov, G. V. Kozlov, S. P. Lebedev, and A. M. Prokhorov, Infrared Phys. **25**, 369 (1985).
19. V. Zelezny, E. Cockayne, J. Petzelt, M. F. Limonov, D. E. Usvyat, V. V. Lemanov, and A. A. Volkov, Phys. Rev. B **66**, 224303 (2002).
20. Yu. M. Gufan and E. S. Larin, Fiz. Tverd. Tela (Leningrad) **22**, 463 (1980) [Sov. Phys. Solid State **22**, 270 (1980)].

Translated by G. Skrebtsov

Physics of the Solid State, Vol. 47, No. 3, 2005, pp. 556–559. Translated from Fizika Tverdogo Tela, Vol. 47, No. 3, 2005, pp. 536–539.

LATTICE DYNAMICS AND PHASE TRANSITIONS

Martensitic Transformation and Electrical Properties of a $Ni_{2.14}Mn_{0.81}Fe_{0.05}Ga$ Alloy in Its Different Structural States

R. N. Imashev, Kh. Ya. Mulyukov, I. Z. Sharipov, V. G. Shavrov, and V. V. Koledov

Institute for Metal Superplasticity Problems, Russian Academy of Sciences, ul. Khalturina 39, Ufa, Bashkortostan, 450001 Russia

e-mail: Ramil_imashev@imsp.da.ru

Received June 22, 2004

Abstract—Phase transformations in a $Ni_{2.14}Mn_{0.81}Fe_{0.05}Ga$ alloy in different structural states are studied from the temperature dependences of its electrical resistivity. The dependences obtained indicate that, in the coarse-grained state, this alloy undergoes two structural phase transformations: intermartensitic modulation transformation and martensite–austenite transformation. In the nanocrystalline state, these transformations are absent. The recrystallization of a nanocrystalline sample at 773 K for 30 min results in the martensite–austenite transformation; however, the phase transformation related to a change in the martensite modulation period does not occur in this state. The resistivity is shown to depend on the structural state of the alloy. © *2005 Pleiades Publishing, Inc.*

1. INTRODUCTION

The unique combination of the physical properties of Ni_2MnGa alloys, which exhibit a shape-memory effect (SME) [1], has recently attracted considerable research interest. This circumstance stems from the fact that the thermoelastic martensitic transformation inducing an SME in these alloys occurs in their ferromagnetic state and that the temperature of this structural phase transition is sensitive to an applied magnetic field [2], mechanical stresses [3], the introduction of impurity atoms, and a deviation from the stoichiometric composition [4–6]. For example, the substitution of Ni for Mn atoms results in an increase in the martensite–austenite transition temperatures and in a decrease in the Curie temperature [5]. Phase transitions in alloys are known to be accompanied by changes in their physical properties. One of the properties that are most sensitive to these processes is the electrical resistivity, whose variation allows one to exactly establish the temperatures of the onset and completion of a structural phase transition.

The formation of a nanocrystalline (NC) state in materials substantially changes their physical properties [7]. However, there are no systematic data on the effect of the structural state of Ni_2MnGa alloys on their physical properties and the character of phase transitions in them. Therefore, in this work, we studied the temperature dependences of the resistivity of a $Ni_{2.14}Mn_{0.81}Fe_{0.05}Ga$ alloy in its different structural states.

2. EXPERIMENTAL

A polycrystalline $Ni_{2.14}Mn_{0.81}Fe_{0.05}Ga$ alloy was fabricated using a technique described in [2]. The NC state was formed by severe plastic deformation (SPD). To this end, flat 0.5-mm-thick disks 6 mm in diameter were cut from the initial polycrystalline ingots. The disks were subjected to shear deformation in Bridgman anvils at a pressure of 7 GPa by rotation through an angle of 10π at room temperature. An intermediate structural state was produced by annealing NC samples in vacuum at a pressure of 10^{-3} Pa at 773 K for 30 min. The resistivities of the samples were measured using the four-point probe method.

The microstructure of a coarse-grained sample was examined on an AXIOVERT 100A optical microscope equipped with a digital video camera and a computer. The microstructures of the NC states of the $Ni_{2.14}Mn_{0.81}Fe_{0.05}Ga$ alloy were examined on a JEM-2000EX transmission electron microscope.

3. RESULTS AND DISCUSSION

The microstructure of the coarse-grained sample at 283 K (low-temperature phase) shown in Fig. 1 demonstrates that this sample is polycrystalline with a mean grain size of about 0.5 mm. The grains contain characteristic martensite plates. The disorientation of the martensite plates in different grains indicates that the grain boundaries are high-angle boundaries. The grain boundaries contain pronounced cracks, which obviously lead to high brittleness of the coarse-grained sam-

1063-7834/05/4703-0556$26.00

ple; the cracks appear after several austenite–martensite–austenite cycles.

Figure 2 shows that an NC sample consists of very small crystallites without clear boundaries between them. The mean grain size of the crystallites is estimated to be 10 nm. The electron diffraction pattern of the sample is a set of diffraction rings consisting of reflections that are strongly diffused in the azimuthal direction. This feature indicates the presence of both significant internal stresses and high-angle misorientations of the crystallographic axes of various crystallites with respect to each other. The structure of the NC sample changes significantly after annealing at 773 K (Fig. 3). Clear boundaries form between crystallites, whose mean size is 200 nm. Some grains have boundaries with a typical fringe contrast, which indicates recrystallization. The color contrast between the grains demonstrates their misorientation. The electron diffraction pattern taken from an area of 0.5 μm^2 contains clear undiffused reflections, which indicate that the internal stresses have relaxed.

Figure 4 shows the temperature dependences of the resistivity ρ for three structural states. The measured values of the resistivity ρ for the three states are seen to differ substantially. The resistivity is maximum in the NC state (Fig. 4c); this should be caused by the small crystallite sizes, a high defect density, and disordering of the alloy. These assumptions are supported by the fact that ρ is minimum in the coarse-grained state (Fig. 4a) and has intermediate values in the annealed state (Fig. 4b).

The $\rho(T)$ dependence for the coarse-grained state is rather complex. Upon heating from 80 to 268 K, the resistivity increases almost linearly. In the range from 270 to 273 K, it increases sharply by 0.15 $\mu\Omega$ m and then again increases linearly up to 294 K. In the range from 294 to 297 K, the resistivity decreases jumpwise by 0.7 $\mu\Omega$ m. At higher temperatures, the resistivity increases smoothly; however, near the Curie point, the curve has a weak discontinuity in slope. Upon cooling, ρ behaves similarly; in the range 294–297 K, ρ varies virtually reversibly, but the change in it that was observed in the range 270–273 K is repeated only in the range 222–242 K.

This complex character of the $\rho(T)$ dependence is obviously due to the fact that a number of different phase transformations occur in the coarse-grained sample. For example, the sharp increase in ρ at 270 K upon heating should be caused by a change in the modulation period of the martensite [8–11], which in turn begins to transform at 294 K into the high-temperature cubic phase (austenite). The latter transformation induces the jumpwise decrease in resistivity observed at this temperature. Indeed, the austenite phase has a higher crystallographic symmetry as compared to the martensite and, hence, should have a lower resistivity. This transformation ends at 297 K. Upon cooling, the reverse austenite–martensite transformation proceeds almost

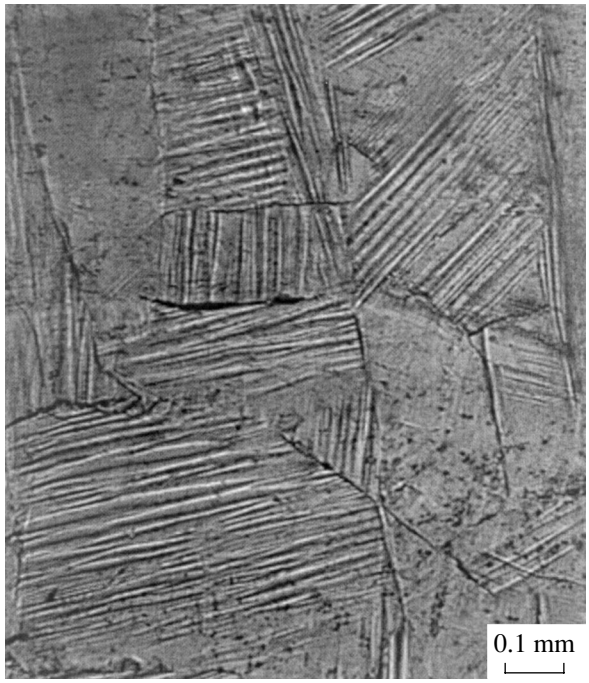

Fig. 1. Microstructure of a coarse-grained sample (the martensite phase).

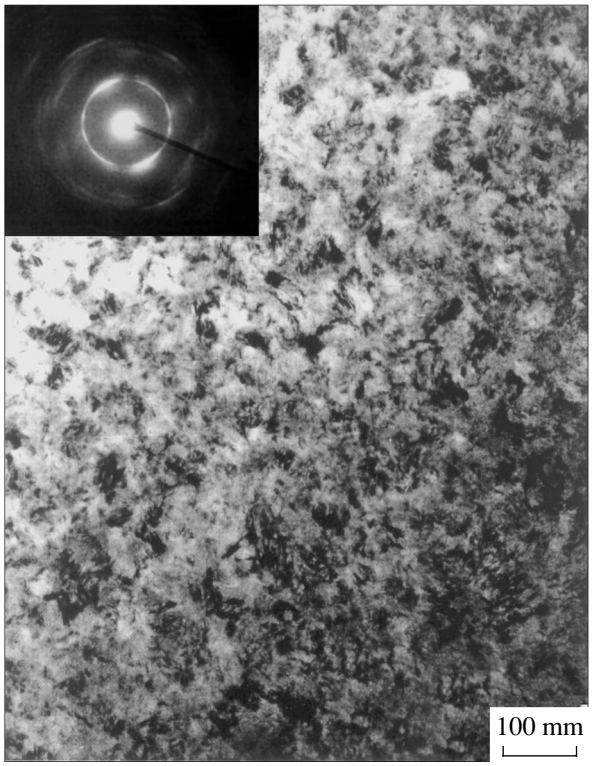

Fig. 2. Microstructure and an electron diffraction pattern of an NC sample.

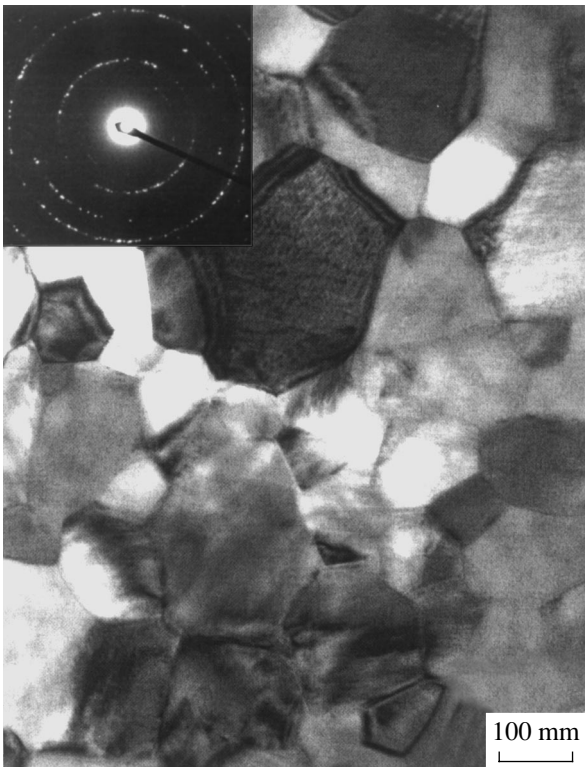

Fig. 3. Microstructure and an electron diffraction pattern of a recrystallized sample (the austenite phase).

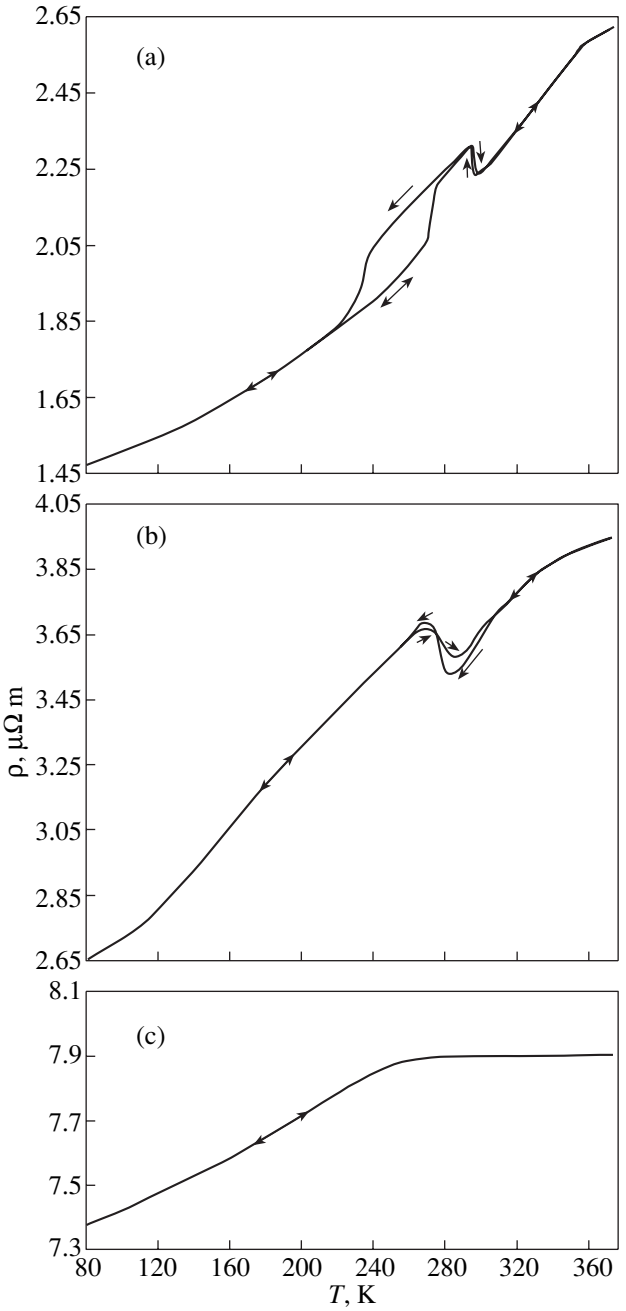

Fig. 4. Temperature dependences of the resistivity of the alloy in (a) the quasi-crystalline, (b) recrystallized, and (c) nanocrystalline states.

reversibly. The transformation related to martensite modulation is significantly delayed and occurs over a wider temperature range.

An analysis of the $\rho(T)$ dependence of the sample with an NC structure shows that, over the entire temperature range, the variation in ρ upon heating and cooling is smooth and reversible, which indicates the absence of structural phase transformations in this state. This feature should be due to both the small crystallite sizes and possible disordering of the compound caused by SPD. The fact that ordering compounds can be disordered during SPD was established in [12–14]. The following circumstance is important here. In the range 260–360 K, ρ remains virtually unchanged, although it increases relatively rapidly at lower temperatures. The character of the $\rho(T)$ dependence is determined by the scattering of free carriers by phonons, lattice defects, and magnetic inhomogeneities. Earlier, we found that, in the NC state, the alloy under study has no ferromagnetic properties [15] and is in a superparamagnetic state. Apparently, the observed $\rho(T)$ dependence is related to a transition from the superparamagnetic to paramagnetic state at about 260 K.

In contrast to the coarse-grained state, the structure forming after annealing at 773 K exhibits only one rather sharp change in ρ during both heating and cooling (Fig. 4b); this change takes place in the range 260–290 K. This specific feature in the $\rho(T)$ dependence is more pronounced upon cooling of the sample and is related to the austenite–martensite phase transformation, which is accompanied, as in the coarse-grained state, by an increase in ρ. However, the intermartensitic modulation transformation is absent in this case. The occurrence of the martensite transition in the recrystallized sample is caused not only by the increased crystallite size and a decreased defect density but also by possible ordering of the $Ni_{2.14}Mn_{0.81}Fe_{0.05}Ga$ compound during annealing. In [16], it was reported that the mar-

tensitic-transformation temperature of stoichiometric and near-stoichiometric Ni_2MnGa alloys increases in proportion to the long-range order parameter squared. However, the structural-transformation temperature should also depend on the grain size. The martensitic transformation is known to occur via the motion of transformation dislocations, which are atomic martensite steps in interphase boundaries. Therefore, the martensitic-transformation temperature depends on the grain size, since grain boundaries are barriers for dislocation motion and, hence, restrict the mean path length of dislocations [17]. The absence of the intermartensitic modulation transformation is likely due to the fact that both the increased degree of ordering of the compound and the increased crystallite size reached under the annealing conditions are insufficient for this phase transformation to occur. The broadening of the temperature range of the structural transformation is explained by the fact that the grain sizes in the recrystallized state vary from 100 to 300 nm and, hence, the martensitic transformation begins at different temperatures throughout the bulk of the sample.

ACKNOWLEDGMENTS

The authors thank V.V. Khovaĭlo for the starting samples.

This work was supported by the state program of support for leading scientific schools of the Russian Federation (project no. NSh-209.2003.8), the Russian Foundation for Basic Research (project no. 03-02-17443), RFBR and Chinese NSF (project no. 03-02-39006), and the Ministry of Education of the Russian Federation (project no. 202.01.01.054).

REFERENCES

1. V. V. Kokorin and V. A. Chernenko, Fiz. Met. Metalloved. **68** (6), 1157 (1989).
2. A. A. Cherechukin, I. E. Dikshtein, D. I. Ermakov, A. V. Glebov, V. V. Koledov, D. A. Kosolapov, V. G. Shavrov, A. A. Tulaikova, E. P. Krasnoperov, and T. Takagi, Phys. Lett. A **291**, 175 (2001).
3. V. V. Kokorin, V. V. Martynov, and V. A. Chernenko, Scr. Metall. **26**, 175 (1992).
4. S. Wirth, A. Liethe-Jasper, A. N. Vasil'ev, and J. M. D. Coey, J. Magn. Magn. Mater. **167**, 7 (1997).
5. A. N. Vasil'ev, A. D. Bozko, I. E. Dikshtein, V. V. Khovailo, V. D. Buchel'nikov, M. Matsumoto, S. Suzuki, V. G. Shavrov, T. Takagi, and J. Tani, Phys. Rev. B **59** (2), 1113 (1999).
6. V. V. Khovailo, K. Oikawa, T. Abe, and T. Takagi, J. Appl. Phys. **93** (10), 8483 (2003).
7. A. I. Gusev and A. A. Rempel', *Nanocrystalline Materials* (Fizmatlit, Moscow, 2000) [in Russian].
8. I. K. Zasimchuk, V. V. Kokorin, V. V. Martynov, A. V. Tkachenko, and V. A. Chernenko, Fiz. Met. Metalloved. **69** (6), 110 (1990).
9. V. V. Martynov and V. V. Kokorin, J. Phys. III, No. 2, 739 (1992).
10. W. H. Wang, Z. H. Liu, J. Zhang, J. L. Chen, G. H. Wu, and W. S. Zhan, Phys. Rev. B **66**, 052411 (2002).
11. W. H. Wang, G. H. Wu, J. L. Chen, S. X. Gao, W. S. Zhan, G. H. Wen, and X. X. Zhang, Appl. Phys. Lett. **79** (8), 1148 (2001).
12. G. F. Korznikova, A. V. Korznikov, and O. Dimitrov, Ann. Chim. Sci. Mater. **27** (3), 35 (2002).
13. A. V. Korznikov, G. Tram, O. Dimitrov, G. F. Korznikova, S. R. Idrisova, and Z. Pakiela, Acta Mater. **49**, 663 (2001).
14. I. Z. Sharipov, R. R. Mulyukov, and Kh. Ya. Mulyukov, Fiz. Met. Metalloved. **95** (1), 47 (2003) [Phys. Met. Metallogr. **95**, 42 (2003)].
15. Kh. Ya. Mulyukov, R. N. Imashev, I. Z. Sharipov, and V. V. Koledov, in *Proceedings of International Seminar on Problems of Magnetism in Magnetic Films, Small Particles, and Nanostructural Objects* (Astrakhan, 2003).
16. H. Hosoda, T. Sugimoto, K. Ohkubo, S. Miura, T. Mohri, and S. Miyazaki, Int. J. Appl. Electromagn. Mater. **12**, 9 (2000).
17. G. A. Malygin, Fiz. Tverd. Tela (St. Petersburg) **42** (8), 1469 (2000) [Phys. Solid State **42**, 1512 (2000)].

Translated by K. Shakhlevich

Physics of the Solid State, Vol. 47, No. 3, 2005, pp. 560–570. Translated from Fizika Tverdogo Tela, Vol. 47, No. 3, 2005, pp. 540–549.

LOW-DIMENSIONAL SYSTEMS AND SURFACE PHYSICS

Interaction of Electrons with Polar Optical Phonons in Semiconductor Superlattices

V. G. Tyuterev

Tomsk State Pedagogical University, Tomsk, 634041 Russia

e-mail: vgt@phys.tsu.ru

Received April 16, 2004

Abstract—On the basis of the microscopic theory of lattice dynamics, simulation of the electric potentials created by optical phonons in semiconductor superlattices is performed. It is shown that the spatial distribution of the amplitudes of electric potentials differs from that in a dielectric continuum predicted by the conventional macroscopic model without dispersion. A modified macroscopic continuum theory is proposed that takes into account the dispersion of short-range interatomic forces and allows one to obtain analytical expressions for the potentials of electron–phonon interaction. © *2005 Pleiades Publishing, Inc.*

1. INTRODUCTION

Polar optical vibrations in semiconductor nanostructures are a source of strong electron–phonon interaction and, therefore, are important for the study of carrier transport. Displacements of the ions participating in optical vibrations create an electric polarization in the crystal. In the absence of free charges, the electric displacement arising in this case satisfies the condition $\nabla(\varepsilon\mathbf{E}) = 0$. In a nonuniform medium like a nanostructure, the permittivity ε depends on spatial coordinates and the calculated electric fields $\mathbf{E}$ and the related potentials appear to be different from those in a bulk material due to quantum confinement of phonons. In an elementary version of the theory (the so-called dielectric continuum model [1]), the frequency dependence of the permittivity $\varepsilon(\omega)$ of a separate layer of the heterostructure is assumed to be the same as in the corresponding bulk material, where it is determined by the phonon spectrum of the material. The calculated potentials for each separate layer are matched using the continuity condition at the heterointerfaces. The solutions obtained are divided into two types. Potentials of the first type are related to bulk phonons confined to a layer. These potentials are also confined to the active layer and vanish at the heterointerfaces. Potentials of the second type are localized near the heterointerfaces and are associated with interface vibrations.

A fundamental difficulty in the dielectric continuum model [1] is given by the incompatibility of the boundary conditions for electric and mechanical components of the envelope function of the phonon field at the interfaces. The amplitudes of mechanical displacements for the confined bulk phonons appear to be discontinuous in this model. The electrostatic contribution is only ~10% of the phonon energy, which makes the predictions from the dielectric continuum model doubtful to a certain degree [2]. On the other hand, the requirement of continuity of the mechanical component leads to discontinuity of the potentials and to the absence of interface potentials [3]. Attempts to resolve this problem by including the dispersion of short-range interatomic forces in the dielectric continuum model [3, 4] result in an unjustified complication of the theory. For this reason, most of the studies of transport processes have been performed using the dielectric continuum model [5] with dispersionless short-range interatomic forces.

2. MICROSCOPIC CALCULATION OF THE POTENTIALS OF ELECTRON–PHONON INTERACTION IN AN $AlAs_nGaAs_m$ [001] SUPERLATTICE

In [6], it was demonstrated that phonon electric fields can be directly calculated on the basis of microscopic theory.

We calculated the phonon spectrum of the superlattice (Fig. 1) using the phenomenological bond charge model [7]. The $AlAs_nGaAs_m$ [001] structure belongs to the D_{2d}^5 symmetry group if $n + m = 2p$ and to the D_{2d}^9 group if $n + m = 2p + 1$. The symmetry classification of long-wavelength vibrations depends on the total number of monolayers in the superlattice unit cell. The decomposition of the vibrational representation at the Γ point can contain one-dimensional fully symmetric Γ_1 representations, one-dimensional Γ_3 representations (which transform as the z component of a vector), and two-dimensional Γ_5 representations (which transform as the x, and y components). The number of different irreducible representations is determined by the total number of monolayers in the unit cell of the specific superlattice.

Calculations show that, in the $AlAs_nGaAs_m$ [001] structure, the ion displacements corresponding to opti-

1063-7834/05/4703-0560$26.00

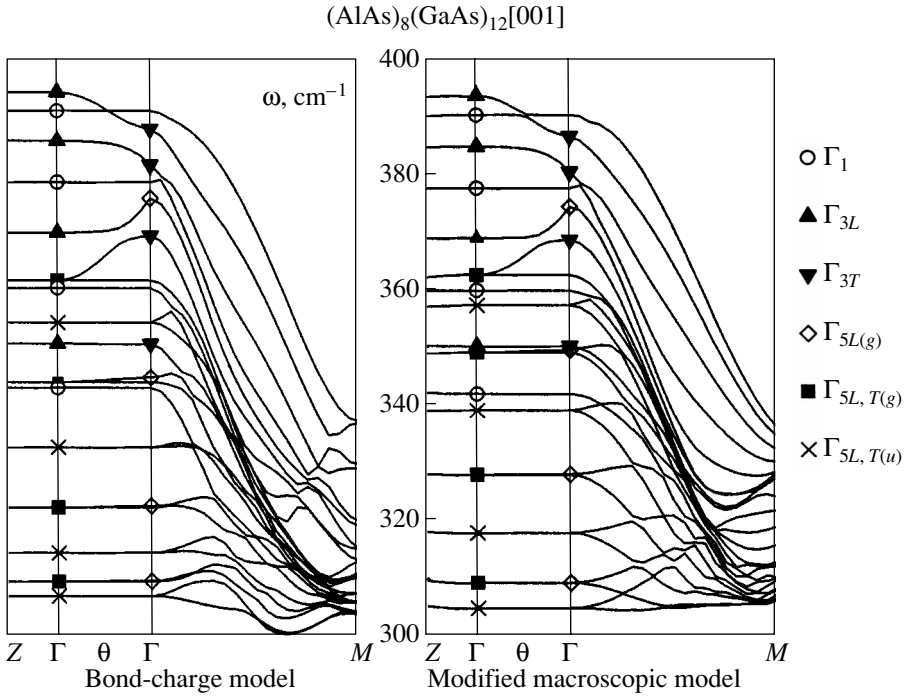

Fig. 1. Frequencies of AlAs-like phonons in the $(AlAs)_8(GaAs)_{12}$ [001] superlattice in two symmetry directions, $Z(0, 0, \pi/D)$ and $M = (\pi/a, 0, 0)$. $D = 10a$ is the superlattice period, and a is the zinc blende lattice constant. In the central part (Γ–Γ), the frequencies of long-wavelength phonons ($\mathbf{q} \longrightarrow 0$) are plotted as functions of the angle θ ($0 \le \theta \le \pi/2$) between the wave vector and the superlattice growth axis (z axis). The left-hand panel corresponds to the microscopic bond charge model, and the right-hand panel shows the calculation in the modified continuum model including dispersion of short-range forces. The irreducible representations at the center of the Brillouin zone are also indicated.

cal vibrations are localized in separate $(AlAs)_n$ or $(GaAs)_m$ sublayers (subcells) and that the phonon frequencies for different sublayers correspond to different energies. The number of representations according to which the long-wavelength phonons in the active subcell transform is determined by the number N_c of monolayers in the subcell. If $N_c = 2m$, the decomposition for phonons of this layer is $\Gamma = m(\Gamma_1 + \Gamma_3 + 2\Gamma_5)$. If $N_c = 2m + 1$, the decomposition for phonons of this sublayer has the form $\Gamma = m\Gamma_1 + (m + 1)\Gamma_3 + (2m + 1)\Gamma_5)$. Calculations [6] show that the vector $\mathbf{s}^n = p_n M_n \mathbf{u}^n$ varies smoothly with the ion number n and is an envelope function for optical vibrations. Here, $p_n = z^n/Z^n$ is the sign of the ion charge ($Z^n = |z^n|$ is the magnitude of the charge) and M_n is the ion mass.

The envelope of ion optical displacements for Γ_1 phonons has only a component parallel to the growth axis of the superlattice (the z axis) and is an odd function with respect to the center of the active sublayer. For Γ_3 phonons, the displacement envelope also contains only a z component and $\mathbf{s}^n$ is an even function. For the two-dimensional Γ_5 representation, the displacements lie in the xy plane (normal to the growth axis) and can be divided into two types: $\Gamma_{5(g)}$ with even displacements $\mathbf{s}^n$ and $\Gamma_{5(u)}$ with odd displacements.

The frequencies of Γ_1 vibrational modes are independent of the direction of the vector $\mathbf{q}$ in the long-wavelength limit.

For any direction of the wave vector, Γ_1 phonons create potentials whose amplitudes are periodic functions (with the period of the superlattice) and even with respect to the center of the active layer ($AlAs_n$ in Fig. 2). They do not create macroscopic fields.

In the long-wavelength limit, the frequencies of Γ_3 vibrational modes have a strongly pronounced dependence on the direction of the wave vector, which is analogous to that for the longitudinal–transverse (L–T) splitting of optical modes in cubic crystals. The potentials created by Γ_3 phonons are odd functions with respect to the center of the active layer (Fig. 2) and exhibit a substantial (nonanalytic) dependence on the direction of the wave vector. When propagating in the direction $\mathbf{q} \perp z$, these phonons are transverse, Γ_{3T}, and create periodic potentials with the superlattice period (local fields).

When propagating in the $\mathbf{q} \parallel z$ direction, Γ_3 phonons are longitudinal, Γ_{3L}, and produce both local and macroscopic fields. The macroscopic electric field $\mathbf{E}_{\text{macro}}$ is directed along the z axis.

In the $\mathbf{q} \parallel z$ direction, all Γ_5 phonons are transverse, their frequencies are doubly degenerate, and these phonons do not create electric fields. For long-wave-

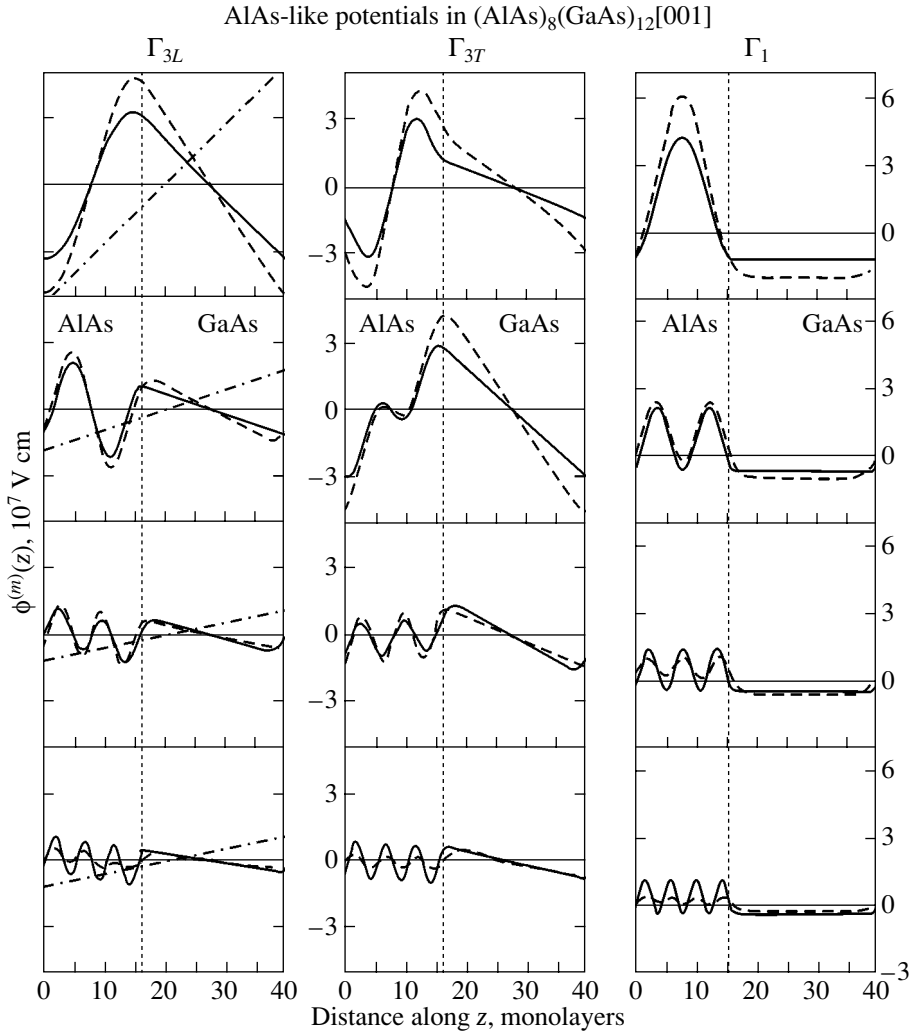

Fig. 2. Periodic part of the amplitude of the electric potentials created by long-wavelength phonons. Dashed lines correspond to the microscopic calculation, and solid lines, to the modified continuum model. For Γ_{3L} phonons propagating in the $\mathbf{q} \parallel z$ direction, the macroscopic component is also shown (dash-dotted lines).

length $\Gamma_{5(g)}$ phonons with $\mathbf{q} \perp z$, the L–T splitting $\Gamma_{5(g)} \longrightarrow \Gamma_{5L(g)} + \Gamma_{5T(g)}$ occurs. Longitudinal $\Gamma_{5L(g)}$ phonons create a macroscopic field $\mathbf{E}_{\text{macro}}$ (in the *xy* plane) directed along the vector $\mathbf{q} \perp z$. In the long-wavelength limit, the potentials created by these phonons do not depend on $\Gamma_{5(u)}$ phonons remain degenerate and, like $\Gamma_{5T(g)}$ phonons, do not create electric fields.

The average potential created by long-wavelength Γ_{3L} and $\Gamma_{5L(g)}$ phonons depends on the wave vector as q^{-1}. The average potential produced by Γ_1 phonons is a constant dependent on the phonon frequency.

We see in Fig. 2 that the form of the potentials of long-wavelength phonons differs substantially from that obtained in the dispersionless continuum model [1–3]. Above all, this is true for the potentials of Γ_3 phonons. In contrast to the potentials of the model developed in [1–3], they are finite at the heterointerface. The phonons whose displacements are localized in one of the layers (AlAs in Fig. 2) also create significant potentials in the inactive layer (GaAs in Fig. 2), where there are no ion displacements for these modes. The potentials of Γ_1 phonons are localized in their active layer; however, they also have nonzero values at the heterointerface.

In the long-wavelength limit, there are no surface vibrations; they appear only at finite values of the phonon wave vector.

Figure 3 shows the amplitudes of the potentials for two short-wavelength AlAs-like phonons in the same superlattice with a wave vector $\mathbf{q} = (201)\pi/D$ (where *D* is the superlattice period) and frequencies $\omega^{(3)}(\mathbf{q}) = 376.6$ cm^{-1} and $\omega^{(5)}(\mathbf{q}) = 372.2$ cm^{-1} generated by the long-wavelength Γ_3 and Γ_5 phonons, respectively. We see in Fig. 3 that, for $q \neq 0$, the interface vibrations are hybridized with bulk modes. As *q* increases, the ampli-

tudes of the potentials decrease and, at $q \approx \pi/a$ (where a is the lattice constant of the bulk material), are an order of magnitude smaller than at the center of the Brillouin zone.

Straightforward application of the simulation results to transport processes is nonproductive, since it requires significant computational effort. However, in our microscopic calculations, the potentials of the electron–phonon interaction exhibit important features that cannot be explained in terms of simplified macroscopic models, such as that considered in [1–3].

In the following section, we suggest a different macroscopic approach, which explains these features and is not hampered by the problem of incompatibility of the boundary conditions. This method is applied to calculate the electric potentials created by phonons with an arbitrary wavelength in a superlattice of the $AlAs_nGaAs_m$ [001] type.

3. ELECTROSTATIC POTENTIALS OF POLAR VIBRATIONS IN CRYSTALS WITH A LARGE UNIT CELL: MACROSCOPIC THEORY

Phenomenologically, the energy of a vibrating crystal lattice in the presence of an electric field can be written in the form [6]

$$W = \frac{1}{2}\sum_{nn'} \mathbf{u}^n \tilde{\Phi}_{nn'} \mathbf{u}^{n'} - \sum_n z^n \mathbf{u}^n \int \tilde{Q}_n(\mathbf{r}) \mathbf{E}(\mathbf{r}, t) d\mathbf{r} - \frac{1}{8\pi}\int \mathbf{E}(\mathbf{r}, t) \tilde{\varepsilon}^{\infty}(\mathbf{r}, \mathbf{r}') \mathbf{E}(\mathbf{r}', t) d\mathbf{r} d\mathbf{r}'. \quad (1)$$

Here, $\mathbf{u}^n$ is the ion displacement at site n of the crystal lattice, z^n is the ion charge, $\mathbf{E}(\mathbf{r}, t)$ is the electric field at the point $\mathbf{r}$, $\tilde{\varepsilon}^{\infty}_{\alpha\beta}(\mathbf{r}, \mathbf{r}')$ is the high-frequency dielectric tensor, $\Phi_{\alpha n, \alpha' n'}$ is the force matrix of the short-range forces, α and β are Cartesian indices, and the quantity $z^n \sum_\alpha u^n_\alpha Q^n_{\alpha\beta}(\mathbf{r})$ determines the β component of the dipole moment density created by the displacement of ion n. As noted above, for structures with a large number of particles in a unit cell, the quantity $\mathbf{s}^n = p_n M_n \mathbf{u}^n$ varies smoothly with the number n and acts as an envelope function for optical vibrations.

The ion displacements $\mathbf{s}^n$ are functions of the discrete variable $\mathbf{r}_n$, whereas the fields are assumed to depend continuously on $\mathbf{r}$. Therefore, a problem regarding transition to the continuum limit arises [8], which can be solved as follows. We introduce a set of functions $\{f_i(\mathbf{r})\}$ localized within a unit cell and satisfying

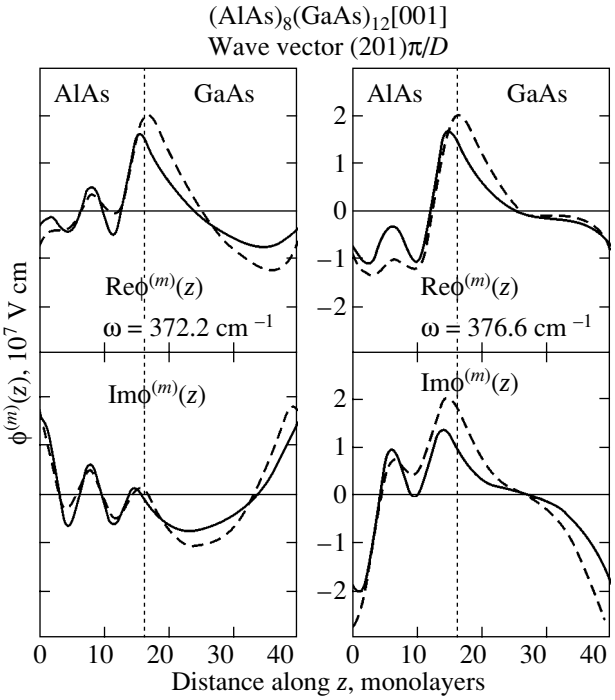

Fig. 3. Periodic part of the amplitude of the electric potentials of two short-wavelength AlAs-like phonons with $\mathbf{q} = (201)\pi/D$. Dashed lines correspond to macroscopic calculations, and solid lines, to the modified continuum model.

the following orthonormalization condition on a discrete set of points:

$$\Omega_a \sum_{n=0}^{n_0-1} f_i^*(\mathbf{r}_n) f_j(\mathbf{r}_n) = \delta_{ij}, \qquad \Omega_a \sum_{i}^{n_0} f_i^*(\mathbf{r}_n) f_i(\mathbf{r}_{n'}) = \delta_{nn'}. \quad (2)$$

Here, $\mathbf{r}_n$ is the equilibrium ion position; n_0 is the number of ions in the unit cell; Ω_a is the volume per atom; and $i, j = 1, \ldots, n_0$. We assume that the transition to the continuum limit for the phonon polarization field implies that the number of atoms in the unit cell n_0 tends to infinity, whereas the volume of the unit cell remains constant, $V_c = \text{const}$; therefore, formally, the volume per atom vanishes, $\Omega_a \longrightarrow 0$. We also assume that $\mathbf{r}_n$ varies quasi-continuously and replace summation by integration according to the rule $\sum_{n=0}^{n_0-1} \longrightarrow \Omega_a^{-1}\int_{V_c} d\mathbf{r}$. Furthermore, we assume that the functions $\{f_i(\mathbf{r})\}$ can be chosen so that, in this continuum limit, the following relations are satisfied:

$$\int_{V_c} f_i^*(\mathbf{r}) f_j(\mathbf{r}) d\mathbf{r} = \delta_{ij}, \quad \sum_{i}^{n_0} f_i^*(\mathbf{r}) f_i(\mathbf{r}') = \delta(\mathbf{r} - \mathbf{r}'). \quad (3)$$

It is convenient to introduce functions of the Wannier type ("standard vibrational modes")

$$F_{i\mathbf{q}}(\mathbf{r}) = N_0^{-1/2}\sum_{\mathbf{L}}\exp(i\mathbf{q}\mathbf{L})f_i(\mathbf{r}-\mathbf{L}). \quad (4)$$

Here, the vector $\mathbf{q}$ is restricted to the first Brillouin zone, $\mathbf{L}$ is a vector of the direct lattice, and N_0 is the number of unit cells in the crystal. Using Eq. (2), we write the ionic displacements as an expansion:

$$u_\alpha^n = \sqrt{\Omega_a}p_n\sum_{ii'}F_{i\mathbf{q}}(\mathbf{r}_n)\tau_{ii'}^{-1}(\mathbf{q})S_{\alpha i'}(\mathbf{q})/M_n, \quad (5)$$

where

$$S_{\alpha i}(\mathbf{q}) = \sum_{i'n}\mu_{ii'}^{-1}(\mathbf{q})F_{i'\mathbf{q}}^*(\mathbf{r}_n)s_\alpha^n. \quad (6)$$

The matrix $\tau_{ii'}(\mathbf{q})$ is related to the positively defined mass matrix

$$\mu_{ii'}^{-1}(\mathbf{q}) = \Omega_a\sum_n F_{i\mathbf{q}}^*(\mathbf{r}_n)M_n^{-1}F_{i'\mathbf{q}}(\mathbf{r}_{n'}) \quad (7)$$

by the relation $\tilde{\mu}^{-1}(\mathbf{q}) = \tilde{\tau}(\mathbf{q})\tilde{\tau}^+(\mathbf{q})$.

The derivative $-\partial W/\partial u_\alpha^n$ determines the α component of the force acting on ion n. We define the electric displacement at the point $\mathbf{r}$ as the variational derivative $\mathbf{D}(\mathbf{r}, t) = -4\pi\delta W/\delta\mathbf{E}(\mathbf{r}, t)$. For atomic displacements and fields, we assume a harmonic time dependence of the form $\exp(i\omega t)$ with a frequency ω. The electric field and the electric displacement are written in the form of an expansion in terms of functions (4), which are considered a basis with a continuous variable. In this case, the condition $\nabla\mathbf{D} = 0$ connects the expansion coefficients of the ionic displacements and fields.

The classical equations of motion for ionic displacements can be reduced to the form

$$\sum_{\beta j}(\Theta_{\alpha i,\beta j}(\mathbf{q}) + W_{\alpha i,\beta j}(\mathbf{q}))S_{\beta j}^{(m)}(\mathbf{q}) = \omega_{(m)}^2(\mathbf{q})S_{\alpha i}^{(m)}(\mathbf{q}), \quad (8)$$

where the matrix

$$\Theta_{\alpha i,\alpha' i'}(\mathbf{q}) = \Omega_a\sum_{jj'}\tau_{ij}(\mathbf{q}) \times\sum_{nn'}F_{j\mathbf{q}}^*(\mathbf{r}_n)p_n\Phi_{\alpha\alpha'}^{nn'}p_{n'}F_{j'\mathbf{q}}(\mathbf{r}_{n'})\tau_{j'i'}^+(\mathbf{q}) \quad (9)$$

is determined by the short-range forces.

Using Eq. (3), we can write the contribution of lVong-range forces as

$$\tilde{W}(\mathbf{q}) = 4\pi\tilde{\zeta}(\mathbf{q})\tilde{V}(\mathbf{q})(\tilde{1} + \tilde{\boldsymbol{\kappa}}(\mathbf{q})\tilde{V}(\mathbf{q}))^{-1}\tilde{\zeta}^+(\mathbf{q}). \quad (10)$$

Here,

$$V_{\alpha j,\alpha' j'}(\mathbf{q}) = \frac{1}{4\pi}\int\frac{F_{\alpha j\mathbf{q}}^*(\mathbf{r})F_{\alpha' j'\mathbf{q}}(\mathbf{r}')}{|\mathbf{r}-\mathbf{r}'|}d\mathbf{r}d\mathbf{r}', \quad (11)$$

$$\zeta_{\alpha i,\alpha' i'}(\mathbf{q}) = \sqrt{\Omega_a}\sum_{nj}\tau_{ij}(\mathbf{q})F_{j\mathbf{q}}^*(\mathbf{r}_n)p_n z^n\int Q_{\alpha\alpha'}^n(\mathbf{r})F_{i'\mathbf{q}}(\mathbf{r})d\mathbf{r}. \quad (12)$$

The matrix $\tilde{\boldsymbol{\kappa}}(\mathbf{q})$ describes the high-frequency polarization

$$\kappa_{\alpha j,\alpha' j'}(\mathbf{q}) = \int F_{j\mathbf{q}}^*(\mathbf{r})\varepsilon_{\alpha\alpha'}^\infty(\mathbf{r},\mathbf{r}')F_{j'\mathbf{q}}(\mathbf{r}')d\mathbf{r}d\mathbf{r}' - \delta_{\alpha\alpha'}\delta_{jj'}. \quad (13)$$

The quantities $F_{\alpha i\mathbf{q}}(\mathbf{r})$ in Eq. (11) are defined as $F_{\alpha i\mathbf{q}}(\mathbf{r}) = \partial F_{i\mathbf{q}}(\mathbf{r})/\partial r_\alpha$. Equation (8) is an eigenvalue problem for the lattice vibration frequencies $\omega_{(m)}(\mathbf{q})$.

For longitudinal fields, disregarding the retardation effects, we have $\mathbf{E}(\mathbf{r}, t) = -\nabla\varphi(\mathbf{r}, t)$, where the potential is given by

$$\varphi(\mathbf{r}, t) = \frac{1}{4\pi}\int\frac{\nabla\mathbf{E}(\mathbf{r}', t)}{|\mathbf{r}-\mathbf{r}'|}d\mathbf{r}'. \quad (14)$$

After performing the standard quantization procedure for atomic displacements (5), the potentials in Eq. (14) produced by these displacements can be found to be

$$\tilde{\varphi}(\mathbf{r}, t) = N_0^{-1/2}\sum_{\mathbf{q}m}\varphi_{\mathbf{q}}^{(m)}(\mathbf{r})(\tilde{a}_{m\mathbf{q}}^+(t) + \tilde{a}_{m\mathbf{q}}(t)), \quad (15)$$

$$\varphi_{\mathbf{q}}^{(m)}(\mathbf{r}) = \sqrt{\frac{\hbar}{2n_0\omega_{(m)}(\mathbf{q})}}\sum_{\alpha i}\phi_{\alpha i}(\mathbf{r}|\mathbf{q})S_{\alpha i}^{(m)}(\mathbf{q}). \quad (16)$$

Here, $\tilde{a}_{m\mathbf{q}}^+(t)$ and $\tilde{a}_{m\mathbf{q}}(t)$ are the phonon creation and annihilation operators, respectively, and $\mathbf{S}^{(m)}(\mathbf{q})$ are the eigenvectors of Eq. (8) corresponding to $\omega_{(m)}(\mathbf{q})$. In Eq. (16), the potential created by a phonon with frequency $\omega_{(m)}(\mathbf{q})$ is expanded in terms of certain "standard" potentials $\phi_{\alpha i}(\mathbf{r}|\mathbf{q})$. These potentials are created by "standard modes" (in which the atomic displacements are directed along the α axis and their magnitudes are given by the functions $F_{i\mathbf{q}}(\mathbf{r}_n)$) and are determined by

$$\phi_{\alpha i}(\mathbf{r}|\mathbf{q}) = \sum_{\beta\beta' jj'V}\int\frac{F_{\beta' j'\mathbf{q}}(\mathbf{r}')}{|\mathbf{r}-\mathbf{r}'|}d\mathbf{r}' \times(\tilde{1} + \tilde{\boldsymbol{\kappa}}(\mathbf{q})\tilde{V}(\mathbf{q}))^{-1}_{\beta' j',\beta j}\zeta_{\beta j,\alpha i}^*(\mathbf{q}). \quad (17)$$

4. POLAR VIBRATIONS IN SEMICONDUCTOR BINARY SUPERSTRUCTURES

We assume that the unit cell of a superstructure consists of subcells made up of different materials, which we denote by index c. For binary compounds, each of the subcells is assumed to contain $2N_c$ atoms, so $n_0 = 2\sum_c N_c$.

If the frequencies $\bar{\omega}_1$ and $\bar{\omega}_2$ of long-wavelength transverse optical phonons in the bulk materials are substantially different, e.g., as is the case with GaAs and AlAs, then the optical vibrations in isolated subcells of the superlattice can be considered independently, which is also confirmed by simulations. The criterion for the applicability of this approximation is $4\pi Z_c^2(\varepsilon^\infty\Omega_a\mu_c|\bar{\omega}_1^2 - \bar{\omega}_2^2|)^{-1} \ll 1$. Here, μ_c and Z_c are the reduced mass and the magnitude of the ionic charge in subcell c, respectively.

In this case, it is convenient to choose the functions $f_i(\mathbf{r})$ so that set (3) is a union of bases, $\sum_{\otimes c}\{f_{\lambda c}(\mathbf{r})\}$, for which each of the functions $f_{\lambda c}(\mathbf{r})$ is nonzero only in its own subcell c.

The model in which $\tau_{c\lambda, c\lambda'}(\mathbf{q}) = \mu_c^{-1/2}\delta_{\lambda\lambda'}$, $\zeta_{\alpha c\lambda, \alpha' c\lambda'}(\mathbf{q}) = (\Omega_a\mu_c)^{-1/2}Z_c\delta_{\lambda\lambda'}\delta_{\alpha\alpha'}$, and $\varepsilon^\infty_{\alpha\beta}(\mathbf{r}, \mathbf{r}') = \varepsilon^\infty\delta_{\alpha\beta}\delta(\mathbf{r} - \mathbf{r}')$ corresponds to the nonpolarizable-ion approximation and to a superstructure fabricated from materials of the zinc blende type with close values of the dielectric constant ε^∞, e.g., a GaAs/AlAs superstructure. In this model,

$$W_{\alpha c\lambda, \alpha' c\lambda'}(\mathbf{q}) = \frac{4\pi Z_c^2}{\varepsilon^\infty\Omega_a\mu_c}V_{\alpha c\lambda, \alpha' c\lambda'}(\mathbf{q}). \tag{18}$$

5. PLANAR GEOMETRY

In the continuum approximation, a superlattice is a periodic repetition of a bilayer of thickness D ($0 < z \le D$) consisting of two layers (subcells) made up of binary compounds with $c = 1$ ($0 < z \le d_1$) and $c = 2$ ($d_1 < z \le D$). The z axis is perpendicular to the layer planes. It is convenient to choose basis (2) in the form $f_{c\lambda}(\mathbf{r}) = S^{-1/2}\exp(i\mathbf{K}\boldsymbol{\rho})\psi_{cn}(z)$, where the vectors $\mathbf{K}$ and $\boldsymbol{\rho}$ lie in the layer planes (i.e., $\mathbf{K}, \boldsymbol{\rho} \perp z$) and S is the area of a layer in the plane normal to the z axis. Accordingly, $\lambda \equiv (n, \mathbf{K})$ becomes a composite index. The Brillouin zone is one-dimensional; therefore, the wave vector is written as $\mathbf{q} = (\mathbf{K}, k)$, where its z component k varies in the limits $-\pi/D \le k < \pi/D$.

Next, we use an approximation in which vibrations in different layers are independent. To be specific, we consider the layer with c = 1 ($0 < z \le d_1$). Passing to the next layer with $c = 2$, it suffices to properly displace the origin, $z_c = z - d_1$, and to make the substitution $d_1 \longrightarrow d_2 = D - d_1$. Therefore, the arguments do not depend on the subcell index, and we write z_c and d_c without the layer index in the subsequent formulas where this does not give rise to any misunderstanding.

In the "active" subcell with $c = 1$ ($0 \le z \le d$), it is convenient to choose functions $\psi_{cn}(z)$ that vanish outside this sublayer and have the form

$$\psi_n(z) = \sqrt{2/d}\sin(\pi nz/d) \tag{19}$$

within this sublayer. In Eq. (19), $n = 1, \ldots, N_c$, where $2N_c$ is the number of atomic monolayers in the subcell. It is convenient to direct one of the coordinate axes, e.g., the y axis, along the vector $\mathbf{K}$. Then, it follows from Eq. (11) that $V_{xn\mathbf{K}'\beta n'\mathbf{K}''}(\mathbf{K}, k) = 0$, whereas for $\alpha, \beta = y, z$ the matrix elements are nonzero only if $\mathbf{K}' = \mathbf{K}'' = \mathbf{K}$; we denote them by $V_{\alpha n\mathbf{K}, \beta n'\mathbf{K}}(\mathbf{K}, k) \equiv V_{\alpha\beta}(nn'|\mathbf{K}, k)$. The calculation of matrix elements (11) reduces to evaluating the expression

$$V_{\alpha\beta}(mn|(\mathbf{K}, k)) = \frac{1}{2KD}\sum_{L=-\infty}^{\infty}e^{ikLD}\int_0^d dz\Psi_\alpha^{m*}(z, K) \times \int_0^d dz' e^{-K|z-z'-LD|}\Psi_\beta^n(z', K). \tag{20}$$

Here, $K = |\mathbf{K}|$, L is an integer, $\Psi_y^n(z, K) = iK\psi_n(z)$, and $\Psi_z^n(z, K) = d\psi_n(z)/dz$. The calculated matrix elements (20) are listed in Appendix 1.

Standard potentials (16) in the planar geometry can be written in the Bloch form

$$\psi_{\alpha n\mathbf{K}}(\mathbf{r}|\mathbf{q}) = S^{-1/2}\exp(i\mathbf{K}\boldsymbol{\rho})\exp(ikz) \times \frac{\bar{\varphi}_1}{\pi(\vartheta^2 + n^2)}U_\alpha^{(n)}(z/(\mathbf{K}, k)). \tag{21}$$

Here, $\vartheta = Kd/\pi$ and $\bar{\varphi}_c = \frac{4\pi Z_c}{\varepsilon^\infty}\sqrt{2d_c/\Omega_a\mu_c}$; the functions $U_\alpha^{(n)}(z|\mathbf{K}, k)$ are calculated using Eq. (17) and given in Appendix 2.

To calculate the contribution of short-range forces (9), we introduce a 3×3 matrix $\tilde{\Delta}_c(Q)$ whose eigenvalues reproduce the spectrum of optical phonons in the bulk binary compound corresponding to $c = 1$ without the polar component, i.e., as if the phonons were nonpolar. This spectrum of "nonpolar" phonons can be obtained using the data from microscopic theory; the

corresponding technique is described in [6]. In this case, the short-range-force matrix can be written as

$$\Phi^c_{\alpha\beta}(\mathbf{r}_n, \mathbf{r}_{n'}) = \frac{1}{N_0}\sum_Q \mu_c p_n \Delta^c_{\alpha\beta}(Q_x, Q_y, Q_z) p_{n'} \times \exp(i\mathbf{Q}(\mathbf{r}_n - \mathbf{r}_{n'})), \quad (22)$$

where $\mathbf{Q}$ varies within the Brillouin zone of the bulk binary crystal. Matrix elements (9) include the quantity

$$\int_0^d \exp(-ikz)\psi_n(z)dz = \sqrt{2d}\frac{\pi n(1-(-1)^n e^{idk})}{((kd)^2 - (\pi n)^2)}. \quad (23)$$

As $k \longrightarrow \pm\pi n/d$, the contribution of integral (23) to matrix elements (9) is maximum and equal to $i\sqrt{d/2}$. Keeping only these leading terms in Eq. (9), we obtain

$$\Theta_{\alpha n\mathbf{K}, \alpha' n'\mathbf{K}'} \approx \delta_{\mathbf{K}\mathbf{K}'}\delta_{nn'}\left\{\Delta^c_{\alpha\alpha'}\left(K_x, K_y, \frac{\pi n}{d}\right) + \Delta^c_{\alpha\alpha'}\left(K_x, K_y, -\frac{\pi n}{d}\right)\right\}. \quad (24)$$

In this approximation, the matrix elements are independent of the longitudinal component k of the wave vector.

6. EXACT SOLUTION IN THE DIELECTRIC-CONTINUUM MODEL

If we disregard the dispersion of short-range forces, matrix (24) becomes

$$\Theta_{\alpha n\mathbf{K}, \alpha' n'\mathbf{K}'}(\mathbf{K}, k) = \bar{\omega}_c^2 \delta_{\mathbf{K}\mathbf{K}'}\delta_{nn'}\delta_{\alpha\alpha'}, \quad (25)$$

where $\bar{\omega}_c^2$ is the frequency of transverse phonons in the bulk material corresponding to layer c.

In the continuum limit, Eqs. (8) form an infinite system whose solution can be found exactly. The details of the solution are not trivial; the calculations were performed using the Maple language in the Scientific Notebook shell and cannot be reproduced in detail in the framework of a journal article. We give only the final result.

The potentials are written in the Bloch form

$$\varphi^{(m)}_{\mathbf{q}}(\mathbf{r}) = S^{-1/2}\exp(i\mathbf{K}\boldsymbol{\rho})\exp(ikz)\phi^{(m)}(z|(\mathbf{K}, k)), \quad (26)$$

where $\phi^{(m)}(z + DL|\mathbf{K}, k) = \psi^{(m)}(z|\mathbf{K}, k)$ and L is an integer. For phonons whose optical displacements $S^{(m)}_{\alpha n\mathbf{K}}(\mathbf{q})$ are confined to the active layer $c = 1$ ($0 < z \le d$), the periodic part extends over the entire unit cell $0 \le z \le D$. The periodic part of the potential $\phi^{(m)}(z|\mathbf{K}, k)$ for these phonons is given below.

The solutions are written as $\phi^{(m)}(z|\mathbf{K}, k) = \bar{\varphi}_1[\hbar/2\omega_{(m)}(\mathbf{K}, k)]^{1/2}\chi^{(m)}(z|\mathbf{K}, k)$. We introduce the notation $\eta = KD$, $\xi = kD$, $\sigma = Kd/2$,

$$U^{(\pm)}_{\mathbf{q}} = \sqrt{(1 \pm H_{\mathbf{q}}/\sqrt{H^2_{\mathbf{q}} + B^2_{\mathbf{q}}})/2},$$
$$H_{\mathbf{q}} = \cosh 2\sigma - \frac{\sinh\eta \sinh 2\sigma}{\cosh\eta - \cos\xi}, \quad (27)$$
$$B_{\mathbf{q}} = \frac{\sin\xi \sinh 2\sigma}{\cosh\eta - \cos\xi}.$$

The function $\Theta(z, d) = 1$ if $0 \le z \le d$ and $\Theta(z, d) = 0$ for all other values of z.

(1) For a given layer, there are two solutions, labeled $m = (\pm)$, which depend on the phonon propagation direction $\mathbf{q} = (\mathbf{K}, k)$:

$$\omega^2_{(\pm)}(\mathbf{K}, k) = \bar{\omega}_1^2 + \frac{2\pi Z_1^2}{\mu_1 \varepsilon^\infty \Omega_a}\left(1 \pm \sqrt{\frac{\cosh(\eta - 2\sigma) - \cos\xi}{\cosh\eta - \cos\xi}}\right), \quad (28)$$

$$\chi^{(\pm)}(z|\mathbf{K}, k) = \exp(-ikz)\frac{\sqrt{\sinh 2\sigma/(2\sigma)}}{2(\cosh\eta - \cos\xi)} \times \left\{\left[U^{(\pm)}_{\mathbf{q}}\cosh(Kz - \eta - \sigma) \pm i\frac{k}{|k|}U^{(\mp)}_{\mathbf{q}}\sinh(Kz - \eta - \sigma)\right] - e^{i\xi}\left[U^{(\pm)}_{\mathbf{q}}\cosh(Kz - \sigma) \pm i\frac{k}{|k|}U^{(\mp)}_{\mathbf{q}}\sinh(Kz - \sigma)\right]\right\} + \frac{1}{2}\exp(-ikz)\Theta(z, d)\sinh(Kz - 2\sigma) \times \left\{U^{(\pm)}_{\mathbf{q}}(\sigma\tanh\sigma)^{-1/2} \mp i\frac{k}{|k|}U^{(\mp)}_{\mathbf{q}}(\tanh\sigma/\sigma)^{-1/2}\right\}. \quad (29)$$

As K and k increase, functions (29) are more and more strongly localized near the interface and are the potentials of interface vibrations.

(2) Longitudinal optical ion displacements correspond to the direction-independent polar solutions $\omega^2_{l(m)} = \bar{\omega}_1^2 + 4\pi Z_1^2/(\mu_1\varepsilon^\infty\Omega_a)$ with infinite degeneracy: $m = 1, \ldots, \infty$. The potentials created by these vibrations are nonzero only in the active layer (the layer $c = 1$, i.e., $0 \le z \le d$), and in this layer they are

$$\chi^{l(m)}(z|\mathbf{K}, k) = i\Theta(z, d) \times \exp(-ikz)\frac{4}{\sqrt{m^2 + \vartheta^2}}\sin(\pi m z/d). \quad (30)$$

(3) Transverse optical ion displacements correspond to direction-independent nonpolar solutions $\omega^2_{t(m)} = \bar{\omega}^2_1$ with infinite degeneracy: $m = 1, \ldots, \infty$. These vibrations do not create electric fields.

For phonons whose ionic displacements are concentrated in the second layer, $c = 2$ ($d < z \le D$), the solutions have a similar form. They can be obtained from Eqs. (28)–(30) by shifting the origin, $z' \longrightarrow z - d$, with the subsequent replacement $d \longrightarrow D - d$ and substitution of the parameters $\bar{\omega}^2_2$, ζ_2, and μ_2 of the bulk phonon spectrum corresponding to this layer.

The fields calculated from Eqs. (28)–(30) and the ionic displacements given in Appendix 3 fully agree with the pattern of the interface vibrations and their potentials (29) and with the confined bulk vibrations and their fields (30) obtained numerically in the continuum model in [1–4]. We note that, as far as we know, the solution in the continuum model has not been previously obtained in an analytical form. An analysis of the solutions obtained shows that potentials (29) are nonanalytic functions at $\mathbf{q} \longrightarrow 0$. In this long-wavelength limit, fields (29) are macroscopic and extend over the entire superlattice if $k \gg K$; in the case of $k \ll K$, these fields are local and have the superlattice period. In the limiting case $d \longrightarrow D \longrightarrow \infty$, Eqs. (28)–(30) reduce to the well-known expression [9] for scattering potentials produced by long-wavelength polar phonons in a bulk cubic crystal. Potentials (29) and (30) are continuous at the interfaces. However, calculations based on Eq. (5) show that the optical ionic displacements are discontinuous for even m, in accordance with the conclusion that the boundary conditions for mechanical and electrodynamic components of optical vibrations are incompatible in the dispersionless continuum model [2]. To achieve simultaneous continuity of fields and ionic displacements, it is necessary to take into account dispersion of short-range forces [2, 3].

7. DIELECTRIC-CONTINUUM MODEL MODIFIED BY INCLUDING DISPERSION OF SHORT-RANGE FORCES

To calculate the spectrum with allowance for the crystal symmetry, we take the matrix $\tilde{\Delta}_c(\mathbf{Q})$ in Eq. (22) in the form

$$\begin{aligned}
\Delta^c_{xx}(\mathbf{Q}) &= \bar{\omega}^2_c(1 + A(k)k_x^2 + B(k)(k_y^2 + k_z^2)),\\
\Delta^c_{yy}(\mathbf{Q}) &= \bar{\omega}^2_c(1 + A(k)k_y^2 + B(k)(k_x^2 + k_z^2)),\\
\Delta^c_{zz}(\mathbf{Q}) &= \bar{\omega}^2_c(1 + B(k)(k_x^2 + k_y^2) + A(k)k_z^2),\\
\Delta^c_{\alpha\beta}(\mathbf{Q}) &= 2\bar{\omega}^2_c G(k)k_\alpha k_\beta, \quad \alpha \ne \beta.
\end{aligned} \tag{31}$$

Here, $A(k) = X_1 + X_2k^2 + X_3k^4$, $B(k) = X_4 + X_5k^2 + X_6k^4$, $G(k) = X_7 + X_8k^2 + X_9k^4$, and $\mathbf{k} = \mathbf{Q}a_c/2\pi$, where a_c is the lattice constant of the material of the layer c. Since there are $3N_c$ degrees of freedom for optical vibrations in the layer c, Eq. (8) involves $3N_c \times 3N_c$ matrices. The parameters of the bulk AlAs and GaAs spectra are chosen by comparing them with the spectra calculated in the bond charge model [6, 7] ($Z_1 = Z_2 = 0.65\sqrt{\varepsilon^\infty}e_0$, $\varepsilon^\infty = 12$, $a_1 = a_2 = 5.65$ Å, $M_{\mathrm{Al}} = 26.98M_p$, $M_{\mathrm{Ga}} = 69.72M_p$, $M_{\mathrm{As}} = 74.92M_p$) and are listed in the table.

Parameters of the short-range force matrix $\tilde{\Delta}$ for bulk materials

Parameter	AlAs	GaAs
$\bar{\omega}$, cm^{-1}	364.39	271.36
X_1	−0.5637	−0.5441
X_2	0.2689	0.2110
X_3	−0.0256	−0.0097
X_4	−0.8293	−0.5771
X_5	0.7346	0.5385
X_6	−0.2001	−0.1535
X_7	−0.1514	−0.1672
X_8	0.1785	0.0369
X_9	−0.0518	0.0199

The basis functions in the form of Eq. (19) do not take into account the short-range interaction of $(\mathrm{AlAs})_n$ and $(\mathrm{GaAs})_m$ sublayers. The agreement with microscopic calculations is improved if we allow for the interaction between the subcells phenomenologically by introducing an effective thickness of the active layer $d_{\mathrm{eff}} = d + \delta$ into the formulas in Appendix 2. For $(\mathrm{AlAs})_n(\mathrm{GaAs})_m$ [001] superlattices with any values of n and m such that $n + m = 20$, the results agree equally well with the simulation results if we take δ to be equal to the thickness of one monolayer.

Figure 1 shows the spectrum of AlAs-like optical phonons in the $(\mathrm{AlAs})_8(\mathrm{GaAs})_{12}$ [001] superlattice ($D = 56.5$ Å, $d_{\mathrm{eff}} = 37.67$ Å) calculated using the microscopic bond charge model (to the left) and the macroscopic model based on Eqs. (8), (24), and (31) (to the right).

We see in Fig. 1 that, in the region $|\mathbf{q}| \le 2\pi/D$, which is important for charge carrier scattering, the agreement is quite good. The deviations near the Brillouin zone boundary $|\mathbf{q}| \sim 2\pi/a$ are more significant and have a qualitative character; this is not surprising, since Eqs. (31) correctly take into account the symmetry of the spectrum of bulk phonons only in the long-wavelength limit.

In the presence of dispersion of short-range forces, bulk modes (30) and interface modes (29) are mixed. As a result of hybridization, both the potentials and optical ionic displacements are now continuous.

The results obtained are illustrated in Figs. 2 and 3 through the example of AlAs-like phonons in the $(AlAs)_8(GaAs)_{12}$ [001] structure. The potentials are calculated using Eqs. (16) and (21) (see also the formulas in Appendix 2). Solid lines show the local components of the potentials:

$$\phi_{\text{loc}}^{(m)}(z|\mathbf{K}, k) = \phi^{(m)}(z|\mathbf{K}, k) - \bar{\phi}^{(m)}(\mathbf{K}, k),$$
$$\bar{\phi}^{(m)}(\mathbf{K}, k) = D^{-1}\int_0^D \phi^{(m)}(z|\mathbf{K}, k)dz. \quad (32)$$

For Γ_{3L} phonons, there also exists a macroscopic component of the potential, $\phi_{\text{macro}}^{(m)}(z, k) = izk\bar{\phi}^{(m)}(0, k)$, shown by the dash-dotted line in Fig. 2. The results shown in Figs. 2 and 3 are typical. We see that the agreement between the two models is quite good. The reasons for the quantitative disagreement are related to the fact that, in the microscopic bond charge model, the high-frequency polarizability of the medium is effectively taken into account, whereas in the macroscopic model we used the rigid-ion approximation.

The agreement between the microscopic calculations and our version of the continuum model for $(AlAs)_n(GaAs)_m$ [001] superlattices is the same for any values of n and m (for both even and odd n and m such that $n + m = 20$) up to $(AlAs)_2(GaAs)_{18}$ [001].

8. CONCLUSIONS

Numerical analysis performed in terms of a realistic model of interatomic interaction has shown that the spatial distribution of the amplitudes of interaction potentials between electrons and optical phonons in a superlattice differs substantially from that predicted by the simple macroscopic dispersionless dielectric continuum model [1–3]. The physical reason for this disagreement is the fact that the simple macroscopic model includes only the long-range component of interatomic forces. The modified macroscopic model developed in this study agrees with the simulation results only if dispersion of the short-range interatomic interaction is taken into account.

The advantage of our modified macroscopic model over our numerical microscopic calculations is that the potentials of electron–phonon interaction are obtained analytically in a form more convenient for calculating scattering probabilities, thus simplifying the analysis of transport processes.

It should be noted that the above features of the behavior of the potentials are important in considering the electron scattering between minibands. For scattering processes inside a miniband, the differences between our model and the dispersionless continuum model are not of crucial importance, since the matrix elements of the potentials of Γ_3 phonons do not make a contribution because of the symmetry and the values of the potentials of Γ_1 phonons at the heterointerface are small, as seen in Fig. 2. Nevertheless, in this case, the use of analytical expressions for electron–phonon interaction potentials also leads to an appreciable reduction in the amount of calculations.

APPENDIX 1

MATRIX $V_{\alpha\alpha' jj'}(\mathbf{K}, k)$ IN THE PLANAR GEOMETRY

We write out only the nonzero intralayer matrix elements for $c = 1$.

$$V_{\alpha cm\mathbf{K}', \beta cn\mathbf{K}''}(\mathbf{q}) = V_{\alpha\beta}(mn|\mathbf{K}, k)\delta_{\mathbf{K}\mathbf{K}'}\delta_{\mathbf{K}\mathbf{K}''},$$
$$V_{yy}(mn|\mathbf{K}, k) = f_{mn}^{\mathbf{K}}(s_{mn}t_m^{\mathbf{K}}R_{\mathbf{q}}^m - ia_{mn}B_{\mathbf{q}}) + \delta_{mn}\vartheta^2/(\vartheta^2 + m^2),$$
$$V_{zz}(mn|\mathbf{K}, k) = f_{mn}^{\mathbf{K}}(-s_{mn}t_m^{\mathbf{K}}R_{\mathbf{q}}^m + ia_{mn}B_{\mathbf{q}}) + \delta_{mn}m^2/(\vartheta^2 + m^2),$$
$$V_{yz}(mn|\mathbf{K}, k) = -f_{mn}^{\mathbf{K}}(s_{mn}t_m^{\mathbf{K}}B_{\mathbf{q}} + ia_{mn}R_{\mathbf{q}}^m) - (1 - \delta_{mn})4imn\vartheta^2 a_{mn}/[\pi(\vartheta^2 + m^2)|m^2 - n^2|].$$

Here, $V_{\alpha\beta}(mn|\mathbf{K}, k) = V_{\beta\alpha}(mn|\mathbf{K}, k)$. In addition to the previous notation, we set

$$f_{mn}^{\mathbf{K}} = 2mn\vartheta/[\pi(\vartheta^2 + m^2)(\vartheta^2 + n^2)],$$
$$t_m^{\mathbf{K}} = (\cosh 2\sigma - (-1)^m)/\sinh 2\sigma,$$
$$s_{mn} = ((-1)^m + (-1)^n)/2, \quad R_{\mathbf{q}}^m = H_{\mathbf{q}} + (-1)^m,$$
$$a_{mn} = ((-1)^m - (-1)^n)/2.$$

The matrix $V_{\alpha\beta}(mn|\mathbf{K}, k)$ is Hermitian, which can be verified by straightforward calculation.

APPENDIX 2

PHONON POTENTIALS IN THE PLANAR GEOMETRY

In the calculation, we used the formulas from Appendix 4. In the chosen coordinate system, we obtain

$$U_x^{(n)}(z|\mathbf{K}, k) = 0,$$
$$U_y^{(n)}(z|\mathbf{K}, k) = -i\frac{nS_n(\sigma)}{2(\cosh\eta - \cos\xi)} \times (C_n(Kz - \sigma - \eta) - e^{i\xi}C_n(Kz - \sigma)) + i\Theta(z, d)\{(-1)^n n\sinh(Kz - 2\sigma) - \vartheta\sin(\pi nz/d)\},$$

$$U_z^{(n)}(z|\mathbf{K}, k) = \frac{nS_n(\sigma)}{2(\cosh\eta - \cos\xi)}$$
$$\times (S_n(Kz - \sigma - \eta) - e^{i\xi}S_n(Kz - \sigma))$$
$$- \Theta(z, d)\{(-1)^n n\cosh(Kz - 2\sigma) + n\cos(\pi nz/d)\}.$$

Here, $S_n(x) = (e^x - (-1)^n e^{-x})/2$ and $C_n(x) = (e^x + (-1)^n e^{-x})/2$.

APPENDIX 3

SOLUTION TO EQ. (8) IN THE DISPERSIONLESS DIELECTRIC CONTINUUM MODEL

In the calculation, we used the formulas from Appendix 4. We write out the eigenvectors $S_{\alpha n\mathbf{K}'}^{(m)}(\mathbf{q}) = S_\alpha^{(m)}(n|\mathbf{K}, k)\delta_{\mathbf{K}\mathbf{K}'}$.

For the direction-dependent frequencies (28), we have $S_\alpha^{(\pm)}(n|\mathbf{q}) = 2nr_\alpha^{(\pm)}(n|\mathbf{K}, k)\sqrt{\vartheta t_n^{\mathbf{K}}/\pi}/(\vartheta^2 + n^2)$, where the quantities $r_\alpha^{(\pm)}(n|\mathbf{K}, k)$ are different for even and odd $r_y^{(\pm)}(2m|\mathbf{q}) = iU_{\mathbf{q}}^{(\pm)}$, $r_z^{(\pm)}(2m|\mathbf{q}) = \mp i\frac{k}{|k|}U_{\mathbf{q}}^{\pm}$, $r_y^{(\pm)}(2m+1|\mathbf{q}) = \mp\frac{k}{|k|}U_{\mathbf{q}}^{\pm}$, and $r_z^{(\pm)}(2m+1|\mathbf{q}) = -U_{\mathbf{q}}^{(\pm)}$. For the chosen coordinate axes, we have $r_x^{(\pm)}(n|\mathbf{K}, k) = 0$.

For the direction-independent polar solutions $\omega_{l(m)}^2$, the eigenvectors are

$$S_y^{(m)}(n|\mathbf{K}, k) = \delta_{mn}\vartheta/\sqrt{m^2 + \vartheta^2},$$
$$S_z^{(m)}(n|\mathbf{K}, k)$$
$$= (1 - \delta_{mn})4imna_{mn}/[(m^2 - n^2)\sqrt{m^2 + \vartheta^2}].$$

For the nonpolar solutions $\omega_{t(m)}^2$, we have

$$S_y^{(m)}(n|\mathbf{K}, k)$$
$$= -(1 - \delta_{mn})4imna_{mn}/[(m^2 - n^2)\sqrt{m^2 + \vartheta^2}],$$
$$S_z^{(m)}(n|\mathbf{K}, k) = \delta_{mn}\vartheta/\sqrt{m^2 + \vartheta^2}.$$

APPENDIX 4

RELATIONS USED IN THE CALCULATIONS

$$\sum_{n=1}^{\infty}(2n)^2/(\vartheta^2 + (2n)^2)^2$$
$$= \pi(2\coth(\pi\vartheta/2) + \pi\vartheta - \pi\vartheta\coth^2(\pi\vartheta/2))/16\vartheta,$$

$$\sum_{n=0}^{\infty}(2n+1)^2/(\vartheta^2 + (2n+1)^2)^2$$
$$= \pi(2\tanh(\pi\vartheta/2) + \pi\vartheta - \pi\vartheta\tanh^2(\pi\vartheta/2))/16\vartheta,$$

$$\sum_{n=0}^{\infty}(2n+1)^2/[((2n+1)^2 - (2m)^2)(\vartheta^2 + (2n+1)^2)]$$
$$= \pi\vartheta\tanh(\pi\vartheta/2)/4(\vartheta^2 + (2m)^2),$$

$$\sum_{n=1}^{\infty}(2n)^2/[((2n)^2 - (2m+1)^2)(\vartheta^2 + (2n)^2)]$$
$$= \pi\vartheta\coth(\pi\vartheta/2)/4(\vartheta^2 + (2m+1)^2),$$

$$\sum_{n=0}^{\infty}(2n+1)^2/[((2n+1)^2 - (2m)^2)$$
$$\times((2n+1)^2 - (2k)^2)] = \delta_{mk}\pi^2/16,$$

$$\sum_{n=1}^{\infty}(2n)^2/[((2n)^2 - (2m)^2)$$
$$\times((2n)^2 - (2k+1)^2)] = \delta_{mk}\pi^2/16.$$

For $0 \le z \le d$, the following relations are valid:

$$\sum_{n=1}^{\infty}n\sin(2\pi nz/d)/((2n)^2 + \vartheta^2)$$
$$= \pi\sinh(\pi\vartheta(d - 2z)/2d)/8\sinh(\pi\vartheta/2),$$

$$\sum_{n=0}^{\infty}(2n+1)\sin(\pi(2n+1)z/d)/((2n+1)^2 + \vartheta^2)$$
$$= \pi\cosh(\pi\vartheta(d - 2z)/2d)/4\cosh(\pi\vartheta/2).$$

ACKNOWLEDGMENTS

This study was supported by a grant from the President of the Russian Federation (no. NSh-1743.2003.2) and INTAS (grant no. 01-0458).

REFERENCES

1. K. Huang and B. Zhu, Phys. Rev. B **38** (18), 13377 (1988); G. Weber, Phys. Rev. B **46** (24), 16171 (1992).
2. K. J. Nash, Phys. Rev. B **46** (12), 7723 (1992); M. P. Chamberlain, M. Cardona, and B. K. Ridley, Phys. Rev. B **48** (19), 14356 (1993).
3. F. Comas and C. Trallero-Giner, Physica B (Amsterdam) **192**, 394 (1993); C. Trallero-Giner, F. Comas, and G. Garcia-Moliner, Phys. Rev. B **50** (3), 1755 (1994);

B. K. Ridley, O. Al-Dossary, N. C. Constantinou, and M. Babiker, Phys. Rev. B **50** (16), 11701 (1994).

4. H. Rucker, E. Molinari, and P. Lugli, Phys. Rev. B **44** (7), 3463 (1991).
5. G. J. Warren and P. N. Butcher, Semicond. Sci. Technol. **1** (2), 133 (1986); I. Dharssi and P. N. Butcher, J. Phys.: Condens. Matter **2**, 119 (1990); F. Comas, F. Castro, and J. L. Gondar, Physica B (Amsterdam) **239** (3–4), 370 (1997); V. G. Litovchenko, D. V. Korbutyak, S. Krylyuk, H. T. Grahn, and K. H. Ploog, Phys. Rev. B **55**, 10621 (1997); J. Pozela, A. Namajunas, K. Pozela, and V. Juciene, Physica E (Amsterdam) **5** (1–2), 108 (1999); S. I. Borisenko, Fiz. Tekh. Poluprovodn. (St. Petersburg) **38** (2), 207 (2004) [Semiconductors **38**, 202 (2004)].
6. V. G. Tyuterev, J. Phys.: Condens. Matter **11** (9), 2153 (1999).
7. K. C. Rustagi and W. Weber, Solid State Commun. **18** (6), 673 (1976); G. Kannelis, Phys. Rev. B **35** (2), 746 (1987); E. Richter and D. Strauch, Solid State Commun. **64**, 867 (1987).
8. B. A. Foreman, Phys. Rev. B **52** (16), 12260 (1995).
9. G. L. Bir and G. E. Pikus, *Symmetry and Strain-Induced Effects in Semiconductors* (Nauka, Moscow, 1972; Wiley, New York, 1974).

Translated by I. Zvyagin

Physics of the Solid State, Vol. 47, No. 3, 2005, pp. 571–577. Translated from Fizika Tverdogo Tela, Vol. 47, No. 3, 2005, pp. 550–555.

LOW-DIMENSIONAL SYSTEMS AND SURFACE PHYSICS

Energy Spectra and Lifetimes of Quasiparticles in an Open Quantum Dot Surrounded by Identical Barriers in a Cylindrical Quantum Wire

N. V. Tkach and A. M. Makhanets

Chernovtsy National University, Chernovtsy, 58012 Ukraine

e-mail: theormyk@chnu.cv.ua

Received April 20, 2004

Abstract—A theory of quasi-stationary states and lifetimes of electrons, holes, and excitons in an open cylindrical semiconductor quantum wire containing a quantum dot surrounded by two identical antidots (with potential barriers of finite height) is developed using the scattering matrix method. The energy spectra and lifetimes of electrons, holes, and excitons in a β-HgS/β-CdS/β-HgS/β-CdS/β-HgS nanoheterosystem are calculated and analyzed as functions of the geometric parameters of the quantum dot involved. It is demonstrated that an increase in the height of the quantum dot leads to a decrease in the energy of quasi-stationary exciton states of the Breit–Wigner type and to an increase in their lifetimes. The lifetime of exciton states is long enough for these states to be observed in the experiment. © *2005 Pleiades Publishing, Inc.*

1. INTRODUCTION

Considerable advances have been made in the study of low-dimensional semiconductor systems since the advent of new techniques for growing nanocrystals. The use of these techniques has opened up strong possibilities for designing and fabricating a great variety of nanoheterosystems (two-dimensional quantum wells, one-dimensional quantum wires, zero-dimensional quantum dots) and their combinations [1, 2].

Virtually all theoretical and experimental investigations of nanoheterosystems have dealt with so-called closed systems, i.e., systems for which the environment is considered a maximum potential barrier for quasiparticles (electrons, holes, excitons). In these systems, states with quasiparticle energies lower than the potential of the environment are always stationary. Excited quasiparticles (for example, excitons) can lose energy only due to interaction either with other quasiparticles or with fields.

The particular interest expressed by researchers in open nanoheterosystems is explained by the fact that, in open systems, unlike closed systems, quasiparticles can always penetrate through the potential barrier into the environment [3]. This provides an additional channel of energy relaxation for excited quasiparticles in a quantum well. This specific feature of open systems can be of great importance in designing lag-free high-speed detectors.

The existing theory of quasi-stationary states of electrons and holes in composite spherical quantum dots and cylindrical quantum wires was developed using the scattering matrix method by Buczko and Bassani [4] and in our previous studies [5, 6]. In those works, the energy spectra and lifetimes of quasiparticles in specific nanoheterosystems were calculated as functions of the geometric parameters of the nanosystems and the dynamical characteristics of quasiparticles (for example, the longitudinal quasi-momentum in the case of quantum wires).

Unfortunately, no satisfactory theory of quasi-stationary states of electron, holes, and excitons in open combined nanoheterosystems has been offered to date. In this respect, it is of interest to investigate the specific features in the behavior of quasi-stationary states even if only in relatively simple systems. One of these systems, which can be fabricated using modern experimental techniques, is a semiconductor quantum wire that contains a quantum dot separated from the other part of the quantum wire by two identical quantum antidots with potential barriers of finite height (Fig. 1).

For this system, two different problems arise depending on the position of the spatial point at which a quasiparticle is initially formed in the nanoheterosystem. The first problem is associated with scattering. It is assumed that a specific physical process occurring in one part of the quantum wire brings about the formation of a free quasiparticle (electron, hole, exciton). This quasiparticle has an energy and a quasi-momentum and

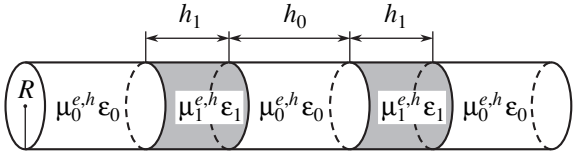

Fig. 1. Schematic drawing of the nanoheterosystem.

1063-7834/05/4703-0571$26.00 © 2005 Pleiades Publishing, Inc.

Material parameters of the system under investigation

	μ^e, μ_0	μ^h, μ_0	U^e, eV	U^h, eV	a, Å	ε	E_g, eV
CdS	0.2	0.7	3.8	6.3	5.818	5.5	2.5
HgS	0.036	0.044	5.15	5.65	5.851	11.36	0.5

moves to another part of the quantum wire through the quantum antidots and the quantum dot. It is necessary to determine the coefficients of transmission and reflection for the "quantum antidot–quantum dot–quantum antidot" system. The second problem deals with quasi-stationary states of a quasiparticle that is originally located within the quantum dot. It is assumed that, upon the initial excitation, the quasiparticle located in the quantum dot will penetrate through the potential barriers into the quantum wire (completely isolated from the environment). It is necessary to determine the energies and lifetimes of the relevant quasi-stationary states. It is this problem that is solved in the present study.

2. HAMILTONIAN AND THE SCATTERING MATRIX OF AN ELECTRON (HOLE) IN A COMPOSITE CYLINDRICAL QUANTUM WIRE WITH AN OPEN QUANTUM DOT

Let us consider a composite semiconductor cylindrical quantum wire that contains a quantum dot surrounded by two identical quantum antidots. The nanowire, the quantum dot, and both quantum antidots have the same radius R. The heights of the quantum dot and the quantum antidots are equal to h_0 and h_1, respectively (Fig. 1). From symmetry considerations, the origin of the cylindrical coordinate system is conveniently chosen at the center of the quantum dot with the OZ axis aligned parallel to the principal axis of the system. It is assume that the materials of the quantum wire and the quantum dot possess identical physical characteristics (effective masses, permittivities), whereas the material of two quantum antidots in the general case has other physical characteristics. The composite quantum wire is in an environment that provides an infinite potential barrier for any quasiparticles in this system.

It is assumed that, at some instant of time, a specific physical action (for example, exposure to an electromagnetic field) brings about the formation of quasiparticles (excitons) located in the quantum dot. Since the height and width of the potential barriers of both quantum antidots are finite, the quantum dot is an open system. As a consequence, excitons can penetrate through the potential barriers; hence, their states become quasi-stationary and have a finite lifetime.

In this paper, the quasi-stationary spectrum and lifetimes of the exciton states generated in an open cylindrical quantum dot located in a quantum wire and separated from the wire by two quantum antidots will be investigated as functions of the geometric parameters of the system.

Before analyzing the spectrum and lifetimes of the exciton states, it is necessary to investigate the quantum states of electrons and holes in the nanosystem under consideration.

Hereinafter, the geometric sizes of the nanoheterosystem components are assumed to be such that the effective-mass approximation will be valid for electrons (holes) and that the interaction between an electron and a hole will be determined by the Coulomb potential with permittivities of the corresponding massive materials.

Therefore, the effective masses of electrons (holes) are considered to be known and equal to the effective masses of these quasiparticles in massive analogs of nanocrystals:

$$\mu^{e,h}(z) = \begin{cases} \mu_0^{e,h}, & z_{-1} \le |z| \le z_1 \\ \mu_1^{e,h}, & z_1 \le |z| \le z_2 \\ \mu_0^{e,h}, & z_2 \le |z| < \infty. \end{cases} \quad (1)$$

We also assume that the lattice constants of the well material a_0 (subscript 0) and the barrier material a_1 (subscript 1) are very close in magnitude. In particular, the lattice constants of the β-HgS and β-CdS compounds used in the nanosystem studied in this work are taken to be such (see table) that $(a_1 - a_0)/a_0 \le 1\%$. As a result, the interfaces between the subsystems are sufficiently abrupt. This makes it possible to use the approximation of rectangular potential energy barriers for electrons and holes; that is,

$$U^{e,h}(\rho, \varphi, z) = \begin{cases} -U_0^{e,h}, & z_{-1} \le |z| \le z_1 \\ -U_1^{e,h}, & z_1 \le |z| \le z_2 \\ -U_0^{e,h}, & z_2 \le |z| < \infty. \end{cases} \quad (2)$$

where $U_{0,1}^{e(h)}$ are the potential energies of the electron and the hole in the corresponding materials with respect to vacuum. For $\rho > R$, we have $U^e(\rho, \varphi, z) = U^h(\rho, \varphi, z) = \infty$.

Since the theories of the quasi-stationary spectrum of electrons and holes in the system under investigation are equivalent, we consider the theory for electrons and temporarily omit the index e.

In order to determine the quantum states of electrons, it is necessary to solve the Schrödinger equation

$$\hat{H}\psi(\mathbf{r}) = E\psi(\mathbf{r}) \quad (3)$$

with the Hamiltonian

$$\hat{H} = -\frac{\hbar^2}{2}\nabla\frac{1}{\mu(z)}\nabla + U(\rho, \varphi, z). \quad (4)$$

By virtue of the symmetry of the problem, the wave function $\psi(\mathbf{r})$ is conveniently sought in the following form [7]:

$$\Psi_{n_\rho m}(\mathbf{r}) = (-\pi R^2 J_{m-1}(x_{n_\rho m}) J_{m+1}(x_{n_\rho m}))^{-1/2} \times J_m\left(\frac{x_{n_\rho m}}{R}\rho\right) e^{im\varphi}\varphi(z), \quad (5)$$

where $m = 0, \pm1, \pm2, \ldots$ is the magnetic quantum number, $J_m(\rho x_{n_\rho m}/R)$ is the Bessel function of integer order, and $x_{n_\rho m}$ are the zeros of the Bessel function (n_ρ is the radial quantum number, which determines the ordinal number of the zero of the Bessel function at a fixed magnetic quantum number m).

After substituting the wave function defined by expression (5) into the Schrödinger equation, we separate the variables and obtain the following equation for the zth component of the wave function:

$$\frac{\partial^2}{\partial z^2}\varphi(z) + \varphi(z)\left[\frac{2\mu(z)}{\hbar^2}(E - U(\rho, \varphi, z)) - \frac{x_{n_\rho m}^2}{R^2}\right] = 0. \quad (6)$$

Since the potential energy of the electron is symmetric with respect to the variable z, Eq. (6) is invariant with respect to the transformation $z \longrightarrow -z$. Therefore, we can restrict our consideration to the range of the variable z from 0 to ∞. It should be noted that, in this case, the solutions to Eq. (6) are divided into even (+) and odd (–) solutions [8]:

$$\varphi^{\pm}(z) = \begin{cases} \varphi_0(z) = A^{\pm}(e^{ik_0 z} \pm e^{-ik_0 z}), & 0 < z \le z_1 \\ \varphi_1(z) = B^{\pm}(e^{-k_1 z} + S_1^{\pm} e^{k_1 z}), & z_1 \le z \le z_2 \\ \varphi_2(z) = C^{\pm}(e^{-ik_0 z} + S^{\pm} e^{ik_0 z}), & z_2 \le z < \infty. \end{cases} \quad (7)$$

Here, $k_0^2 = 2\mu_0/\hbar^2 E - x_{n_\rho m}^2/R^2$, $k_1^2 = 2\mu_1/\hbar^2(U - E) + x_{n_\rho m}^2/R^2$, $U = U_0 - U_1$, and $S^{\pm}$ is the scattering matrix (S-matrix). The energy is reckoned from the top of the potential well (material 0).

Then, by using the continuity conditions for the wave function and the probability density flux at all the interfaces,

$$\varphi_0(z)|_{z=z_1} = \varphi_1(z)|_{z=z_1}, \quad \varphi_1(z)|_{z=z_2} = \varphi_2(z)|_{z=z_2},$$
$$\frac{1}{\mu_0}\varphi_0'(z)|_{z=z_1} = \frac{1}{\mu_1}\varphi_1'(z)|_{z=z_1}, \quad (8)$$
$$\frac{1}{\mu_1}\varphi_1'(z)|_{z=z_2} = \frac{1}{\mu_0}\varphi_2'(z)|_{z=z_2},$$

and the normalization conditions for the wave function

$$\int_0^\infty \varphi_{k_0}^{*\pm}(z)\varphi_{k_0'}^{\pm}(z)dz = \delta(k_0 - k_0'), \quad (9)$$

it is possible to derive analytical relationships for the coefficients $A^{\pm}$, $B^{\pm}$, and $C^{\pm}$ and the scattering matrix in the form

$$S^{\pm} = \frac{S_1^{\pm}(\mu_0 k_1 + i\mu_1 k_0)\exp[(k_1 - ik_0)z_2] - (\mu_0 k_1 - i\mu_1 k_0)\exp[-(k_1 + ik_0)z_2]}{(\mu_0 k_1 + i\mu_1 k_0)\exp[-(k_1 - ik_0)z_2] - S_1(\mu_0 k_1 - i\mu_1 k_0)\exp[(k_1 + ik_0)z_2]}, \quad (10)$$

where

$$S_1^{\pm} = \frac{\exp(-2k_1 z_1)\left[k_1\mu_0\begin{Bmatrix}\cos(k_0 z_1)\\ \sin(k_0 z_1)\end{Bmatrix} \mp k_0\mu_1\begin{Bmatrix}\sin(k_0 z_1)\\ \cos(k_0 z_1)\end{Bmatrix}\right]}{k_1\mu_0\begin{Bmatrix}\cos(k_0 z_1)\\ \sin(k_0 z_1)\end{Bmatrix} \pm k_0\mu_1\begin{Bmatrix}\sin(k_0 z_1)\\ \cos(k_0 z_1)\end{Bmatrix}}. \quad (11)$$

In this study, we do not analyze the specific features of the wave functions for quasi-stationary states of electron and holes. Therefore, we can omit rather cumbersome analytical expressions for the coefficients $A^{\pm}$, $B^{\pm}$, and $C^{\pm}$ and restrict our consideration to a theoretical treatment and calculation of the scattering matrix.

According to the general theory [3], the real and imaginary parts of the poles of the scattering matrix in the complex energy plane

$$\tilde{E}_{n_\rho m n_z} = E_{n_\rho m n_z} - i\Gamma_{n_\rho m n_z}/2 \quad (12)$$

determine the energies $E_{n_\rho m n_z}$ and the half-widths $\Gamma_{n_\rho m n_z}$ of the quasi-stationary states, respectively. The quantum number n_z numbers the poles of the scattering matrix at fixed values of the quantum numbers n_ρ and m. The half-width of the level and the lifetime of elec-

trons and holes in the states $|n_\rho m n_z\rangle$ are related by the expression

$$\tau_p = \frac{\hbar}{\Gamma_\rho} \quad (p = n_\rho m n_z). \tag{13}$$

Therefore, relationships (10)–(13) describe the energy spectrum and the lifetimes of exciton electrons and exciton holes in quasi-stationary states that are generated in an open cylindrical quantum dot located in a cylindrical quantum wire.

3. ENERGY SPECTRUM AND LIFETIMES OF QUASI-STATIONARY STATES OF EXCITONS IN AN OPEN CYLINDRICAL QUANTUM DOT LOCATED IN A CYLINDRICAL QUANTUM WIRE

In order to solve the problem of the quasi-stationary spectrum of an exciton produced in a cylindrical quantum dot separated from the cylindrical quantum wire by two quantum antidots, we need to solve the Schrödinger equation

$$\hat{H}_{\text{ex}}(\mathbf{r}_e, \mathbf{r}_h)\psi_{\text{ex}}(\mathbf{r}_e, \mathbf{r}_h) = E_{\text{ex}}\psi_{\text{ex}}(\mathbf{r}_e, \mathbf{r}_h) \tag{14}$$

with the Hamiltonian

$$\hat{H}_{\text{ex}}(\mathbf{r}_e, \mathbf{r}_h) = \hat{H}_e(\mathbf{r}_e) + \hat{H}_h(\mathbf{r}_h) + U(|\mathbf{r}_e - \mathbf{r}_h|) + E_{g0}. \tag{15}$$

Here, E_{g0} is the band gap of the quantum dot material; $H_{e,h}$ are the Hamiltonians of noninteracting electrons and holes, which are determined by formula (4) for each quasiparticle; and

$$U(|\mathbf{r}_e - \mathbf{r}_h|) = -\frac{e^2}{\varepsilon(\mathbf{r}_e, \mathbf{r}_h)|\mathbf{r}_e - \mathbf{r}_h|} \tag{16}$$

is the electron–hole interaction potential, in which the permittivity $\varepsilon(\mathbf{r}_e, \mathbf{r}_h)$ is a composite function of the electron and hole positions in the nanosystem.

Equation (14) cannot be solved exactly. In this respect, the quasi-stationary states of excitons will be examined using the results obtained in the previous section and the perturbation theory approach.

The lifetimes $\tau_{p_h}^{p_e}$ and the energy spectrum $E_{p_h}^{p_e}$ of excitons in the quasi-stationary states can be calculated under the assumption that the electron–hole interaction energy is less than the difference between the quantum-confinement energies (the validity of this assumption will be confirmed by numerical calculations). Since the electron–hole interaction is relatively weak, the lifetimes of exciton states can be determined from the relationship [9]

$$\frac{1}{\tau_{p_h}^{p_e}} = \frac{1}{\tau_{p_e}} + \frac{1}{\tau_{p_h}}. \tag{17}$$

However, the quantity $\Delta E_{p_h}^{p_e}$ cannot be calculated from the wave functions $\psi_{n_\rho m n_z}^{e,h}$ of the quasi-stationary states for the open nanosystem, because their components $\varphi_{n_z}^{e,h}(z_{e,h})$ are normalized to the δ function (9) rather than to unity. Nonetheless, the quantity $\Delta E_{p_h}^{p_e}$ can be calculated with a good accuracy if it is remembered that the electron and hole energy levels expressed through the poles of the scattering matrix [formula (10)] for the open quantum dot and those found by solving the Schrödinger equation for the closed quantum dot (when the barrier antidots are extended over the entire length of the quantum wire) are very close to each other. This means that the electron–hole binding energy can be calculated as the diagonal matrix element:

$$\Delta E_{p_h}^{p_e} = -e^2 \iint \frac{\left|\psi_{p_h}^{p_e}(\mathbf{r}_e, \mathbf{r}_h)\right|^2}{\varepsilon(\mathbf{r}_e, \mathbf{r}_h)|\mathbf{r}_e - \mathbf{r}_h|} d\mathbf{r}_e d\mathbf{r}_h, \tag{18}$$

where the wave functions of the stationary states of the exciton

$$\psi_{p_h}^{p_e}(\mathbf{r}_e, \mathbf{r}_h) = \psi_{p_e}(\mathbf{r}_e)\psi_{p_h}(\mathbf{r}_h) \tag{19}$$

are determined by the wave functions of the stationary states of the electron and the hole in the closed quantum dot; that is,

$$\begin{aligned}\Psi_{n_\rho^{e,h} m^{e,h} n_z^{e,h}}(\mathbf{r}_{e,h}) &= (-\pi R^2 J_{m^{e,h}-1}(x_{n_\rho^{e,h} m^{e,h}}) \\ &\times J_{m^{e,h}+1}(x_{n_\rho^{e,h} m^{e,h}}))^{-1/2} J_{m^{e,h}}\left(\frac{x_{n_\rho^{e,h} m^{e,h}}}{R}\rho_{e,h}\right) \\ &\times e^{im^{e,h}\varphi_{e,h}} \varphi_{n_z^{e,h}}^{s\pm}(z_{e,h}).\end{aligned} \tag{20}$$

Here, the axial wave functions $\varphi_{n_z^{e,h}}^{s\pm}(z_{e,h})$ of the stationary (s) states of the electron and the hole are derived from the corresponding Schrödinger equations with the Hamiltonian for the closed nanosystem. These equations are solved in a trivial way. As a result, we have

$$\begin{aligned}&\varphi_{n_z^{e,h}}^{s\pm}(z_{e,h}) \\ &= \frac{\exp(k_1(z_0 - z_{e,h})\theta(z_{e,h} - z_0))\begin{Bmatrix}\cos(k_0 z_{e,h}) \\ \sin(k_0 z_{e,h})\end{Bmatrix}}{\sqrt{\dfrac{2k_0 z_0 \pm \sin(2k_0 z_0)}{4k_0} + \dfrac{\begin{Bmatrix}\cos^2(k_0 z_0) \\ \sin^2(k_0 z_0)\end{Bmatrix}}{2k_1}}},\end{aligned} \tag{21}$$

where $\theta(z_{e,h} - z_0)$ is the Heaviside theta function.

The quantity $\Delta E_{p_h}^{p_e}$ is calculated in the cylindrical coordinate system taking into account that the permittivity as a composite function of the variables $\mathbf{r}_e$ and $\mathbf{r}_h$ can be approximately represented in the form

$$\frac{1}{\varepsilon(\mathbf{r}_e, \mathbf{r}_h)} \approx \frac{1}{\bar{\varepsilon}} = \frac{\rho^0_{p_e, p_h}}{\varepsilon_0} + \frac{\rho^1_{p_e, p_h}}{\varepsilon_1}, \quad (22)$$

where $\rho^{0,1}_{p_e, p_h}$ are the probabilities of finding the exciton in the quantum dot (index 0) and in both antidots (index 1), respectively.

Therefore, the relationship describing the quantity $\Delta E_{p_h}^{p_e}$ takes the form

$$\Delta E_{p_h}^{p_e} = \int_0^\infty\int_0^\infty dz_e dz_h \int_0^\infty\int_0^\infty d\rho_e d\rho_h \int_0^{2\pi}\int_0^{2\pi} d\varphi_e d\varphi_h \times \frac{J^2_{m^e}(\rho_e x_{n_\rho^e m^e}/R) J^2_{m^h}(\rho_h x_{n_\rho^h m^h}/R) \rho_e \rho_h \varphi^{s\pm}_{n_e}(z_e) \varphi^{s\pm}_{n_h}(z_h)}{\bar{\varepsilon}\sqrt{(z_e - z_h)^2 + \rho_e^2 + \rho_h^2 - 2\rho_e\rho_h\cos(\varphi_e - \varphi_h)}}. \quad (23)$$

In relationship (23), two integrals are taken in the general form and the last four integrals are calculated using a computer at specified parameters of the systems.

4. ANALYSIS AND DISCUSSION OF THE RESULTS

Before proceeding to an analysis of the energy spectrum and the lifetimes of exciton states in the nanoheterosystem as functions of its geometric parameters, it is necessary to investigate the corresponding characteristics for electrons and holes that form excitons.

The energies $E^{e,h}_{n_\rho m n_z}$ and the lifetimes $\tau^{e,h}_{n_\rho m n_z}$ of electrons (e) and holes (h) as functions of the height h_0 of the cylindrical quantum dot at a fixed value of its radius ($R = 10a_{\mathrm{HgS}}$) and a fixed height of the quantum antidots ($h_1 = 4a_{\mathrm{CdS}}$) were calculated in terms of the theory described in the preceding sections. The material parameters of the system are listed in the table. The results of the calculations are presented in Fig. 2.

It is evident that the energy spectra and the lifetimes of electrons and holes exhibit qualitatively identical behavior and that the quantitative differences are associated only with the differences in their effective masses and potential energies. Consequently, we can restrict our consideration to an analysis of the spectrum and the lifetimes of electronic states.

As can be seen from Fig. 2, an increase in the height h_0 of the cylindrical quantum dot brings about a shift of all the quantum energy levels $E^e_{n_\rho m n_z}$ to the low-energy range and an increase in the lifetimes $\tau^e_{n_\rho m n_z}$ in the corresponding states. The spectral levels form groups in

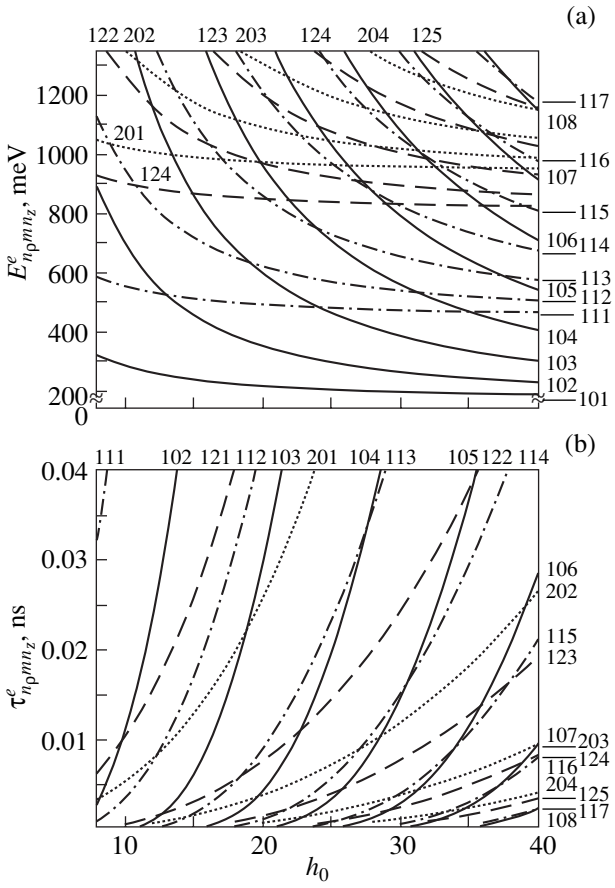

Fig. 2. Dependences of (a) the energy $E^e_{n_\rho m n_z}$ and (b) the lifetime $\tau^e_{n_\rho m n_z}$ of an electron on the quantum dot height h_0 for the quantum antidot height $h_1 = 4a_{\mathrm{CdS}}$ and the quantum dot radius $R = 10a_{\mathrm{HgS}}$.

which levels have the same quantum number n_ρ. These groups consist of subgroups composed of levels with the same quantum number m. In turn, the subgroups include levels with different quantum numbers n_z. An increase in any one of the three quantum numbers (n_ρ, m, n_z) results in an increase in the energy of the corresponding state and a decrease in the lifetime. Therefore, the group of levels with the quantum number $n_\rho = 1$ corresponds to the lowest energies. In this group, the subgroups of levels with the quantum numbers $m = 0, 1, 2, \ldots$ are located on the energy scale in order of increasing energy from bottom to top. These subgroups each involve levels with the quantum numbers $n_z = 1, 2, 3, \ldots$. The groups of levels with the quantum numbers $n_\rho = 2, 3, \ldots$ lie at higher energies. These groups contain their own subgroups with the quantum numbers m and n_z.

The analysis demonstrates that all the electronic states are doubly degenerate with respect to the quantum number m (except for $m = 0$). Furthermore, it can be seen from Fig. 2a that there is an accidental degeneracy of different states, because the levels of all the

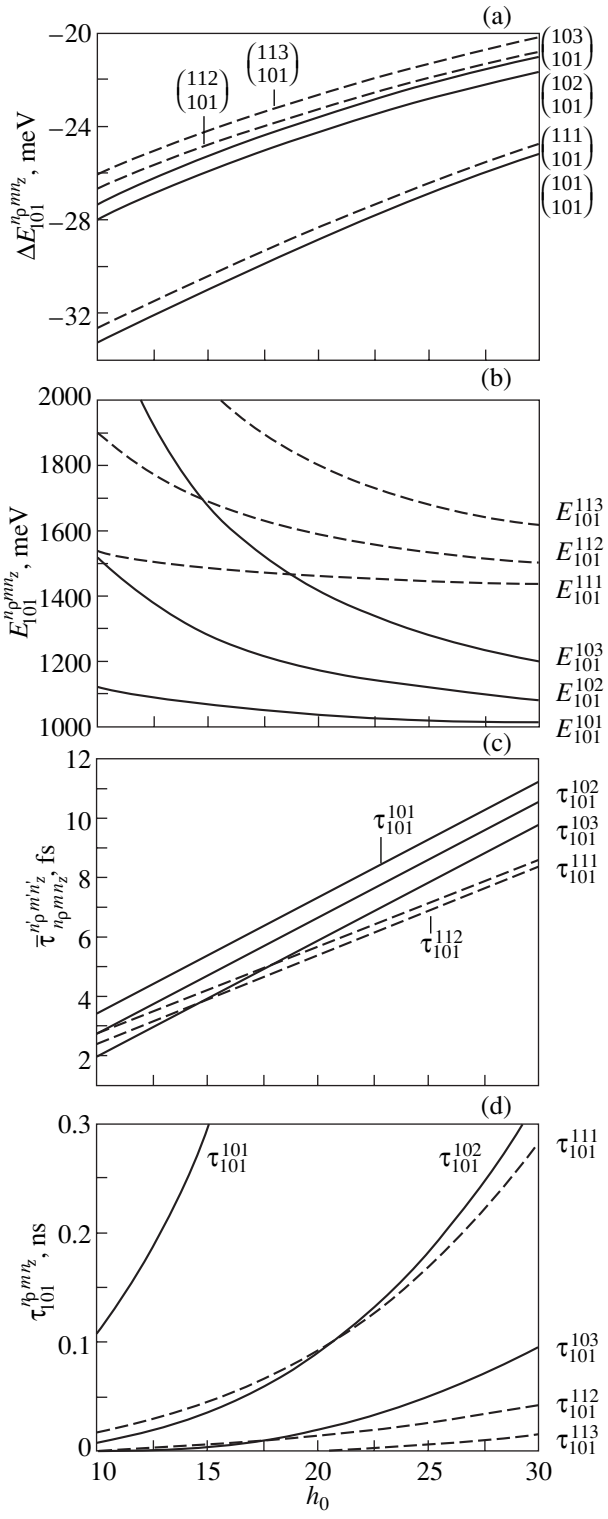

Fig. 3. Dependences of (a) the binding energy $\Delta E_{101}^{n_\rho m n_z}$, (b) the excitation energy $E_{101}^{n_\rho m n_z}$, (c) the time $\bar{\tau}_{101}^{n_\rho m n_z}$ of flight of an exciton along the quantum dot, and (d) the lifetime $\tau_{101}^{n_\rho m n_z}$ of the exciton on the quantum dot height h_0 for the quantum antidot height $h_1 = 4a_{\mathrm{CdS}}$ and the quantum dot radius $R = 8a_{\mathrm{HgS}}$.

groups and subgroups (except for the levels of the same subgroup) intersect each other with a change in the height h_0 or the radius ρ_0 of the quantum dot. Note that, when the levels of different subgroups within the same group intersect each other ($E_{n_\rho m n_z} = E_{n_\rho m' n_z'}$), the inequality $\tau_{n_\rho m n_z} > \tau_{n_\rho m' n_z'}$ holds for $m > m'$ at the intersection points. If the levels of the different subgroups belonging to different groups cross each other ($E_{n_\rho m n_z} = E_{n_\rho' m n_z'}$), the inequality $\tau_{n_\rho m n_z} > \tau_{n_\rho' m' n_z'}$ is satisfied at $n_\rho > n_\rho'$. Physically, this hierarchy of lifetimes is associated with the fact that, at equal energies, quasiparticles in the states in which they are more smeared in the plane perpendicular to the direction of motion along the principal axis penetrate through the potential barrier harder.

The calculated dependences of the binding energy $\Delta E_{101}^{n_\rho m n_z}$, the excitation energy $E_{101}^{n_\rho m n_z}$, and the lifetime $\tau_{101}^{n_\rho m n_z}$ of an exciton on the quantum dot height h_0 are plotted in Figs. 3a, 3b, and 3d, respectively. For comparison, Fig. 3c shows the dependences of the time $\bar{\tau}_{101}^{n_\rho m n_z}$ of flight of the exciton along the quantum dot on the quantum dot height h_0. The latter dependences were calculated under the assumption that the exciton, which is a quasiparticle formed by an electron and a hole, moves at a mean velocity estimated as $v_{\mathrm{ex}} = 1/2(v_e + v_h)$. As a result, we have

$$\tau_{n_\rho m n_z}^{n_\rho' m' n_z'} = \frac{2h_0}{v_{n_\rho m n_z}^{e} + v_{n_\rho' m' n_z'}^{h}} = \sqrt{2}h_0\left(\sqrt{\frac{E_{n_\rho m n_z}^{e}}{m_e}} + \sqrt{\frac{E_{n_\rho' m' n_z'}^{h}}{m_h}}\right)^{-1}.$$

The calculations were performed for the states in which the hole in the ground state $|101\rangle$ interacts with the electron residing in several quantum states $|n_\rho m n_z\rangle$.

It can be seen from Fig. 3 that a decrease in the quantum dot height h_0 leads to an increase in the magnitude of the exciton binding energy for all the states, because this favors a spatial approach of the exciton electron and the exciton hole.

For fixed sizes of the quantum dot, the specified quasi-stationary state $|101\rangle$ of the hole, and the quantum numbers n_ρ and m of the electron, an increase in the quantum number n_z of the electron is accompanied by a decrease in the binding energy. This can be explained as follows: the hole retains its position in the quantum dot, the electron penetrates into the barrier with a higher probability, and, hence, the mean distance between the electron and the hole increases.

An increase in the quantum dot height h_0 results in a decrease in the energies of the exciton in all the states

(Fig. 3b), because the shifts of the corresponding energy levels of the electron and the hole are more significant than the decrease in the magnitude of the binding energy of these quasiparticles.

The increase in the exciton lifetime $\tau_{101}^{n_\rho m n_z}$ with an increase in the quantum dot height h_0 (Fig. 3d) is due to the aforementioned dependences of the lifetimes $\tau_{n_\rho m n_z}^{e}$ and $\tau_{n_\rho m n_z}^{h}$ on the quantum dot height h_0 and their total contribution to the time $\tau_{n_\rho m n_z}^{n'_\rho m' n'_z}$ in accordance with relationship (17).

A comparison of the times $\bar{\tau}_{101}^{n_\rho m n_z}$ of exciton flight along the quantum dot (Fig. 3c) and the lifetimes $\tau_{101}^{n_\rho m n_z}$ of the exciton in the same states (Fig. 3d) demonstrates that the latter times are several orders of magnitude longer than the former times. This implies that all the states under investigation are resonance quasi-stationary states of the Breit–Wigner type. Therefore, the exciton states are fairly well localized within the quantum dot and their lifetimes are long enough to be observed experimentally.

In conclusion, we should note that the theory developed in this study is also applicable to analyzing the energy spectra and the lifetimes of excitons in other similar heterosystems composed of different semiconductor materials.

REFERENCES

1. Zh. I. Alferov, Fiz. Tekh. Poluprovodn. (St. Petersburg) **32** (1), 3 (1998) [Semiconductors **32**, 1 (1998)].
2. N. N. Ledentsov, V. M. Ustinov, V. A. Shchukin, P. S. Kop'ev, Zh. I. Alferov, and D. Bimberg, Fiz. Tekh. Poluprovodn. (St. Petersburg) **32** (4), 385 (1998) [Semiconductors **32**, 343 (1998)].
3. A. I. Baz', Ya. B. Zel'dovich, and A. M. Perelomov, *Scattering, Reactions, and Decays in Nonrelativistic Quantum Mechanics*, 2nd ed. (Nauka, Moscow, 1971; Israel Program for Scientific Translations, Jerusalem, 1966).
4. R. Buczko and F. Bassani, Phys. Rev. B **54** (4), 2667 (1996).
5. N. V. Tkach and V. A. Golovatskiĭ, Fiz. Tverd. Tela (St. Petersburg) **41** (11), 2081 (1999) [Phys. Solid State **41**, 1911 (1999)].
6. M. Tkach, V. Holovatsky, and O. Voitsekhivska, Physica E (Amsterdam) **11**, 17 (2001).
7. N. V. Tkach, I. V. Pronishin, and A. M. Makhanets, Izv. Vyssh. Uchebn. Zaved., Fiz., No. 2, 96 (1998).
8. S. Flugge, *Practical Quantum Mechanics* (Springer-Verlag, Berlin, 1971; Mir, Moscow, 1974), Vol. 1.
9. L. D. Landau and E. M. Lifshitz, *Course of Theoretical Physics*, Vol. 3: *Quantum Mechanics: Non-Relativistic Theory*, 3rd ed. (Nauka, Moscow, 1974; Pergamon, New York, 1977).

Translated by O. Borovik-Romanova

Physics of the Solid State, Vol. 47, No. 3, 2005, pp. 578–586. Translated from Fizika Tverdogo Tela, Vol. 47, No. 3, 2005, pp. 556–564.

LOW-DIMENSIONAL SYSTEMS AND SURFACE PHYSICS

Specific Features of Transmission of an Elastic Shear Wave through a Finite Acoustic Thin-Layer Superlattice of the Magnet–Ideal Diamagnet Type

O. S. Tarasenko, S. V. Tarasenko, and V. M. Yurchenko

Donetsk Physicotechnical Institute, National Academy of Sciences of Ukraine, Donetsk, 83114 Ukraine

e-mail: tarasen@mail.fti.ac.donetsk.ua

Received May 17, 2004

Abstract—The effect of the equilibrium magnetic configuration on the conditions for transmission of an elastic-wave through a finite magnetic superlattice consisting of ferromagnetic and superconducting layers is studied within an effective-medium approximation with correct inclusion of the dynamic coupling between the spin and elastic subsystems. The superlattice is assumed to be sandwiched between nonmagnetic media. © *2005 Pleiades Publishing, Inc.*

1. INTRODUCTION

Currently, analysis of the specific features of transmission of a bulk elastic wave through an acoustic multicomponent coupled system exhibiting one-, two-, or three-dimensional ordering (phononic crystal) is of particular interest in view of the potential practical applications of these composite materials [1, 2]. In this respect, studying the elastic dynamics of phononic crystals containing magnetic components (magnetic photonic crystals [3, 4]) is of importance, because the dimensionless linear dynamic magnetoelastic coupling constant ξ can be varied within a wide range ($0 < \xi < 1$) by varying an external magnetic field or the temperature. Up to now, however, phononic crystals consisting of nonmagnetic components have been primarily studied. One simple example of a one-dimensional magnetic phononic–photonic crystal is a two-component magnetic superlattice consisting of alternate, equidistant, acoustically coupled magnetic and nonmagnetic layers. If the nonmagnetic medium in this superlattice is an ideal diamagnet, e.g., a superconductor ($2\lambda/t \longrightarrow 0$, where λ is the London penetration depth, t is the thickness of the superconducting layer), then this structure can be considered a one-dimensional magnetic phononic crystal, because the acoustic interlayer coupling is the only mechanism that forms the spectrum of collective excitations in this case. To describe the dynamics of this crystal consistently, the magnetoelastic and magnetic dipole–dipole interactions should be taken into account simultaneously. However, in the case of an acoustic superlattice of the ferromagnet–superconductor type, calculating the spectrum of normal elastic SH waves by the transfer-matrix method involves matrices with minimum dimensions of 4×4 [5]. If we restrict ourselves to the case of sufficiently small wavenumbers (thin-layer superlattice), the spectrum of collective excitations of a finite acoustic magnetic superlattice can be found using the effective-medium approximation [6]. We note that the elastic dynamics of an infinite, uniform, magnetized ferromagnet exhibits the following important property: an elastic shear SH wave with wave vector $\mathbf{k}$ not directed along the equilibrium magnetization vector $\mathbf{M}$ can propagate only if $\mathbf{k} \perp \mathbf{M} \parallel \mathbf{u}$ (where $\mathbf{u}$ is the elastic atomic displacement of the lattice). However, the effect of gyrotropy on the reflection and refraction of a bulk elastic shear wave incident on the surface of a finite acoustic superlattice of the easy-axis ferromagnet–ideal diamagnet type has not yet been studied.

In this paper, we consider the influence of the magnetoelastic interaction on the reflection and transmission of an elastic SH wave incident on a finite, acoustic, thin-layer superlattice of the easy-axis ferromagnet–ideal superconductor type.

2. BASIC RELATIONS

We consider a magnetic superlattice consisting of equidistant ferromagnetic (medium 1) layers with a thickness of d_1 each that are acoustically coupled via identical superconducting layers of an ideal superconductor (medium 2) with a thickness of d_2 each. Therefore, in each superconducting layer, the London penetration depth satisfies the condition $2\lambda \ll d_2$. It is well known that a shear surface acoustic wave (SAW) of the SH type can propagate near the surface of an easy-axis ferromagnet if the atomic-displacement vector $\mathbf{u}$ in this wave with wave vector $\mathbf{k}_\perp$ satisfies the condition $\mathbf{n} \perp \mathbf{u} \parallel \mathbf{M} \perp \mathbf{k}_\perp$ ($\mathbf{M}$ is the equilibrium magnetization of the ferromagnet) [7].

We assume that medium 1 of the superlattice is a single-sublattice easy-axis ferromagnet [7] (with the

1063-7834/05/4703-0578$26.00

easy axis along the z axis) and that the elastic properties of both magnetic and nonmagnetic media are isotropic. In this case, the energy density W of the single-sublattice uniaxial ferromagnet (medium 1), including the interaction energy between the spin and elastic subsystems, is given by [7]

$$W = -0.5\,bm_z^2 - mh_m + \gamma m_i m_k u_{ik} + \lambda_1 u_{ii}^2 + \mu_1 u_{ik}^2, \quad (1)$$

where b is the uniaxial-anisotropy constant, γ is the magnetoelastic (isotropic) interaction constant, λ_1 and μ_1 are the Lamé coefficients of the magnetic medium, u_{ik} is the elastic strain tensor, and h_m is the magnetic dipole field. The dynamics of the nonmagnetic medium (medium 2, with Lamé coefficients λ_2, μ_2) is described by the basic equation of elasticity theory. For the magnetic medium, this equation is supplemented by the Landau–Lifshitz equations and the magnetostatics equations. The requirement that the superlattice be acoustically continuous at the interfaces between the magnetic and nonmagnetic layers leads to the equations

$$u_1 = u_2, \quad \xi = d_1 + N(d_1 + d_2); \quad N(d_1 + d_2), \quad (2)$$

$$\sigma_{ik}^{(1)} n_k^{(1)} = \sigma_{ik}^{(2)} n_k^{(2)}, \quad \xi = d_1 + N(d_1 + d_2); \quad N(d_1 + d_2), \quad (3)$$

where $N = 0, 1, \ldots$; ξ is the coordinate along the interfaces between the magnetic and nonmagnetic layers; σ_{ik} is the elastic stress tensor; and labels 1 and 2 indicate the medium which the corresponding quantity describes. Since the superconducting medium is assumed to be an ideal diamagnet, the electromagnetic boundary conditions at the interfaces between the magnetic and nonmagnetic layers have the form

$$\mathbf{B}_1\mathbf{n} = 0, \quad \xi = d_1 + N(d_1 + d_2); \quad N(d_1 + d_2). \quad (4)$$

Thus, the only mechanism that forms the spectrum of collective excitations in the superlattice is the indirect interaction between the layers via phonons; that is, this superlattice is a magnetic phononic crystal.

As mentioned above, an elastic shear wave can propagate through an infinite easy-axis ferromagnet described by Eq. (1) only if its wave vector is perpendicular to the easy axis and $\mathbf{u} \parallel \mathbf{M} \parallel z$ [7]. Therefore, in what follows, we assume that (i) $\mathbf{k} \in xy$, (ii) the equilibrium magnetization points along the same direction in all magnetic layers of the easy-axis (z axis) ferromagnet–superconductor superlattice and is perpendicular to the normal $\mathbf{n}$ to the interfaces, and (iii) $\mathbf{n} \parallel x$ (without loss of generality, because the magnetic medium is assumed to be isotropic in the xy plane).

In the absence of an external magnetic field, two essentially different types of equilibrium magnetic configurations can exist in the superlattice at hand, namely, with parallel (configuration A) and antiparallel (configuration B) orientation of the magnetizations of any pair of adjacent ferromagnetic layers. In terms of translation symmetry, these two structures are different. Indeed, in configuration A, the period of the magnetic superlattice (D_A) consists of two layers (a magnetic layer of thickness d_1 and a superconducting layer of thickness d_2); that is, we have $D_A = d_1 + d_2$. In configuration B, the superlattice period (D_B) consists of four layers: two ferromagnetic layers with a thickness of d_1 each and two superconducting layers of thickness d_2 acoustically coupled with the former; that is, $D_B = 2D_A$. As already mentioned, we restrict our consideration to the ranges of frequencies ω and wave vectors $k_\perp$ for which the superlattice can be considered to be thin-layered [6]. Therefore, the wave-vector component ($\mathbf{k}_\parallel$ parallel to the normal to the superlattice surface for the elastic shear wave in the magnetic ($\mathbf{k}_{\parallel,1}$) and superconducting ($\mathbf{k}_{\parallel,2}$) layers of the building block of the superlattice is much less than the inverse thickness of the respective layer (d_1, d_2):

$$k_{\parallel,1} d_1 \ll 1, \quad k_{\parallel,2} d_2 \ll 1. \quad (5)$$

Thus, for both configurations A and B, the acoustic superlattice can be considered a spatially uniform effective medium characterized by the components of the elastic stress tensor ($\langle\sigma_i\rangle$) and elastic strain tensor ($\langle u_i\rangle$) averaged over the superlattice period D_A or $D_B = 2D_A$ for configurations A and B, respectively. Introducing the relative thicknesses of the magnetic (medium 1) and nonmagnetic (medium 2) layers

$$f_1 = \frac{d_1}{d_1 + d_2}, \quad f_2 = \frac{d_2}{d_1 + d_2}, \quad (6)$$

we can write any physical quantity P averaged over the superlattice period in the form

$$\langle P\rangle = f_1 P_2 + f_2 P_2 \quad (7)$$

for configuration A and

$$\langle P\rangle = 0.5[f_1(P_1 + P_3) + f_2(P_2 + P_4)] \quad (8)$$

for configuration B.

In Eq. (8), labels 1 and 3 correspond to neighboring ferromagnetic layers (each with a thickness of d_1) whose magnetizations are opposite in direction and labels 2 and 4 correspond to two identical nonmagnetic layers (each with a thickness of d_2) that, together with the two magnetic layers, make up one building block of the acoustic magnetic superlattice of thickness $D_B = 2(d_1 + d_2) = 2D_A$.

The relation between the averaged elastic stress tensor $\langle\sigma_{ik}\rangle$ and the elastic strain tensor $\langle u_{ik}\rangle$ is determined by the effective elastic moduli c_{ik} and can be found by taking into account that σ_{ix} and u are continuous at the interfaces between neighboring layers. In the case of $\mu_1 = \mu_2 = \mu$ and for the chosen geometry of propagation of the elastic SH wave ($\mathbf{M} \parallel \mathbf{u} \parallel z$, $\mathbf{k} \in xy$, $\mathbf{n} \parallel x$), the effective moduli associated with the tensor components $\langle\sigma_i\rangle$ and $\langle u_i\rangle$ of interest to us have the form

$$\bar{c}_{55}/\mu = c_{\parallel} = \frac{\omega_2^2 - \omega^2}{\omega_1^2 - \omega^2},$$
$$\bar{c}_{44}/\mu = c_{\perp} = \frac{\omega_3^2 - \omega^2}{\omega_1^2 - \omega^2}, \quad (9)$$
$$\bar{c}_{54}/\mu = c_* = \frac{f_1\omega\omega_{me}}{\omega_1^2 - \omega^2}$$

for configuration *A* and

$$\bar{c}_{55}/\mu = c_{\parallel} = \frac{\omega_2^2 - \omega^2}{\omega_1^2 - \omega^2},$$
$$\bar{c}_{44}/\mu = c_{\perp} = \frac{\omega_4^2 - \omega^2}{\omega_2^2 - \omega^2} \quad (10)$$

for configuration *B*. Here, $\omega_3^2 = \omega_0(\omega_0 - \omega_{me}) + \omega_{me}^2 f_1 f_2$, $\omega_1^2 = \omega_0^2 - f_2\omega_0\omega_{me}$, $\omega_2^2 = \omega_0^2 - \omega_0\omega_{me}$, and $\omega_4^2 = \omega_0^2 - \omega_{me}\omega_0(1 + f_1) + \omega_{me}^2 f_1$. For any values of $k_\perp$, f_1, and f_2, we have $\omega_1 > \omega_3 > \omega_2$ and $\omega_1 > \omega_2 > \omega_4$.

Thus, in contrast to the effective elastic moduli $\tilde{c}_{44}$, $\tilde{c}_{55}$, and $\tilde{c}_{45}$ of an infinite ferromagnet (with $\mathbf{M} \parallel z$) calculated neglecting the magnetic dipole–dipole interaction and given by

$$\tilde{c}_{44}/\mu = \tilde{c}_{55}/\mu = \frac{\omega_0(\omega_0 - \omega_{me}) - \omega^2}{\omega_0^2 - \omega^2},$$
$$\tilde{c}_{45}/\mu = -\tilde{c}_{54}/\mu = \frac{\omega\omega_{me}}{\omega_0^2 - \omega^2}, \quad (11)$$

the effective moduli of the acoustic magnetic superlattice in Eqs. (9) and (10) not only exhibit time dispersion but also depend strongly on the relative thicknesses of the magnetic and nonmagnetic layers. It should be particularly emphasized that, although the acoustic magnetic superlattice at hand contains gyrotropic (ferromagnetic) layers, the effective uniform elastic medium characterized by moduli (9) or (10) may either possess (in configuration *A*, $\bar{c}_{54} = -\bar{c}_{45} \neq 0$) or not possess (in configuration *B*, $\bar{c}_{54} = \bar{c}_{45} = 0$) gyrotropic properties.

It is easy to verify that, in the case of $\gamma \longrightarrow 0$ (where there is no magnetoelastic interaction), the effective elastic moduli in Eqs. (9) and (10) coincide with the respective elastic moduli of a nonmagnetic bilayer superlattice [6].

In Eqs. (9) and (10), in accordance with the notation used in [7], $\omega_{me} = gH_{me4}$ is the magnetoelastic band gap, $\omega_0 = g(H_A + H_{me4})$ is the FMR frequency, H_A is the uniaxial magnetic anisotropy field, H_{me4} is the magnetoelastic field, and g is the gyromagnetic ratio. Since we are studying the elastic dynamics of a magnet–ideal diamagnet acoustic superlattice using the effective-field method, conditions (4) are satisfied in the bulk of each magnetic layer. For this reason, in the wavenumber range under study, the inclusion of the magnetic dipole–dipole interaction does not lead to additional (other than magnetoelastic) mechanisms of time dispersion of the elastic moduli given by Eqs. (9) and (10). In the $\mathbf{k} \in xy$ and $\mathbf{u} \parallel z$ geometry, this interaction reduces to renormalization of the uniaxial magnetic anisotropy constant $\beta \longrightarrow \beta - 4\pi$. In what follows, we also assume that the densities of the magnetic (ρ_1) and nonmagnetic (ρ_2) media of the superlattice are equal, $\rho_1 = \rho_2 = \rho$. In this case, for an elastic SH wave propagating through an infinite acoustic superlattice of the easy-axis ferromagnet–ideal superconductor type with $k \in xy$, $\mathbf{n} \parallel x$, and $\mathbf{u} \parallel z$ (considered in the effective-medium approximation with inclusion of the magnetoelastic and magnetic dipole–dipole interactions), the frequency spectrum for both magnetic configurations is given by

$$\omega^2 = s_t^2(c_\perp k_y^2 + c_\parallel k_x^2), \quad (12)$$

where $s_t^2 = \mu/\rho$. It follows from Eqs. (9)–(12) that, in the presence of magnetoelastic and magnetic dipole interactions, the elastic shear wave is a single-component excitation of the type

$$\langle u_z \rangle = A\exp(ik_\parallel x)\exp(ik_\perp y - i\omega t) \quad (13)$$

for both configurations *A* and *B*. The case of $k_\parallel^2 > 0$ corresponds to a propagating bulk (trigonometric) elastic SH wave, whereas at $k_\parallel^2 < 0$ ($k_\parallel^2 = -\alpha^2 k_\perp^2$) the only wave that can propagate along the surface of the magnetic superlattice at hand is a hyperbolic elastic shear wave, for which

$$\langle u_z \rangle \longrightarrow 0, \quad x \longrightarrow -\infty, \quad (14)$$

if the superlattice occupies the lower half-space, $x < 0$.

It is known that the conditions for reflection and transmission of a wave incident on a medium are closely related to the topology of the isofrequency surface of the corresponding type of normal vibrations [8]. For the infinite acoustic superlattice under study, according to Eq. (12), the structure of the cross section of the isofrequency surface of the normal elastic SH wave by the plane of incidence remains qualitatively unchanged with a variation in the equilibrium magnetic configuration but depends critically on the sign of the quantities $c_\parallel$ and $c_\perp$ (Figs. 1–3). In order to determine the conditions for transmission of an elastic shear wave through a finite layer of this effective magnetic medium, it is necessary to investigate the reflection of the SH wave in the case where this wave is incident from a semi-infinite nonmagnetic medium onto the acoustically continuous interface between this medium and a semi-infinite superlattice of the type under study.

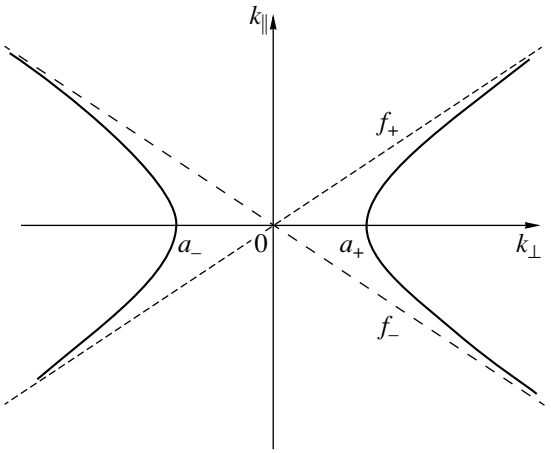

Fig. 1. Cross section of the isofrequency surface of Eq. (12) by the *xy* plane for a bulk elastic SH wave propagating in an easy-axis ferromagnet–ideal superconductor superlattice with the *A* or *B* configuration in the case where $\mathbf{k}_\perp \parallel y$, $\mathbf{u} \parallel z$, $\mathbf{n} \parallel x$, $c_\parallel < 0$, and $c_\perp > 0$; $f_\pm = \pm k\sqrt{c_\perp/|c_\parallel|}$ and $\alpha_\pm = \pm\omega k_\perp/(s_t\sqrt{c_\perp})$.

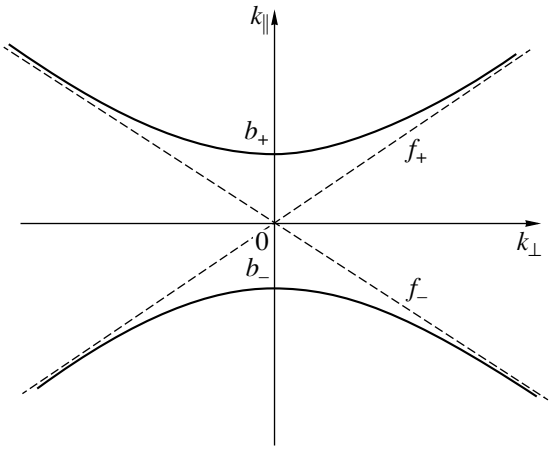

Fig. 2. Cross section of the isofrequency surface of Eq. (12) by the *xy* plane for a bulk elastic SH wave propagating in an easy-axis ferromagnet–ideal superconductor superlattice with the *B* configuration in the case where $\mathbf{k}_\perp \parallel y$, $\mathbf{u} \parallel z$, $\mathbf{n} \parallel x$, $c_\parallel > 0$, and $c_\perp < 0$; $f_\pm = \pm k_\perp\sqrt{|c_\perp|/c_\parallel}$ and $b_\pm = \pm\omega k_\parallel/(s_t\sqrt{c_\parallel})$.

3. SPECIFIC FEATURES OF THE REFLECTION OF A BULK ELASTIC SH WAVE FROM A SEMI-INFINITE ACOUSTIC SUPERLATTICE OF THE MAGNET–SUPERCONDUCTOR TYPE

Within the effective-medium approximation, the conditions at the acoustically continuous interface ($x = 0$) between a semi-infinite ferromagnetic superlattice ($x < 0$) and a semi-infinite superconductor ($x > 0$) have the form

$$\sigma_{ik}^{+} = \langle\sigma_{ik}\rangle, \quad u_i^{+} = \langle u_i\rangle, \quad x = 0. \tag{15}$$

Here and henceforth, the superscript plus sign denotes quantities related to the upper half-space. By carrying out a standard calculation [8] and using Eqs. (9)–(13) and (15), it can be shown that, for a bulk transverse SH wave that is incident from the nonmagnetic medium onto the boundary of the semi-infinite acoustic magnetic superlattice and is polarized perpendicular to the plane of incidence ($\mathbf{u} \parallel \mathbf{M} \parallel z$, $\mathbf{k} \in xy$), the reflection coefficient R for two types of equilibrium magnetic configuration (*A*, *B*) is given by

$$R_{AS} = \frac{a\tilde{k}_\parallel - (c_\parallel k_\parallel - ic_*\sigma k_\perp)}{a\tilde{k}_\parallel + (c_\parallel k_\parallel - ic_*\sigma k_\perp)} \quad (A\text{–S configuration}), \tag{16}$$

$$R_{BS} = \frac{a\tilde{k}_\parallel - c_\parallel k_\parallel}{a\tilde{k}_\parallel + c_\parallel k_\parallel} \quad (B\text{–S configuration}), \tag{17}$$

where $k_\parallel^2 = (\omega^2/s_t^2 - k_\perp^2)/c_\parallel$, $\tilde{k}_\parallel^2 = (\omega^2/s_t^2 - c_\perp)/c_\parallel$, and $a = \mu_+/\mu$. Here and henceforth, *A*–S and *B*–S indicate the interface between the semi-infinite superconductor (S) and the semi-infinite magnetic superlattice for the case of the *A* and *B* equilibrium magnetic configurations, respectively.

It follows from Eqs. (16) and (17) that, if both inequalities $k_\parallel^2 > 0$ and $\tilde{k}_\parallel^2 > 0$ are simultaneously true, the bulk elastic SH wave can pass through the interface between the nonmagnetic and magnetic half-spaces at $x = 0$ without reflection in the case of the *B* configuration ($R_{BS} = 0$). For the *A* configuration, due to acoustic gyrotropy, there is no angle of incidence at which transmission of the wave is possible without reflection ($0 <$

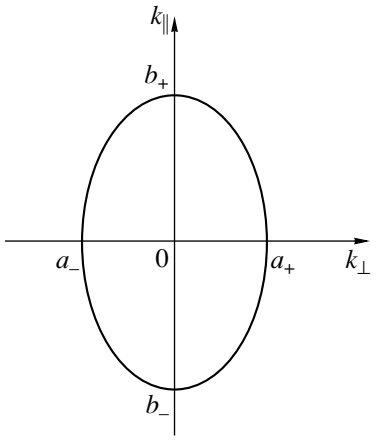

Fig. 3. Cross section of the isofrequency surface of Eq. (12) by the *xy* plane for a bulk elastic SH wave propagating in an easy-axis ferromagnet–ideal superconductor superlattice with the *A* or *B* configuration in the case where $\mathbf{k}_\perp \parallel y$, $\mathbf{u} \parallel z$, $\mathbf{n} \parallel x$, $c_\parallel > 0$, and $c_\perp > 0$.

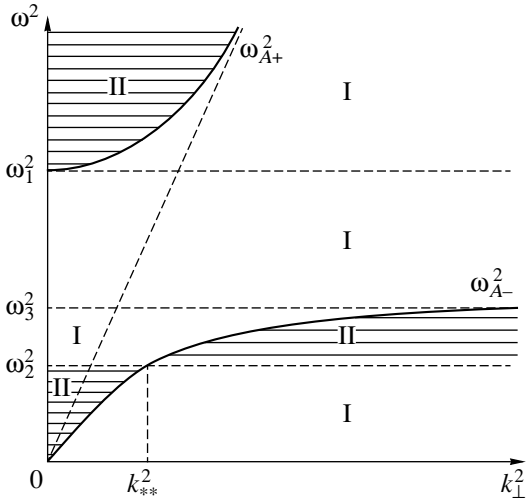

Fig. 4. Region I corresponds to the total internal reflection of a bulk elastic SH wave [Eq. (16) with $k_\parallel^2 = -\alpha^2 k_\perp^2$, $\alpha^2 > 0$ incident from outside onto an easy-axis ferromagnet–ideal superconductor superlattice with the *A* configuration in the case of $\mathbf{k}_\perp \parallel y$, $\mathbf{u} \parallel z$, and $\mathbf{n} \parallel x$; $\omega_{A\pm}$ is determined from Eqs. (9) and (12) for $k_x = 0$, and k_{**} is defined by the condition $\omega_2 = \omega_{A-}$.

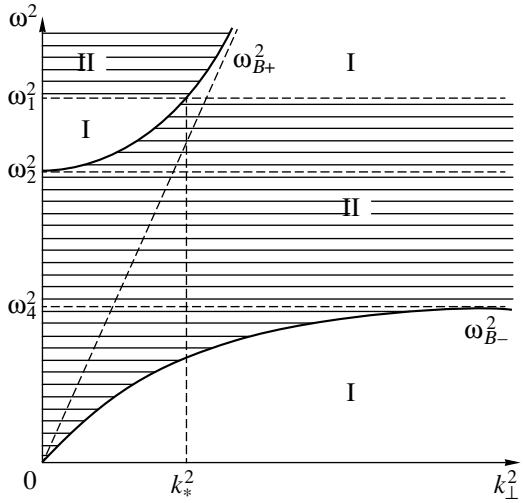

Fig. 5. Region I corresponds to the total internal reflection of a bulk elastic SH wave [Eq. (17) with $k_\parallel^2 = -\alpha^2 k_\perp^2$, $\alpha^2 > 0$] incident from outside onto an easy-axis ferromagnet–ideal superconductor superlattice with the *B* configuration in the case where $\mathbf{k}_\perp \parallel y$, $\mathbf{u} \parallel z$, and $\mathbf{n} \parallel x$; $\omega_{B\pm}$ is determined from Eqs. (10) and (12) for $k_x = 0$.

$|R_{AS}| < 1$). Both the transmitted and reflected bulk shear waves undergo a phase shift (ϕ_A and ψ_A, respectively) with respect to the bulk elastic SH wave incident on the superlattice surface:

$$\tan\phi_A = \frac{\operatorname{Im} R_{AS}}{\operatorname{Re} R_{AS}}, \qquad \tan\psi_A = \frac{\operatorname{Im}(1 + R_{AS})}{\operatorname{Re}(1 + R_{AS})}. \tag{18}$$

It should be noted that, for the *A* configuration and given values of ω and k_1, the phase shifts ϕ_A and ψ_A calculated from Eqs. (18), in combination with Eqs. (9) and (16), are nonreciprocal with respect to the replacement $k_\perp \longrightarrow -k_\perp$.

For the values of ω and $|k_\perp|$ at which the inequality $k_\parallel^2 < \mathrm{O}(\tilde{k}_\parallel^2 > 0)$ is true (Figs. 4, 5), the bulk SH wave incident on the interface is totally reflected for both magnetic configurations of the magnetic superlattice, with the reflected shear wave undergoing an additional phase shift ϕ ($R = \exp i\phi$). For the *A* configuration and given values of ω and $k_\perp$, the additional phase shift is nonreciprocal with the replacement $k_\perp \longrightarrow -k_\perp$ and depends, according to Eq. (16), not only on the gyrotropic properties of the superlattice but also on the relationship between the acoustic parameters of the two media:

$$\tan(\phi/2) = \frac{(c_*\sigma - c_\parallel\alpha)}{a}\frac{k_\perp}{k_\parallel}, \quad \sigma = k_\perp/|k_\perp|, \tag{19}$$

where $k_\parallel^2 = -\alpha^2 k_\perp^2$.

It follows from Eqs. (16) and (17) that $R = -1$ for $\tilde{k}_\parallel = 0$. Therefore, in the case where $a \neq 0$, the bulk uniform shear SH wave cannot propagate along the acoustically continuous interface ($x = 0$) between the magnetic superlattice and a superconductor. For the *B* configuration, this effect is independent of the frequency ω and wavenumber $k_\perp$ of the bulk shear wave. As for the *A* configuration, it can be seen from Eq. (16) that $R = 1$ along the line

$$c_\parallel\alpha = c_*\sigma k_\perp \tag{20}$$

in the ω–$k_\perp$ plane. Therefore, the bulk uniform shear wave with $\tilde{k}_\parallel = 0$ can propagate in the nonmagnetic half-space along the acoustically continuous interface between this half-space and the magnetic superlattice with the *A* configuration. This effect is also due entirely to acoustic gyrotropy ($c_* \neq 0$).

The reflection coefficient *R* given by Eqs. (16) and (17) with substitutions $k_\parallel \longrightarrow i\alpha k_\perp$ and $\tilde{k}_\parallel \longrightarrow iqk_\perp$ can have a pole in the ω–$k_\perp$ plane, which, according to the

general theory of wave processes [8], corresponds to the dispersion law $\Omega_s(k_\perp)$ of the SH SAW propagating in the geometry in question ($\mathbf{n} \parallel x$, $\mathbf{u} \parallel z$, $\mathbf{k}_\perp \parallel y$) along the acoustically continuous [satisfying Eqs. (15)] interface between a superconductor and a superlattice with configuration *A* or *B*.

For the shear SAW propagating along the interface $x = 0$, we have

$$\begin{aligned} k_\perp^2 &= \omega^2[(c_\perp - c_\parallel\alpha^2)s_t^2]^{-1}, \\ \alpha &= aq\frac{(\omega + \sigma\tilde{\omega}_-)(\omega - \sigma\tilde{\omega}_+)}{\omega_2^2 - \omega^2} > 0, \\ \sigma\tilde{\omega}_\pm &= \left(\frac{f_1^2\omega_{me}^2}{4a^2q^2} + \omega_1^2\right)^{1/2} \mp \frac{f_1\omega_{me}}{2aq}, \end{aligned} \tag{21}$$

for the *A* configuration and

$$\begin{aligned} k_\perp^2 &= \omega^2[(c_\perp - c_\parallel\alpha^2)s_t^2]^{-1}, \\ \alpha &= -aq(\omega_1^2 - \omega^2)/(\omega_2^2 - \omega^2) > 0 \end{aligned} \tag{22}$$

for the *B* configuration. In both cases, $q^2 = 1 - \omega^2/s_+^2k_\perp^2 > 0$, $s_+^2 = \mu_+/\rho_+$, $a = \mu_+/\mu$, and $\mu_1 = \mu_2 = \mu \neq \mu_+$. It follows from Eqs. (21) that the dispersion law of the SH SAW propagating along the interface ($x = 0$) between a superconductor and a superlattice with the *A* configuration is nonreciprocal under reversal of the direction of wave propagation, $\omega(k_\perp) \neq \omega(-k_\perp)$.

For the branch of spectrum (21) with $\sigma = -1$, we have $\omega > \omega_2$. However, this branch can have not only the long-wavelength but also a short-wavelength limiting point, for which the wave number can be determined from Eq. (21) by putting $\omega = \tilde{\omega}_-$ ($\tilde{\omega}_- > \omega_1$). Therefore, following the terminology accepted in polariton dynamics [9], this SH SAW is a virtual shear SAW or a shear SAW of the second type. In the case of $\sigma = 1$, it follows from Eqs. (21) that at $a \neq 0$ the structure of the spectrum of the SAW in question depends critically on the ratios of $\tilde{\omega}_+$ ($\tilde{\omega}_+ < \omega_1$) to ω_2 and ω_3 ($\omega_2 < \omega_3$). Analysis of Eqs. (21) shows that, in the case where $\sigma = 1$ and where the interface is acoustically continuous, the SAW in question has only one branch; its long-wavelength limiting point can be determined from Eq. (21) at $q = 0$. If $\tilde{\omega}_+ > \omega_3$, the dispersion curve of the SH SAW described by Eq. (21) is defined for $\omega > \omega_2$. Beginning at the $q = 0$ line, this curve asymptotically approaches the frequency $\tilde{\Omega}_+$ as the wavenumber increases (for $d_1 > d_2$). In the elastostatic limit $\omega/s_tk_\perp \longrightarrow 0$ ($q \longrightarrow 1$), in the case where $a \neq 1$ ($\mu_2 = \mu_*$, $\mu_1 = \mu$), this frequency is given by

$$\tilde{\Omega}_+ = \omega_0 - \frac{\omega_{me}}{1 + a}. \tag{23}$$

In the specific case where $a = 1$ and $d_1 > d_2$, we have $\tilde{\Omega}_- = \omega_0 - 0.5\omega_{me}$.

If $\omega_2 < \omega < \omega_3$ and $\sigma = 1$, then dispersion relation (21) also has a long-wavelength limiting point [which can be found from Eq. (21) at $q = 0$] and the spectrum lies in the range $\omega > \omega_2$. However, now, the spectrum has a short-wavelength limiting point; its wavenumber can be found from the relation

$$\omega_+^2 = s_t^2k_\perp^2\frac{\omega_3^2 - \tilde{\omega}_-^2}{\omega_1^2 - \tilde{\omega}^2}. \tag{24}$$

Therefore, this branch corresponds to a shear SAW of the second type, whereas at $\tilde{\omega}_+ > \omega_3$ this branch is found to correspond to a SAW of the first type.

Finally, at $\omega_2 > \tilde{\omega}_+$ and $\sigma = 1$, it follows from Eqs. (21) that the dispersion curve of the shear SAW lies in the range $\omega < \omega_2$ for all values of $k_\perp$ and the frequency $\omega = \tilde{\omega}_+$ is the long-wavelength limiting point. In the elastostatic limit, this dispersion curve approaches the frequency $\tilde{\Omega}_+$ given by Eq. (23).

Thus, at $\sigma = 1$ and -1 and $\omega_2 < \tilde{\omega}_+ < \omega_3$, dispersion relation (21) corresponds to a shear SAW of the second type. Otherwise, the dispersion relation has only a long-wavelength limiting point, which is typical of SAWs of the first type.

By comparing Eqs. (21) and (22), it can be seen that the distinctive feature of the collective shear SAW propagating in the magnetic superlattice with the *B* configuration, described by Eq. (22), is the reciprocity of its spectrum under reversal of the direction of wave propagation, $\omega(k_\perp) = \omega(-k_\perp)$, despite the fact that the superlattice contains magnetic layers that exhibit acoustic gyrotropy in the geometry in question. The spectrum of this wave has both a long-wavelength (at $q = 0$) and a short-wavelength limiting point ($\omega_* = \omega_1$, $k_*^2 = \omega^2/c_\perp s_t^2$; that is, this wave is a virtual shear SAW.

The specific features of the reflection of the bulk elastic SH wave from the interface between the magnetic superlattice and a superconductor have a significant effect on the conditions of transmission of this wave through an acoustically continuous structure, such as a superconductor–magnetic superlattice–superconductor (S–*A*–S or S–*B*–S) sandwich.

4. SPECIFIC FEATURES OF THE REFLECTION OF A BULK ELASTIC SH WAVE FROM THE SURFACE OF A FINITE ACOUSTIC SUPERLATTICE OF THE MAGNET–SUPERCONDUCTOR TYPE

We consider a finite magnetic superlattice made up of layers of an easy-axis ferromagnet (medium 1) and of an ideal superconductor (medium 2). The superlat-

tice has a thickness $2d$ ($-d < x < d$) and is embedded in an infinite superconducting medium. We assume that Eqs. (2)–(4) are satisfied at the interfaces of this sandwich; therefore, the sandwich is an acoustically continuous structure. Using the effective-medium approximation and the energy density given by Eq. (1), the boundary conditions at the outer surfaces of the finite superlattice $x = \pm d$ can be written in the form

$$\begin{aligned} \sigma_{ik}^{+} &= \langle \sigma_{ik} \rangle, \quad u_i^{+} = \langle u_i \rangle, \quad x = d, \\ \sigma_{ik}^{-} &= \langle \sigma_{ik} \rangle, \quad u_i^{-} = \langle u_i \rangle, \quad x = -d. \end{aligned} \tag{25}$$

In this case, for a bulk elastic shear wave (with $\mathbf{u} \parallel z$ and $\mathbf{k} \in xy$) incident from the upper half-space onto the magnetic superlattice–superconductor interface $x = d$, the reflection coefficient V is given by

$$V = \frac{V_{32} + V_{21}(1 + V_{23} + V_{32})\exp(i4k_\parallel d)}{1 - V_{23}V_{21}\exp(i4k_\parallel d)}, \tag{26}$$

where

$$\begin{aligned} V_{23} &= \frac{c_\parallel k_\parallel + ic_*\sigma k_\perp - ak_\parallel}{c_\parallel k_\parallel - ic_*\sigma k_\perp + ak_\parallel}, \\ V_{21} &= \frac{c_\parallel k_\parallel - ic_*\sigma k_\perp - ak_\parallel}{c_\parallel k_\parallel + ic_*\sigma k_\perp + ak_\parallel}, \\ V_{32} &= \frac{a\tilde{k}_\parallel - c_\parallel k_\parallel + ic_*\sigma k_\perp}{a\tilde{k}_\parallel + c_\parallel k_\parallel - ic_*\sigma k_\perp} \end{aligned} \tag{27}$$

for the S–*A*–S configuration and

$$V_{23} = V_{21} = -V_{32} = \frac{c_\parallel k_\parallel - ak_\parallel}{c_\parallel k_\parallel + ak_\parallel} \tag{28}$$

for the S–*B*–S configuration.

Here, in the notation introduced in [8], V_{ij} is the reflection coefficient for the bulk single-component SH wave incident from the ith medium onto the interface between the ith and jth media, subscript 3 corresponds to the medium in the region $x > d$, subscript 2 corresponds to the superlattice ($-d < x < d$), and subscript 1 corresponds to the medium in the region $x < -d$. At $d \longrightarrow \infty$, Eq. (26) for V reduces to Eqs. (16) and (17) for the reflection coefficient of the elastic shear SH wave incident on the acoustically continuous interface between the magnetic superlattice and a semi-infinite superconductor with the *A*–S ($V = R_{AS}$) and *B*–S ($V = R_{BS}$) configurations, respectively. The poles of expressions (26)–(28) for the reflection coefficients with the substitution $ik_\parallel \longrightarrow \pm\alpha k_\perp$ ($ik_\parallel \longrightarrow \pm q k_\perp$) in the ω–$k_\perp$ plane give the spectrum of the SH SAW propagating along a finite acoustic magnetic superlattice of the easy ferromagnet–ideal superconductor type that is in acoustic contact at $x = \pm d$ with a nonmagnetic medium:

$$\frac{c_*^2 - (c_\parallel\alpha + aq)^2}{c_*^2 - (c_\parallel\alpha - aq)^2} = \exp(-2qd) \tag{29}$$

(S–*A*–S configuration),

$$\frac{c_\parallel\alpha + aq}{c_\parallel\alpha - aq} = \pm\exp(-qd) \tag{30}$$

(S–*B*–S configuration).

By analyzing the magnitude of the reflection coefficient V given by Eqs. (26)–(28), it can be verified that the elastic SH wave can pass through the finite superlattice without reflection ($|V| = 0$) for both the *A* and *B* configurations if the superlattice is a half-wave plate [8]: $2\tilde{k}_\parallel d = m\pi$, where $m = 1, 2, \ldots$ ($\tilde{k}_\parallel^2 > 0$). Furthermore, transmission of the bulk elastic wave without reflection is also possible if

$$V_{32} = 0. \tag{31}$$

For this condition to be satisfied, the finite magnetic superlattice must be nongyrotropic; i.e., its magnetic configuration must be of the *B* type, for which Eq. (28) takes place. Equation (31) coincides with the condition that the acoustically continuous interface between a semi-infinite magnetic superlattice and a semi-infinite superconductor be reflectionless. It should be stressed that condition (31) cannot be satisfied for the superlattice with the *A* configuration because it exhibits acoustic gyrotropy.

The situation for the S–*A*–S and S–*B*–S magnetic sandwich structures under study is similar to that for the interface between two semi-infinite media considered above; namely, the uniform ($k_\parallel = 0$) bulk SH wave can propagate through the nonmagnetic medium only for the S–*A*–S configuration and only if $c_\parallel k_\parallel - ic_*\sigma k_\perp = 0$ ($k_\parallel^2 < 0$).

In the case where $k_\parallel^2 < 0$, transmission without reflection, as well as the total reflection, is impossible for the elastic bulk wave ($\tilde{k}_\parallel^2 > 0$) incident on the finite ($-d < x < d$) magnetic superlattice, $0 < |V| < 1$. Furthermore, it follows from Eqs. (26)–(28) that the reflected and transmitted bulk elastic SH waves undergo a phase shift with respect to the incident wave.

In the case where the superlattice (with the *A* or *B* configuration) occupies the lower ($x < -d$) and upper ($x > d$) half-spaces between which a superconducting layer ($-d < x < d$) is sandwiched and tightly bound to them, the reflection coefficient of the bulk elastic SH wave incident on the surface of the layer vanishes as $d \longrightarrow 0$. We note that, under certain conditions, the bulk SH wave ($\tilde{k}_\parallel^2 > 0$) can also pass without reflection

($|V| = 0$) through the acoustic superlattice in question in the case where $\alpha^2 > 0$ ($k_\parallel^2 < 0$). Let us consider the case where the antiferromagnet–ideal superconductor superlattice ($-d < x < d$) is tightly bound (e.g., at $x = d$) to an elastically isotropic nonmagnetic layer (with thickness t and elastic parameters μ_0, ρ_0) and this bilayer structure is in acoustic contact (at $x = -d$ and $x = d + t$) with semi-infinite identical ideal diamagnetic media ($x \geq d + t$ and $x \leq -d$) with elastic parameters μ_+ and ρ_+. The elastic parameters of the magnetic superlattice ($\mu_1 = \mu_2 = \mu$, $\rho_1 = \rho_2 = \rho$, $s_t = \mu/\rho$) are assumed to be such that

$$s_t < s_0 = \mu_0/\rho_0. \tag{32}$$

Calculations show that, in this case, the reflection coefficient of the bulk elastic SH wave ($\tilde{k}_\parallel^2 > 0$, $\mathbf{u} \parallel z \parallel \mathbf{M}$, $\mathbf{n} \parallel x$) incident from the upper half-space onto the surface $x = d + t$ of this structure with the A or B equilibrium magnetic configuration is given by (see also [8])

$$W = \frac{Z_{in} - Z_+}{Z_+ + Z_{in}},$$

$$Z_{in} = \frac{Z_+ Z - Z_+ Z_0 p p_t - iZ(Zp + Z_0 p_t)}{Z_0 Z - Z^2 p p_t - iZ_+(Z_0 p + Z p_t)} Z_0, \tag{33}$$

$Z_0 = (i\mu_0 k_0, \quad Z_+ = i\mu_+ \tilde{k}_\parallel, \quad Z) = i\mu(c_\parallel k_\parallel - ic_* \sigma k_\perp)$.

$p = \tan(k_\parallel 2d), \quad p_t) = \tan(k_0 t), \quad k_0^2) = \omega^2/s_0^2 - k_\perp^2 >$

In the limit as $d \longrightarrow 0$, Eq. (33) reduces to Eq. (26) for the reflection coefficient V of the acoustically continuous structure consisting of a finite magnetic $2t$-thick superlattice sandwiched between two semi-infinite identical nonmagnetic media.

It follows from Eq. (33) that the bulk SH wave ($\tilde{k}_\parallel^2 > 0$) passes without reflection ($|W| = 0$) through this finite acoustic superlattice with a nonmagnetic coating on one side if

$$Z = -Z_0, \quad p = p_t \tag{34}$$

($q_0^2 = -k_0^2 k_\perp > 0$, $\alpha^2 > 0$). Note that the first of equations (34) can be satisfied only for $c_\parallel < 0$ and gives the spectrum of the shear SAW (at $\alpha^2 > 0$, $\omega < s_0 k_\perp$) propagating along the acoustically continuous interface between the semi-infinite superlattice in question and a semi-infinite elastically isotropic ideal diamagnet (with shear modulus μ_0 and density ρ_0). Therefore, the transmission of the bulk shear wave without reflection ($W = 0$) is in this case resonant in nature and is accompanied by excitation of a shear SAW near the superlattice–nonmagnetic coating interface. Naturally, in the case of the superlattice with the A magnetic configuration, which exhibits acoustic gyrotropy, the total-transmission effect and the spectrum of the shear SAW will be nonreciprocal in nature.

It should be noted that, if the excited shear SAW is of the first type, resonant transmission under conditions (34) occurs at any angle of incidence of the bulk ($k_\parallel^2 > 0$) SH wave. In the case where a virtual shear SAW is generated under conditions (34), the condition for resonant transmission of the bulk SH wave ($k_\parallel^2 > 0$) without reflection is more restrictive, because the virtual shear SAW propagates along the interface between the semi-infinite superlattice and its nonmagnetic coating. In addition to Eqs. (34), in this case, the condition $k_\perp \geq k_*$ must be satisfied, where k_* is the short-wavelength limiting point of the spectrum, $\alpha(\omega_*) = 0$, of the excited virtual SH SAW.

So far, we have considered the transmission of a bulk shear elastic wave through a finite magnetic superlattice ($-d < x < d$) in acoustic contact with nonmagnetic media on both sides, $x > d$ and $x < -d$, with equal elastic parameters. It is also of practical interest to analyze the transmission of the bulk SH wave through this acoustically continuous structure in the case where the elastic parameters of the nonmagnetic media in the regions $x > d$ and $x < -d$ are different (μ_+, ρ_+ at $x > d$ and μ_-, ρ_- at $x < -d$, where $\mu_+ \neq \mu_-$, $\rho_+ \neq \rho_-$). Calculations analogous to those described above show that transmission without reflection is possible only in the case of the superlattice with the B configuration and a thickness satisfying the condition $4k_\parallel d = \pi\nu$ ($\nu = 1, 2, \ldots$); furthermore, the surface impedances of the outer media must satisfy the condition

$$\begin{gathered} Z^2 = Z_+ Z_-, \\ Z_+ = i\mu_+ k_{\parallel+}, \quad k_{\parallel+}^2 = \omega^2/s_+^2 - k_\perp^2 > 0, \quad x > d, \\ Z = i\mu c_\parallel k_\parallel, \quad -d < x < d, \\ Z_- = i\mu_- k_{\parallel-}, \quad k_{\parallel-}^2 = \omega^2/s_-^2 - k_\perp^2 > 0, \quad x < -d. \end{gathered} \tag{35}$$

These conditions, according to [8], correspond to the case of a quarter-wave antireflective layer.

5. CONCLUSIONS

We have considered the transmission of a bulk elastic shear wave through a finite acoustic superlattice of the easy-axis ferromagnet–superconductor type using the effective-medium approximation with consistent inclusion of the magnetoelastic interaction. An analysis has been performed for a superlattice with in-plane magnetized ferromagnetic layers in the case where the equilibrium magnetic moments of neighboring layers are parallel or antiparallel to each other (the A and B configurations, respectively). Although an infinite ferromagnetic medium exhibits gyrotropy in the Voigt geometry, the propagation of the elastic wave through the magnetic superlattice in this geometry reveals macroscopic acoustic gyrotropy only in the A configuration, whereas the B configuration does not exhibit acoustic

gyrotropy (in the long-wavelength limit). Therefore, for given values of the frequency ω and wavenumber $k_\perp$, the conditions for the transmission of a bulk SH wave through a thin-layer magnetic acoustic superlattice depend critically on its equilibrium magnetic configuration. In particular, in addition to the "half-wave" mechanism for transmission without reflection that is known to exist for nonmagnetic layers [8], there is another (resonance) mechanism for reflectionless transmission in a finite magnetic superlattice of the easy-axis–superconductor type with the *B* equilibrium configuration. In a finite magnetic superlattice with the *A* configuration, this resonance does not occur. It has been shown that, in a magnetic superlattice with the *A* configuration in acoustic contact with a nonmagnetic medium, the uniform elastic shear wave can propagate along the interface. This will be the case if the frequency and wavenumber of the wave satisfy the dispersion relation of a shear SAW propagating, in this geometry, along the mechanically free surface of a semi-infinite magnetic superlattice of this type. It has been shown for the first time that the bulk elastic SH wave can pass without reflection through a finite easy-axis ferromagnet–superconductor thin-layer superlattice with the *A* or *B* configuration in acoustic contact with a nonmagnetic coating of finite thickness. Physically, this effect is due to the fact that the incident bulk elastic wave causes resonance excitation of a shear SAW propagating along the interface between the finite magnetic superlattice and the nonmagnetic coating of finite thickness.

Due to gyrotropy, the effects indicated above are nonreciprocal under a change in sign of the wave vector projection of the elastic SH wave onto the superlattice surface in the case of the superlattice with the *A* magnetic configuration.

A study of the influence of nonuniform exchange interaction on the effects considered in this paper is currently underway.

ACKNOWLEDGMENTS

One of the authors (S.V.T.) is grateful to I.E. Dikshteĭn for supporting the idea behind this study and for helpful discussions.

REFERENCES

1. T. T. Wu, Z. G. Huang, and S. Lin, Phys. Rev. B **69** (9), 094301 (2004).
2. R. Sainidou, N. Stefanou, and A. Modinos, Phys. Rev. B **69** (6), 064301 (2004).
3. Yu. I. Bespyatykh, I. E. Dikshteĭn, V. P. Mal'tsev, S. A. Nikitov, and V. Vasilevskiĭ, Fiz. Tverd. Tela (St. Petersburg) **45** (11), 2056 (2003) [Phys. Solid State **45**, 2160 (2003)].
4. A. Figotin and I. Vitebsky, Phys. Rev. E **63**, 066609 (2001).
5. M. G. Cottam and D. R. Tilley, *Introduction to Surface and Superlattice Excitations* (Cambridge Univ. Press, Cambridge, 1989).
6. S. M. Rytov, Akust. Zh. **2** (1), 72 (1956) [Sov. Phys. Acoust. **2**, 68 (1956)].
7. Yu. V. Gulyaev, I. E. Dikshteĭn, and V. G. Shavrov, Usp. Fiz. Nauk **167** (7), 735 (1997) [Phys. Usp. **40**, 701 (1997)].
8. L. M. Brekhovskikh, *Waves in Layered Media*, 2nd ed. (Nauka, Moscow, 1973; Academic, New York, 1980).
9. *Surface Polaritons: Electromagnetic Waves at Surfaces and Interfaces*, Ed. by V. M. Agranovich and D. L. Mills (North-Holland, Amsterdam, 1982; Nauka, Moscow, 1985).

Translated by Yu. Epifanov

Physics of the Solid State, Vol. 47, No. 3, 2005, pp. 587–594. Translated from Fizika Tverdogo Tela, Vol. 47, No. 3, 2005, pp. 565–571.

LOW-DIMENSIONAL SYSTEMS AND SURFACE PHYSICS

Effect of the Correlation Properties of One- and Three-Dimensional Inhomogeneities on the High-Frequency Magnetic Susceptibility of Sinusoidal Superlattices

V. A. Ignatchenko and Yu. I. Mankov

Kirensky Institute of Physics, Siberian Division, Russian Academy of Sciences, Akademgorodok, Krasnoyarsk, 660036 Russia
e-mail: vignatch@iph.krasn.ru

Received June 30, 2004

Abstract—The effect of one- (1D) and three-dimensional (3D) inhomogeneities on the high-frequency magnetic susceptibility at the boundary of the first Brillouin zone of a ferromagnetic superlattice is studied. The study is performed with an earlier developed method of random spatial modulation (RSM) of the superlattice period. In this method, structural inhomogeneities are described in terms of the random-phase model, in which the phase depends on three coordinates in the general case. The frequency spacing $\Delta\nu_m$ between two peaks in the imaginary part of the averaged Green's function, which characterizes the gap width in the frequency spectrum at the boundary of the Brillouin zone, is calculated as a function of both the root-mean-square fluctuations γ_i and the correlation wavenumbers η_i of phase inhomogeneities (i = 1 and 3 for 1D and 3D inhomogeneities, respectively). The function $\Delta\nu_m(\gamma_1, \eta_1)$ for 1D inhomogeneities is shown to be symmetric with respect to interchanging the variables γ_1^2 and η_1, whereas the function $\Delta\nu_m(\gamma_3, \eta_3)$ for 3D inhomogeneities is strongly asymmetric with respect to interchanging γ_3^2 and η_3. This effect is associated with the difference in form between the correlation functions of 1D and 3D inhomogeneities and can be used to determine the dimensionality of inhomogeneities from the results of spectral studies of such superlattices. © *2005 Pleiades Publishing, Inc.*

1. INTRODUCTION

One-dimensional periodic structures (superlattices) have been extensively applied in various devices. Despite the progress made in the production of such structures, their characteristics are still far from ideal in many cases. This is caused by the fact that the properties of real superlattices depend on technological factors, such as random scatter of the layer thicknesses (one-dimensional structural inhomogeneities) and randomly strained interfaces between layers (two- and three-dimensional inhomogeneities). Therefore, it is challenging to theoretically study the effect of random structural inhomogeneities on the physical properties of superlattices and, in particular, on the characteristics of waves propagating in such materials. Apart from the applied aspects of such studies, it should be noted that partly randomized superlattices are convenient objects for the development of new methods in theoretical physics to investigate media without translational symmetry. At present, different-type models and methods are being used to develop a theory of randomized superlattices. In initially sinusoidal superlattices, one-dimensional randomization is taken into account by introducing a random phase [1, 2]. In superlattices with a rectangular profile of the coordinate dependence of a material parameter along the superlattice axis, randomization is modeled by a disturbance in the sequence of layers of two different materials [3–9] or by random deviations of the layer–layer interfaces from their initial arrangement [10–12]. There are also methods based on the superlattice correlation functions of a postulated shape [13, 14], applications of the geometrical-optics approach [15], and the development of a dynamic theory of elastic composite media [16].

In [17], we proposed another method for investigating the effect of superlattice inhomogeneities on the wave spectrum, which we called the method of random spatial modulation (RSM) of the superlattice period. Let us briefly review this method. The spectral properties of any inhomogeneous medium are known to be best described in terms of averaged Green's functions. The only characteristic that describes a random medium and enters into an expression for an averaged Green's function is the correlation function $K(\mathbf{r})$, which depends on the distance $\mathbf{r} = \mathbf{x} - \mathbf{x}'$ between two points in the medium. Therefore, the first part of the problem reduces to finding the function $K(\mathbf{r})$ for a superlattice that contains certain structural inhomogeneities. The second part of the problem consists in extracting spectral characteristics from the Green's function that contains this correlation function by using standard

approximate methods. To describe structural inhomogeneities in a sinusoidal superlattice, we used the model of a random phase, which was considered a random function of all three coordinates with an arbitrary correlation radius (the authors of [1, 2] considered only a one-dimensional δ-correlated random function). To find the correlation function $K(\mathbf{r})$ of the superlattice, we have developed a method which is a generalization of the well-known method of determining the time correlation function for a randomly frequency-(phase-)modulated radio signal [18, 19] to the case of spatial (in general, three-dimensional) modulation of the superlattice period (phase). This method is advantageous in that the shape of the correlation function of a superlattice is derived under general assumptions about the character of random spatial modulation of the superlattice period rather than being postulated. It has been shown that, in general, this function has a complex form, which depends on the inhomogeneity dimensionality, the structure of the interface between layers, etc. Knowledge of the correlation functions corresponding to different types and dimensionalities of inhomogeneities allowed us to use the averaged Green's functions to find the eigenfrequencies, damping, and other wave characteristics of superlattices [17, 20–28]. The RSM method allowed us to consider inhomogeneities of different dimensionalities in terms of a single model. The effect of one- (1D) and three-dimensional (3D) inhomogeneities on a wave spectrum has been studied for sinusoidal superlattices and superlattices with zero and arbitrary thicknesses of the interfaces between layers. We have also studied the effect of a mixture of 1D and 3D inhomogeneities [26, 27] and the effect of the anisotropy of a correlation function [28]. However, some important problems have not been solved. For example, the authors of [25–28] showed how the difference in form between correlation functions for 1D and 3D inhomogeneities manifests itself in the characteristics of the wave spectrum of a superlattice when the root-mean-square phase modulation varies in magnitude. In this work, we study the dependences of the wave-spectrum characteristics on both the root-mean-square phase fluctuations and the correlation radii of inhomogeneities and demonstrate radical differences in character between these dependences for 1D and 3D inhomogeneities. We use the true correlation functions obtained by us earlier in [17]. With these functions, we determined the range of applicability of the approximate analytical expressions for the correlation functions of 3D inhomogeneities that were used in [25–28] to simplify computations.

2. CALCULATION PROCEDURE

Let us recall, in brief, the main features of the RSM method, which was developed in [17] to find the correlation functions of a superlattice having 1D, 2D, or 3D inhomogeneities of its period. The coordinate dependence of the uniaxial magnetic anisotropy of a ferromagnetic superlattice was taken to be

$$\beta(\mathbf{x}) = \beta_0 + \Delta\beta\rho(\mathbf{x}), \quad (1)$$

where β_0 is the mean value of the anisotropy, $\Delta\beta$ is its root-mean-square deviation, and $\rho(\mathbf{x})$ is a centered ($\langle\rho\rangle = 0$) and normalized ($\langle\rho^2\rangle = 1$) function. The function $\rho(\mathbf{x})$ describes the periodic variation in the magnetic-anisotropy parameter along the z axis, as well as random spatial modulations of this parameter. Angle brackets mean averaging over an ensemble of random realizations. In [17], this function was taken in the form

$$\rho(\mathbf{x}) = \sqrt{2}\cos[q(z - u(\mathbf{x}) + \psi)], \quad (2)$$

where $q = 2\pi/l$ is the wavenumber of the superlattice and l is its period. Inhomogeneities are characterized by a random spatial phase modulation $u(\mathbf{x})$, which in general is a function of all three coordinates: $\mathbf{x} = \{x, y, z\}$. By introducing the function $\chi(\mathbf{x}, \mathbf{r}) = q[u(\mathbf{x} + \mathbf{r}) - u(\mathbf{x})]$ and averaging the product $\rho(\mathbf{x})\rho(\mathbf{x} + \mathbf{r})$ over χ with a Gaussian distribution and over the coordinate-independent phase ψ with a uniform distribution (see [17] for more details), we obtain the correlation function of the superlattice in the form

$$K_i(\mathbf{r}) = \cos qr_z \exp\left[-\frac{Q_i(\mathbf{r})}{2}\right], \quad (3)$$

where the structure function $Q_i(\mathbf{r})$ has the form

$$Q_1(r_z) = 2\gamma_1^2[\exp(-k_\parallel r_z) + k_\parallel r_z - 1], \quad (4)$$

$$Q_3(r) = 6\gamma_3^2\left[1 - \frac{2}{k_0 r} + \left(1 + \frac{2}{k_0 r}\right)\exp(-k_0 r)\right], \quad (5)$$

for 1D and 3D inhomogeneities, respectively. Here, $k_\parallel$ and k_0 are the correlation wavenumbers of 1D and 3D inhomogeneities, respectively ($r_\parallel = k_\parallel^{-1}$ and $r_0 = k_0^{-1}$ are the correlation radii of inhomogeneities), and

$$\gamma_1 = \sigma_1 q/k_\parallel, \quad \gamma_3 = \sigma_3 q/k_0, \quad (6)$$

where σ_1 and σ_3 are the root-mean-square fluctuations of the gradients of the functions $u_1(z)$ and $u_3(\mathbf{x})$.

We consider the situation where an external magnetic field $\mathbf{H}_0$, the static part of the magnetization $\mathbf{M}_0$, and the magnetic-anisotropy axis are directed along the superlattice axis (z axis). By linearizing the Landau–Lifshitz equation for the magnetization ($M_x, M_y \ll M_0$, $M_z \approx M_0$) and introducing circular projections for the resonance (positive) components of the magnetization and the external magnetic field, we obtain an equation for spin waves in the form [20]

$$\nabla^2 m - \left[\nu - \frac{\Lambda}{\sqrt{2}}\rho(\mathbf{x})\right]m = -\frac{h}{\alpha}. \quad (7)$$

Here, $m = M_x + iM_y$, $h = H_x + iH_y$, $\Lambda = \sqrt{2}\,\Delta\beta/\alpha$, and the frequency ν (measured in wave-vector units) is equal to

$$\nu = \frac{\omega - \omega_0}{\alpha g M_0}, \quad (8)$$

where ω_0 is the frequency of uniform ferromagnetic resonance, g is the gyromagnetic ratio, and α is the exchange constant.

The high-frequency spin-wave susceptibility $\chi(\nu, k)$ is proportional to the averaged Green's function $G(\nu, k)$ of Eq. (7):

$$\chi(\nu, k) = \langle m(\nu, k)\rangle/h_0 = a(k)G(\nu, k), \quad (9)$$

where h_0 is the high-frequency field amplitude. The proportionality coefficient $a(k)$ for the case of a spin-wave resonance in a thin magnetic film was analyzed in detail in [20]. The averaged Green's function for Eq. (7) has the form

$$G(\nu, k) = \frac{1}{\nu - k^2 + \frac{1}{2}\Lambda^2 M(\nu, k)}, \quad (10)$$

where $M(\nu, k)$ is the classical analog of the mass operator. It was shown in [23] that, using an approximation similar to the Bourret approximation [29], this quantity can be represented in general in the form

$$M_i(\nu, \mathbf{k}) = -\frac{1}{4\pi}\int \frac{K_i(\mathbf{r})}{|\mathbf{r}|}\exp[-i(\mathbf{kr} + \sqrt{\nu}|\mathbf{r}|)]d\mathbf{r}, \quad (11)$$

where the correlation function $K(\mathbf{r})$ for a sinusoidal superlattice is determined by Eq. (3).

For 1D and isotropic 3D inhomogeneities, integration over angles in Eq. (11) can be preformed exactly. As a result, the following expressions were obtained in [23]:

$$M_1 = -\frac{1}{2i\sqrt{\nu}}\int_0^\infty \exp\left[-\frac{1}{2}Q_1(r_z) - i\sqrt{\nu}r_z\right] \times [\cos(k-q)r_z + \cos(k+q)r_z]dr_z, \quad (12)$$

for 1D inhomogeneities and

$$M_3 = -\frac{1}{2}\int_0^\infty \exp\left[-\frac{1}{2}Q_3(r) - i\sqrt{\nu}r\right] \times \left[\frac{\sin(k-q)r}{k-q} + \frac{\sin(k+q)r}{k+q}\right]dr \quad (13)$$

for 3D inhomogeneities. (Note that in [23] there is a misprint in the expression corresponding to Eq. (12).) Further integration in these expressions with the true functions $Q_1(r_z)$ and $Q_3(r)$ specified by Eqs. (4) and (5) cannot be conducted analytically. Therefore, the dispersion, damping, and susceptibility were studied in our previous papers by using the following approximating correlation functions:

$$K_1(r_z) \approx \cos qr_z \begin{cases} \exp(-\gamma_1^2 k_\parallel r_z), & \gamma_1^2 \ll 1 \\ \exp(-\gamma_1^2 k_\parallel^2 r_z^2/2), & \gamma_1^2 \gg 1, \end{cases} \quad (14)$$

for 1D inhomogeneities and

$$K_3(r) = \cos qr_z[(1-L)\exp(-\gamma_3^2 k_0 r) + L], \quad (15)$$

for 3D inhomogeneities, where $L = \exp(-3\gamma_3^2)$ is the asymptotic expression of $K_3(r)$ at $r \longrightarrow \infty$. The approximate expressions (14) for $K_1(r_z)$ were grounded in [17], whereas the range of applicability of approximation (15) for $K_3(r)$ has not been determined. We will return to this problem later.

3. SPIN-WAVE SPECTRUM AND THE HIGH-FREQUENCY SUSCEPTIBILITY OF A SUPERLATTICE

The dispersion and damping of spin waves are specified by a transcendental equation for the complex frequency $\nu = \nu' + i\nu''$; this equation is obtained by equating the denominator of Green's function (10) to zero:

$$\nu - k^2 + \frac{1}{2}\Lambda^2 M(\nu, \mathbf{k}) = 0. \quad (16)$$

The high-frequency susceptibility of a ferromagnet is proportional to the complex Green's function $G(\nu, \mathbf{k}) = G'(\nu, \mathbf{k}) + iG''(\nu, \mathbf{k})$, which depends on the real frequency ν of the external high-frequency field and the real wave vector $\mathbf{k}$. The wave spectrum $\nu = \nu(k)$ in a superlattice is known to have a band structure. At the value $k = nq/2$ corresponding to the boundary of the nth Brillouin zone, a gap (forbidden band) forms in the frequency spectrum. For sinusoidal superlattices, the boundary of the first Brillouin zone is of special interest, since the widths of the subsequent band gaps decrease rapidly with increasing zone number [22]. In superlattices with sharper interfaces between layers, the decrease in the band-gap width with an increase in n is less pronounced (such situations were considered in [22, 24, 25]). Here, we restrict ourselves to the study of the magnetic susceptibility of a sinusoidal superlattice at the boundary of the first Brillouin zone: $k = k_r \equiv q/2$. In the case where there are no inhomogeneities and natural wave attenuation can be neglected, the gap width in the spectrum at $k = k_r$ is equal to Λ [this is the distance between the split-spectrum levels $\nu_+(k_r)$ and $\nu_-(k_r)$]. The $G''(\nu)$ dependence at $k = k_r$ exhibits two δ peaks spaced Λ apart. As the root-mean-square fluctuation γ of inhomogeneities increases, the spacing $\nu'_+ - \nu'_-$ between the spectrum levels decreases and the gap in the spectrum closes at a certain critical γ value. An increase in γ is accompanied by an increase in the damping $\nu''(k)$; this function of k reaches a maximum at

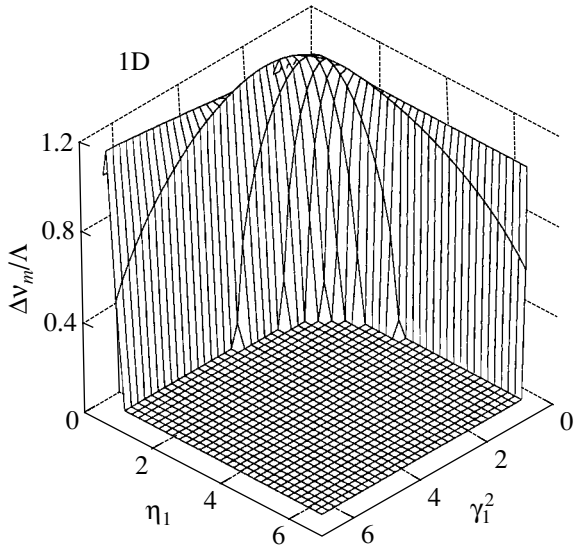

Fig. 1. Effect of γ_1^2 and η_1 on the spacing between peaks in the imaginary part $G_1''(\nu)$ of the Green's function at the boundary of the first Brillouin zone of a superlattice with 1D inhomogeneities.

$k = k_r$. As γ increases, the peaks in the $G''(\nu)$ dependence weaken and approach each other until merging at a certain value of γ. Qualitatively, the variation in the spacing between the peak maxima $\Delta\nu_m$ corresponds to the variation in the difference $\nu_+' - \nu_-'$ between the eigenfrequencies; however, there is no exact quantitative relation between these quantities at $\gamma \neq 0$ [20]. This qualitative description of the variation in the spectral gap width and in the spacing between the $G''(\nu)$ maxima with increasing root-mean-square fluctuations is valid for both 1D and 3D inhomogeneities. However, the quantitative differences between the effects of 1D and 3D inhomogeneities are very substantial. For example, in the presence of 1D inhomogeneities, the band gap is closed (or two $G''(\nu)$ maxima merge) at a critical value of γ_1, which is well below the corresponding critical value γ_3 for 3D inhomogeneities [23].

As noted above, approximate correlation functions (14) and (15) were used in [17, 20–28] to analyze the eigenfrequencies, damping, and magnetic susceptibility of a superlattice. These approximations make it possible to study the $\nu(k)$ spectrum; otherwise, transcendental equation (16) for $\nu(k)$ cannot be represented in an explicit form without integrating in Eqs. (12) and (13) for the mass operator. However, the susceptibility can be studied without making assumptions regarding $K(\mathbf{r})$, since numerical integration can be performed for each value of ν in Eqs. (12) and (13) to construct the $G(\nu)$ dependence. Therefore, to calculate the dependences of $G''(\nu)$ on γ_i and η_i, we use both approximate expressions and true expressions (4) and (5) for the structure functions of 1D and 3D inhomogeneities in Eqs. (12) and (13) for the mass operator, respectively.

3.1. 1D Inhomogeneities

With the approximate expression for $K_1(r_z)$ in Eq. (14) corresponding to the condition $\gamma_1^2 \ll 1$, the integral in Eq. (12) for M_1 can easily be calculated. At the boundary of the first Brillouin zone ($k = k_r$), we thus obtain a simple expression for the Green's function in the two-wave approximation under the condition Λ, $k_\parallel^2 \ll \nu$:

$$G_1(\nu) \approx \frac{1}{\Lambda}\frac{X - i\eta_1\gamma_1^2}{X(X - i\eta_1\gamma_1^2) - 1/4}, \qquad (17)$$

where $X = (\nu - k_r^2)/\Lambda$ is the dimensionless frequency detuning from the value $\nu = k_r^2$ and $\eta_1 = k_\parallel q/\Lambda$ is the dimensionless correlation wavenumber. By equating the denominator of this function to zero, we obtain a quadratic equation for the complex frequency ν, from which we find

$$\nu = k_r^2 + \frac{\Lambda}{2}[i\eta_1\gamma_1^2 \pm \sqrt{1 - \eta_1^2\gamma_1^4}]. \qquad (18)$$

As follows from this expression, the spectral gap $\Delta\nu = \nu_+' - \nu_-'$ is closed at $\eta_1\gamma_1^2 \geq 1$. From Eq. (17) with the real frequency ν, we find that the function $G_1''(\nu)$ has two peaks; the spacing $\Delta\nu_m$ between them decreases with increasing γ_1 and η_1, and at $\eta_1\gamma_1^2 \geq 1/\sqrt{2}$, these peaks merge to form one peak.

Figure 1 shows the dependence of $\Delta\nu_m$ on γ_1^2 and η_1 calculated by substituting exact structure function (4) into Eq. (12) for the mass operator and performing the integration numerically. As is seen from Fig. 1, the function $\Delta\nu_m$ is symmetric with respect to interchanging the variables γ_1^2 and η_1 and is a function of their product with a rather high accuracy. This symmetry is clearly visible for approximate analytical expressions (17) and (18) and is due to the fact that the effective correlation radius of a one-dimensional sinusoidal superlattice at $\gamma_1^2 \ll 1$ is equal to $(\gamma_1^2 k_\parallel)^{-1}$, i.e., is inversely proportional to the product $\gamma_1^2\eta_1$. This symmetry is not so obvious for the $\Delta\nu_m(\eta_1, \gamma_1^2)$ dependence calculated with the exact correlation function. At small values of the product $\gamma_1^2\eta_1$, the spacing $\Delta\nu_m$ between the peaks is slightly in excess of Λ, which agrees with the analogous effect obtained for the gap width in the wave spectrum in [17]. In that work, this effect was explained in terms of Gaussian correlations, which correspond to the lower line in Eq. (14).

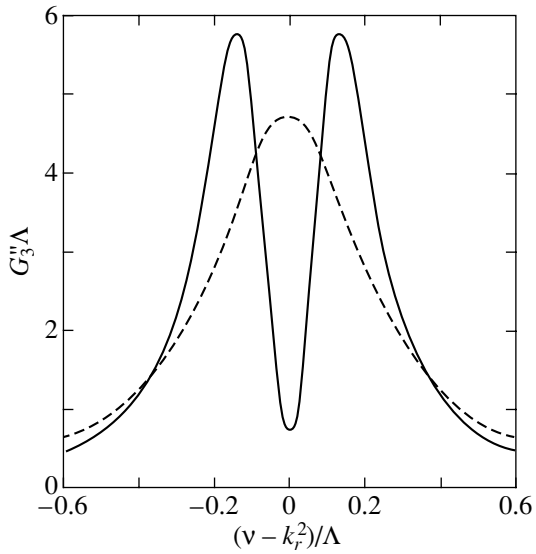

Fig. 2. Frequency dependence of the imaginary part $G_3''(\nu)$ of the Green's function at the boundary of the first Brillouin zone of a superlattice with 3D inhomogeneities for $\gamma_3^2 = 1$ and $\eta_3 = 4$ (solid line) and for $\gamma_3^2 = 4$ and $\eta_3 = 1$ (dashed line).

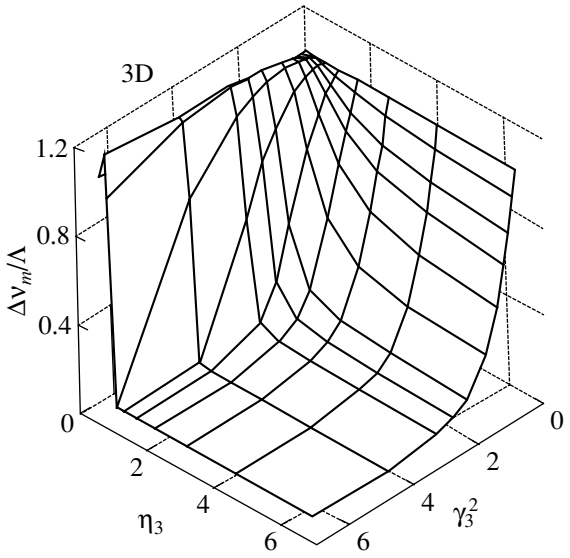

Fig. 3. Effect of γ_3^2 and η_3 on the spacing between peaks in the imaginary part $G_3''(\nu)$ of the Green's function at the boundary of the first Brillouin zone of a superlattice with 3D inhomogeneities.

3.2. 3D Inhomogeneities

With approximate expression (15) for the correlation function of 3D inhomogeneities, the integral in Eq. (13) for M_3 can be calculated exactly. At the boundary of the first Brillouin zone, the Green's function in the two-wave approximation and under the condition Λ, $k_0^2 \ll \nu$ takes the form

$$G_3 \approx \frac{1}{\Lambda}\frac{X(X - i\eta_3\gamma_3^2)}{X^2(X - i\eta_3\gamma_3^2) - 1/4(X - i\eta_3\gamma_3^2 L)}, \qquad (19)$$

where $\eta_3 = k_0 q/\Lambda$ is the dimensionless wavenumber of 3D inhomogeneities.

By equating the denominator of this function to zero, we obtain a cubic equation for the complex frequency; the dependence of the frequency on γ_3^2 was analyzed numerically in [25]. As follows from Eq. (19), the Green's function is not symmetric with respect to interchanging the parameters γ_3^2 and η_3 in the case of 3D inhomogeneities. Indeed, unlike function (17), which contains only the product $\gamma_1^2\eta_1$, function (19) contains not only the product $\gamma_3^2\eta_3$ but also the asymptotic value L of the correlation function, which depends on γ_3^2 alone.

Figure 2 shows the frequency dependence of the function G_3'' at the boundary of the first Brillouin zone of the superlattice ($k = k_r$) calculated numerically with exact structure function (5) in Eq. (13) for the mass operator. Both curves in Fig. 2 correspond to $\gamma_3^2\eta_3 = 4$. However, the solid line was plotted at $\gamma_3^2 = 1$ and $\eta_3 = 4$, whereas the dashed line was plotted at $\gamma_3^2 = 4$ and $\eta_3 = 1$. In the first case, the function $G_3''(\nu)$ is seen to have two pronounced peaks (i.e., there is a gap in the wave spectrum), whereas in the second case both peaks merge to form one broad peak (the gap in the spectrum is closed). Figure 3 shows the dependence of the spacing between the peaks $\Delta\nu_m$ on γ_3^2 and η_3 calculated using exact structure function (5). This dependence differs radically from the $\Delta\nu_m(\gamma_1^2, \eta_1)$ dependence for the 1D inhomogeneities shown in Fig. 1: the function $\Delta\nu_m$ for 3D inhomogeneities is asymmetric with respect to interchanging γ_3^2 and η_3. The difference between the spectral characteristics of superlattices with 1D and 3D inhomogeneities is due to the radically different correlation functions of 1D and 3D inhomogeneities. This difference can clearly be illustrated using approximate analytical expressions (14) and (15), whose asymptotic behavior coincides with that of the exact functions $K_1(r_z)$ and $K_3(r)$. For 1D inhomogeneities, the correla-

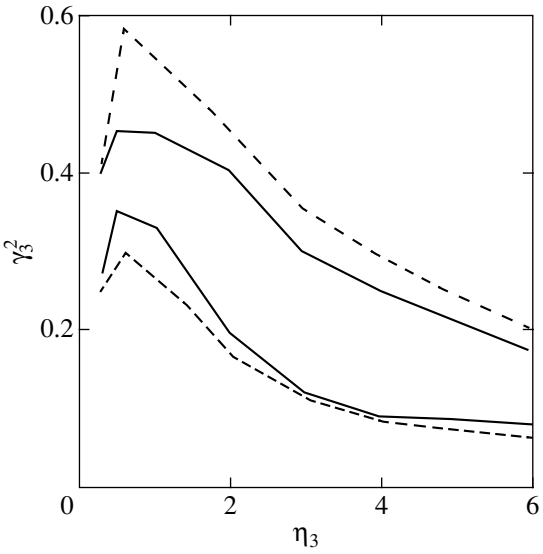

Fig. 4. Ranges of applicability of approximate expression (15) for the correlation function and approximate expression (19) for the Green's function. The differences between Eq. (19) and the Green's function as calculated using the exact correlation function do not exceed 10% in the region between the solid lines and 20% in the region between the dashed lines.

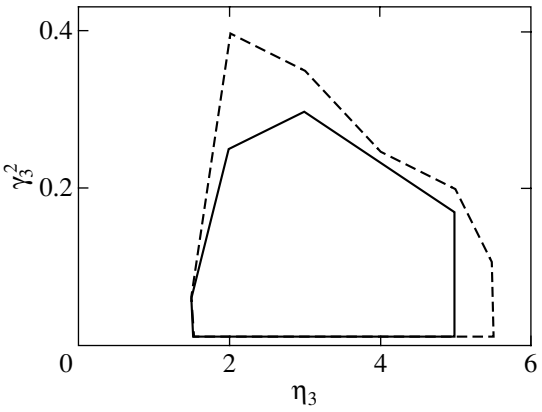

Fig. 5. Ranges of applicability of approximate expressions (20) for the correlation function and (21) for the Green's function. The differences between Eq. (21) and the Green's function as calculated using the exact correlation function do not exceed 10% in the region restricted by solid lines and 20% in the region restricted by dashed lines.

tion function tends to zero at $r_z \longrightarrow \infty$, whereas the descending portion of $K_3(r)$ at $r \longrightarrow \infty$, tends to a nonzero asymptotic value L, which depends on γ_3^2 and is independent of η_3.

In this work, the magnetic susceptibility of a partly randomized sinusoidal superlattice is calculated for the first time using the exact correlation functions $K_1(r_z)$ and $K_3(r)$. This allowed us to compare the exact results and the results calculated with approximate correlation functions (14) and (15) and determine the range of applicability of the latter functions. For 3D inhomogeneities, the range of applicability of approximate expression (15) for the correlation function and approximate expression (19) for the Green's function is shown in Fig. 4. To find this range, we compared both the spacing between the peaks in the imaginary part of the Green's function and the peak widths obtained using the approximate and exact correlation functions. Then, on the (γ_3^2, η_3) parametric plane, we determined the region where the difference between these characteristics did not exceed 10% (solid lines) or 20% (dashed lines). It should be noted that the peak width was found to be a critical characteristic in most cases. The spacing between the peaks is described by approximate expression (19) with a much higher accuracy than is the peak width. As is seen from Fig. 4, there is a rather broad region of parameters γ_3^2 and η_3 in which the approximate analytical expression for the Green's function (19) is valid. The fact that this expression gives bad results for small values of γ_3^2 came as a surprise.

For this reason, we calculated the Green's function for 3D inhomogeneities using another approximating correlation function,

$$K_3(r) = \cos qr_z\left[(1-L)\exp\left(-\frac{\gamma_3^2 k_0^2 r^2}{2}\right) + L\right]. \quad (20)$$

This function differs from Eq. (15) in that it falls off as a Gaussian rather than exponentially, as is the case in Eq. (15). With Eq. (20), the integral in Eq. (13) for M_3 can also be calculated exactly. In the two-wave approximation and under the conditions used above (Λ, $k_0^2 \ll \nu$), the Green's function at the boundary of the first Brillouin zone can be found to be

$$G_3 \approx \frac{1}{\Lambda}\left\{X - \frac{1-L}{2\sqrt{2}\eta_3\gamma_3}\left[D\left(\frac{X}{\sqrt{2}\eta_3\gamma_3}\right) - i\frac{\sqrt{\pi}}{2}\exp\left(-\frac{X^2}{2\eta_3^2\gamma_3^2}\right)\right] - \frac{L}{4X}\right\}^{-1}, \quad (21)$$

where $D(s) = e^{-s^2}\int_0^s e^{t^2}dt$ is Dawson's integral. The frequency dependence of the function $G_3''(\nu)$ as described by Eq. (21) is compared with $G_3''(\nu)$ calculated using the exact correlation function. The characteristics for comparison were the same as above, namely, the spacing between the peaks and the peak width. As a result, we obtained the range of applicability of Eq. (21) and approximate correlation function (20) of a superlattice (Fig. 5). It is seen that this region overlaps only partially with the region shown in Fig. 4. A comparison of these

regions shows that, e.g., at small values of η_3 and $\gamma_3^2 \approx 0.3$–0.5, the approximation of the correlation function by Eq. (15) is more exact as compared to Eq. (20). At small values of γ_3^2 and $\eta_3 \approx 2$–5, the situation is reversed and Eq. (20) is more exact. Thus, approximations (15) and (20) complement each other.

4. CONCLUSIONS

We have studied the effect of the correlation properties of 1D and 3D structural inhomogeneities of an initially sinusoidal ferromagnetic superlattice on its high-frequency magnetic susceptibility. To describe the stochastic properties of inhomogeneities, we used correlation functions derived earlier using the method of random spatial modulation of the superlattice period [17]. In this method, structural inhomogeneities in a superlattice are described in terms of the model of a random phase, which is assumed to depend on the z coordinate in the case of 1D inhomogeneities and on all three coordinates (x, y, z) for 3D inhomogeneities. The random phase is characterized by a monotonically decreasing correlation function with arbitrary values of the relative root-mean-square fluctuations γ_i and normalized correlation wavenumbers η_i, where $i = 1$ and 3 for 1D and 3D inhomogeneities, respectively. As shown earlier in [17], the form of the correlation functions $K_i(r)$ of the superlattice obtained using this model and the RSM method depends only weakly on the form of the correlation functions characterizing the stochastic properties of the random phase. However, this form depends strongly on the dimensionality of inhomogeneities: for 1D inhomogeneities, we have $K_1(r_z) \longrightarrow 0$ as $r_z \longrightarrow \infty$, whereas for 3D inhomogeneities $K_3(r)$ tends to a nonzero asymptotic value $L = \exp(-3\gamma_3^2)$ as $r \longrightarrow \infty$.

These correlation functions have been used to calculate the averaged Green's function $G_i(\nu, k)$ from which the high-frequency susceptibility is determined in the case of 1D and 3D inhomogeneities. The mass operator of the Green's function was found in the Bourret approximation by performing numerical integration of expressions containing the exact correlation functions $K_1(r_z)$ and $K_3(r)$ for the 1D and 3D cases, respectively. The frequency dependence of the imaginary part $G''(\nu)$ of the Green's function was studied at a fixed value of the wave vector k corresponding to the boundary of the first Brillouin zone of the superlattice (experimentally, the wavenumber can be fixed due to the size effect in the situation corresponding to a spin-wave resonance in a superlattice film [20]). In this case, the $G_i''(\nu)$ dependence exhibits two peaks and the spacing between the peaks $\Delta\nu_m$ approximately corresponds to the gap width in the wave spectrum at the boundary of the Brillouin zone. The dependence of $\Delta\nu_m$ on γ_i was studied earlier in [20, 23] using approximate expressions for $K_1(r_z)$ and $K_3(r)$. In this work, we have studied the dependences of $\Delta\nu_m$ on both γ_i and η_i using exact expressions for $K_1(r_z)$ and $K_3(r)$. For 1D inhomogeneities, the two-dimensional function $\Delta\nu_m(\gamma_1, \eta_1)$ was shown to be symmetric with respect to interchanging the variables γ_1^2 and η_1 (Fig. 1), whereas in the case of 3D inhomogeneities the function $\Delta\nu_m(\gamma_3, \eta_3)$ is strongly asymmetric with respect to interchanging γ_3^2 and η_3 (Fig. 3). This effect is associated with the difference in form between the correlation functions for 1D and 3D inhomogeneities. For the correlation function $K_1(r_z)$, the correlation radius is inversely proportional to the product $\gamma_1^2\eta_1$, which causes the function $\Delta\nu_m$ to be symmetric with respect to interchanging γ_1^2 and η_1. The correlation radius of the function $K_3(r)$ is inversely proportional to the analogous product $\gamma_3^2\eta_3$. However, the function $K_3(r)$ differs from $K_1(r_z)$ in terms of the asymptotic value L, which divides the entire correlation volume into two parts, one of which is characterized by a finite correlation radius (above the asymptotic value L) and the other by an infinite correlation radius (below L). This asymptotic value depends on γ_3^2 and is independent of η_3, which leads to asymmetry of the function $\Delta\nu_m(\gamma_3, \eta_3)$ with respect to interchanging γ_3^2 and η_3. This effect can be used to determine the dimensionality of structural inhomogeneities in a superlattice by spectral methods if independent changes in the values of γ_i^2 and η_i can be controlled technologically.

We have also compared the functions $\Delta\nu_m(\gamma_3, \eta_3)$ as calculated using either the exact correlation function $K_3(r)$ or approximate analytical expressions for this function. This comparison allowed us to construct diagrams in the (γ_3^2, η_3) plane (Figs. 4, 5) that determine the range of applicability of the approximate analytical expressions for $K_3(r)$, namely, Eq. (15), which was used earlier in [25–28], and Eq. (20), which was derived in this work. These diagrams also specify the range of applicability of approximate analytical expressions (19) and (21) for the Green's function.

ACKNOWLEDGMENTS

This work was supported by the Russian Foundation for Basic Research (project no. 04-02-16174) and the Krasnoyarsk Regional Science Foundation (grant no. 12F0013C).

REFERENCES

1. J. B. Shellan, P. Agmon, and P. Yariv, J. Opt. Soc. Am. **68** (1), 18 (1978).

2. Yu. Ya. Platonov, N. I. Polushkin, N. N. Salashchenko, and A. A. Fraerman, Zh. Tekh. Fiz. **57** (11), 2192 (1987) [Sov. Phys. Tech. Phys. **32**, 1324 (1987)].
3. J. M. Luck, Phys. Rev. B **39** (9), 5834 (1989).
4. S. Tamura and F. Nori, Phys. Rev. B **41** (11), 7941 (1990).
5. N. Nishiguchi, S. Tamura, and F. Nori, Phys. Rev. B **48** (4), 2515 (1993).
6. G. Pang and F. Pu, Phys. Rev. B **38** (17), 12649 (1988).
7. J. Yang and G. Pang, J. Magn. Magn. Mater. **87** (1–2), 157 (1990).
8. D. H. A. L. Anselmo, M. G. Cottam, and E. L. Albuquerque, J. Appl. Phys. **87** (8), 5774 (1999).
9. L. I. Deych, D. Zaslavsky, and A. A. Lisyansky, Phys. Rev. E **56** (4), 4780 (1997).
10. B. A. Van Tiggelen and A. Tip, J. Phys. I **1** (8), 1145 (1991).
11. A. R. McGurn, K. T. Christensen, F. M. Mueller, and A. A. Maradudin, Phys. Rev. B **47** (20), 13120 (1993).
12. M. M. Sigalas, C. M. Soukoulis, C.-T. Chan, and D. Turner, Phys. Rev. B **53** (13), 8340 (1996).
13. V. A. Ignatchenko, R. S. Iskhakov, and Yu. I. Mankov, J. Magn. Magn. Mater. **140–144**, 1947 (1995).
14. A. G. Fokin and T. D. Shermergor, Zh. Éksp. Teor. Fiz. **107** (1), 111 (1995) [JETP **80**, 58 (1995)].
15. A. V. Belinskiĭ, Usp. Fiz. Nauk **165** (6), 691 (1995) [Phys. Usp. **38**, 653 (1995)].
16. B. Kaelin and L. R. Johnson, J. Appl. Phys. **84** (10), 5451 (1998); J. Appl. Phys. **84** (10), 5458 (1998).
17. V. A. Ignatchenko and Yu. I. Mankov, Phys. Rev. B **56** (1), 194 (1997).
18. A. N. Malakhov, Zh. Éksp. Teor. Fiz. **30** (5), 884 (1956) [Sov. Phys. JETP **3**, 701 (1956)].
19. S. M. Rytov, *Introduction to Statistical Radiophysics*, 2nd ed. (Nauka, Moscow, 1976), Part 1 [in Russian].
20. V. A. Ignatchenko, Yu. I. Mankov, and A. V. Pozdnyakov, Zh. Éksp. Teor. Fiz. **116** (4), 1335 (1999) [JETP **89**, 717 (1999)].
21. V. A. Ignatchenko, Yu. I. Mankov, and A. A. Maradudin, Phys. Rev. B **59** (1), 42 (1999).
22. V. A. Ignatchenko, Yu. I. Mankov, and A. A. Maradudin, J. Phys.: Condens. Matter **11** (13), 2773 (1999).
23. V. A. Ignatchenko, A. A. Maradudin, and A. V. Pozdnaykov, Phys. Met. Metallogr. **91** (Suppl. 1), 69 (2001).
24. V. A. Ignatchenko, Yu. I. Mankov, and A. A. Maradudin, Phys. Rev. B **62** (3), 2181 (2000).
25. V. A. Ignatchenko, Yu. I. Mankov, and A. A. Maradudin, Phys. Rev. B **65** (2), 024207 (2002).
26. V. A. Ignatchenko, Yu. I. Mankov, and A. A. Maradudin, Pis'ma Zh. Éksp. Teor. Fiz. **77** (6), 335 (2003) [JETP Lett. **77**, 285 (2003)].
27. V. A. Ignatchenko, Yu. I. Mankov, and A. A. Maradudin, Phys. Rev. B **68** (2), 024209 (2003).
28. V. A. Ignatchenko, A. A. Maradudin, and A. V. Pozdnaykov, Pis'ma Zh. Éksp. Teor. Fiz. **78** (9), 1082 (2003) [JETP Lett. **78**, 592 (2003)].
29. R. C. Bourret, Nuovo Cimento **26** (1), 1 (1962); Can. J. Phys. **40** (6), 782 (1962).

Translated by K. Shakhlevich

Physics of the Solid State, Vol. 47, No. 3, 2005, pp. 595–598. Translated from Fizika Tverdogo Tela, Vol. 47, No. 3, 2005, pp. 572–574.

LOW-DIMENSIONAL SYSTEMS AND SURFACE PHYSICS

Dependence of the Condensation Coefficient of Bismuth on the Energy of Particles Deposited from an Ion Beam on Silicon Substrates

V. E. Pukha, I. F. Mikhaĭlov, A. N. Drozdov, and L. P. Fomina

National Technical University, Kharkov Polytechnical Institute, Kharkov, 61002 Ukraine

e-mail: puch@kpi.kharkov.ua

Received April 1, 2004; in final form, July 1, 2004

Abstract—The dependence of the condensation coefficient of bismuth ions on the energy of particles deposited from an ion beam on silicon substrates is investigated experimentally. It is found that, as an accelerating voltage is applied to the substrate, the condensation coefficient of bismuth ions drastically increases at voltages ranging from 0 to 10 V and monotonically decreases at voltages higher than 60 V. The critical temperature of condensation of bismuth particles deposited from the ion beam is 100 K higher than that from the vapor phase. © *2005 Pleiades Publishing, Inc.*

1. INTRODUCTION

The considerable interest expressed by researchers in the behavior of bismuth particles on a solid surface is explained by the possibility of using this metal as a surfactant for the growth of heteroepitaxial films on semiconductor crystals (Si, Ge, etc.) [1]. At present, cleaning of silicon substrates from contaminants and natural amorphous oxide films has been performed using a complex technology of heating under ultrahigh vacuum [2].

Ion sputtering is an efficient method for cleaning surfaces of materials. The use of this method at low ion energies does not lead to radiation damage of the substrate [3] but can provide sputtering of an oxide film and the formation of active nucleation centers for the growth of epitaxial layers on the surface. The occurrence of these processes on the surface can be judged from an increase in both the condensation coefficient of the deposited material and the critical deposition temperature.

In this connection, the purpose of the present work was to determine experimentally the dependence of the condensation coefficient of bismuth ions on the ion energy and the substrate temperature.

2. EXPERIMENTAL TECHNIQUE

Low-energy bismuth ions were deposited under vacuum at a residual pressure of approximately 5×10^{-4} Pa on heated Si(001) substrates coated with a natural amorphous oxide film. The operating vacuum was maintained by an Orbitron getter-ion pump.

Bismuth ions were produced by a vacuum arc discharge plasma separated from neutral components (atoms, molecules, microparticles) with the use of a curved plasmaguide to preclude spatial separation of singly and doubly charged ions (Fig. 1). The flux density of bismuth ions was characterized by an ionic current through the substrate. The ionic current density was equal to 0.2 mA cm^{-2}. This value corresponded to a particle flux density of 1.25×10^{15} cm^{-2} s^{-1}. The ion energy was measured with a multigrid probe according to the technique described by Ionov [4] and was then used to construct the energy distribution of bismuth ions $N(E)$ (Fig. 2). The mean energy of bismuth ions in the ion beam with respect to the cathode was determined to be $E_0 = 18$ eV, and the half-width of the energy distribution was approximately equal to 12 eV. In order to increase the energy of deposited particles, an accelerating voltage U was applied to the substrate and varied in the range from 0 to 100 V. This was accompanied by a shift in the ion energy distribution $N(E)$; as a result, the energy of each ion arriving at the substrate increased by a value U and reached $E = E + U$ (eV). The condensation coefficient of bismuth ions k was determined from the ratio between the effective thickness h of the film deposited under specific conditions and the thickness h_R of the film deposited on a cold substrate (T = 25°C) in the absence of an electric potential at a constant ionic current and at a constant time of arc combustion (τ = 5 min). The arc-discharge sputtering was carried out in parallel with the deposition of bismuth ions evaporated from an effusive cell. The equality of the ion flow to the vapor flow was checked against the thickness of the films deposited on cold substrates. The effective thickness was determined from the intensity of the Bi $L\alpha$ analytic line in the x-ray fluorescence spectrum measured on a Sprut-2 spectrometer.

1063-7834/05/4703-0595$26.00

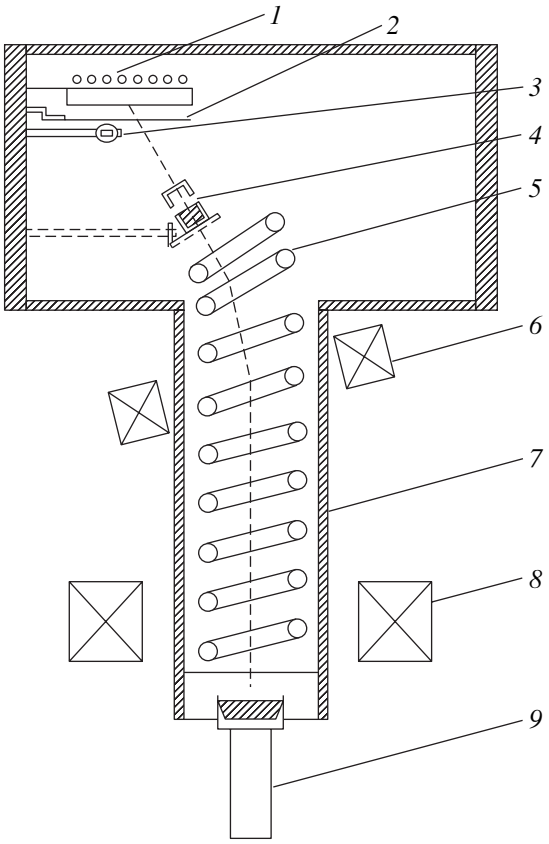

Fig. 1. Schematic diagram of the experimental setup: (*1*) substrate holder, (*2*) shutter, (*3*) quartz sensor for measuring the thickness of a coating, (*4*) effusion cell, (*5*) plasmaguide, (*6*) magnetic system for ion-beam rotation, (*7*) vacuum chamber, (*8*) magnetic system for ion-beam focusing, and (*9*) cathode unit.

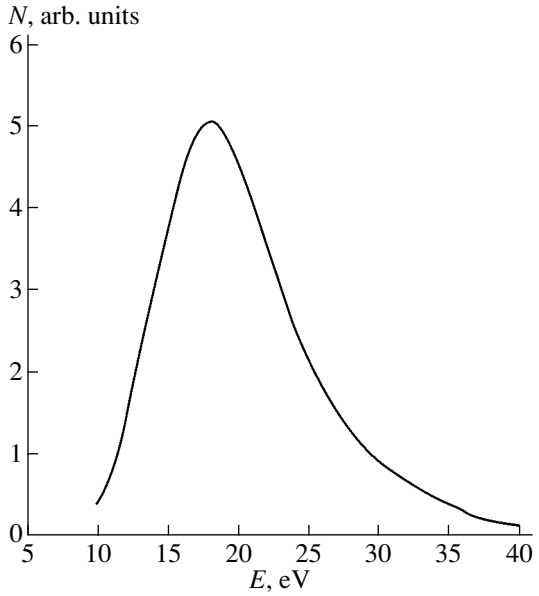

Fig. 2. Energy distribution $N(E)$ of bismuth ions produced by the vacuum arc discharge plasma.

3. RESULTS AND DISCUSSION

The dependence of the condensation coefficient of bismuth ions on the accelerating voltage can be divided into the following three portions (Fig. 3): (i) the first portion (from 0 to 10 V) corresponds to an abrupt increase in the condensation coefficient of bismuth ions, (ii) the second portion (from 10 to 60 V) is characterized by a constant value of the condensation coefficient, and (iii) the third portion (from 60 to 100 V) corresponds to a monotonic decrease in the condensation coefficient.

The observed jump in the condensation coefficient of bismuth ions in the first portion of the experimental curve indicates that some process occurs on the substrate surface with a threshold energy below which no condensation takes place. This means that only bismuth ions with an energy higher than the critical value E_{cr} ($E > E_{cr}$) can be retained on the substrate. The number $K(E_k, U)$ of these ions is determined by an integral of the energy distribution function $N(E)$, for which the threshold energy of condensation serves as the lower limit of integration.

If the energy distribution of bismuth ions $N(E)$ is known, the critical energy of nucleation can be determined from the experimental dependence of the condensation coefficient on the ion energy. In actual fact, when an accelerating voltage is applied to the substrate, the energy distribution of bismuth ions is displaced by a value U with respect to the threshold energy. With a set of values U, we can obtain a system of integral equations for numerically calculating the critical energy E_{cr}:

$$K(E_{cr}, U) = \int_{E_{cr}}^{\infty} N(E + U)dE. \quad (1)$$

Figure 3 presents the results of numerically solving the above system of integral equations for different critical energies E_{cr}. It can be seen from Fig. 3 that the experimental dependence of the condensation coefficient of bismuth ions on the accelerating voltage is approximated well by a theoretical curve obtained for the threshold energy $E_{cr} = 24$ eV.

According to Mesyats and Barengol'ts [5], doubly charged ions account for ≈17% of the total number of charged bismuth particles. Therefore, the energy distribution function obtained in our case is the sum of the energy distribution functions for singly and doubly charged ions. Since these distributions are independent of charge multiplicity [5], their shape can be described by the same energy distribution function $N(E)$. In this case, the system of integral equations (1) takes the following form:

$$K(E_{cr}, U) = \int_{E_{cr}}^{\infty} N(E + U)dE + \int_{E_{cr}}^{\infty} N(E + 2U)dE. \quad (2)$$

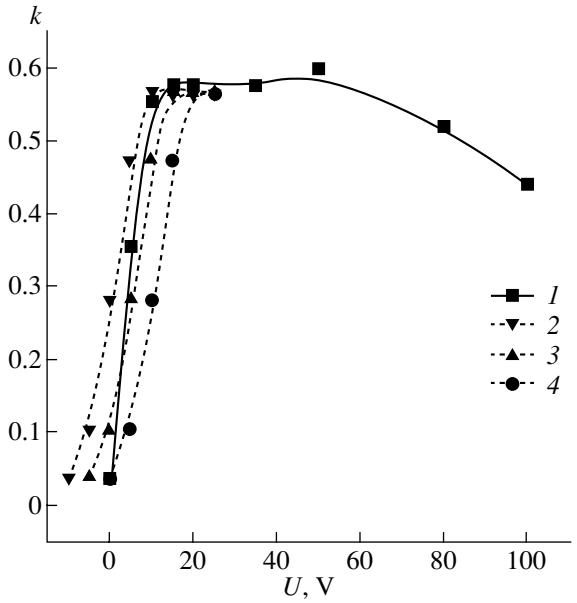

Fig. 3. Dependences of the condensation coefficient of bismuth ions $k = h/h_R$ on the accelerating voltage U according to (*1*) the experimental data and (*2–4*) the results of numerical integration of expression (1) for threshold energies E_{cr} = (*2*) 20, (*3*) 25, and (*4*) 30 eV.

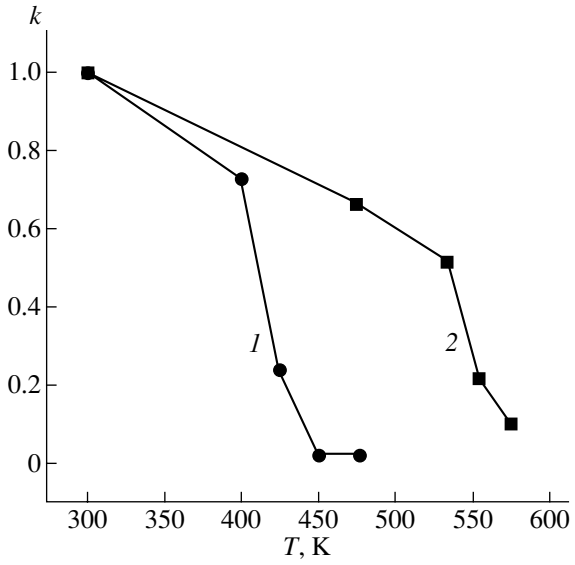

Fig. 4. Dependences of the condensation coefficient of bismuth ions on the substrate temperature upon deposition from (*1*) the vapor phase and (*2*) the ion beam (U = 10 V).

The numerical solution of the system of integral equations (2) gives the best fit to the experimental curve at the critical energy E_{cr} = 25 eV, which corresponds to the threshold energy of the process.

This threshold energy can be associated with the activation of the surface due to the destruction of the amorphous oxide film and the formation of nucleation centers. According to Samsonov [6] and Goronovskiĭ *et al.* [7], the dissociation energy for amorphous silicon oxide SiO_2 is estimated as U_0 = 8 eV per molecule. As follows from the estimates made in accordance with Isaev [8], the dissociation energy for this oxide at a temperature of 270°C decreases and amounts to 7.6 eV per molecule. The threshold energy of sputtering can be estimated from the formula $E \approx 4U_0$ [9]. For SiO_2, this energy is equal to 30 eV, which entirely corresponds to the critical energy E_{cr} obtained in our case. With a further increase in the ion energy, the condensation coefficient of bismuth ions remains almost unchanged and does exceed 0.6 at the substrate temperature T_s = 270°C. The observed decrease in the condensation coefficient of bismuth ions in the third portion of the curve can be associated with the processes of reflection and self-sputtering of bismuth atoms from the substrate at high energies of the deposited ions. The temperature dependences of the condensation coefficients for bismuth films deposited from the ionic beam and the vapor phase are compared in Fig. 4. As can be seen from this figure, the critical temperature of condensation of bismuth ions with a mean energy of 30 eV is approximately 100°C higher than that upon deposition from the vapor phase and reaches 300°C. This increase in the critical temperature can be caused by a change in the dominant mechanism of nucleation due to the penetration of bismuth ions into the surface layer of the substrate and the formation of active nucleation centers.

4. CONCLUSIONS

(1) It is found that an increase in the ion energy is accompanied by a jump in the condensation coefficient of bismuth ions. This jump can be associated with the destruction of the natural amorphous oxide film on the silicon surface. The threshold energy of the onset of condensation is determined to be E_{cr} = 25 eV.

(2) A monotonic decrease in the condensation coefficient of bismuth ions is observed at accelerating voltages higher than U = 60 V. This decrease is caused by the processes of reflection and self-sputtering of bismuth ions from the growth surface.

(3) Upon condensation of bismuth ions with an energy higher than 30 eV, the critical condensation temperature increases to 300°C due to a change in the nucleation mechanism.

This behavior of the condensation coefficient of bismuth ions indicates that the surface undergoes an activation due to cleaning from contaminants and the destruction of the amorphous oxide film. The results of this work can be used to prepare bismuth nanolayers and to produce nucleation centers for the growth of epitaxial layers.

ACKNOWLEDGMENTS

This work was supported by the Government of Ukraine within the research program "Fullerene Compositions Formed from Fluxes of Particles of High-Energy Components," project no. M5462.

REFERENCES

1. K. Sakamoto, K. Kyoya, K. Miki, H. Matsuhata, and T. Sakamoto, Jpn. J. Appl. Phys., Part 2 **32** (2A), L204 (1993).
2. S. Yu. Bulavenko, Candidate's Dissertation (KNU, Kiev, 2002).
3. M. D. Gabovich, N. V. Pleshivtsev, and N. N. Semashko, *Beams of Ions and Atoms for Controlled Thermonuclear Fusion and Technological Applications* (Énergoatomizdat, Moscow, 1986), p. 117 [in Russian].
4. N. I. Ionov, Zh. Tekh. Fiz. **34**, 769 (1964) [Sov. Phys. Tech. Phys. **9**, 591 (1964)].
5. G. A. Mesyats and S. A. Barengol'ts, Usp. Fiz. Nauk **172** (10), 1113 (2002) [Phys. Usp. **45**, 1001 (2002)].
6. G. V. Samsonov, *Physicochemical Properties of Oxides* (Metallurgiya, Moscow, 1978) [in Russian].
7. I. T. Goronovskiĭ, Yu. P. Nazarenko, and E. F. Nekryach, *A Brief Handbook on Chemistry* (Naukova Dumka, Kiev, 1965) [in Russian].
8. S. I. Isaev, *The Course of Chemical Thermodynamics* (Mashinostroenie, Moscow, 1975) [in Russian].
9. *Sputtering by Particle Bombardment*, Ed. by R. Behrisch (Springer, Berlin, 1981; Mir, Moscow, 1984).

Translated by I. Volkov